University of Southampton

Faculty of Natural and Environmental Sciences

School of Ocean and Earth Sciences

Origins and implications of Si-Fe cap rocks from extinct seafloor massive sulphide deposits from the TAG Hydrothermal Field, 26˚N, Mid-Atlantic Ridge

By

Iain James Stobbs, MSci ARSM

Thesis for the degree of Doctor of Philosophy

March 2020

University of Southampton

Faculty of Natural and Environmental Sciences

School of Ocean and Earth Sciences

Thesis for the degree of Doctor of Philosophy

Origins and implications of Si-Fe cap at extinct seafloor massive sulphide deposits from the TAG Hydrothermal Field, 26˚N, Mid-Atlantic Ridge

Iain J. Stobbs, MSci ARSM

Abstract

The deep ocean is considered the largest unexplored environment left on the earth. Since the discovery of active hydrothermal venting on the seafloor over 40 years ago, deep ocean research has furthered our understanding on the role that hydrothermal systems have in transferring heat and elements from the earth's interior, and the unique chemosynthetic biota that inhabit vents provide a potential analogue for the origins of life on earth. With a global shift towards the development of green technologies, and the general decreasing grades of on-land mineral deposits, mineral reserves in the deep ocean could prove to be of economic interest in the future. Seafloor massive sulphide (SMS) deposits form at hydrothermal vent sites at a wide range of ocean spreading centres, however due to their high venting temperatures and unique life, are not considered viable for mineral exploitation. However, extinct seafloor massive sulphide (eSMS) deposits are an understudied aspect of modern seafloor hydrothermal activity, and are thought to be a potential resource for base and precious metals. The transition from active to inactive sulphide deposits poses important, but as yet, unanswered questions about their preservation as hydrothermal venting ceases. Upon cessation of hydrothermal activity, oxygenated ocean water has the potential to destroy the metal tenor and grade in SMS deposits, unless they are somehow protected. Surface study of inactive mounds from the TAG Hydrothermal Field has been undertaken, and reveals that with one hydrothermal field, multiple eSMS deposits present a range of surface weathering features, indicating that if deposits remain on the seafloor they begin to oxidise. However, upon

drilling three eSMS deposits, Si-Fe caps, in the order of 3-5 m thick, were discovered at each deposit, directly overlying the massive sulphide ore bodies.

This project brings together historical data based on comparable Si-Fe material from volcanogenic massive sulphide deposits (the geological equivalent of SMS deposits), and uses a range of petrological and geochemical techniques to assess their origins, to identify the range of processes which have combined to form these cap rocks, and to determine what effect these caps may have on the preservation of eSMS deposits.

Petrological assessment of the Si-Fe cap rocks and the overlying sediments has identified a range of comparable textures and mineralogy to determine that the cap is a product of silicification of hydrothermal sediments. Preserved textures imply that the sediments have formed by a combination of seafloor weathering processes including mass-wasting, and likely involve microbial mediation and abiological precipitation of iron oxides. Late-stage, low temperature, reduced, diffuse hydrothermal fluids are interpreted to have silicified these sediments, thus forming the Si-Fe cap. Three dimensional connected porosity and permeability simulations undertaken on Si-Fe cap rock samples show that they are impermeable to vertical fluid movement (i.e. seawater ingress or hydrothermal upflow) in their current form. Two of the eSMS deposits show evidence of hydrothermal resurgence which has resulted in deep bleaching and sulphide precipitation within the base of the Si-Fe cap, and provides evidence that the formation of the Si-Fe cap has imparted a significant control on the hydrological regime of the eSMS deposit.

Ultimately, the processes that are interpreted to have formed these Si-Fe cap rocks are generic and are likely to occur at other seafloor hydrothermal deposits. Combined with the fact that the Si-Fe cap is impermeable to fluid flow, their presence is identified as a potential auto-preservation mechanism to protect eSMS deposits from losing their metal tenor and grade as they move off-axis. Therefore, occurrence of these Si-Fe features in eSMS deposits could have significant implications for the potential for exploitation of eSMS deposits, and the future of deep-sea mining.

Table of Contents

Table of Tables

Table of Tables

Table of Tables

Table of Tables

Appendix Tables

Table of Figures

Table of Figures

Table of Figures

Table of Figures

Table of Figures

Research Thesis: Declaration of Authorship

Print name:	Iain James Stobbs
Title of thesis:	Origins and implications of Si-Fe cap rocks at extinct seafloor massive sulphide deposits from the TAG Hydrothermal Field, 26˚N, Mid-Atlantic Ridge

I declare that this thesis and the work presented in it are my own and has been generated by me as the result of my own original research.

I confirm that:

1. This work was done wholly or mainly while in candidature for a research degree at this University;
2. Where any part of this thesis has previously been submitted for a degree or any other qualification at this University or any other institution, this has been clearly stated;
3. Where I have consulted the published work of others, this is always clearly attributed;
4. Where I have quoted from the work of others, the source is always given. With the exception of such quotations, this thesis is entirely my own work;
5. I have acknowledged all main sources of help;
6. Where the thesis is based on work done by myself jointly with others, I have made clear exactly what was done by others and what I have contributed myself;
7. Parts of this work have been published as:

Murton, B.J., Lehrmann, B., Dutrieux, A.M., Martins, S., Gil de Iglesia, A., Stobbs, I.J., Barriga, F.J.A.S., Bialas, J., Dannowski, A., Vardy, M.E., North, L.J., Yeo, I.A.L.M., Lusty, P.A.J., Petersen, S. (2019) Geological fate of seafloor massive sulphides at the TAG hydrothermal field (Mid-Atlantic Ridge), Ore Geology Reviews, 107, pp 905-923.

Murton, B.J. and Scientific Part (2018) Cruise Report: Expedition JC 138: 29th June – 8th August 2016, Mid-Atlantic Ridge, 26˚N 8.38'N, 44˚ 49.92'W, Southampton, p 285.

The Ore Geology Reviews paper is a summary of the Cruise Report data, and the seafloor mapping and surface description presented in Chapter 3 of this thesis is the main contribution to both works.

Signature: Date: 18/03/2020

Acknowledgements

I've been both dreading and longing for this moment. Time to write the acknowledgements. Throughout the PhD I've thought about what I would write in this section, who to thank, whether to try to be witty, and during the odd dark day that most PhD students get, whether it would even happen. Well, looks like it has, so here goes!

First, I would like to thank my supervisor Dr Bramley Murton. Without Bram I wouldn't have been able to undertake this project, and without his support I would not have been able to experience half of the things I've done over these last 4.5 years. For that alone, I will be forever grateful. I may not be the most academic of students, but I think we have had fun throughout, and who can say no to another 4 years student discount, eh?

I'd also like to thank my other supervisors, Professor Steve Roberts, Dr Chris Pearce, and Dr Doug Connelly. I certainly haven't made the most of having any of you attached to the project, but you've always been available to help when asked.

Next on the list are my fellow deep-sea mineral resource partners in crime. Dr Adeline Dutrieux, Sarah Howarth (soon to be Dr), Dr Isobel Yeo, Dr Berit Lehrmann. Adeline, sharing an office with you for 4 years and being able to chat about our interlinked projects at pretty much any time got me through quite a lot of this PhD. Add in the two cruises, a wide range of conferences on a couple of continents, the support you've given me throughout, the least I can say is thank you. Sarah and Izzy, relatively sure I wouldn't have had as much fun without you guys being here, oh yeah, and the science, yeah. Berit, thank you for your help with microscope work, particularly the sulphides, my favourite part of the jasper. Although not part of the deep sea research crew, I'd also like to thank Dr Catriona Menzies, for giving me some company in the stark north of East Kilbride, offering me a place to stay in Aberdeen during labwork, and generally being welcoming and very helpful with any science questions, despite how simple and silly they were.

I'd also like to thank a wide range of people for help with the wide range of work attempted as part of this thesis. John Ford, Dan Doran and Matt Beverly-Smith, again, I am so sorry about the project being about jasper, but without your thin section making abilities and entertainment, it would've been a bumpier ride. Dr Matt Cooper, Dr Richard Pearce, Professor Ian Croudace, and Dr Katsia Pabortsava, thank you for all your help with the range of analytical techniques I was able to use at NOC. I'd also like to thank a whole host of people for their scientific help and friendship throughout both Blue Mining Cruises M127 and JC138, Sven, John, Florian, Sophia, Fernando, Meike, Sebastian (x2), Nico, Alba, Paul, Laurence, Kate, Romina, Eric, Ian, Gavin.

Acknowledgements

One of the things that kind of amazed me about doing a PhD at NOC was the PhD community as a whole. I don't know if anywhere else has such a high number of PhDs in the same building, and the general camaraderie throughout has been fantastic. I suppose I'll get told off if I don't name some names, so I'll mention a few of you guys… The Aryan robot James, who has a plethora of nick names I won't go into right now, thank you for being a great target and at least keeping me company at mineral deposit conferences, not exactly a common research interest at an oceanography centre. Members of the 'NOC' lunch crew, Vlad, Stephen, Rachael (honorary member), Duncan, Dan, Chelsey, Amber, Aled (that's right, I went reverse alphabetical order so none of you moan about who's first), oh and that 'ex-workplace acquaintance' what was his name… Colin? Callum? Carl? Something like that. The countless number of surreal conversations from oxo cube related comments to gorillas in the NOC canteen, and general tomfoolery both in and outside NOC has kept me smiling, despite my outwardly grumpy persona. I'd also like to give a little shout out to my snooker pals, Steve, Rob, Xiaodong, and Jonny, although you're all spread out across the country/even further, I think we had quite a bit of fun, always up for a rematch. On the same vein, I'd also like to acknowledge the NOC cricket team, particularly Pete, Ben, Robbie, and Jon, it's been a pleasure to play with you guys, I only wish I'd be able to play a bit more! There are load more PhD's and other people from NOC, Highfield, and a whole host of other universities who I've met through conferences, and field trips, the list is too long, but I've appreciated all of your friendship throughout, and can only hope it continues!

I'd like to also thank my family for their support, Mum, Dad, and Laura, not just through this PhD, but just in general, whatever I've wanted to do (and not in a bratty way), you've always been there to support me. Finally, my better half, Dr Robyn Pointer, I was immensely proud to see her complete her PhD and graduate last year, and she's had to sacrifice a lot supporting me while I finish mine for which I will be eternally grateful. As I write this she's current out getting 'apocalypse supplies' for the impending doom of the Covid-19 coronavirus, and giving me a live-action report on the amount of people wearing face-masks around Southampton. It looks like I'll be preparing for my PhD viva in self-quarantine, an interesting end to say the least…

I feel like there are two quotes by the great Michael Gary Scott can summarise this PhD in a nutshell:

"I knew exactly what to do. But in a much more real sense, I had no idea what to do"

And:

"Sometimes I'll start a sentence and I don't even know where it's going. I just hope I find it along the way"

Adios all.

xxx

Chapter 1 Introduction

1.1 Seafloor Hydrothermal Activity

Although the existence of seafloor hydrothermal venting was first suggested in 1965 (Elder, 1965), active venting was not discovered until 1977 (Corliss *et al.*, 1979). This discovery not only triggered over 40 years of continued exploration for active venting, but has also had a significant impact on the scientific community's understanding of global heat and elemental fluxes from the earth's interior to the surface, provided an example of extreme environments where life can thrive, and provided evidence for the origin of life on Earth.

Hydrothermal vent systems are products of convective hydrothermal cells (Figure 1), where cold seawater percolates through ocean crust, becomes heated, buoyant, chemically altered, and rises resulting in transfer of heat and elements (such as base metals from water-rock interaction, and addition of magmatic volatiles) from the deep oceanic crust to the shallow crust and ocean reservoir (Fontaine *et al.*, 2009). Depending on a range of temperature and geochemical conditions (i.e. pH, or Eh) elements are either deposited at or near the seafloor, or are exhaled into the ocean by concentrated flow (as hydrothermal plumes), or by diffuse flow. One of the most interesting features of concentrated hydrothermal venting is the precipitation and accumulation of base metal-rich massive sulphides at or near the seafloor-ocean interface (Figure 1). These are known as seafloor massive sulphide (SMS) deposits and are classified as 'active' at currently venting hydrothermal sites, or extinct (eSMS deposits) at inactive hydrothermal vent sites.

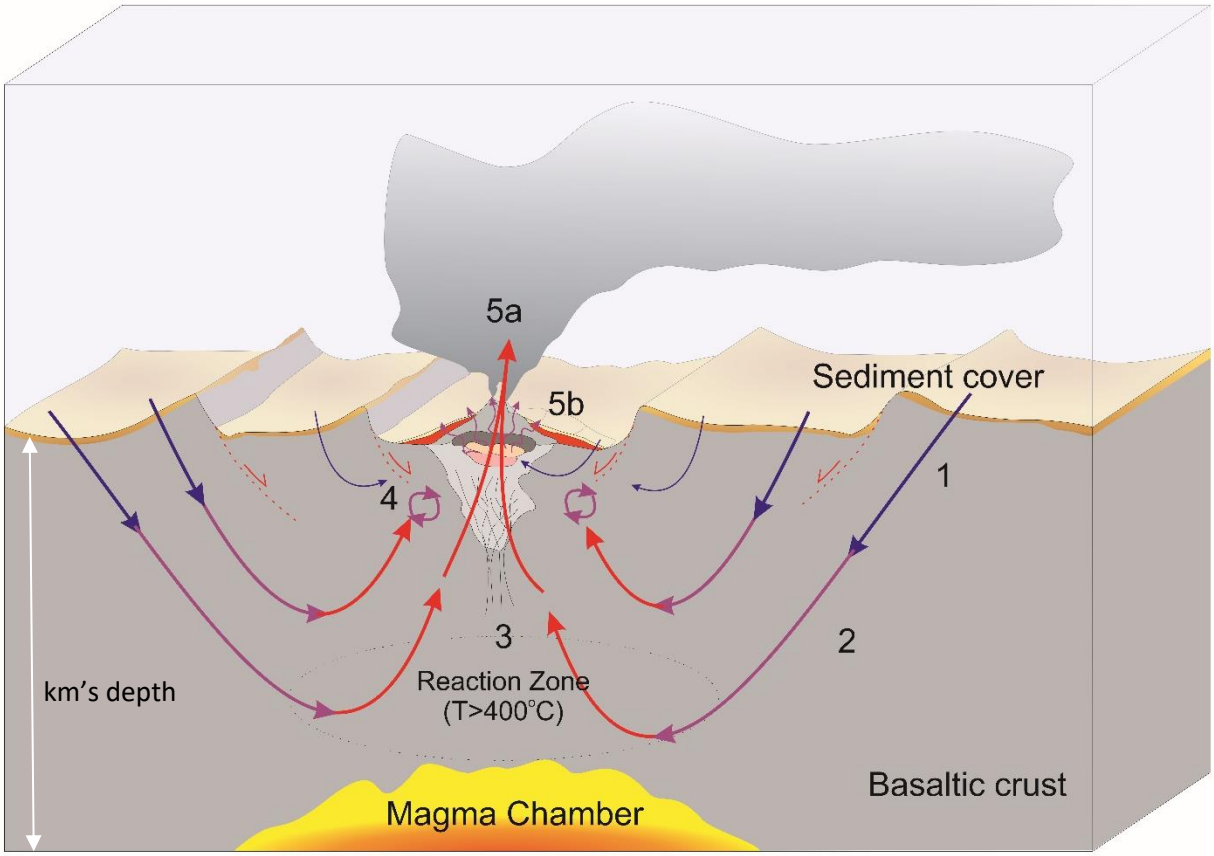

Figure 1: Schematic sketch of a convective cell of hydrothermal fluid at a mid-ocean ridge forming a SMS deposit. Step 1) At surface, cold seawater infiltrates and percolates through kilometers of oceanic crust. Step 2) As this seawater descends it gets closer to a heat source (i.e. magma chamber) and starts to increase in temperature, thus increasing its ability to scavenge metals from the surrounding basalt or other oceanic crustal rocks. Step 3) At a certain point, when the fluid reaches super-criticality, it will become positively buoyant and start to rise, continuing to scavenge metals. This area is known as the 'reaction zone' and is the principal site of elemental enrichment of the fluid. This results in a high temperature reduced, low pH, hydrothermal fluid containing a range of elements leached from the oceanic crust. Step 4) As this fluid ascends it likely mixes with cold, oxygenated seawater within saturated shallow oceanic crust. This change in Eh, pH, and temperature can cause precipitation of a range of minerals at, or below the surface. This is the dominant mechanism for seafloor massive sulphide formation. Step 5) Residual fluid is emitted from the seafloor into the ocean either by focussed venting (i.e. hydrothermal vents, (5a)) or by diffuse flow (5b). Cold seawater recharge occurs distally to the heat source, thus completing the cycle.

Heat sources driving hydrothermal circulation at ocean spreading centres are attributed to decompression melting of the mantle. This melt is buoyant and rises through the oceanic lithosphere, transferring heat from the upper mantle to the oceanic crust (Coogan *et al.*, 2019). This

heat transfers to fluids within the oceanic crust, making them rise due to an increase in buoyancy, and hence forming part of the hydrothermal cell. This enables the flux of heat from the mantle, to transfer through the shallow oceanic crust to the ocean (Coogan *et al.*, 2019). Hydrothermal heat flux is considered to approximately represent a third (~ 11 x 10^{12} W) of predicted global oceanic heat flux (~ 32 x 10^{12}W), with mid-ocean ridge axial hydrothermal fluxes representing ~18-36% of the global hydrothermal total (~2-4 x 10^{12} W) (Stein and Stein, 1994).

From a geochemical point of view, elements such as Fe and Mn are enriched in hydrothermal fluids with respect to seawater by a factor or ~10^6 (Elderfield *et al.*, 1993) and are considered good tracers for calculating hydrothermal fluxes (Baker *et al.*, 1993) in the ocean. At individual vent field scales, hydrothermal Fe and Mn fluxes have been calculated using a combination of vent fluid analysis, hydrothermal plume analysis, and a fluid mixing model (assuming the hydrothermal plume has formed by a combination of discrete high temperature and diffuse low temperature fluid flows) (Baker *et al.*, 1993; Massoth *et al.*, 1994). These studies indicate that discrete high temperature vent fluids contribute >90% of dissolved Fe and >60% dissolved Mn to hydrothermal plumes, but only contribute ~ 3% of the total water flux from hydrothermal discharge (Baker *et al.*, 1993). Conversely, diffuse flow contributes <10% dissolved Fe, and <40% dissolved Mn, but is interpreted to have ~30 times higher water flux, and ~2 times higher heat flux. Monitoring at a single vent site indicates hydrothermal fluxes are constant on a timescale of 3-7 years (Massoth *et al.*, 1994).

Early estimates of global hydrothermal fluxes were calculated geochemically by using inputs from fluvial environments, hydrothermal fluids, submarine weathering, and volcanic effusion (Wolery and Sleep, 1976). More recent estimates of iron flux from hydrothermal vents conclude a contribution of ~10% (9% (Sander and Koschinsky, 2011), 10% (Raiswell, 2006)), but could potentially be between 12 and 22% (Bennett *et al.*, 2008), of the total iron flux into the oceans.

Compared with seawater, hydrothermal fluids are enriched in Fe, Mn, Be, Al, H^+, Ba, Rb, Li, and Si, have comparable Sr, K, Ca, Na, and Cl concentrations, and are depleted in Mg, SO_4^{2-} (Elderfield *et al.*, 1993; Baker *et al.*, 1995). However, hydrothermal plumes can act as a sink for a range of elements dissolved in seawater: Cr, V, As, P, U, Mo, Be, Ce, Nd, and Lu (Elderfield and Schultz, 1996). Coupled with the observation that seafloor massive sulphide deposits can accumulate base, trace, and precious metals in sulphides (Petersen *et al.*, 2016), hydrothermal activity in general likely imparts controls on a wide range of elemental fluxes and potential reservoirs in the ocean and oceanic crust.

1.2 Occurrences of active hydrothermal vents

As of 2016, 697 hydrothermal vent sites are known from around the world, either as confirmed or inferred (Table 1). Over 70% of these are recorded as being in water deeper than 1500 meters below sea level, and approximately 50% of the sites are 'inferred' from water column signals. Because of their water column signatures, that are relatively easy to locate, the 2016 database is biased towards active (both inferred and confirmed) SMS over inactive deposits, with only 56 eSMS deposits known, representing ~ 8% of the total (Table 1, Figure 2).

Table 1: Summary of vent sites from the InterRidge vent database v3.4. Depth data is maximum depth, or single reported depth.

Meters below sea level (mbsl)	Active Confirmed	Active Inferred	Inactive
<500	68	26	1
500 - 1000	25	20	5
1000 - 1500	25	24	3
1500 - 2000	45	26	10
2000 - 2500	43	78	6
2500 - 3000	63	104	12
3000 - 3500	10	42	8
3500 - 4000	5	25	3
4000 - 4500	2	8	2
4500 - 5000	2	0	4
> 5000	0	0	2
Total	288	353	56

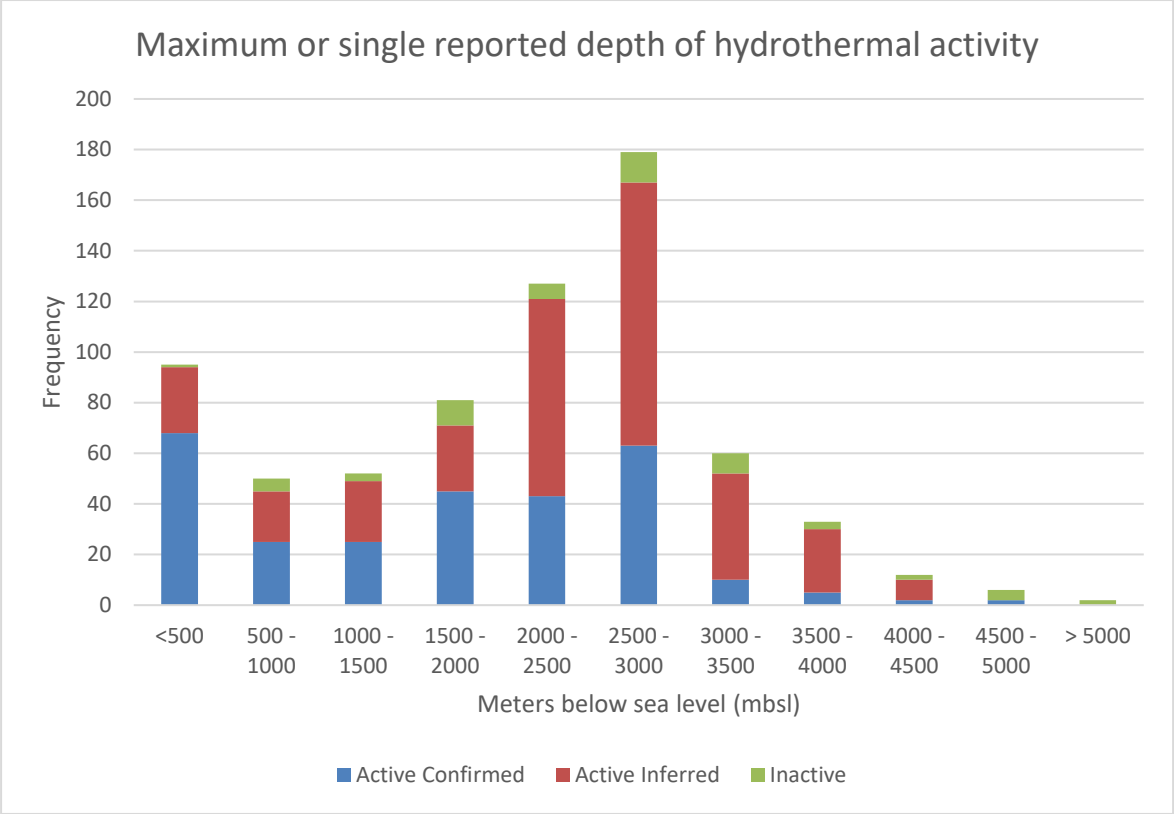

Figure 2: Histogram of InterRidge vent database v3.4, based upon depth.

The ease by which new hydrothermal vents are found is also the reason why inactive one are overlooked; features typical of active hydrothermal vents (such as geochemical or turbidity anomalies in the water column i.e. plume signatures) include: temperature and Eh anomalies, dissolved particulates, methane and other chemical indicators, are not present at inactive vent sites (Murton *et al.*, 2019). Recent changes in investigation methods (e.g. geophysical) have started to increase the number of inactive deposits found and include those discovered off-axis, and/or beneath sediment cover (e.g. Murton *et al.* 2019; Hannington *et al.* 2015; Petersen *et al.* 2019). There remains a general lack of knowledge regarding the size, volume, distribution, and frequency of eSMS deposits. It is thought that eSMS deposits are likely far greater in number than active deposits (Murton *et al.*, 2019), and have the potential to be present under sediment cover over a significantly larger area than is currently being investigated on the mid-ocean ridges and their near off-axis flanks.

1.3 SMS deposits as a resource?

With the continuing increase in global population, increasing demand for modern technology, the shift towards the use of green technology enable low-carbon economies (Zepf *et al.*, 2014), and the decrease in ore grades from terrestrial deposits (Calvo *et al.*, 2016) the demand for base and critical

metals continues to grow. This has resulted in consideration of alternative mineral sources, with deep-sea mineral deposits such as ferromanganese crusts, manganese nodules, and SMS deposits presenting a potential future source for both critical and base metals.

To be commercially viable, SMS deposits must have both grade and tonnage. Tonnages are poorly estimated, and the grades are biased towards metal-rich hydrothermal chimney sampling. Comparison of 142 SMS deposits from the InterRidge database (v3.4) show that only 91 have average metal contents that make them of potential economic interest (shown in red in Figure 3). SMS deposits show a wide range of geochemical and mineralogical variation within a single hydrothermal field, at deposit, at hand specimen, and even at thin section scales, and the current bias towards surface sulphide samples may not represent the average composition of sulphides within the main orebody at depth. Out of the 91 SMS deposits of potential economic interest, only 13 have resource estimates based on (albeit sparse) three dimensional data (Petersen *et al.* 2016 and references therein), showing the widespread lack of volumetric information for SMS deposits.

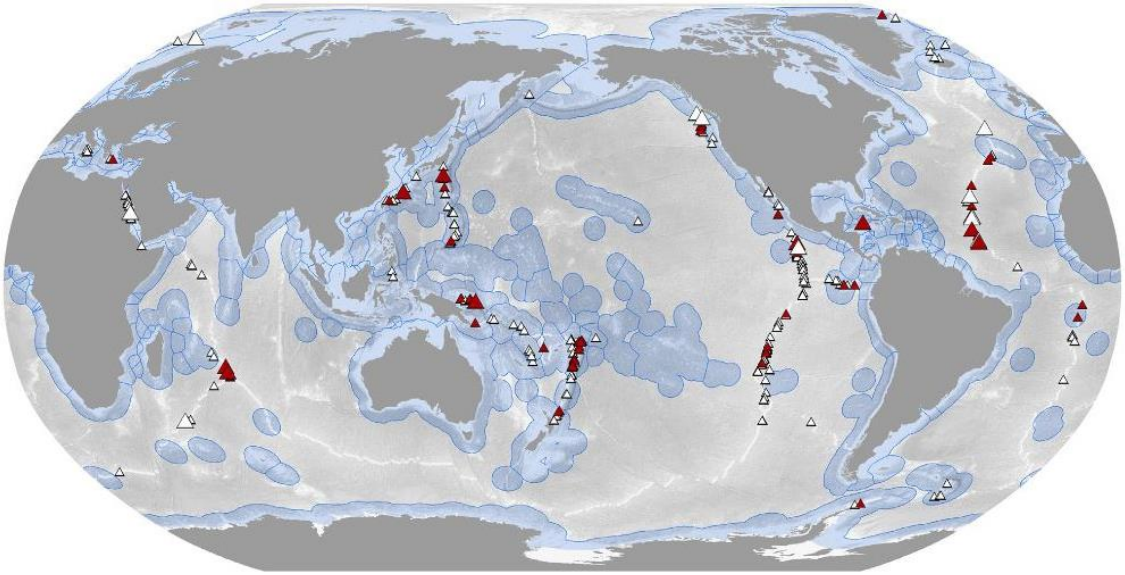

Figure 3: Distribution of high-temperature seafloor hydrothermal systems and associated seafloor mineralisation from Petersen *et al.(*2016). Red = average grade of deposit is either > 5 wt% Cu, >15 wt% Zn, or > 5 ppm Au; large symbols have size estimate of > 1 million tonnes.

Studies of the frequency of occurrence of hydrothermally active SMS deposits against parameters such as spreading rate, back-arc length, etc. (Beaulieu *et al.*, 2015) yield estimates that ~40% of the active systems have been discovered, with the majority of the undiscovered deposits being at mid-ocean spreading ridges (Hannington *et al.*, 2011; Beaulieu *et al.*, 2015). This unknown deposit occurrence rate, combined with limited geochemical and three dimensional deposit information,

makes global resource estimates difficult. One estimate extrapolates deposit occurrence data over 10,000km of mid-ocean ridges, arc, and back arc spreading centres, to estimate the tonnage of SMS deposits in the neovolcanic zones using a median grade of 5 wt% Cu and Zn, resulting in ~30MT Cu+Zn (Hannington *et al.*, 2010). This total metal tonnage estimate is considered similar to the total metal content for all on-land Cenozoic volcanogenic massive sulphide (VMS) deposits (Hannington *et al.*, 2010, 2011). Another method uses *Monte Carlo* modelling to estimate Cu, Zn, Pb, Ag, and Au contents across SMS deposits within mafic (256,000 km^2) and felsic/bimodal (100,000 km^2) tracts, resulting in median undiscovered metal contents at 6.4Mt (Zn), 4.6Mt (Cu), 1.2Mt (Pb), 10,000t (Ag), and 390t (Au) (Singer, 2014). This second estimate is significantly lower than the first, and highlights the lack of knowledge and potential range of global resource estimations for SMS deposits.

Neither global SMS resource estimates include 'off-axis' (Hannington *et al.*, 2010) or >4km off axis (Singer, 2014) deposits, and rely on median grades and metal distribution of VMS analogues respectively to estimate metal contents. More importantly, neither estimates includes inactive 'eSMS' deposits, although they may represent up to ~ 600Mt of Cu and Zn off-axis (Hannington *et al.*, 2010). Yet, due to the unique chemosynthetic biota, high temperatures, and low pH environments created by ongoing hydrothermal fluid expulsion, actively forming SMS deposits are not currently considered prospective for exploitation. Instead, it is much more probably that eSMS deposits will be the first to be exploited. As such, the unknown and currently unquantifiable eSMS metal tonnage estimates could represent a significant reserve of economically interesting metals at or near the seafloor of potential interest for deep-sea mineral exploitation (Murton *et al.*, 2019).

1.4 Comparing SMS deposits with VMS deposits

SMS deposits are broadly considered to be the modern day, actively forming equivalent of some types of volcanogenic massive sulphide deposits (VMS), a significant source of base metals, preserved as sulphide bodies within ophiolites (oceanic crust obducted onto continental crust). Both SMS deposits and VMS deposits occur at a wide range of geological settings, where active magmatism and tectonics combine to create suitable environments for hydrothermal circulation. These settings are often extensional, and include mid-ocean spreading centres, volcanic arcs, back arcs, intraplate volcanoes, rifted continental margins and strike-slip basins (USGS 2012, Figure 4)

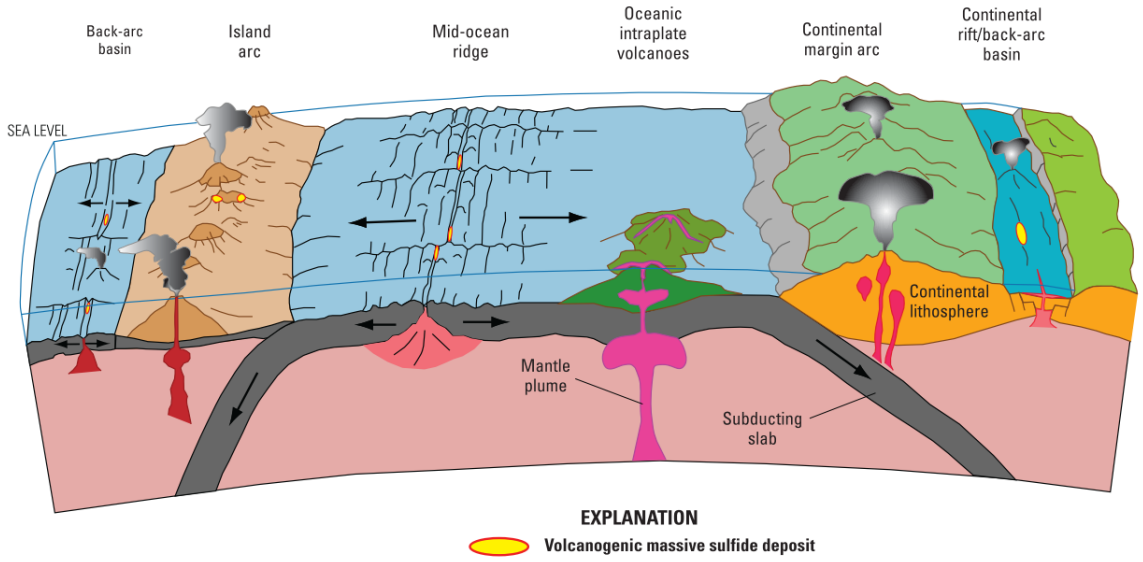

Figure 4: Geological formation environments for Volcanogenic Massive Sulphide (VMS) deposits, a product of seafloor hydrothermal activity (USGS, 2012)

VMS deposits are classified into five different groups by the USGS 'Volcanogenic Massive Sulfide Occurrence Model' (USGS, 2012), summarised in Table 2.

Table 2: VMS classification summary

VMS classification	**Tectonic Setting**
Siliciclastic-felsic	Epi-continental back arcs
Bimodal-felsic	Continental margin arcs and back arcs
Bimodal-mafic	Rifted intra-oceanic volcanic arcs
Siliciclastic-mafic	Sediment covered back arcs (includes sediment covered mid-ocean spreading ridges)
Mafic-ultramafic	Mature back arc spreading centres (includes un-sedimented mid-ocean spreading ridges)

To enable VMS and SMS deposits comparison, an understanding of the geological setting of each deposit is necessary due to their inherent variability between geological settings. In SMS deposits, variable geological setting is thought to result in variable metal content e.g. slow spreading ridges tend to have higher Cu and Au than intermediate-fast ocean ridges due to the increased interaction

with ultramafics (German *et al.*, 2016), and arcs and back arcs have variable source rocks and volatile input resulting in higher Cu, Zn, Pb, Ag, and Au concentrations than mid-ocean settings (Petersen *et al.*, 2016). Different geological settings can also result in variable contributions from non-sulphide materials into the system, i.e. mid-ocean deposits are likely only to have deep water carbonate or hydrothermal sediments associated with deposits; arc and back arc settings likely have more input from volcaniclastics and potentially a contribution from continental sediments.

With these variations in mind, this study focusses on a comparison between three eSMS deposits of the same type: from an un-sedimented, slow-spreading, mid-ocean ridge setting. The closest geological analogy to these eSMS characteristics are (ultramafic-)mafic dominated VMS deposits. Figure 5 shows a comparison of the stratigraphy between a 'type' deposit for mafic extrusive-dominated VMS deposit and a comparable SMS deposit. There are some similarities in stratigraphy, for example multiple zones defined by sulphide assemblages or alteration mineralogy and an overall structure including a massive ore body and underlying stockwork. The main difference appears to be the presence of overlying material, understandably lacking in modern hydrothermally active or recently inactive SMS deposits.

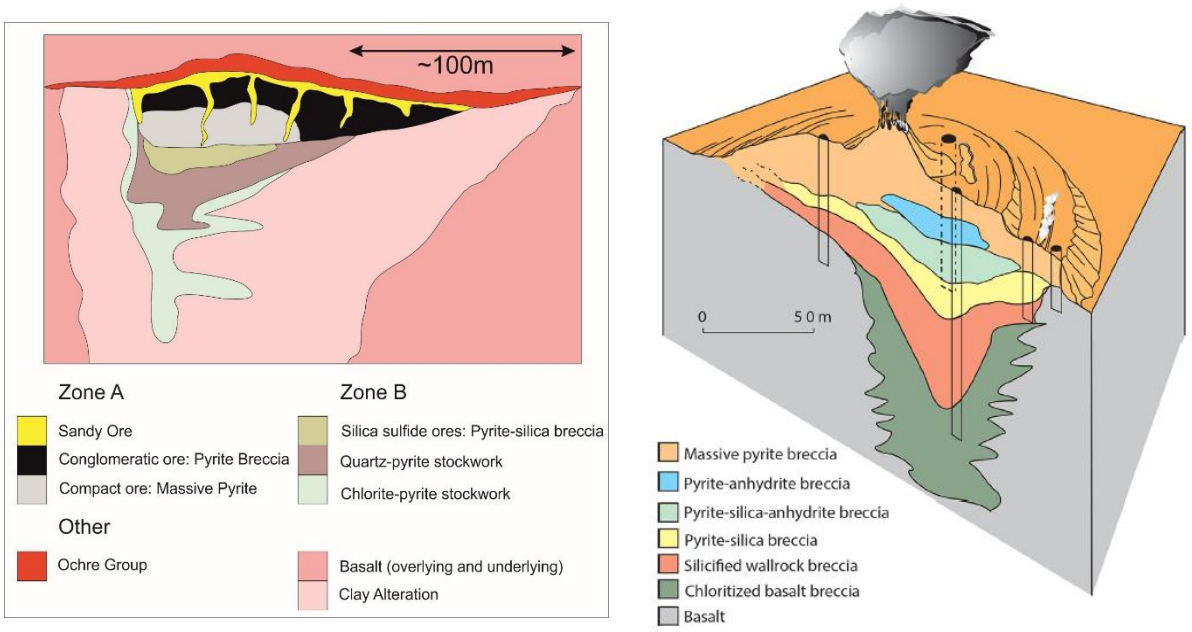

Figure 5: Comparison of 'Mafic'-type VMS deposits vs the TAG Active Mound SMS deposit. Left) Mafic-extrusive VMS deposit type model (Cyprus-type), edited from Hannington *et al.* (1998), Right) Active TAG Mound, mafic hosted SMS deposits on the Mid-Atlantic Ridge, from Humphris & Tivey (2015).

In general, eSMS deposits represent a missing link between active SMS deposits, and preserved VMS deposits. In comparison to modern active SMS deposits (i.e. Active TAG Mound), eSMS and

VMS deposits (i.e. Cyprus-type) have gone through processes relating to the reduction and cessation of hydrothermal activity. Comparison between active SMS deposits, eSMS deposits, and ancient VMS deposits can potentially identify late-stage geochemical, fluid dynamic and, hydrothermal processes that are particular to hydrothermal closure, and that may lead to modification of these deposits with implications for their fate.

1.5 Preservation of VMS deposits through time

It is clear from the geological record that VMS deposits have been preserved throughout geological history, from the Archaean to the Tertiary (Franklin *et al.*, 2005; Groves *et al.*, 2005). Until the Palaeozoic Era, deep ocean anoxia provided a reduced environment for the precipitation of seafloor massive sulphides, and is one of the most likely mechanisms that explains the preservation of early VMS deposits (Groves *et al.*, 2005). Since the ocean oxidation event at the beginning of the Palaeozoic Era (Fike *et al.*, 2006), deep ocean water has been oxidised, and as such has represented a large reservoir of oxidising fluid that had the potential to oxidise VMS deposits after they had formed on the seafloor. Despite this, VMS deposits have still been preserved, which begs the question of how and why? Key processes that are linked to preserving VMS deposits include: localised or widespread ocean bottom anoxia (Eastoe and Gustin, 1996; Slack and Grenne, 2018); rapid burial by clastic and/or volcaniclastic sediments and/or exhalites; and burial under extrusive volcanic materials (e.g. lava flows) (Eastoe *et al.*, 1987; Eastoe and Gustin, 1996; USGS, 2012). A common factor linking all of these processes is the protection of these seafloor sulphides from weathering by oxidation.

Continued circulation of chemically reduced hydrothermal fluids after burial is apparent in many VMS deposits and indicated by the acidic leaching and alteration of hanging wall rock stratigraphically overlying massive sulphide ore bodies or sub-surface sulphide emplacement and/or replacement (Doyle and Allen, 2003; Herrington *et al.*, 2005; Galley *et al.*, 2007). Regardless of the type of hanging wall lithology, such alteration implies that cover existed over the ore bodies before hydrothermal activity ceased, supporting the idea that burial of deposits increases the chance of preservation. However, this is not always evident and there is often a long period of time between the formation of SMS and their burial during which the deposits remain exposed and susceptible to destruction by oxidation. Hence the question arises: by what processes, if any, do eSMS deposits persist on the modern seafloor and become part of the metal inventory embedded in the oceanic crust, that could act as a reservoir for base metals?

1.6 Thesis rationale, Blue Mining Project, and aims of the study

One of the most important unanswered questions is if, and how, eSMS deposits are preserved on the seafloor. During hydrothermal activity, the emitted reduced fluids enable sulphide precipitation and preservation while hydrothermal fluids dominate over oxygenated seawater. Upon cessation of hydrothermal flow, it is likely that cold oxygenated seawater would infiltrate, diffuse, and otherwise permeate though and penetrate the deposit, resulting in oxidation, weathering and chemical dissolution of the massive sulphide ore, and the mobilisation and loss of economic metals to the ocean. The evidence from the geological record is that VMS deposits are typically preserved by processes that physically or chemically limit oxidation (Chapter 2). But many of these processes do not appear to apply to modern eSMS deposits (or at least to the same extent).

A simple calculation yields a theoretical abundance of eSMS deposits on the axis and flanks of mid-ocean ridges. For slow-spreading ridges, SMS deposits form over a period of 10-50ka (Lalou *et al.*, 1995). Assuming an average of 50-100ka for each deposit from start to finish (including multiple hydrothermal events at the same site), and extrapolating out across the ridge flanks to crust that is 1Ma old on both sides of the spreading axis, then there may be 20-40 times as many eSMS deposits than hydrothermally active ones. If the metal grade and tenor is preserved during the transition from an SMS to an eSMS deposit, and continues to be preserved as the deposits move off-axis and are buried by increasingly thick pelagic sediment, they could potentially act as a significant reservoir for base and precious metals. Although these observations are based upon a series of assumptions that cannot be confirmed at this current time, they are all linked to the question of preservation.

Considering the problem of preservation alone, many questions are broadly unanswered, such as: is the metal tenor of reduced SMS deposits preserved as eSMS deposits, despite being in direct contact or likely influenced by a reservoir of oxidised fluids? If so, how are they preserved? Are there any common features between eSMS deposits and VMS deposits that could explain preservation? These questions can only be answered by comprehensive study of eSMS deposits.

This research presented here is derived from a European Union commissioned project 'Blue Mining', which produced the most comprehensive 2D and 3D multidisciplinary investigation of eSMS deposits to date. A range of geological and geophysical techniques were used to investigate a series of eSMS deposits within the TAG Hydrothermal Field (TAGHF), that hosts one of the largest and most well known hydrothermally active SMS deposits known (the Active TAG Mound). Here, the TAGHF is used as a natural laboratory to address many of the outstanding questions around the fate of eSMS deposits at slow spreading ridges. This thesis focuses on the hitherto unique finding of a sequence of Si-Fe lithologies, forming a substantial thickness (up to 5 metres), overlying massive sulphide ore bodies at each of three separate eSMS deposits that were drilled by the 'Blue

Mining' project in the TAGHF at 26˚N, Mid-Atlantic ridge. Here, I set out to test the premise that this cap may have formed by late-stage hydrothermal processes during the final stages of hydrothermal activity, and that this process may act as an auto-preservation mechanism for retention of the metal tenor of eSMS deposits. Discovery of these Si-Fe lithologies, at each of the three eSMS mounds investigated, implies that their occurrence may be the product of common processes that preserve SMS deposits after hydrothermal activity ends. Understanding the formation mechanisms and role that these Si-Fe caps may play in metal preservation can shed further understanding of the resource potential of eSMS deposits, and raises the prospect of re-evaluating the magnitude of the ocean crust as a reservoir for base metals with implications for global fluxes and cycles.

In summary, the main aims of this study are:

- to characterise and interpret the origins and paragenesis of Si-Fe capping lithologies recovered from the three eSMS deposits;
- to understand the role of Si-Fe capping lithologies, and whether it has the potential to be involved in the preservation of the underlying orebody in eSMS deposits.

It is important to note that the study of the mineralogy and geochemistry of the underlying massive sulphide ore body, quantification of the metal tenor and whether it is preserved in the underlying eSMS deposits is outside of the scope of this project. Instead, this project focuses on the unique discovery, on the modern seafloor, of a silica cap overlying massive sulphide ore bodies, and the potential of this material to influence metal preservation in eSMS deposits.

1.7 Outline of dissertation

Chapter 2 aims to provide a review of literature relating to the formation of silica and iron lithologies and the evidence for the formation processes from both geological analogues (VMS deposits) and modern seafloor environments (SMS deposits) to understand their distribution and historical and current interpreted formation mechanisms of Si-Fe materials. Chapter 3 summarises the Trans-Atlantic Geotraverse (TAG) Hydrothermal field and knowledge of the active hydrothermal mound, and inactive deposits, including through both historical work and the presentation of geological mapping and surface surveying undertaken as part of this study. Chapter 4 presents the range of analytical techniques used to conduct this research, including methodologies, and accuracy and precision assessments. Chapter 5 summarises and presents the physical characterisation of the Si-Fe lithologies using a range of analytical techniques (thin section petrography, XRD, SEM, FTIR), including macro- and micro-textural assessment. Chapter 6 presents the geochemical characterisation of the Si-Fe lithologies, including whole rock geochemistry (major

elements and trace elements), and stable isotope investigations which highlight changes in physicochemical conditions such as temperature, eH, and pH. Chapter 7 presents results from CT scanning, analysis of total porosity, connected porosity, and permeability simulations Si-Fe and underlying massive sulphide samples. Chapter 8 is the main discussion chapter where, firstly, the genesis of the three main constituents of the Si-Fe cap are considered, followed by the presentation of the interpreted paragenesis of the Si-Fe cap. Secondly, the role of the Si-Fe capping materials within the context of the hydrothermal cycle and the potential preservation of the sulphide ore body are discussed, and some wider implications of the presence of SI-Fe caps is considered. Finally, Chapter 9 will discuss the wider implications of this research, and present conclusions and further work which would complement this body of work.

Chapter 2 Background

As stated in Chapter 1, one of the key questions, which is yet to be fully answered, is if and how eSMS deposits are preserved on the seafloor. Recent three dimensional investigation of three eSMS deposits at the TAG hydrothermal field discovered variable thicknesses of Si-Fe material directly overlying the massive sulphide orebody (fully described in Chapter 3 and Chapter 4), which could potentially contribute to the preservation of the underlying orebody.

Similarities between SMS deposits and VMS deposits enable general comparison, with the main differences highlighting the presence or lack thereof of overlying material. The occurrence of Si-Fe material directly overlying sulphide ore bodies in TAG hydrothermal field eSMS deposits, leads to various questions: Are there any examples of comparable material at other SMS or VMS deposits to this material? If so, how have they formed? Are there any comparable formation mechanisms that can explain the formation of this material?

In order to answer these questions, a review of potentially comparable Si-Fe material from a series of VMS deposits and modern seafloor hydrothermal systems has been undertaken. This review is not exhaustive, but focusses on the distribution of Si-Fe material (thicknesses, spatial distribution, and stratigraphic relationship to the massive sulphide orebodies), the interpreted origins of the material (including formation mechanisms of both silica and iron oxide), and how or if they may have acted to preserve underlying massive sulphide ore bodies (for VMS deposits only).

Literature review for Si-Fe materials is not as simple as it sounds as a wide range of terminologies exist including: iron stone, jaspers, jaspilloids, tetsusekiei, jasperite, iron rich cherts, and more (Hollis *et al.*, 2015) and are used to describe Si-Fe lithologies throughout geological analogues, but all share the dominant silica and iron oxide/oxyhydroxide mineralogy. In order to try to normalise the wide range of literature descriptions of what appear to be similar materials a few terms have been defined (Section 2.1). These terms relate to defining the physical state of the silica and iron, both chemically and in their host crystal structures (i.e. specific iron and silica hosted mineralogy, and the degree of crystallinity of these minerals etc.). The differences between these terms are important as they are determined by the formation processes and environments and include temperature, pH, Eh, alkalinity, kinetics, and general chemical environment. Understanding the characteristics of the material in these terms thus yields information on their formation history.

2.1 Si-Fe lithologies, their definitions and modes of formation

2.1.1 Difference between Si-Fe and Fe-Si materials

In this thesis, the term Si-Fe material or lithology denotes either a sediment, or rock, which is predominantly composed of silica (amorphous silica, opal-A, opal-CT, quartz) and iron oxides or oxyhydroxides (haematite, goethite, or ferrihydrite) with silica being the dominant phase (e.g. SiO_2/silica minerals > 50 wt%). The term Fe-Si material is used to denote a sediment or rock sample where iron oxides or hydroxides are the dominant phase (e.g. Fe_2O_{3T}/iron oxide or oxyhydroxide minerals > 50 wt%). Si-Fe or Fe-Si will be used where possible to group Si-Fe lithologies together and make the literature comparable, as a wide range of names exist in the literature for Si-Fe lithologies (Table 3).

Table 3: Summary of Si-Fe terminologies from Hollis et al. 2015

Term	Definition	References
Ironstone (sensu stricto)	Sedimentary rock that contains >15 wt.% Fe. Includes: iron formations, metalliferous sediments, Fe–Mn nodules, pavements and crusts.	Stow (2005)
Iron formation	Layered, bedded or laminated rocks with >10 wt.% Fe, where iron minerals are interlayered with quartz, chert or carbonate. Divisible into Superior- and Algoma-types. Referred to as banded iron formation (BIF) in Precambrian terranes.	Gross (1980), Spry et al. (2000), Bekker et al. (2010)
Chert	Fine-grained siliceous sedimentary rock of biogenic, biochemical or chemogenic origin. Composed predominantly of fine-grained silica with small quantities of impurities. Green colors are typically associated with chlorite or smectite clays from volcaniclastics, and dark colors with clays and organic carbon.	Stow (2005)
Hematitic chert/jasper	Red colored chert, with its color imparted by finely disseminated hematite. May be recrystallized or show poikilitic textures with cryptocrystalline hematite dispersed in a silica matrix. Of variable thickness (few cm to >10 m).	Maslennikov et al. (2012)
Sulfidic chert/mudstone	Chert/mudstone with visible sulfide minerals above trace amounts (i.e. >1%).	Defined herein
Iron-rich chert	Chert with a high content of iron oxide minerals and 5–15 wt.% Fe.	
Jaspillite	Interbedded jasper and hematite. Australian term for a banded iron formation (BIF).	Allaby (2013)
Tetsusekiei	Iron quartz in Japanese. Generic name used for silica-iron rich chemical sedimentary rocks of the Kuroko district, Japan. Interpreted as a mixture of both clastic (tuffaceous) and exhalative (chemical) material.	Kalogeropoulos and Scott (1983)
Tuffite (sensu lato)	Generic name used for tuffaceous chemical sedimentary rocks (often referred to as tuffaceous exhalites) in the Abitibi greenstone belt, Canada. Examples: Key Tuffite, Main Contact Tuff.	Kalogeropoulos and Scott (1989)
Tuffite (sensu stricto)	A rock which contains a mixture of pyroclastic (25–75%) and epiclastic material. May be divided according to average clast size into tuffaceous conglomerate/breccias, tuffaceous sandstone, tuffaceous siltstone, and tuffaceous mudstone/shale.	Le Maitre (2004)
Umber (or umbrite)	A sedimentary deposit of Fe–Mn oxyhydroxides admixed with variable amounts of biogenic and detrital material (e.g., chlorite, silica and carbonate) forming trace-metal enriched mudstones.	Maslennikov et al. (2012) and references therein
Ochre	Gossan-derived unmetamorphosed ferruginous sediments (e.g., Semail Nappe and Troodos, Cyprus).	
Jasperite	Orange hematite–quartz rocks differentiated from jaspers on account of microbreccia-like textures and abundant features indicative of replacement inherited from former hyaloclastite. Fragments of fine grained hematite–quartz aggregates are cemented by a blocky quartz matrix. Jasperites can occur as veins, interpillow interstitial infillings, stratiform lenses, beds and interbeds.	
Gossanite	A submarine gossan-derived sedimentary rock and the lithified analogues of ochres. Generally comprise oxidized clastic sulfides mixed with hematitized carbonate and/or hyaloclastic material almost entirely replaced by silica, chlorite and hematite.	
Exhalite	A unit formed through precipitation of mainly amorphous Fe ± Mn ± Si ± S ± Ba ± B phases from VMS-related hydrothermal vents and plumes at or below the seafloor.	Peter and Goodfellow (1996, 200 Grenne and Slack (2005), Slack (Slack (2012)
Vasskis	Beds of silicate- and sulfide-facies iron formation in Norway (e.g., Løkken district).	

2.1.2 Gossan vs. exhalite

When associated with hydrothermal systems, Si-Fe lithologies are typically described as either a gossan or an exhalite. These two terms, by definition, imply specific environmental and/or chemical

processes involved with the formation of the Si-Fe material. It is important to understand the differences between these terminologies when describing Si-Fe lithologies because of the inherent implication of formation mechanism with the use of the terms.

An exhalite is defined as an 'exhalative chemical sediment' and refers to typically stratiform or lenticular units of variable composition that have ultimately been precipitated from an exhalative hydrothermal source (Spry, Peter and Slack, 2000). Banded iron Formations (BIFs) are considered to be exhalites (Isley and Abbott, 1999; Klein, 2005; Posth *et al.* 2011; Gourcerol *et al.*, 2016), and commonly Si-Fe exhalite beds are spatially associated with VMS deposits (Davidson *et al.*, 2001; Grenne and Slack, 2005; Bekker *et al.*, 2010; USGS, 2012; Hollis *et al.*, 2015). Their origin is typically linked to the accumulation of precipitated amorphous mineral phases (mainly Fe ± Mn ± Si ± S ± Ba ± B) from hydrothermal vents and/or plumes (USGS, 2012). The term exhalite also includes examples such as hydrothermally altered volcaniclastic materials that can overly VMS deposits. This type of exhalite has likely undergone silicification as a result of seafloor or subseafloor precipitation of silica from diffuse venting (Jones et al., 2006) and although different to hydrothermal plume related deposits, are still classified as exhalites.

A gossan is defined as a lithology typically composed of fine grained iron oxide or oxyhydroxides (i.e. goethite, limonite etc.) and quartz which has been derived from oxidation and weathering of existing massive sulphide material (Velasco 2013). It is commonly accompanied by secondary enrichment of base and/or precious metals (USGS, 2012; Velasco *et al.*, 2013). Two different types of gossans have been identified from VMS deposits: 1) a gossan derived from subaerial weathering and enrichment related to circulating meteoric water, a process that can act on a deposit post-obduction assuming it is located within a water table (Andrew, 1984; Velasco *et al.*, 2013), and 2) seafloor gossans formed *in-situ* by seafloor weathering by exposure of massive sulphide material to circulating oxygenated seawater where a massive sulphide deposit may be located at or just below the seafloor (Hannington, 1993; Herrington *et al.*, 2005; Gablina *et al.*, 2006).

The main difference between the two gossan types are their timing, the contrasting hydrological settings, and the processes forming them. It is also likely that VMS deposits contain both types of gossan, but post depositional processes such as faulting or erosion may have destroyed evidence of seafloor gossan formation. Furthermore, it may also be difficult to determine whether a gossan has formed as a preserved seafloor gossan, or as a subaerial gossan in on land VMS deposits.

For comparison between modern day and geological analogues, it is important to realise the differences between gossans and exhalites, and between subaerial and submarine gossans. Where geological examples are presented and comparisons drawn, the interpreted origin of the iron-silica units in question should be discussed within the context of these three endmembers.

2.2 Origins of iron oxide, iron oxyhydroxides, and silica in hydrothermal environments.

To consider the origins of Si-Fe material from geological analogues one must consider the separate mechanisms of formation or accumulation of both of the iron and silica components. Iron oxides can form from gossan formation, plume fallout, exhalite precipitation or biologically mediated precipitation in hydrothermal environments, and silica is predominantly thought to be a low temperature hydrothermal precipitate. Each of these formation mechanisms is summarised below, presenting an understanding of the geochemical conditions and scenarios in which they are prevalent.

2.2.1 Iron oxide/oxyhydroxide - Gossan Formation

During the formation of both SMS deposits and VMS deposits, massive sulphides are stable under reduced conditions, from prevailing reduced hydrothermal fluids. At some point after cessation of hydrothermal activity, ambient fluids are allowed to ingress into the deposit so that the prevailing conditions become more oxygenated, i.e. seawater or meteoric water (depending on environment). Upon ingress or exposure of massive sulphide material to oxygenated water, sulphides begin to weather as a result of this redox change. The main difference between subaerial and submarine gossans is obviously the fact that one is in a marine environment, the other accreted and uplifted into a terrestrial environment. However, another significant detail is the amount and extent of oxidised water available to influence weathering of the massive sulphide orebody. Due to water mobility and fluctuating water tables subaerial gossans often are subject to secondary enrichment, where metal content of weathered ore material (i.e. base and precious metals) are either mobilised and reprecipitated within the gossan as secondary oxides (i.e. malachite for copper), or left as residual native metals (i.e. gold). In a marine environment the entire shallow crust will be saturated, and therefore sulphide would likely be always in contact with, or have a simple pathway to oxygenated water. Prolonged residence time at or near the seafloor for any sulphide material would result in oxidation and loss of metal content into the ocean reservoir, rather than be retained as oxides in a secondary gossanous deposit.

Main sulphide minerals are typically associated with VMS deposits include: pyrite (FeS_2) (and its metastable polymorph marcasite), chalcopyrite ($CuFeS_2$) and sphalerite ((Zn,Fe)S). Weathering of pyrite, marcasite and chalcopyrite by oceanic water (i.e. near neutral pH as a result of oceanic buffering) can form ferrihydrite or ferric hydroxide (Fallon *et al.*, 2017, 2018; Knight *et al.*, 2018) as shown in the equations below:

$2FeS_{2\,(S)} + 7.5O_{2\,(aq)} + 4H_2O \rightarrow Fe_2O_{3\,(s)} + 4SO_4^{-2} + 8H^+$ (pyrite to iron oxide)

$FeS_2 + 3.75O_{2\,(aq)} + 3.5H_2O \rightarrow Fe(OH)_{3(S)} + 2SO_4^{-2} + 4H^+$ (pyrite to iron oxyhydroxide)

$CuFeS_{2(s)} + 8.5O_{2\,(aq)} + 5H_2O \rightarrow CuO_{(S)} + Fe(OH)_3\,(s) + 4SO_4^{-2} + 8H^+$ (chalcopyrite to iron oxyhydroxide)

Ferrihydrite is metastable and, as such, would alter to goethite (α-FeO.OH) or haematite (Fe_2O_3), a reaction that has been experimentally shown to be pH and/or temperature dependent under experimental conditions (Schwertmann, 1983).

Gossanous products in VMS systems often manifest as thick of accumulation of fine-grained sedimentary iron oxide and oxyhydroxides, are referred to as 'Ochres' (defined in Table 3). However, sometimes it can be difficult to differentiate between gossanous iron oxide formation and accumulation of iron oxide directly precipitated from a hydrothermal fluid. When this is the case, other features such as textural evidence (relict sulphide structures and pseudomorphs), and geochemical data (high residual base metal content), need to be used to determine the origin of the iron oxide material.

2.2.2 Iron oxide/oxyhydroxide – Precipitation from hydrothermal fluids

Precipitation of iron oxides as direct products from low temperature hydrothermal fluids, or as particles within hydrothermal plumes, are included within the definition of exhalites.

The predominant mechanism for exhalite formation is the mixing of chemically reduced hydrothermal fluids with low temperature, oxidised seawater. The resulting change in temperature and redox state is thought to be the main mechanism driving subsurface precipitation and mineralisation from fluids (both sulphides and oxides), the growth on the seafloor of sulphide structures (e.g. chimneys), as well as the formation of hydrothermal plumes.

Iron oxides/oxyhydroxides can precipitate within both buoyant and non-buoyant plumes due to the change in oxidation state upon mixing of reduced hydrothermal fluids with the cold oxygenated seawater. After precipitation the particulate iron can act as a sink for a range of trace elements including Y, Be, Th, V, As, Cr, Zn, Co, and Pb (German *et al.*, 1991). Buoyant material has the potential to travel large distances before fallout (Lilley *et al.* 1995; Gurvich 2005 and references therein), and likely contribute components to seafloor sediments both proximal and distal to hydrothermal vent fields (Lilley *et al.*, 1995).

Iron is mobilised under reduced conditions, iron oxides/oxyhydroxides can precipitate from hydrothermal fluids which a limited dissolved sulphur component, i.e. fluids which have formed massive sulphide minerals at depth exhausting dissolved sulphur, but still contained excess iron

(Kalogeropoulos and Scott, 1983). If a reduced fluid contained significant amounts of dissolved sulphur and dissolved iron, then iron sulphide would preferentially precipitate over iron oxide/oxyhydroxide.

2.2.3 Involvement of biology

Since the discovery of iron oxide coated, micron scale, filamentous material, which resemble iron oxidising bacteria, at modern hydrothermal vent systems, comparisons have been drawn with ancient Si-Fe material from VMS deposits. Although no carbon based material remains, the morphologies of filaments within iron oxide deposits have typically been interpreted to represent ancient iron oxidising bacteria. This interpretation is not without criticism, as morphologically similar abiological filamentous material has been produced experimentally (García Ruiz *et al.*, 2002), and feasible abiological formation mechanisms have been attributed to similar material form the TAG active Mound (Hopkinson *et al.*, 1998).

Iron oxidising bacteria metabolise energy produced from the oxidation of reduced iron in solution, resulting in precipitation of iron oxides. Direct metabolism of Fe^{2+} to Fe^{3+} results in the nucleation of nanometric-scale iron oxide particles directly onto the cell walls or organic sheaths of the bacteria (Little *et al.*, 2004; Fortin and Langley, 2005). Continued metabolic oxidation or abiological iron oxide absorption onto the existing structures would increase the amount of iron forming, and likely would result in the movement of the bacteria leaving a mineralised sheath (Little et al. 2004). This movement lengthens the filament and even a small amount of bacteria moving together can create a complex filamentous network, and existing filaments can provide surfaces for further abiological dendritic growth (Emerson and Moyer, 2002a; Little *et al.*, 2004). This is supported by the observation of active bacteria in ~7% of iron oxide sheaths within a microbial mat (Emerson and Revsbech, 1994).

2.2.4 Silica in marine sediments

There are two main sources of silica in seafloor silica deposits: biologically derived silica (radiolarians, etc.) or hydrothermal silica. Biologically derived silica typically refers to cherts (quartz dominated) and porcellanites (opal-CT dominated) which have formed by replacement of carbonate sediment, or as a primary bedded feature within a carbonate sediment sequence. Although the origin of the silica is biogenic, the precipitation and recrystallisation mechanisms are interpreted to be inorganic (Adachi *et al.*, 1986).

Exact causes of silica precipitation at low temperatures remains enigmatic. On one hand, quartz has been experimentally precipitated from seawater containing 4.4 ppm dissolved silica, at 20˚C, and 1

atmosphere (Mackenzie and Gees, 1971), and on the other, silica can remain in solution despite being supersaturated with respect to quartz, interpreted to be a function of slow kinetics (Krauskopf 1956). Silica precipitation within hydrothermal systems is commonly attributed to cooling by direct mixing of seawater and hydrothermal fluids, or conductive cooling of hydrothermal fluids. Silica saturation is controlled by silica polymorph solubility, and therefore varies with temperature (Krauskopf, 1956; Zarrouk *et al.*, 2014, Figure 6)

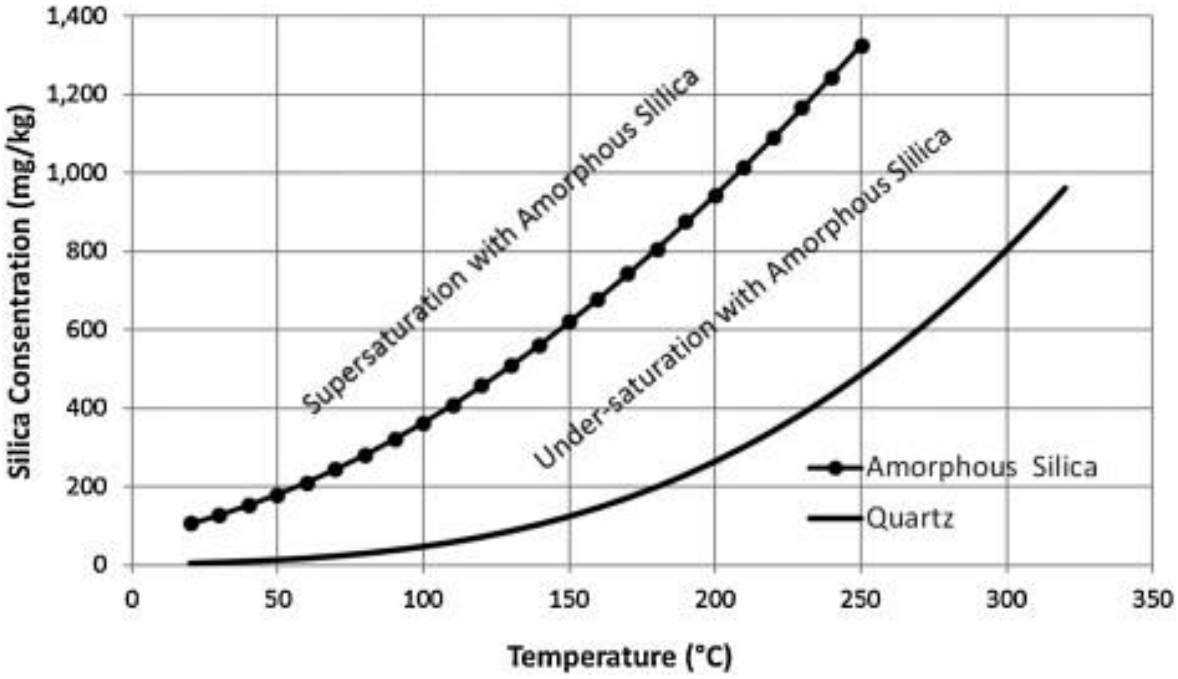

Figure 6: Silica solubility concentrations with respect to amorphous silica and quartz (Zarrouck *et al.* 2014)

High temperature hydrothermal fluids require concentrations > 1000 ppm of dissolved silica to be supersaturated with respect to quartz, and even higher dissolved silica concentrations are required to be supersaturated with respect to other silica polymorphs.

In hydrothermal chimneys, silica precipitates due to the sharp temperature gradient between the interior fluid conduit (i.e. ~350˚C) and ocean bottom temperatures (~2-4˚C) over distances of the order of centimeters. This promotes rapid cooling of hydrothermal fluids resulting in silica precipitation. This process typically occurs after the precipitation of high temperature massive sulphides (i.e. chalcopyrite) followed by lower temperature sulphides (i.e. pyrite, sphalerite), before an outer ring of silica is formed (Koski *et al.* 1994). The same cooling principle can be applied to sub-surface silicification of existing material (i.e. sediment) where hydrothermal fluids mix with entrained seawater resulting in a silica saturated, conductively cooled fluid, thus promoting silica precipitation within the 'host' material.

Despite typically being supersaturated with respect to quartz, at low temperatures, silica is precipitated as the metastable hydrous polymorph opal-A (amorphous silica)(Jones and Segnit, 1971; Zhu, 2005) and, similar to non-hydrothermal diagenetic chert, it is often thought to form as a silica rich gel. This amorphous gel transitions through the metastable polymorphs of opal-CT, and opal-C before becoming α-quartz, with dehydration (by heat or pressure) driving crystallisation and structural ordering (Zhu, 2005).

2.3 Geological Analogues

Si-Fe materials have been described throughout the geological record at a range of different submarine depositional settings including, but not limited to: ocean spreading centres, back and fore-arc basins, intraplate submarine volcanoes, and anoxic shallow marine basins (e.g. (Hannington *et al.*, 1998; Cope *et al.*, 2010; Hollis *et al.*, 2015; Brusnitsyn and Zhukov, 2018)). They commonly occur as a feature of two main types of economic ore deposits: Banded Iron Formations (BIFs), and volcanogenic massive sulphide (VMS) deposits, both interpreted to be authigenic products of seafloor hydrothermal activity (USGS, 2012; Gourcerol *et al.*, 2016).

The main focus of this project is the potential involvement of Si-Fe materials on the preservation of massive sulphide mineralisation. Although Si-Fe materials at BIF deposits may form by similar mechanisms (i.e. Sun 2015), the lack of accompanying massive sulphide mineralisation does not make them comparable to VMS deposits. Similarly, if Si-Fe materials exist at pre-Palaeozoic VMS deposits, the presence of widespread ocean anoxia could explain their preservation, and therefore would also not provide a suitable comparison in this study. Si-Fe materials from VMS deposits from the Palaeozoic to Tertiary provide the most suitable material for comparison.

2.3.1 Si-Fe material in VMS type models

'Type' models for VMS deposits are hybrids derived from a range of observed VMS deposits which fit into the same general classification (i.e. Mafic-Ultramafic, see Figure 7). They often depict key structures and lithologies that are common between deposits, but potentially do not exist at every deposit. This is supported from descriptions of specific examples of VMS deposits in the geological record (Table 4, Figure 7). Each of the examples presented in Table 4 are discussed later in this chapter and have been selected to illustrate a range of Si-Fe lithologies, each with unique traits that are not necessarily included on the equivalent 'Type deposit' model.

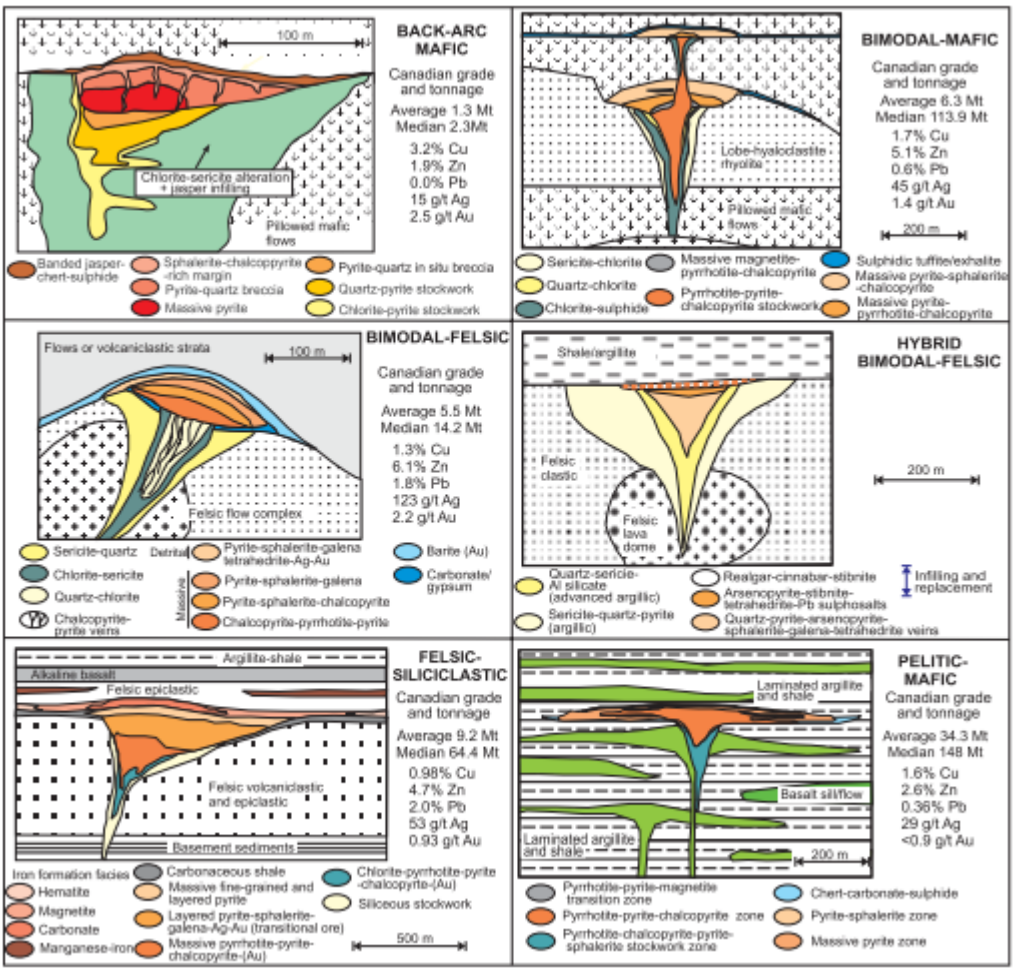

Figure 7: Summary of VMS type deposits from Galley *et al.* (2007)

2.3.2 VMS deposit analogues

Si-Fe materials in VMS deposits, although generally quite similar mineralogically, can form from variable combinations of iron oxide, oxyhydroxide, and silica formation processes. Ultimately a range of factors including stratigraphic thickness, location and distribution, geochemistry, mineralogy, and textural observations can help determine the combination of formation mechanisms, which varies on a deposit scale, and have been assessed (Section 2.3.3 to 2.3.8).

The following section describes a series of geological analogues that have a range of iron oxide sediment, Si-Fe lithologies, and silicified material not associated within iron oxide formation. Each example is typically described at a district scale, however if interesting and relevant individual deposits exist, they have been highlighted (Table 4, Figure 8).

Table 4: Selected occurrences of Si-Fe lithologies associated with VMS deposits

Location	**Geological Setting and Age**	**Description/Occurrence of Si-Fe or Fe-Si material**	**Relevant formation mechanisms of Si-Fe or Fe-Si material**
1) Troodos ophiolite, Cyprus	Fore-arc spreading or subduction initiation, Late Cretaceous	As an apron zone around VMS deposits, tens of meters wide, interbedded with sulphides". Also commonly found within stockwork alteration and within pillow lavas sequences as veins and open-space infill.	Gossan formation (directly overlying ore bodies). Plume fallout, mass wasting, general low temperature silicification distal from orebodies.
References: Hannington *et al.* 1998; Constantinou 1972; Constantinou & Govett 1973; Antivachis 2015; Adamides 1984; Adamides 2010a; Adamides 2013; Boyle 1984; Richards & Boyle 1986			
2) Kuroko deposits, Japan	Back arc basin, Tertiary	Tetsusekiei – 'iron quartz' facies: thin discontinuous beds of haematite and silica overlying massive sulphide ore bodies that extend over ~ 2 times the area of the underlying orebody.	Predominantly exhalites, with minor gossan formation.
References: Ohmoto *et al.* 1983; Tsutsumi & Ohmoto 1983; Kalogeropoulos & Scott 1983; Cathles 1983			
3) Iberian Pyrite Belt, Spain and Portugal	Early intracontinental rifting or back arc thinning, Devonian – Carboniferous	'Red haematitic chert ± magnetite' - Locally developed at the expense of the volcanic or sedimentary host and is reworked as pebbles in overlying tuffaceous and epiclastic beds (pre- to syn-diagenetic).	Predominantly exhalites with minor gossan formation, directly overlies massive sulphide orebodies.
References: Leistel *et al.* 1997; Barriga 1983; Barriga & Kerrich 1984; Barriga & Fyfe 1988			

4) Urals, Russia	Island arc, inter-arc and back arc, Devonian	Directly overlying basaltic volcanics, or associated with flanks of VMS ore bodies. Dominated by quartz and iron oxides within variable carbonate fragments and altered volcanic clasts.	Hydrothermal replacement of volcaniclastic rocks. 'Halmyrolysis' mechanism. Contribution from gossans and biological iron oxide precipitation.
References: Maslennikov *et al.* 2012; Ayupova & Maslennikov 2013; Ayupova *et al.* 2017			
5) Løkken ophiolite, Norway	Back arc system, Ordovician	Massive or laminated beds (extending over several kilometres) and iron silica-sulphide debris-flow deposits, locally abundant near VMS ore bodies.	Exhalites (Plume fallout), minor degree of gossan related mass-wasting
References: Grenne & Slack 2003a; Grenne & Slack 2003b; Grenne & Slack 2005; Grenne & Slack 2018			
6) Myra Falls, Canada	Arc related volcano-sedimentary terrane , Devonian	Semi-continuous horizon of chert 'cap' rock, interbedded with a range of lithologies including siltstone, rhyolitic sandstone and conglomerate, rhyolite, mixed andesite-dacite-rhyolite volcaniclastics, and sulphide/ore related horizons	Exhalite, hydrothermal replacement of clastic material.
References: Jones *et al.* 2006; Jones 2001			

Figure 8: Global distribution of VMS districts, selected here to describe the range of settings, ages and occurrences. Numbers correlate to Table 4.

In addition to this summary, multiple studies provide a more general review of VMS deposits and systematics (Lydon, 1984; Galley *et al.*, 2007; USGS, 2012).

2.3.3 VMS deposits of the Troodos Ophiolite

The closest geological analogue to the mafic-hosted, mid-ocean ridge hydrothermal field studied in this thesis are VMS deposits from the Troodos Ophiolite, Cyprus. The ophiolite has been the focus of a wide range of studies of VMS deposits, from a district scale (Constantinou, 1972; Constantinou and Govett, 1973; Oudin and Constantinou, 1984; Herzig *et al.*, 1991; Adamides, 2010b) down to individual deposit systematics (Pantazis and Govett, 1973; Adamides, 2013; Keith *et al.*, 2016). Study of VMS deposits within the Troodos ophiolite resulted in the creation of the type deposit model for Mafic type VMS (i.e. Figure 5). Furthermore, out of the main VMS 'type' deposits, this is the only model to display iron oxide-rich material directly overlying the massive orebody as a cap, implying that similar processes may have occurred at both Troodos VMS deposits, and the eSMS deposits of the TAG hydrothermal field.

The Troodos Ophiolite is interpreted to represent a Mesozoic spreading centre, possibly relating to a triple junction, or fore-arc spreading in the Cretaceous (Gass, 1968; Moores *et al.*, 1984; Regelous *et al.*, 2014) and has undergone comparatively little deformation (Varga and Moores, 1985; Dilek *et al.*, 1990). This lack of deformation, combined with the presence of multiple large VMS deposits (Adamides, 2010a) enables one of the best comparisons between modern spreading centre settings and a geological analogue.

VMS deposits of Cyprus are typically observed at the contact between 'Lower', comparatively altered pillow basalts, and 'Upper' comparatively unaltered pillow basalts (Figure 9).

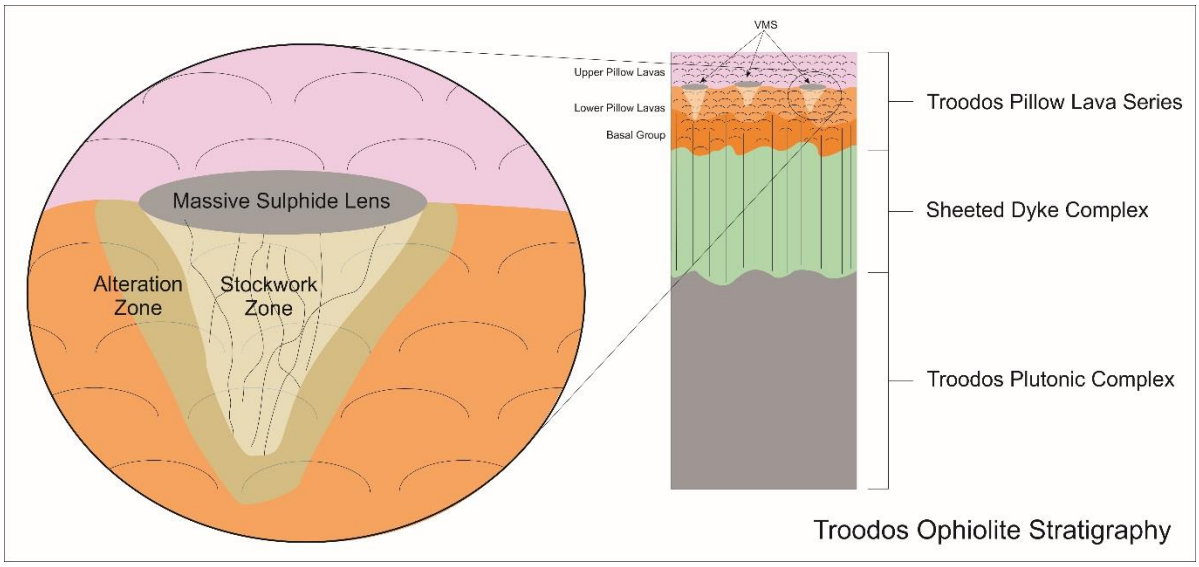

Figure 9: Troodos Ophiolite Stratigraphy and location of VMS deposits within the sequence.

Table 5 shows a summary of Si-Fe and iron oxide dominated materials from individual VMS deposits throughout the Troodos VMS deposits. In this context, Si-Fe materials have been described in the literature by a range of terms from jaspers to iron oxide stained and banded cherts. 'Iron oxide dominated materials' are typically described in the literature as ochres (or of the 'Ochre Group' (Constantinou, 1972; Boyle, 1984)), a term relating to unmetamorphosed iron-rich sediments derived from weathering of massive sulphides).

Table 5: Summary of Si-Fe materials, and iron oxide dominated materials distribution in Troodos VMS deposits (summary from Constantinou 1972; Antivachis 2015; Adamides 1984; Adamides 2010b; Adamides 2013)

Ore body	**Description of Si-Fe material**	**Description of iron oxide dominated material**
Skouriotissa	Jasper occurred as veins and nodules within the Upper part of the Basal Group. Patches of strong gossanitised pillow basalt associated with silicification and abundant red jasper in the lower pillow lavas. Silica cemented brecciated ore (directly over the centre of the ore body) grading upward into	9 m thickness of 'Ochre Group' overlying the massive sulphide orebody. Includes red-brown-orange ochre with graded banding and bedded chert with sulphide.

	banded chert with sulphides. Bands varying in colour from grey, grey-green, pink, brown to haematitic red.	
Kokkinopezula	Jasper associated with silicified lavas within the upper part of the basal group. Pillow structures within basalts associated with the ore body surrounded by pyrite, quartz, and jasper. Red jasper is common in the ore body as variable sized nodules and veins.	-
Agrokipia A	-	Intercalated layer of ochre between the upper and lower pillow lavas.
Agrokipia B	-	-
Kokkinoyia	Abundant red jasper within uplifted, weathered, blocks of the Upper basalt group in the vicinity of the ore body. Red jasper within Zone B of the ore body, associated with pyrite, chalcopyrite, and rare sphalerite.	
Mathiatis North	Red jasper as veins but more commonly nodules up to 30 cm within Zone B of the ore body.	Ochre group overlies the ore body at 3 – 8 m thick. Alternating beds of brown-yellow ochre, siliceous limestone, and siliceous calcareous tuff.
Mathiatis South	Jasper present at various levels and have a 'close spatial relationship' to the mineralisation.	-

	Present as veins in the mineralised zone and surrounding rocks	
Mousoulos	Jasper associated with silicified lavas in the Upper Basal Group. Jasper associated with an 'appreciable portion' of the silica within Zone B of the orebody.	Thin band of ocherous sediment between upper and lower pillow lavas (and directly overlying the ore body). 'Ochre fault' with red haematic ochre and brecciated lava along the fault plane. Ocherous material found within 'inter-volcanic sediments' in the Upper Pillow Lavas.
Apliki	Jasper is widely present in the brecciated lavas and veins or open-space filling between pillows, often associated with epidotisation. Jasper and quartz veining characterises the stockwork zone	Ochre overlies the massive sulphide and underlies a thickness of upper pillow lavas.
East Lefka	Red pyritic jasper occurs within the mineralised zone	-

Si-Fe materials from within the Troodos ophiolite can be separated into three different manifestations: a group of iron oxide dominated sediments that can directly overly the massive sulphide orebodies (and occasionally contain Si-Fe materials), Si-Fe materials which occur as pods and enclaves within the massive sulphide orebodies, and Si-Fe material which occur distally from sulphide dominated ore bodies.

Out of the ten ore bodies summarised in Table 5, five deposits have iron oxide dominated sedimentary material directly overlying the massive sulphide ore bodies. The other five deposits had either already been eroded down into the massive sulphide ore body, thus creating a sub-aerial gossan (and destroying any evidence of potential capping materials) or were directly overlain by the Upper Pillow lava unit. Agrokipia B was the only deposit described to have no significant occurrences of Si-Fe material nor 'ochre group'.

Skouriotissa provides the best example of the iron oxide dominated sediment package, and also contains examples of Si-Fe lithologies. Two units described as 'Bedded chert with sulphides', and 'Red haematitic ochre' material were typically restricted to the ochre-ore contact (Constantinou,

1972). The bedded, finely banded chert unit was observed to directly overlie the massive ore in the central area, and conformably overlie altered lavas to the east and south of the orebody (Constantinou, 1972). Banding is a result of the variable quartz:sulphide ratio, and colouration from the amount and dispersion of iron oxides within the silica at a microscopic level (Constantinou, 1972). The fact that the sulphidic chert unit was conglomeratic near the ore body-sediment interface, and was conformable with both the orebody and the adjacent lava, implies that this unit was the product of silicification of mass wasted sulphide material.

The haematitic ochre was best developed in the centre of the eastern orebody at or close to the top of the ore, and consisted of repeating bands of sulphides, sulphide rich ochre and sulphide poor ochre material (Constantinou, 1972). Highly corroded pyrite material, completely devoid of zoning (unlike pyrite within the underlying massive sulphides), was consistently observed within the ochre units, and the occurrence of chalcopyrite (rimmed by covellite and rarely digenite) was limited to <50 cm above the ore-body sediment, beyond which no copper sulphides were observed (Constantinou, 1972).

Based upon the geochemistry, textures, and association with submarine lithologies, the iron oxide dominated material in Troodos deposits is interpreted to be a direct result of submarine leaching and oxidation of the underlying massive sulphide ore, i.e. submarine gossan formation (Constantinou, 1972; Adamides, 1984; Boyle, 1984). Two different formation mechanisms of the iron oxide dominated material have been suggested: 1) the dissolution of pyrite and precipitation of iron hydroxides and oxides, or 2) alteration of pyrite to iron oxide by a solid-state reaction (Constantinou, 1972; Constantinou and Govett, 1973).

Si-Fe materials were more commonly described within 'Zone B' of the massive sulphide ore bodies, which, when present, is located above the stockwork zone, but below the main massive sulphide ore zone (Zone A) (See Figure 9). The occurrence of Si-Fe material has been interpreted to represent either:

- late stage replacement of conglomeratic massive sulphide ore by silica, where zoned quartz are supposedly pseudomorphs of zoned pyrite material formed by acid leaching of the pyrite and infill of the relict structure by silica (Constantinou, 1972)
- or more likely, entrained fragments of precursor Si-Fe deposits, formed by low temperature diffuse flow at or near the palaeoseafloor during the onset of hydrothermal activity (Hannington *et al.*, 1998).

The fact that this material was observed within the orebody implies that its formation did not likely influence the preservation of the ore body.

In the South Mathiatis deposit, Si-Fe jasper is 'spatially associated' with massive sulphides as veins in the mineralised and surrounding rocks (Adamides 2013). Jasper textures include spherulitic silica, filamentous and ellipsoid structures, and dendritic structures (Figure 10) and are interpreted to be of mixed biological and abiological origin, with evidence of silica crystallisation from a gel precursor (Adamides 2013). Jasper veins are cross-cut by sulphide mineralisation implying that the Si-Fe materials formed earlier than the main sulphidation event (Adamides 2013).

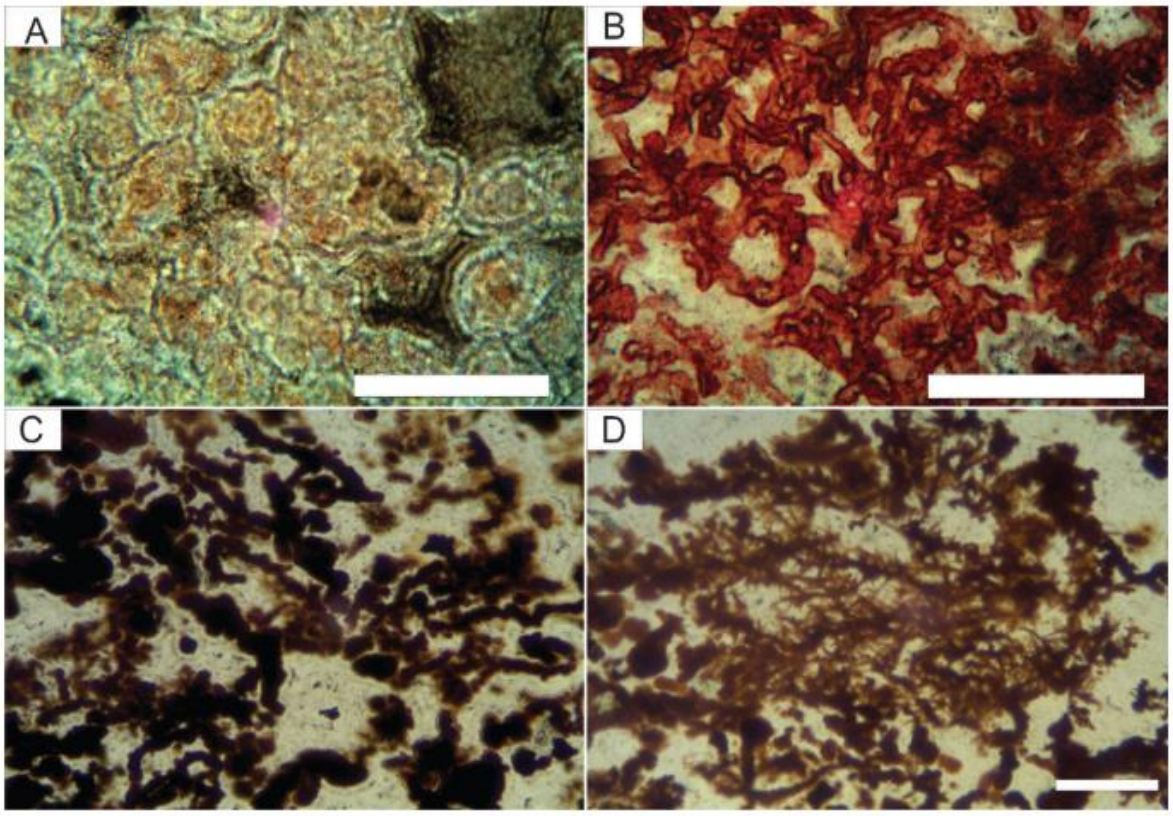

Figure 10: Spherulitic and filamentous/dendritic material from Si-Fe rocks from South Mathiatis (Adamides 2013) Scales are 100 µm.

The final type of Si-Fe materials in the Troodos ophiolite typically occur as interpillow deposits (Figure 11). The iron oxide or oxyhydroxide component is considered to derive from either low temperature sub-seafloor weathering of basalts within a volcanic stack (Richards and Boyle, 1986), or as accumulations of iron rich sediment (i.e. hydrothermal plume fallout, or transported iron oxides from sulphide weathering material) in relict seafloor topography (evidenced by preserved skeletal ostracod remains)(Boyle, 1984). Silicification of this iron oxide material is attributed to low-high temperature hydrothermal fluids, exploiting faulting and factures in the volcanic sequence enabling silicification of the interpillow material (Boyle, 1984; Richards and Boyle, 1986; Hannington *et al.*, 1998). Distribution of iron oxide (haematite) against iron oxyhydroxides (predominantly goethite), is attributed to the temperature of silicification; low temperature fluids (<100°C) may

have preserved goethite, but higher temperature fluids (>100°C) may have transformed goethite into haematite (Boyle, 1984). Pyrite is observed within interpillow basaltic material, despite being distal from massive sulphide ore bodies. This could imply that the pyrite was preserved during sediment accumulation (i.e. mass wasting or plume fallout), or may have been precipitated during late-stage silicification, but this is a speculation without evidence.

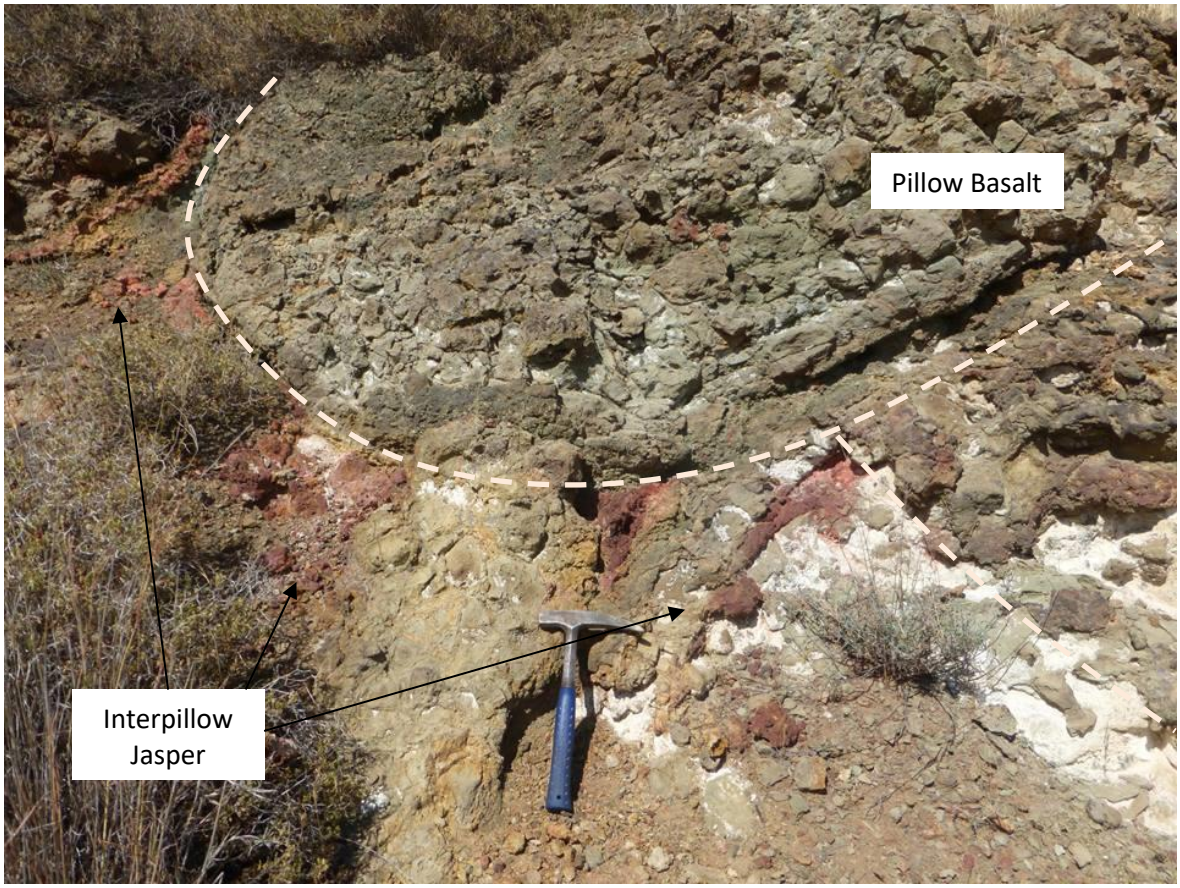

Figure 11: Interpillow jasper and unsilicified iron oxide sediment at Mathiatis, Cyprus. Hammer is ~ 20 cm long.

Some 'Type' deposit diagrams for 'Cyprus-type' VMS deposits show a chert and iron oxide dominated cap directly overlying the ore bodies (Franklin *et al.*, 2005; Galley *et al.*, 2007). Review of individual Troodos ophiolite deposits show that this is likely representing the iron oxide dominated sediment (with minor Si-Fe materials) of the 'Ochre Group', which only occurs at half of the sites described, and in turn does not exhibit the same degree of silicification as implied by the description of a unit of 'banded chert and iron oxide'.

In fact the interpretation that the overlying iron oxide dominated material is derived from the massive sulphides, and that no sulphide minerals are present >50 cm above the ore body in a seafloor weathering profile, implies a relatively efficient oxidation on the palaeoseafloor. The fact that these deposits are preserved in the geological record (without significant synchronous Si-Fe

formations), implies another mechanism is responsible for deposit preservation. Study and modelling of dyke emplacement within the Troodos ophiolite implies that VMS deposits are initially preserved by rapid burial to depths where seawater is unable to weather the deposits, but also requires burial to depths where the deposits are not subject to destruction by dyke emplacement (0.1 km above the 25 percent dyke density surface (Hall and Yang 1994)). This is estimated to be depths between 200 m and 800m beneath the volcanic surface (Figure 12 from Hall and Yang 1994).

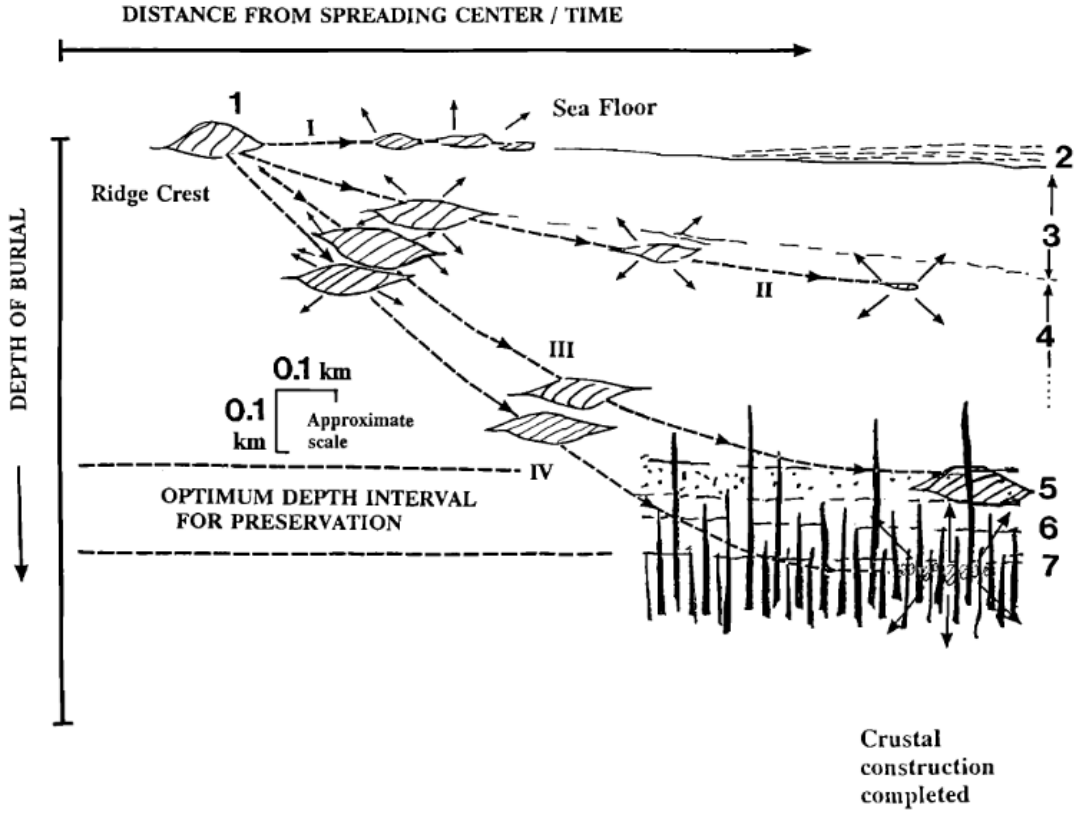

Figure 12: Ideal preservation depth for Troodos VMS deposits from Hall and Yang 1994. Multiple pathways of potential VMS deposit burial within an ophiolite sequence. Too shallow burial would result in seawater oxidation and metal loss/transport (Pathway II). Too deep burial (Pathway IV) would result in destruction by dyke emplacement at depth. 'Optimum burial' (Pathway III), is buried deep enough to be protected from seawater oxidation, but not to be destroyed by dyke emplacement.

2.3.4 Tetsusekiei, Kuroko deposits, Japan

''Tetsuskiei'', literally translated as 'iron quartz', are described as a product of VMS deposits of the Kuroko district, Japan. In contrast to Cyprus VMS deposits, Kuroko-type VMS deposits fall into the siliciclastic felsic type (but contain subordinate basaltic material), and were formed in a Tertiary back arc basin. This difference in geological setting would cause a range of differences within the VMS system, including: differing host lithologies (associated with more siliceous volcanism); a

potential change in hydrothermal geochemistry as a result of differing source rocks; and a likely significant input of volcaniclastic material during ore deposit genesis.

In general, tetsusekiei are interpreted to be a late stage formation product at low temperatures (Cathles, 1983; Eldridge *et al.*, 1983; Kalogeropoulos and Scott, 1983; Tsutsumi and Ohmoto, 1983), that typically directly overlies the massive sulphide ore deposits (Figure 13).

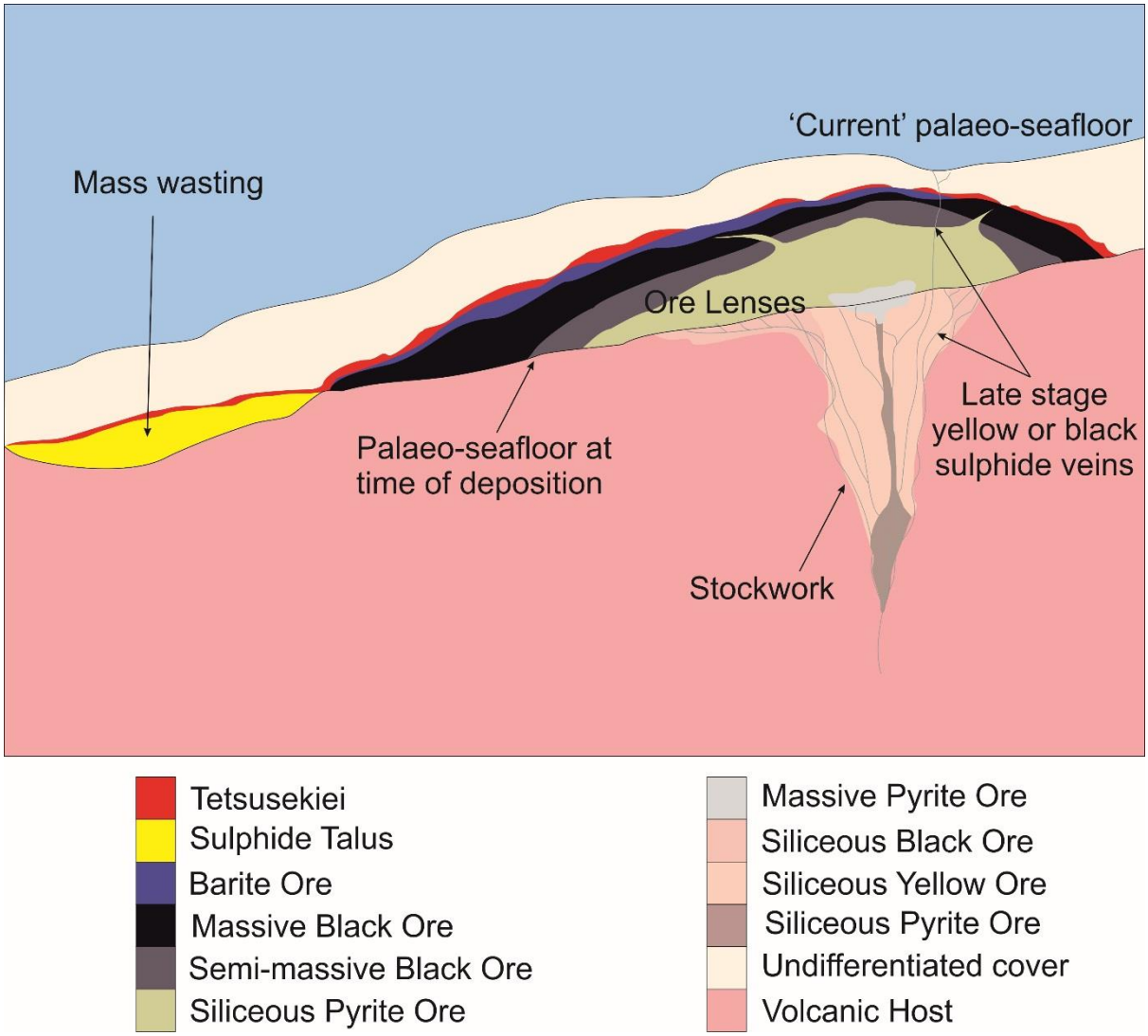

Figure 13: Idealised Kuroko-type VMS model, edited from (Eldridge *et al.*, 1983)

Tetsusekiei occurs discontinuously over roughly double the area of the underlying massive sulphide ore body and is commonly less than 20 to 30 cm in thickness (Kalogeropoulos and Scott, 1983). In its bedded form, tetsusekiei occurs conformably over the massive sulphide ore bodies (or the ore-horizon's tuffaceous host), and is overlain by basaltic tuff/breccia material (Kalogeropoulos and Scott, 1983). Alternating clastic and chemical sediments of bedded tetsusekiei are composed of the same minerals in differing proportions. The clastic beds share textural characteristics with the overlying hanging-wall tuff, the ore horizon tuff, and the upper layered part of the orebody,

whereas the chemical layers are less similar with increased chemical components (Kalogeropoulos and Scott, 1983). As a breccia matrix, tetsusekiei is dominated by quartz, haematite, and pyrite, all of chemical origin.

A three-stage formation model for tetsusekiei in the Kuroko deposits summarised in Table 6 (Kalogeropoulos and Scott, 1983).

Table 6: Three stage formation of tetsusekiei in the Fukazawara VMS deposit

Stage 1	**Stage 2**	**Stage 3**
Initial formation of tetsusekiei (precipitation from low temperature hydrothermal fluids) away from the main locus of sulphides, possibly from satellite vents.	Waning in hydrothermal activity, increased cold oxygenated seawater cooling the system enabling precipitation of tetsusekiei interlayed with tuffaceous material to form a laminated unit overlying the massive sulphide deposit	Resurgence of higher temperature activity resulted in partial sulphidation of iron oxides within the tetsusekiei. This process was aided by the inhibition of seawater ingress after silica precipitation and formation of the tetsusekiei overlying the orebody.

Tetsusekiei are considered to represent an exhalite by precipitation from slow mixing of hydrothermal fluids and seawater within hydrothermal sediments (in this case volcaniclastic material) as the likely mechanism of formation (Ohmoto and Skinner, 1983). The precipitation of haematite is interpreted to potentially represent an excess of iron over dissolved sulphur within the ore-forming fluids, resulting in initial sulphide precipitation (possibly at depth), and subsequent haematite precipitation once the sulphur supply was exhausted, and mixing with oxygenated seawater occurred (Ohmoto *et al.*, 1983). Estimated formation temperatures from oxygen isotopes (including margins of error) range from a minimum of 40°C to a potential maximum of 370°C (Tsutsumi and Ohmoto, 1983). Despite the fact that a back arc setting of the Kuroko VMS deposits is not comparable with a mid-ocean spreading centre or mafic type deposits, the stratigraphic occurrence and broadly comparable mineralogy of tetsusekiei share some important characteristics with the Si-Fe material of this study.

Post-ore intrusion of dacite bodies is interpreted to have aided the mechanical break up of some ore bodies, and chemical modification by fluid circulation (including magmatic fluids, pore water, and seawater/meteoric water) are both interpreted to have a potential role in preservation of Kuroko deposits (Kumita *et al.* 1982). The deposits are interpreted to have been overlain by fine grained basaltic tuffs and mudstones, which were considered to be relatively impermeable (Kumita

et al., 1982). Evidence of continued fluid circulation is apparent by alteration of the hanging wall material (Iijima, 1972) but the overlying consolidated mudstones and tuffs likely hinder fluid movement, limiting further alteration of the orebody (Kumita *et al.* 1982).

2.3.5 Aljustrel and chert in the Iberian Pyrite Belt (IBP), Spain and Portugal

The IBP hosts the Feitais ore body, Aljustrel, Portugal, where an 'up to 15 m thick', stratiform Si-Fe layer, directly overlies and extends laterally away from the massive sulphide ore has been studied (Figure 14, Barriga and Fyfe, 1988). Feitais provides one of the best examples of a thick Si-Fe material which directly overlies a massive sulphide orebody, potentially comparable with the Si-Fe material investigated in this study.

Si-Fe materials at the Feitais orebody appear to be directly related to the generation of underlying massive sulphide. Referred to as the Aljustrel jasper formation, this layer has differing mineralogy proximal to the VMS orebody, compared to distal. The predominant distal end-member is described as a typical jasper (haematitic red chert), and is often accompanied by black manganiferous chert and Mn-oxides. However, the cherts proximal to the ore deposits are interpreted to have been altered to a bluish-grey pyritic chert, with evidence of alteration of haematite to magnetite (muschketovitization) and the occurrence of pyrite indicative of reduced conditions.

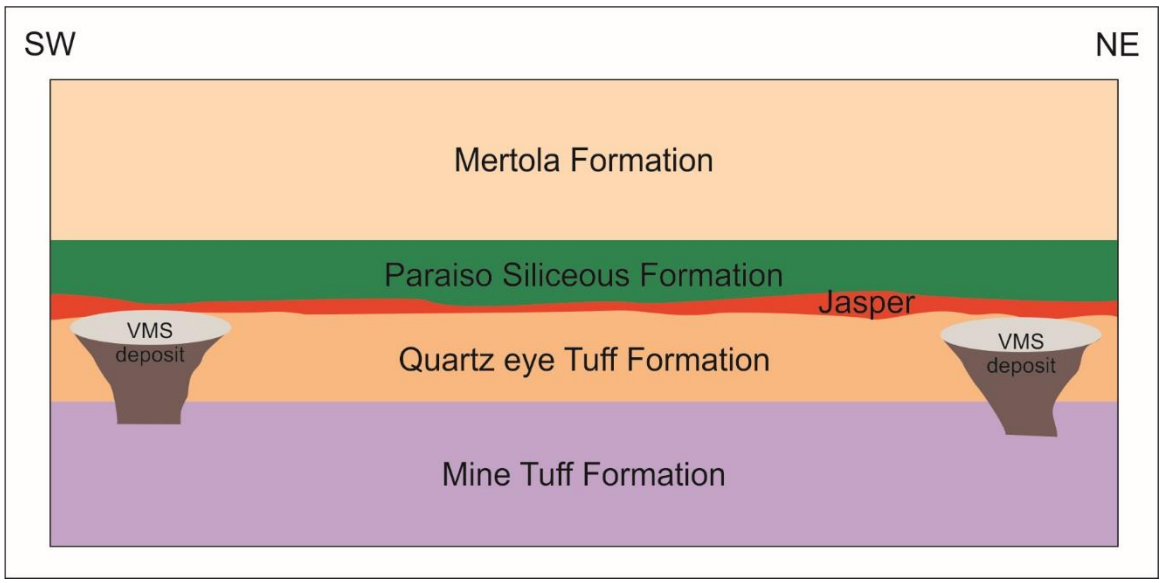

Figure 14: Schematic cross section of the IBP stratigraphy at Aljustrel, with the Aljustrel jasper directly overlying VMS deposits. Diagram modified from Barriga and Fyfe (1988).

Evidence of reduction haloes around veins cross-cutting unaltered jasper, the restriction of red jasper proximal to the ore bodies as relics on the decimeter scale, and the pre-tectonic, likely syn-sedimentary, deformation of these alteration features all imply that the proximal chert is the

reduced, altered, equivalent of the same distal red jasper unit. Quartz separates were analysed for oxygen isotopes were found to be between +17.9% and +20.1% $\delta^{18}O$ (Barriga, 1983; Barriga and Kerrich, 1984), which correlates to silica precipitation at 100-120°C. Primary textures within the jasper were destroyed by recrystallisation, and similar material from elsewhere within the IBP showed evidence of radiolarians in comparable red jasper material, but were noted to not be present proximal to underlying massive sulphide ore bodies (Barriga, 1983; Barriga and Fyfe, 1988), either implying that they were not present, or more likely were recrystallised during hydrothermal activity.

Three formation hypotheses for the origin of the alteration of the Aljustral jasper, and the relationship between the formation of the jasper and the underlying massive sulphide deposits, are discussed (Barriga and Fyfe, 1988) (Table 7), with Hypothesis three the preferred formation mechanism.

Table 7: Three hypothesis for the formation of the Aljustrel jasper formation by Barriga *et al.* 1988

Hypothesis 1	**Hypothesis 2**	**Hypothesis 3**
Early massive sulphide precipitation, followed by jasper precipitation during the waning stage of a hydrothermal cycle. Alteration of the jasper would have taken place during compaction and diagenesis of both sulphide ores and the jasper.	Initial pile of sulphides covered by the jasper, and subsequent hydrothermal venting through both, caused the jasper alteration and possibly modification of the sulphides as well.	Jasper formation took place first, and the sulphides precipitated under the blanket of unconsolidated siliceous sediment, probably as a silica gel. Hanging wall alteration would represent leakage of the impermeable blanket

Chert throughout the IBP has also been studied with four different types recognised (Table 8) and with observed cherts at two different levels within the stratigraphy (Leistel *et al.*, 1997):

- 1) At the lower level – directly at the top of the youngest of three acidic volcanic sequences (VA1), or a few meters above within the tuffite, pelite, and black schist hanging wall
- 2) At the upper level – within the second acidic volcanic sequence (VA2) often a few meters above massive sulphide mineralisation which overlies VA1 facies.

Table 8: Summary of chert facies in the Iberian Pyrite belt after (Leistel *et al.*, 1997)

Chert member	**Main mineralogy**	**Characteristics of the unit**
Red haematitic chert ± magnetite	Microcrystalline quartz, finely crystalline haematite, magnetite, chalcedony	Haematite being altered to magnetite (muschketovitization). At least two stages of silica + haematite with the second event microbrecciating the first and being richer in haematite. Sulphides not abundant, and where present post-date the oxides and are associated with patches of carbonate.
Radiolarian and conglomeratic chert	Same as red haematitic chert ± magnetite, with the inclusion of radiolarians (microcrystalline quartz)	Lateral and vertical variations of red haematitic chert. Conglomeratic chert likely a result of erosion of a partly silicified unit within an unconsolidated mud.
Pale sulphidic chert	Microcrystalline quartz, pyrite, marcasite, pyrrhotite, chalcopyrite, sphalerite, galena, and arsenopyrite	Widespread and cuts the red haematitic chert ± magnetite. Two phases of silica genesis. First phase hosts haematite grains and needles. Second phase hosts sulphides depositing within brecciation of first genesis of silica. Late stage veins and veinlets of quartz do not contain sulphides and may represent infilled tension gashes.
Rhodonite and/Mn carbonate ± magnetite facies	Siderite, ankerite, Mg-kutnahorite, rhodochrosite	Fe or Mn carbonates present as veins cross-cutting chert facies. Younger origin to the cherts, and can locally form large beds

Cherts in the IBP are interpreted to be predominantly hydrothermal with a three stage paragenesis: 1) silica and haematite formation; 2) silicification and sulphidation; 3) carbonate and Mn silicate formation (Leistel *et al.*, 1997). The main observation of these three stages is switches in redox conditions between oxidising (Stages 1 and 3), to reducing (Stage 2), and the apparent change in chemistry with the introduction of Mn and Ca in Stage 3.

Although no stratigraphic links between the range of cherts in the IBP and VMS deposits were identified, the Aljustrel jasper presents an example where the chert can be directly linked to hydrothermal activity, and provides an example of post-depositional alteration of Si-Fe material.

IBP VMS deposits are commonly observed to be stratigraphically overlain, or closely associated with black shales, chert horizons, silts stones, and volcaniclastics (Barriga and Fyfe, 1988; Saez *et al.*, 1996; Gonzalez Clavijo and Spire, 1998; Matos *et al.*, 2011; Oliveira *et al.*, 2013), including Aljustrel. The formation and subsequent preservation is attributed to prolonged hydrothermal activity during volcanic quiescence combined with localised anoxia (implied by occurrences of black shales) (Saez *et al.*, 1996), but this does not include the potential for the Aljustrel jasper and chert horizons associated with the volcaniclastics in aiding preservation of ore bodies.

2.3.6 South Urals, Russia

The Urals present a well-preserved accreted island arc system, where VMS deposits are preserved at multiple levels, unlike other VMS districts (Herrington *et al.*, 2005). Furthermore deposits fall into a range of VMS classifications including mafic, pelitic-mafic, bimodal-mafic, and bimodal-felsic deposit types (Herrington *et al.*, 2005). The lack of metamorphic overprinting has resulted in a range of seafloor related textures and features to be preserved, and in particular a halmyrolysis model for the formation of Si-Fe materials has been proposed (Herrington *et al.*, 2005; Maslennikov *et al.*, 2012). Studies have also used the high degree of preservation within the VMS deposits and Si-Fe materials to study filamentous and other textures interpreted to be biological in origin (Herrington *et al.*, 2005).

Similar to VMS deposits, Si-Fe materials are distributed throughout and are not always in direct contact or associated with sulphide mineralisation (Maslennikov *et al.* 2012 and references there in) including:

- within and overlying sulphide lenses;
- intercalated with layered sulphide turbidites lateral to VMS deposits;
- interlayered with dacitic and basaltic hyaloclastic sandstones;
- directly overlying basaltic volcanics and associated with limestone or ‘carbonates’;
- in basal basalt formations as ‘jasper’, ‘cherts’ and as interpillow infill

Four different members of Si-Fe or Fe-Si materials (summarised in Table 9) throughout a series of VMS deposits in the Urals, are interpreted to be either replacement materials or products of gossan formation (Maslennikov *et al.*, 2012).

Table 9: Summary of Si-Fe material in the Urals (Maslennikov *et al.*, 2012)

Si-Fe type	**Occurrence and morphology**	**Formation mechanism**
Jasperite	Veins, interpillow infill, stratiform beds, lenses, and interbedded with volcanic units.	In-situ replacement of hyaloclastic material
Gossanite	'Sedimentary dispersion haloes around sulphide mounds' formed peripheral to the mounds, 1-10 up to 50-60 mm thick layers directly overlying clastic sulphide ores or sulphide turbidites	In-situ oxidation/replacement of massive sulphide material
Umber or Umberite	Sedimentary sequences, horizons, and lenses. Often associated with gossanites forming peripheral to sulphide mounds. Ranging in thickness from 0.01 – 1 m, averaging 0.3 m.	Seafloor replacement of hyaloclastic material, gossanites or jasperites.
Jasper and sulphidic chert	'Lateral or distal end members of the jasperites, gossanites, and umberites'	In-situ replacement of hyaloclastic material, associated with felsic deposits

In contrast to Troodos, Kuroko, and IBP deposits a different mechanism of Si-Fe generation has been suggested for Si-Fe materials from the Urals, a halmyrolysis model (Herrington *et al.*, 2005; Maslennikov *et al.*, 2012). This model relates to sub-seafloor weathering of volcaniclastic materials resulting in the precipitation of iron oxide and silica and called 'jasperites' (Maslennikov *et al.*, 2012). Hyaloclastic components within the Si-Fe materials increase with distance from massive sulphide ore bodies, and correlates with the disappearance of sulphide minerals. Proximal Si-Fe units are dominated by gossanous material (weathered sulphides), and distal by jasperites (replacement of hyaloclastites) (Maslennikov *et al.*, 2012; Ayupova and Maslennikov, 2013).

Filamentous haematite and quartz bacterial pseudomorphs (examples in Figure 15) were commonly observed (Maslennikov *et al.*, 2012; Ayupova and Maslennikov, 2013; Ayupova *et al.*, 2017). The filamentous material was interpreted to be derived from relict *siboglinids, polychaetes*, and calcareous *serpulids*, fossilised during diagenetic alteration of the primary sediments (Ayupova and Maslennikov, 2013). Haematite associated with fossil material was also determined to be 'geochemically similar' to the surrounding haematite, with the exception of As and P, implying both As and P may be important in the biomineralisation process (Ayupova and Maslennikov, 2013).

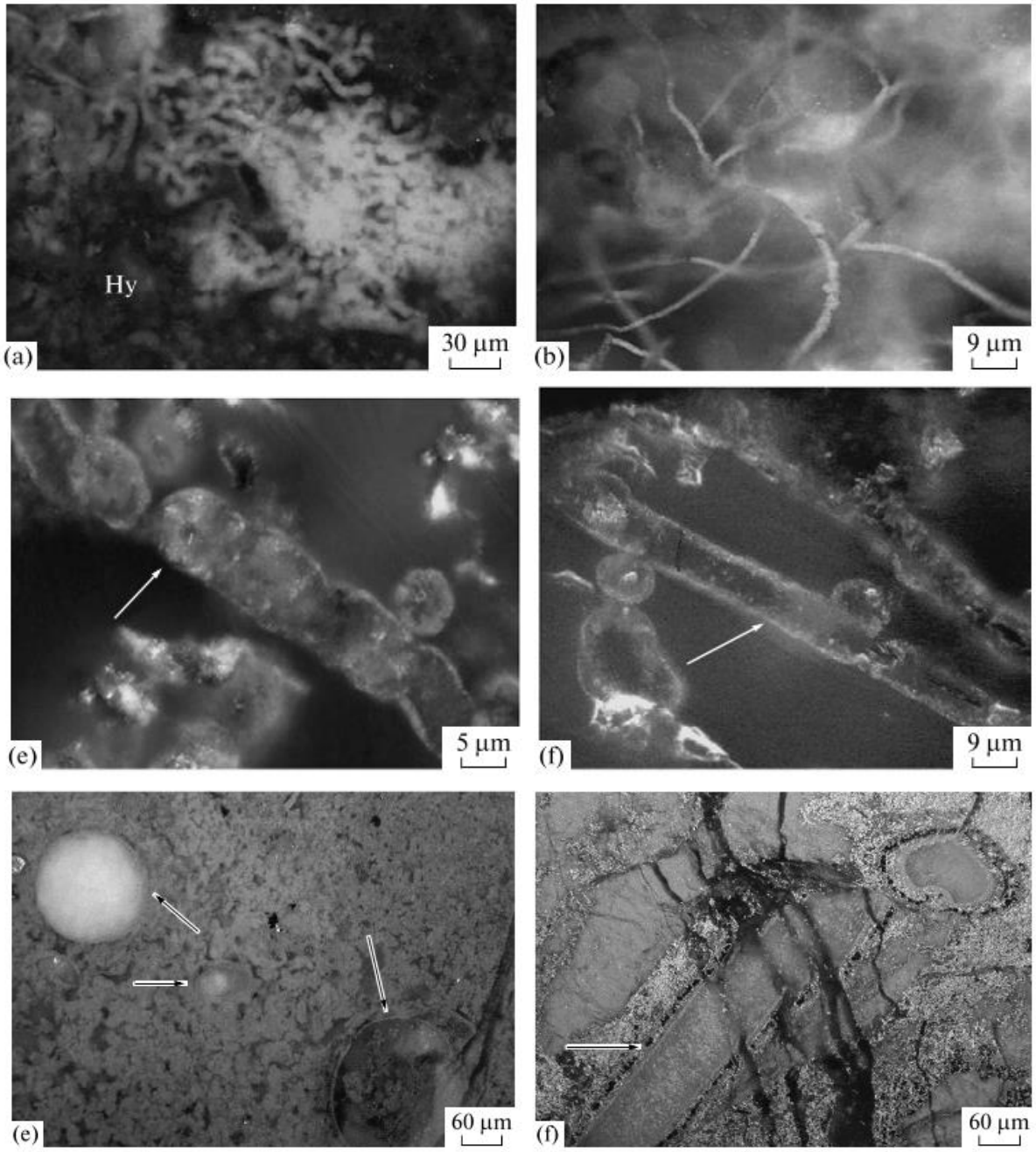

Figure 15: Bacteriomorphic textures in Si-Fe rocks from the Urals (Ayupova *et al.* 2018). (Top left) Haematite filaments. (Top right) twisted-fibrous filaments on chlorite-heamatite-quartz gossan. (Middle left) chain of spheroids. (Middle right) longitudinal cross sections of filaments. (Bottom row) relicts of 'tubular' organisms.

The preservation of VMS deposit research for the Urals focuses more on the preservation from accretion to modern day (i.e. lack of significant deformation or metamorphism) (Herrington *et al.*, 2005) rather than specific deposit type preservation. Based upon the wide range of volcanic, volcaniclastic, and siliciclastic materials often associated with hanging wall strata (Maslennikov *et al.*, 2012) it is likely that preservation is simply attributed to burial. In addition to this, black shale

horizons are observed within clast materials implying that localised anoxia could have also affected ore deposit preservation.

The halmyrolysis model interprets Si-Fe materials to have formed as a function of seawater interaction with volcaniclastic material thus implying the inherent permeability in said volcaniclastic material. It is possible that the Si-Fe product of halmyrolysis may represent a more impermeable material and if this process occurred directly above an ore body it could aid in preservation, but this is a speculative observation.

2.3.7 Løkken Ophiolite

Typically in the VMS districts described in earlier sections, Si-Fe materials occur as lenses, or layers which are not laterally continuous over large areas (i.e. >100s of m). In contrast, Si-Fe materials from the Løkken ophiolite (and associated VMS deposits) are laterally continuous over kilometres (Grenne and Slack, 2003a, 2003b, 2005, 2018).

The Si-Fe lithologies within the Løkken ophiolite are present at thicknesses ranging from several centimeters to over 10m of typically massive or laminated beds that were commonly at or near the stratigraphic level of the VMS orebodies (Løkken and Høydal). Four types of Si-Fe material have been identified throughout the ophiolite (Table 10).

Table 10: Summary of the variation in Si-Fe lithologies in the Løkken Ophiolite

Si-Fe Type	**Description**
Massive	Rare, dense aphanitic distribution of haematite grains (< 3 μm) and matrix quartz.
Laminated	Most abundant. 1-5mm thick laminae with syn-sedimentary disruptions and folding. Primary laminations not laterally continuous, commonly modified or destroyed by redistribution of iron oxides or brecciation.
Brecciform	Common. Beds of angular red haematite clasts within grey-black matrices. Often cross cut by quartz veins which replace laminations, or the matrix is replaced by quartz. Clasts can show both diffuse and sharp contacts with the matrix.
Clasts within sulphide debris flow	Jasper fragments (up to 1m diameter) are angular to rounded, and show characteristics of both laminated and brecciform jaspers.

Si-Fe clasts are commonly intermixed with volcanic rocks as debris-flow breccias. Basaltic lavas distal from the Løkken ore body (200-400 m from interpreted feeder zone of the ore body), generally do not show any evidence of hydrothermal alteration (i.e. alteration minerals or textures) and directly underlie the jaspers. At Høydal, beds of Si-Fe material up to 5m thick directly overlie massive sulphide, or sulphide-jasper-basalt debris flow deposits, and directly underlie the massive sulphide ore body (Grenne and Slack, 2003a, Figure 16). The underlying jasper is bleached by stockwork veining with only a few small haematite patches implying a jasper protolith (Grenne and Slack, 2003a).

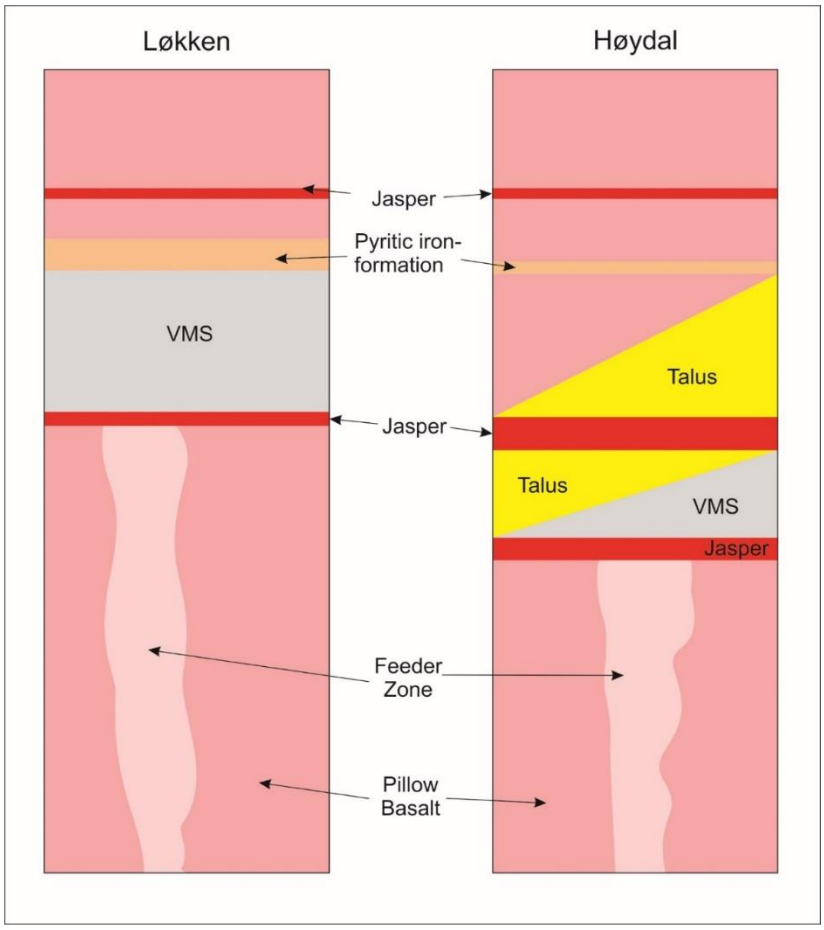

Figure 16: Simplified stratigraphy of the Løkken and Høydal VMS deposits. Modified from (Grenne and Slack, 2005)

The Si-Fe lithologies within the Løkken ophiolite are interpreted to be products of Fe oxide-rich silica-gels, formed from the combination of iron rich hydrothermal plume material and silica rich seawater (Grenne and Slack, 2003a, 2005). This interpretation was principally based on a range of textural and morphological features observed in thin section and hand specimen (examples in Figure 17), Ge/Si ratios (an indication of a plume diluted by seawater with a low hydrothermal component) and similar REE patterns to modern hydrothermal plumes (Grenne and Slack, 2003a, 2005). The high silica ocean content is interpreted to be a feature of Cretaceous seawater, which

transitioned to silica-depleted seawater through the Phanerozoic by the emergence of diatoms (Grenne and Slack, 2003a). Variation in plume output would account for the formation of laminations within the jasper (i.e. variable iron oxide content) and the brecciation and syn-sedimentary deformation of the non-massive jasper units is taken as evidence that volcanism was contemporaneous with plume fallout.

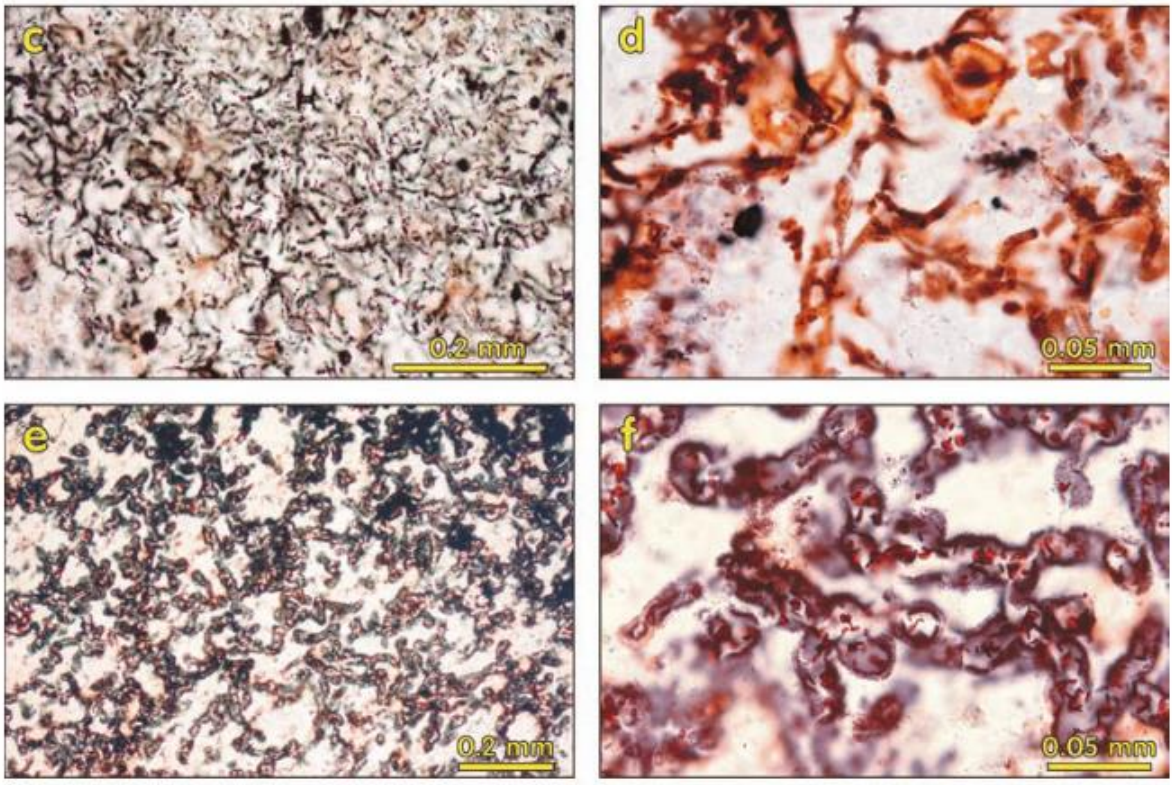

Figure 17: Filamentous material from the Løkken ophiolite, Grenne and Slack, 2003. (Top left) thin curved filaments, (Top right) thin tubular filaments, likely formed during silica gel maturation. (Bottom row) Thick tubular filaments from ~0.8km east of the Høydal deposit

The interpretation of a hydrothermal plume origin for these jaspers accounts for the widespread and stratigraphically repetitive nature of the beds. However, the widespread nature is only attributed to the unusual oceanic conditions (silica-rich ocean) during the early Proterozoic. Modern oceanic conditions are not silica saturated therefore widespread jasper formation as observed in the Løkken ophiolite is not expected. However, textural and potentially geochemical indicators of plume fallout material may be similar. Thus the Løkken ophiolite presents a hydrothermal plume dominated formation end-member example of Si-Fe lithologies. Filamentous material within the Løkken ophiolite (Figure 17) is likely a combination of plume material, and biogenic features.

The widespread and laterally extensive Si-Fe materials imply oxic to suboxic bottom waters during precipitation and, thus during VMS formation (Slack and Grenne, 2018). Recent interpretation of an early Ordovician extinction event has been linked to seafloor anoxia, and the Løkken hydrothermal system has been suggested as a source of exhaled reductants (H_2, H_2S, Fe^{2+}, and Mn^{2+} (Hannington *et al.*, 2005)) that could have contributed to this event (Slack and Grenne, 2018). If this is the case, it could indicate that sustained hydrothermal activity exhaling reductants could cause localised seawater anoxia, thus increasing the chance of seafloor sulphide preservation.

2.3.8 Myra Falls, Vancouver Island

In all previous VMS examples summaries the main focus has been on the occurrence and distribution of Si and Fe containing materials. In general all of the above examples show a relationship between the formation of iron oxides and silica, with both predominantly associated with hydrothermal activity, but not necessarily interpreted as forming a 'cap' directly overlying massive sulphide orebodies. Myra Falls provides one of the few examples of VMS deposits which has a defined capping material, however it is classified as a silica cap, and has no association with iron oxide material. Si-Fe materials are identified within the same basin as the VMS mineralisation, but occur distally on the basin flanks (Jones *et al.*, 2006).

This cap-rock was split into three different units: white chert, black chert, and argillite (Jones *et al.*, 2006) with the most prominent occurrence of the cap directly overlying the Battle VMS orebody. The white chert is best developed directly above the sulphide orebodies; at between 3 and 5m thick, it distally grades into the black chert (Figure 18). Clasts of Si-Fe material exist within the cap and are interpreted to be mass-wasted from basin flank Si-Fe deposits, and not representative of in-situ formation (Jones, 2001).

Fluid micro-thermometry, geochemistry, and textural evidence from the Battle chert cap implies silica precipitation from a hydrothermal fluid at between 100 and 215°C, by replacement and silicification of pre-existing overlying sediments (Jones *et al.*, 2006). In contrast, the nearby 'HW' ore body does not have the same overlying silicified cap as the Battle orebody. This is interpreted this to be a result of the timing of hydrothermal activity in relation to the deposition of the overlying sediments (Jones *et al.*, 2006). The Battle orebody formed syn- and post-deposition of the mudstone, where the sediment cover provided a trap enabling conductive cooling of the hydrothermal fluids, and nucleation sites for the silica to precipitate (Jones *et al.*, 2006). In contrast, the 'HW' ore body formed pre-mudstone deposition.

The lack of high iron content in the silica cap, the lack of benthic fauna, and the distal occurrence of Si-Fe materials both support the hypothesis of stratified oxic-anoxic waters in the basin (Jones 2001), likely increasing the preservation potential of the VMS mineralisation.

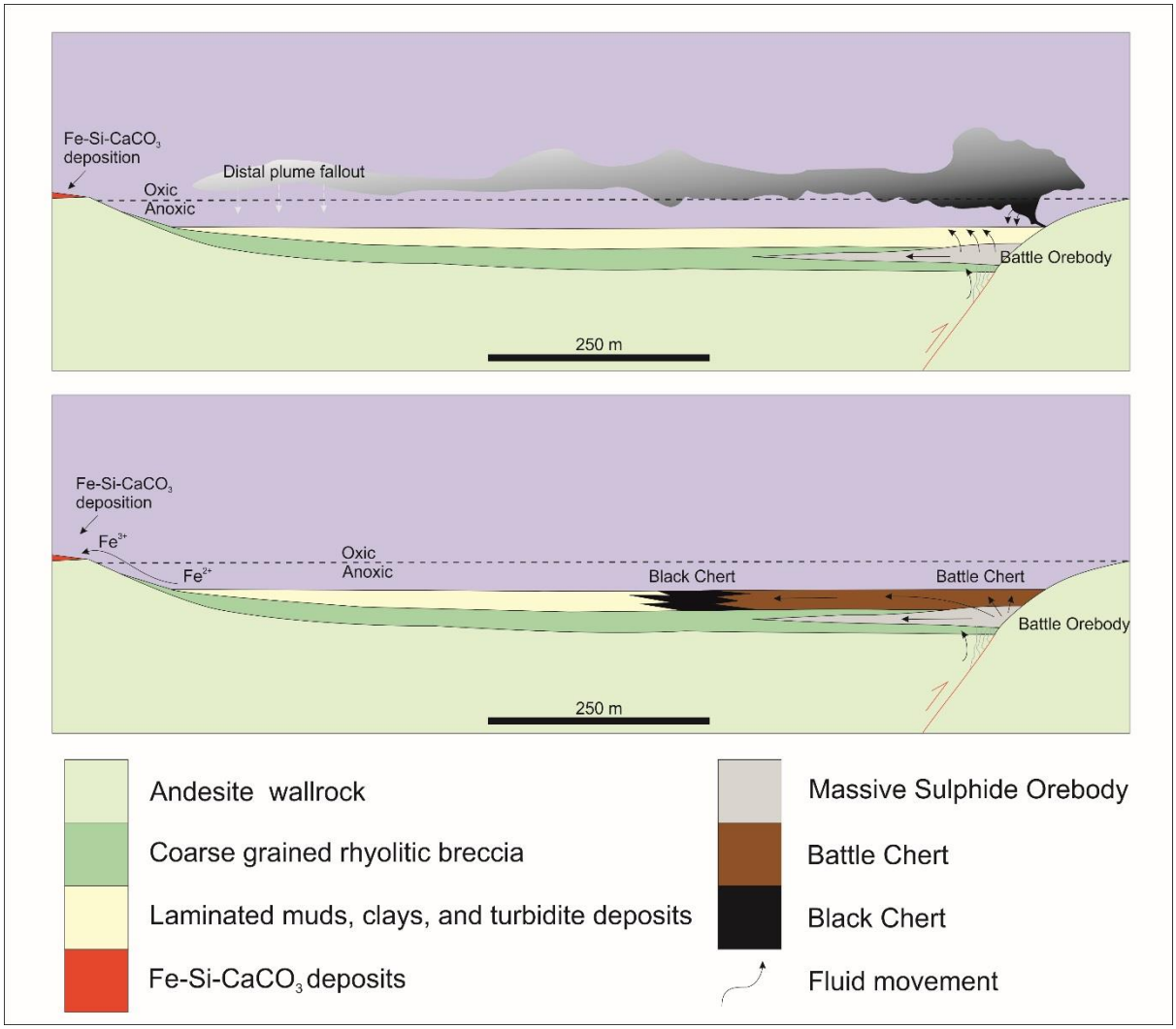

Figure 18: Interpretive chert formation diagram after Jones (2001). Silica rich fluids rose through the overlying siliciclastic sediments and precipitated silica, resulting in the formation of an iron oxide free silica cap.

2.4 Modern Seafloor Environments

Comparison between VMS deposits, and modern day areas of seafloor hydrothermal activity could potentially help understand the role of the Si-Fe lithologies in both the modern and ancient environments.

Similar to VMS deposits, modern seafloor hydrothermal deposits have a wide range of terminologies for referring to iron-silica materials including: red and grey chert, Fe-Si-

oxyhydroxides, Si-Fe oxyhydroxides, jasper, opalite, and Fe-Si crusts, but for simplification are referred to as Si-Fe or Fe-Si materials.

In order to summarise the range of Si-Fe materials associated with seafloor hydrothermal systems different occurrences have been separated into subcategories as follows:

- 'Hard rock' features – surface and sub-surface samples from mounds, and Si-Fe /Fe-Si chimney materials
- Sedimentary deposits – weathered sulphide products, abiological low temperature precipitates, and biologically mediated low temperature precipitates.

Sedimentary related Si-Fe materials have been recovered at significantly more hydrothermal sites, and represent a much greater sample size than hard rock Si-Fe material. Iron oxide dominated sedimentary deposits have also been included within this review, as they can provide evidence of iron oxide formation mechanisms associated with hydrothermal activity which may or may not be independent of silica formation.

A range of modern day examples of deposits (Table 11, Figure 19) where Si-Fe, and iron oxide or oxyhydroxide lithologies have been recovered, inclusive of the TAG active mound, are summarised in Table 11:

Table 11: Selected examples from modern seafloor settings

Location	**Geological Setting**	**Si-Fe or iron oxide dominated material**	**References**
1) TAG active mound/TAG Hydrothermal Field	Ocean spreading ridge	Hard rock Si-Fe material Weathered Sulphide sediment	Hannington *et al.* 1998 Bogdanov *et al.* 2008; Scott *et al.* 2015
2) MESO Hydrothermal field, CIR	Ocean spreading ridge	Hard rock Si-Fe material	Lalou *et al.* 1998; Halbach *et al.* 2002
3) Blanco Fracture Zone	Ocean spreading ridge	Hard rock Si-Fe material	Hein *et al.* 2008; Hein *et al.* 1999
4) East Pacific Rise (multiple sites)	Ocean spreading ridge	Si-Fe chimney Weathered sulphide-derived sediment	Alt, 1988a; Hekinian *et al.*, 1993; Zeng *et al.*, 2008; Dekov *et al.*, 2015

		Abiological/Biological derived, iron oxide-dominated sediments	
5) Lau Basin	Back arc	Si-Fe chimney Abiological/Biological derived iron oxide-dominated sediments	ZhiLei Sun *et al.* 2012
6) Franklin Seamount	Intraplate volcano	Si-Fe chimney	Boyd & Scott 2001; Binns *et al.* 1993
7) Lucky Strike 8) Broken Spur 9) Snake Pit	Ocean spreading ridge (MAR)	Weathered sulphide derived sediment	Bogdanov *et al.* 2008
10) Wocan Field, Carlsberg Ridge	Ocean spreading ridge	Weathered sulphide derived sediment	Popoola *et al.*, 2019
11) Green Seamount	Intraplate volcano	Weathered sulphide derived sediment	Alt 1988b; Alt *et al.* 1987
12) Lilliput Hydrothermal Field (MAR)	Ocean spreading ridge	Abiological/Biological derived iron oxides dominated sediments	Dekov *et al.* 2010
13) Hydrothermal field between segments 27 and 28, SWIR	Ocean spreading ridge	Abiological/Biological derived iron oxides dominated sediments	Li *et al.* 2013; Sun *et al.* 2015
14) Society, Austral, and Pitcairn hotspots	Intraplate volcanos	Abiological/Biological derived iron oxides dominated sediments	Hekinian *et al.* 1993
15) Loihi Seamount	Intraplate volcano	Abiological/Biological derived iron oxides dominated sediments	Karl *et al.* 1989; Emerson & Moyer 2002

16) PACMANUS	Back arc	Abiological/Biological derived iron oxides dominated sediments	Zeng *et al.* 2012; Yang *et al.* 2015
17) Vanuatu back-arc	Back arc	Abiological/Biological derived iron oxides dominated sediments	Iizasa *et al.* 1998
18) Bent Hill and ODP mound	Ocean spreading ridge	Non iron oxide silicified material	Zierenberg *et al.* 1998; Zierenberg & Miller 2000; Fouquet *et al.* 1998

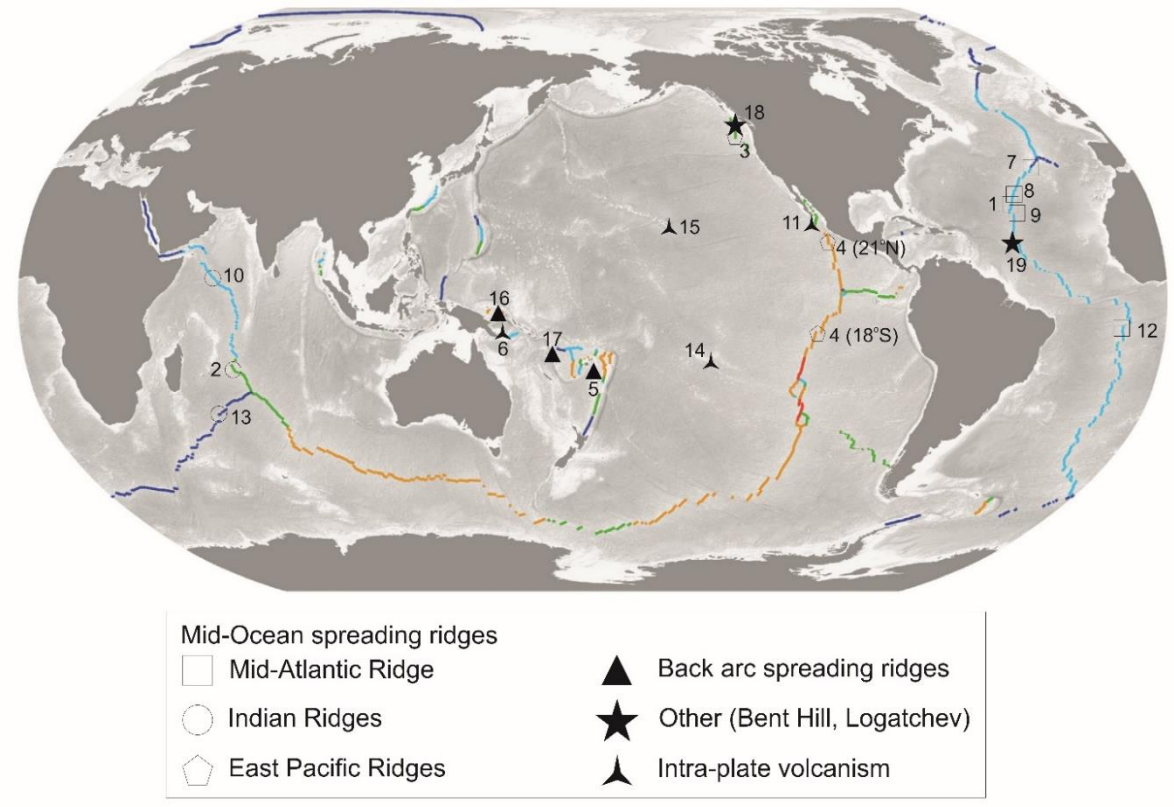

Figure 19: Modern seafloor hydrothermal examples of SMS where Si-Fe deposits have been reported, discussed in this section. Figure adapted from Petersen *et al.* (2016). Numbered sites correlate with Table 11 (No. 14 = approximate location of 3 locations). Colours correlate with seafloor spreading rate (Ultraslow (<20 mm/year) = dark blue, Slow (20-40 mm/year) = light blue, Intermediate (40-60 mm/year) = green, Fast (60-140 mm/year) = orange, Ultrafast (>140 mm/year) = red)

2.4.1 Si-Fe material associated with SMS mounds

In contrast to VMS deposits, solid Si-Fe material is not a common product observed or recovered from active hydrothermal systems. This could be due to the lack of systematic investigation of both SMS and eSMS deposits, the bias of surface samples over sub-surface samples from SMS or eSMS deposits (to date), or that the processes which formed Si-Fe materials in VMS deposits have not yet occurred in SMS deposits.

The few Si-Fe 'hard rock' samples recovered from SMS deposits present the best possible comparison between Si-Fe materials from both SMS and VMS deposits, outside of the samples studied as part of this project (Table 12).

Table 12: Summary of 'hard rock' surface samples of Si-Fe material from modern day hydrothermal vent fields

Location	Description	References
TAG active mound*	Two types of silicified weathered massive sulphide material, differentiated by interpreted initial base metal content	Herzig *et al.* 1991
MESO Zone	Sulphate-sulphide rich jasper	Lalou *et al.* 1998; Halbach *et al.* 2002
East Blanco	Opal-CT and haematite low temperature mound	Hein *et al.* 2008
EPR	Si-Fe chimney	Dekov *et al.* 2015
Lau Basin	Si-Fe chimney	Zhilei Sun *et al.* 2012
Franklin Seamount	Fe-(Mn)-Si chimneys and Mounds	Binns *et al.* 1993; Boyd & Scott 2001
* Only surface samples are discussed in this section. Si-Fe material recovered from drilling of the active mound is discussed in Chapter 3.		

2.4.1.1 TAG Active Mound

Two facies of Fe-Si material were identified from surface samples from the TAG active mound. The first: amorphous iron oxide and silica with atacamite, jarosite and goethite, characterised by a high Au and Cu concentrations and base metal content (up to 23 ppm Au, > 18% wt Cu (Herzig *et al.*, 1991)). The second: amorphous iron oxide and silica with layers of crystalline goethite and locally abundant jarosite, characterised by lower Au and low Cu concentrations (<0.71 ppm Au, < 0.59% wt Cu)(Herzig *et al.*, 1991). These two facies of Fe-Si lithologies were considered to be gossan material, with their base and precious metal differences attributed to the initial sulphide base/precious metal content before weathering.

As the TAG active mound is within the same hydrothermal field as the eSMS deposits that form the focus of this study, a separate short review of historical work at TAG hydrothermal activity, and other relevant information regarding Si-Fe materials has been conducted in Chapter 3. This review of the active TAG mound is presented with the description of the eSMS deposits, and includes the three dimensional stratigraphy of the TAG active Mound (from IODP drilling), and the three dimensional stratigraphy of the investigated eSMS deposits.

2.4.1.2 MESO Zone, Central Indian Ridge (CIR)

The Si-Fe material recovered from the MESO Zone potentially represents the closest analogue to Si-Fe materials associated with VMS deposits.

Si-Fe material was recovered from the surface of the central area of the inactive Sonne Field hydrothermal vent site in the MESO Zone (Lalou *et al.*, 1998; Halbach*et al.*, 2002). A wide range of textures characterised the iron oxide fraction of the material including laminations, dendritic, coral and fan like structures, individual filaments, and potential relict worm tubes (Halbach *et al.*, 2002). Additional silica related textures, including spheres, rods, and filaments were also observed within the samples (Figure 20).

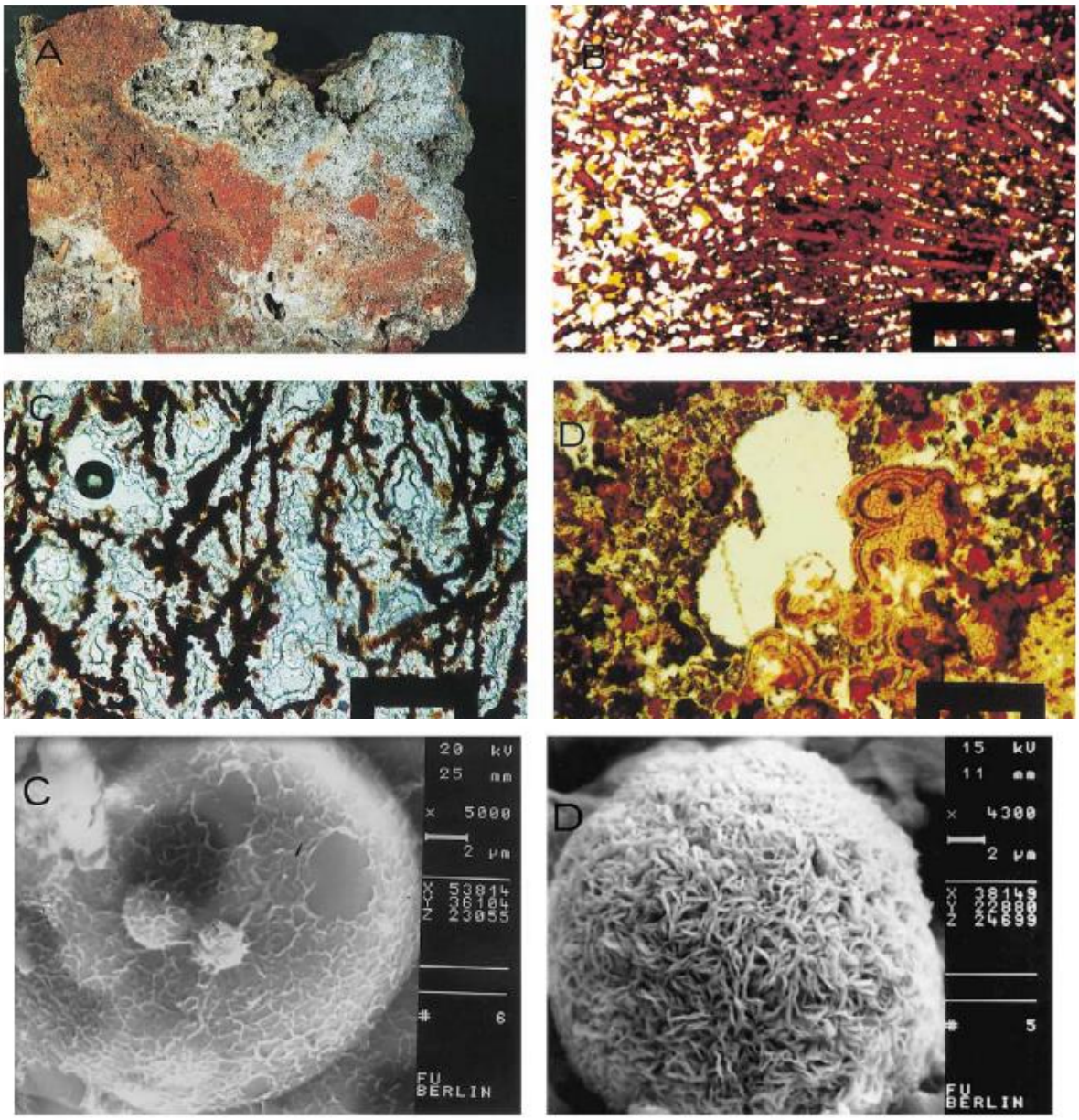

Figure 20: Range of biogenic and iron oxide/oxyhydroxide dominated textures from Si-Fe material of the MESO zone (Halbach *et al.* 2002)

The Si-Fe material is interpreted to represent a late-stage, low temperature hydrothermal environment (supported by silica formation temperature obtained by oxygen isotopes of ~ 63.2˚C) where the origin of the iron oxides was difficult to determine, but the paragenesis was determined from first order observations (Halbach *et al.*, 2002, Table 13)

Table 13: Paragenesis of the sulphide impregnated jaspers of the MESO zone (Halbach *et al.*, 2002)

Formation Phase	**Description**
Iron oxy-hydroxide	Formation of a sedimentary sequence of iron oxides with syn-sedimentary deformation and slumping structures. Origins of the iron oxy-hydroxides difficult to determine (i.e. weathered sulphides, low temperature precipitate, microbial mediation of iron oxide precipitation)
Silica I	Impregnation of the iron rich mud to form the 'jasper'. Silica precipitation from conductively cooled hydrothermal fluids. Desiccated micro-cracks occur within the denser parts of the concentric botryoidal/agate like jasper textures, potentially a result of opal dehydration (opal-A → opal-CT). Fluids ~ 65°C.
Silica II and Pyrite I	mm- to cm- thick rims of massive, white silica hosting small euhedral pyrite grains. Partial recrystallisation and hydrothermal leaching of the jasper to enable localised creation of sulphides. Fluids between 170 and 215°C.
Barite I	Precipitation of an early barite generation, subsequently corroded/dissolved.
Sphalerite I, Pyrite II, Chalcopyrite I	Fe-rich sphalerite, pyrite II and chalcopyrite formed from fluids approaching ~ 225°C. Highest temperature, comparable with white smoker fluids.
Sphalerite II and III	Fe-poor sphalerite (II) followed by Fe-free sphalerite
Marcasite I	Replacement of existing pyrite
Barite II	Sometimes co-precipitated with sphalerite, considerable seawater-hydrothermal fluid mixing.
Silica III	Spheroidal silica coating all older surfaces at ~ 15µm thick and 'solidified' the jasper.

The paragenesis in Table 13 is a general definition, due to the apparent co-precipitation of sulphides (Halbach *et al.*, 2002). Two of the three silica formation stages (Silica I and III) are interpreted to be independent of the main 'leaching' or hydrothermal addition of sulphides and sulphates to the jasper material.

2.4.1.3 East Blanco Depression (EBD)

A 'unique' opal-CT-haematite mound, measuring ~ 5m across by ~1m high, was discovered within a diffuse-flow hydrothermal field, EBD (Hein *et al.*, 2008) and potentially provides an example of modern day Si-Fe material occurring distally to massive sulphide mineralisation. Samples were described as containing millimetre diameter tubular structures and discontinuous wavy laminations, with thin section analysis showing a porous network of dendritic and filamentous silica and haematite (Figure 21, examples from Hein *et al.*, 2008). Hard rock samples were described as being coated by haematite rich mud.

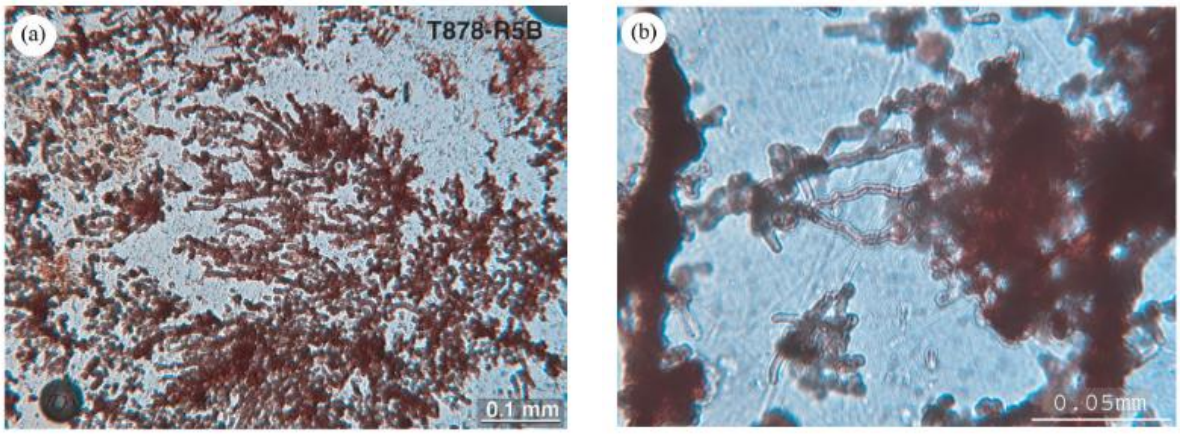

Figure 21: Haematite sheaths and biogenic structures from the Blanco fracture zone low temperature deposit (Hein *et al.* 2008).

The mound is interpreted to represent a partially fossilised microbial mat, altered by diffuse, low temperature, strongly oxidised, silica- and iron-rich, sulphur-poor fluid (Hein *et al.*, 2008). Bacterial mats elsewhere within the EDB hydrothermal field were mineralised by opal-A and barite precipitated from hydrothermal fluids at ~50°C and 100°C (Hein *et al.*, 1999). The presence of haematite (not goethite, nor ferrihydrite), implies a formation temperature greater than ~115°C (Hein *et al.*, 2008). This higher temperature could also explain the presence of opal-CT within a porous medium, implying that the opal-CT did not mature from a precursor opal-A (which would have resulted in a decrease in porosity, something not observed)(Lynne and Campbell, 2003; Hein *et al.*, 2008), but precipitated directly from hydrothermal fluid.

2.4.2 Si-Fe hydrothermal sulphide chimneys

Iron oxides and silica are common as minor phases associated with massive sulphide hydrothermal chimney formation and alteration and are typically products of seawater oxidation of sulphides, and interaction with hydrothermal fluids respectively. On rare occasions, iron oxides and silica can

form the dominant structure within chimneys, implying variation in the physico-chemical properties of hydrothermal fluids (from sulphide dominated chimneys) but forming by similar formation mechanisms. Although sulphide chimney fragments are observed and have been described in VMS ore bodies, Si-Fe chimney fragments have not.

Two silica-dominated hydrothermal chimneys (18°S EPR, and Lau Basin) are interpreted to have comparable formation mechanisms, and are composed of iron oxide/oxyhydroxide filaments, coated by opal-A (Figure 22). Both examples show a clear relationship of early iron oxide/oxyhydroxide filament formation (likely of biological origin) which have acted as nucleation sites for late silica precipitation (ZhiLei Sun *et al.*, 2012; Dekov *et al.*, 2015). The early iron oxides are interpreted to exert a control on seawater-hydrothermal fluid mixing, enabling rapid cooling of hydrothermal fluids, super-saturation of silica, and precipitation as opal-A (ZhiLei Sun *et al.*, 2012; Dekov *et al.*, 2015). Both chimney examples imply growth from outside inwards with silica precipitation acting as a self-sealing mechanism (ZhiLei Sun *et al.*, 2012; Dekov *et al.*, 2015). Oxygen isotope formation of opal-A materials from both chimneys were broadly similar (ranging from +26.6 to + 32.6 (ZhiLei Sun *et al.*, 2012; Dekov *et al.*, 2015)) with calculated formation temperatures between ~ 40 and 70°C. A combination of isotopically light carbon isotope composition of organic material (EPR chimney), and morphological and RNA studies (chimney from the COMRA Discover Expedition (CDE) vent field), provide strong evidence for biological involvement in the formation of filamentous iron oxide materials in both chimneys.

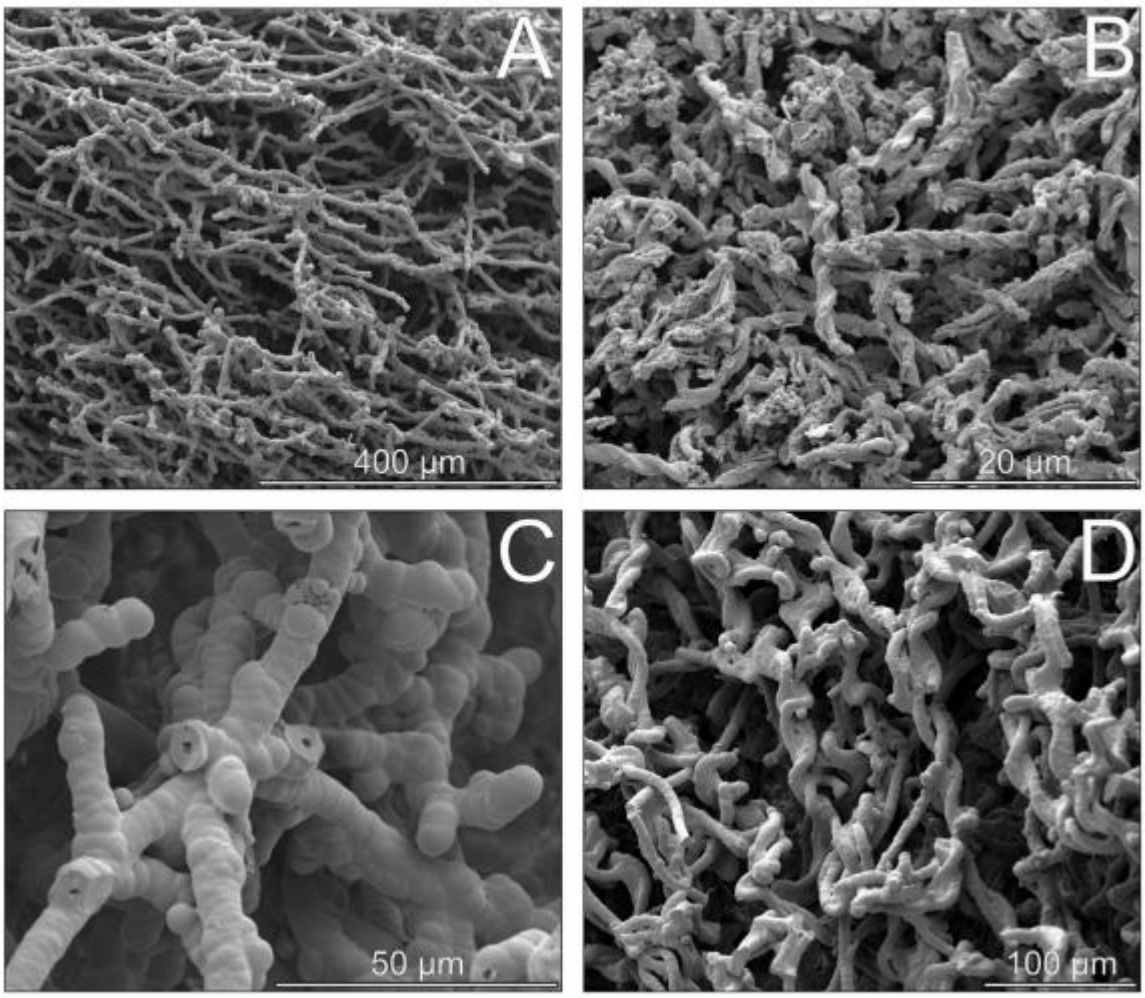

Figure 22: Microbial and bacterial filamentous material from Si-Fe chimneys (Zhilei *et al.* 2012)

Hydrothermal Fe-(Mn)-Si chimneys and mounds have been described and sampled from the Franklin Seamount, Western Woodlark Basin, Papua New Guinea (Binns *et al.*, 1993; Boyd and Scott, 2001). In contrast to the aforementioned Si-Fe chimneys, the Fe-(Mn)-Si chimneys are interpreted to be have early silica filaments formed (likely influenced by biology), with later stage iron oxides/oxyhydroxides, Mn, and nontronite (Binns and Scott, 1993; Boyd and Scott, 2001). Volumetrically significant microbial filamentous material (including fossil remains of iron oxidising bacteria *Leptothrix* and *Gallionella*) and non-biological agglomerates were common across Franklin Seamount (Boyd and Scott, 2001). Thermodynamic and kinetic controls of iron at Franklin Seamount have been investigated, implying that the pH conditions of fluids are close to the triple point of dissolved Fe^{2+}, ferrosic hydroxide, and ferric hydroxide, implying the potential for large quantities of abiological iron oxide precipitation (Boyd and Scott, 2001). Microbial influence is inferred to have converted ferrosic hydroxides into ferric hydroxides, resulting in filamentous textures (Boyd and Scott, 2001).

2.4.3 Iron oxide/oxyhydroxide dominated sediments

There is significantly more un-silicificed, iron oxide/oxyhydroxide related materials observed at modern day hydrothermal vent sites, than observed in VMS deposits. Understanding the sediment accumulation and iron oxide/oxyhydroxide formation mechanisms of these materials (in lieu of Si-Fe material) may provide evidence for the paragenesis of the modern day Si-Fe material investigated in this study.

Sediments that are dominated by amorphous to crystalline iron oxide and/or oxyhydroxides commonly occur at a wide range of hydrothermal sites. These sediments can contain a wide range of other non-iron minerals including: volcanic glass, barite, sulphides, amorphous silica, gypsum/anhydrite, and carbonate (e.g. (Popoola *et al.*, 2019)). Typically, iron oxide/oxyhydroxide dominated sediments are interpreted to have formed by a combination of accumulation processes, with three main inputs: mass wasting of gossan related mechanisms, hydrothermal plume fallout, or abiological or biological accumulation. All three of these mechanisms are comparable with iron oxide material in VMS deposits described in Section 2.3.

2.4.3.1 Gossan related sediment input

Materials recovered from close proximity with existing massive sulphide material (e.g. exterior and plugging massive sulphide chimneys, or loose powdery deposits associated with off axis inactive vents) are likely to be in-situ, or directly associated with massive sulphide weathering processes. However, when sediments have been recovered without this context, occurrence of high base metal content (including Cu, Co, Zn, Ni) often coupled with the presence of trace sulphides enable (Zeng *et al.*, 2008) interpretation of gossan related input to iron oxide/oxyhydroxide dominated sediments.

An example of this is an investigation of ~100 samples of dredged loose amorphous iron oxide material from along the EPR. The modal sediment was interpreted to have a significant gossan derived component because of the presence of trace sulphides, with Cu+Co+Zn+Ni values > 0.1 wt% (Zeng *et al.*, 2008).

Examples of this kind of material have been recovered from a wide range of geological settings and are summarised in Table 14:

Table 14: Gossan related hydrothermal sediments associated with modern day hydrothermal vent fields

Location	**General description**	**References**
East Pacific Rise	Loose amorphous iron oxy-hydroxides	Zeng *et al.*, 2008
Central Indian Ridge	Amorphous to poorly crystalline iron oxyhydroxides with minor goethite and manganese oxides, and silica.	Popoola *et al.*, 2019
Green Seamount	Fine grained goethite with variable smectite content	Alt *et al.*, 1987; Alt, 1988b)

In addition to iron oxide/oxyhydroxide sediments, at least one study has focussed on thin iron oxide films, and coating of massive sulphide boulders and chimneys along the MAR (Table 15). These films could represent in-situ seafloor oxidation of the massive sulphide materials, which could contribute to iron oxide/oxyhydroxide sediments upon collapse and mass wasting of the sulphide chimneys, or potentially represent direct precipitation of iron oxides by the mixing of hydrothermal fluids and seawater during diffusion through sulphide deposits (Bogdanov *et al.*, 2008).

Table 15: Example of non-sediment related low temperature iron oxide deposits along the MAR (Bogdanov, Vikent'ev, *et al.*, 2008)

Hydrothermal Site	**Sample 'type'**
Snake Pit	'Ironshot' film coating sulphide chimney, oxide and sulphide 'crust' coating the chimney, crust on basalt
TAG	'Low temperature' mound, oxide films, massive sulphide loads, and films on sulphide chimneys
Broken Spur	Films on surface of chimneys, films on sulphide plates
Lucky Strike	Films on surface of chimneys, films on sulphide plates

2.4.3.2 Plume related sediment input

It is difficult to identify hydrothermal plume material by textural assessment mainly due to the fact that plume material is very fine-grained or colloidal (Figure 23). Plume contributions to sediments are typically inferred from geochemical studies (Cave *et al.*, 2002; Lough *et al.*, 2019).

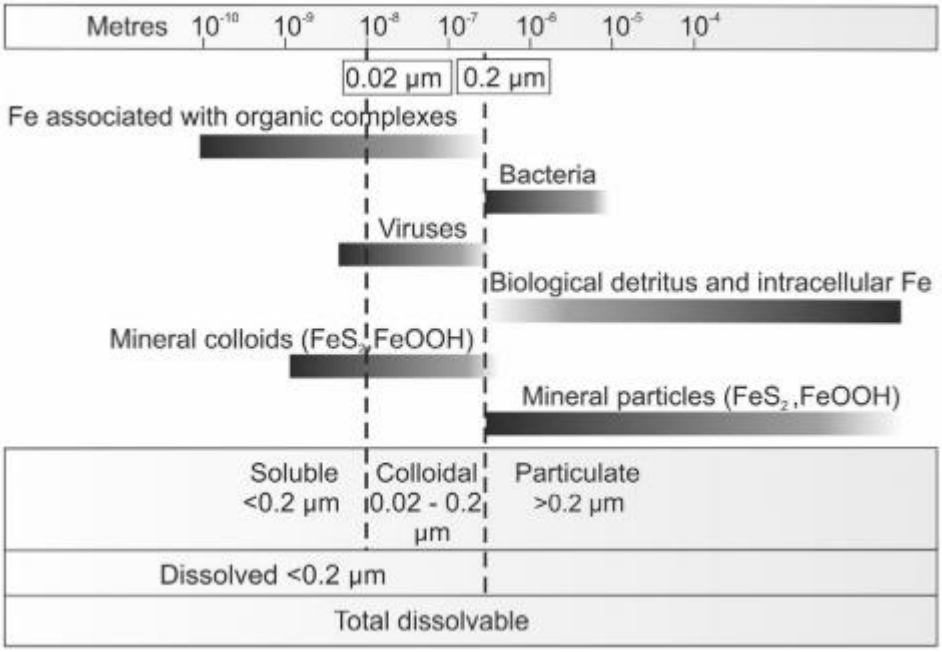

Figure 23: Plume material particle size distribution from Lough (2019)

Plume related iron oxide/oxyhydroxide sediment input has been identified from increased total REE, V and P concentrations, elements which have been scavenged from seawater during dispersal (Zeng *et al.*, 2008).

2.4.4 Abiotic/Biotic iron oxide growth

Another main feature of Si-Fe and Fe oxide sediments across seafloor hydrothermal sites is the presence of complex, microscopic textures of filamentous and dendritic iron oxide/oxyhydroxide materials of contested origin. These textures are commonly interpreted as either evidence for microbial (or bacterial) activity, or as abiological precipitation of iron oxides. Discovery and evidence from modern systems has enabled interpretation and understanding of the role biology can play in iron oxide accumulation and formation throughout time.

A range of modern day hydrothermal sites with iron oxide/oxyhydroxide, or Si-Fe materials which have been studied with respect to biological formation mechanisms are summarised in Table 16. This description also includes a summary of the identified biological or abiological morphologies to highlight the range and ambiguity of the textures.

Table 16: List of hydrothermal sites with Si-Fe and Fe oxide sediments with descriptions, and interpretation of biological vs abiological formation mechanism

Hydrothermal Site	**Description**	**Abiological vs Biological**
MAR vent sites (inc. Snake Pit, TAG, Broken Spur, Lucky Strike)	Early proto-ferrihydrite iron oxide minerals identified in low temperature hydrothermal deposits can often exhibit characteristic filamentous textures, which have been preserved during recrystallisation (commonly into ferrihydrite and goethite)(Bogdanov *et al.*, 2008). Iron oxide mats (Snake Pit and TAG) interpreted to be the product of iron oxidising *Zetaproteobacteria* (Scott *et al.*, 2015).	Predominantly biological
Lilliput	Thin and fragile crust-like layers forming channel and chamber like structures, comprised goethite and x-ray amorphous Fe-Si-oxyhydroxides, goethite and ferrihydrite. At micron-scales the samples were composed of web-like and mesh-like bacterial structures, coated with goethite (observed by SEM analysis) and microbial-like structures resembling iron oxidising bacteria were identified from white and reddish mat-like material coating goethite (by transmitted light microscopy). (Dekov *et al.*, 2010) (Figure 24)	Predominantly biological with some abiological interaction
Segments 27 to 28, SWIR	Sediments/semi-consolidated iron-silica materials, recovered from an area of metal sulphides, relict chimneys and yellow-brown low temperature hydrothermal deposits. The recovered iron-silica samples were composed predominantly of iron oxyhydroxide filamentous structures, sometimes surrounded by amorphous silica or opal-A. The filamentous structures were formed by oxidation and precipitation of iron from hydrothermal fluids creating mineralised sheaths of iron oxidising neutrophilic bacteria (FeOB)(Li *et al.*, 2013; Sun *et al.*, 2015), but the possibility of auto-catalysed abiotic iron oxide growth is not discounted. (Figure 26)	Predominantly biological with potential for abiological contribution

EPR, Society, Austral, and Pitcairn hotspots	Type 1 – Purple-red Fe oxyhydroxides. Typically amorphous Fe oxides with only goethite as well-crystallised phase. Rarely contain nontronite. Sometimes interbedded with brecciated volcanic material formatted as hyaloclastic deposits. Type 3 - Alternating layered nontronite-rich lamellae and purple-red limonite goethite deposits. Also can form as concentric concretions or as powdery precipitates. Type 4 – Opaline Si-Fe oxyhydroxides. Soft lightweight material forming a gel-like precipitate. Forms as edifices or small mounds. Dominated by silica (> 40%) containing amorphous silica, quartz and amorphous iron oxides. (Karl *et al.*, 1989)	All types abiological
EPR - Alt	Fe-oxyhydroxide deposits forming as laminated muds with fragments of more lithified material, both mud and fragments are composed of amorphous iron oxides (with haematite and goethite identified in a few samples). Red Seamount deposits are also associated with laminated nontronite-oxides with variable detrital grains of quartz and pyrite. Proximal to hydrothermal activity, dominant textures include filament morphologies, with rare spherules, and aggregates composed of iron oxide, with at the inactive site deposits comprising broken filaments and sheaths (Alt, 1988a).	Biological
Loihi	Iron oxide deposits recovered as flocculated mats of hydrous ferric oxides, and are texturally amorphous, or occur as sheaths, or twisted or irregular filaments (Emerson and Moyer, 2002b). The bacterial mat deposits are composed of tubular filaments in the order of 1-2 microns diameter, and 200-500 microns in length (Figure 25). Organic material was identified within 1-2% of filament cross sections, with only ~1.8 wt% organic carbon in the mat samples(Karl, Brittain and Tilbrook, 1989). Cultures from Loihi samples enabled isolation of two strains of iron oxidising bacteria, both interpreted to be dominant at hydrothermally low temperatures (i.e. 20-30°C)(Emerson and Moyer, 2002b).	Biological

PACMANUS	Loose, fragile, low density iron-silica-manganese samples (Zeng *et al.*, 2012). Three sample suites were determined based upon colour (black, yellow, and yellow-green)(Zeng *et al.*, 2012). The Fe-Si-oxyhydroxide samples were composed of opal-A, iron oxides, manganese oxides, and nontronite, and displayed a wide range of microtextures that resembled bacteria-like strands encrusted with Fe-Se oxyhydroxides. Samples obtained from the same cruise were described with a range of textures described, including rod-like, twisted, and sheath-like filaments, along with globular and spherical grains. (Yang *et al.*, 2015)	Both abiological and biological growth.
Lau Basin	Yellow to orange-yellow and green, laminated, semi consolidated materials and are texturally dominated by filamentous materials, including radiating and mesh-like patterns, composed of single and branching rod-like and thread filaments, and twisted stalks of iron oxides.(Zhilei Sun *et al.*, 2012) interprets two silica generations with the first co-precipitating and adsorbing onto the surface of microbially mediated iron oxides, and the second precipitating from conductively cooled hydrothermal fluids utilising the iron oxide-silica filaments and mats as nucleation sites resulting in a coating of opal-A.	Biological
Vanuatu – Futuna Trough	Semiconsolidated amorphous Fe-Si precipitates and manganese oxides, with trace barite, pyrite, marcasite, chalcopyrite, and sphalerite. The deposits are typically either massive or filamentous, displaying web-like networks of filaments with tube-like voids and colloform textures (Iizasa *et al.*, 1998). Goethite is present as amorphous in the upper layer to well crystallised at depth in the Futuna Trough gravity core and interpreted to be a direct hydrothermal precipitate rather than weathered sulphide material (Iizasa *et al.*, 1998). The increase in crystallisation with depth is interpreted to reflect aging of the material where relatively unstable ferric oxyhydroxides partially dehydrate to more stable crystalline goethite (Schwertmann, 1983).	Unknown – but abiological mechanisms evidenced.

Table 16 covers Si-Fe material across a range of geological settings, which display a range of common textures, but also show variable interpretations as to whether the material is biologically or abiologically controlled. Loihi Seamount was the location of a series of studies focussed specifically on the biological aspects of these deposits, and provided solid evidence of biological involvement by isolating bacteria from filaments. However, this study also highlights the difficulty in the determination of biological activity, even in active modern systems with only 1-2% of the filamentous material containing organic material (Karl *et al.*, 1989).

Other than the difficulty in interpreting the exact origins of the iron oxide components, the origin of the silica is often interpreted as a product of conductively cooled hydrothermal fluids. Generally, the iron oxide filamentous material pre-dates the silica, and is often interpreted to represent a network of nucleation sites for silica precipitation. This mechanism may be the main difference between an iron oxide/oxyhydroxide only sediment, and an Si-Fe sediment.

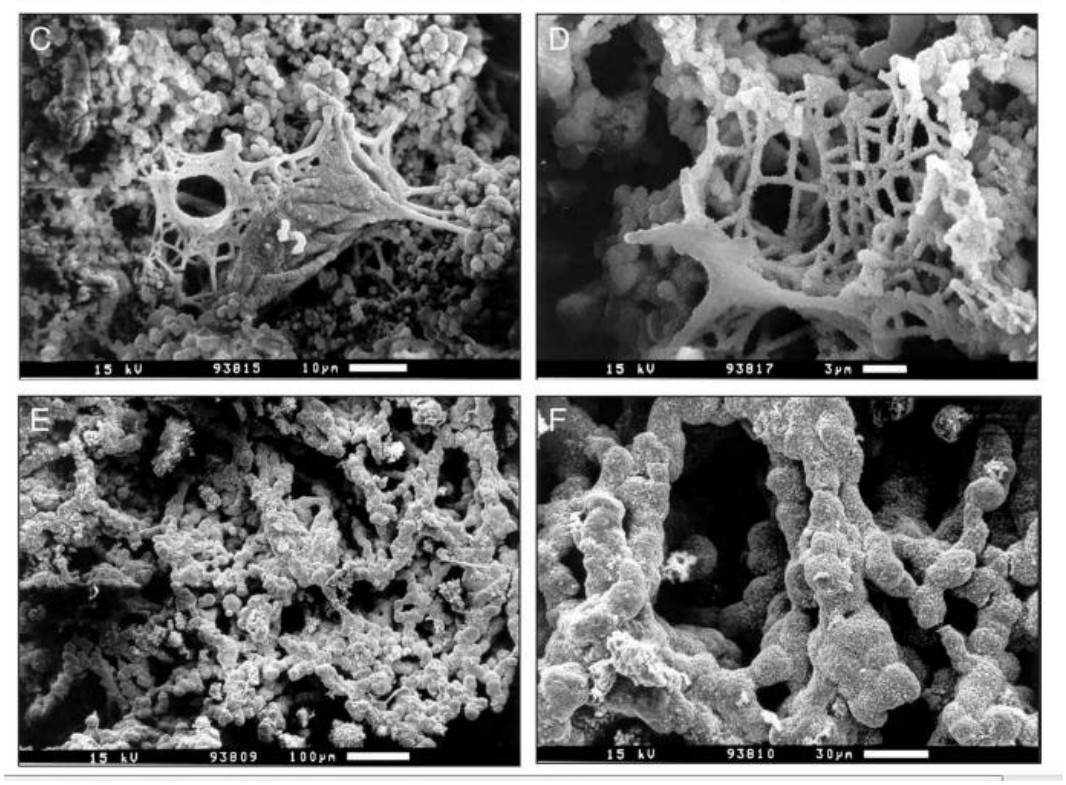

Figure 24: Microbial and bacterial material from the Lilliput hydrothermal field

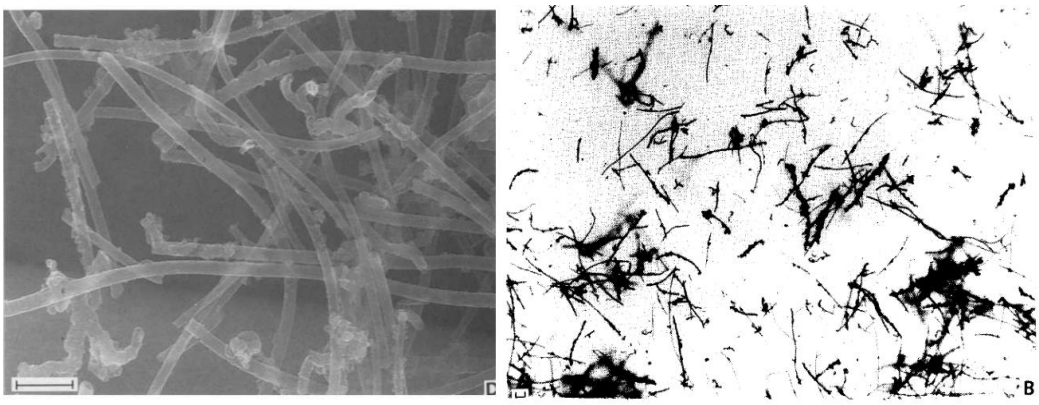

Figure 25: Bacterial filamentous iron oxides from the Loihi Seamount (Karl 1989)

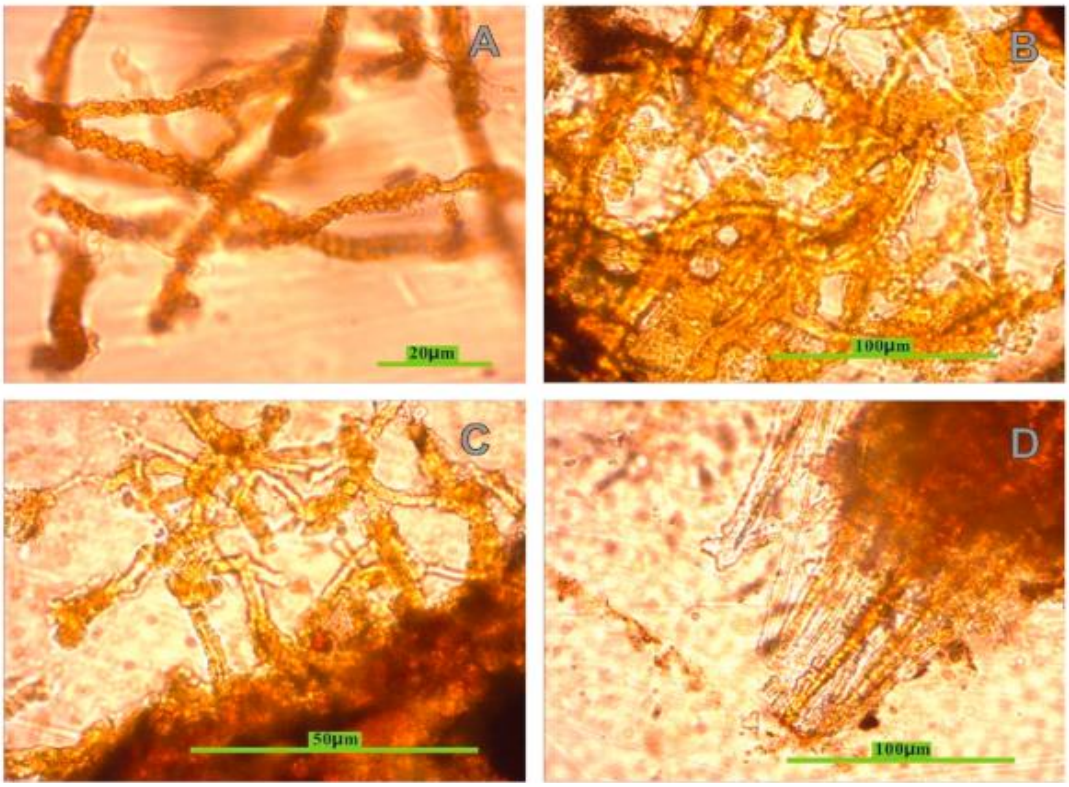

Figure 26: Si-Fe filamentous material from SWIR, including twisted filaments (Sun *et al. 2015*)

2.4.5 Non-iron oxide related silicification

Silicified material that is comparable to the Myra Falls VMS deposit, and considered a direct product of hydrothermal activity but not associated with iron oxides, is also observed within modern day analogues.

Bent Hill and ODP mounds are located on the Juan de Fuca spreading ridge and were the subject of drilling during ODP Leg 169 (Zierenberg and Miller, 2000). Both SMS mounds are hosted within a thick of sediment sequence (100s m), with Bent Hill showing a typical single ore lens over a feeder zone structure, and ODP mound revealing three stacked ore lenses and feeder zone complexes,

with both overlying an anomalous deep copper zone (DCZ). The DCZ is a thickness of sulphide-impregnated sediments, directly overlain by a layer of intensely silicified sediments. Sulphides present as subhorizonal veins and replacing sedimentary features such as parallel and cross bedding, and burrows (Fouquet *et al.*, 1998) in the DCZ. Other silicified layers with associated pyrrhotite and lesser pyrite were determined to be at comparable depths to the DCZ but did not host significant copper mineralisation.

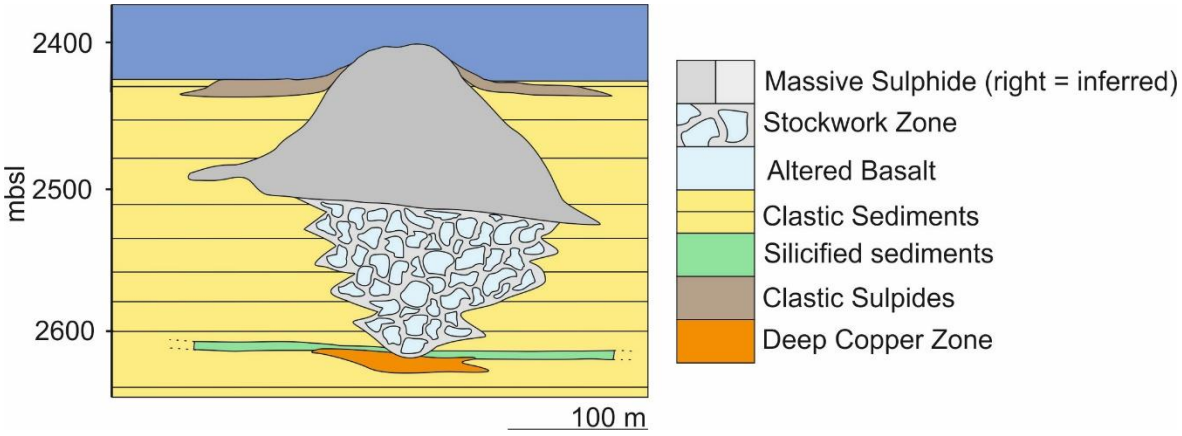

Figure 27: Simplified Bent Hill cross section, modified after Zierenberg *et al.* (1998). Silicified sediment represents an impermeable barrier which delineates the top of the DCZ unit. Note that this unit and the DCZ are both deeper than both the main ore body and stockwork zone.

The silicified layers are interpreted to form as a result of lateral movement of fluids through a permeable sandstone unit with subsequent conductive cooling promoting silica precipitation (Fouquet *et al.*, 1998). This silica precipitation provided a hydrological control on the system, forming an impermeable cap (Zierenberg *et al.*, 1998), similar to the mechanisms of Si-Fe chimney growth where silica precipitation limits fluid mobility (Dekov, 2015). Subvertical veins within the DCZ are interpreted to represent high permeability fluid pathways through the silicified unit. When the veins closed, the decrease in porosity facilitated further lateral movement and mass deposition of Cu-Fe sulphides (Zierenberg *et al.*, 1998).

The Myra Falls deposit discussed in Subsection 2.3.7 provides an interesting analogue to the Bent Hill and ODP mound deposits, with the presence of a sedimentary protolith enabling silicification to take place, and promoting lateral fluid flow and further silicification.

2.5 Summary of comparison between ancient VMS and modern SMS Si-Fe lithologies

A summary of the main comparative features of Si-Fe material at VMS vs SMS deposits in summarised in Table 17, however it is important to consider the inherent sample bias between VMS and SMS deposits. One of the benefits of VMS deposits is that they have been preserved and emplaced onto continental crust during obduction of ophiolite sequences. They present a much easier environment for exploration and recovery of materials throughout the VMS system including 'palaeo'-subseafloor samples, hanging and footwall materials, a wide range of ore body samples, and deeper and more widespread alteration assemblages associated with hydrothermal activity. In contrast, sampling of SMS deposits have historically been limited to surface sample recovery by dredges or ROV grab arms, with very limited three-dimensional data available.

Ironically the presence of subaerial gossanous material (e.g. those observed at a range of Troodos VMS deposits), commonly used to discover VMS deposits on land, means that the overlying material has been eroded away, likely removing paleo-seafloor weathering products, the predominantly sampled material type at SMS deposits. Si-Fe materials recovered from the VMS analogues described in this chapter are all interpreted to have formed at or near the palaeo-seafloor and likely present the best comparison with samples from modern day SMS deposits.

Table 17: Summary of comparison of iron-silica lithologies between VMS deposits and SMS deposits

	VMS deposits	**SMS deposits**
Type of Si-Fe materials recovered	Predominantly Si-Fe material, dominated by high silica contents. Some iron oxide dominated sediments, typically attributed to sub-seafloor or sub-aerial gossans.	Generally not recovered as Si-Fe materials, typically semi consolidated or unconsolidated iron oxide dominated material.
Spatial distribution of Si-Fe materials at each deposit time	Commonly recovered at the periphery of sulphide mineralisation, at basal alteration zones, as interpillow infill and as veins and clasts within stockwork zone. This Chapter presents examples of both common and uncommon Si-Fe materials which overly massive sulphide orebodies.	Sampling is generally limited to surface samples, but Si-Fe materials have been recovered at or near the seafloor. Unsilicified material is associated with pillow basalts, massive sulphide ore bodies, or general sediment substrate.

Mineralogy	Typically dominated by quartz and haematite, can contain a range of accessory minerals including calcite, chlorite, magnetite, manganese oxides, and fragments of volcanic glass.	Iron oxides: typically goethite, ferrihydrite, and/or amorphous. Silica: typically amorphous silica or opal-A, and rarely opal-CT. Quartz and haematite samples observed from limited sub-surface material.
Silicification mechanism interpretation	Silicification typically interpreted as a product of conductive cooling of hydrothermal fluids (low temperature)	Silicification typically interpreted as a product of conductive cooling of hydrothermal fluids (low temperature)
Iron oxide formation mechanisms	Iron oxides form from a range of processes including: weathering/alteration of massive sulphides or hyaloclastic material, hydrothermal plume fallout, and direct low temperature precipitation (abiological and biological)	Iron oxides form from a range of processes including: weathering/alteration of massive sulphides, hydrothermal plume fallout, and direct low temperature precipitation (abiological and biological).
Potential role of biology?	Filamentous textures are common, likely a result of biological activity, but this often remains ambiguous due to lack of biological material.	Filamentous textures common and resemble bacteria strands or microbes, organic carbon preservation and RNA analysis directly imply biological involvement in at seafloor.

Chapter 3 The TAG Hydrothermal field and the discovery of the Si-Fe cap

Review of VMS deposits and modern seafloor hydrothermal activity, has determined that it is difficult to compare typical VMS preservation mechanisms (i.e. rapid burial by impermeable material and/or sustained localised seafloor anoxia during deposit formation), with modern deposits. The lack of ocean anoxia, the bias towards surface sampling (at both SMS and eSMS deposits), with 3D assessment typically restricted to active SMS deposits makes this the case. Only review of the evolution of SMS deposits to eSMS deposits, including 3D characterisation, can provide insight on the degree of preservation in eSMS deposits and investigate if and how preservation occurs on the seafloor.

The TAG Hydrothermal field was selected for study as part of the Blue Mining Project, an EU FP-7 funded collaboration to understand the range of processes that can occur as SMS deposits transition to eSMS deposits, which may or may not aid deposit preservation. The active TAG mound is considered one of the most well studied and constrained examples of an actively forming SMS deposits, but the eSMS deposits in the same field were understudied. Hence, characterisation and comparison of surface and sub-surface features of the eSMS deposits with the active TAG mound could elucidate common processes that occur after hydrothermal activity ceases.

Review and comparison of the surface features of eSMS deposits in the TAG hydrothermal field with the active TAG mound can provide an example of the range of destructive processes that have affected SMS deposits, during the transition to eSMS deposits. Furthermore, if the surface assessment of eSMS deposits can indicate the degree of seafloor weathering of eSMS deposits, assessment and comparison of the sub-surface geology of both eSMS and SMS deposits can provide an indication of the degree of preservation of eSMS deposits.

Part of the work presented in this Chapter (predominantly Section 3.2 and 3.3) was contributed to the following journal article:

Murton, B.J., Lehrmann, B., Dutrieux, A.D., Martins, S., Gil de la Iglesia, A., Stobbs, I.J., Barriga, F.J.A.S, Bialas, J., Dannowski, A., Vardy, M.E., North, L.J., Yeo, I.A.L.M, Lusty, P.A.J., Petersen, S., 2019, Geological fate of seafloor massive sulphides at the TAG hydrothermal field (Mid-Atlantic Ridge), Ore Geology Reviews, **107**, 903-925.

3.1 Historical and modern investigation of the TAG Hydrothermal Field

The TAG hydrothermal field (Figure 28) is a ~5km by ~5km area at water depths ranging from ~2300 m to 4000 m, located at 26°N along the Mid-Atlantic ridge (Rona *et al.*, 1993). It is one of the best studied hydrothermal fields with an active mound, two areas of inactive mounds (ALVIN zone and MIR zone), and an area of low temperature activity (Rona *et al.*, 1993; Rona *et al.*, 1993). Since its discovery in 1972 (Scott *et al.*, 1974), multiple research expeditions have investigated the hydrothermal field including Leg 158 of the Ocean Drilling Programme (ODP) when the TAG active mound was drilled (Humphris et al. 1996). Historically, research has been focused on the TAG active mound including detailed geological (Humphris and Kleinrock, 1996; You and Bickle, 1998; Petersen et al., 2000), geochemical (Fouquet *et al.*, 2000; Humphris and Tivey, 2000) and geophysical (Tivey *et al.*, 1995; Tivey et al., 1996; Humphris and Tivey, 2015) studies.

As part of the Blue Mining project, two research cruises were completed in the summer of 2016 focussing on a multidisciplinary approach to investigating extinct seafloor massive sulphide deposits. This included ship based and Autonomous Underwater Vehicle (AUV) based bathymetry, multichannel seismic surveys, 2D and 3D electromagnetic surveys, robotic underwater vehicle (RUV) surveys, deployment of a robotic seafloor drill (the BGS's RD2), the recovery of a range of surface grab samples, and the recovery of sediment cores.

High-resolution (~2 m) bathymetric mapping obtained by GEOMAR's AUV, during the M127 research cruise in 2016, shown in Figure 28 depicts the areas of interest and focus, including the known areas of eSMS deposits: Alvin Zone and the MIR zone.

Surveys of the surfaces of the SMS deposits indicates the extent of sediment cover, the degree of seawater weathering, and where exposed, the shallow interior including sulphide material. In describing their surface geology, it is useful first to consider the hydrothermally active TAG mound.

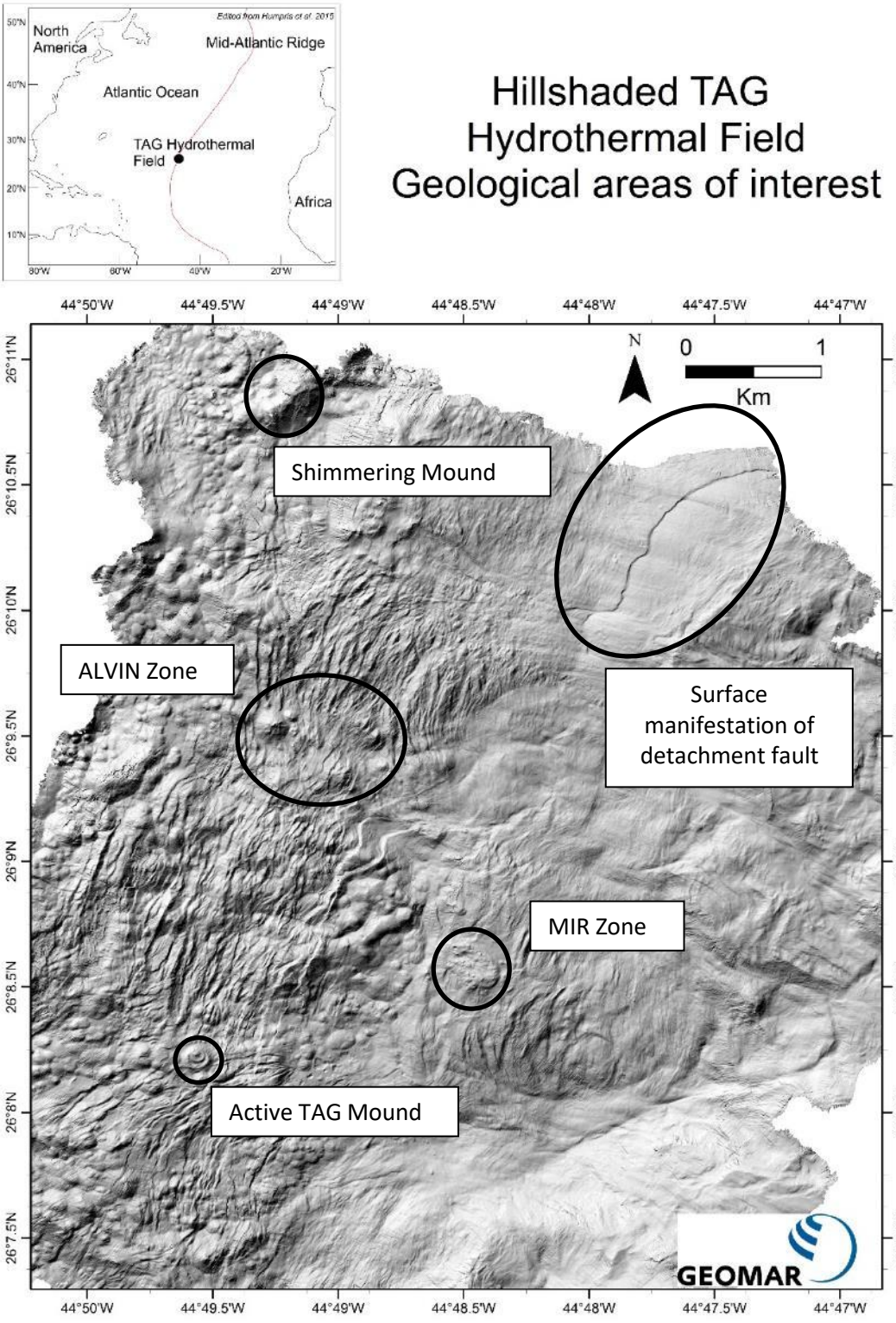

Figure 28: TAG Hydrothermal Field 2 m resolution AUV map obtained during M127 cruise (2015). Illumination direction ~NW. Main areas of interest include the TAG active mound, ALVIN zone and MIR zone. Location map edited from Humphris *et al.* 2015 (Humphris and Tivey, 2015).

3.1.1 TAG Active Mound

The active TAG mound is located proximal to the eastern wall of the Mid-Atlantic ridge rift valley (~1 km west) and ~2.4 km east of the rift axis. The mound itself resembles a 'double doughnut' composed of two circular terraces. The larger, lower terrace is ~150 m in diameter with escarpments of variable heights with slop angles in the order of 25° – 45°(Humphris *et al.*, 1995). The smaller, upper terrace is asymmetrically superimposed on the lower platform and is ~ 90 m in diameter, with ~ 5m high escarpments (Humphris and Kleinrock, 1996). High temperature hydrothermal fluids (~360-370˚C) vent from a cluster of 'black smoker' chimneys at the top of a ~12 m conical structure on the upper terrace (Parker *et al.*, 2005; Humphris and Tivey, 2015). Lower temperature (~220-300˚C) 'white smoker' more diffuse venting, has also been observed from small (~2 m high, ~1 m diameter) mounds on the upper terrace also referred to as the 'Kremlin Area' (Becker *et al.*, 1996). Low temperature diffuse fluid flow (≤ 25˚C) was also measured at multiple sites across the active mound (Tivey *et al.*, 1995; Schultz *et al.*, 1996), with evidence of higher temperature fluids (up to 50 ˚C) during heat flow measurements (Becker *et al.*, 1996). Proximal conductive heat flow (within ~20 m of the conical black smoker structure) was high and showed a large temporal variation (0.1 - > 100 W/m^2) (Becker *et al.*, 1996). Distal measurements (> 20 m from black smoker structure) in pelagic sediment were consistently high (3.7 - > 25 W/m^2) and showed little temporal variation (Becker *et al.*, 1996).

Drilling of the active mound, during ODP leg 158 yielded a three-dimensional model for the TAG active mound (Figure 29), and gave the first insight into the internal structure of an active SMS deposit. The deposit was split into different lithological zones based upon the drilling results, originally defined by Humphris *et al.* (1995) and expanded upon by Petersen *et al.* (2000):

- Zone 1 - metalliferous sediments - predominantly composed of sand grade oxidised sulphides, chert and iron-oxyhydroxides.
- Zone 2 - Massive sulphides and sulphide dominated breccias - composed of clast supported massive sulphide (pyrite) in a pyritic sandy matrix with minor anhydrite.
- Zone 3 - central anhydrite-rich zone - anhydrite matrix supported pyrite-anhydrite breccias.
- Zone 4 - pyrite silica breccias.
- Zone 5 - a deeper stockwork zone of silicified wall rock and chloritized basaltic breccias.

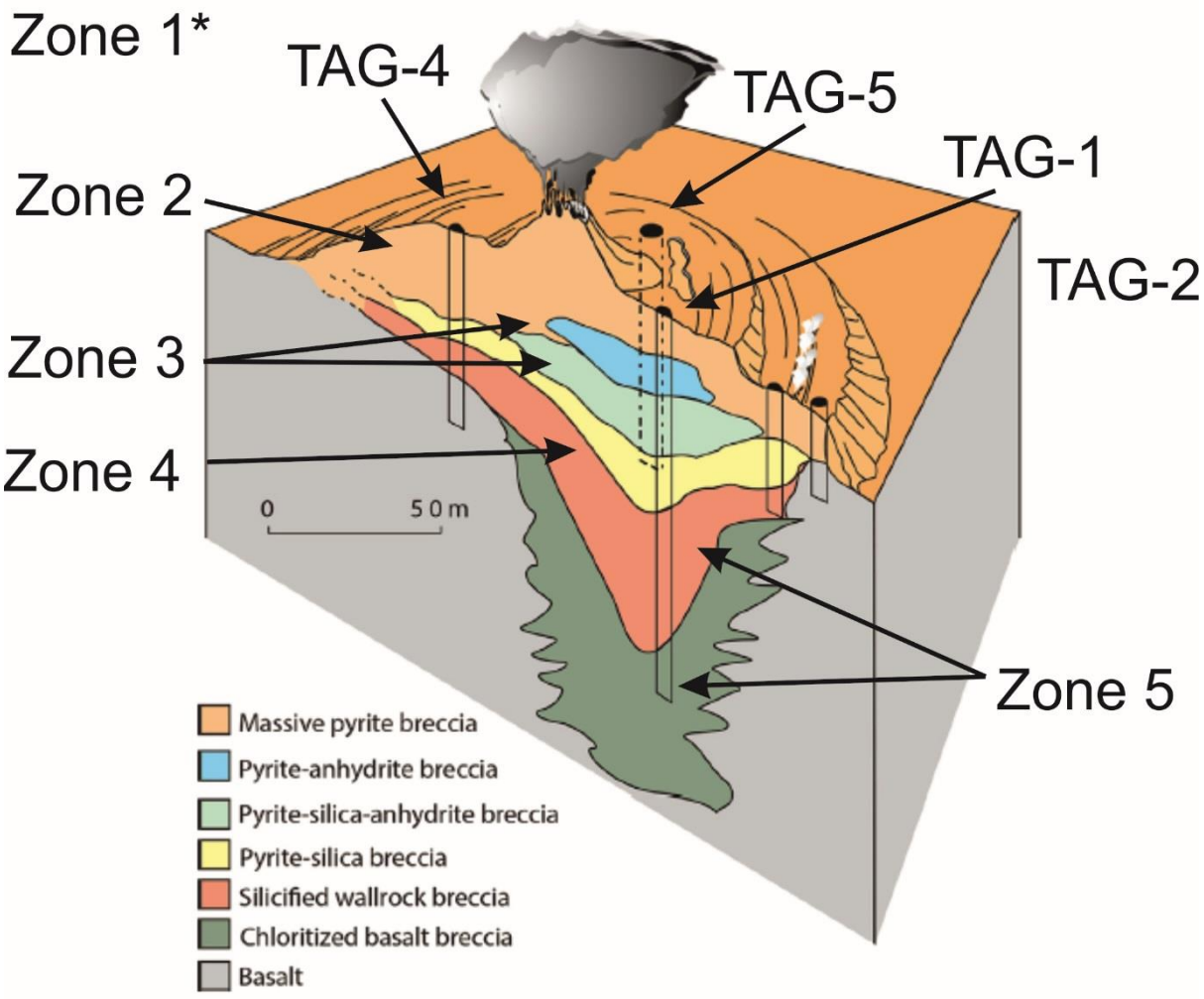

Figure 29: Cross section of the TAG active Mound from Humphris and Tivey, 2015. Zone 1 is not shown on diagram and overlies Zone 2 at surface. Vertical columns on figure represent drilling locations TAG-1 to TAG-5 from ODP Leg 158.

Zones 2-5 represent the main ore body and underlying stockwork, while Zone 1 represents the weathered sulphide apron and surface products of hydrothermal activity. ^{234}U - ^{230}Th dating of sulphides and anhydrite throughout the mound revealed at least 4 periods of hydrothermal activity during the lifespan of the active mound (50kya – 11kya, ~8kya -7kya, 6kya – 4kya, and < 50 years to present) (Lalou *et al.*, 1995), showing a complex mound growth history.

Silica is a major component of the subsurface material recovered from the TAG active mound (Hopkinson *et al.*, 1999). Throughout the mound two types of silica were identified: low temperature (<360˚C) 'Type-B' quartz (chalcedony, micro- and macro-crystalline quartz), and high temperature 'Type A' (>360˚C) quartz (macro-crystalline, includes trace Al up to ~1 wt%) (Hopkinson *et al.*, 1999).

Distribution of 'type-A' quartz was observed proximal to the central high temperature zone through the mound, with 'type-B' quartz dominant distally (Figure 30). Silica within the mound is interpreted to have transformed from an 'impure silica gel', or silica solution through 'Type B' quartz (to chalcedony then through micro- and macro-crystalline quartz) to 'type-A' quartz by the loss of water and increasing temperature (Hopkinson *et al.*, 1999).

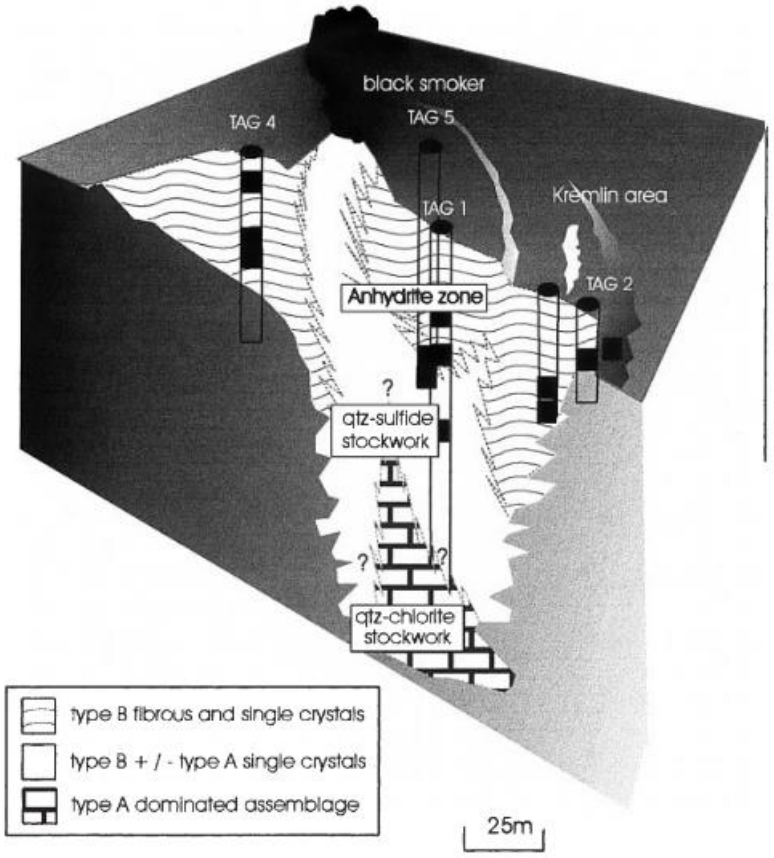

Figure 30: Schematic diagram of the likely silica domains within the TAG Active Mound, from Hopkinson *et al.* 1999.

Despite the abundance of silica throughout the deposit, and the fact that Fe was usually the dominant trace metal impurity in quartz (Hopkinson *et al.*, 1999), Si-Fe materials were not a common feature. Si-Fe material was recovered as small (< 4cm) fragments (Knott *et al.*, 1998) of grey and red, sphalerite bearing chert (Tivey *et al.*, 1995) from within the top 10 m of borehole TAG-4 (See Figure 29), and as clasts (< 2cm) throughout the whole massive sulphide ore body and stockwork zone (Zones 2 through to Zone 5)(Knott *et al.*, 1998). The grey and red chert in TAG-4 was interpreted to represent fragments of a 'thin' layer (< 1m thick) overlying massive porous pyrite ± sphalerite between ~1 and 10 m below the seafloor on the periphery of the mound ('TAG-4 Area', 1996). Si-Fe material enclaves throughout the deposit were interpreted to be early low temperature

precipitates entrained during later stage mound growth (Knott *et al.*, 1998). The low quantities of Si-Fe material throughout the active mound appear to be due to fact that Si-Fe materials are a product of low temperature hydrothermal activity, and therefore would not be present within the bulk of a high temperature mound. Observation of red and grey chert on the periphery of the mound interpreted is interpreted to have formed by low temperature hydrothermal activity (Tivey *et al.*, 1995; Hopkinson *et al.*, 1999; Petersen, 2000) and as such would be restricted to lower temperature areas.

3.1.2 Inactive Deposits – ALVIN and MIR Zones

The 'Alvin Zone' is a cluster of SMS deposits that comprises at least three large mounds (Southern, Shinkai and Alvin, see Figure 28) up to 200 m diameter (Rona, *et al.*, 1993; Rona, *et al.*, 1993; White *et al.*, 1998). It is located ~2.4 km NNE of the TAG active mound, and aligned parallel to a set of axis-parallel faults (trending ~020°). Previous work identified standing and toppled chimneys, hydrothermal crusts, and hydrothermal material interlayered with carbonate ooze and pillow lava talus (Rona *et al.*, 1993). Sulphide boulders exposed on the seafloor were seen to be mainly composed of pyrite, minor chalcopyrite and trace sphalerite, with an iron oxide veneer (Lisitsyn *et al.*, 1989). Gravity coring in the area revealed evidence of sulphide debris within the surrounding sediment sequence, likely derived by turbidity flows from mass wasting of existing mound material (Metz *et al.*, 1988; Rona, *et al.*, 1993).

Si-Fe samples were recovered by dredge from the ALVIN zone, and described as 'dark red chert', being composed of red-brown iron oxides cementing basalt and volcanic glass grains (Petersen, 2000). Silicified samples range in composition from slightly silicified carbonate sediment, to amorphous silica, to opal-C, and smectite hydrothermal precipitates (Petersen, 2000). Along with lithified samples, semi-consolidated orange Fe-oxyhydroxide sediments, dominated by goethite with traces of manganese oxides, were recovered from the surface of the ALVIN Zone (Petersen, 2000). One Si-Fe lithology sample from the ALVIN zone was analysed for oxygen stable isotopes ($\delta^{18}O_{VMSOW}$ = 30.2%), indicating a formation temperature of ~ 50˚C (Petersen, 2000).

The 'MIR Zone' is a large mound of discontinuous sulphide outcrop, located on the eastern rift valley wall, at ~ 3450 m depth. It is partially buried beneath pelagic sediment, making it difficult to fully delineate. The zone consists of a series of juxtaposed and superimposed inactive hydrothermal deposits in various stages of weathering, dissection by faulting, and degrading by mass wasting, delineating the MIR zone into 3 subzones (Figure 31):

- Subzone 1: Mixed hydrothermal debris and sediments with areas of hydrothermal breccia exposed in stepped normal faults.

- Subzone 2: Semi-continuous sulphide outcrop with a carbonate and metalliferous sediment substrate.
- Subzone 3: Hummocky topography with low temperature hydrothermal products (Fe-Mn staining), and fractured pillow lavas and talus.

Surface grab samples recovered sulphide chimney fragments (pyrite-marcasite and pyrite-chalcopyrite assemblages), many with iron oxide coatings, Fe-rich gossan and Mn oxide crust (Rona *et al.*, 1993; Rona *et al.*, 1993; Krasnov *et al.*, 1995; Stepanova *et al.*, 1996). Anhydrite and amorphous silica are absent from all samples, including sulphide chimney pieces, and is interpreted to have been removed during hydrothermal recrystallisation that also obscured primary texture (Rona *et al.*, 1993).

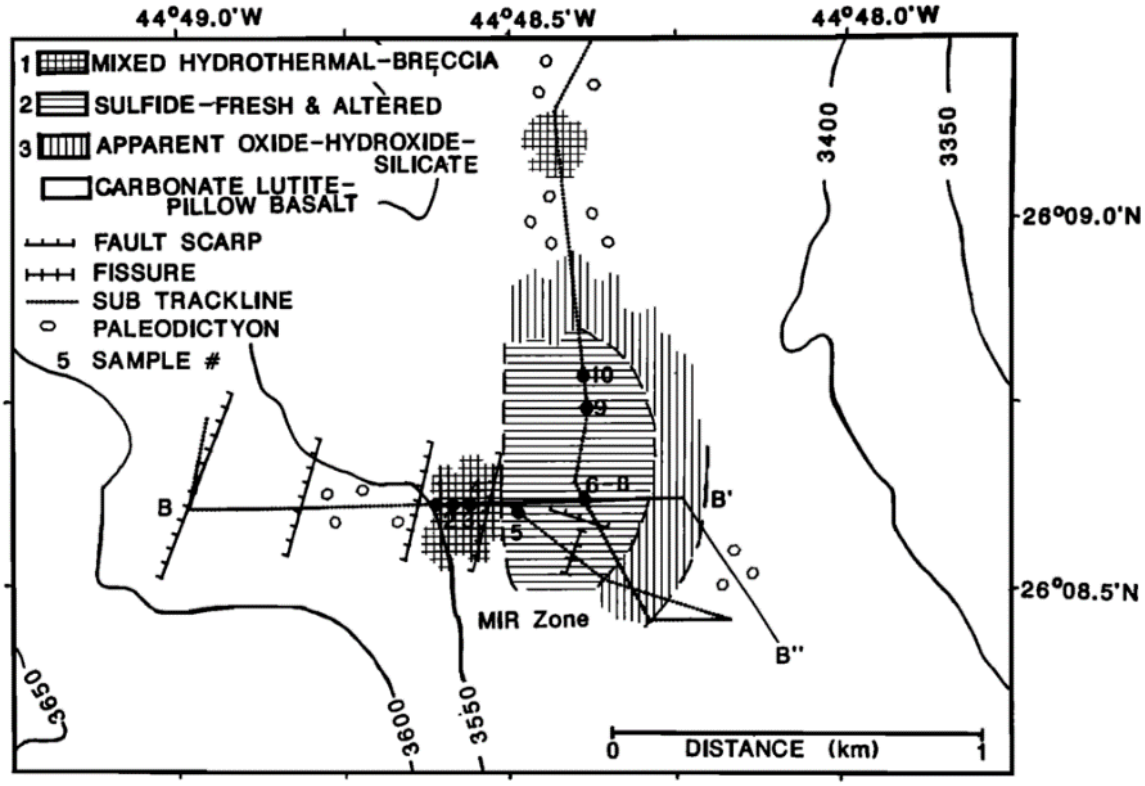

Figure 31: Three subzones of the MIR Zone, from Rona *et al.* (1993)

Varying degrees of silicification have been observed from samples dredged from the MIR zone including: sulphides silicified by late stage, globular and thread like amorphous silica; strongly silicified haematitic clasts in a matrix of Fe- and Mn- oxyhydroxides, with late sulphide rims; sulphide chimney material coated with a (up to 3 cm) layer of porous siliceous material; and part of an Si-Fe chimney in which fluid conduits were clogged by late-sate amorphous silica (Petersen, 2000). Four of these samples were analysed for stable oxygen isotopes ($\delta^{18}O_{VMSOW}$ ranging from 25.2 % to 30.2 %), with calculated formation temperatures of between ~ 40˚C and 80˚C (Petersen, 2000).

3.2 Current state of preservation of eSMS deposits – New data

Until now, the eSMS deposits and mounds at the TAG hydrothermal field have been poorly studied. Navigation was poor, sampling sparse and often by dredge, and there was not any accurate, precise, or high-resolution bathymetry. Some mounds within the ALVIN zone have been referred to by different names reflecting the lack of accurate positioning data between different expeditions such that the same sites were 'discovered' several times. This all changed with the 2016 AUV surveys that acquired high-resolution bathymetry of eight eSMS deposits from the ALVIN zone (See Figure 32), and the MIR Zone. The bathymetric maps enabled targeted HyBIS robotic underwater vehicle (RUV) surveys that acquired surface video and sampling from five eSMS deposits in the ALVIN Zone.

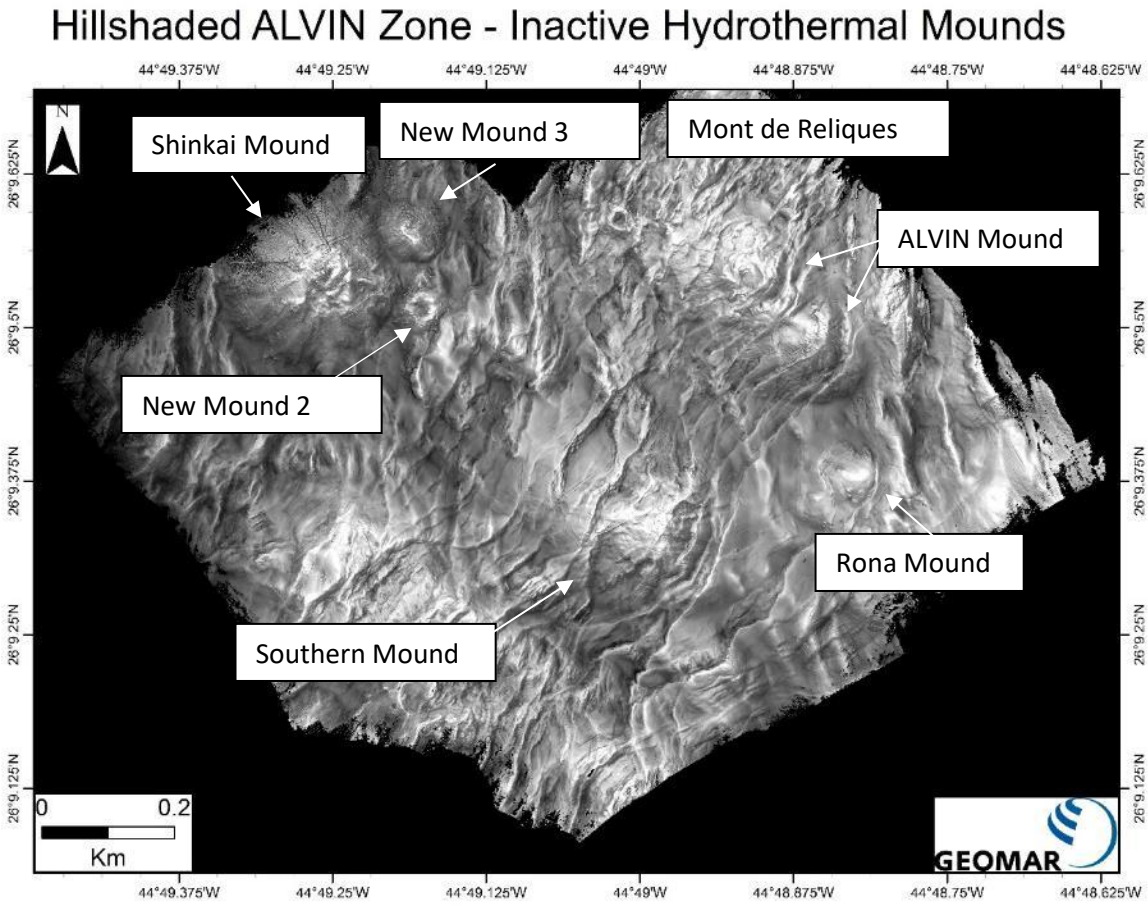

Figure 32: Inactive mounds within the ALVIN Zone: Southern Mound, Rona Mound, Shinkai Mound, New Mound 2, New Mound 3, Mont de Reliques, and ALVIN/Double Mound.

The surface video footage and bathymetry of five eSMS deposits enabled comparison of surface features and mound profiles from the active TAG mound to the inactive deposits. These five eSMS deposits can be separated into a 'Northern' cluster of three mounds (Shinkai Mound, New Mound 2, and New Mound 3), and a 'Southern' cluster of two mounds (Southern Mound, and Rona Mound)

(Figure 32). ALVIN Mound and Mont de Reliques were not visited during HyBIS dives and so are not considered further.

3.2.1 ALVIN Zone - Southern cluster

Southern Mound and Rona Mound are located at the south eastern corner of the ALVIN Zone, within a terrane dominated by spreading-ridge axis parallel NE-SW faults that stretch from the TAG active mound, through the southern cluster of eSMS deposits and extend ~1.5km to the NE of the ALVIN Zone (White *et al.*, 1998).

Southern Mound is an oval shaped, faulted, sulphide mound (~40 m high, ~260 x 220m wide), and Rona Mound is a roughly dome shaped, faulted, sulphide mound (~30m high, ~170m diameter) located ~0.5km east of Southern Mound. The overall profiles of both mounds are smooth with relatively low ~19˚ slope angles in comparison to the active TAG Mound and were mapped during the JC138 research cruise (Figure 33).

NE-SW-trending, graben forming, inward-facing, fault scarps dissect both Southern mound (4 scarps), and Rona Mound (2 scarps) exposing the sub-surface geology to a depth of ~5m below the seafloor at Southern, and <~1m at Rona. These faults clearly post-date mound formation and are observed to curve round the centre of both mounds, implying some degree of local influence on the fault by volume loss of each mound.

Summits of both mounds are covered by carbonate sediment ~30-50 cm thick, with a few areas of sulphide outcrop, and rare manganese crust material. These include several meter-sized blocks of massive sulphide, derived from highly-weathered and fallen chimneys, and several small relict *in situ* chimneys Figure 34) at Southern Mound, and a single *in-situ* ~2m tall, ~2m diameter, highly weathered sulphide chimney at Rona Mound (Figure 35).

Evidence of the onset and cessation of hydrothermal activity in the area can be interpreted from surface features. At the northern extent of the distal NE-SW fault at Southern Mound hydrothermal material is clearly on-lapping brecciated basaltic material, implying that mound growth post-dates the formation of this volcanic material. This also appears to be the case at Rona Mound where brecciated pillow basalt was present at the south western and western base of the mound, implying that Rona may represent the formation of hydrothermal material at the summit of an existing pillow basalt dome.

The presence of pelagic material covering the flanks and large areas of both mounds implies a clear quiescence of hydrothermal activity as both high and low temperature hydrothermal fluids are typically acidic so hydrothermal flow would result in carbonate dissolution, a process interpreted

from the active TAG Mound (Section 3.1.1). Cessation of hydrothermal activity would enable carbonate accumulation atop the mound. Only a small plateau area to the west of the summit of Southern Mound showed little pelagic cover. Surface sediments were predominantly iron oxide with two samples of silicified, barite containing, iron oxide material recovered by HyBIS grabs. This area was also home to multiple holothurians and yellow bacterial mats supporting the idea of 'recent' hydrothermal activity, inhibiting carbonate sediment accumulation.

The general coverage of pelagic sediment across both mounds, the smoothness of both mound profiles, the occurrence of late-stage faults, and indication of mound volume loss at both of these deposits represent a mature stage of seafloor weathering. If the NE-SW trending faults were not present, only the sporadic and highly weathered sulphide material on both mounds provides an indication that the underlying material is a massive sulphide mound.

Investigation of the exposed material within NE-SW trending fault scarps resulted in ~ 5 m of shallow subsurface material at Southern Mound being exposed at the seafloor, and not only gives an indication of the sub-surface stratigraphy, but also shows evidence of seafloor processes which would have affected the whole mound.

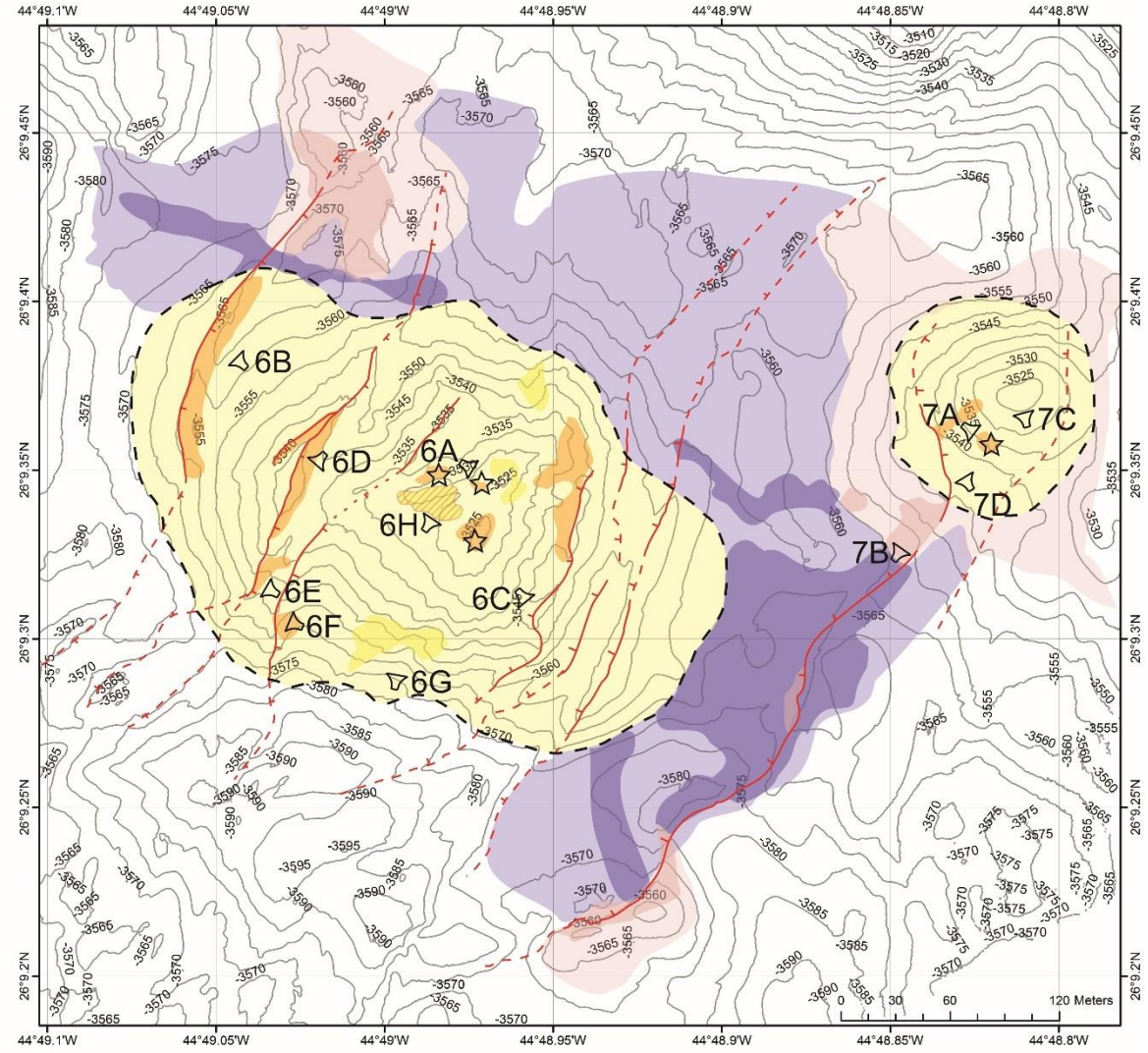

Basalt outcrop observed
Basalt outcrop inferred
Sediment cover (predominantly pelagic) observed
Sediment cover inferred
Sulphide talus and hydrothermal sediment
Sulphide outcrop inferred (under sediment pelagic/hydrothermal)
Sulphide outcrop observed (including fault scarps)

Low temperature zone (?)

Fault observed
Fault inferred
Inferred extent of mound sulphide
Inactive Chimneys
Photo location and viewing direction (e.g. = 315°)

Figure 33: Interpreted geological map with photo locations for Figure 34 and Figure 35. Geology is interpreted from surface observations, HyBIS grab samples, and bathymetry.

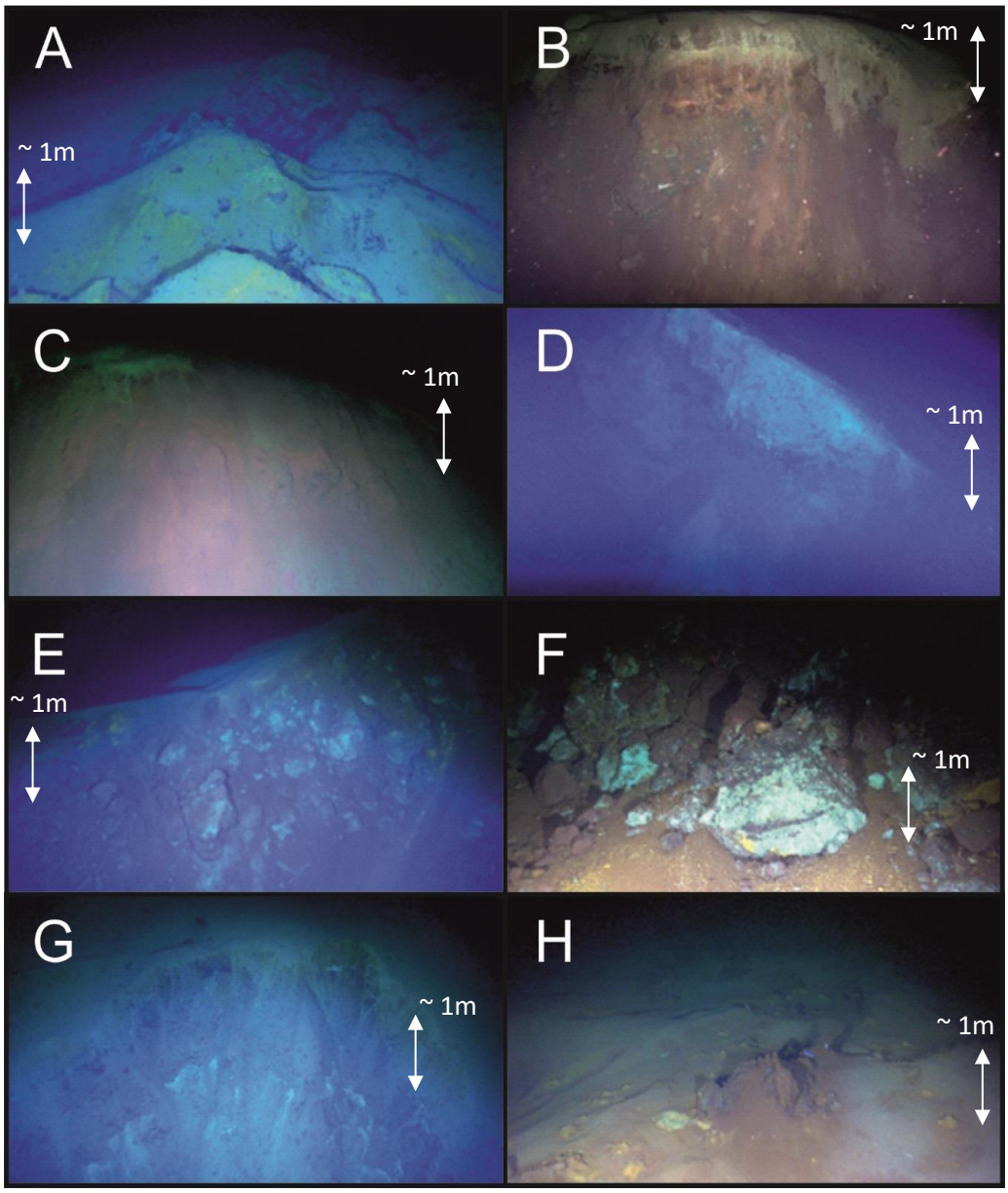

Figure 34: Evidence of sulphide materials within the constructional part of Southern Mound: (A) Small chimneys near the summit, areas of yellow bacterial mats observed across the mound (B) Typical iron oxide coated massive pyrite boulders observed in the distal western fault scarp, overlain by oxidised and pelagic sediments. (C) Dark red oxidised sediment draping over the proximal eastern fault scarp, occasional sulphide boulders observed within sediments. (D) Competent sulphide layer observed within northern sections of the proximal western fault scarp. (E) Sulphide boulders within the proximal western fault scarp, slight green colouration is secondary copper mineralisation on sulphide boulders. (F) Base of proximal western fault scarp, meter size boulders of 'secondary' copper-coated massive sulphide. (G) Horseshoe scarp on the southern slope, sulphide boulders and oxidised sediments visible within and at the base of the slope. (H) Area of potential low temperature flow, dominated by oxidised sediment with little evidence of carbonate material, holothurians and yellow bacterial mats.

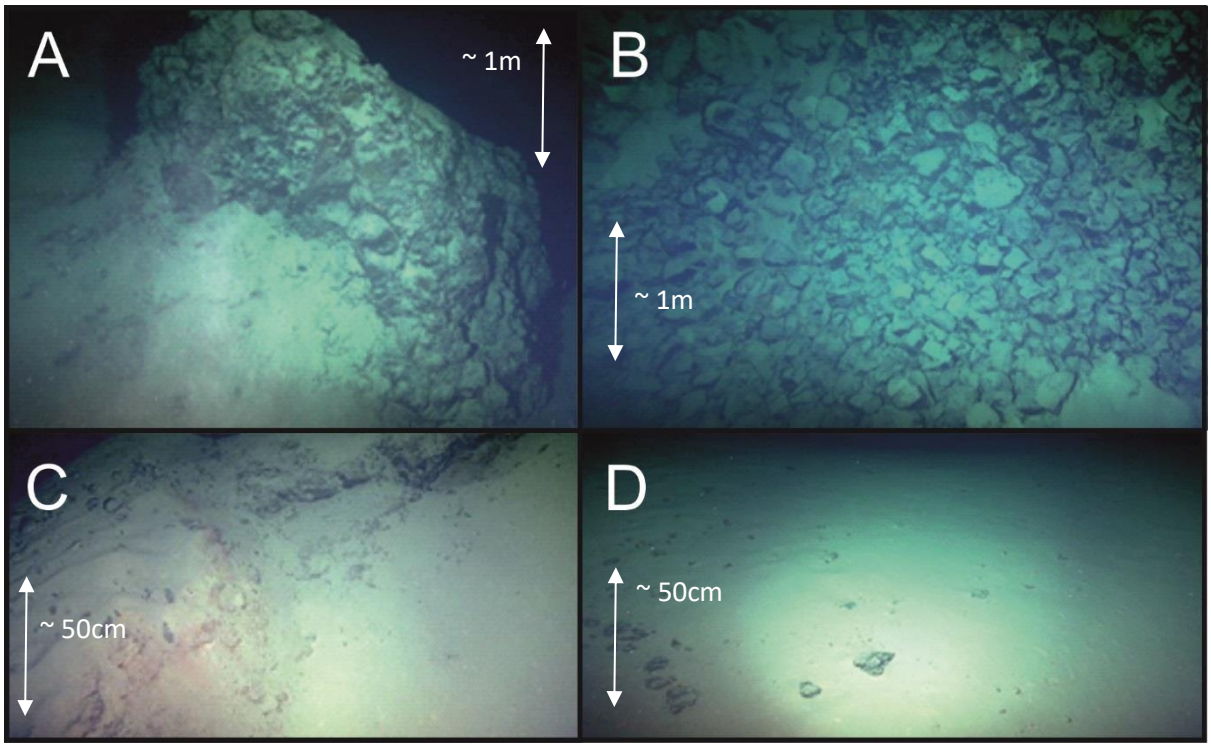

Figure 35: Surface characteristics of Rona Mound: A) Highly weathered, massive sulphide chimney near the summit of Rona Mound ~ 2 m high. B) Pillow basalt talus at the base of Rona Mound. C) Fault scarp at Rona Mound, hints of competent material near surface. D) Carbonate sedimented summit of Rona Mound with occasional manganese/iron rich crust patches visible. Scale is for all images

3.2.1.1 Evidence of seafloor weathering processes and sub-surface geology

At Southern Mound, fault scarps typically expose a sequence of pelagic sediment with patches of Mn-Fe oxide 'crust' material (≤0.3 m thickness) overlying a sequence of orange to brown sediments (~0.3 - > ~1 m thick, likely composed of iron oxides/oxyhydroxides) with weathered massive sulphide blocks, underlain by weathered massive sulphide granular material and boulders (Figure 36).

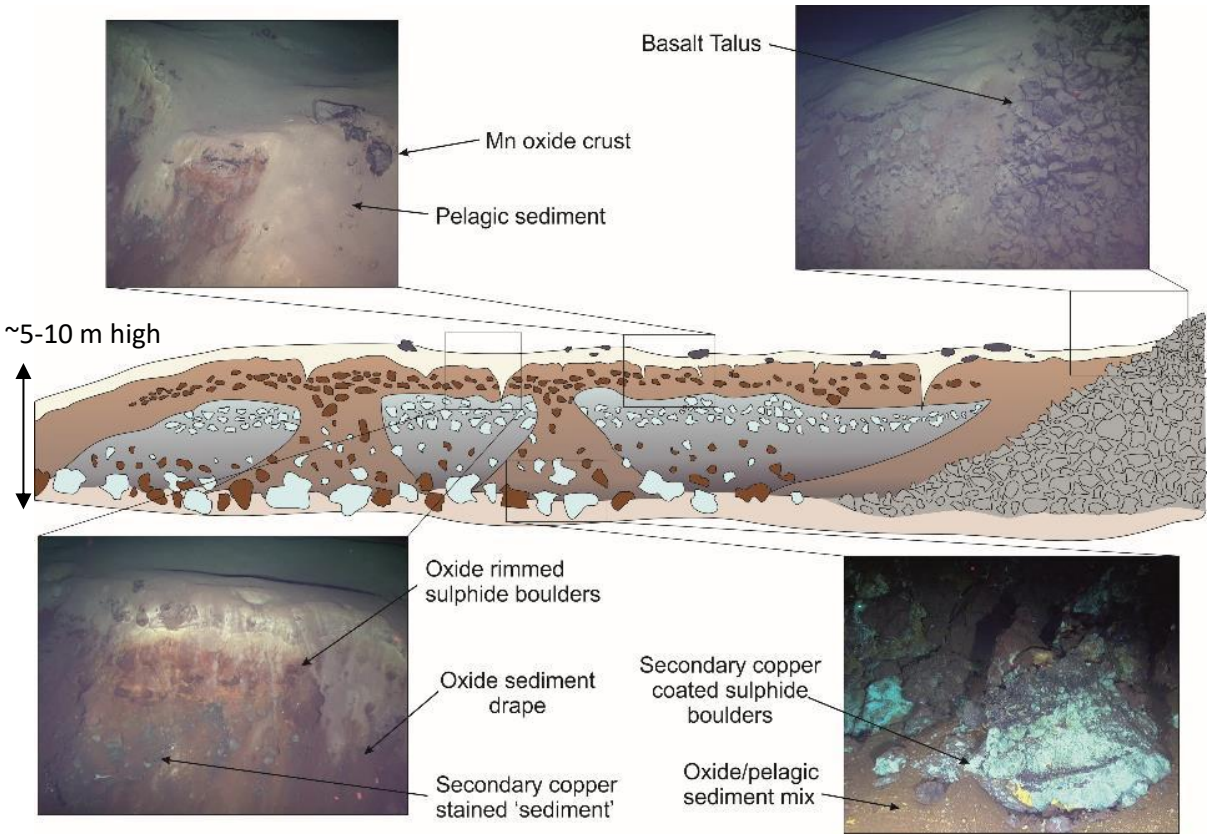

Figure 36: Sketch of the distal NW fault scarp dissecting Southern Mound Stratigraphy within fault scarp shows pelagic sediment overlying mixed hydrothermal sediment and red-brown oxide coated sulphide boulders, overlying sulphide and oxidised sediments and green secondary copper coated sulphide boulders.

One of the first observations from the fault scarp stratigraphy is that massive sulphide material appears *in-situ* as shallow as ~50-60 cm. If this is the case across the mound, it implies that there is little to no surficial cover of the massive sulphides, one of the key conditions identified for VMS preservation (See Section 2.3).

Seafloor weathering is evidenced by the occurrence of iron oxide (dark red), and copper chloride (green) coatings of massive sulphide boulders and granular material where weathering product likely relates to the base metal content of the sulphides (i.e. copper rich material would form copper rich weathering products). It is also likely that the red-orange hydrothermal sediments are at least in part derived from weathering of massive sulphide materials as they direct overly, and are closely associated with, weathered massive sulphide material. Mass wasting processes, linked to seafloor weathering are indicated by sediment drape, and the accumulation of large weathered sulphide material at the base of each fault scarp.

This sequence of lithologies was observed within three fault scarps at Southern Mound, and within the two horseshoe collapse scarps along the southern slope of the mound. The only significant

variation of this trend is the proximal southern eastern fault scarp. This fault scarp had a similar thickness of pelagic sediment (~30cm) overlying a greater thickness of dark red sediment (likely iron oxide) than observed in other fault scarps. The thickness of iron oxide sediment appears to be ~ 5-8 m. No secondary copper chloride coated sulphide boulders were observed, but small dark red coated boulders were present within the fault scarp (interpreted to be massive sulphide, based upon observations only; no samples were obtained from this scarp). The iron oxide sediment thickness may be an exaggeration based upon sediment drape indicating a higher degree of mass wasting at this scarp, and covering the interpreted underlying *in-situ* massive sulphide material.

3.2.2 ALVIN Zone - Northern Cluster

Shinkai, New Mound 2, and New Mound 3 are ~1.2 km NW of the Southern cluster. Shinkai is the largest of the three mounds (~65 m high, and ~260 m in diameter), followed by New Mound 3 (~30 m high, ~120 m diameter), and New Mound 2 (~20 m high, ~80 m diameter). The mounds are hosted within an unfaulted terrane, to the west of the NE-SW trending faults that have dissected the Southern Cluster, closer to the spreading axis. All three mounds are therefore unfaulted, and exhibit simple conical profiles with average slope angles ~ 27˚ (Figure 37).

The summit of Shinkai is dominated by a large, ~ 15 m sulphide 'spire' with the eastern slope surveyed dominated by smaller relict chimneys and chimlets with little sediment cover (Figure 38). In contrast, the western slope was dominated by large weathered sulphide blocks and chimneys, and orange-brown oxidised hydrothermal sediments. Similar surface features were observed at both New Mounds 2 and 3, with little sediment cover on both mounds, and ~15 standing and collapsed chimneys (~1-2 m) observed near the summit of New Mound 2. Basaltic material was observed at the base of the western flank of Shinkai, between the bases of the southern flank of New Mound 3 and around ~ 60% of New Mound 2 (from the northern to south eastern flank). In fact, the basaltic material at New Mound 2 appeared to be a basaltic mound with hydrothermal growth atop, similar to Rona Mound.

Higher angle mound slopes, more conical mound profiles, general lack of pelagic material on the hydrothermal mounds, and the presence of more primary hydrothermal vent features (relict standing and collapsed chimneys) all support the interpretation that the Northern cluster represents a series of eSMS deposits that are less weathered than the Southern cluster. This is also

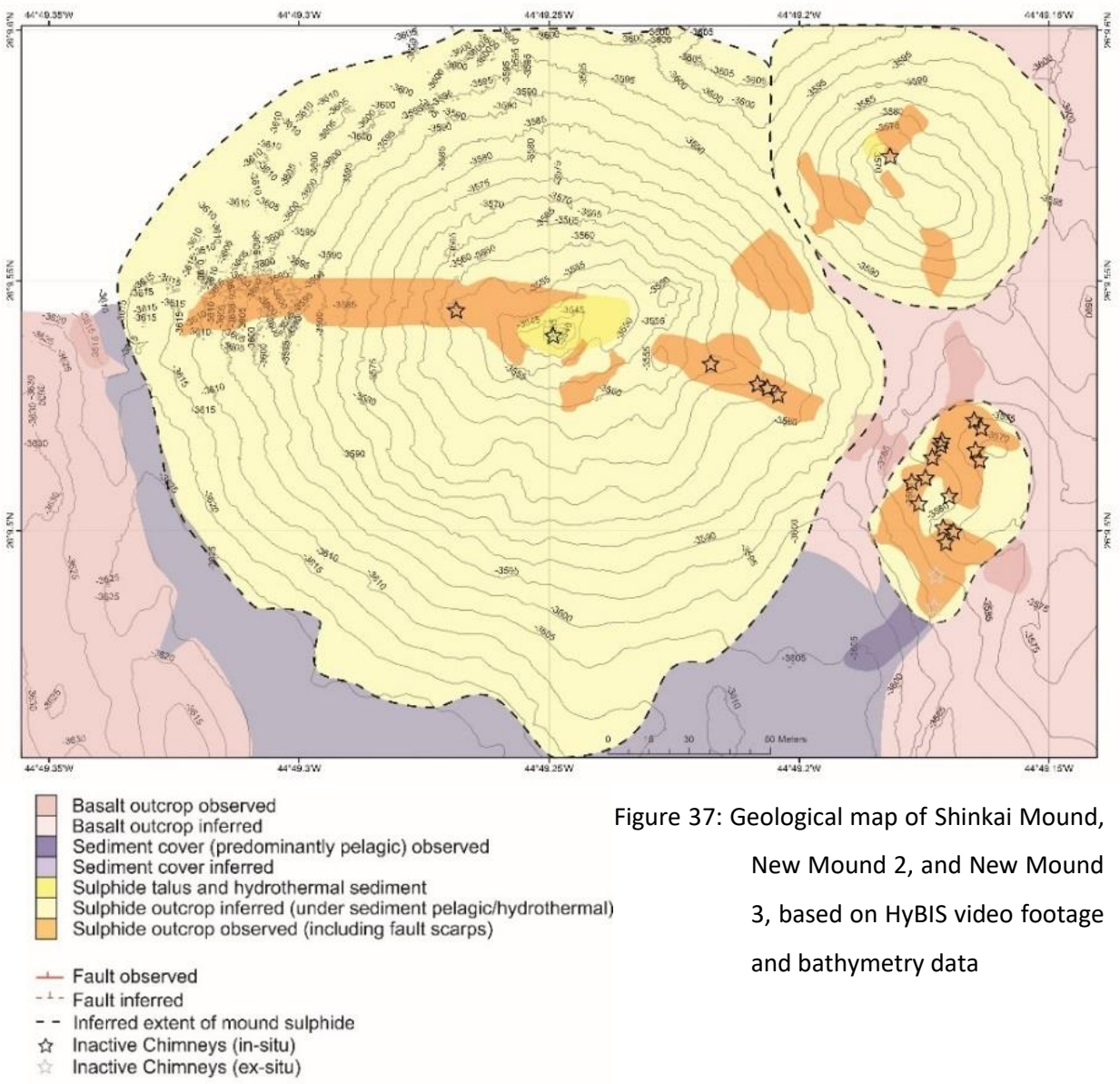

Figure 37: Geological map of Shinkai Mound, New Mound 2, and New Mound 3, based on HyBIS video footage and bathymetry data

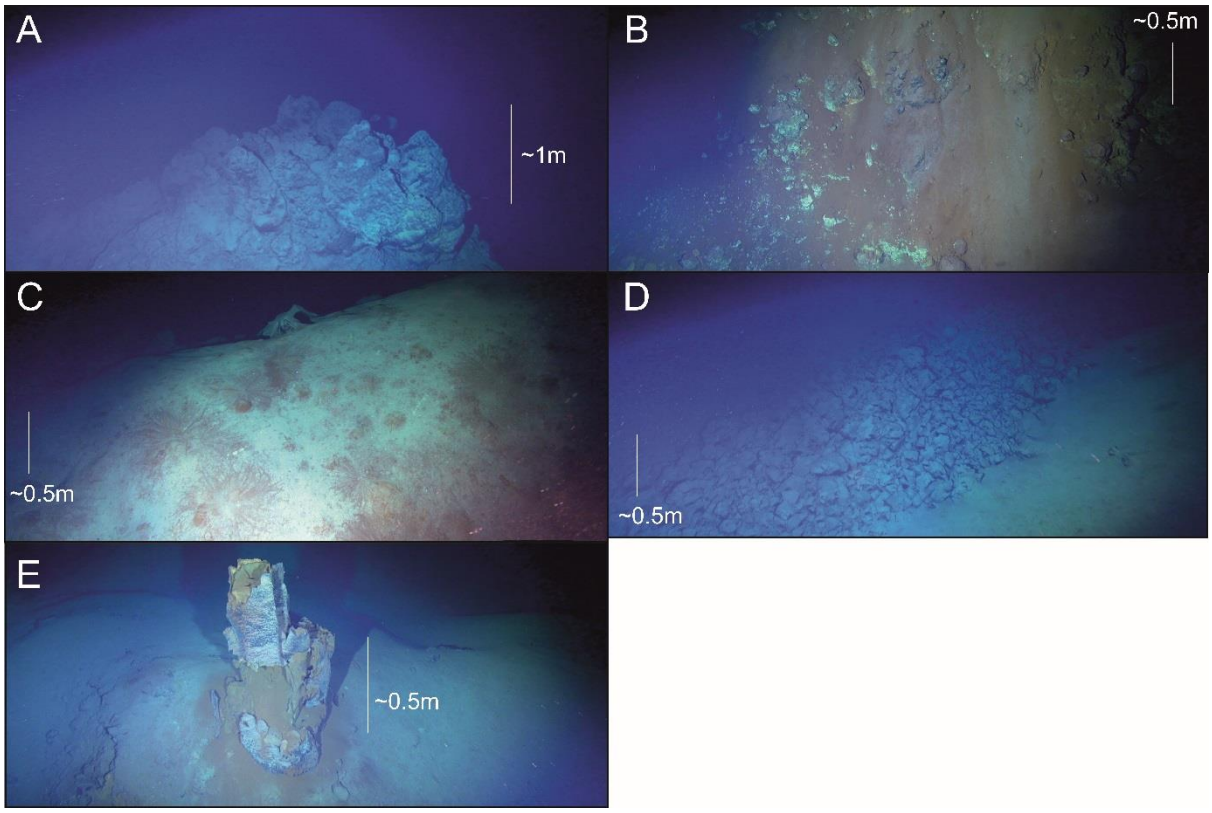

Figure 38: Range of surface features from Shinkai Mound, New Mound 2, and New Mound 3. A) Top of the 'spire' of Shinkai, viewing ~ North. B) Hydrothermal iron rich sediment with boulders of green copper coated secondary copper sulphides boulders on the eastern flank of Shinkai Mound, viewing ~ East. C) Proximal western fault scarp adjacent to Shinkai Mound, burrows show hydrothermal sediment at depth under pelagic sediment, viewing ~ West. D) Angular basalt talus at the base of Shinkai (left of image) and New Mound 2 (right of image), viewing ~ West. E) Single partially weathered standing sulphide chimney near the summit of New Mound 2, viewing ~ North East.

3.2.3 MIR Zone

The MIR Zone is located ~ 2km ENE from the active TAG Mound, on an elevated block that has been upthrust by a ~N-S trending, west-facing fault. It is roughly oval shaped (~450 by 300 m) with small mound-like features around the circumference with slump features incising the deposit in the NW and SE. No surface geology surveys were undertaken over the MIR Zone during data collection in 2016, however, some examples of the seafloor morphology at MIR Zone have been obtained from historical video footage (Figure 39). Limitations with navigation data made comparison of this footage to the new bathymetry impossible.

The morphology of the MIR zone is considerably different from both of the ALVIN Zone clusters, with no real defined 'single' mound feature. Based upon the observation of large standing sulphide

chimneys on historical footage, and some degree of carbonate deposition around the deposit imply that MIR may fit somewhere between the two ALVIN clusters with respect to seafloor weathering. However, the interpretation of multiple superimposed constructional hydrothermal features could also explain the presence of 'younger' hydrothermal chimneys as 'more recent' hydrothermal activity, rather than a true representation of seafloor weathering. Uplift and dissection of the MIR Zone by the N-S faulting likely promoted the mass-wasting of the mound, further obscuring the potential degree of seafloor weathering

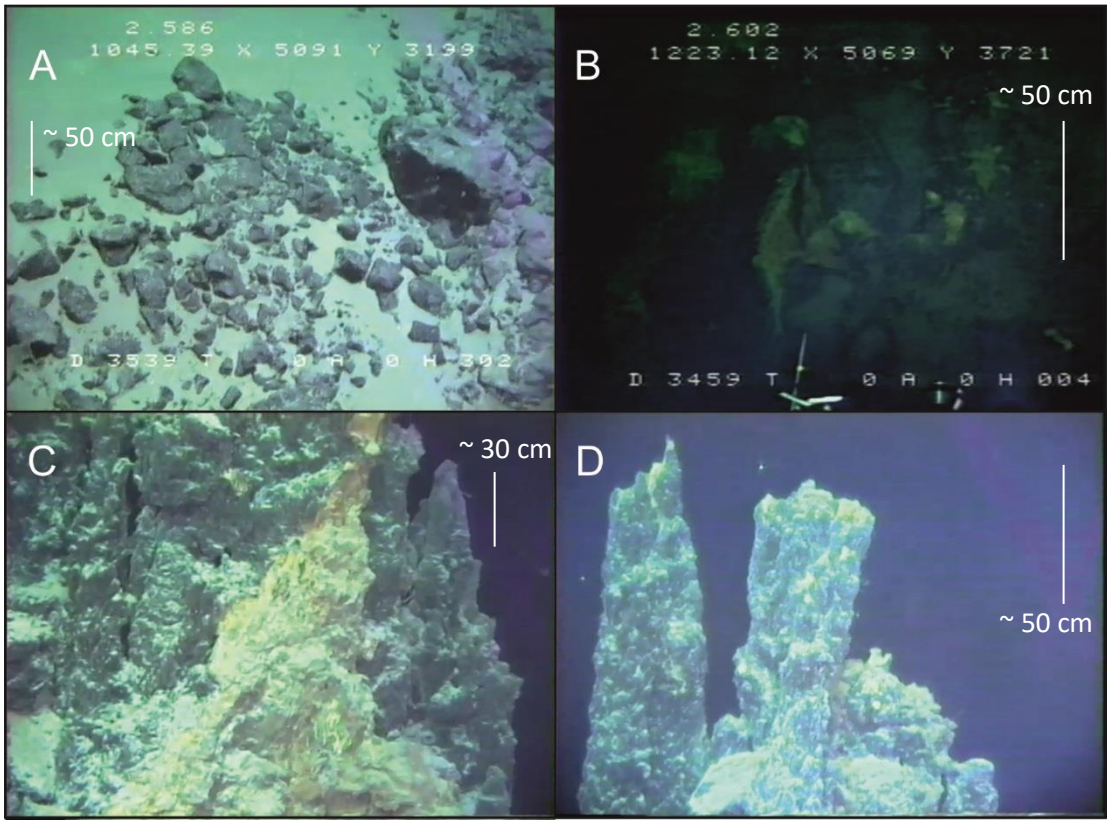

Figure 39: Screenshots from two ALVIN dives (2586 and 2592) to MIR Zone. A) Carbonate sediment with likely basaltic boulders, interpreted to be within a sulphide debris zone. B) Yellow and black bacterial mats. C) Yellow bacterial staining on inactive sulphide chimney. D) Top of spire of inactive massive sulphide chimney.

3.3 eSMS subsurface stratigraphy - the discovery of an Si-Fe cap

Surface observations indicated that the Northern cluster of eSMS deposits in the ALVIN Zone, represented a less weathered end member of eSMS deposit (compared to the Southern cluster), however the high slope angles of each mound meant that seafloor drilling was not possible. The more degraded eSMS deposits from the Southern cluster and the MIR Zone presented more opportunities for drilling. Drill sites were located by interpretation of HyBIS surface video, and

bathymetry data, enabling subsequent sub-surface drilling, of Southern Mound, Rona Mound, and the MIR Zone.

Drilling of all three mounds recovered Si-Fe materials in the order of 3-5 m thick, a feature that was not anticipated based upon the implied sub-surface geology as exposed at surface. The Si-Fe lithologies are subdivided into three different units based on a range of physical and mineralogical information from Southern Mound.

- **Unit A –** Partially silicified, 'low' density, iron oxyhydroxides
- **Unit B – '**Jasper' - silicified iron oxides
- **Unit C –** Transitional material of silicified iron oxides/oxyhydroxides with grey silica

Hydrothermal sediments were recovered at Southern Mound, and interpreted to be present at both Rona Mound and the MIR Zone, but were not recovered.

3.3.1 Southern Mound

Three boreholes (022RD, 031RD and 050RD) were drilled in a sedimented hollow near the summit of Southern Mound, at approximately the same location (within ~10m^2 area) (Figure 40).

Boreholes 022RD and 031RD recovered a comparable sequence of hydrothermal sediments overlying samples of Si-Fe material ~3.2 and ~2.7 mbsf respectively before drilling was terminated. Hole 050RD subsequently penetrating a thicker and variable sequence of Si-Fe materials (between ~ 2.9 to 6.5 mbsf), and recovered a sulphide pebble at termination depth (6.7mbsf).

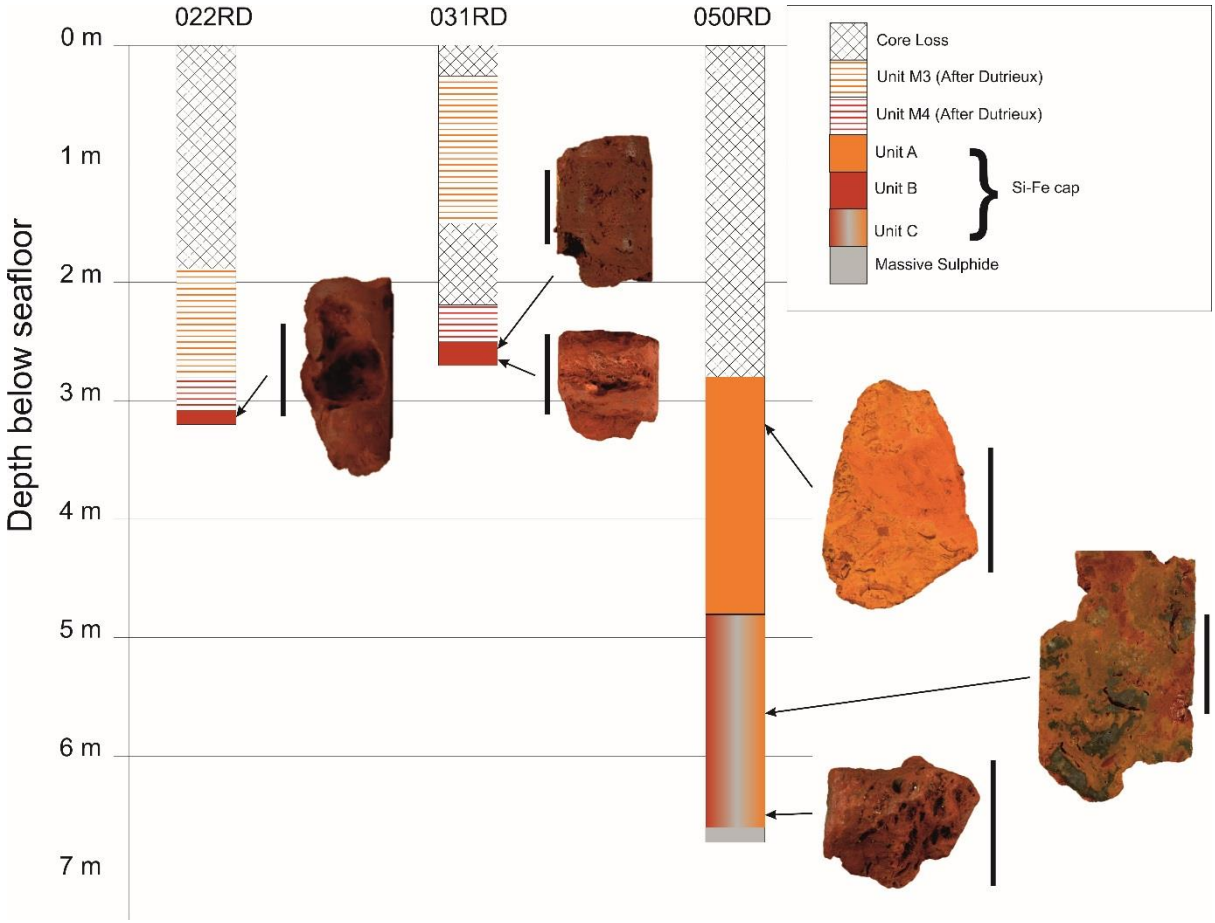

Figure 40: Summary of recovered drill core materials from Southern Mound. Hard rock material dominated by Fe-Si lithologies, further separated into 3 sub-units. Scale bars = 5cm.

The maximum depth penetrated was ~6.7 m (at borehole 050RD). Weighted average recoveries for each RD2 drilling site were calculated for each borehole: 022RD = 50.9%, 031RD = 72.5%, and 050RD = 16.6%. High recovery rates from 022RD and 031RD are due to the recovery of sediment above the Si-Fe material, with each location penetrating <20 cm into the Si-Fe material. The third borehole, 050RD was 'open holed' through the sediments (marked as 'core loss' on Figure 40), therefore the low recovery is representative of hard rock material.

3.3.1.1 Sediments overlying the Si-Fe cap

Southern Mound was the only eSMS deposit where overlying hydrothermal sediments were recovered along with hard rock material enabling an insight into the sediment-hard rock interface. Hydrothermal sediments were recovered from hole 022RD and hole 031RD (as shown in Figure 40) and the stratigraphy, mineralogy, and geochemistry have been described in detail (Dutrieux, 2019). Dutrieux separated the mound summit sediments into four sub-units M1 – M4. M1 refers to a layer of ~20 to 40cm thick pelagic material composed predominantly of carbonate ooze. Unit M2 represents a thin (~ 10cm) heterogeneous sediment composed of iron oxides and manganese

oxides (Dutrieux, 2019). Unit M3 occurs as an orange-red-brown heterogeneous sediment, principally dominated by iron oxyhydroxides. Unit M4 occurs as a blood red homogenous sediment, dominated by haematite. At both hole 022RD and hole 031RD the sediment-rock interface occurred within Unit M4, with the underlying Si-Fe material described in the following subsection.

3.3.1.2 Unit A

Unit A is dominated by orange-red-brown iron oxides and oxyhydroxides which exhibit a characteristic wide range of complexly textured 'clasts' implying it is a kind of breccia material (Figure 41). Comparative to the underlying units it is notably low density, and is friable.

Figure 41: 050RD/Piece3, a characteristic hand specimen from Unit A. Multiple individual iron oxide 'clasts' can be seen as brecciated laminations and subrounded to subangular gravel sized pieces. Scale bar = 5 cm.

3.3.1.3 Unit B

Unit B is typically dark red in colour with a higher density than Unit A and recovered in 022RD and 031RD, but not in 050RD. The increased density and dark red colour is characteristic of the unit. Unit B material was present at the sediment-rock interface in both holes 022RD and 031RD, occasionally with unsilicified iron oxide dominated M4 sediment within void spaces when recovered (Figure 42).

Figure 42: 031RD/107/CC, example of sample from Unit B. Material is dominated by red iron oxide and is notably harder than Unit A. Pore spaces visible at cm scale. Scale bar = 5cm.

3.3.1.4 Unit C

Unit C is a similar density to Unit B but defined by the presence of patches of grey chert and the presence of massive sulphides (Figure 43). The siliceous material appears grey due to the presence of interstitial sulphides and is not visible within Units A or B. Red and orange iron oxides are commonly intermixed within this unit, similar to Unit A, but the characteristic textures observed in Unit A were not observed in Unit C. Upon cutting Unit C, patches of orange sediment were recovered from within pore spaces. Samples 050RD/P12 and P13 (the deepest Si-Fe sample from

Southern Mound), did not exhibit the sulphidic grey chert, and was visually similar to Unit B material, however, due to the presence of massive sulphides, they were classified as Unit C.

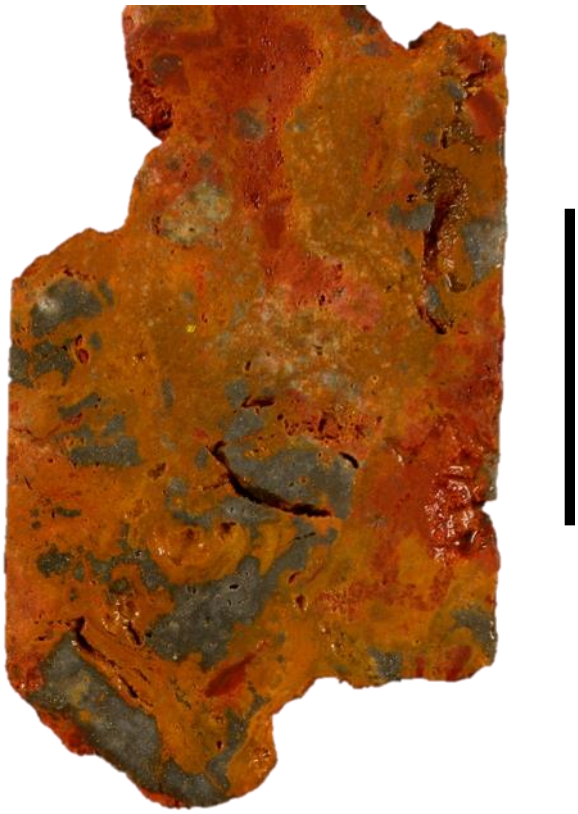

Figure 43: 050RD/P11, example of Unit C. Material recovered is dominated by yellow brown iron oxides with patches of darker red iron oxides. A characteristic feature of this unit is patches of grey silica with disseminated sulphide within. Scale bar = 5cm.

3.3.2 Rona Mound

Three holes were drilled at the summit of Rona Mound (holes 057RD, 065RD, and 068RD, see Figure 44) and the maximum penetrated depth was ~ 12.5m in 065RD. Hole 068RD was open-holed to ~12m depth before being terminated and only 0.16 m of disturbed samples were recovered. Drilling results of holes 057RD and 065RD are summarised within Figure 44. Hole 057RD was drilled without coring through sediments to ~1.7m depth, and penetrated Si-Fe materials (Unit B and C) and massive sulphides before being terminated at ~10.5m depth. Hole 065RD was drilled without coring until 7.7 m depth and cored until termination through massive sulphides only. Unit A was not recovered from Rona Mound.

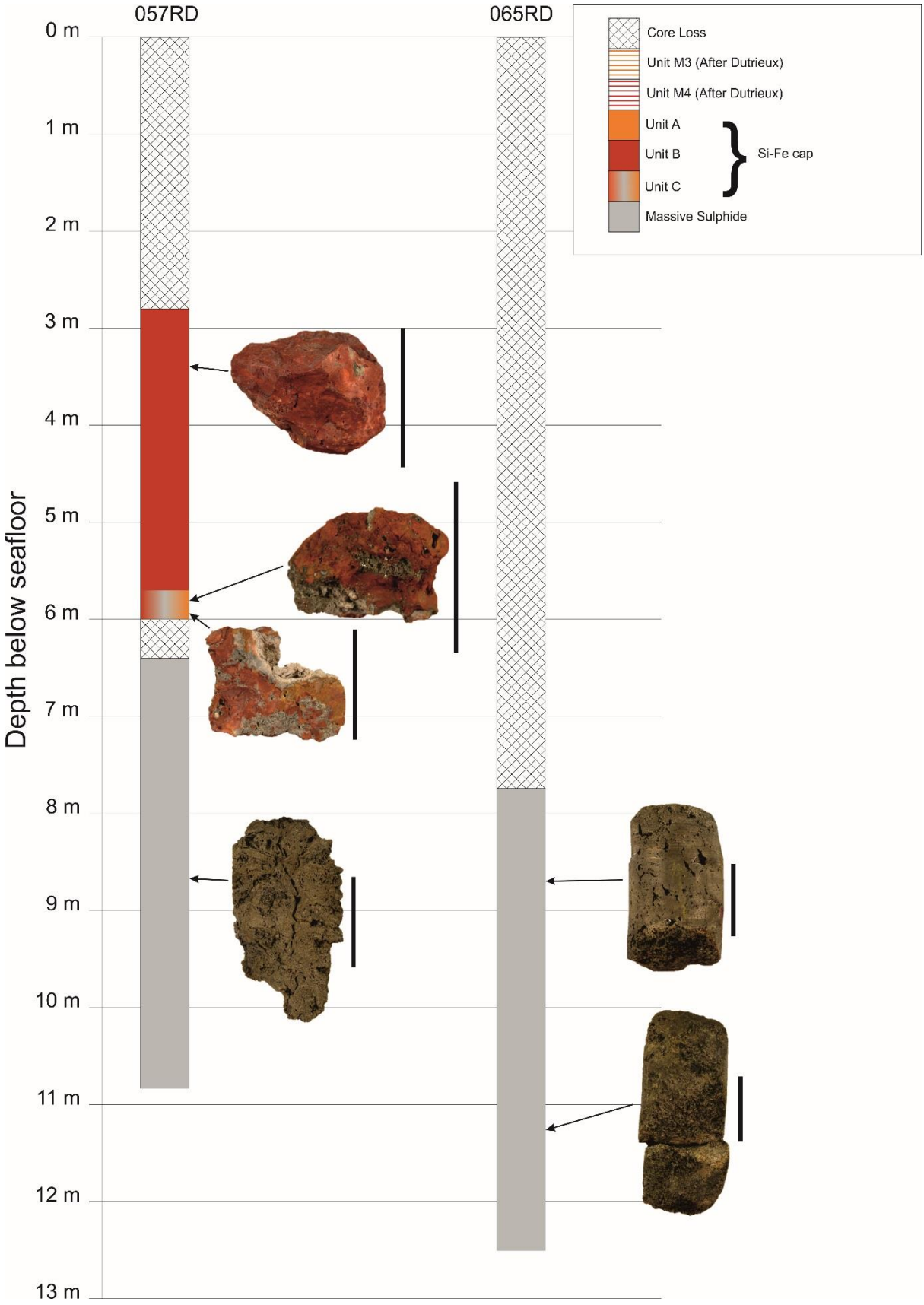

Figure 44: Summary core logs of 057RD and 065RD from Rona Mound. 057RD fully penetrated iron silica lithologies, whereas 065RD was drilled without coring through the iron silica materials. Scale bars = 5cm.

Weighted average recoveries for each RD drilling location were calculated from the percentage recovery from each run length for 057RD (10.9%) and 065RD (32.2%). Drilling without coring was recorded as 'core loss' in Figure 44.

3.3.2.1 Unit B

Unit B was recovered as a series of gravel sized pebbles throughout the drilling (e.g. Figure 45) with few competent core pieces, and was lower density, closer to that of Unit A. It was classified as Unit B due to the lack of macro-textures and colour variation observed in Unit A. Rare areas of sulphide grains were visible in hand specimen, and small patches of grey chert type material were observed, but these were localised and not considered enough to categorise this material as Unit C.

Figure 45: 057RD/Piece2, single pebble of Unit B. Visually similar to Southern Mound samples, however less dense. Small area of grey silica present in top right hand side of image. Scale bar = 5 cm.

3.3.2.2 Unit C

Unit C material was not recovered as easily as visually comparable Unit C material from Southern Mound. Recovered material was a mixture of red and orange brown iron oxides/oxyhydroxides, and exhibited the characteristic grey silica and sulphide enclaves enabling classification as Unit C material (Figure 46). However, recovered samples also shared characteristics with Unit A material in Southern Mound with apparent clasts, or visible clast like textures in the iron oxide portions.

Figure 46: Unit C sample with characteristic grey silica patches, material is silicified red and orange brown iron oxides/oxyhydroxides. Scale bar = 5cm.

3.3.3 MIR Zone

Two drill cores (073RD and 076RD) were recovered from a central area of the MIR mound from within Subzone 2 (Figure 47). The deepest hole (073RD) was cored to ~7.5m depth and fully penetrated sediments overlying iron silica materials and was terminated within massive sulphide material. 076RD did not fully penetrate iron silica material. Only Unit B material was recovered from both 073RD and 076RD no evidence of Units A or C was recovered.

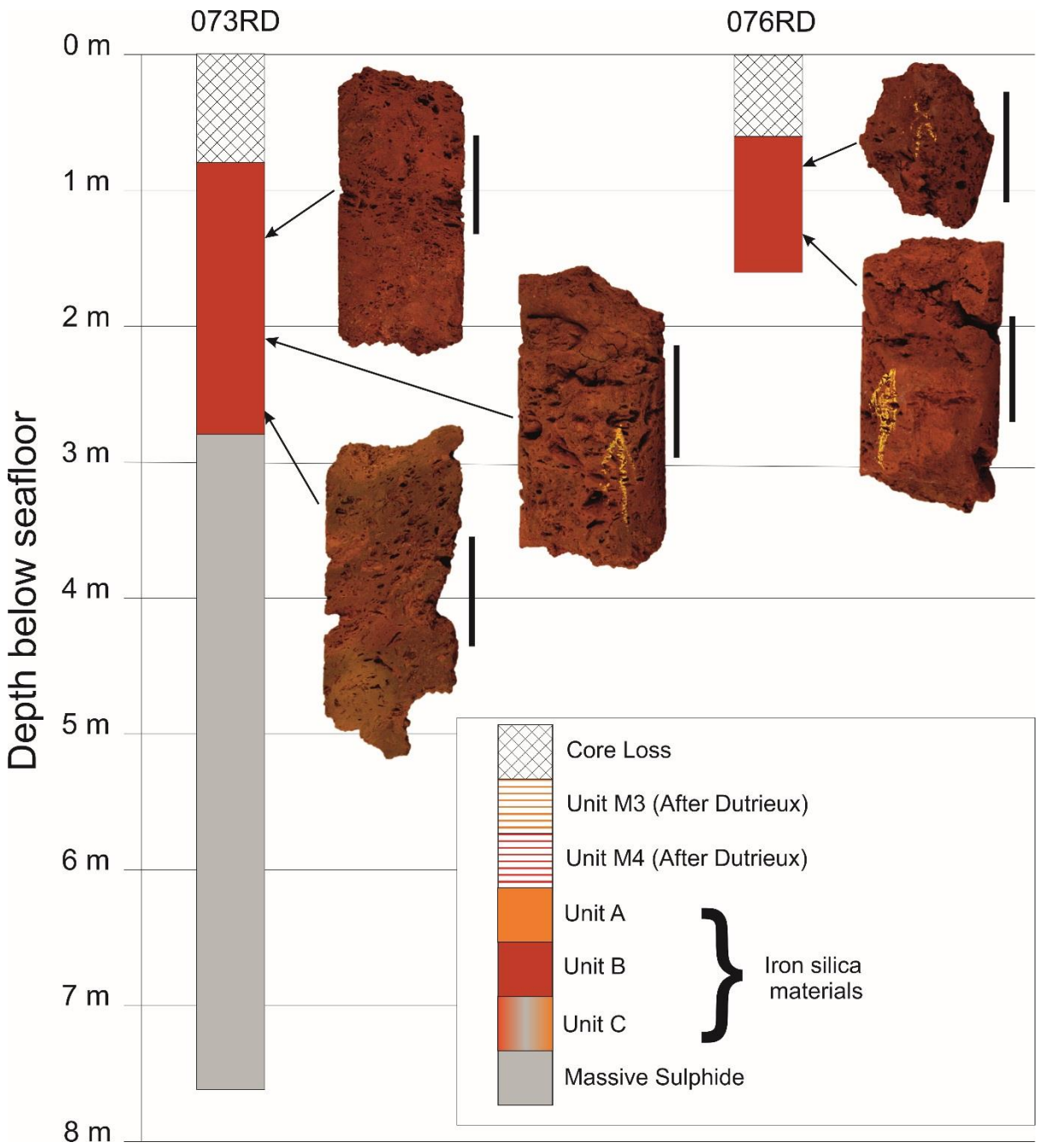

Figure 47: Summary drillcore logs from MIR Zone, all iron silica materials are from Unit B. Core loss is actually coring without drilling and represents the sediment cover. Scale bars = 5cm.

Weighted average recoveries for each RD drilling location were calculated from the percentage recovery from each run length for 073RD (24.7%) and 076RD (24.4%).

3.3.3.1 Unit B

Unit B was generally similar in appearance to material recovered at Southern and Rona mound, with observable void space in hand specimen, and the characteristic blood red haematite colour.

One exception to this was an orange-brown colour between ~2.9 m and 3.2 m depth in 073RD Figure 48, likely a product of differing iron oxide mineralogy. In hand specimen, the MIR zone Unit B appears to have more centimetre scale pores or voids, and typically has more visible disseminated sulphides and rare areas of apparent brecciation (Figure 49).

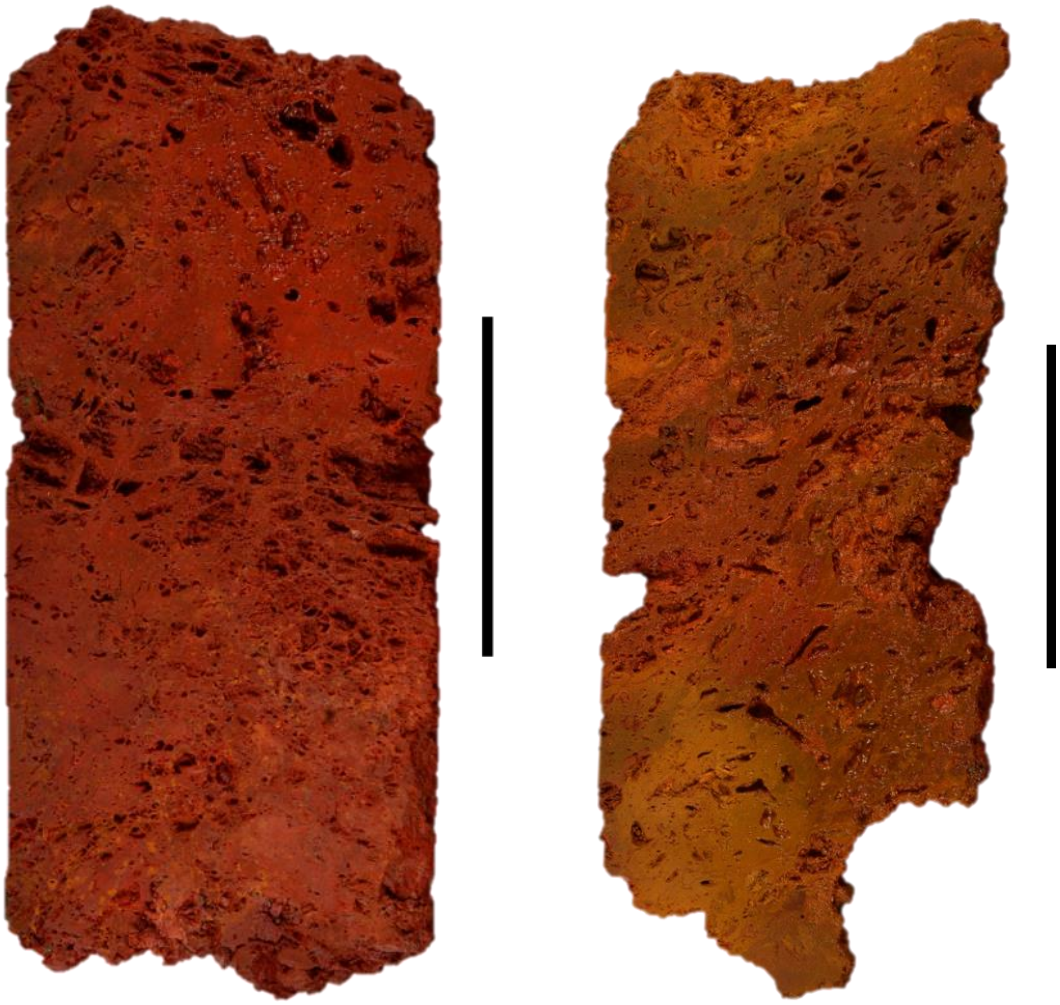

Figure 48: 073RD/Piece 6 (left) and 073RD/Piece 14 (right) shows the variation in colour composition of Unit B material at the MIR mound. Scale bars = 5cm.

3.3.4 Summary of Si-Fe occurrences across the three mounds

Figure 49 shows a comparative summary of the drilling results across the three eSMS mounds of interest. Iron silica lithologies were recorded at each eSMS deposit, overlying massive sulphide material and divided into three Units: A, B, and C.

Unit A was recovered as a comparably 'low' density, partially silicified, breccia of iron oxide and oxyhydroxides showing a wide range of centimetre scale textures. Unit B was recovered as a 'jasper' composed of silicified iron oxide with minor iron oxydroxides and locally disseminated sulphides.

Unit C was recovered as silicified iron oxides and oxyhydroxides with characteristic grey silica enclaves (composed of silica and disseminated sulphide).

The distribution of Units A-C across the three mounds is complicated, and although the three units are defined above, comparison is difficult (Figure 49). Unit A was only recovered from one out of three boreholes at Southern Mound, and was not recovered from Rona Mound nor the MIR Zone. The other two boreholes at Southern recovered hydrothermal sediment directly overlying Unit B material. Furthermore, the uppermost Unit B samples had large cavities infilled with dark red, iron oxide sediment indicating a clear stratigraphic and mineralogical relationship between Unit B and the overlying M4 sediments.

Unit B material from Southern Mound, is broadly comparable with MIR Zone; however both are significantly higher density then Unit B from Rona Mound.

Unit C material was recovered from one borehole at Southern Mound (050RD), and one borehole Rona Mound (057RD). Material from Southern Mound showed a more varied iron oxide component and seemed to be a higher density than Rona Mound Unit C samples (similar to the observations for Unit B). Unit C material was not recovered from the MIR Zone but the lack of penetration of Unit B (in one borehole), does not discount the occurrence of Unit C at depth. Despite fully penetrating the iron silica stratigraphy in 073RD, Unit C material was not recovered from MIR Zone.

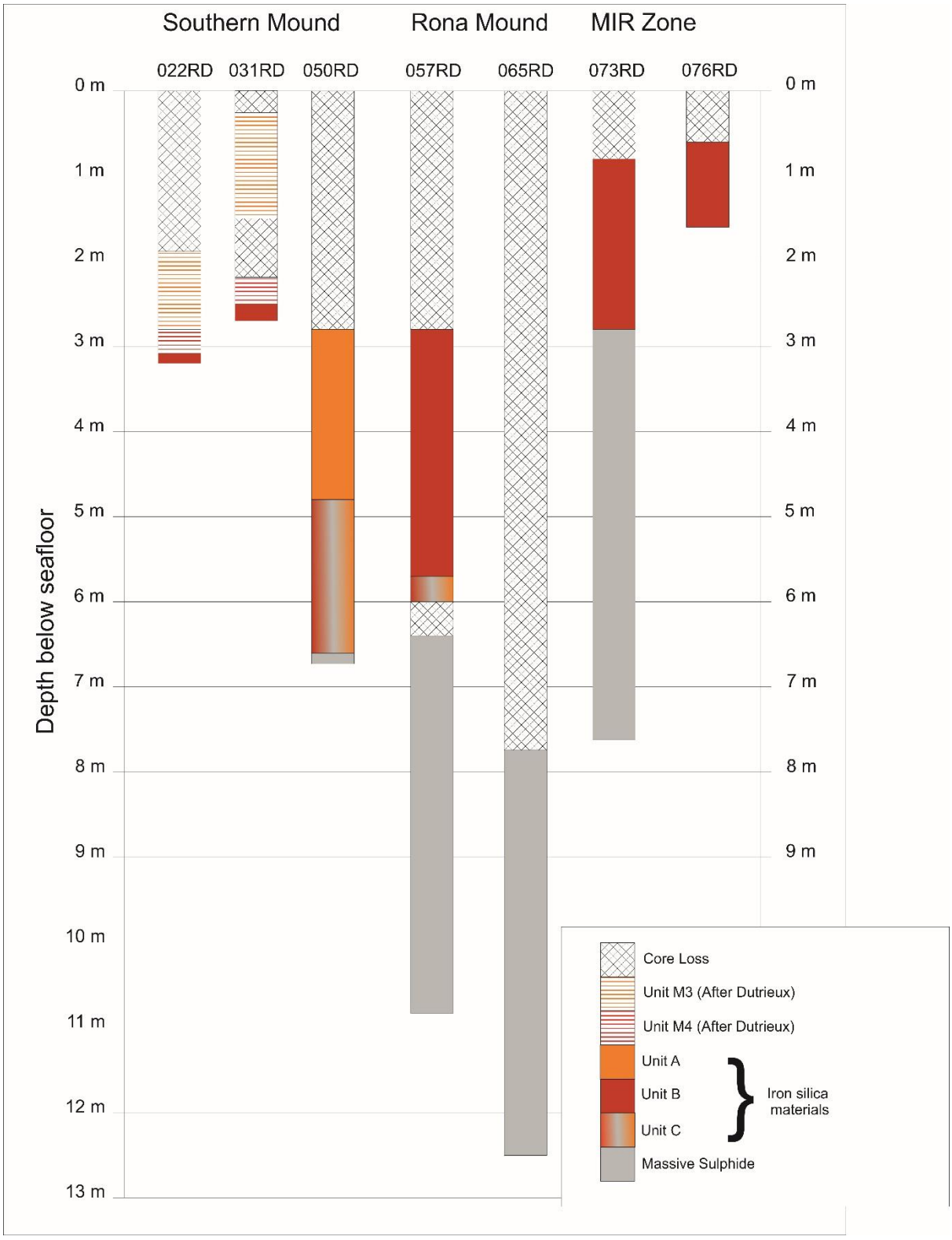

Figure 49: Drill core material recovered from each of the successful RD2 drilling locations. Core loss includes open hole drilling within 050RD, 057RD, 065R. Iron silica cap and sulphide thicknesses presented here are maximum possible thicknesses.

3.4 Cap Rock Dimension Estimation

An estimation of the lateral extent of the occurrence of the Si-Fe cap can be undertaken, based upon drill-core data, surface video surveying (where present), bathymetric interpretation, and the understanding of typical 3D characteristics of SMS deposits. The lateral extent of the Si-Fe cap can give an indication of the area over which a Si-Fe cap can form, and thus act as a barrier between oxidised seawater and the underlying massive sulphide.

3.4.1 Estimated lateral extent of the Si-Fe cap

3.4.1.1 Southern Mound

The capping unit was recorded as ~4m thick at the top of Southern mound based upon thickness obtained from 050RD. Assuming that Si-Fe material is a product of low temperature hydrothermal activity, the cap is interpreted to be thickest at the centre of the mound (i.e. a main conduit for hydrothermal fluids), and to taper distally. No evidence of a Si-Fe cap rock was observed within the shallow surface stratigraphy in the proximal western fault scarp, and although a thickness of red oxide sediment was observed in the eastern scarp, no visible competent material was observed. The Si-Fe cap is therefore not interpreted to extend further than the two proximal fault scarps from the centre of the mound. This data, combined, with bathymetric data, enables a NW-SE cross section of the cap rock to be constructed (Figure 50).

Very little evidence for the cap rock is present at the seafloor, and the northern and southern extent of the cap rock is difficult to determine. A ‘horse-shoe’ shaped fault scarp, likely a result of mass wasting, is present on the southern slope of Southern Mound. Video footage of this scarp showed no evidence of either iron oxide sediment, or Si-Fe cap rock material. The northern slope of Southern Mound is covered in a thickness of carbonate sediment, with little evidence of the substrate beneath. It is therefore probable that the cap rock does not extend past the horseshoe scarp to the south, and does not outcrop on the northern slope.

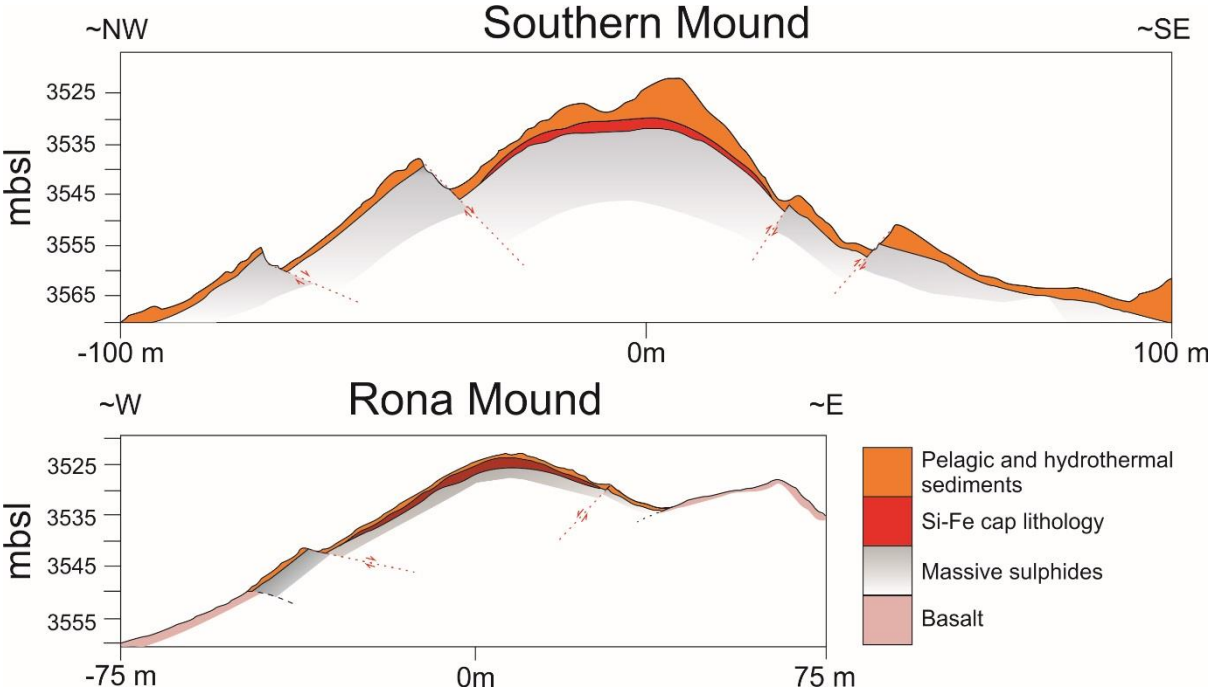

Figure 50: Schematic cross sections of Southern Mound and Rona Mound. Thicknesses are estimated based upon drill core data, bathymetry and surface geological information.

3.4.1.2 Rona Mound

A NW-SE cross section for Rona Mound can be constructed based on bathymetry and drill core data. Surface surveying was limited at Rona Mound, with only a short period of one HyBIS dive spent investigating the mound. No Si-Fe material was observed in the eastern fault scarp, and the western scarp was not observed during surface surveying. As the eastern fault appears to have a throw of ~ 1m, it is possible that the faults could post-date cap formation and the displacement is not enough to expose the cap at the seafloor. However, based upon the observations at Southern Mound, and the lack of Si-Fe material in the eastern fault scarp, it is interpreted that the Si-Fe cap does not extent past the fault scarp (Figure 50).

A part of the southern flank was surveyed, and was covered in pelagic sediment, showing no iron oxide sediment or Si-Fe material. The northern flank was not surveyed. Therefore, the NE-SW cross section of Rona Mound is estimated based upon based upon drill core data and the interpreted cross section for Southern Mound.

3.4.1.3 MIR Zone

MIR Zone was not surveyed during this investigation, therefore only drill core data cross section data and interpretation of bathymetry was available to estimate the morphology of the MIR Zone cap-rock. However, unlike Southern Mound and Rona Mound the interpretation of superimposed

constructive hydrothermal features of MIR Zone makes any kind of estimation of Si-Fe cap delineation difficult. Therefore no volume estimation calculation was undertaken for the MIR Zone.

3.4.2 Cap rock volume calculation

The 'footprint' of the Si-Fe cap rock in plan view can be approximated by oval shapes, based upon the aforementioned features and interpretation of the extent of the cap rock.

Based upon the oval plan view shape, and the NW-SE cross section of the cap rock, the volume of the cap rock can be approximated by the difference between two, oval based, conical volumes (Figure 51):

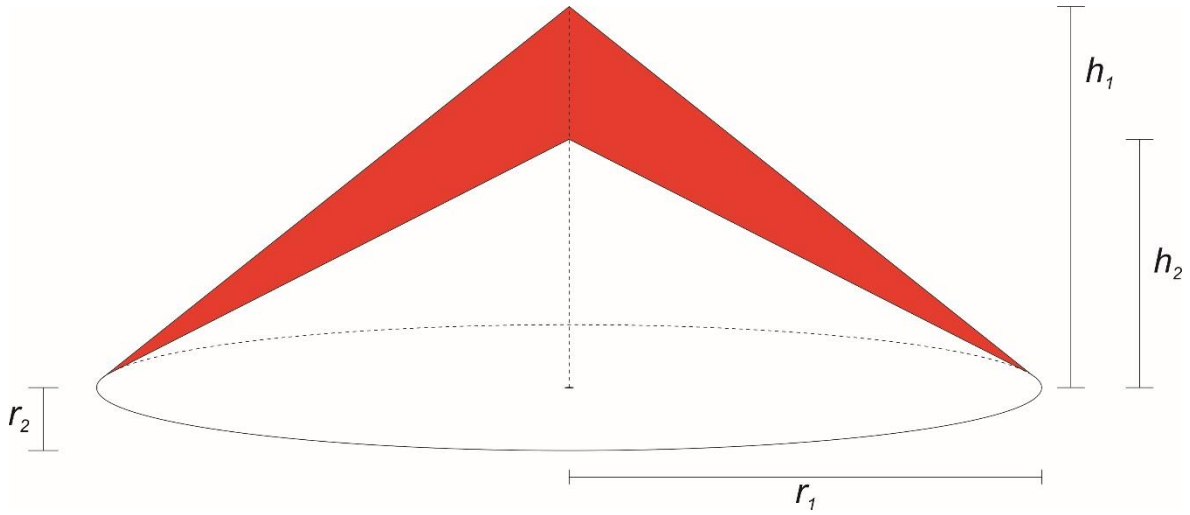

Figure 51: Simplified visualisation of the volume estimation of cap-rock material

$$Volume\ of\ cap\ rock = \frac{1}{3}r_1 r_2 h_1 - \frac{1}{3}r_1 r_2 h_2$$

Where dimensions are as follows:

r_1 = 'long' radius of estimated cap rock (along NW-SE cross section for Southern and Rona Mounds) in m

r_2 = 'short' radius of estimated cap rock along NE-SW line (along NW-SE cross section for Southern and Rona Mounds) in m

h_1 = 'height' from estimated shallowest depth of the top of the cap rock (mbsf) and deepest depth of the top of the cap rock (mbsf)

h_2 = 'height' from estimated shallowest depth of the bottom of the cap rock unit (mbsf) and deepest depth of the 'bottom of the cap rock unit (mbsf).

Estimated foot prints of the Si-Fe caps at both Southern and Rona Mound can be found in Figure 52 with r_1 and r_2 dimensions marked, and are calculated at ~43,020 m^2, and ~15,080 m^2 respectively. Values for h_1 and h_2 have been calculated based upon: seafloor depth at borehole locations, depth (mbsf) of the shallowest and deepest occurrence of the Si-Fe cap drilled, seafloor depth at the periphery of the estimated Si-Fe cap footprint, and an estimation of the depth (mbsf) at which the Si-Fe cap pinches out (Table 18). It is important to note that this estimation assumes a regular and uniform shape to the cap. This is likely not the case, but is the most sensible option for this calculation. Table 19 summarises the dimensions used for the calculation, and presents the two volume estimates for Southern Mound, and Rona Mound.

Table 18: Summary of depths from drill core data used to calculated h_1 and h_2

	Top surface (mbsl)	**Bottom surface (mbsl)**	**Terminal lateral depth (mbsl)**	**h_1 (m)**	**h_2 (m)**
Southern Mound	3537.5	3541.6	~3550	3550 – 3527.5 = 12.5 m	3550 – 3541.6 = 8.4 m
Rona Mound	3532.8	3535.9	~ 3545	3545-3532.8 = 12.2 m	3545-3535.9 = 9.1 m

Where:

Top surface of the Si-Fe cap from borehole data = seafloor depth of borehole - depth below seafloor of the shallowest Si-Fe material

Bottom surface of the Si-Fe cap from borehole data = seafloor depth of borehole – depth below seafloor of the deepest Si-Fe cap material

Terminal lateral depth = Estimated depth where the cap ‘pinches’ out

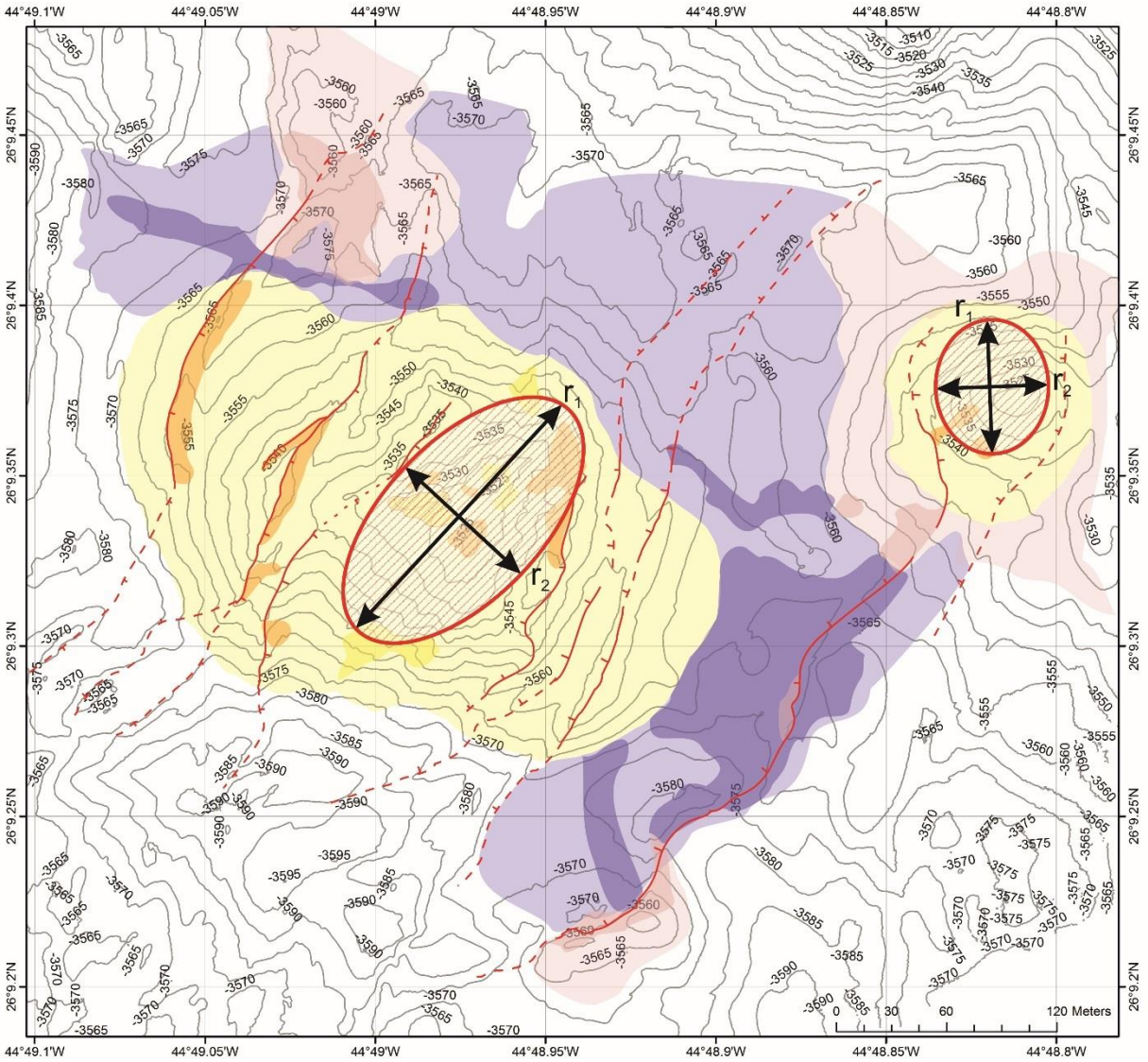

Figure 52: Estimated maximum footprints of the Si-Fe cap at both Southern Mound and Rona Mound, based upon lack of surface evidence within fault scarps.

Table 19: Dimensions used, and estimated cap rock volume calculation result

	r_1 (m)	r_2 (m)	h_1 (m)	h_2 (m)	Estimated Cap rock volume (m^3)
Southern Mound	165	83	12.5	8.4	18,716.5
Rona Mound	80	60	12.2	9.1	4960

Si-Fe capping materials are interpreted to have formed at the centres of both mounds and based on the above observations, are not interpreted to cover the whole footprint of the underlying massive sulphide orebodies. The Fe-Si caps were estimated to cover ~24% and ~48% of the interpreted massive sulphide orebody extent for Southern Mound and Rona Mound respectively.

3.5 Summary

The evidence presented in Section 3.2 highlights the role of seafloor weathering and evolution from an active SMS deposit (i.e. active TAG Mound) to a recently active eSMS deposit (ALVIN Zone Northern cluster) to a more mature weathered eSMS (ALVIN Zone – Southern cluster). The decay of these deposits is expected, and little evidence exists of any kind of potential preservation mechanisms from surface observations.

The observation and recovery of Si-Fe material from the three most weathered eSMS deposits studied in the TAG hydrothermal field is the first recovery of a thick sequence of *in-situ* Si-Fe material directly overlying massive sulphide material in eSMS deposits. The Si-Fe cap is overlain by several meters of iron oxide and oxyhydroxide rich sediment, in turn overlain by a thin iron oxyhydroxide and manganese oxide sediment, with pelagic sediment as the surface (proven at Southern Mound, assumed for Rona, and MIR Zone). Little to no evidence of the existence of a Si-Fe cap is present at the surface or within the fault scarps that dissect mounds (where present), only upon drilling of each mound was the Si-Fe discovered.

The Si-Fe cap can be separated into three different Units, which are not always present at each mound, or even at different locations on the same mound. It is important to understand that although similarities exist between the Si-Fe caps, each mound appears to have undergone slightly different formation mechanisms, resulting in three different Si-Fe facies, present across the mounds.

Limited Si-Fe material was recovered from the drilling of the active TAG mound, interpreted to be associated with low temperature, diffuse hydrothermal flow, and limited examples of Si-Fe surface samples have been recovered historically from the TAG hydrothermal field. The distribution of silica within the TAG active mound is well studied, but not as a Si-Fe cap.

The occurrence of Si-Fe materials, directly overlying massive sulphide materials, presents the first evidence of Si-Fe lithologies potentially comparable to Si-Fe materials associated with VMS deposits in the geological record (See Chapter 2). The observation of Si-Fe lithologies is not uncommon in VMS systems (discussed in detail in Chapter 2) but typically they do not form thick capping layers, directly overlying massive sulphide ore bodies as observed in the eSMS deposits.

In VMS systems, the preservation of massive sulphide orebodies is typically attributed to processes which either physically or chemically restrict the weathering of the sulphide ore bodies (i.e. rapid burial by comparatively impermeable material, or occurrence and burial associated with anoxia). However, the common preservation mechanisms throughout geological time, have not occurred to eSMS deposits, still at or near the seafloor. Thus another process which would either act as a physical or chemical barrier to massive sulphides would have to have occurred in eSMS deposits to enable preservation.

Surface observations of three areas of eSMS deposits are interpreted to show a range of seafloor weathering processes that generally show sequential and persistent weathering of deposits as they move off-axis. Prominent late-stage faults are observed to dissect two of the most weathering deposits (Southern Mound and Rona Mound), providing evidence that shallow massive sulphide material had been buried by < 1m of hydrothermal and pelagic sediment.

Upon drilling, Si-Fe caps were discovered at three eSMS deposits in the TAGHF, which present the first *in-situ* recovery of such material from eSMS deposits, and providing a potential candidate for an auto-preservation mechanism of eSMS deposits. Quantification of the extent of this cap rock (See Section 3.4), coupled with investigation of physical and chemical characterisation, and interpretation of the Si-Fe material paragenesis, could help determine whether or not this cap could be a common product at eSMS deposits, and if it could aid in their preservation. Understanding whether eSMS deposits are preserved on the seafloor could have a significant effect on the future of deep-sea mining, and possibly help understand what contribution eSMS deposits can have to global metal fluxes. The following chapter describes the range of physical and geochemical analysis undertaken to characterise these Si-Fe cap materials.

Chapter 4 Methodologies

4.1 Ship-based data collection

4.1.1 Seafloor Mapping – HyBIS RUV

The HyBIS robotic underwater vehicle (RUV) was deployed 7 times during the JC138 research cruise focussing on surface mapping and exploration of the eSMS deposits within the TAG hydrothermal field (Table 20).

Table 20: Summary of HyBIS dive workflow to produced interpretive maps

HyBIS workflow	
Dives and Dive Locations	A total of 6 dives were completed on Southern Mound, with part of one of the dives visiting Rona Mound. The seventh dive was completed over Shinkai, New Mound 2 and New Mound 3 deposits. The main features of the HyBIS RUV used were: two forward facing high-definition (HD) video cameras, a hydraulic manipulator arm, and a hydraulic powered sample storage drawer. A total of ~52 hours of HD video footage was recorded during the exploration dives across the eSMS deposits. The following stages were used to interpret the seafloor geology and produce geological maps of the eSMS deposits:
Real-time observation	Preliminary linking of observed features (e.g. fault scarps, bathymetric highs etc.) with previously obtained bathymetry data. Recording of sample locations and general characteristics to permit these to be linked to subsequent laboratory-based observations, imagery and mapping.
Post-dive location error correction	Post-dive comparison of RUV location based on USBL (Ultra short baseline) positioning data, and temporary shifting of base map so that the dive track corresponds to the bathymetry. Subsequent geological interpretation was all undertaken on this single 'master' base map.

Combining real-time observations with new locations.	Review of dive video footage. Interpretation of seafloor features and plotting of 'outcrop' on the master base map, to produce an 'outcrop' map showing all notable geological features. The outcrop maps are restricted to visual observations based upon the HD imagery, with limited extrapolation of seafloor features (e.g. faults) when they were not clearly observed during the survey.
Additional geological information	Obtained from the processed grab samples is used to validate bathymetric and image-based observations and interpretation.
Final product	Production of interpretive geological maps based on the outcrop mapping and bathymetry data.

4.1.2 Sub-surface drilling - BGS RD2

The British Geological Survey's (BGS) robotic drilling rig (RD2) was deployed at three different eSMS deposits during the JC138 cruise: Southern Mound, Rona Mound, and MIR Mound (summarised in Table 21). The rig is theoretically capable of drilling up to 55 m below the seafloor in 1.7 m long continual vertical sections.

Table 21: Summary of the RD2 drilling of the three eSMS deposits as part of the Blue Mining Research Cruise - JC138

Station	**Site**	**Latitude**	**Longitude**	**Depth (m)**	**Penetration (m)**	**Recovery (%)**
022RD	Southern	26°9.34'N	44°48.95'W	3535	3.5	50.9
031RD	Southern	26°9.34'N	44°48.94'W	3535	2.7	72.5
050RD	Southern	26°9.34'N	44°48.95'W	3535	6.7	16.6
057RD	Rona M.	26°9.36'N	44°48.79'W	3535	10.8	10.9
065RD	Rona M.	26°9.39'N	44°48.80'W	3530	12.5	32.2
068RD	Rona M.	26°9.37'N	44°48.79'W	3530	11.7	1.4
073RD	Mir Zone	26°8.60'N	44°48.39'W	3430	7.6	24.7
076RD	Mir Zone	26°8.61'N	44°48.39'W	3429	1.7	24.4

Out of the eight drilling locations, Si-Fe material was recovered from six, with only 065RD and 068RD at Rona Mound drilling into sulphides only.

The following flow chart (Figure 53) summarises the core handling protocol employed during both the M127 and JC138 cruises for both sediment and hard rock drill cores:

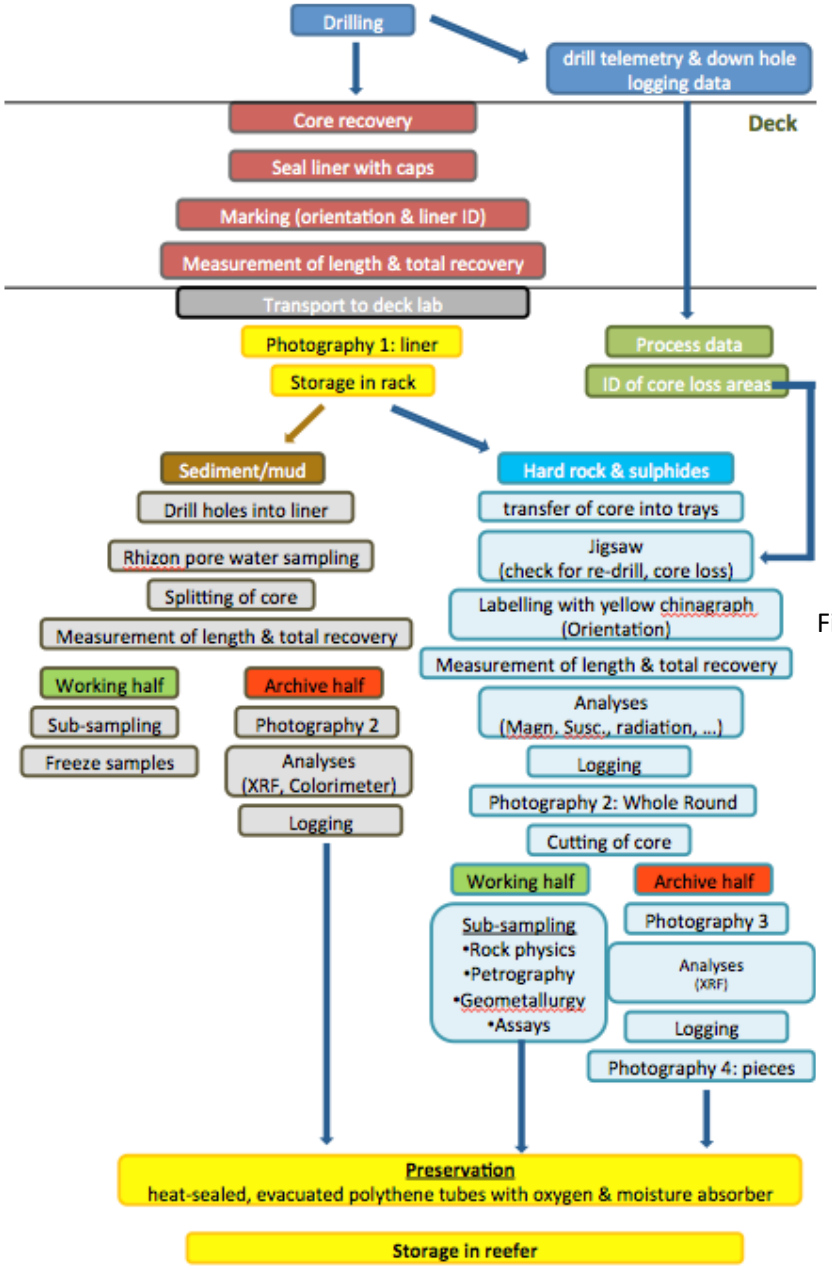

Figure 53: Workflow of sediment and drill core handling on the research cruise JC138 - applied to all sediment and hard rock samples

4.2 Petrology

A total of 13 polished thick (~100-150 µm) sections of hydrothermal sediments (Units M3 and M4) and 27 Si-Fe capping lithologies (Units A-C) were analysed using transmitted and optical light microscopy. All sections were later reduced to polished thin sections (~30 µm) and are summarised in Table 22.

Table 22: Summary of thin sections from the various Si-Fe cap rocks

Southern Mound			Rona Mound		MIR Zone
A	B	C	B	C	B
4	3	5	2	3	10

Photomicrographs were taken at the University of Southampton digital camera attachments on the microscope. Six polished block sections were prepared for LA-ICP-MS, and $\delta^{34}S$ investigation, and were also used for reflective light microscopy.

4.3 X-ray diffraction (XRD)

X-ray diffraction analysis works on the principle that x-rays are diffracted by crystal structures of minerals, therefore every mineral has a characteristic diffraction pattern enabling identification. 32 samples were analysed by XRD, where enough material was available quantitative analysis was undertaken, where not, qualitative analysis was undertaken (Table 23). Analysis was undertaken at the University of Southampton.

Table 23: Summary of XRD methodology and processes

Methodology	For each sample, 1.5g of material was weighed out, to which an internal standard of 25% by weight of corundum was added. Thereafter, samples were ground in a McCrone mill for 8 minutes under iso-propanol. To avoid preferred mineral orientation, the ground 'slurry' was dried and side-loaded in XRD sample holders. Any samples with insufficient material to side-load were placed on a silicon disc (non-diffracting crystal face), without the addition of corundum.
Instrument	PANalytical X'Pert pro diffractometer machine fitted with a Cu X-ray tube.
Operating conditions	The machine operating conditions were set at 35kV, 40mA utilising automatic slits and a step size of 0.02º 2θ at 1 second/ step.

Processessing	Semi-quantitative analysis of the sample was undertaken using XRD software (Siroquant V4.0, Sietronics Pty Ltd) that utilises the "Rietveld" technique. The data are corrected to remove the %corundum analysis. For samples in which the %corundum differs significantly from 25%, its abundance can be used to quantify the presence of amorphous, non-diffracting material.
Error estimates	The %error values are equal to one standard deviation of the total. Precision values and detection limits for bulk mineral analysis of crystalline materials are generally of the order of ±0.5-2%. Minerals quoted as present, but which are close to the detection limit should not be relied upon as an accurate record. For clay minerals and probably for opaline silica, accuracy is at best ±10% of the amounts present for concentrations >20%, and ±20% of the amounts present for minerals at concentrations <20%.

4.4 Scanning Electron Microscope

A selection of polished thin sections were chosen for SEM analysis using a Leo 1450VP SEM with an Oxford Instruments X-ACT 10mm^2 area SEM-energy Dispersive Spectrometer (EDS) at the University of Southampton. Whole slide backscatter electron images were obtained for six Si-Fe samples. Thin sections were carbon coated for the analysis. Topographic images were obtained from gold coated broken core samples to investigate the three dimensional textures.

4.5 Fourier Transform Infrared (FTIR) Spectroscopy

FTIR Spectroscopy is based upon the principle that samples absorb or reflect light differently, and that characteristic absorption or reflectance patterns of light at over a range of different wavelengths (reconstructed using Fourier Transforms). Absorption or reflectance is controlled by molecular vibrations, therefore minerals can be identified by characteristic spectra that correspond to the different molecular bonds (See Table 24). It is used here to assess the distribution of the four major minerals that form Si-Fe materials, as characteristic peaks can theoretically distinguish them. It is difficult to understand their distribution fully in thin section as the optical properties of both the iron oxides/oxyhydroxides interfere with each other. Understanding the distribution of the silica and iron oxides/oxyhydroxides can provide information that relates to the interpreting the

paragenesis of the Si-Fe cap, and determining whether they can form from typical hydrothermal processes.

Table 24: Summary of FTIR characteristics of relevant minerals from the Si-Fe cap

Mineral	Formula	Elemental Bonds	Characteristic wavenumber for peaks
Quartz	SiO_2	Si-O	Si – O = ~1180 cm^{-1} (prominent shoulder peak) ~ 1090 cm^{-1}, ~ 800 cm^{-1} and ~ 450 cm^{-1}
Opal-CT	$SiO_2.xH_2O$	Si-O, O-H	Si – O = ~1180 cm^{-1} (less prominent or no shoulder peak) ~ 1090 cm^{-1}, ~ 800 cm^{-1} and ~ 450 cm^{-1} O-H = 3400-3600 cm^{-1}
Haematite	Fe_2O_3	Fe-O	~ 1000 cm^{-1}, ˜550 cm^{-1}, ~480 cm^{-1}
Goethite	FeO.OH	Fe-O, O-H	~ 1000 cm^{-1}, ˜550 cm^{-1}, ~480 cm^{-1}. 900 cm^{-1} 800 cm^{-1} O-H = 3100 cm^{-1} and 3700 cm^{-1}

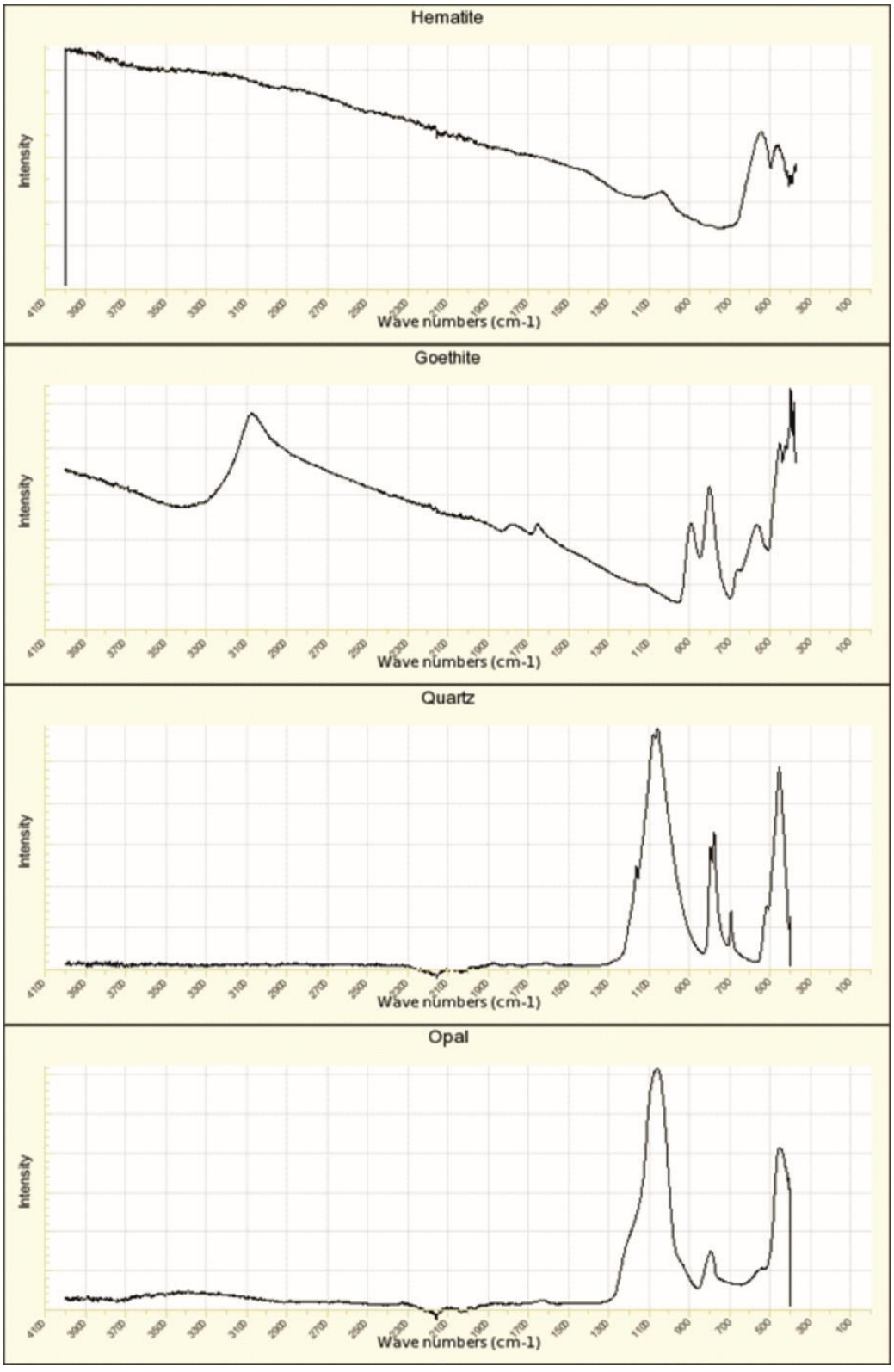

Mixed materials are also difficult to unambiguously interpret, in which strong Si-O band at ~ 1090 cm^{-1} overlap the haematite band at ~ 1000 cm^{-1}, and the quartz and opal-CT bands at ~ 800 cm^{-1} and ~480 cm^{-1} also overlap and interfere with the goethite bands at 800 cm^{-1}, and 450cm^{-1}. Both FTIR methods used in this investigation are summarised in Table 25 and were both undertaken at the University of Southampton.

Table 25: Summary of both FT-IR methodologies attempted as part of this project

Bulk Powders	Instrument	Nicolet Protege 460 FTIR
	Samples analyses	32
	Methodology	Approximately 0.1g of powdered material was subsampled from the bulk rock powder and mixed with KBr within an agate mortar. The material was thoroughly mixed with a metal spatula and transferred to a metal holder/mould. The sample was compressed into a thin in the holder/mould disc using a manual pneumatic. The holder is transferred to the FTIR machine and aligned with the infrared emission source. Each sample was analysed three times, with the holder rotated ~ 120°, producing 3 separate wavelength spectra per sample.
	Output	Range of .csv files from which spectra can be plotted in Excel
In-situ	Instrument	Perkin Elmer Spotlight 400 FT-IR microscope
	Samples	Range of thin sections from Units M3, M4, A, B, and C
	Methodology	Maps are produced from a series of 'point' analysis spectra to identify similar or different material across an area of investigation. The thin section stage is mounted in a sealed Perspex box (which helps limit atmospheric interference), and background scans are automatically subtracted from all individual spectra upon scanning. The analysis is limited to between 650 and 4000 cm^{-1} wavenumbers, therefore direct comparison between the bulk spectra and the in-situ spectra is only possible between these wavenumbers.

4.6 Whole Rock Geochemistry

Thirty Si-Fe whole-rock samples were processed at the University of Southampton for analysis of major and trace elements. Major elements were obtained by X-Ray Fluorescence (XRF) analysis, and traces were obtained by inductive coupled plasma mass spectrometry (ICP-MS) (Summarised in Table 26). Additional analysis of Total Sulphur, Total Carbon (TC), and Total Organic Carbon (TOC), were undertaken using a LECO CS225 elemental analyser, at the University of Aberdeen.

Table 26: Summary of major and trace elements discussed in this thesis, and the methods by which they were obtained. Where elements were analysed by both XRF and ICP-MS (i.e. Zn) the data from the most accurate and precise method was chosen. This is represented in this table.

XRF		**ICP-MS**		**LECO**	
Majors	**Trace**	**Majors**	**Trace**	**Majors**	**Other**
SiO_2, Fe_2O_{3T}, MgO, CaO, K_2O, Na_2O, P_2O_5	Zn	Al_2O_3, TiO_2, MnO	V, Cr, Co, Ni, Cu, Sr, Mo, Cd, Ba, Pb, Th, U REEs: La, Ce, Pr, Nd, Sm, Eu, Gd, Tb, Dy, Ho, Er, Tm, Yb, Lu, Hf	S	TC, TOC

4.7 X-Ray Fluorescence (XRF)

Table 27: Summary of XRF Methodology

Instrument	Philips MagiX PRO XRF
Majors analysed	SiO_2, TiO_2, Al_2O_3, Fe_2O_{3T}, MnO, MgO, CaO, K_2O, Na_2O, and P_2O_5
Trace elements analysed	Sr, Zr, Ni, Cr, Pb, Zn, Cu, Co, V, Ba
Sample processing	Approximately 0.5 g of sample powder was subsampled and oven dried overnight. Dried powders were mixed with Lithium Tetraborate flux at a 10:1 flux to sample ratio (±0.001%). Sample and flux material was added to platinum crucibles and fused into a bead using a Vulcan Fusion Machine.
Standards and CRMs	Pre-made: JR-1, GSP2-3, NIM-G, BHVO2 (5:1 flux to powder ratio) Made for this study: FER-1, FER-2, FER3, FER-4 (10:1 flux:powder ratio) Synthetic Fe_2O_3:SiO_2 beads at 40:60, 25:75, and 5:95 ratios.

4.8 Inductively Coupled Plasma – Mass Spectrometry (ICP-MS) - X Series

4.8.1 Standards and blanks

A suite of igneous rock standards (BCR-2, JB-2, BIR-1, JGb-1, BRR-1, BAS 206, JA-2, JB1a, BHVO2, AGV-2, JB-3) of basaltic to andesitic composition were included within the analysis to calibrate the data. Existing mother solutions of the rock standards had dilution factors of ~350, requiring 0.5 ml subsample in a 5 ml vial to get ~4000 times dilution (comparable with trace elements anticipated from the sample set). A further rock standard (JR-2) was also included in the analyses, however this was digested from powder rather than subsampled from existing mother solutions.

Samples were digested in 3 batches, the first and second batches included one blank each, with the third batch including 2 blanks. Each blank sample underwent the same digestion routine and subsampling protocol as the unknown samples. Two other blanks 'C blank' and 'As blank' were also run. 'C blank' underwent the same digestion routine as the rock standard mother solutions, and As blank underwent the same digestion routine as the other As standard solutions.

4.8.2 REE elements

Due to the generally low concentrations of rare earth elements within the samples, a separate analysis was undertaken with differing dilutions for samples and standards. Mother solutions of sample digests were diluted to ~1000 times, compared to the previous ~4000 times. Standards (BIR-1, JB-3, JGb-1, BHVO2, JB1a, JB-2, BCR-2, AGV-2, JA2, BAS206, and BRR-1) and CRMs JA-2 and JR-2 were diluted to ~40,000 times dilution. These two dilution factors resulted in broadly comparable raw counts for REEs and therefore would enable better precision for REE elements.

Where REEs are normalised (denoted by (REE symbol$_N$) they are normalised to carbonaceous chondrite values from Evensen *et al.* 1978. Light rare earth elements (LREEs) are defined as La, Ce, Pr, Nd, and Sm, and heavy rare earth elements (HREEs) are defined as Eu, Gd, Tb, Dy, Ho, Er, Tm, Yb, and Lu.

Europium anomalies (Eu/Eu*) were calculated after Worrall and Pearson(Worrall and Pearson, 2001), using the following formula:

$$\frac{Eu}{Eu^*} = \frac{Eu_N}{\sqrt{(Sm_N{}^2 + Gd_N{}^2)}}$$

Cerium anomalies (Ce/Ce*) were calculated after Worrall and Pearson(Worrall and Pearson, 2001), using the following formula:

$$\frac{\boldsymbol{Ce}}{\boldsymbol{Ce^*}} = \frac{\boldsymbol{Ce_N}}{\sqrt{(\boldsymbol{La_N}^2 + \boldsymbol{Pr_N}^2)}}$$

4.9 LECO CS225

30 samples of Si-Fe materials were analysed for sulphur (S), total organic carbon (TOC), and total carbon (TC) using a LECO CS225 elemental analyser at the University of Aberdeen. Samples are combusted and carbon and sulphur are oxidised to CO_2 and SO_2 respectively. CO_2 and SO_2 concentrations were analysed by non-dispersive infra-red cells (NDIR), which analyses the incident IR energy with respect to calibrated standards.

4.9.1 Standards and blanks

Four CRMs were run throughout the analyses, for both carbonised and decarbonised samples, standards were analysed in both the non-filtration crucibles, and the filtration crucibles for each respective sample set.

The selected CRMs were BCS-CRM 362, LECO 501-024 lot no. 1027, 501-502 LN 192-100-2, and 501-505 LN 1351 represented a range of carbon and sulphur values which were predicted to cover the anticipated carbon and sulphur values of the sample set.

A total of 24 blank analyses were undertaken throughout the analysis of standards and samples. Blanks were undertaken at certain intervals throughout the run of samples to establish a baseline for 'background' levels in the crucibles. Additional blanks were run at the beginning and end of each day, and after cleaning, or manual inspection, of any of the internal components of the LECO. These blanks were analysed to 'clean' the internal components and ensure that any relict carbon or sulphur materials were vaporised before any samples were analysed.

4.10 Accuracy and Precision calculations for geochemical analysis

For XRF, ICP-MS, and LECO analysis, accuracy is represented by "% Average Relative Error", which is defined as the average value of the % relative errors of the given element across all standards analysed. I.e. the accuracy of any given element across a range of standard materials.

'% Average Relative Error' is calculated by:

$$\%\ Average\ Relative\ Error = 100 * \frac{Absolute\ Error}{Standard\ elemental\ concentration}$$

'Absolute Error' is the difference between the average measured concentration for a given element (from repeated analyses of CRMs) and the reported concentration for the same given element in the CRM. 'Standard element concentration' is the published concentration of the given element in the CRM.

Precision is represented by relative standard deviation for 2 standard deviations (2σ RSD %), calculated by:

$$2\sigma \text{ RSD } (\%) = 100 * \frac{2 * Absolute\ Standard\ Deviation}{Standard\ elemental\ concentration}$$

Where 'Absolute Standard Deviation' is the standard deviation across the repeated analyses and 'Standard element concentration' is defined above.

According to (Jenner, 1996) 0-3% is excellent, 3-7% is very good, 7-10% is good and >10% is poor, and the following accuracy and precision information are highlighted as displayed in Table 28. Where concentrations of elements or elemental oxides are close to the instrument detection limits, accuracy values are not considered representative of the overall accuracy of the dataset, but have been included where calculated.

Table 28: Definitions and colour coding of accuracy and precision for all types of analysis

Excellent	Very Good	Good	Poor	N/A
0 - 3%	3 - 7 %	7 - 10 %	> 10 %	CRM concentration near detection limits of instrument

4.10.1 XRF

To assess the accuracy of the XRF data, eight CRMs (JR-1, GSP2-3, NIM-G, BHVO2, FER-1, FER-2, FER-3, and FER-4) and three synthetic standards of known SiO_2 and Fe_2O_{3T} ratios (95:5, 75:25, 60:40) were analysed. To assess precision of the XRF dataset, one random sample was repeated 10 times, and one CRMs (FER-2) were repeated 6 times each. Accuracy and precision values are calculated using the formulae in Section 4.10, and presented in Tables Table 29 - Table 31.

Table 29: Calculated accuracy of XRF data from CRMs

Accuracy (%)				
Element	**JR-1**	**GSP2-3**	**NIM-G**	**BHVO2**
SiO_2	2.07	1.55	0.76	0.61
TiO_2	7.82	4.05	-*	5.48
Al_2O_3	3.21	3.15	1.95	3.13
Fe_2O_{3T}	6.63	5.33	0.25	6.73
MnO	2.53	40.63	25.00	37.67
MgO	17.50	2.92	23.33	2.88
CaO	12.09	4.52	2.44	4.68
K_2O	5.10	5.76	3.07	1.35
Na_2O	1.92	3.71	2.59	4.68
P_2O_5	23.81	2.07	-$^+$	0.37
* = certified value below DL $^+$ = no certified value for CRM				

Table 30: Additional calculated accuracy of SiO2 and Fe2O3 XRF data from CRMs and synthetic beads

Accuracy (%)			
		SiO_2	**Fe_2O_{3T}**
SYN-1	Fe:Si = 5:95	0.62	2.50
SYN-2	Fe:Si = 25:75	0.11	2.77
SYN-3	Fe:Si = 40:60	0.19	3.01
FER-1		7.49	5.85
FER-2		0.88	2.03
FER-3		0.30	3.14
FER-4		5.63	6.09

FER-2 was repeated six times to test precision of the method for Fe and Si and one Si-Fe sample was selected at random and analysed 10 times to further test precision with an 'unknown' sample. Table 31.

Table 31: Summary of precision from CRM and 'unknown' sample

Precision (2σ RSD %)		
	FER-2	**'Unknown'**
Repeats	6	10
SiO_2	0.60	0.53
Fe_2O_{3T}	0.85	0.51
MnO	-	13.0
MgO	-	3.70
CaO	-	4.21
K_2O	-	4.80
Na_2O	-	1.17
P_2O_5	-	2.05

In general XRF accuracy of data in excellent or very good with the exception of poor accuracy when CRM concentrations were close to detection limits, and CaO in JR-1. Precision of SiO_2 and Fe_2O_{3T} was excellent to very good for FER-1 to FER-4, synthetic standards and an 'unknown' sample. Other major element oxides had excellent to good precision in the unknown sample with the exception of MnO where concentrations were close to the detection limits of the XRF.

4.10.2 ICP-MS

Accuracy and precision of the trace element ICP-MS data was tested by running two CRMs (JA-2 and JR-2) with each run throughout the analysis (Table 32).

Table 32: Accuracy and precision for a range of trace elements and select major elements obtained by ICP-MS

	JA2	JR-2	JA2	JR-2
	Precision (%)	Precision (%)	Accuracy (%)	Accuracy (%)
Al	0.14	0.72	1.93	3.23
Mn	1.34	0.32	5.43	9.32
P	3.37	32.18	6.08	33.72
Ti	4.67	3.11	5.93	14.76
Ba	1.94	0.97	1.04	29.61
Co	1.75	4.79	5.75	74.35
Cr	1.08	4.79	9.86	34.31
Cu	0.87	0.18	1.43	13.90
Mo	21.64	5.53	5.08	22.18
Ni	3.37	2.10	1.50	55.90
Pb	6.49	1.64	11.25	4.42
Sr	0.78	1.99	0.79	3.40
U	1.23	4.77	4.03	3.39
V	4.29	27.9	8.41	27.93
Zn	18.11	0.51	12.33	39.86

Precision of trace elements is typically excellent very good with respect to both JA2 and JR2. Accuracy is typically excellent to good for JA2, but is predominantly poor with respect to JR-2. This could be due to human error during the dilution process.

Accuracy and Precision of the rare earth elements (and Ba) ICP-MS data was tested by repeating two CRMs (JA2 and JR-2) three times each during the run (Table 33).

Table 33: Accuracy and precision for Ba, Y, and REEs from ICP-MS analysis

	JA2	JR-2	JA2	JR-2
	Precision (%)	Precision (%)	Accuracy (%)	Accuracy (%)
Ba	3.74	3.43	9.54	28.6
Y	5.71	7.48	1.39	1.05
La	3.75	0.55	6.16	11.04
Ce	4.39	0.58	4.94	3.43
Pr	6.52	0.46	7.66	1.19
Nd	5.94	0.77	0.89	6.65
Sm	6.39	1.35	5.29	6.00
Eu	6.41	3.08	4.30	29.35
Gd	8.45	0.94	5.24	4.72
Tb	13.41	0.90	7.14	6.09
Dy	10.98	0.95	0.73	0.38
Ho	9.25	0.81	17.30	4.70
Er	8.09	0.47	13.72	4.56
Tm	9.02	0.59	11.70	2.10
Yb	12.50	0.90	2.06	0.65
Lu	10.35	1.35	8.90	4.06

Accuracy and precision of REEs with respect to JA2 Is typically very good to good, with several values between 10 % and 17 % being poor. Accuracy and precision with respect to JR-2 is excellent to very good.

4.10.3 XRF vs ICP comparison

Nine elements were analysed by both XRF and ICP-MS and the results compared to observe the differences between the two methodologies. However, out of the nine elements only Mn, P, Cr, Cu, and Zn have sizable data populations from XRF that were significantly above the detection limits.

All five elements show good correlation ($R^2 > 0.7$) between XRF and ICP-MS analysis. Although the graphs shown in Figure 54 show that Cu and Zn appear to be skewed by 2 results up to two orders

of magnitude higher, removal of those two data points still give R^2 values of 0.96 and 0.92 for Cu and Zn respectively.

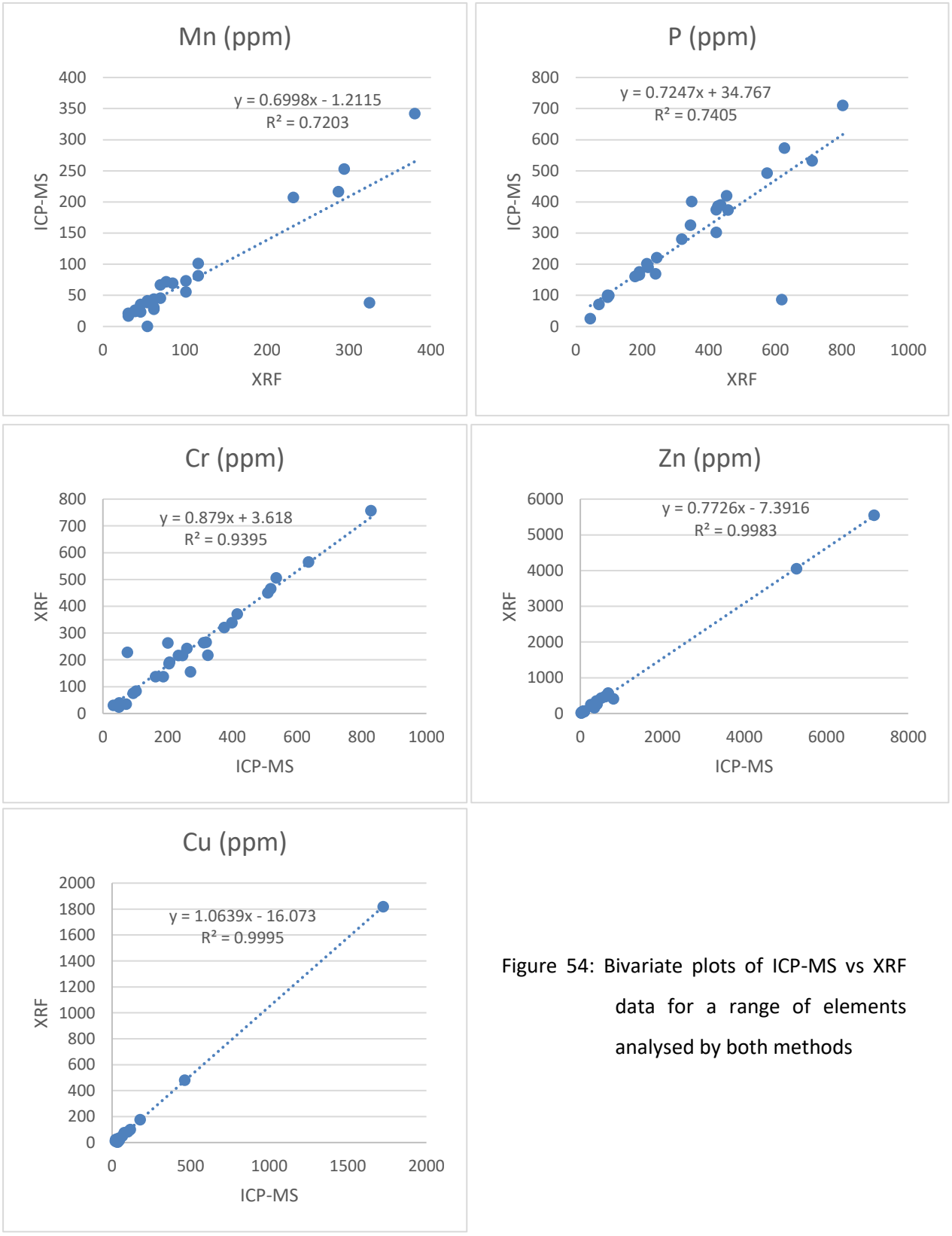

Figure 54: Bivariate plots of ICP-MS vs XRF data for a range of elements analysed by both methods

4.10.4 LECO CS225

To assess accuracy and precision of sulphur, TC, and TOC, a series of 4 CRMs were included within the analysis: BCS-CRM 362 (powder), LECO 501-024 lot no. 1027 (powder), 501-502 LN 192-100-2 (carbon steel rings), and 501-505 LN 1351 (carbon steel rings). Standards were repeated between analysis of carbonated and decarbonated samples, as well as at multiple points within the analysis procedure. Precision and accuracy for all four standards were excellent to good. (Table 34)

Table 34: Summary of accuracy and precision of LECO data from CRMs

	n	Avg measured TC (wt%)	Avg measured S (wt%)	Certified TC (wt%)	Certified S (wt%)	Precision C (%)	Precision S (%)	Average RSD (%) C	Average RSD (%) S
BCS-CRM 362	22	9.57	1.49	-	1.48	-	1.59	-	1.67
Leco 501-024 lot no. 1027	8	3.23	0.04	3.33	0.05	3.00	1.69	0.34	3.67
501-502 LN 192-100-2	10	0.06	0.02	0.06	0.01	0*	1.88	9.03	3.92
501-505 LN 1351	8	0.54	0.02	0.54	0.02	0*	2.20	0.81	4.29

* All result recorded the certified TC values to 2 d.p.

4.11 Oxygen Stable isotopes

A total of 30 whole rock powders, and 30 leached 'silica' powders were analysed for oxygen isotopes, were analysed at Scottish Universities Environmental Research Centre (SUERC), East Kilbride.

4.11.1 Laser Fluorination

The laser fluorination technique used at SUERC is a variation on the methodology described by Sharp (1990) where full details can be found, but the methodology is summarised in Table 35.

Table 35: Methodology of laser fluorination undertaken at SUERC, East Kilbride

Step 1	Combust a sample using a carbon laser within an atmosphere enriched in fluorine (in this case using a chlorine trifluoride (CLF_3) reagent) to replace the oxygen in the silica with fluorine, and produce gaseous O_2
Step 2	Once the sample has been combusted the residual atmosphere is pumped through a system of metal piping, through two liquid nitrogen cold finger traps. This freezes the excess reagent, but not the oxygen released from the sample.
Step 3	The oxygen is then passed through a mercury trap, and a slush trap (made from acetone and dry ice) to remove any non-reacted reagent not condensed by the liquid nitrogen traps, and any other elemental impurities.
Step 4	The sample passes into a glass flask with a heated carbon coil. This coil converts all O_2 to CO_2 which is then transferred to another glass chamber to measure the pressure of gas samples (to calculate yield from the sample).
Step 5	Finally, the gaseous CO_2 is transferred to a mass spectrometer tube, and sent to the mass spectrometer to analyse the oxygen isotopic composition
Step 6	The system is then pumped under low vacuum, then high vacuum, to remove any residual gaseous material before another sample is passed through.

4.11.2 Silica Leached Powders

Due to the intrinsic 'sub-microscopic bonding' of iron oxide and silica within the samples, bulk oxygen isotope values would be a mixture of both the iron oxide and silica materials. Therefore, separation of the silica material from iron oxides by acid leaching was undertaken at the University of Southampton based upon a technique described by Cope *et al.* (2002) (See Table 36). This would enable the silica leached powders to be analysed separately from bulk material, and enable calculation of oxygen isotopic composition of both the iron oxide and silica fractions. Several randomly selected samples were analysed by XRF to determine the silica content before being analysed for oxygen stable isotopes, with all tested samples showing SiO_2 concentrations > 99 wt%.

Table 36: Leaching methodology used to obtain silica powders from bulk sample powders

Step 1	Approximately 1 to 2g of powdered sample was added to a 50 ml plastic centrifuge tube and then made up to between 20 ml and 30 ml with ~ 25% HNO_3. Samples were left in a warm (~30°C - 40°C) ultrasonic water bath and checked every hour for progress.
Step 2	Once no more reaction was observed, samples were centrifuged and the acid pipetted off, and more acid added to ~20-30 ml.
Step 3 (optional)	If a sample had recorded or observed sulphides, the HNO_3 was replaced with HCl until all reaction ceased, then continued with HNO_3.
Step 4	This method was repeated with increasing acid concentrations until eventually concentrated HNO_3 was used.

4.12 Laser ablation ICP-MS (LA-ICP-MS)

A Nu Wave laser was attached to a Thermo Scientific Fisher X Series ICP-MS to undertake the analysis. Laser spots of 20, 25, 30, 40, and 50 microns were selected based upon the size of the grain/area of analysis. NIST 610, NIST 612, and MASS1 CRMs were analysed at all five different spot sizes chosen for the various analyses to calibrate the data. Use of particular CRMs for certain elements is restricted by the range of certified elements for each CRM (Table 37).

Table 37: CRMs and elements where certified values enabled calibration

Calibration CRMs	**Element**
NIST610, MASS-1	Cr
NIST610, NIST612, MASS-1	Fe, Co, Cu, Zn, As, Ag, Sb, Au
MASS-1	V, Ga, Ge, Mo, In, Sn, Hg, Bi
NIST610, NIST612	Ni, Se, Ba, Tl, Pb, U

4.12.1 Internal Standards

SEM EDS spectra (a mixture of spot and area analysis) of sulphide composition was used to determine appropriate internal standard concentrations to use for each sulphide group, with average values used (Table 38). Fe was used as an internal standard for pyrite, Cu for chalcopyrite, and Zn for sphalerite.

Table 38: SEM EDS spectra results for internal standard use for sulphides

	Pyrite			**Chalcopyrite**			**Sphalerite**		
	n = 28			**n = 4**			**n = 34**		
	Fe (wt%)	**S (wt%)**		**Cu (wt%)**	**Fe (wt%)**	**S (wt%)**	**Fe (wt%)**	**Zn (wt%)**	**S (wt%)**
Average	45.98	53.37		33.10	31.45	35.43	10.91	54.89	33.38
Maximum	48.30	55.90		34.40	32.70	35.80	17.22	62.22	34.60
Minimum	44.10	51.70		32.00	30.40	35.10	3.56	48.18	32.56

4.13 O isotope analysis - silica

4.13.1 Accuracy and Precision

Three different internal standards were analysed in conjunction with the unknown samples, YP2 ($\delta^{18}O$ = 16.4, quartz), JJB8 ($\delta^{18}O$ = 30.3, agate), and UWG2 ($\delta^{18}O$ = 5.6, garnet). These standards were chosen as they represent the anticipated range of oxygen isotopic values for the unknown samples. Eight samples of YP2 were not included within the calculation based upon unusually low yields during analysis. Accuracy is represented by the Error (%) and precision is represented by the standard deviation, both are classed as excellent to good (Table 39)

Table 39: Accuracy and precision of oxygen isotopic data

Standard	Repeats (n)	Expected value	Average value	Standard Deviation (σ)	2 σ relative standard deviation (%)	Error (%)
YP2	33	16.4	16.39	0.30	3.66	0.05
JJB8	27	30.3	30.24	0.22	1.46	0.19
UWG2	27	5.6	5.80	0.24	8.28	3.45

4.13.2 Formation Temperature Calculations

Formation temperatures can be calculated for both the iron oxide and silica fractions using the principle of oxygen isotope geothermometry, using Kita (1985) and Sharp (2016) equations for the appropriate mineral-water system.

In order to calculate the formation temperatures the oxygen isotopic fractionation factor between the mineral and water (α) is required, where α is calculated by:

$$\alpha = \frac{(1 + 10^{-3}\delta^{18}O_{MINERAL})}{1 + 10^{-3}\delta^{18}O_{WATER}}$$

Where $\delta^{18}O_{MINERAL}$ is analysed for each silica sample using the laser fluorination technique (described in Section 4.11.1), and in this case $\delta^{18}O_{WATER}$ is assumed. The fluids which are involved in precipitating these minerals are likely a result of mixing of Atlantic bottom water (SW = $\delta^{18}O$ ~ 0 ‰ (Frew *et al.*, 2000)), and hydrothermal fluids (HF = $\delta^{18}O$ = + 1.7‰, based upon end member hydrothermal fluid from active TAG mound, (Shanks III *et al.*, 1995)). Therefore theoretical maximum and minimum values are be calculated by assuming either seawater dominated or hydrothermal fluid dominated $\delta^{18}O_{WATER}$.

4.13.2.1 Kita (1985) – Amorphous Silica/opal-CT

Kita's formulae were derived from experimental work of oxygen isotope fractionation between amorphous silica and water at low temperature (34-93˚C)(Kita *et al.*, 1985). The oxygen isotope fractionation factor between silica and water (α), and the relationship between α and formation temperature are defined as follows:

Formation temperature (T (in Kelvin)) vs. α:

$$10^3 ln\alpha = 3.52(10^6 T^{-2}) - 4.35$$

4.13.2.2 Sharp (2016) – Quartz

Sharp provides a more updated version of the formation temperature calculations from oxygen isotopes derived from a different equation from a range of high temperature experiments (250˚C - 800 ˚C), of :

$$1000.ln\alpha = \frac{4.20(0.11)10^6}{T^2} - \frac{3.3(0.2)1000}{T}$$

This equation was combined with a series of published low temperature samples (including Kita 1985 data) and diatom data (Sharp *et al.*, 2016), to include low temperature quartz assemblages, with the equation as follows:

$$1000.ln\alpha = \frac{4.28(0.07)10^6}{T^2} - \frac{3.5(0.2)1000}{T}$$

This equation including low temperature data was described as 'near identical' as the above 'high temperature' formula, thus extending the range of valid temperatures for the SiO_2 – H_2O system.

4.14 Sphalerite geothermometry

The geothermometer works on the basis that the amount of iron, which substitutes for Zn, in sphalerite is a function of temperature.

Formation temperature can be estimated using the following equation from(Keith *et al.*, 2014):

$$\frac{Fe}{Zn_{Sphalerite}} = 0.0013\,T(^{\circ}\mathrm{C}) - 0.2953$$

Simplistically rearranged to:

$$T(^{\circ}\mathrm{C}) = \frac{\frac{Fe}{Zn_{Sphalerite}} + 0.2953}{0.0013}$$

Where iron and zinc are in weight percent, and T is in Celsius.

4.15 Three dimension (3D) X-ray microtomography

Simplistically, a series of two dimensional (2D) X-ray absorption images are taken 360° around a single sample. Following this, a three dimensional volume can be produced, using the mathematical principals of tomography, where each voxel (three dimensional equivalent of a pixel) represents the x-ray absorption of a 3D volume. X-ray absorption is controlled by the density of the material

being scanned, therefore the internal structure of the sample can be determined from the three dimensional reconstruction, assuming the sample exhibits variable density.

All X-ray CT scans were undertaken at the µ-VIS facility at the University of Southampton. Eight samples were analysed on a 'Modified 225 kVp Nikon/X-tek HMX micro-focus X-Ray CT system' to assess the porosity and permeability of the three Si-Fe cap units (A-C) and the underlying massive sulphide. The aimed resolution for these scans was to between 20 and 40 microns, and to achieve this samples would typically be scanned in two, or three parts which were concatenated digitally as the first step of image processing (Table 40).

Table 40: Low resolution sample catalogue

Sample	**Lithology**	**Low resolution whole core scan voxel size (µm)**
050RD/P3	Unit A	34.7
050RD/P8	Unit A	34.7
073RD/P14	Unit B	34.7
076RD/P6	Unit B	34.7
050RD/P11	Unit C	34.7
057RD/P11	Unit C	34.7
065RD/P15	Massive sulphide	34.7
073RD/P28	Massive sulphide	34.7

3 samples were analysed in the Zeiss 160 kVp Versa 510 to assess filamentous/mesh networks of iron oxides and silica within the samples. The aims of these scans were to focus on these complex 3D structures at a high resolution aiming to ~ 1-2 micron resolution (Table 41)

Table 41: High resolution scan sample catalogue

Sample	**Sample Area**	**Dimensions**	**Voxel size (µm)**	**Scanned volume (mm^3)**
050RD/P8	1	1980x2026x1990	1.689	38.46
	2	1984x2026x1990	1.689	38.54
	3	1976x2026x1989	1.689	38.37
050RD/P11	1	1980x2026x1988	1.789	45.66
	2	1984x2026x1990	1.804	46.96
076RD/P6	1	1976x2026x1987	1.891	53.79
	2	1972x2026x1985	1.764	43.53

Chapter 5 Mineralogical characteristics of Si-Fe cap rock

5.1 Introduction

Having determined that Si-Fe deposits have formed a capping rock over the central zones of each of three different SMS mounds, with the potential to act as a barrier or seal between the underlying massive sulphide and seawater, it is important to determine how the material has formed and what it tells us of the paragenesis of the deposit.

Review of Si-Fe material from VMS deposits and modern day SMS deposits reveal that a wide range of hydrothermal and sedimentary processes can combine to form comparable material, including: precipitation from hydrothermal fluids, weathering of massive sulphide material, and also highlight the potential role of microbes or bacteria in Si-Fe deposit formation.

Interpretation of the formation processes that have formed the Si-Fe materials at the eSMS deposits can enable understanding of whether these deposits could have formed from generic hydrothermal processes (i.e. as interpreted from VMS deposits), or whether they have a unique formation mechanism, and are unlikely to form at other deposits. This has specific implications for the global potential for eSMS preservation rather than just a few unique deposits.

As such a range of techniques have been used to define and describe the mineralogy, physical textures, and characteristics of both the overlying hydrothermal sediment cover (Units M3 and M4), and the Si-Fe capping materials (Units A-C) in order to understand the formation processes of the cap. Techniques employed include thick and thin section petrography, reflected light petrography, X-ray Diffraction (XRD), Scanning Electron Microscopy (SEM), Fourier transform infrared spectroscopy (FTIR). Full analytical processes can be found in Chapter 4 regarding the methodologies.

5.2 Overlying sediments – Units M3 and M4

Hydrothermal sediments overlying the Si-Fe deposit are recovered from holes 022RD and 031RD, both from Southern Mound, and provide a continuous record of the transition from unconsolidated sediment to hard rock at the mounds. The sediment stratigraphy was split into four different units (See Section 3.3), with the two lower ones, Units M3 and M4, representing hydrothermal material that share characteristics with the underlying Si-Fe materials at Southern Mound.

Unit M3 was recorded between ~1m and ~3 m at Southern Mound as a thickness of orange-red goethite and amorphous fraction dominated sediment (Table 42). Although no crystalline silica minerals have been identified by XRD, the presence of amorphous silica is identified by transparent clasts interpreted to be Si-Fe material. Individual iron oxide/oxyhydroxide and Si-Fe clasts exhibit a wide range of heterogeneous textures including: filamentous, dendritic, and colloform growth textures, as well as massive and laminated clasts throughout. More homogeneous, clast free, fine-grained iron oxyhydroxides that show few millimetric scale textures occur in one section, from ~2mbsf.

Unit M4, the lowest sediment unit at Southern Mound was recovered at ~2.9 and ~2.3 mbsf in the two boreholes. Units M3 and M4 are differentiated by a marked colour change (orange-red-brown to dark red), which is a product of a change in dominant iron mineralogy. In contrast to the goethite and amorphous mineralogy of Unit M3, Unit M4 is dominated by fine-grained haematite with rare goethite and quartz. Quartz is present within the unit as rare clasts of Si-Fe material (~250µm), identified by their transparent nature.

Table 42: XRD analysis of Unit M3 and M4 sediments, (from Dutrieux, 2019)

Sample	**Unit**	**Mineralogy %**							
		Qz	**Tridy**	**Crist**	**Haem**	**Goe**	**Non**	**Hal^{+}**	**Amor**
022RD – 193 cm	M3	-	-	-	-	36.0	-	-	64.0
022RD – 225 cm	M3	-	-	-	-	100.0	-	-	-
022RD – 261 cm	M3	-	-	-	-	57.9	-	-	42.1
022RD – 275 cm	M3	-	-	-	-	72.2	4.6	-	23.2
022RD – 289 cm	M3	-	-	-	-	35.1	-	-	64.9
031RD – 105 cm	M3	-	-	-	-	51.1	-	-	48.9
031RD – 125 cm	M3	-	-	-	15.5	29.4	-	-	55.1
031RD – 155 cm	M3	-	-	-	-	69.7	-	-	30.3
022RD – 289 cm	M4	-	-	-	64.9	35.1	-	-	-
022RD – 305 cm	M4	8.8	-	-	91.2	-	-	-	-
031RD – 229 cm	M4	10.6	-	-	89.4	-	-	-	-
Qz = Quartz, Tridy = Tridymite, Crist = Cristobalite, Haem = haematite, Goe = goethite, Non = nontronite, Hal = halite, Amor = Amorphous fraction. $^{+}$Halite removed from analysis									

Sparse pyrite grains, present either individually or as cores surrounded by later growths of haematite, and identified in Unit M4 by reflected light microscopy, but are not observed in Unit M3. The amount of pyrite was not present in sufficient quantities to be identified by XRD analysis. Discovery of rare pyrite indicated that although the hydrothermal sediments are dominated by oxidised iron minerals, some evidence of reduced conditions exists in the sediments.

5.2.1 Distribution of silica

The presence of free silica in the samples is indicated by the presence of transparent colourless amorphous grains often filling pore space or mixed within a matrix of iron oxide and iron oxyhydroxides.

In Unit M3, zonation and boundaries within the matrix indicates heterogeneous cementation (i.e. variable patches of radial growth (Figure 55)), likely by amorphous silica, but the extent is masked by the opacity of the iron-rich mineralisation. Unit M4 exhibits a similar relationship, but the extent of masking is higher as haematite is more opaque than goethite. Silica free of iron oxide pigmentation was not observed within the sediments, and there is little information on the morphology or structure of silica within individual Si-Fe clasts.

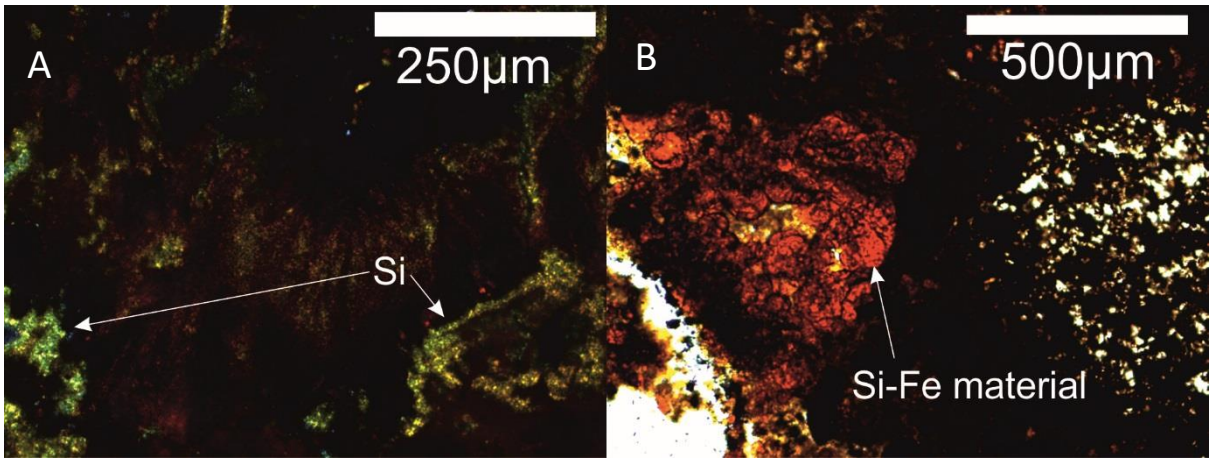

Figure 55: (A) Amorphous silica surrounding iron oxide/oxyhydroxide material – TL-XPL (B) Si-Fe clast exhibiting radial growth textures in Unit M3 – TL-PPL.

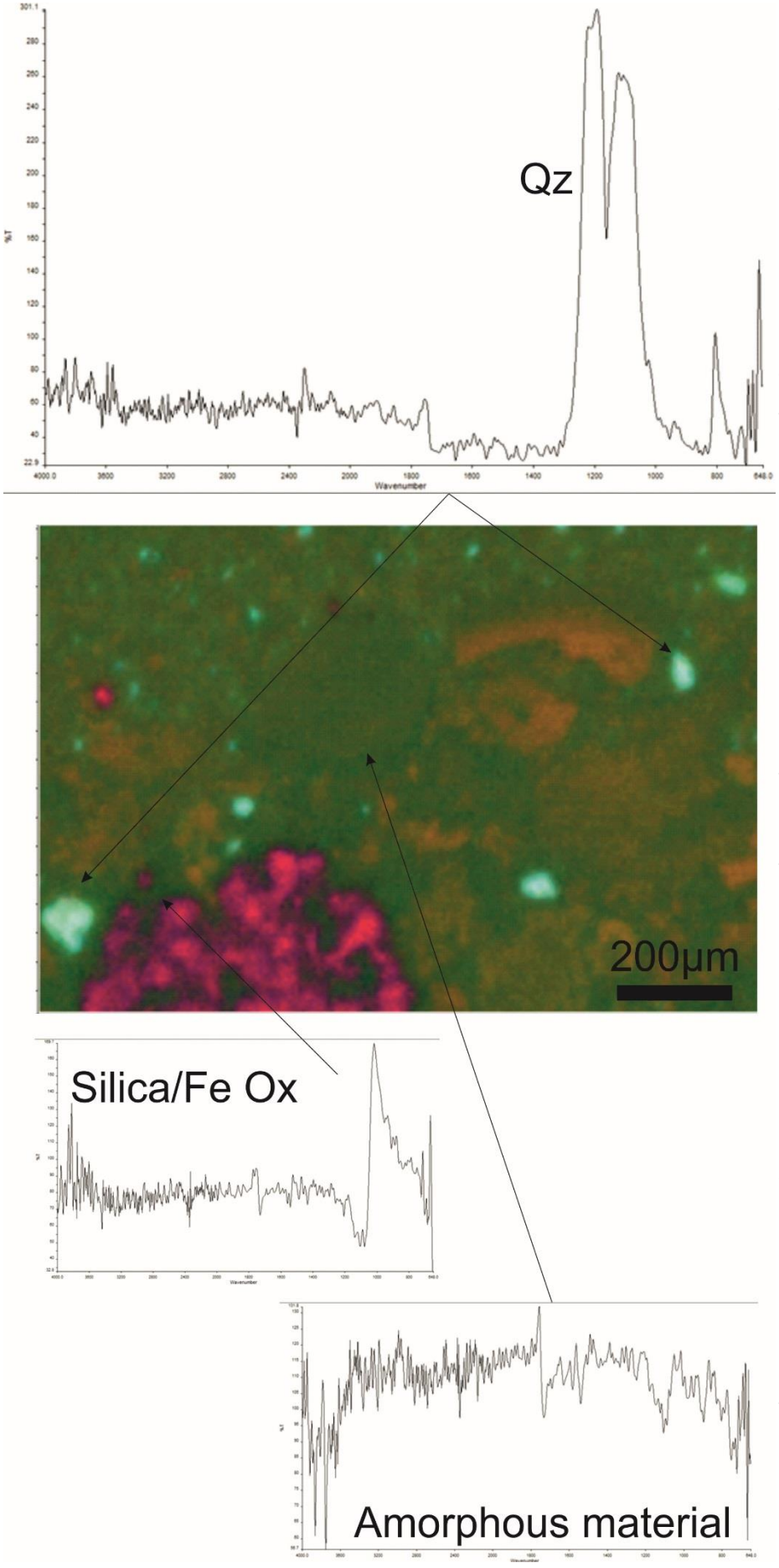

Figure 56: FTIR Map of Unit M4 Sediment. Amorphous material (Orange and green) material dominates the section and share similar spectra. Neither have significant peaks between 4000 and 650 cm^{-1}, and they are therefore likely associated with haematite. Si-Fe clast (magenta) spectrum has a strong peak at ~ 1000 cm^{-1} which is likely to be associated with haematite, however in transmitted light this area is a translucent clast, and therefore not likely to be haematite, but more likely a shifted peak from silica. Quartz/silica (blue) exhibit the characteristic ~1190 cm^{-1} shoulder on a ~1090 cm^{-1} peak, along with further peak at ~ 780cm^{-1}. This is diagnostic of quartz and is a key observation, showing that quartz is present within the Unit M4 sediment.

5.2.2 Dendrite and colloform growth textures

Textural variation across the hydrothermal sediments presents a way of identifying the range of potential accumulation of formation processes that have occurred. This would enable determination of whether the sediments have formed by common processes of if they represent a unique formation.

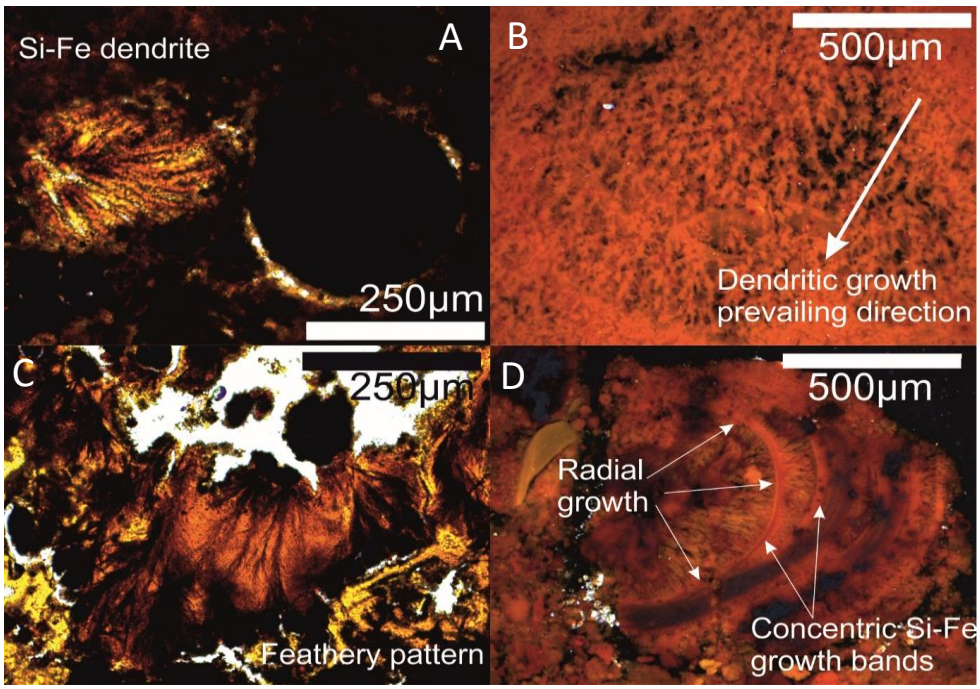

Figure 57: Range of dendritic patterns in the hydrothermal sediments. (A) Radial Si-Fe growth next to a near circular iron oxide grains – TL-PPL (B) Intra-clast dendrites with a single prevailing growth texture – RL-XPL. (C) 'Feathery' iron oxide dendrites within a Si-Fe clast – TL-PPL. (D) Radial dendrites from a single point with concentric growth bands – RL-XPL.

Dendritic growth textures, typically exhibiting radial growth, or feathery features are common in the shallower Unit M3 sediments, and are present, but less common in the deeper M4 sediments. No distinct preferred growth directions of dendritic material occur throughout the cores, implying that they may not have formed *in-situ*, but represent clasts of material that have been brecciated and remobilised. Alternatively, the lack of organisation could be explained by random localised growth forcing mechanisms (i.e. localised fluid flow, or preferred growth by location of nucleation sites). Colloform and zoned textures in Unit M3 are observed in clasts of Si-Fe material, and appear to be a result of accretion of material with oscillatory variations in iron oxide and silica ratios through clast growth. The best example of this texture in M3 (Figure 57D) appears to have formed as a combination of radial dendritic growth and concentric rings of iron oxide/oxyhydroxide material.

In Unit M4, clear concentric oscillatory banding of crystalline haematite, indicative of colloform growth, occurs in discrete clasts up to 250 microns in size, Figure 58A) within a fine-grained iron oxide/oxyhydroxide matrix.

In addition, both regular and irregular void spaces appear to have been in-filled by clusters of platy crystalline haematite indicative of growth that radiated out from the centre outwards. These haematite clusters are also surrounded by fine grained iron oxides/oxyhydroxides (Figure 58).

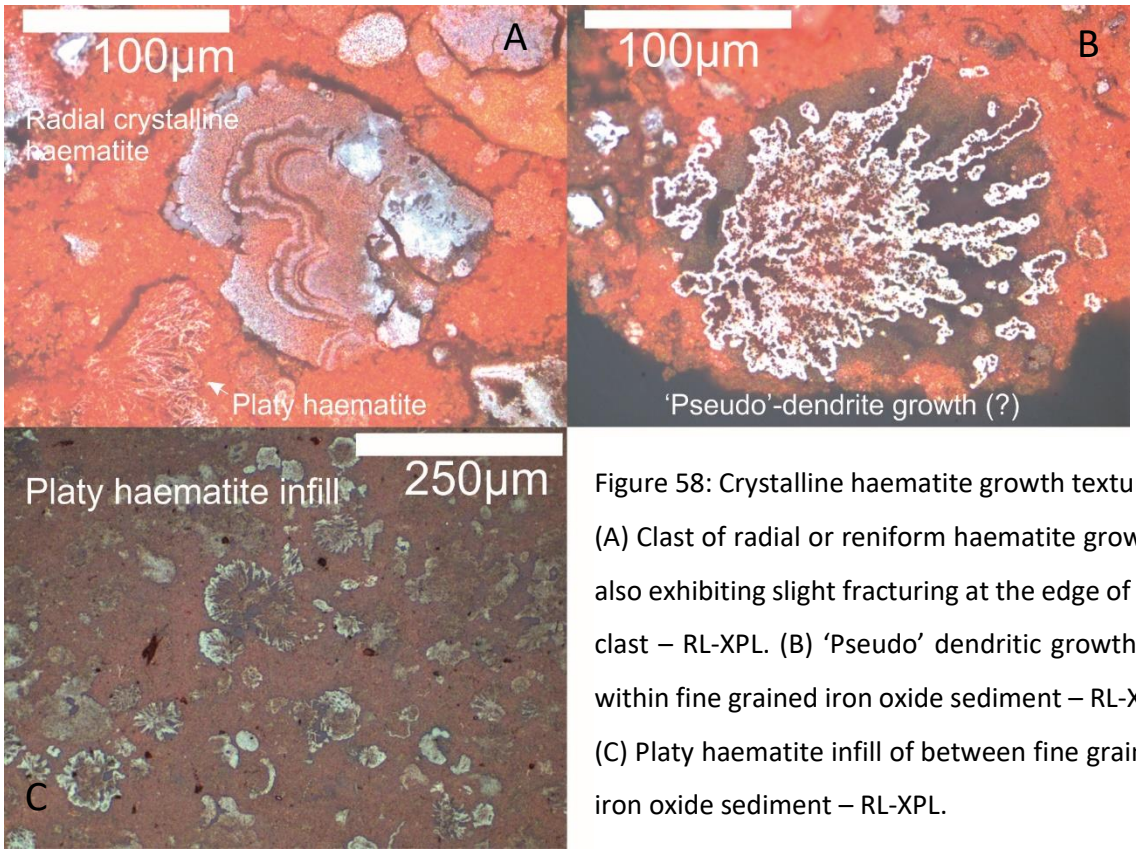

Figure 58: Crystalline haematite growth textures. (A) Clast of radial or reniform haematite growth, also exhibiting slight fracturing at the edge of the clast – RL-XPL. (B) 'Pseudo' dendritic growth (?) within fine grained iron oxide sediment – RL-XPL. (C) Platy haematite infill of between fine grained iron oxide sediment – RL-XPL.

Both colloform and dendritic growth textures represent prolonged cyclical or continual precipitation of iron (and/or silica) minerals. The higher amount of dendritic and colloform growth textures in Unit M3 over Unit M4 indicates a higher degree of 'organised' (i.e. structured) precipitation.

Although it is difficult to infer the origins of the fine grained iron oxide/oxyhydroxide material on texture alone, the larger clasts of iron oxide/oxyhydroxide and Si-Fe materials exhibit textures which are commonly thought to be related to precipitation from fluids (i.e. colloform (Roedder, 1968; Barrie *et al.*, 2009). This growth mechanism implies that some contribution to the hydrothermal sediments is likely from direct precipitation from hydrothermal fluids.

5.2.3 Sulphides

The hydrothermal sediments are dominated by iron oxide/oxyhydroxides, and only rare subhedral pyrite grains were observed in one sample of Unit M4 sediment (Figure 59). The general lack of sulphides and dominant iron oxides/oxyhydroxides shows that the sediments were deposited within an oxidative environment. The pyrite grains are often surrounded by haematite, potentially implying direct weathering of sulphides, with relict 'core' remaining.

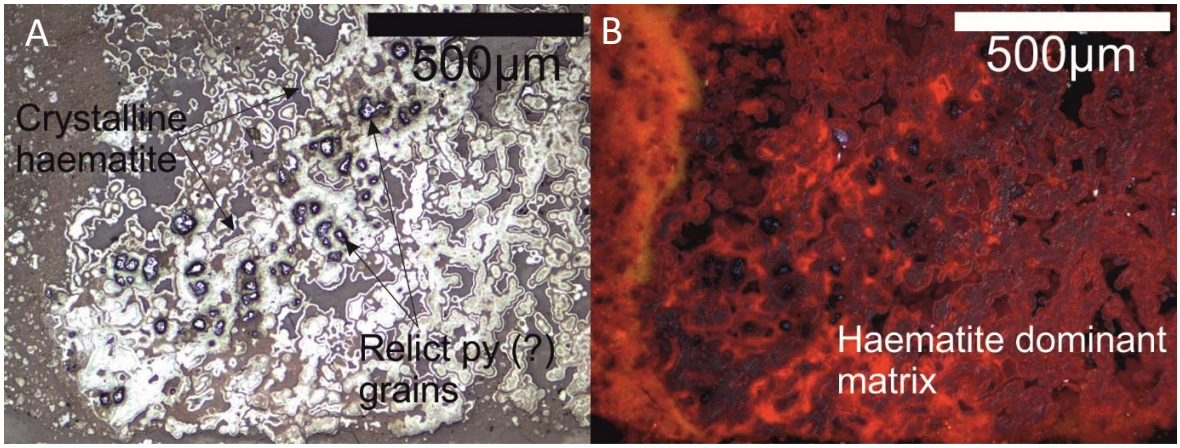

Figure 59: Subhedral to anhedral pyrite within a hematite dominated matrix (A = RL-PPL, B = RL-XPL).

5.2.4 Filaments

Filamentous material is common throughout M3 sediment and manifests as a wide range of morphologies, lengths and diameters. They are observed within Si-Fe clasts, or silica free areas and are composed of quasi-crystallised or very fine grained iron oxides/oxyhydroxide cores, typically surrounded by haloes of amorphous iron oxides/oxyhydroxides (i.e. Figure 60). Generally, filaments show no preferred orientation throughout and exhibit a range in morphologies from straight to curved, and lengths from 20 to over 200 microns. Diameters of filaments are typically consistent within discrete areas and range from 1 to 10 microns (Table 43).

Filamentous material is less common in Unit M4, and where observed occurs as up to 500 micron wide patches of poorly crystallised iron oxide filaments, with fine grained iron oxide coatings (Figure 60). These filaments are typically curved, 30 to 70 microns long and 5 to 7 microns in diameter with an apparently random orientation (Figure 60).

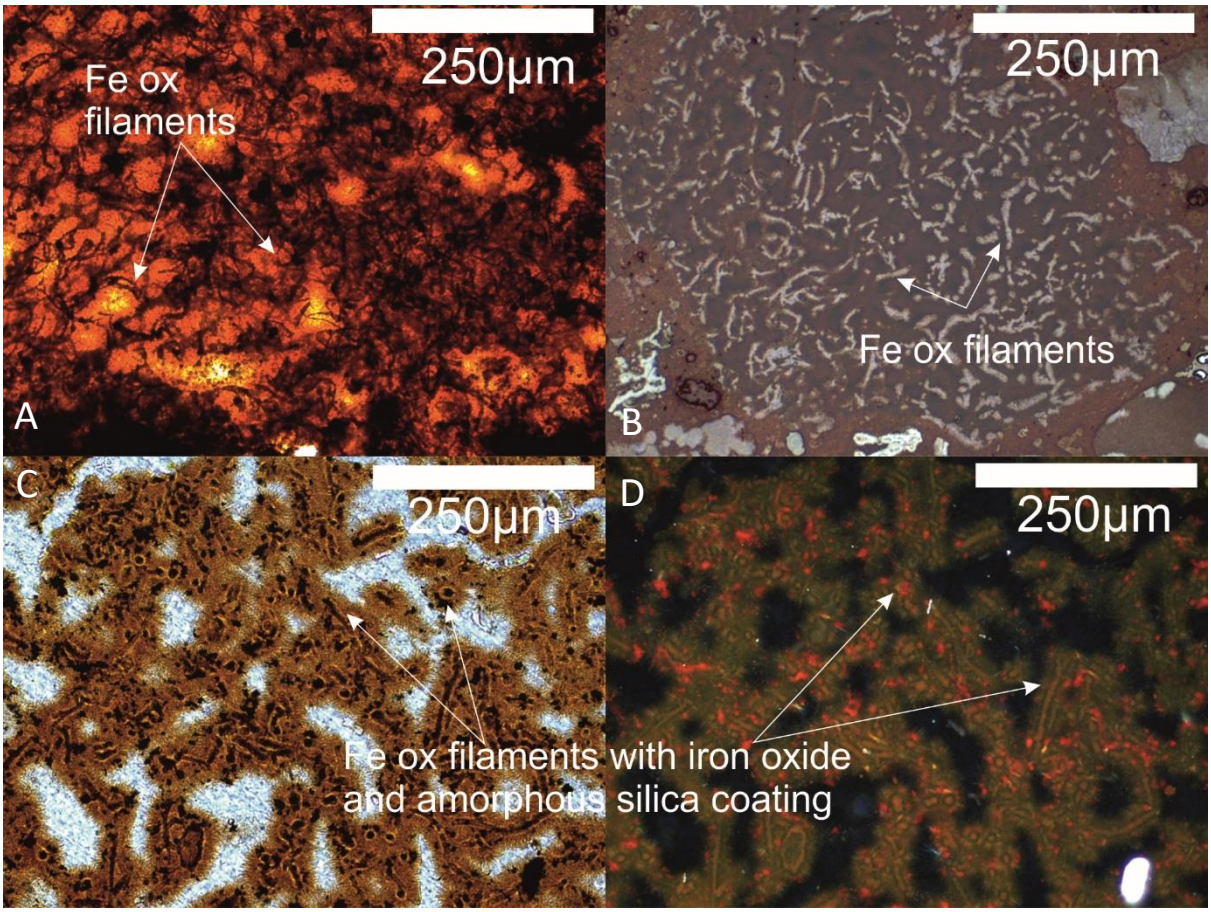

Figure 60: Range of iron oxide filaments throughout the hydrothermal sediments. (A) Fe ox filamentous within a Si-Fe clast – TL-PPL. (B) Similar scale filaments within a discrete area surrounded by fine-grained iron oxides not visible in TL – RL-PPL. (C,D) Fe oxide filaments with bladey amorphous silica and iron oxide coatings. C = TL-PPL, D = RL-XPL.

As detailed in Section 2.2.3, it is difficult to determine whether filamentous material is biological or abiological in both modern and ancient seafloor hydrothermal environments. Certain features such as filament thickness, filament morphology, and bifurcation of filament networks can imply a potential biological origin.

The general random orientation of filaments material, both within enclaves and in general throughout the deposits implies that their formation is unlikely to be the result of self-organised precipitation mechanism (i.e. Hopkinson *et al.*, 1998 and references therein). However, the lack of characteristic identification features (i.e. nodular features, or helical morphology), the small filament diameters, and the fact that most filaments appear to have an iron oxide/oxyhydroxide core imply more of a biological origin (Little *et al.*, 2004).

Table 43: Filamentous material throughout Unit M3 material

Borehole – depth (mbsf)	Morphology	Relative orientations	Length (µm)	Diameter (µm)
022RD – ~1.1	1) Straight 2) Curved 3) Curved	1) Random 2) Parallel and Random 3) Random	1) 40 – 170 2) 30 – 70 3) 20 - 50	1) 1 – 3 2) 1 – 5 3) 5
022RD – ~ 3.1	Curved	Random	≥ 40	1 - 2
022RD – ~ 2.7	1) Straight and curved 2) Curved 3) Straight 4) Straight	1) Random 2) Random 3) Random 4) Random	1) 30 – 80 2) 50 – 100 3) 90 – 220 4) 50 - 120	1) 1 – 3 2) 10 3) 5 4) 5
031RD - ~3.0	Curved	Random	30-70	5-7

The occurrence of filamentous material is commonly associated with microbial and bacterial material in modern hydrothermal sites and interpretation of filament morphology is used to imply significant biological involvement in the formation of Si-Fe materials at VMS deposits. Non-biological filaments are also interpreted to have formed in similar environments, with a lot of filamentous material remaining ambiguous in origin.

5.2.5 Micro-fractures

Fractures in the materials are important as they can also help identify processes that can help with interpretation of the paragenesis and origin of the hydrothermal sediments. Due to the unconsolidated nature of hydrothermal sediments, it is difficult to determine whether open fractures are representative of fractures within the sediment sequence, or are artefacts of sampling. However, fractures preserved by or associated with Si-Fe or iron oxide/oxyhydroxide clasts, or that have been infilled with other fine grained material can be interpreted to be representative of the sediment material.

Large clasts (i.e. mm to cm scale) can be fractured and show a clear relationship between clast growth textures and the timing of fracturing. Growth textures can be traced across fractures, and do not appear to have been altered by fractures, implying that in general the processes forming the clasts occurred pre-fracturing.

Intra-clast fractures are observed in Si-Fe clasts in Unit M3, and within crystalline haematite grains in Unit M4. They are typically polygonal (and linear in Unit M4), ~1-2 microns wide, and can either be infilled with fine grained iron oxide/oxyhydroxide material, or unfilled. Some examples show near optimal ~120˚ angles where three fractures meet (Figure 61). These intra-clast fracture networks are likely indicative of volume decrease, potentially during silicification or crystallisation.

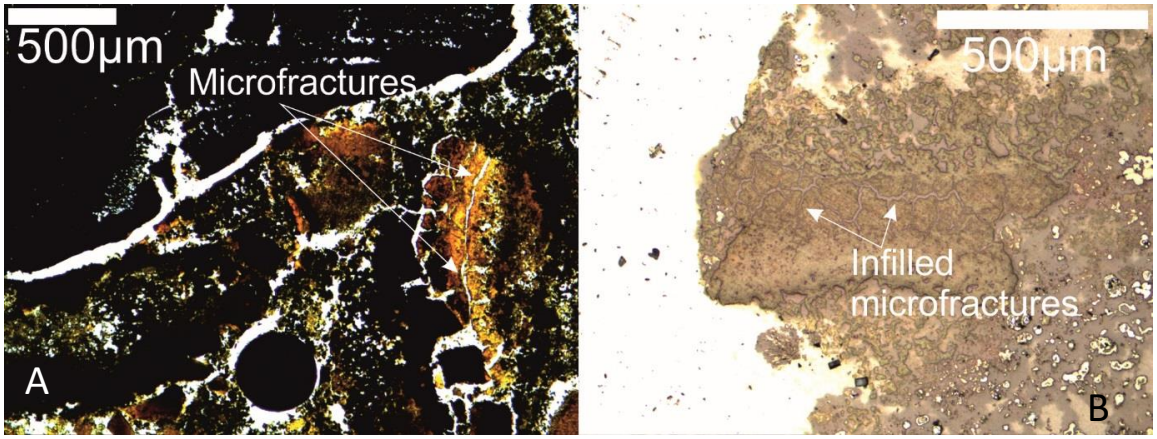

Figure 61: Microfractures in hydrothermal sediments. (A) Si-Fe clast exhibiting intra-clast fractures – PL-PPL. (B) Infilled ~120 cracks potentially linked to desiccation – TL-PPL.

5.3 Unit A of the Si-Fe lithology

Unit A lies directly beneath unconsolidated sediment (interpreted from drilling telemetry) and is the uppermost of the lithified Si-Fe capping lithologies recovered from one borehole (050RD) at Southern Mound. Unit A is dominated by opal-CT (tridymite, cristobalite) and quartz, with a variable amount of iron oxides/oxyhydroxides (haematite and goethite) and amorphous fraction forming the matrix (Table 44). It is not known whether the amorphous fraction is iron oxides/oxyhydroxides or silica. Although Unit A is mineralogically homogenous (silica and iron oxides/oxyhydroxides), it has a highly diverse range of textures visible from centimeter to micrometer scales.

Table 44: Mineralogy identified in Unit A samples from XRD

Sample	Mineralogy %						
	Qz	**O-CT**	**Haem**	**Goe**	**Py**	**Hal**	**Amor**
050RD/P3	20.8	37.4	1.8	9.8	-	0.7	29.5
050RD/P5	22.8	14.5	0.7	24.4	-	0.1	37.5
050RD/P7	-	32.4	2.2	19.6	-	0.5	45.3
050RD/P8	-	87.5	-	12.5	-	-	-
Qz = Quartz, O-CT = opal-CT, Haem = haematite, Goe = goethite, Py = pyrite, , Hal = halite, Amor = Amorphous fraction							

Unit A appears to be a conglomeratic mixture of individual Si-Fe fragments supported by a light orange-yellow matrix. It is often difficult to differentiate between clasts and matrix in thin section; however, two different types of clasts are easily identifiable: laminated fragments, and massive fragments (Figure 62).

Laminated fragments are typically irregularly shaped, with one or more curved boundaries along the line of previous lamination. Laminations are up to 3 mm thick and 20 mm long, and are often revealed by a gradation or sharp change in colour (ranging from dark brown to light orange).

Massive fragments are irregular in size and range from millimetre scale to centimetre scale and are typically more homogenous in colour (orange-red).

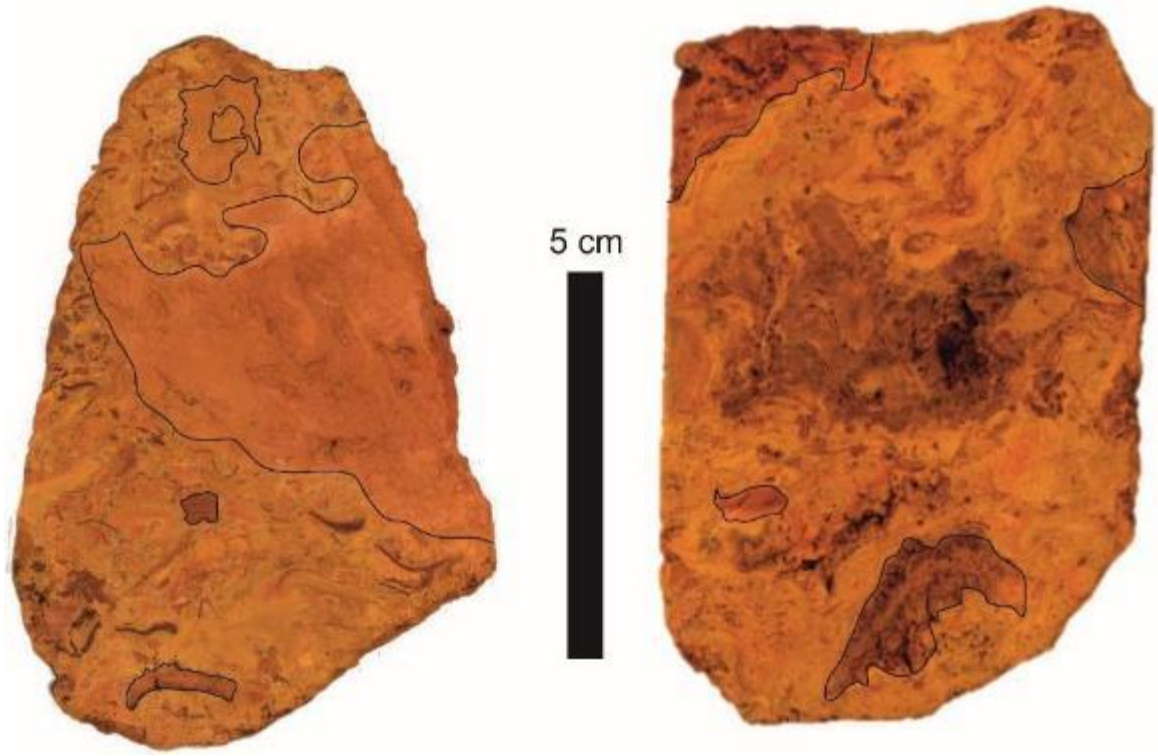

Figure 62: Comparison of 050RD/P3 and 050RD/P8. Some jasperoidal 'clasts' highlighted by black borders. 050RD/P3 is dominated by more laminated clasts, whereas 050RD/P8 my more massive and differentiated textures.

In thin section, individual clasts are generally composed of a mixture of microcrystalline, inter-grown filamentous, or dendritic iron oxides with variable silica content. Iron oxides and oxyhydroxides are opaque to sub-translucent; therefore the degree of transparency of the material is an indication of the silica content of each clast. The clasts are randomly distributed and show no preferred orientation within any sections of Unit A material (Figure 63).

Internally laminated fragments often exhibit some degree of deformation with the majority of fragments showing slight open folding. Laminations appear to correlate with colour change (change in dominant iron oxide or oxyhydroxides) or variable transparency (a result of the silica:iron oxide ratio) in thin section (Figure 63A,B). Both gradational and sharp transitions between laminations are observed within individual fragments. Microfractures, which can occur both perpendicular and parallel to lamination trends, are easily recognisable within laminated fragments. Some

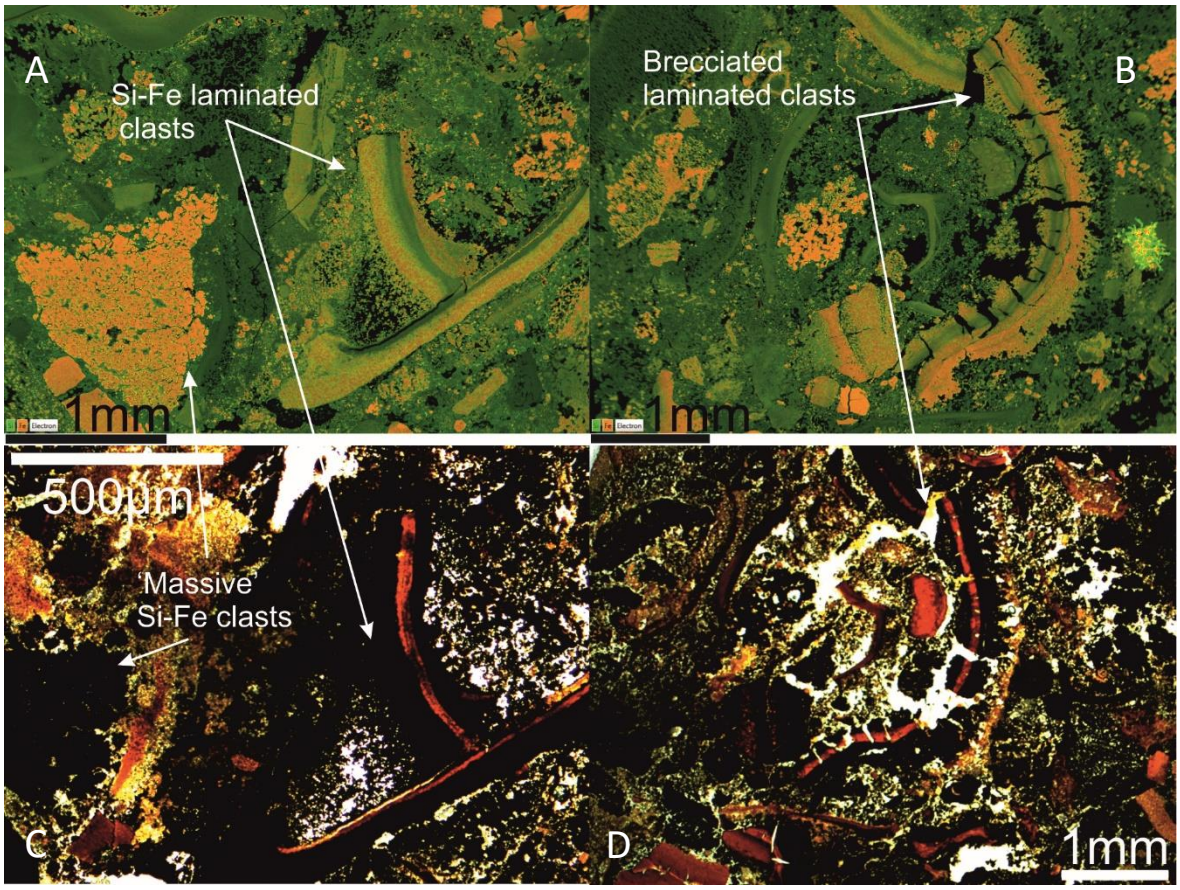

Figure 63: SEM and transmitted light (TL) images of Unit A: (A,B) SEM images of Si (green) and Fe (orange) distribution in massive and laminated clasts. (C,D) TL images of comparable areas showing laminations as a function of opacity.

perpendicular microfractures completely bisect fragments and enable slight displacement of sections of laminated fragments with offsets not typically exceeding 0.5 mm.

Laminated clasts imply a sedimentary origin as material deposited in a low energy environment, which underwent limited soft sediment deformation during consolidation. However, the current random organisation, the brecciation of the clasts, and suspension within the amorphous matrix indicates a change from a low energy environment to higher energy, and imply that the clasts have been transported and brecciated before lithification.

Some massive textured fragments are typically homogenous (Figure 64), but occasionally show gradational colour change and transparency change across a clast, likely as a result of variable iron oxyhydroxide to oxides, and silica:iron oxide/oxyhydroxide ratio. Occasional relict textures can be observed within massive clasts, including traces of dendrites, filaments, and colloform growth zones (e.g. Figure 64, fully described in later subsections). Microfractures are also present within some clasts, but are not as prominent as within laminated fragments.

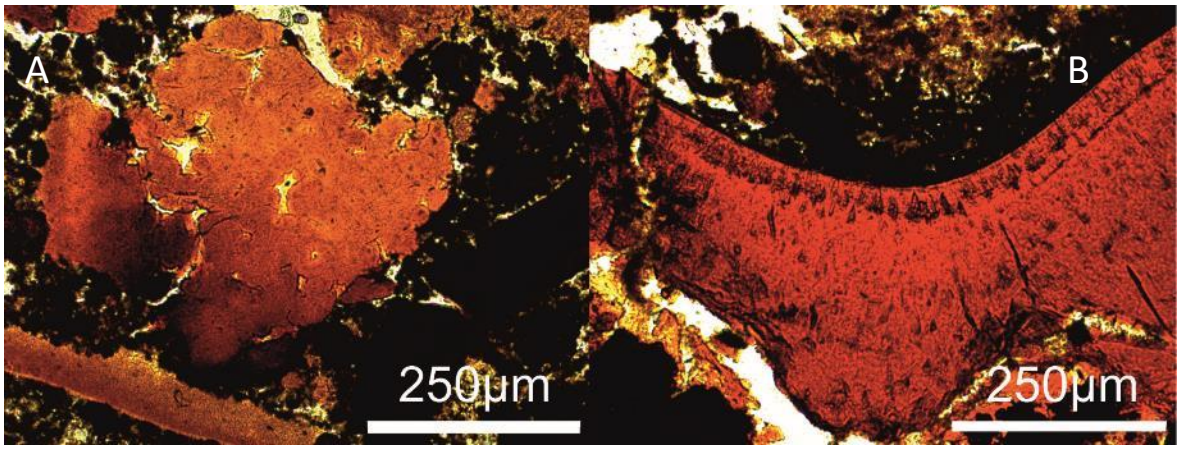

Figure 64: Massive Si-Fe clasts from Unit A. (A) Si-Fe clast showing trace colloform growth patterns. (B) Si-Fe clast reminiscent of a massive sulphide chimney fragment

The matrix material is heterogenous, but similar to the clast material, and it is often difficult to determine matrix from clast. In general, the matrix appears to have a more silica than iron oxide or oxyhydroxide (Figure 64), as can be seen on SEM images, and displays a range of heterogenous, undifferentiated textures.

5.3.1 Silica morphology

Although silica (opal-CT and quartz), is the dominant mineral in Unit A (Table 44), silica textures are typically obscured by the presence and textures of iron oxide, therefore it is difficult to differentiate quartz from opal-CT in thin section. Poorly crystallised or cryptocrystalline silica forms part of the matrix, stained with iron oxyhydroxides or oxides, and where present in Si-Fe clasts is 'sub-microscopic' or cryptocrystalline.

Silica (likely composed of opal-CT, based on XRD results), that is free of iron oxide material is rare but where present, exhibits radial growth with banding, nucleated off iron oxide filaments. Under high-resolution SEM imaging, this is confirmed by the silica often taking the form of lepispheres, a rosette of bladey poorly crystalline authigenic silica (Florke *et al.*, 1990). Considerable amounts of visible surfaces are coated by silica lepispheres, particularly filamentous or pseudo-filamentous areas, or void spaces, eventually forming coalescent aggregates of the lepispheres (Figure 65).

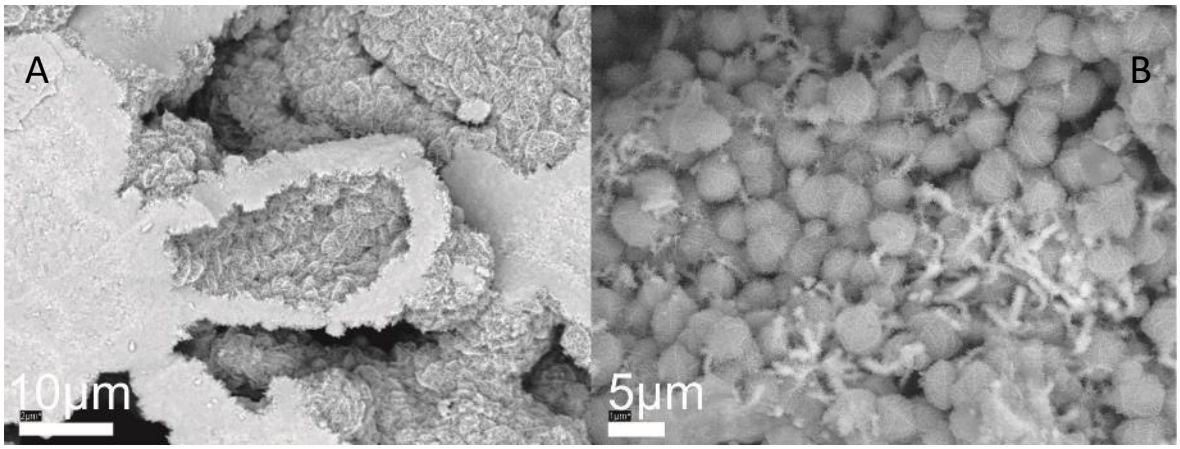

Figure 65: SEM images of coalesced lepispheres (A) and individual aggregates of lepispheres and strands of Si (B).

In-situ FTIR mapping of Unit A was conducted to investigate the distribution of quartz and opal-CT across the sample, due to the difficulty in interpreting the distribution of silica polymorphs in thin section.

Quartz appears to be randomly distributed throughout the cryptocrystalline matrix, and appears not associated with individual clasts of Si-Fe material, implying homogenous silicification of the whole Unit, and silica polymorphs represent a partially matured opal-CT- quartz assemblage (Figure 66).

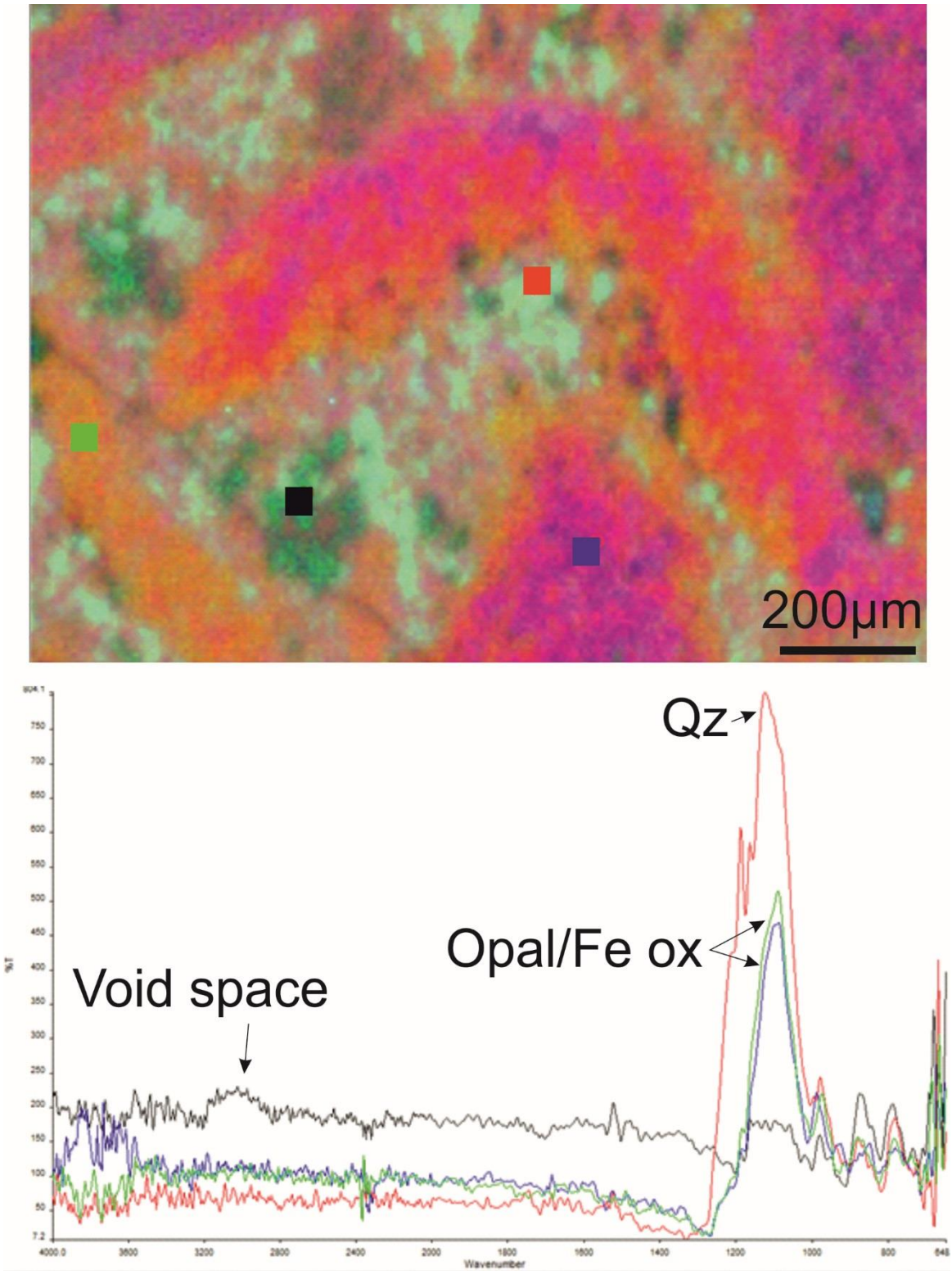

Figure 66: *In-situ* FTIR map from Unit A (050RD/P3). Each colour corresponds to a characteristic FTIR spectrum on the graph. Strong peaks at ~1090 and ~1180 in the red spectra identifies quartz from the opal-CT and iron oxyhydroxide peaks (in the blue and green spectra).

5.3.2 Dendrite and colloform growth textures

Classic dendritic textures can be observed throughout the Unit A material. The dendrites variably occur emanating off clast boundaries or from point sources, indicative of growth infilling spaces between fragments. Some examples of more 'amorphous' fragments show rare traces of dendritic material, implying amorphous material may have been formed by multiple generations overprinting and obliterating earlier dendritic textures. Some amorphous 'massive' fragments also show colloform growth textures that have grown to infill void space, similar to other dendritic textures.

Dendrites appear similar between Unit A and Unit M3 sediment and are typically Si-Fe material, with transparency controlled by the Si:Fe ratio similar to the other Si-Fe textures. Reflective light images of dendritic and colloform growth often show that the outer layers of the growth zones appear to be more iron oxide rich, with the central zones more silica rich. Under reflective crossed polarised light, a range of internal reflection colours from orange to dark red are seen, indicative of changes in goethite and haematite content respectively (Figure 67). However, some caution should be given to this observation as it is likely that silica may affect the optical properties of the iron oxide material.

The dendrite and colloform growth textures observed throughout Unit A are broadly comparable to the textures observed in the shallow, goethite dominated, Unit M3 sediment. Both colloform and dendritic growth textures represent prolonged cyclical or continual precipitation of iron (and/or silica) minerals, implying a similar paragenesis of Unit A and Unit M3 materials.

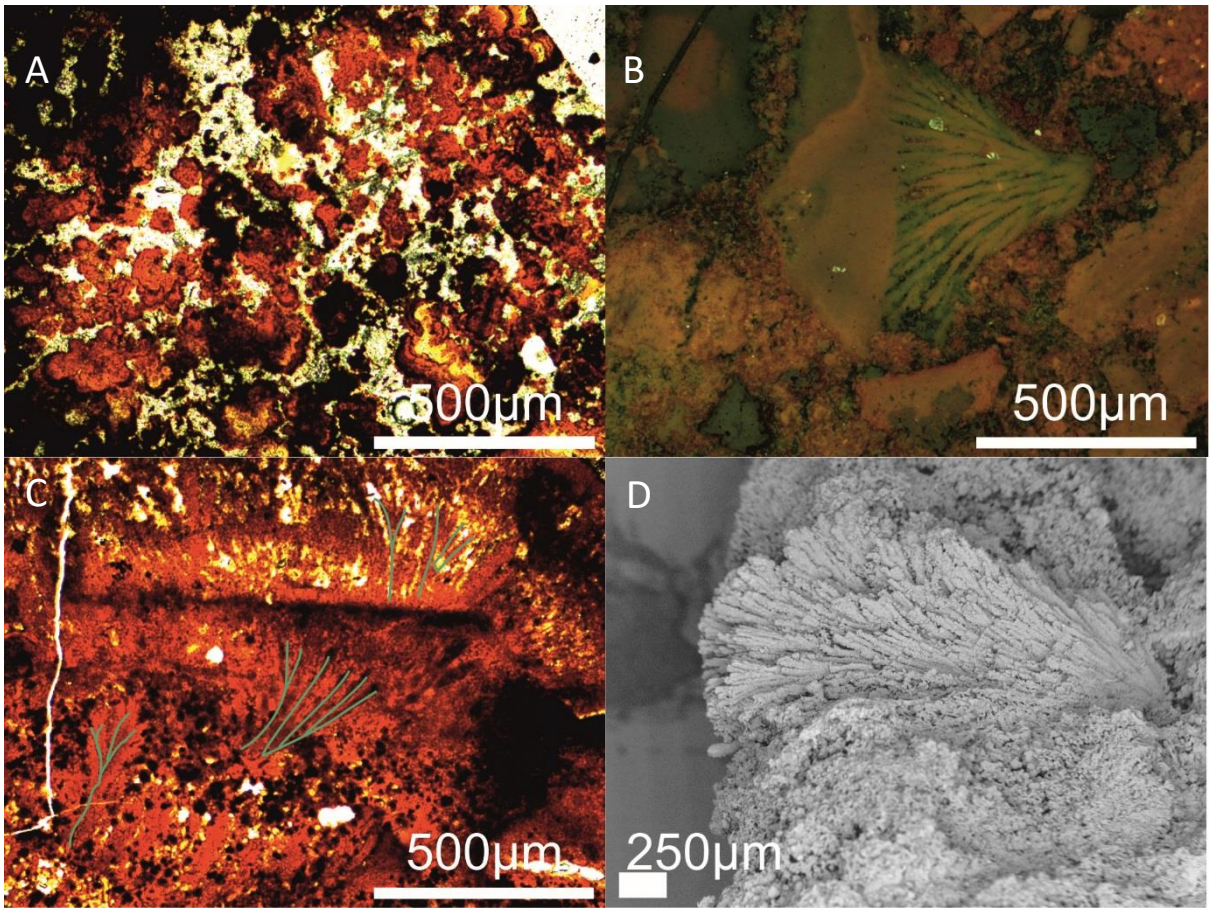

Figure 67: Range of colloform and dendrite textures in Unit A. (A) Colloform Si-Fe growths with banding exhibiting variable opacity. (B) Truncated fan-like dendritic growth, likely grown into void space. (C) Pervasive dendritic growth textures within an Si-Fe dominated area, not clast related. Green lines = prevailing dendrite growth direction. (D) SEM image of a fan-like Si-Fe dendrite.

5.3.3 Filaments and tubes

Filamentous textures are observed within massive or laminated Si-Fe fragments, infilling voids space between clasts, or as fragment size enclaves. Inter-fragment filaments are typically ~5µm diameter, short (~10 to 60 µm long), individual, and are the least common. Void space infill filaments are typically ~3-5 µm diameter, individual, short (50 – 100 µm length), but overlay each other to form randomly orientated and unordered swarms with occasional mesh-like appearances. Filamentous enclaves (discrete area composed of filamentous material only), of comparable size to massive or laminated clasts, typically show more ordered textures of a filamentous network, including radial and mesh-like growth patterns where elongated individual filaments are crosscut by shorter perpendicular filaments. Filaments within enclaves are coated with a thin layer, over an iron oxide tube or sheath like-feature that has been infilled with silica (i.e Figure 68B). High magnification images of some filaments show detailed central structures with four different zones:

1) central ‘speckled’ silica and iron oxide core; 2) iron oxide ring with offshooting threads of iron oxide; 3) iron oxide free silica coating; 4) thread like late stage silica growth of the whole filament.

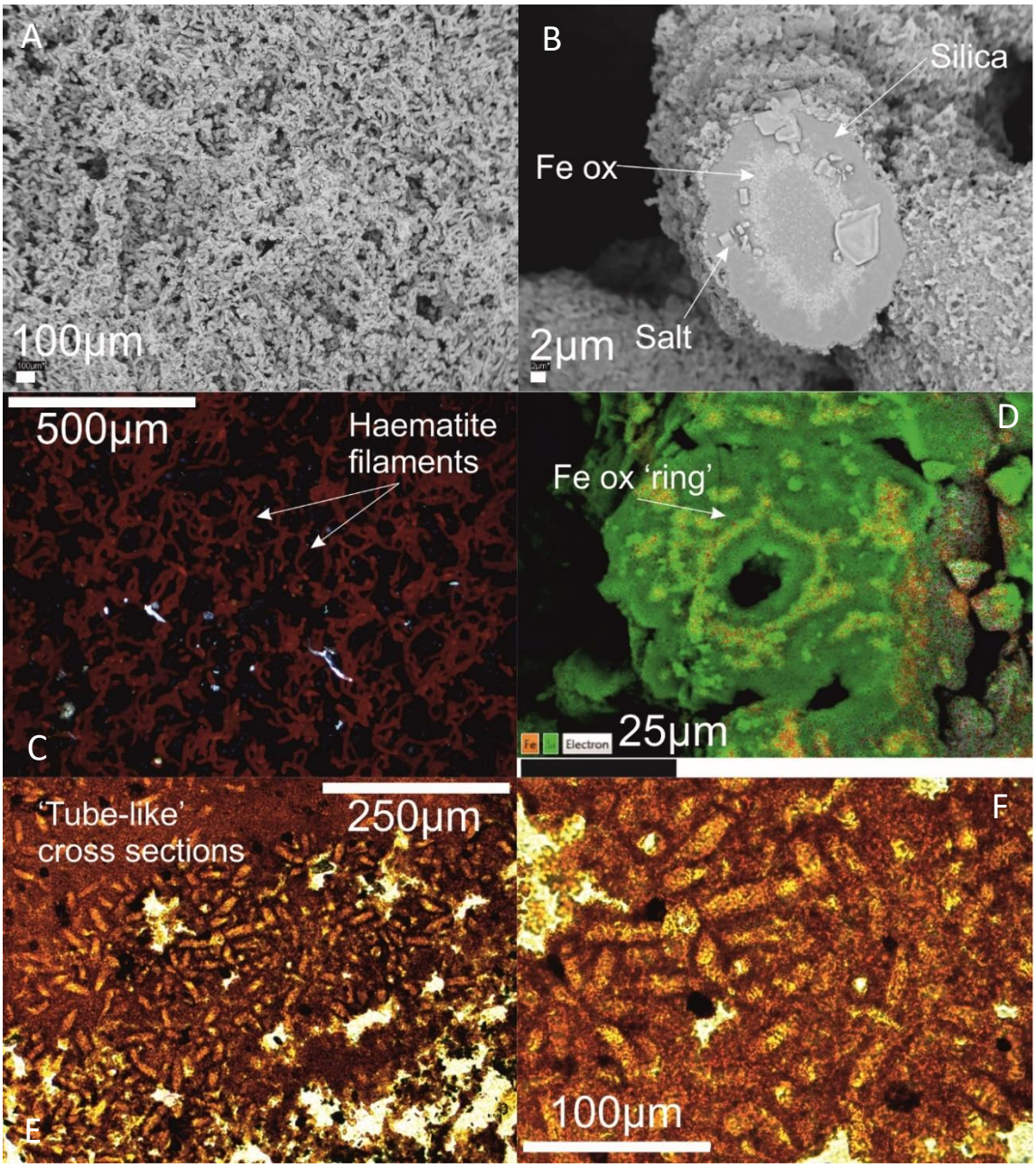

Figure 68: SEM, TL and RLXPL images of filaments in Unit A. (A) SEM - Inter-connected mesh of Si-Fe filaments with no preferred orientations. (B) SEM - Cross section through an individual filament showing complex growth zones. (C) RL-XPL image of randomly orientated haematite filaments. (D) SEM with EDS - Filament cross section showing a Fe-rich (orange) ‘hexagonal’ ring surrounded by Si (green). (E,F) TL-PPL - Oblique cross sections of a cluster of tube-like shapes in a larger Si-Fe clast.

Tube-like structures are observed within one thin section of a massive, amorphous clast. The tubes are delineated by variable iron oxide content in the silica and form short tube-like oblique cross sections (i.e. Figure 68B). These tube-like features are ~10 µm wide, and show no preferred orientation and although they are within the same fragment do not appear to show any branching or chains with the other tube-like casts.

Filamentous material observed in Unit A shows similarities with Unit M3 material (similar to the observations within dendrites and colloforms in Section 5.2.2), but also displays a more diverse range of filamentous material.

In contrast to filamentous material from the hydrothermal sediments, Unit A filaments show both iron oxide/oxyhydroxide cores, and iron oxide/oxyhydroxide 'sheaths', which are coated and infilled by silica. These hollow iron oxide/hydroxide sheaths with diameters ~10µm fit more criteria for interpretation of biological involvement, potentially similar to *Lepothrix* iron oxidising bacteria.

5.3.4 Microfractures

Unlike in the unconsolidated sediment Units M3 and M4, microfractures within Unit A material, whether they are filled or unfilled are representative of the Si-Fe material. Microfractures are observed within, or disrupting, individual clasts throughout the Unit, similar to fragments in sediment Unit M3. They are either contained within the fragment or have propagated through and completely fractured the clast. Laminated clasts shows fracturing at two different magnitudes, smaller order fractures that are contained within the fragment (predominantly perpendicular to laminations, but also extending parallel), and larger order fractures that are lamination parallel and break up the clast into multiple sections, occasionally propagating into the surrounding material. Fractures which partially disrupt and displace clasts can also be partially infilled by the fine grained silica-iron oxide matrix or have a thin silica coating, implying that they pre-date the matrix formation.

When viewed in three dimensions, the small-scale fractures resemble polygonal desiccation cracks (Figure 69C), indicative of dehydration of iron oxyhydroxides before consolidation or lithification, or maturation by dewatering of silica as it undergoes phase transition (opal-A to opal-CT, or opal-CT to quartz). The presence of opal-CT and quartz, and haematite and goethite, within Unit A supports this as a possible mechanism.

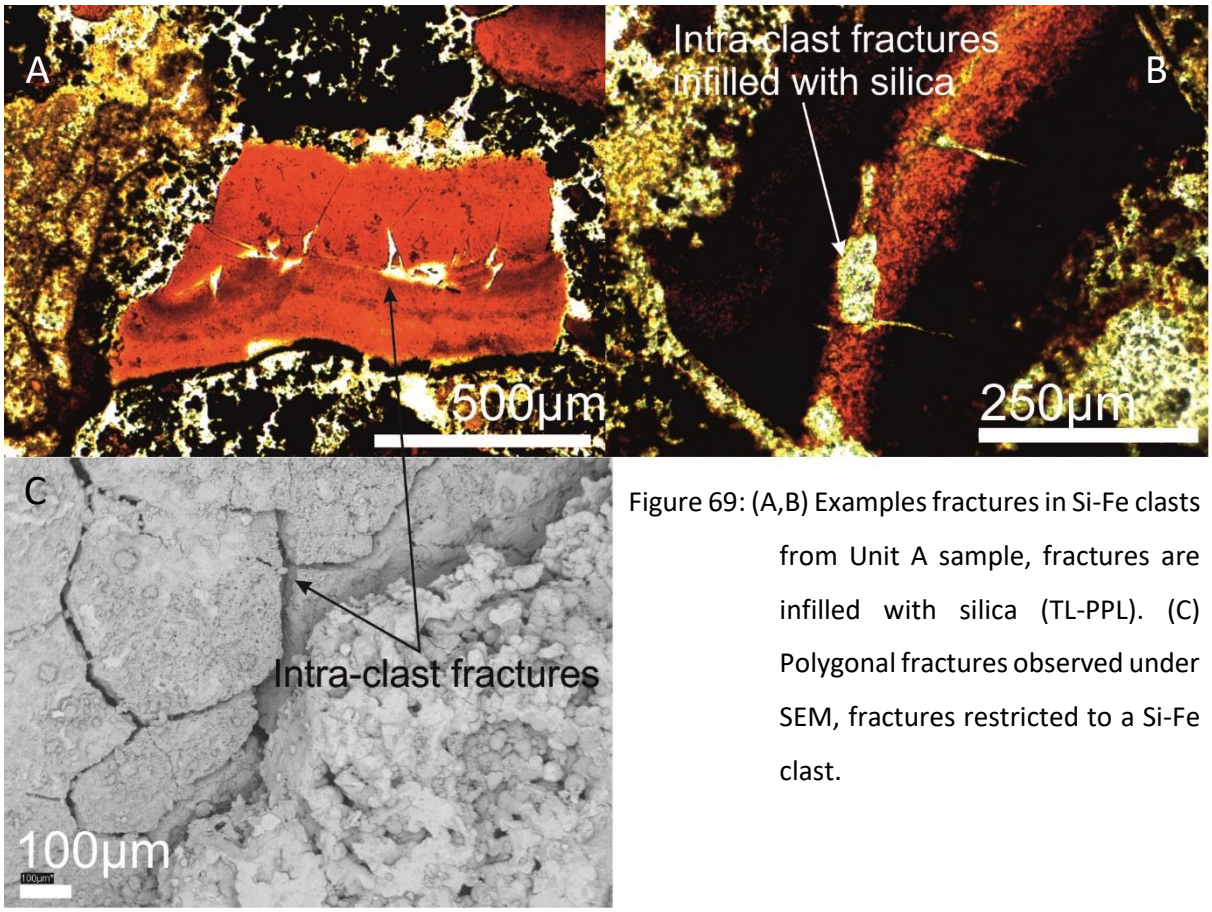

Figure 69: (A,B) Examples fractures in Si-Fe clasts from Unit A sample, fractures are infilled with silica (TL-PPL). (C) Polygonal fractures observed under SEM, fractures restricted to a Si-Fe clast.

5.4 Unit B of the Si-Fe lithologies

Unit B material was recovered from two boreholes at Southern Mound, the one borehole targeting Si-Fe material at Rona Mound, and both boreholes at the MIR Zone. Although it is the only Si-Fe Unit that was recovered from all three mounds, the Unit has both shared and variable characteristics and relationships with underlying material at each deposit.

At Southern Mound Unit B material was recovered at the sediment-Si-Fe interface, in direct contact with unconsolidated, haematite rich Unit M4 sediment. Large, millimeter and even centimeter scale, void spaces are observed in the core samples, and some were infilled with Unit M4 sediment upon recovery. The overlying Unit M4 sediment and Unit B Si-Fe material have a shared mineralogy (See Table 42 for sediment mineralogy, and Table 45 andTable 46 for Unit B mineralogy) of hematite (responsible for the blood red colour) and quartz, with rare pyrite observed in one sample of Si-Fe material. The main difference between the two is the significant increase in quartz from sediment (~ 10%) to hard rock (between ~60 and ~95%). This comparison leads to the interpretation that the overlying hydrothermal sediment Unit M4 appears to be the unlithified equivalent of the underlying Unit B material, with a significant increase in silica likely responsible for the lithification process.

Table 45: XRD analysis of Unit B material from Southern Mound

Sample	Mineralogy %					
	Qz	O-CT	Hae	Goe	Py	Amor
022RD/CC	59.2	-	40.8	-	(x)	-
031RD/007/CC	95.1	-	4.9	-	-	-
031RD/109/CC	96.0	-	4.0	-	-	-
Qz = quartz, Tridy = tridymite, Cryst = crystobalite, Hae = haematite, Goe = goethite, Py = pyrite, Amor = amorphous fraction, (x) = observed in thin section						

Only Unit B material was recovered from MIR Zone with no evidence of either Unit A or Unit C material in either borehole. It is dominated by quartz, and minor haematite in similar ratios to Unit B material from Southern Mound, with a localised sequence of co-existing haematite and goethite observed in one borehole between ~ 1.8 and 3.0 mbsf (See Table 46 and Figure 70). The samples were typically porous, similar to Southern Mound, but no entrained hydrothermal sediment nor evidence of entrained sediment is observed. Trace pyrite was also observed within several Si-Fe Unit B samples again suggesting that Unit B recovered from the MIR Zone is broadly comparable with Southern Mound.

Although sediment was interpreted to be present overlying the MIR Zone, it was not recovered. Based upon the intimate relationship between Unit B and the overlying Unit M4 sediment at Southern Mound, it seems reasonable that similar haematite rich sediment may have been present overlying the Si-Fe material at the MIR Zone.

Table 46: XRD results from Unit B material from the MIR Zone

Sample	Mineralogy %					
	Qz	O-CT	Hae	Goe	Py	Amor
073RD/P1	93.6	-	6.4	-	-	-
073RD/P6	96.9	-	3.1	-	-	-
073RD/P7	83.7	-	16.3	-	-	-
073RD/P9	72.7	-	11.0	16.3	-	-
073RD/P10	84.0	-	9.0	7.0	-	-
073RD/P12	87.4	-	2.1	10.5	-	-
073RD/P14	93.1	-	1.2	5.7	-	-
076RD/P2	68.5	-	31.5	-	-	-
076RD/P3	92.1	-	7.9	-	-	-
076RD/P4	93.9	-	6.1	-	-	-
076RD/P6	84.5	-	15.5	-	(x)	-
076RD/P7	91.4	-	8.6	-	-	-
076RD/P8	95.5	-	4.5	-	(x)	-

Qz = quartz, O-CT = opal-CT, Hae = haematite, Goe = goethite, Py = pyrite, Am = Amorphous fraction, Amor = amorphous fraction, (x) = observed in thin section

Figure 70: Range of Unit B core samples from Southern Mound (top) and the MIR Zone (bottom). Scale bars = 5cm long. Large void in top left sample (022RD/CC) was infilled with Unit M4 sediment. Colour difference between two MIR Zone samples is due to the presence of goethite in the orange-brown sample (073RD/P14).

Unit B material from Rona Mound was recovered as gravel to pebble sized fragments, in contrast to the short competent core sections (~10-15 cm long) recovered from both Southern Mound and the MIR Zone (Figure 71). Individual fragments are comparatively lower density than other Unit B material from both Southern Mound and MIR Zone and is closer in density to Unit A material. Visually Unit B material from Rona Mound is similar to other Unit B samples, exhibiting the characteristic 'blood red' colouration attributed to the presence of haematite (See Table 47). However, the dominant silica phase within Rona Mound Unit B samples is opal-CT (crystobalite-

tridymite) an immature, hydrated silica polymorph, with no quartz identified. XRD analysis of one sample recorded a high amount of amorphous material (27%), possibly associated with amorphous silica based on the immature silica assemblage observed, and comparable low concentrations of haematite/iron oxides in other Unit B samples. If the sample is reprocessed assuming no amorphous fraction, opal-CT is interpreted to be ~91% of the sample, supporting the interpretation that the majority of the amorphous fraction is silica.

Table 47: XRD analysis of Unit B material from Rona Mound

Sample	**Mineralogy %**					
	Qz	**O-CT**	**Hae**	**Goe**	**Py/Mc**	**Amor**
057RD/P2	-	45.4	54.6	-	(x)	-
057RD/P3-8	0.5	66.3	6.2	-	(x)	27.0
Qz = quartz, O-CT = opal-CT, Hae = haematite, Goe = goethite, Py/Mc = pyrite/marcasite, Amor = Amorphous fraction, (x) = observed in thin section						

Figure 71: Gravel sized rounded clast of Unit B from Rona Mound. Note the small areas of grey silica present at the surface of the clast

5.4.1 Silica morphology

The predominant silica mineral in Unit B samples at Southern Mound and the MIR Zone is quartz with no hydrous silica polymorphs identified (via XRD). Quartz is present as two main morphologies, as cryptocrystalline and 'sub-microscopically' mixed with haematite within Si-Fe clasts, and as veins of spherulitic or radial quartz growth (Figure 72 and Figure 73). The radial growth zones and

undulatory extinction, may represent recrystallisation of radial opal-CT to quartz, or could be described as chalcedonic 'type-B' quartz growth (comparable to Hopkinson *et al.*, 1998).

In general, opaque haematite in Si-Fe clasts obscures any internal silica growth textures, however rare occurrences of radial growth textures of silica occurs within clasts pigmented with iron oxide material. These samples were recovered from the mixed goethite-haematite zone from the MIR Zone, and potentially provide evidence of early radial opal-CT or chalcedonic textures. This observed could support the interpretation of cracks from dewatering of opal-CT to quartz during recrystallisation.

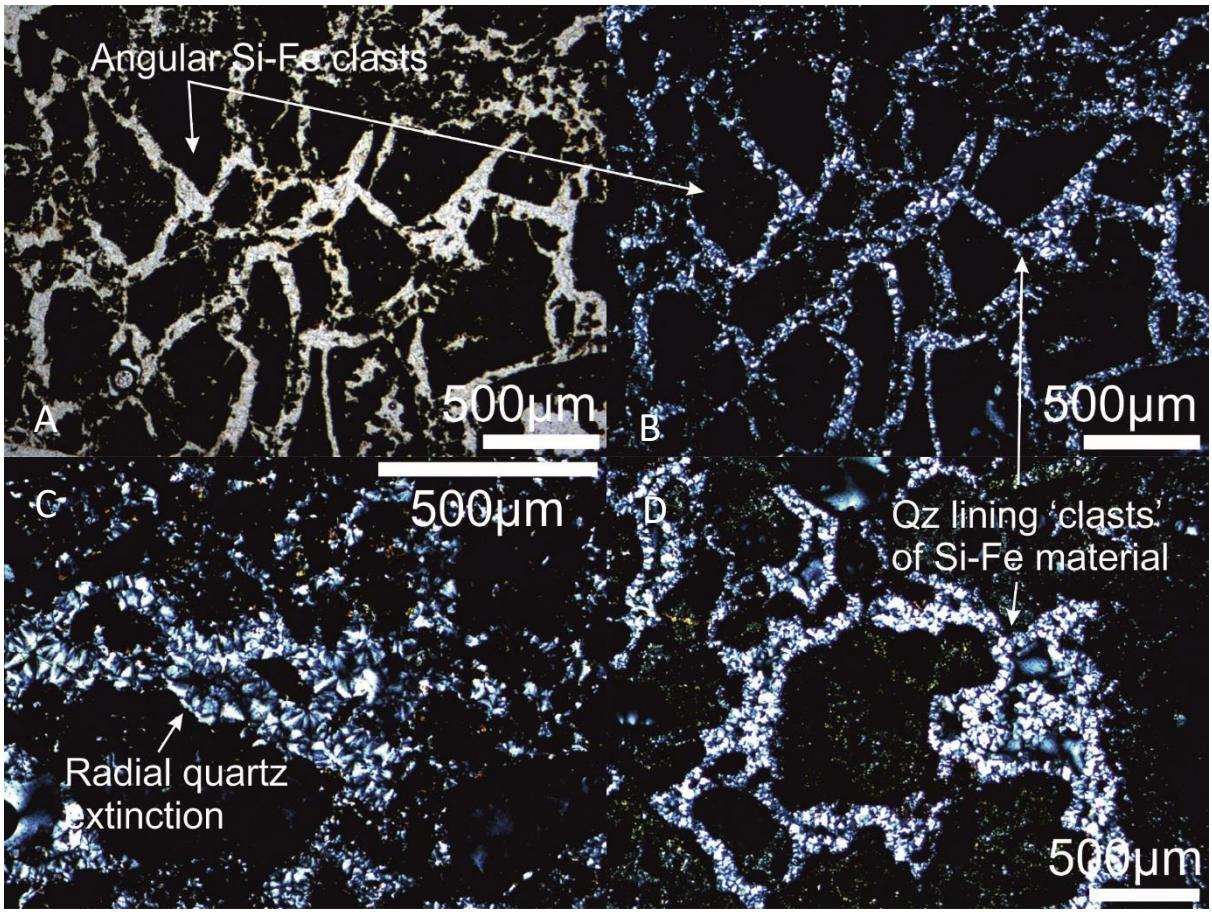

Figure 72: Silica within Unit B samples from Southern Mound. (A,B) Angular jigsaw brecciated Si-Fe clast with vein-like quartz infill (left = TL-PPL, right = TL-XPL). (C,D) Two areas of 'late-stage' iron oxide free quartz with radial and undulatory extinction – TL-XPL.

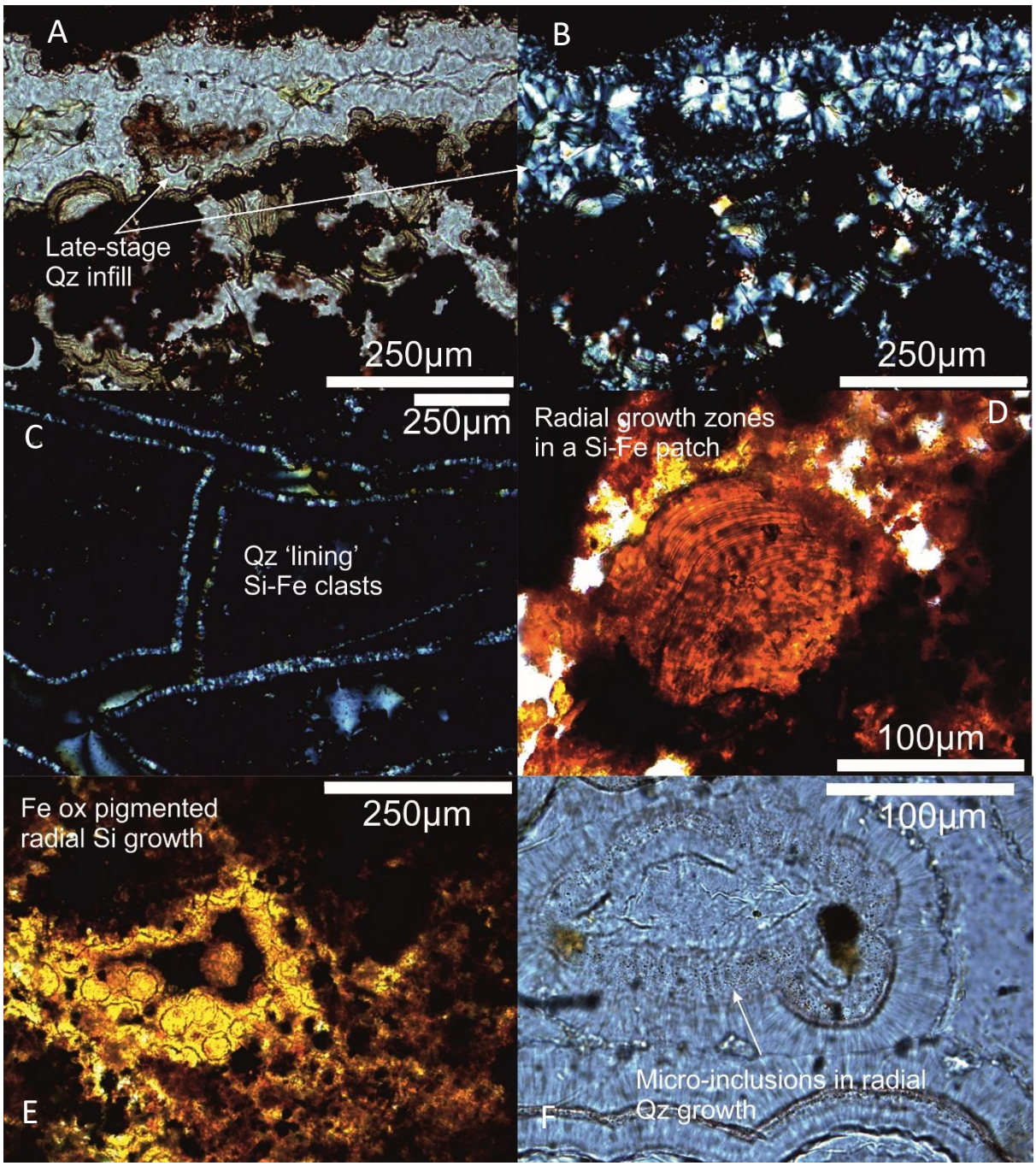

Figure 73: Silica textures within Unit B (cont.) – MIR Zone. (A,B) TL and XPL radial growth zones implying early opal-CT recrystallisation to quartz. (C) XPL image showing thin (< 50 micron) coating of silica on angular 'jigsaw brecciated' Si-Fe clasts. (D,E) Colloform bands of radial growth interpreted to be silica growth banding stained by iron oxide. (F) Textures of adjacent radial growth zones, with rare iron oxide grains and < 1micron inclusions.

In contrast to both Southern Mound and the MIR Zone, opal-CT is the dominant silica mineral in Rona Mound with <1 % quartz identified by XRD. Opal-CT is present overgrowing haematite filaments and dendritic material. Poorly defined radial growth lines are often observed in thin

section around filaments and dendrites, indicating that the haematite provided nucleation sites for silica precipitation (Figure 74). SEM microscopy often revealed zoning of silica overgrowth on filamentous and dendritic material where the outermost layer is composed of hemispherical silica lepispheres giving a globular appearance, or as bladed authigenic silica, similar to lepispheres. The zoned growth and lack of lepisphere textures preserved near the haematite cores support the idea that silica nucleated upon the iron oxides, with the outermost layer exhibiting the least mature bladey silica textures (Figure 74).

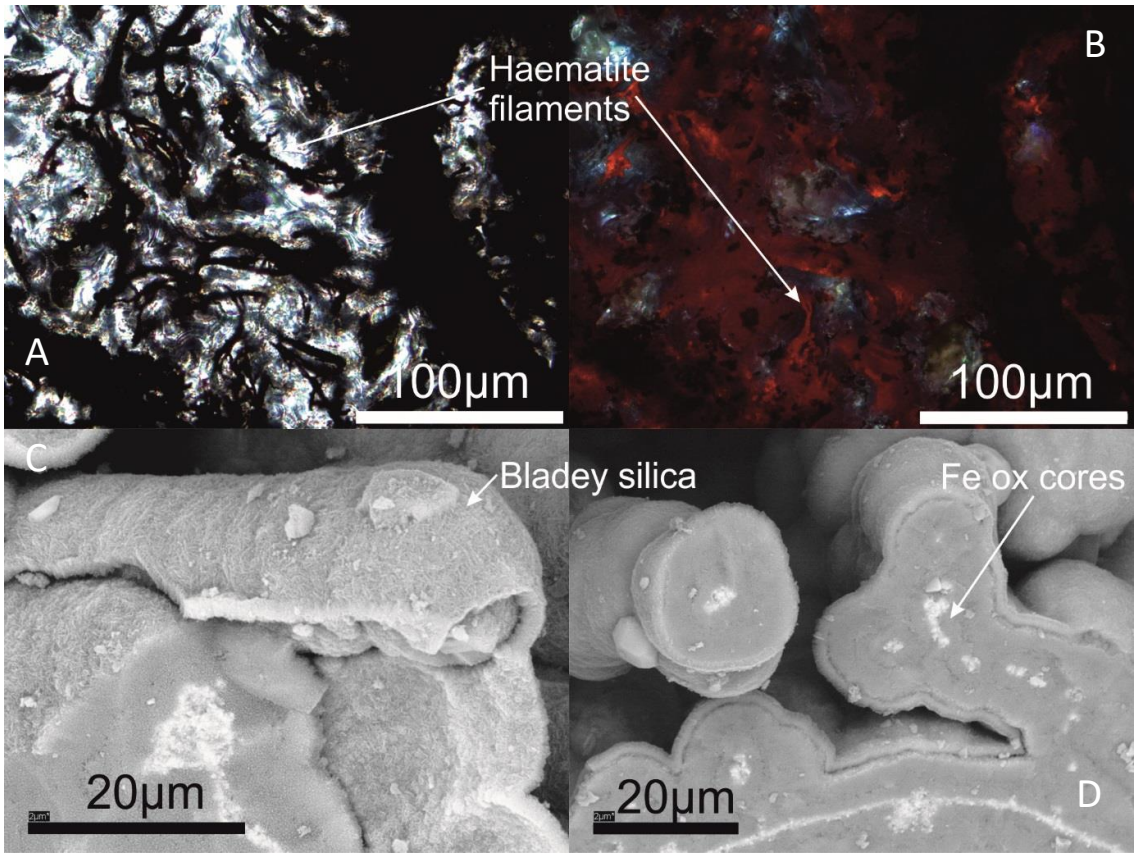

Figure 74: Silica coated filaments at Rona Mound. (A,B) Individual short haematite filaments coated in silica (TL and RL-XPL). (C,D) Backscatter SEM images of haematite (white) cores coated in at least two generations of silica with the outer layer exhibiting bladed silica.

5.4.2 Sulphides

Sulphides are typically rare within Unit B material across all three mounds but show variation of habit, and degree of weathering (fresh to comparatively weathered) throughout, potentially implying variable formation processes and timings. Sulphides throughout Unit B are either pyrite or marcasite (Figure 75).

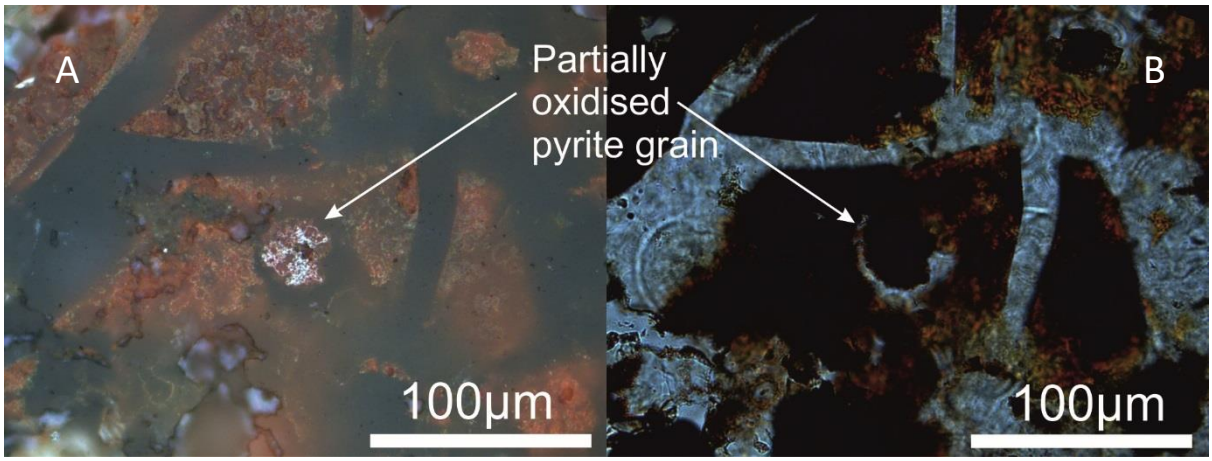

Figure 75: Single grain of partially oxidised 'grubby' pyrite at Southern Mound, within an angular clast of Si-Fe material. Partial halo of iron oxide free silica visible (A = RL-XPL, B = TL-PPL).

Grubby, or partially oxidised subhedral to euhedral pyrite that exhibit variable surface oxidation are observed at each mound. Weathering products are interpreted as grey iron oxide/oxyhydroxide material in reflected light (Figure 76). Larger (~250 micron) near euhedral grains of pyrite in the MIR Zone exhibit surface iron oxide/oxyhydroxides, and also show a pitted surface, potentially related to dissolution by weathering. The degree of weathering of these sulphide grains likely implies early precipitation and weathering, before being incorporated and preserved in the Si-Fe capping material.

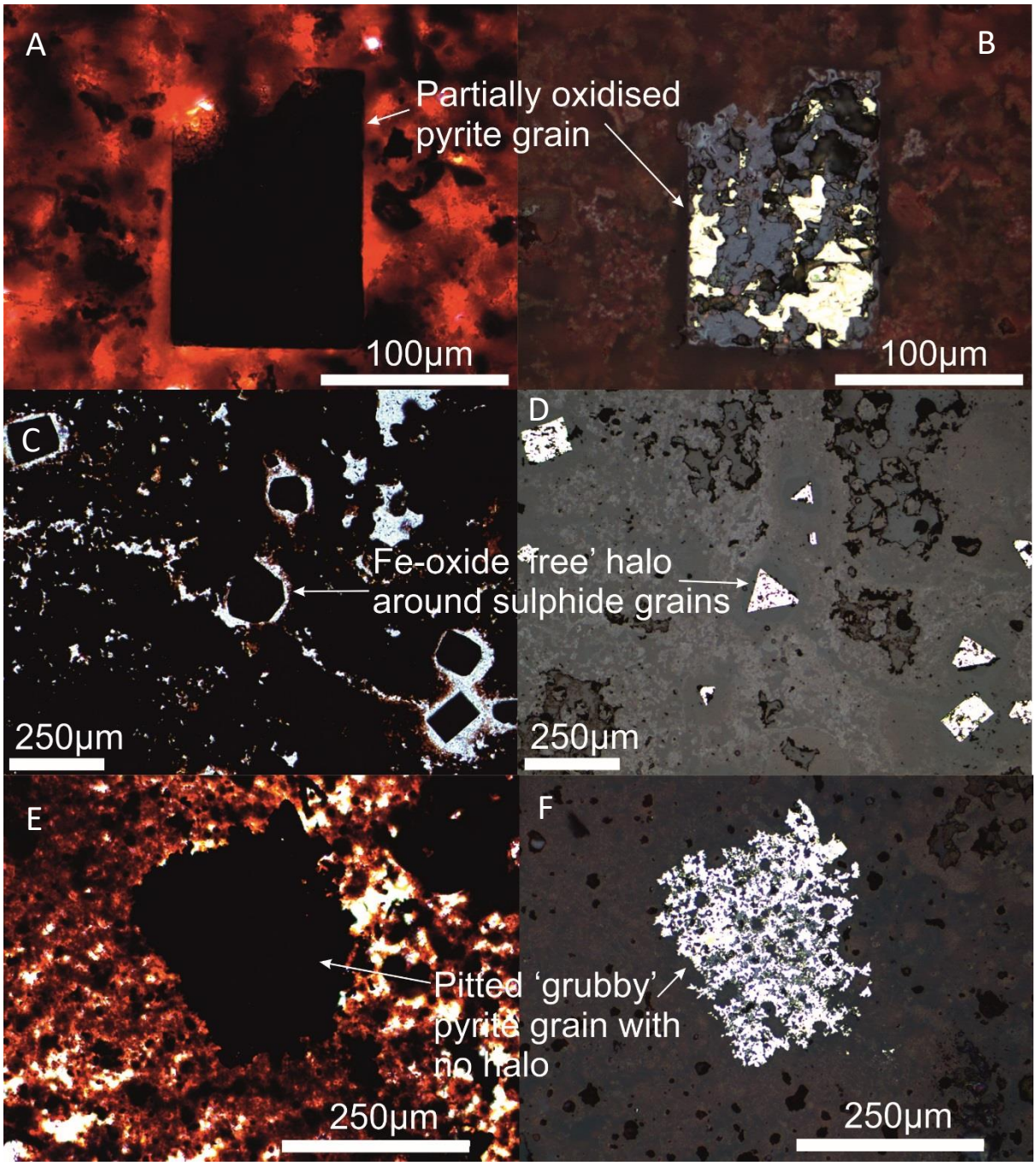

Figure 76: Selection of Unit B sulphides from Unit B at the MIR Zone. (A,B) partially oxidised pyrite grain within Si-Fe material (left = TL, right = RL). (C,D) Individual grubby subhedral pyrite grains often exhibiting iron free silica haloes (left = TL, right = RL). (E,F) Large near euhedral pitted grubby pyrite grain, seemingly overgrowing Si-Fe material (left = TL, right = RL).

Larger irregularly shaped areas of grubby sulphides are texturally different from the subhedral to euhedral grains and appear to be controlled by or related to the dendritic/filamentous textures of the Si-Fe material, implying that their formation post-dates formation of the Si-Fe material (Figure 77).

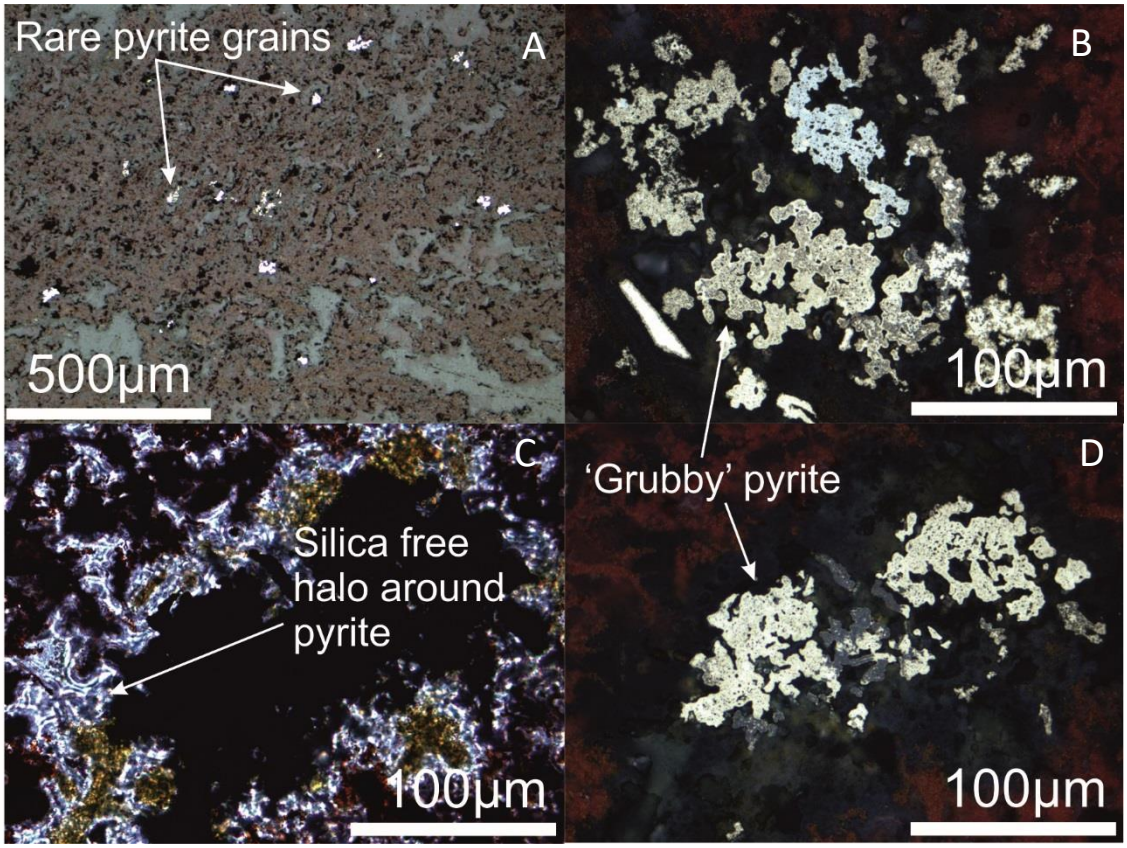

Figure 77: Sulphides throughout Rona Mound Unit B. (A) rare subhedral to euhedral grubby pyrite grains. (B,C,D) anhedral pyrite growth controlled by existing silica coated haematite filaments, with iron free haloes around the sulphide growths (B,D = RL, C = TL).

Most irregularly grown sulphides at Rona Mound (Figure 77), and comparatively fresh near-euhedral grains at the MIR zone (Figure 76) exhibit haloes of iron-free silica. The existence of these haloes is interpreted to be associated with the late-stage (i.e. post silicification) precipitation of sulphide grains. The assumption is that reduced fluids are locally constrained by the silica, enabling dissolution and scavenging of existing iron oxides, and re-precipitation of iron as a sulphide. This would result in iron-free silica zones separating reduced iron (pyrite) from the oxidised iron (haematite). The predominant filamentous/dendritic textures at Rona Mound enabled irregularly shaped precipitation almost pseudomorphic of the silica-coated dendrite/filament material. In comparison, silica appears to be relatively homogenously distributed in Si-Fe clasts at the MIR zone, enabling near euhedral growth.

Unique filamentous pyrite is present in both Unit B samples analysed from Rona Mound. Unlike the irregular grubby pyrite observed, pyrite and marcasite occur as ~ 3µm diameter filament cores, and appear to be coated by haematite and silica (Figure 78). Unlike the other irregular grubby sulphides

no iron free silica halo, separating out oxidised and reduced iron exists, and it is not clear whether the filament cores are early or late-stage in Si-Fe cap formation.

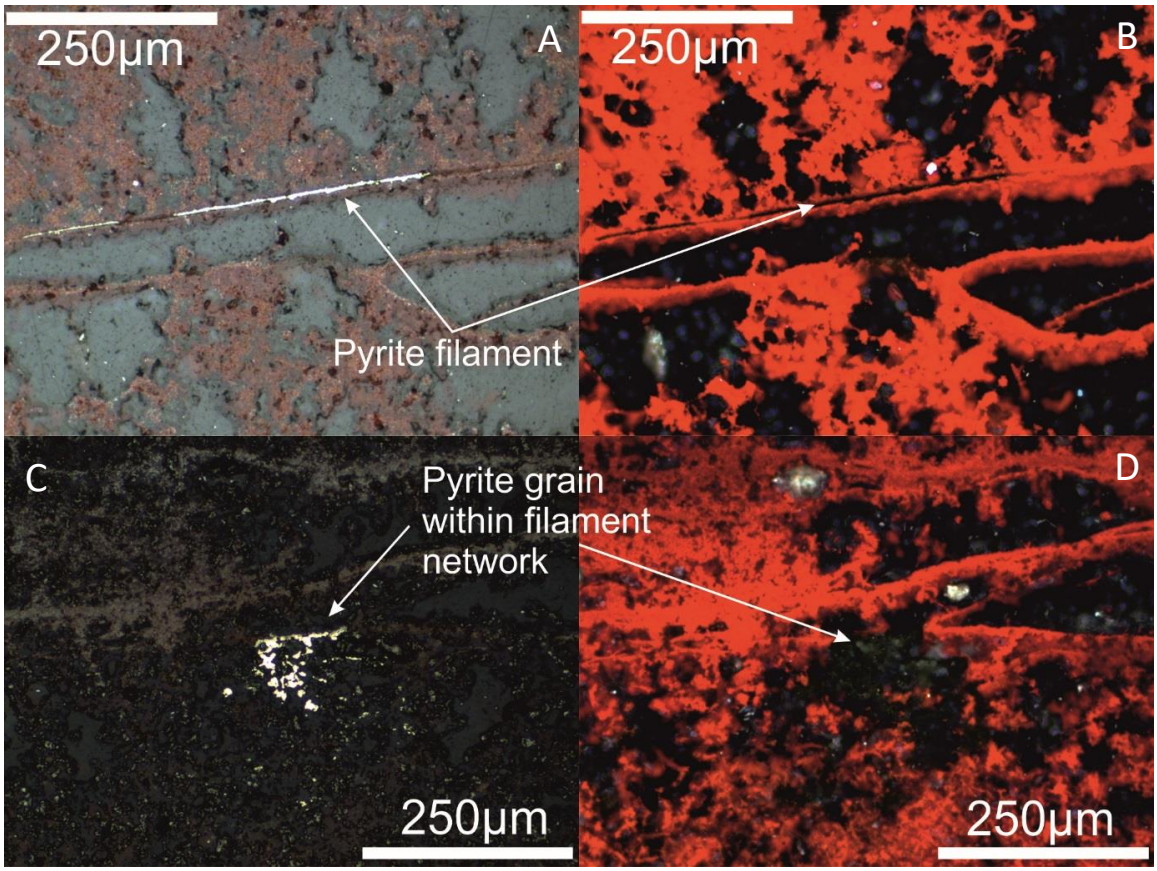

Figure 78: Filamentous pyrite in Rona Mound Unit B. (A,B) Pyrite 'core' present or lost during polishing, coated by Si-Fe material. (C,D) Larger anhedral pyrite associated with a filament section. (A,C = RL, B,D = RL-XPL).

Similar to the filamentous pyrite, other comparatively fresh subhedral to euhedral pyrite grains at the MIR Zone exist in close proximity with iron oxides and do not exhibit a halo of iron oxide-free silica. Based on observation alone, it is not clear why this is the case.

5.4.3 Dendrite and colloform growth

Neither dendrite nor colloform materials were identified in Unit B material from Southern Mound, and only two samples of Unit B material from the MIR Zone exhibit dendritic growth textures, preserved by iron oxide mineralogy (Figure 79). Both examples from the MIR Zone exhibit growth patterns from a point source, within one preserved as a relict texture in a clast of Si-Fe material, and the other a well-defined fan over an area of ~ 1 mm^2, within an area of un-brecciated Si-Fe material. The low amounts of dendrite and colloform growth textures or clasts containing said textures, further supports the idea that Unit B material from Southern Mound and the MIR Zone

are comparable with the haematite rich Unit M4 sediment Unit. Iron oxide (and oxyhydroxide) morphology in Unit B materials (at both mounds) and the Unit M4 sediment is typically homogenous with little to no 'organised' iron oxide structure or growth textures, outside of rare filamentous patches.

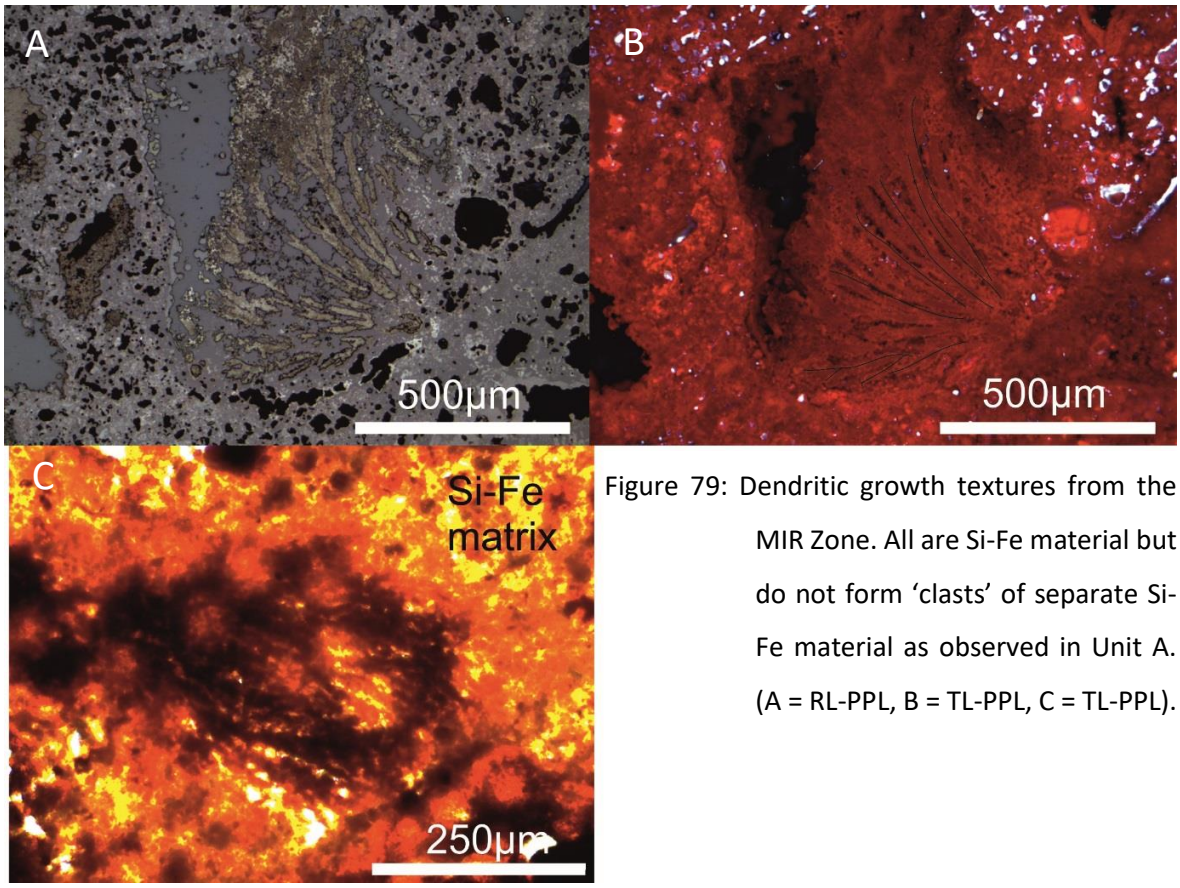

Figure 79: Dendritic growth textures from the MIR Zone. All are Si-Fe material but do not form 'clasts' of separate Si-Fe material as observed in Unit A. (A = RL-PPL, B = TL-PPL, C = TL-PPL).

Unit B dendritic material at Rona Mound has no preferred orientation, but within localised areas a single prevailing growth direction of dendrites occurs. An area of approximately 1 x 2 mm is composed of a series of 'feather-like' dendrites, which all shared a common orientation is a good example of this (Figure 80B). In contrast, another comparable area in the same section contained 6 smaller discrete patches of dendrites orientated in different directions (Figure 80A). These discrete areas are characterised by prevailing growth patterns, within a general area of disorganised iron oxide material. The dominance of dendritic materials in Unit B material at Rona Mound, contrasted with the homogenous fine-grained haematite within Unit B material at both Southern Mound and the MIR Zone, implies two different mechanisms of formation. It is unlikely that Unit B material from Rona Mound formed by silicification of fine-grained hydrothermally derived sediment, but both samples have undergone some degree of silicification.

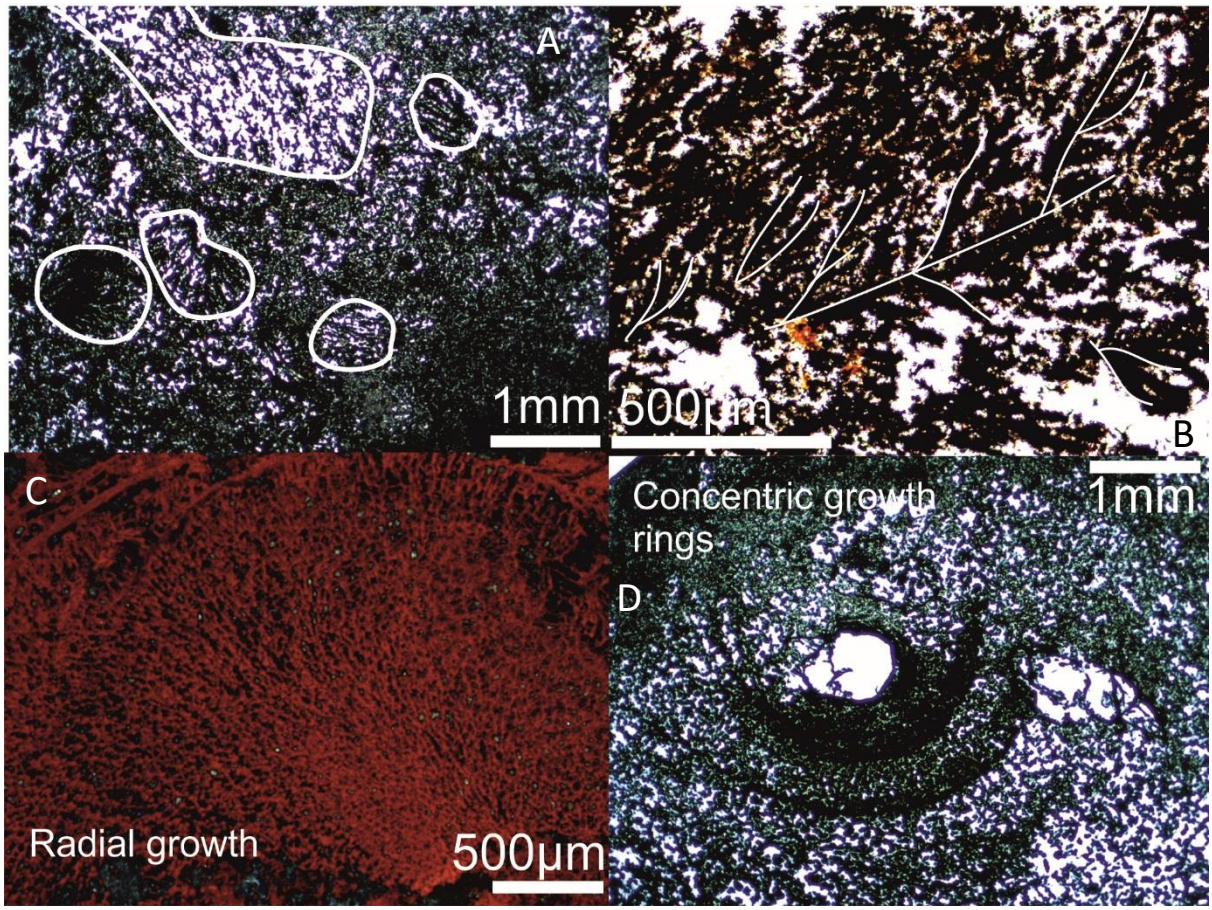

Figure 80: Dendritic and radial growth textures at Rona Mound. (A) Randomly distributed discrete areas of preferential growth zones – TL-PPL. (B) Classic 'tree-like' dendritic growth patterns (highlighted by white lines) – TL-PPL. (C) Fan-like growth radiating from a single point – RL-XPL. (D) 'Tube-like' central void with radial growth bands – TL-PPL

Radial growth patterns are also observed in some Unit B samples from Rona Mound, both as concentric 'rings' of material from a central void space, but also as a mesh radiating out from a single point (Figure 80C,D). This growth pattern shares a striking resemblance to a clast of colloform and dendritic material observed in the goethite rich Unit M3 sediment at Southern Mound, although mineralogy and surrounding materials differ (See Section 5.2.2).

Growth textures from clasts within hydrothermal sediments and Unit B from Rona Mound are comparable, likely indicating formation by similar mechanisms. It is still unlikely that Unit B material from Rona Mound has formed from fine grained, homogenous, hematite rich sediment.

5.4.4 Filaments

Filamentous material is rare within Unit B samples from both Southern Mound and the MIR Zone. At Southern Mound, a single ~ 50 micron long, ~2 micron thick filament was observed within iron

oxide free silica. Additionally an area of filaments or 'pseudo'-filaments up to ~ 100 microns and varying in thickness from ~ 5 to 10 microns are observed (Figure 81, Figure 82). Within MIR Zone Unit B samples filaments are typically short (≤ 100 microns), ~3-5 microns in diameter, single or in small clusters, and are composed of iron oxides (predominantly haematite) and silica, giving a translucent appearance.

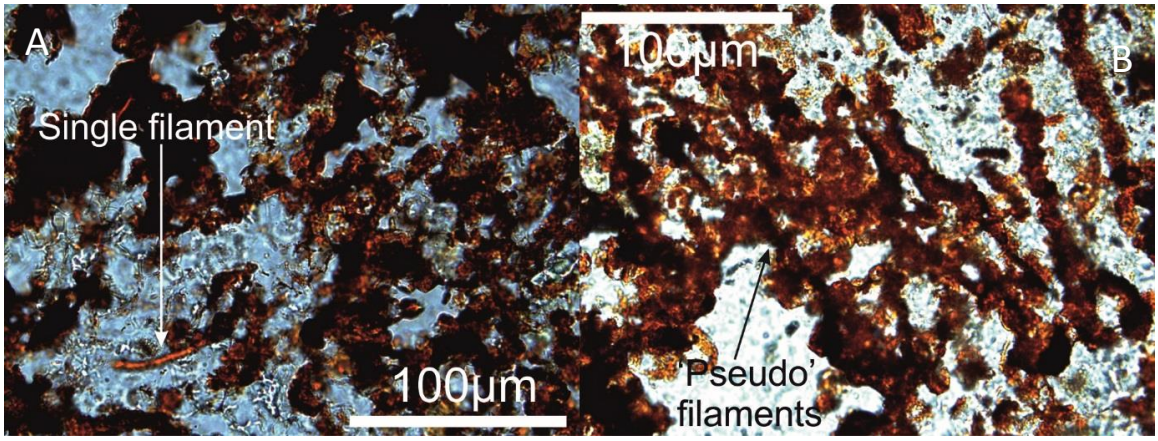

Figure 81: Filamentous textures from Southern Mound. (A) Single filament within quartz infill – TL-PPL. (B) 'Pseudo'-filament textures, thick Si-Fe features that may resemble thicker tube like filaments – TL-PPL.

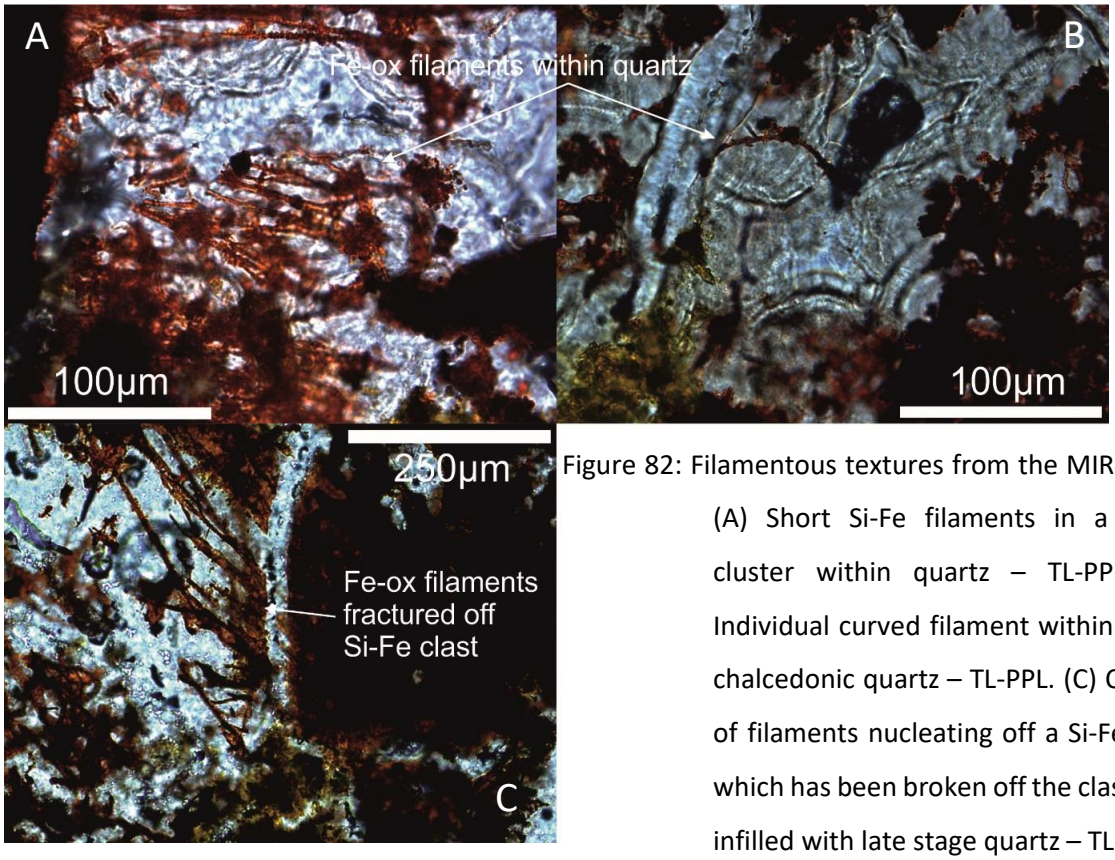

Figure 82: Filamentous textures from the MIR Zone. (A) Short Si-Fe filaments in a small cluster within quartz – TL-PPL. (B) Individual curved filament within radial chalcedonic quartz – TL-PPL. (C) Cluster of filaments nucleating off a Si-Fe clast which has been broken off the clast, and infilled with late stage quartz – TL-PPL.

In contrast to Unit B material at both Southern Mound and the MIR Zone, filaments are a major textural component at Rona Mound. Filamentous material has two main morphologies: Group 1 - as long (~mm to cm length) single or grouped linear filaments; and Group 2 - as discrete areas of single and intergrown, short filaments (Table 48).

Group 1 filaments are less common, and are predominantly composed of hematite core, with silica coatings, but rarely show discrete sections of pyritic cores, surrounded by haematite and silica. These longer filaments are typically straight with little to no deformation and often show braiding with strands branching and reconnecting to a central filament.

Group 2 filaments are more dominant and are composed of haematite cores, coated in silica. Shorter filaments exhibit a more complex filament surface texture with a more nodular-like appearance and show divergent directions and more randomised branching within a single area. This often results in randomly distributed interconnected networks of filaments over ~ 1 mm^2 areas

Both filament morphologies exhibit random orientation implying a lack of localised directional growth mechanisms apparent in dendritic materials (Figure 83).

Table 48: Two types of filaments within Unit B material at Rona Mound

	Morphology	**Relative orientations**	**Length (µm)**	**Diameter (µm)**
Group 1	Straight – single or grouped	Random	mm to cm scale	~ 3 microns
Group 2	Straight or curved - individual	Random	µm to mm scale	~ 3 microns

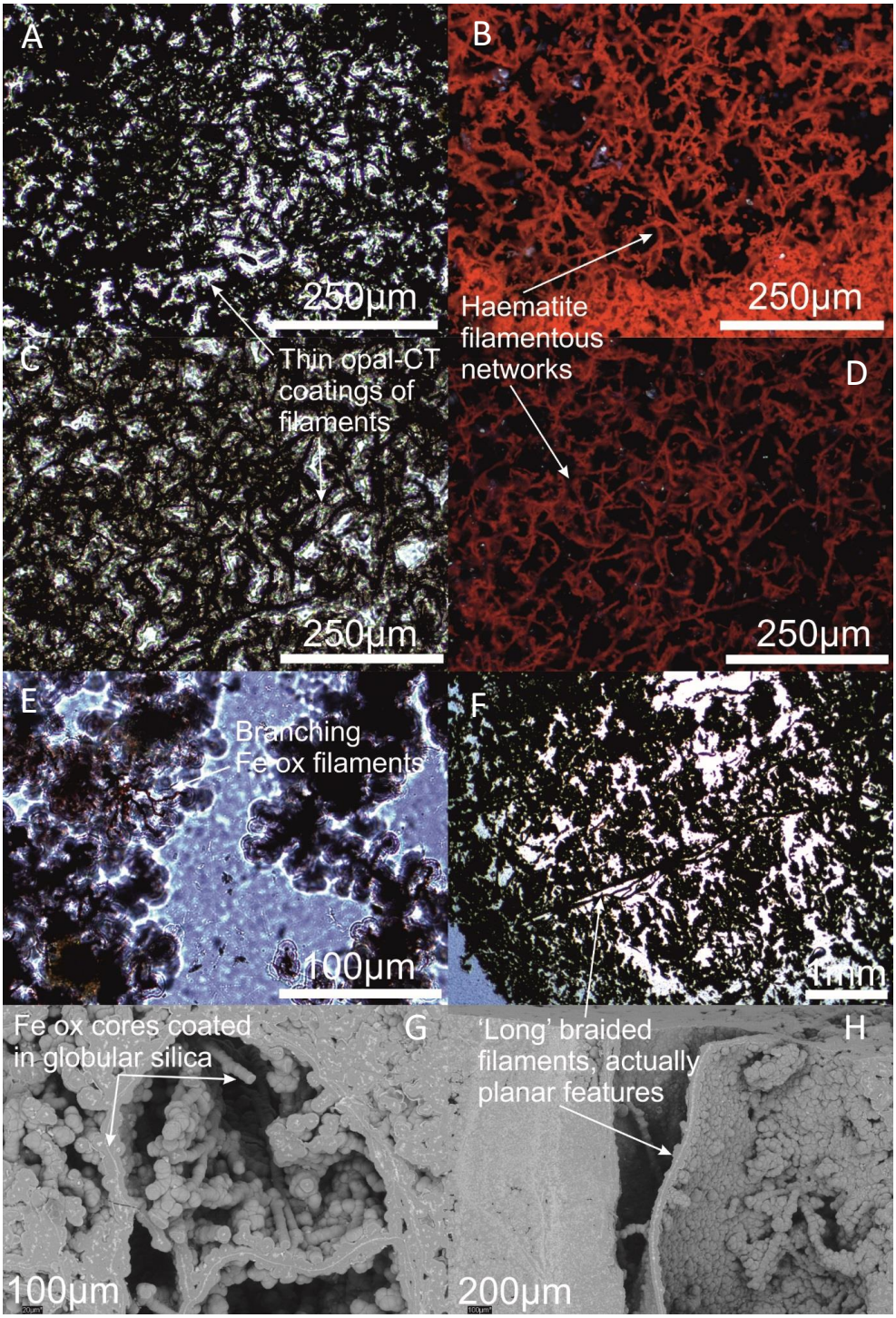

Figure 83: Filamentous material from Rona Mound. (A-D) Group 2 – randomly orientated haematite filaments with thin opal-CT coatings (left = TL-PPL, right = RL-XPL). (E) Group - 2: Branching iron oxide filaments with opal-CT coating – TL-PPL (F) Group 1 – elongate braided haematite filaments – TL-PPL. (G,H) SEM images of Group 1 (G) and Group 2 (H) filaments/planar features.

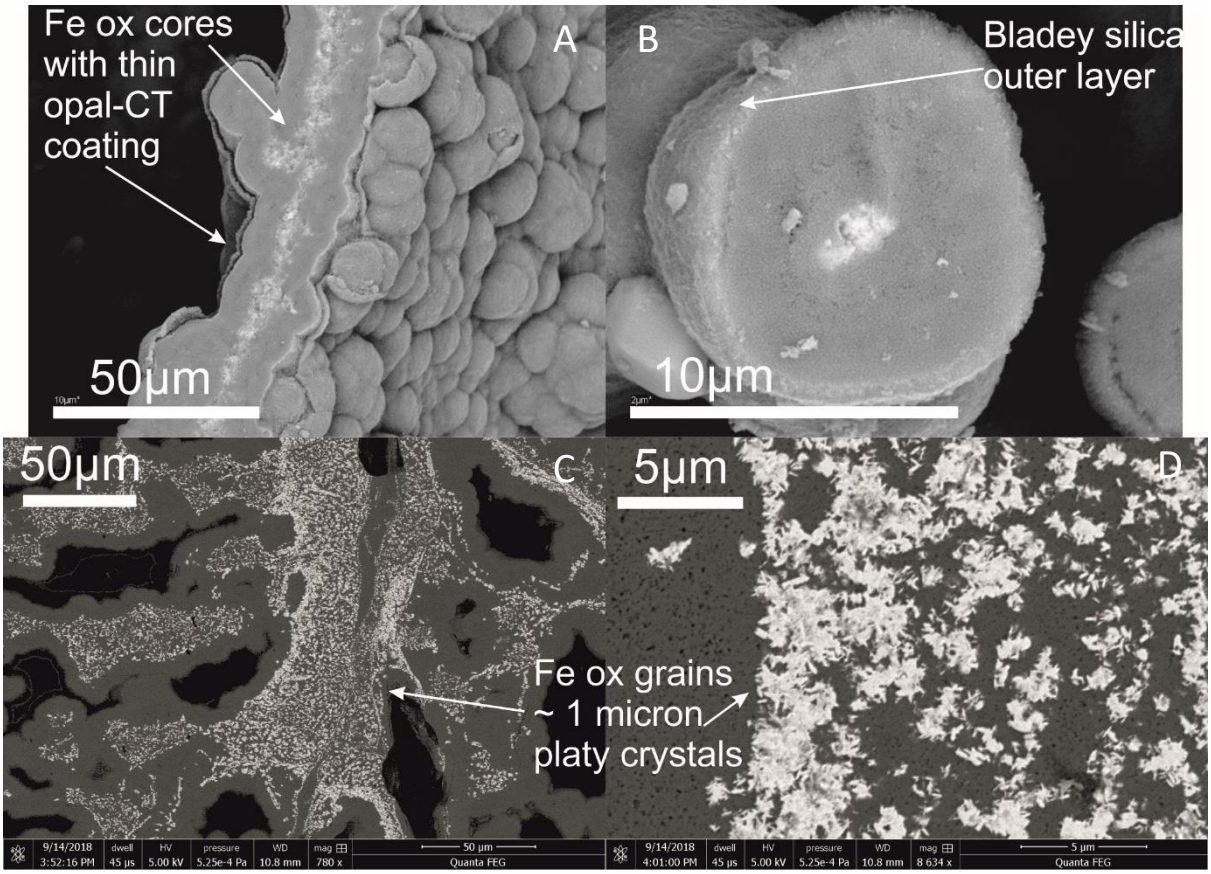

Figure 84A-D: Haematite cores of filamentous and dendritic material coated in ~2 generations of silica. <1 mm platy haematite crystals, potentially indicating abiotic growth rather than biological.

SEM images show that some Group 1 filaments observed in thin section could actually be planar features in three dimensions leading some degree of doubt to other filamentous features observed in section (Figure 83). Additionally individual filaments appear to have continuous cores of haematite coated by silica, but in reality are composed of clusters of platy or bladey haematite crystals that are typically not greater than 1 micron in length (Figure 84C,D).

Unit B at Rona Mound shows significantly more filamentous material than Unit B material at both Southern Mound and Rona Mound. The apparent lack of iron oxide 'sheaths', and the haematite cores being composed of discrete clusters of micron scale haematite crystals, implies that this filamentous material may be abiological (aggregations of haematite crystals) rather than a biological controlled precipitation pattern, but this is a speculative.

5.4.5 Microfractures

Angular Si-Fe fragments cemented by silica (jigsaw brecciation) is a characteristic texture of Unit B material at both Southern Mound and the MIR Zone (Figure 85). The fracture networks do not

appear to have any preferred orientation and the angular clasts occur at a range of sizes (µm to cm scales) and orientations. Displacement between fragments is typically between 20 and 50 microns and they are infilled with iron oxide-free quartz resulting in angular silica-iron fragments 'floating' within the silica matrix. On occasion some clasts show ~120° 'triple junction' fracture patterns that indicate a minimal energy configuration, e.g. from contraction. Rare textured Si-Fe clasts, similar to Si-Fe clasts observed in Unit A material, that have been preserved can also exhibit similar textures, but are not necessarily infilled by silica. These cracks are interpreted to be associated with volume loss from the dehydration of hydrous silica or iron oxyhydroxide (i.e. goethite). A similar mechanism could be responsible for these cracks in Unit B material as typically haematite and quartz (the non-hydrous equivalents) are observed. Unit B at Rona Mound typically does not exhibit these kind of fractures. This could be a function of the lack of Si-Fe clasts which appear to have been brecciated in other Unit B samples, or the fact that opal-CT is the predominant silica mineral. The presence of opal-CT over quartz could imply that significant dehydration has not occurred, and that a similar dehydration of opal-CT to quartz could be responsible for the brecciation in Unit B samples from Southern Mound and the MIR Zone.

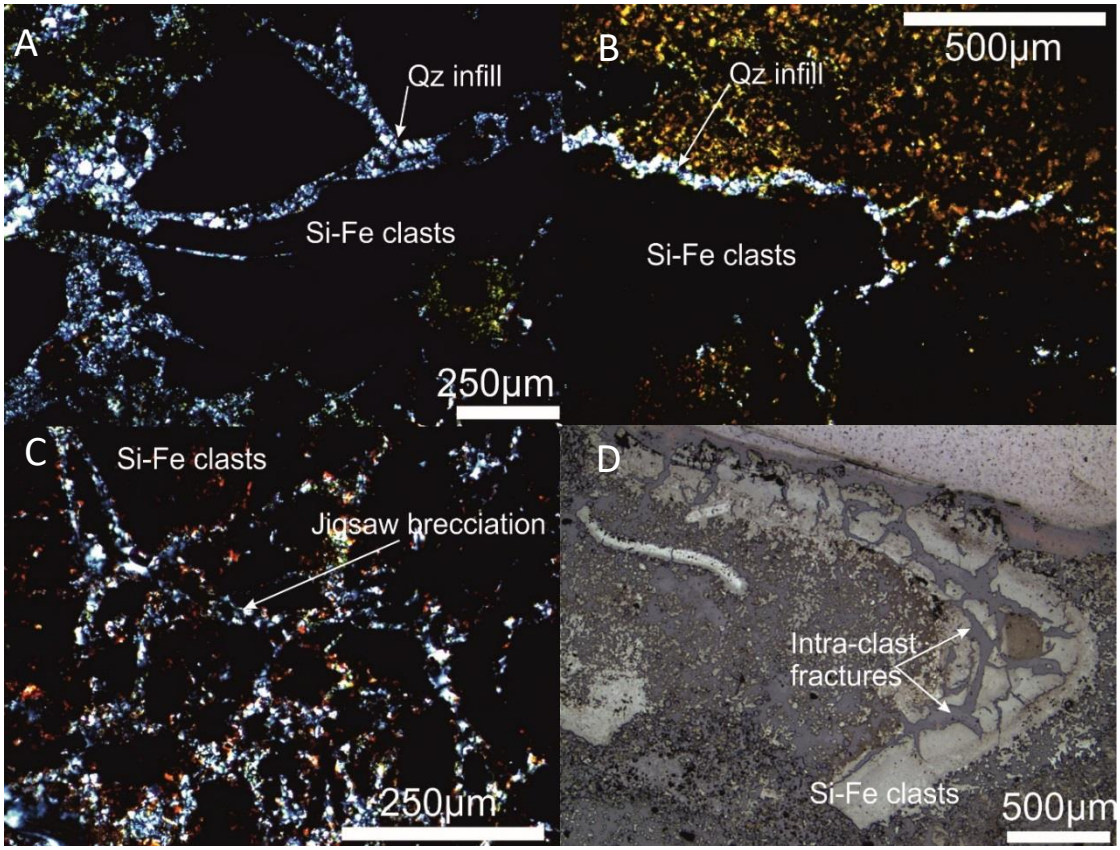

Figure 85: Range of jigsaw and desiccation fractures from the MIR Zone, typically infilled by silica in Unit B material. (A-C = TL-XPL, D = RL-PPL).

5.5 Unit C of the Si-Fe capping lithologies

Unit C was recovered from both Rona Mound and Southern Mound, but not the MIR Zone. At both Southern and Rona mounds Unit C underlies other units of the Si-Fe cap (Unit A at Southern, Unit B at Rona), and directly overlies massive sulphide material. The presence of grey sulphidic silica or massive sulphides are the defining features of this Unit, with each sample showing a variable sulphide assemblage (Section 5.5.2).

Mineralogically Unit C samples are broadly similar to the comparative Unit B material at each mound. Southern Mound Unit C samples are composed of quartz (>93%) and haematite (~1-4 wt%), and Rona Mound Unit C samples are dominated by opal-CT (~60%) and amorphous material (~30%), with iron oxides (~2%) (Table 49). If no amorphous fraction is assumed, opal-CT increases to between ~84 and 92%, supporting the interpretation that amorphous silica is present in both Unit B and C samples Rona Mound.

Table 49: XRD analysis of Unit C material from Southern Mound and Rona Mound

Sample	Mineralogy %								
	Qz	O-CT	Haem	Goe	Py/Mc	Sph	Cpy	Nj	Amor
Southern Mound									
050RD/P11	99.2	-	0.8	-	(x)	(x)	-		-
050RD/P12	93.9	-	3.4	-	2.7	(x)	(x)		-
050RD/P13	96.3	-	3.7	-	(x)	-	(x)		-
Rona Mound									
057RD/P10	0.2	60.0	1.9	-	3.4	(x)	-	-	34.5
057RD/P11	0.3	58.5	2.3	-	8.1	(x)	-	2.3	28.5
Qz = Quartz, O-CT = Opal-CT, Haem = haematite, Goe = goethite, Py/Mc = pyrite/marcasite, Sph = sphalerite, Cpy = chalcopyrite, Nj = Natrojarosite Amor = amorphous fraction									

Although the Unit C samples from Southern Mound are mineralogically similar, they are visually and texturally variable (Figure 86). 050RD/P11, one of the shallowest Unit C samples at Rona Mound, is typically light orange-red in colour with the characteristic grey silica enclaves (silica and sulphide) being present at mm-cm scale. Typically, this colour change is associated with goethite in other samples, but is likely a result of significant dilution by silica as haematite is interpreted to be < 1%.

The deepest two samples of Unit C material do not appear to exhibit the characteristic grey sulphidic silica in hand specimen but show the homogenous 'blood red' haematitic colouring similar to Unit B. Millimeter scale sulphidic silica enclaves are observed in 050RD/P12 in thin section, but not in the underlying sample (050RD/P13). 050RD/P13, the deepest sample of Unit C at Southern Mound, is the only sample of Si-Fe material that exhibits millimetric to centimetric laminations. These laminations are sub parallel to the vertical z-axis of the core.

Unit C samples from Rona Mound exhibit both the characteristic grey sulphidic silica enclaves and high sulphide content. Both samples contains clasts of massive-textured silica-iron, and laminated Si-Fe within a silica matrix observed as grey sulphidic silica enclaves in hand specimen (Figure 86). These textures are broadly comparable with Unit A material from Southern Mound, implying that they may share a comparable paragenesis. Only five samples of Unit C were recovered across both

Southern (3 samples) and Rona Mounds (2 samples), but present a wider range of textures and mineralogy, than the overlying hydrothermal sediments, Unit A or Unit B material.

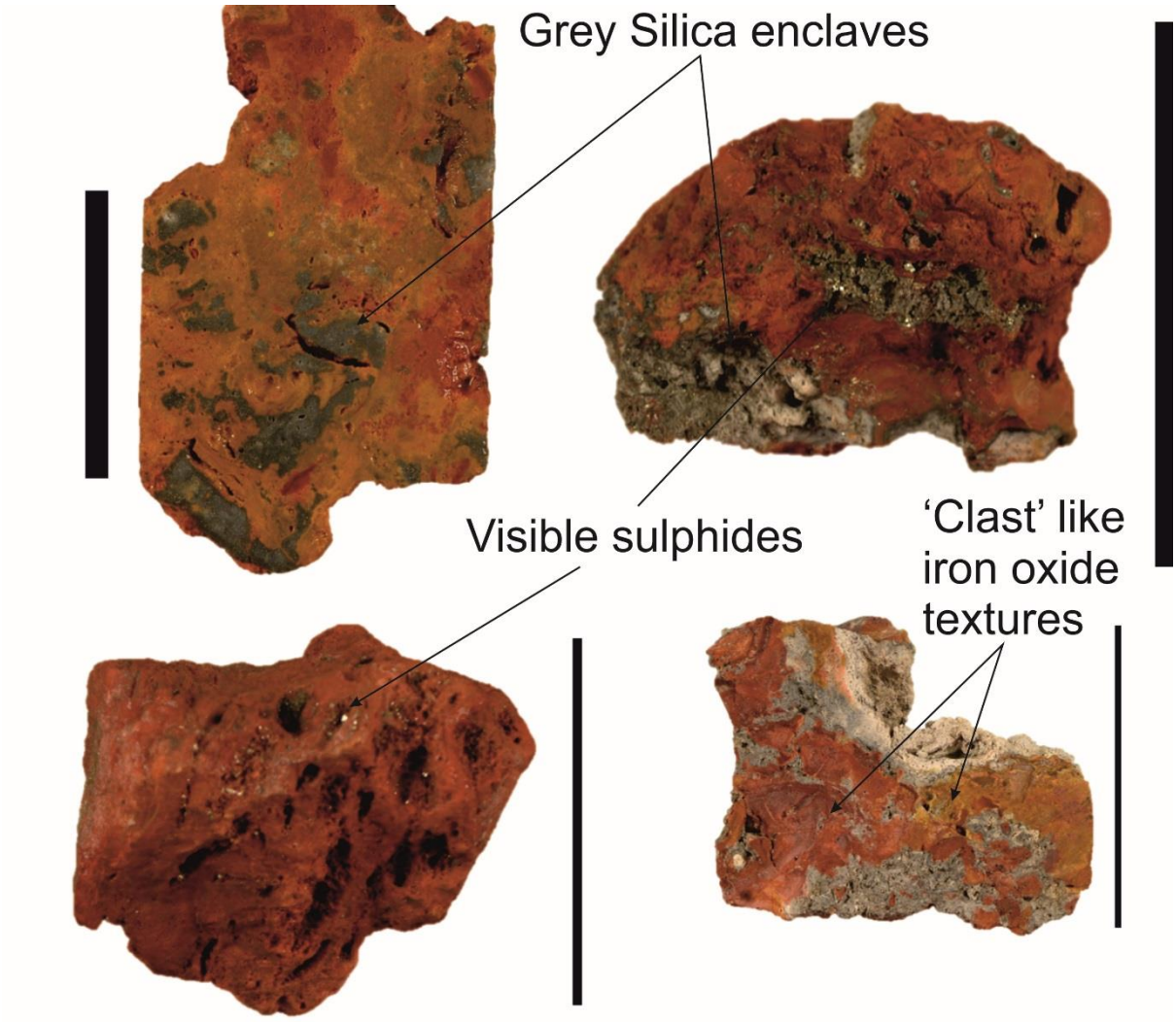

Figure 86: Range of Unit C samples from Southern Mound (Top left = 050RD/P11, Bottom left = 050RD/P13), and Rona Mound (Top right = 050RD/P10, Bottom right = 050RD/P11). Characteristic grey silica enclaves present in three samples, with all showing sulphide mineralisation. Scale bars = 5 cm.

5.5.1 Silica morphology

Variable silica habits, textures, and relationships are be observed across all Unit C samples including: interlocking polygonal quartz crystals, spherulitic and radial/chalcedonic growth textures (opal-CT/amorphous silica), to micro- or cryptocrystalline quartz and opal-CT/amorphous silica. As Southern Mound Unit C samples only contain quartz, and Rona Mound samples only contain opal-CT/amorphous silica, they have been considered separately in the following sections.

5.5.1.1 Quartz – Southern Mound

Interlocking polygonal quartz crystals are observed in the shallowest Unit C sample (050RD/P11), and the deepest (050RD/P13) at Southern Mound only (Figure 87). In the shallowest sample, it is possibly only visible due to the very low concentrations of haematite, and is associated with areas pigmented by haematite. The interlocking polygonal grains show radial and undulatory extinction, indicating that they are the product of recrystallisation. It is likely that the recrystallisation is associated with the bleaching and leaching of iron oxide material, leading to the low haematite concentration.

Interlocking polygonal silica crystals in the deepest Unit C sample (050RD/P13) are not easily observed within Si-Fe clasts as grain boundaries are obscured by finely disseminated iron oxide grains resulting in pigmentation. However, defined grain boundaries can be observed in reflected light indicating at least three generations of overgrowing interlocking polygonal growth, and often exhibit a < 1μm layer of iron oxide-free quartz at the boundary between quartz materials. Often the outermost layer of quartz is partially or wholly iron free, indicating localised leaching, and dissolution and removal of iron oxides after complete silicification, or precipitation within void space. Void spaces are infilled by polygonal and drusy quartz grains, which often exhibit zonation near crystal boundaries.

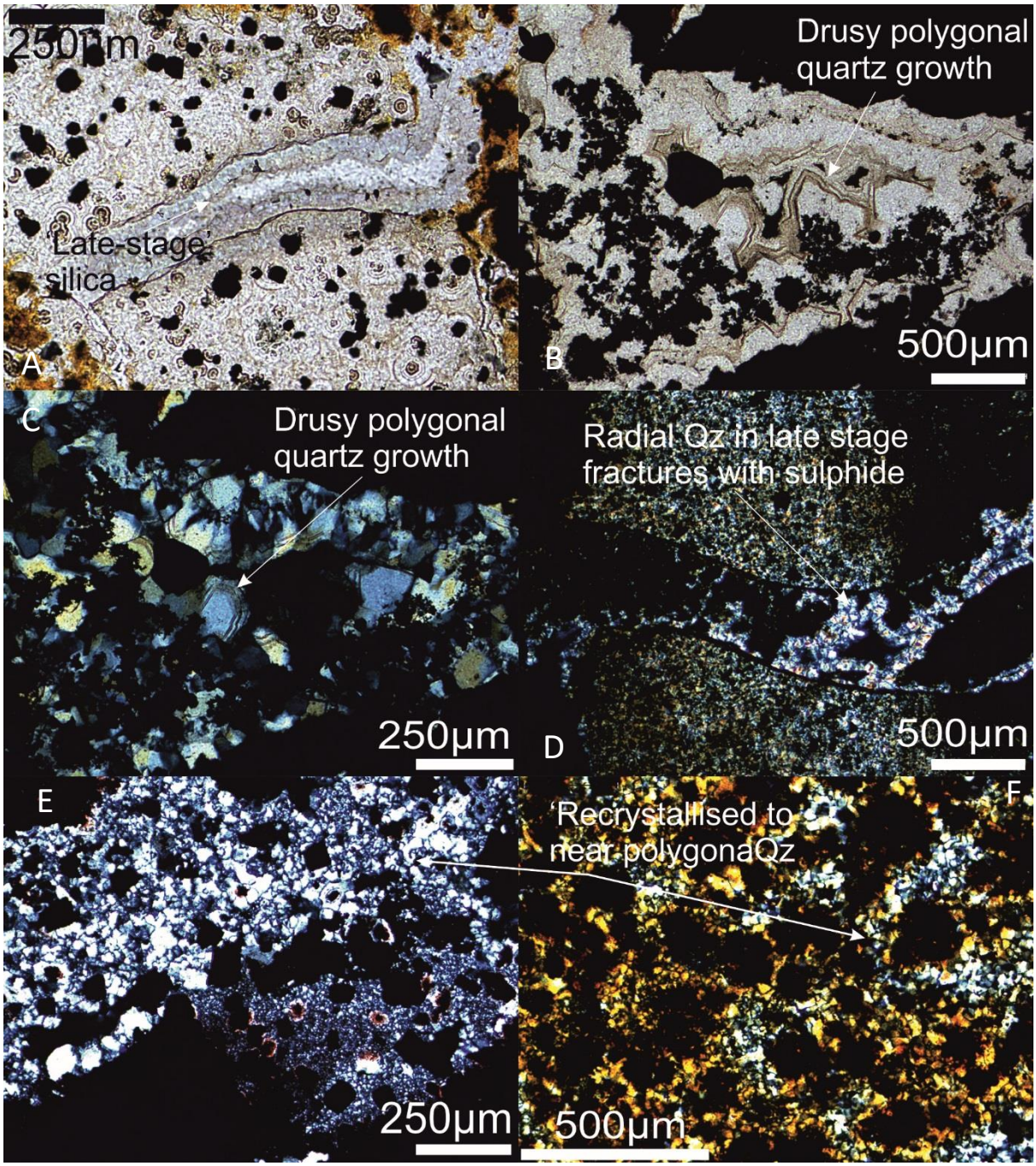

Figure 87: Range of quartz habits throughout Unit C material at Southern Mound. (A-D) Late-stage drusy and polygonal quartz growth within fractures or void space (A,B = TL-PPL, C,D = TL-XPL). (E) Varying quartz grain size from macrocrystalline to microcrystalline in Unit C sample 050RD/P12 – TL/XPL. (F) Near polygonal quartz recrystallisation textures pigmented with iron oxide – TL-XPL.

Microcrystalline, spherulitic, and radial/chalcedonic quartz textures are associated with the centimetre scale grey sulphidic silica enclaves in 050RD/P11, and the millimeter scale enclaves in 050RD/P12 (Figure 88). Radial/chalcedonic quartz textures dominate the grey silica enclaves, with silica textures nucleating off Si-Fe clasts or sulphide grains. In some areas, microcrystalline quartz

infills around the existing radial growth textures, and can be seen infilling small fractures within the radial material (50-100 µm wide), forming the rest of the silica enclave. In 050RD/P11, larger scale fractures post-date both radial/chalcedonic and microcrystalline quartz growth and are partially infilled by a second generation of radial/chalcedonic silica with undulatory and radial extinction. This sequence implies at least three separate generations of silica formation and alteration.

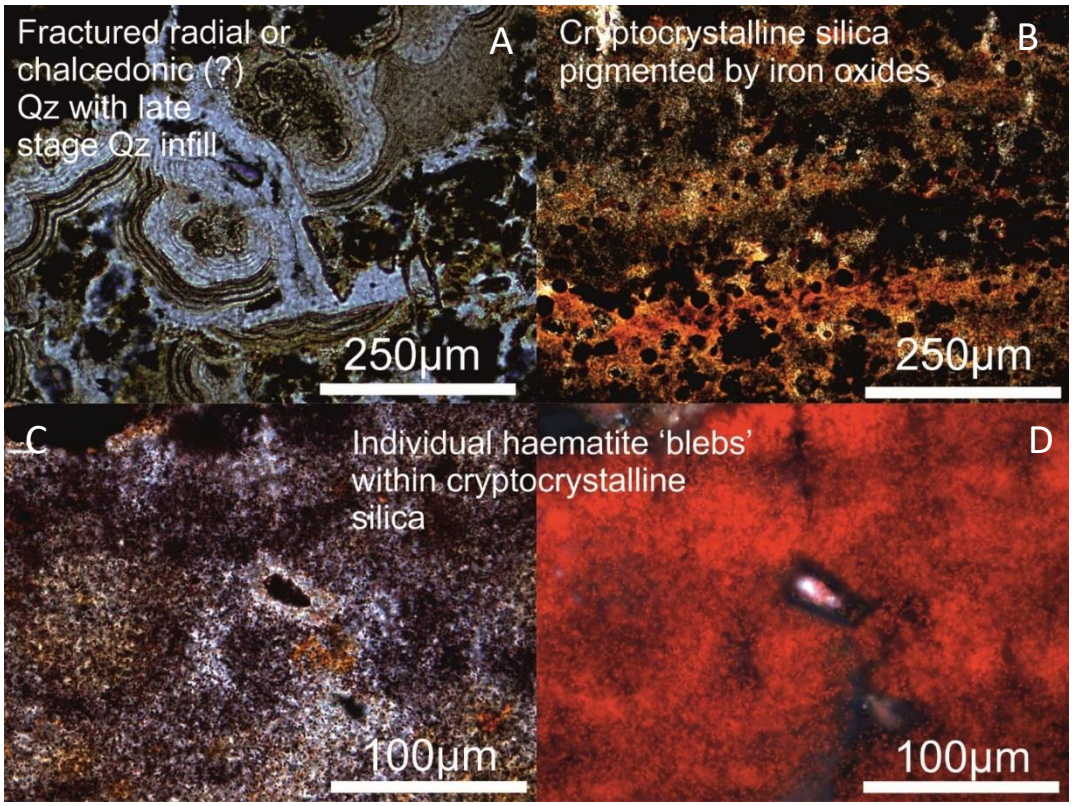

Figure 88: Range of cryptocrystalline quartz textured in Unit C at Southern Mound. (A) Radial/chalcedonic quartz showing fractures and late stage quartz infill – TL-PPL. (B) Fine grained, heterogeneously distributed iron oxides throughout the sample giving the appearance of banding – TL-PPL. (C,D) haematite evenly distributed throughout the cryptocrystalline quartz (C = TL-PPL, D = RL-XPL).

Cryptocrystalline quartz is dominant in the deepest two Unit C samples (050RD/P12 and 050RD/P13), with fine grained (≤5 micron) haematite clusters evenly distributed throughout the cryptocrystalline quartz, likely responsible for the classic 'blood red' jasper colouration, despite only containing <4wt% haematite.

Globular silica (~ 10-20 micron diameter) is observed in the high magnification SEM imagery, with what appears to be a silica 'sheet' connecting individual globules (Figure 89). Microcrystalline euhedral quartz crystals (≤10 microns) are visible as 'strands' or as globular infill of void space. This is most likely recrystallisation from opal-CT lepispheres resulting in the preservation of the

hemispherical textures, but composed of euhedral quartz rather than bladed opal-CT. This implies that during the formation of the grey sulphidic enclave, silica likely precipitated as either opal-CT or amorphous silica. Subsequent dehydration and recrystallisation has occurred resulting in quartz being the dominant polymorph throughout the Unit C material.

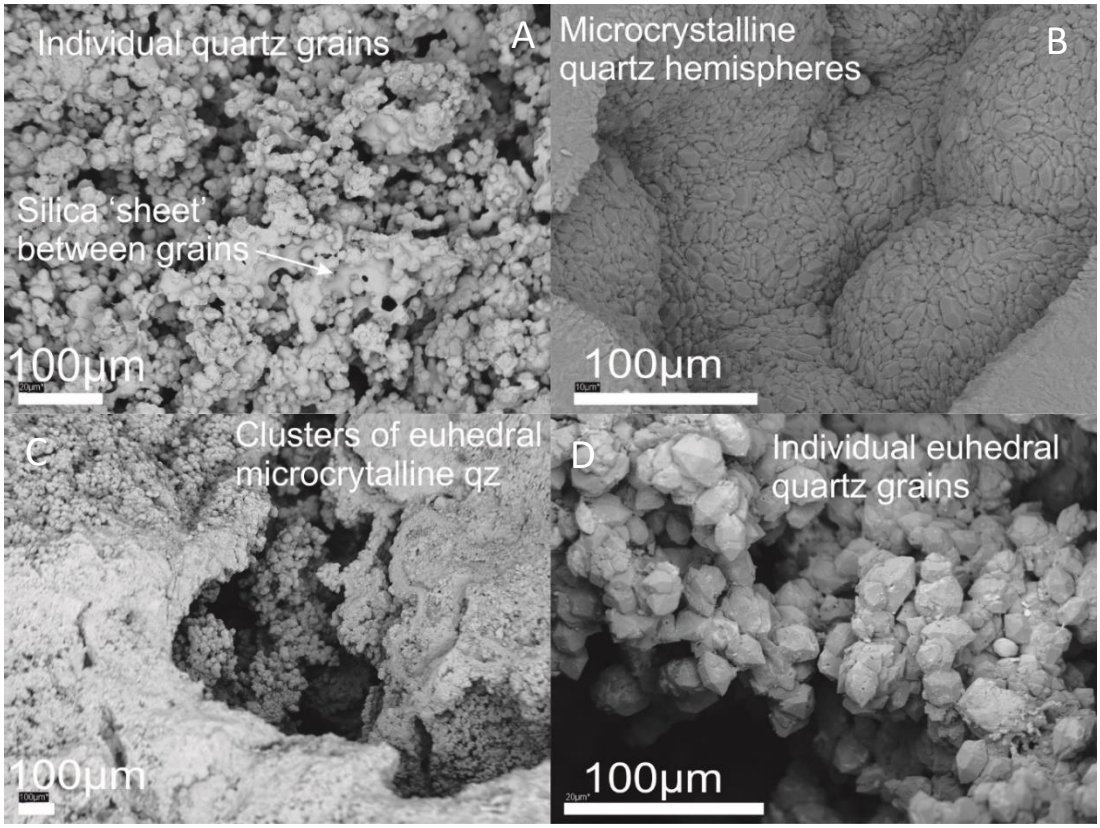

Figure 89: (A-D) SEM images of microcrystalline quartz at Southern Mound. Individual euhedral quartz grains < 10 microns long, and globular hemisphere macro structures composed of euhedral quartz crystals, likely quartz after opal-CT.

5.5.1.2 Opal-CT/Amorphous silica – Rona Mound

Silica textures in thin section at Rona Mound are either cryptocrystalline, spherulitic, or radial growth. Radial growth textures are common throughout and occur as thin (< 10 micron) coating nucleating off Si-Fe fragments, sulphide grains, and filamentous iron oxides of clasts and filamentous material throughout Unit C (Figure 90).

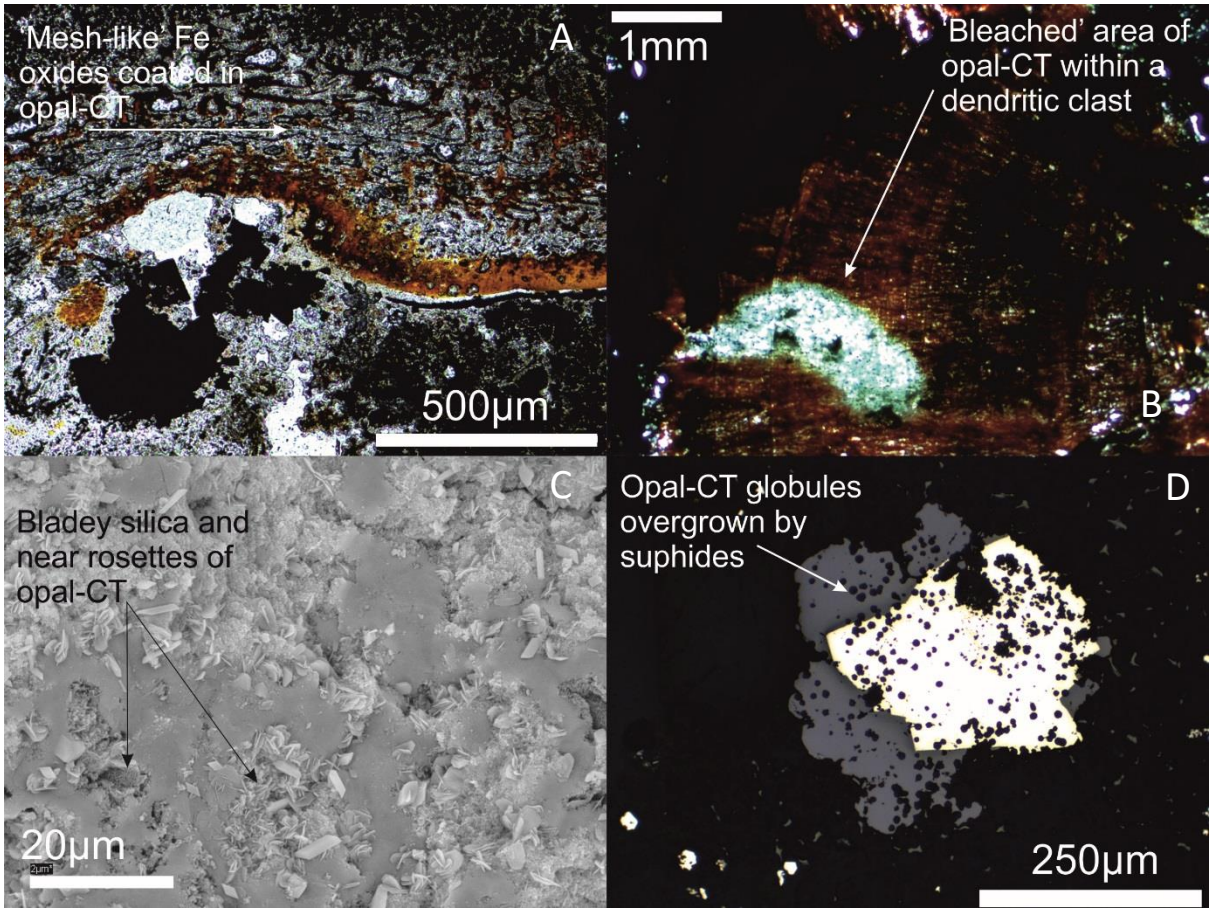

Figure 90: Range of silica textures from Rona Mound. (A) 'Mesh-like' iron oxides coated by opal-CT – TL-PPL. (B) Area of bleached iron oxide free opal-CT in a clast of dendritic fan-like iron oxides – TL-PPL (C) SEM image of bladey opal-CT and lepisphere growth. (D) Individual opal-CT globules being overgrown and incorporated into sulphides – RL-PPL.

Rarely small individual grains (likely iron oxide) also act as nucleation points where radial silica growth occurs evenly around the grain, forming globules or spherules of silica. In some cases the small grains remain, but other cases show no central nucleating point, likely indicating the remobilisation of the nucleation grain, or is an artefact of the three dimensional structure of the sample (i.e. nucleating material is not present within thin section). High-resolution SEM imagery shows that these globules are commonly opal-CT lepispheres with blady silica grains also commonly observed.

5.5.2 Sulphides

The presence of sulphides is one of the defining features of Unit C material, with pyrite, marcasite, sphalerite and chalcopyrite observed in hand specimen and by reflected light microscopy (summarised in Table 50). Sulphides are not disseminated throughout the samples, but are commonly associated within bleached, iron oxide free silica enclaves. These enclaves can be clearly delineated in both thin section and SEM imagery, with the change from reduced iron (sulphide) to oxidised iron (within Si-Fe clasts) being a sharp contact.

Table 50: Sulphide assemblages throughout Si-Fe Unit C samples

Sample	**Sulphides present (descending quantities)**
Southern Mound	
050RD/P11	pyrite, sphalerite, marcasite
050RD/P12	pyrite, sphalerite, marcasite, chalcopyrite
050RD/P13	pyrite, chalcopyrite
Rona Mound	
057RD/P10	Pyrite and marcasite, sphalerite
057RD/P11	Pyrite and marcasite, sphalerite

5.5.2.1 Pyrite/marcasite

Pyrite is the modal sulphide throughout the Si-Fe cap, and is observed in all five Unit C samples across both Southern and Rona Mound (Table 51).

Table 51: Pyrite (and marcasite) variation throughout Si-Fe Unit C samples

	Morphology	**Size (µm)**	**Zonation?**	**Marcasite?**
Southern				
050RD/P11	Euhedral to subhedral (one example of filamentous)	10-50	Yes, in grains (>30µm)	Occasionally intergrown within the larger pyrite grains (>30µm)

050RD/P12	Euhedral to subhedral	30-100	Yes, in grains (>~50µm)	Rarely intergrown with pyrite in larger grains (>3 µm)
050RD/P13	Euhedral to subhedral	≤ 50	No	Not present
Rona				
057RD/P10 057RD/P11	Euhedral to anhedral, Filamentous	10 – 500	No	Commonly intergrown with large pyrite grains (200-500µm), or present at similar sized grains

Euhedral to subhedral pyrite occurs throughout Unit C material at Southern Mound, with large grains often exhibiting marcasite intergrowth (metastable pyrite polymorph). Large pyrite grains also show simple two-stage growth zones in the shallowest two Unit C material from Southern Mound. Zones are delineated by a thin ~ 1 micron layer of what appears to be iron oxyhydroxide. Smaller grains (i.e. < ~30 microns) do not exhibit any internal growth zones or marcasite intergrowths (Figure 91).

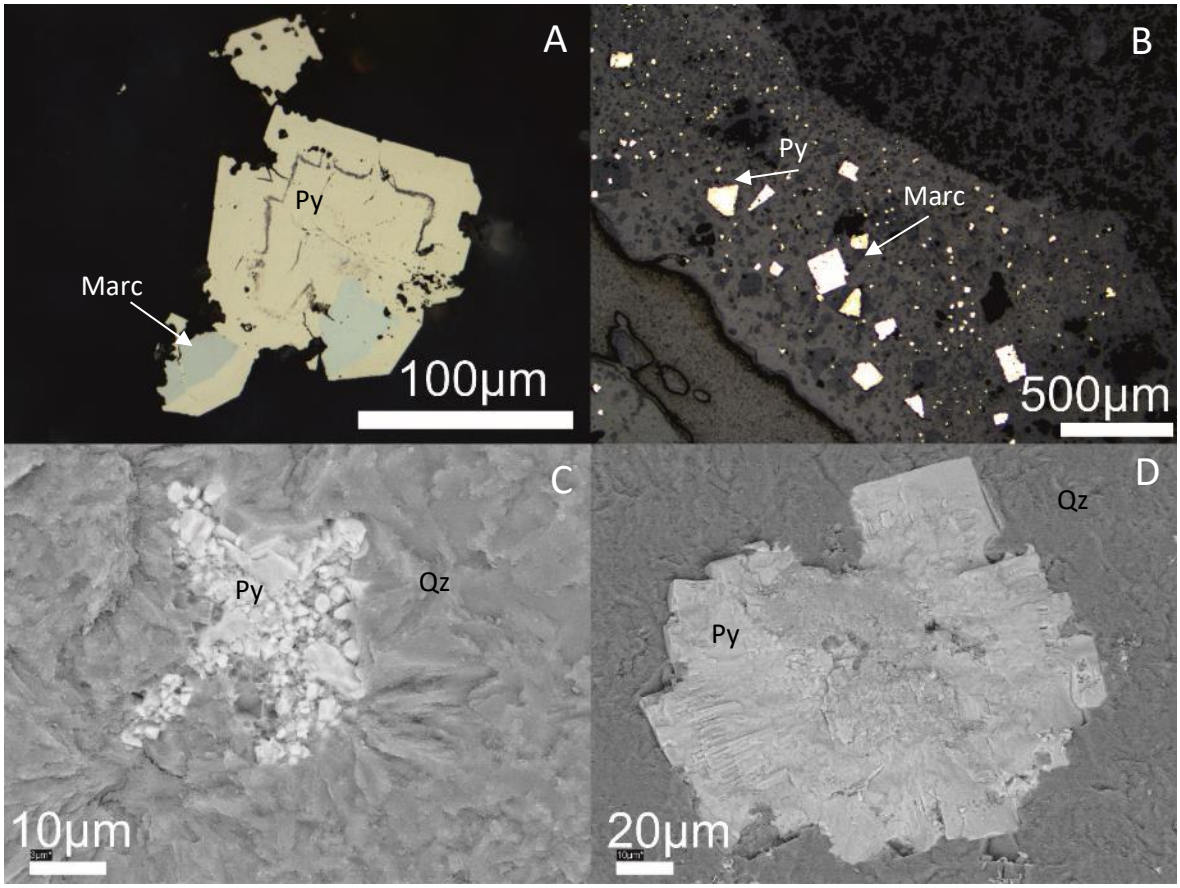

Figure 91: Range of pyrite/marcasite from Unit C - Southern Mound. (A) Zoned pyrite grain with two areas of intergrown marcasite. Zone appears to be delineated by thin layer of iron oxide. (B) euhedral and subhedral pyrite and marcasite grains within late-stage quartz. (C,D) SEM images of pyrite within the microcrystalline quartz.

The edges of larger pyrite grains in 050RD/P12 are often 'pitted' similar to grains observed in Unit B material from the MIR Zone (Section 5.4.2). The pitted edges of these grains often correlate with spherulitic or globular Si-Fe textures where the sulphide grains have grown over silica and started to incorporate it into the structure, this pitted texture is often accompanied by a halo of less iron oxide surrounding the sulphide grain, however this is not always the case (Figure 92). At least one large intergrown euhedral pyrite grain exhibits growth zones with the zone boundaries delineated by grey iron oxyhydroxides.

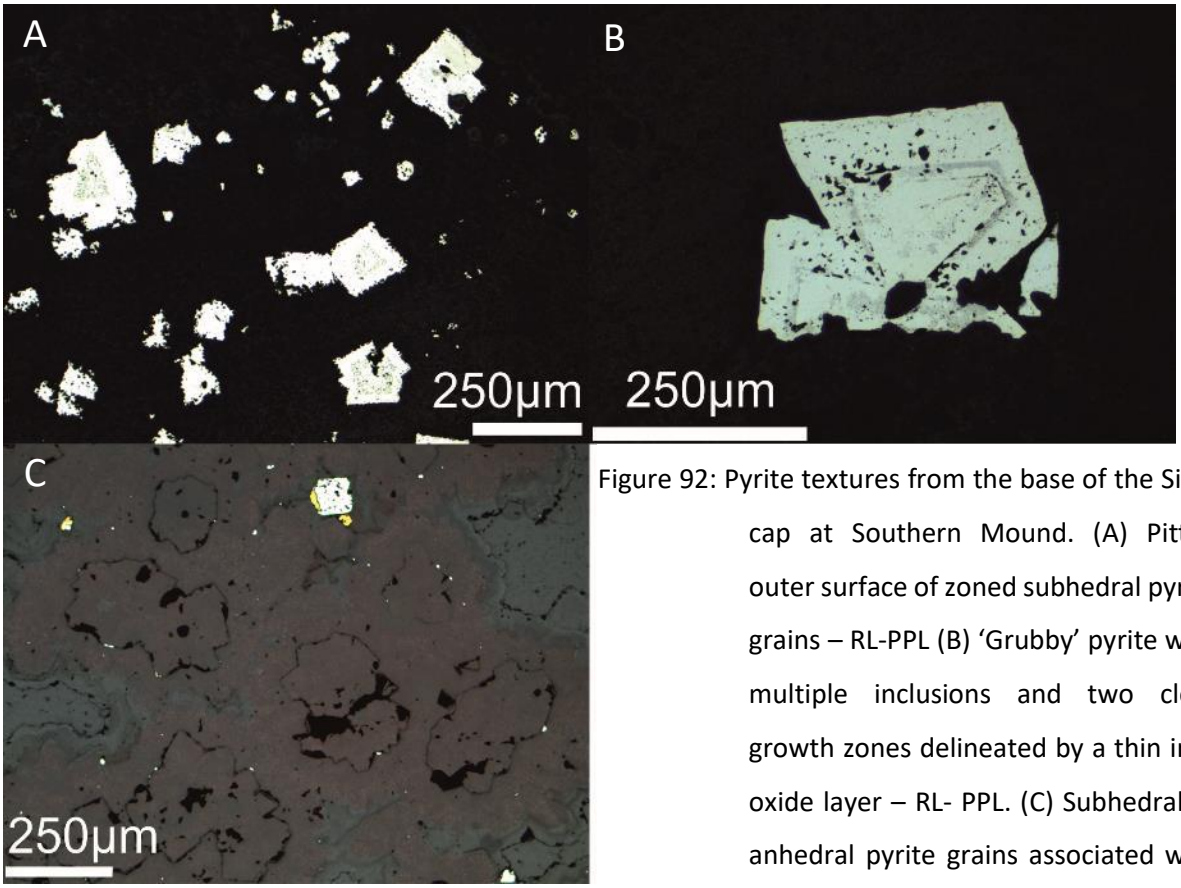

Figure 92: Pyrite textures from the base of the Si-Fe cap at Southern Mound. (A) Pitted outer surface of zoned subhedral pyrite grains – RL-PPL (B) 'Grubby' pyrite with multiple inclusions and two clear growth zones delineated by a thin iron oxide layer – RL- PPL. (C) Subhedral to anhedral pyrite grains associated with polygonal quartz crystal boundaries – RL-PPL.

In contrast to the two shallow Unit C samples in Southern Mound, large pyrite (and chalcopyrite, Section 5.5.2.3) in the deepest sample (050RD/P13) have grown interstitially between late stage drusy zoned quartz grains, which have infilled void space (Figure 92). Small (< 1µm) anhedral pyrite grains can also be found at the crystal boundaries between earlier interlocking polygonal quartz growths, accompanied by < 1µm thin layers of iron oxide-free quartz at the grain boundaries. This implies multiple generations of sulphide formation, potentially accompanied by synchronous silicification.

At Rona Mound, pyrite occurs as disseminated euhedral to anhedral crystals, ranging in size from ~ 10 microns up to ~500 microns. Larger grains (~500 microns) are composed of either only pyrite, or intergrown pyrite and marcasite, but rarely only marcasite. These large grains often show straight grain boundaries, indicative of equilibrium growth, although their final euhedral form is morphologically controlled by pre-existing silica phases (Figure 93).

Overgrowth of the existing silica material by sulphides trying to form euhedral grains results in a speckled texture of silica material bring incorporated into the sulphide. This is nearly identical to the pitted texture observed in Unit C material at Southern Mound (050RD/P12), however the grains

at Rona Mound are larger and show clear overgrowth and inclusion of silica material. Figure 93 shows intergrown euhedral pyrite grains that exhibit the pitted texture with clear silica inclusions, however later stage growth appears to be without silica inclusions. Grains that exhibit this speckled texture are not necessarily associated with haloes of iron oxide free silica as observed in Southern Mound Unit C samples.

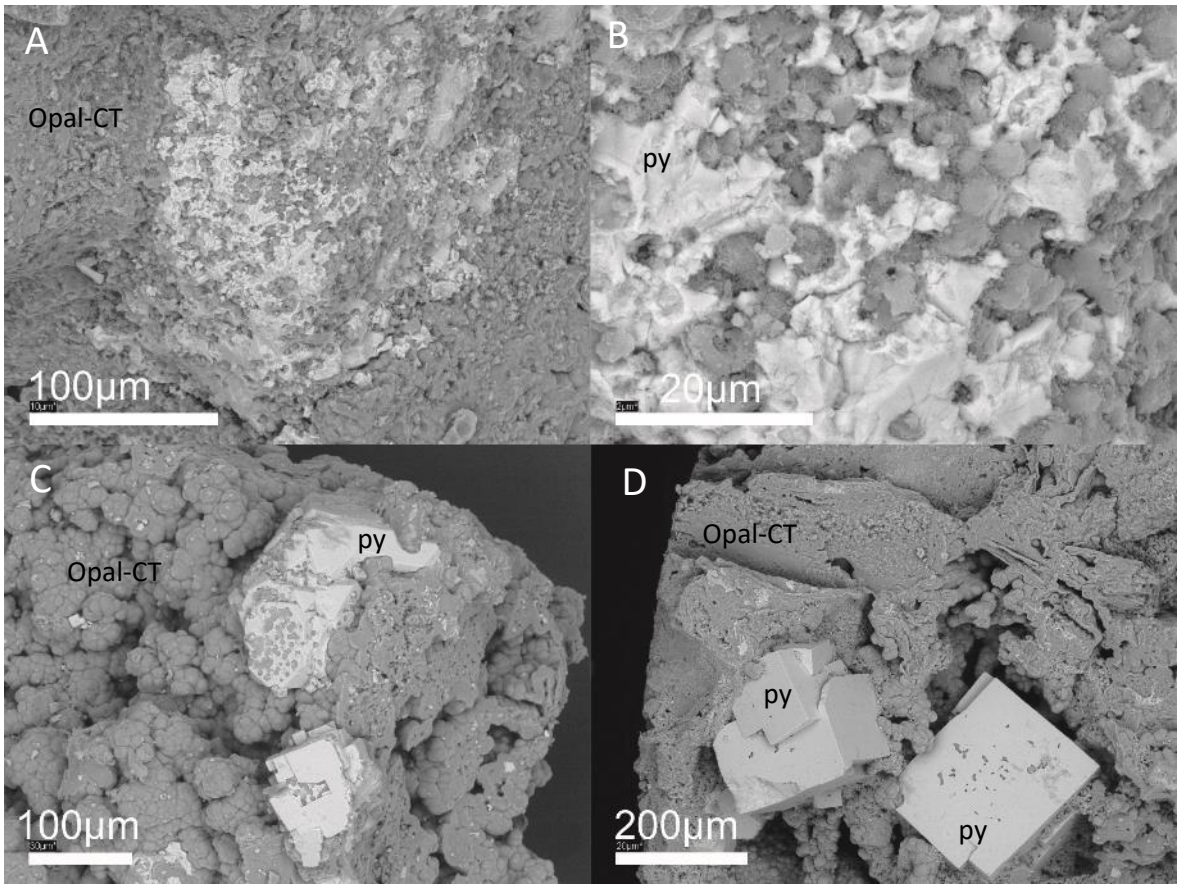

Figure 93: SEM images of pyrite grains from Rona Mound. (A,B) Pyrite overgrowing opal-CT lepispheres. (C,D) Central cores of pyrite with silica globule overgrowth, however outer-most layers of pyrite are commonly silica-free.

Subhedral, <~500 micron, intergrown pyrite and marcasite grains exhibit the pitted texture where in contact with pre-existing silica, but where they have grown into void space, tend towards near euhedral growth.

Unit C at Rona Mound displays the most diverse sulphide textures observed in all the Si-Fe samples recovered from the TAGHF. Pyrite is the dominant sulphide, and occurs as disseminated euhedral to anhedral crystals, ranging in size from ~ 10 microns up to ~500 microns. Larger grains (~500 microns) are composed of either only pyrite, or intergrown pyrite and marcasite, but rarely only

marcasite. These large grains often show straight grain boundaries, indicative of equilibrium growth, although their final euhedral form is morphologically controlled by pre-existing silica phases (Figure 94).

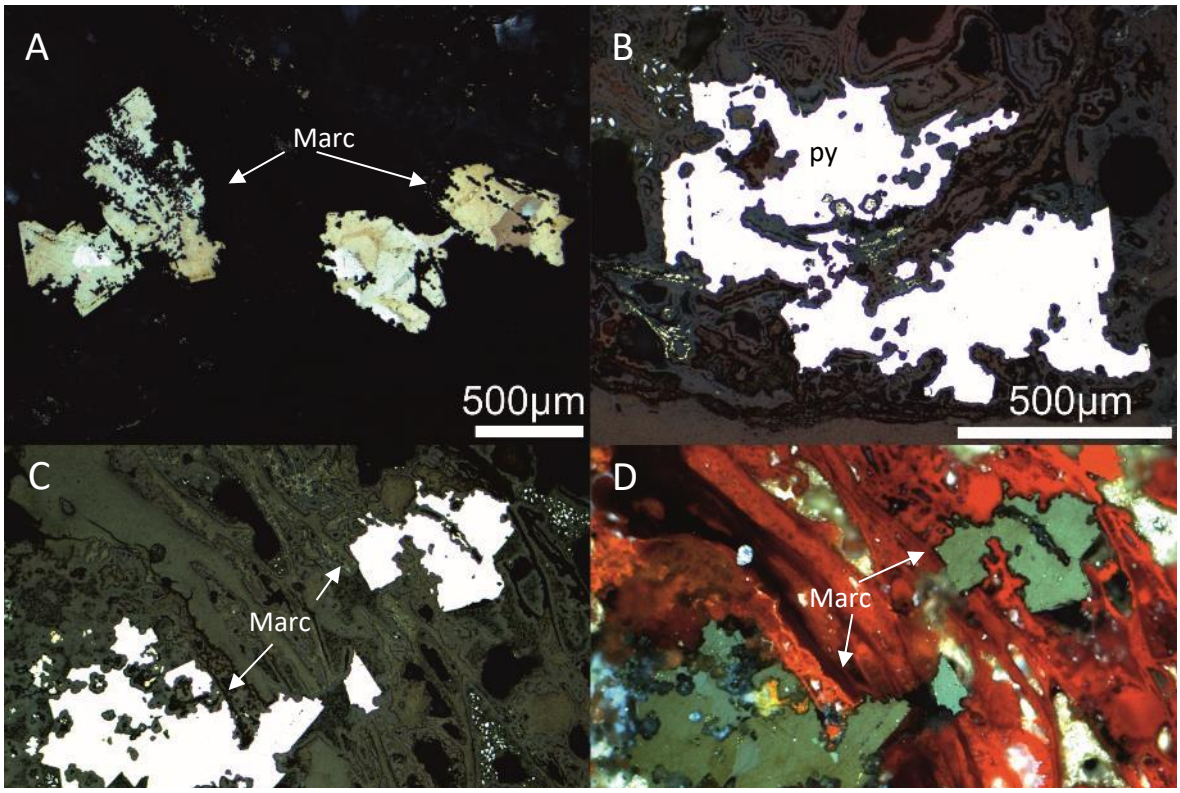

Figure 94: (A-D)Pyrite and marcasite at Rona Mound, pitted and growth limited pyrite and marcasite grains. Existing silica and iron oxide material inhibiting euhedral sulphide growth. (A = marcasite RL-XPL, B = pyrite RL-PPL, C,D = marcasite RL-PPL (C) and RL-XPL (D)).

Unit C material at Rona Mound potentially provides evidence of biogenic features preserved by sulphides. Two spherical shapes with associated sulphide are observed within one sample of Unit C material at Rona Mound (Figure 95). One is a near spherical opal-CT/amorphous silica structure hosting small (<20 micron) anhedral pyrite grains. The second is a circular Si-Fe structure that has a thin halo of pyrite (~ 3 micron wide). Both structures appear to be similar in shape and dimensions to fossilised worm tubes that are commonly associated with hydrothermal systems (Ayupova *et al.*, 2017). Filamentous pyrite is morphologically similar to the sulphide filaments observed in Unit B material at Rona mound and elsewhere (i.e. ~3 micron diameter and up to 1-2 mm in length), but do not exhibit the iron oxide coatings observed elsewhere. In one area, a long sulphide filament is seen to be a nucleation site for subhedral pyrite growth into open pore space (Figure 96). Filaments of haematite are present adjacent to the sulphide grains indicative of bleaching by reduced fluids, but without complete remobilisation of the iron.

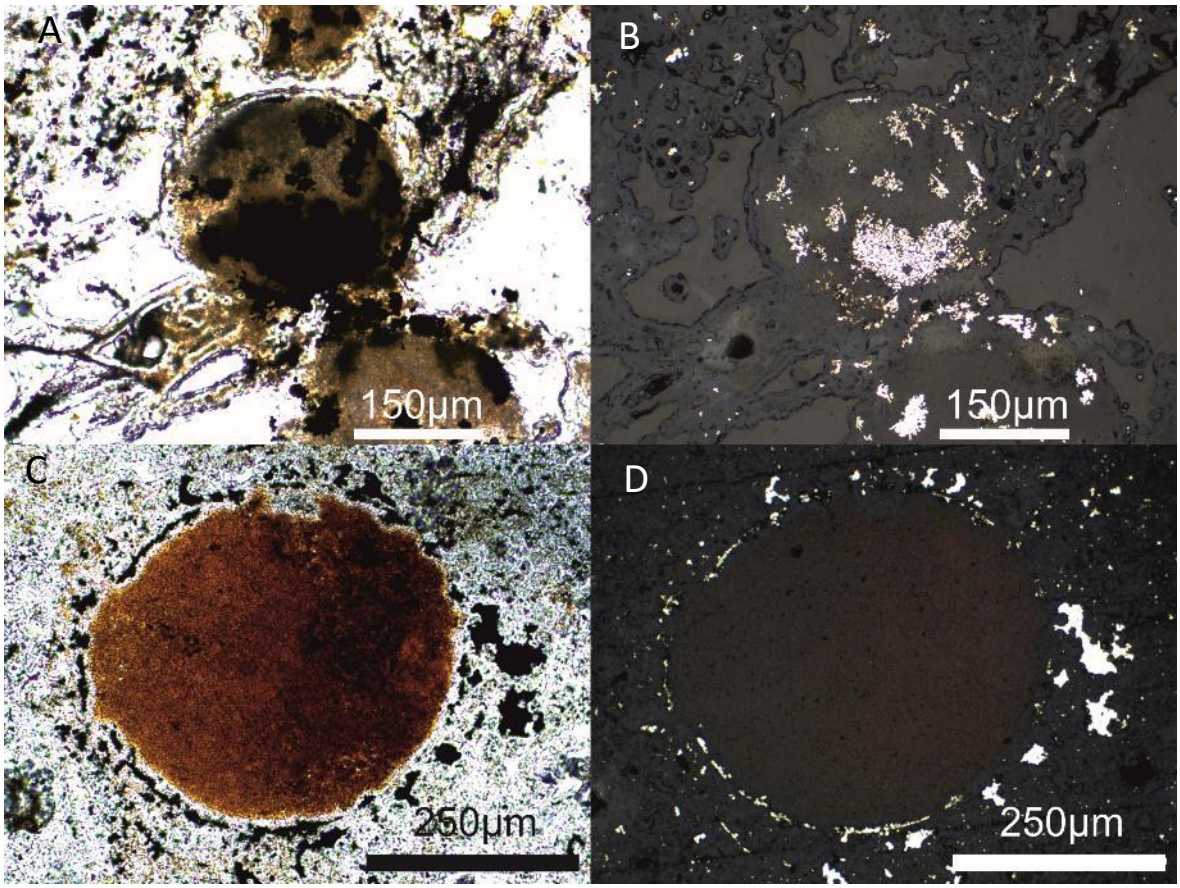

Figure 95: Circular sulphide features from Rona Mound. (A,B) Opal-CT or amorphous circular feature containing pyrite (A = TL-PPL, B = RL-PPL). (C,D) Circular ring of pyrite around a Si-Fe infilled features (C = TL-PPL, D = RL-PPL).

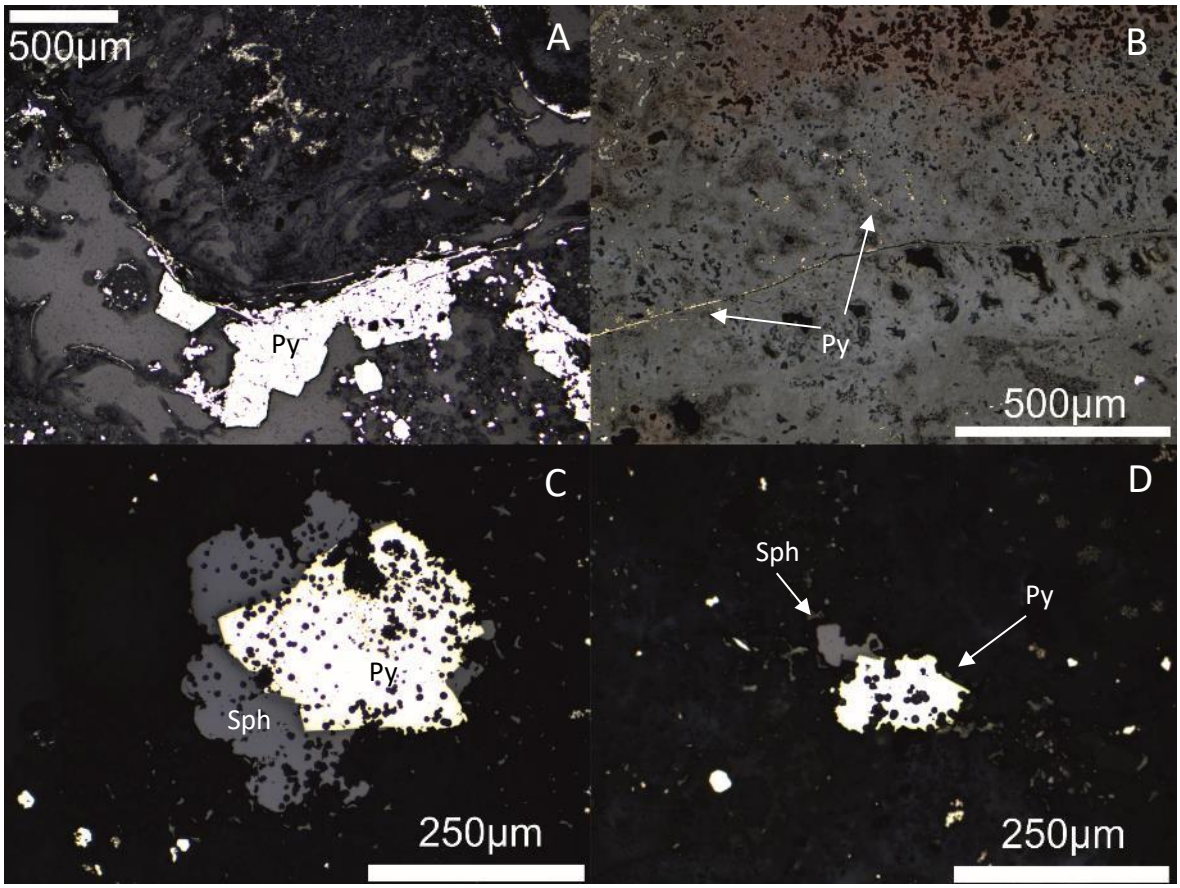

Figure 96: Filamentous pyrite and pyrite-sphalerite relationship at Rona Mound. (A) filamentous pyrite with subhedral pyrite nucleating off the filament into void space – RL-PPL. (B) Relict/trace pyrite filaments – RL-PPL. (C,D) Early subhedral pyrite overgrowing silica with sphalerite typically growing on pyrite grains RL-PPL.

5.5.2.2 Sphalerite

Sphalerite is the next most common sulphide at both Southern Mound and Rona Mound, and is often closely related to pyrite. At Southern Mound, sphalerite is either separate subhedral grains (~30-40 microns), intergrown with pyrite, or nucleating off existing pyrite grains (Figure 97). At Rona Mound, rare subhedral grains of sphalerite are present and often associated with areas of subhedral pyrite, or appear to have nucleated off existing pyrite grains (Figure 96C,D). Sphalerite also shows the same pitted and interstitial textures as pyrite, indicating that both sulphides have overgrown pre-existing silica.

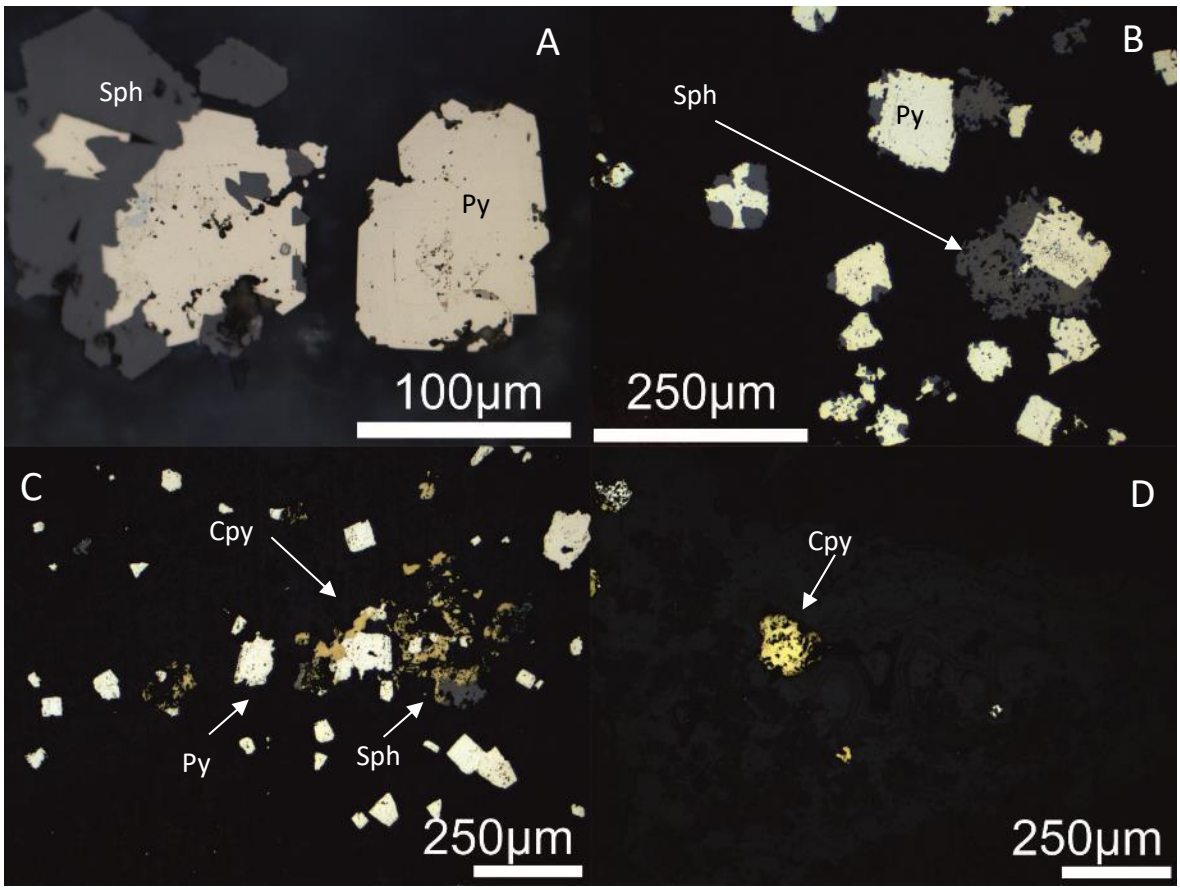

Figure 97: Pyrite-sphalerite, and pyrite-chalcopyrite associations in Unit C at Southern Mound. (A) 'Grubby' pyrite and overgrowth of sphalerite – RL-PPL. (B) Sphalerite nucleating on pyrite grains. (C) Subhedral to euhedral pyrite and interstitial anhedral chalcopyrite growth – RL-PPL. (D) rare interstitial subhedral chalcopyrite grains (RL-PPL).

5.5.2.3 Chalcopyrite

Chalcopyrite is observed as anhedral growths associated with pyrite and sphalerite grains in within millimeter scale 'grey sulphidic enclaves) 050RD/P12 at Southern Mound. In contrast, chalcopyrite grains in the deepest sample (050RD/P13) are subhedral and either individual (up to ~ 50 microns) or intergrown with pyrite (Figure 97C,D).

5.5.2.4 Summary of sulphide distribution and features

Sulphides in 050RD/P11 and P12 at Southern Mound are associated with iron oxide free-silica and often show iron oxide-free, or diminished iron oxide containing silica haloes (Figure 98). In 050RD/P13, the sulphides are interstitial, and have grown within void spaces between euhedral and subhedral quartz crystals. Small subhedral grains of sulphide (typically pyrite or rarely chalcopyrite) are present at crystal boundaries of multiple overgrown euhedral quartz generations, but there

appears to be no pattern to where they are distributed at crystal boundaries, or which silica generation they occur at/within.

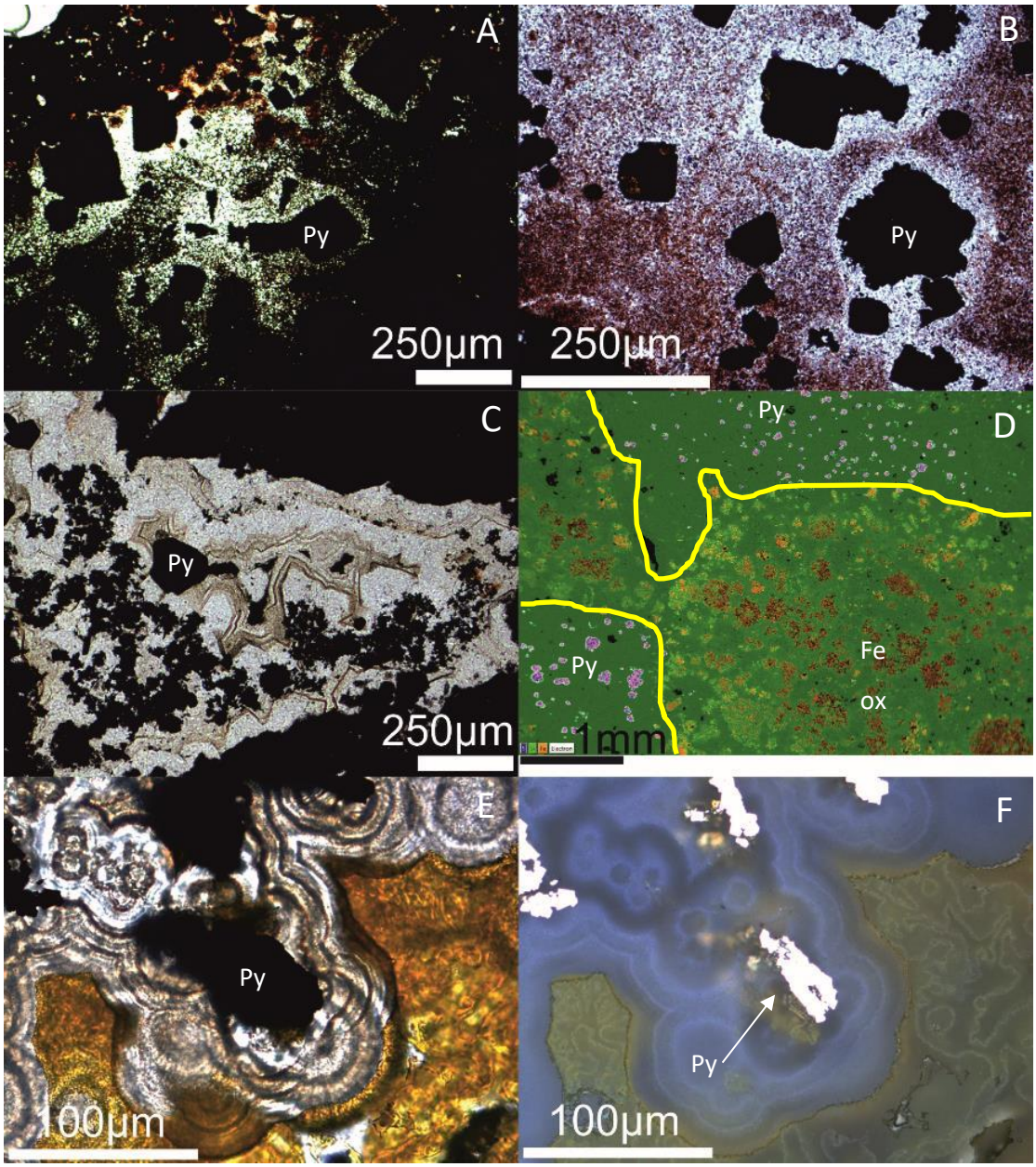

Figure 98: Clear delineation between areas of sulphide growth and areas of iron oxide and silica throughout Unit C at Southern Mound. (A,B) Iron oxide 'free' or poor haloes around subhedral pyrite grains – TL-PPL. (C) interstitial sulphide between drusy quartz growth – TL-PPL. (D) SEM EDS map of bleached grey silica zones. Reduced iron sulphide (pink) and oxidised iron (orange) within microcrystalline silica (green) can delineate zones. (E,F) Subhedral pyrite showing silica nucleation and concentric growth and clear areas of iron oxide free areas (E = TL-PPL, F = RL-PPL).

Evidence from all three Unit C samples shows contrasting relationships between silicification and sulphidation. Sulphides appear to be synchronous with, or post-date, silicification. The inclusion of silica grains within sulphide growth likely implies the co-precipitation or overgrowth of existing silica. However, concentric growth lines indicate that central sulphide grains acted as nucleation sites for silica growth, implying early sulphide formation.

5.5.3 Filaments and tubes

Silicified iron oxides filaments are not observed within Unit C material at Southern Mound. Certain areas of Si-Fe material show possible filamentous textures, but they have been partially obscured and bleached resulting in little to no evidence of the original iron oxide filaments.

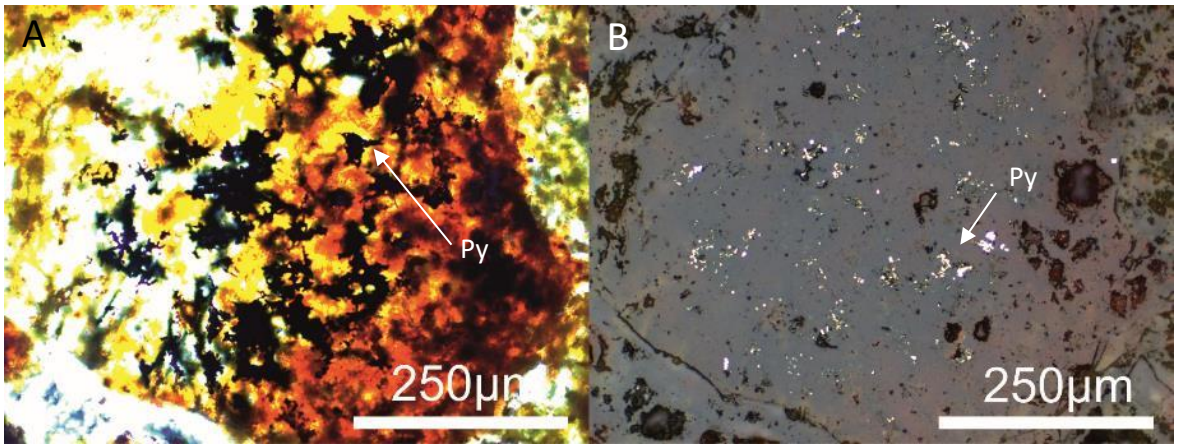

Figure 99: Sulphide filaments, potentially biological in origin from Southern Mound (A = TL-PPL, B = RL-PPL).

Possible sulphide filaments are observed within an amorphous Si-Fe clast in one sample of the shallowest Unit C material (050RD/P11). These filaments are observed in clusters and are typically ~ 3 microns in diameter, with one area potentially exhibiting twisted helical strands (Figure 99).

A large iron oxide sheath approximately 50 microns in diameter composed of a lattice of iron oxyhydroxides, with a central void space was observed within 050RD/P11 (Figure 100). Three sections of potentially the same sheath are observed with a circular cross section and two oblique oval cross sections. The whole sheath is cemented by silica, including the central void, and several small unsilicified voids remain within the centre of each section of filament.

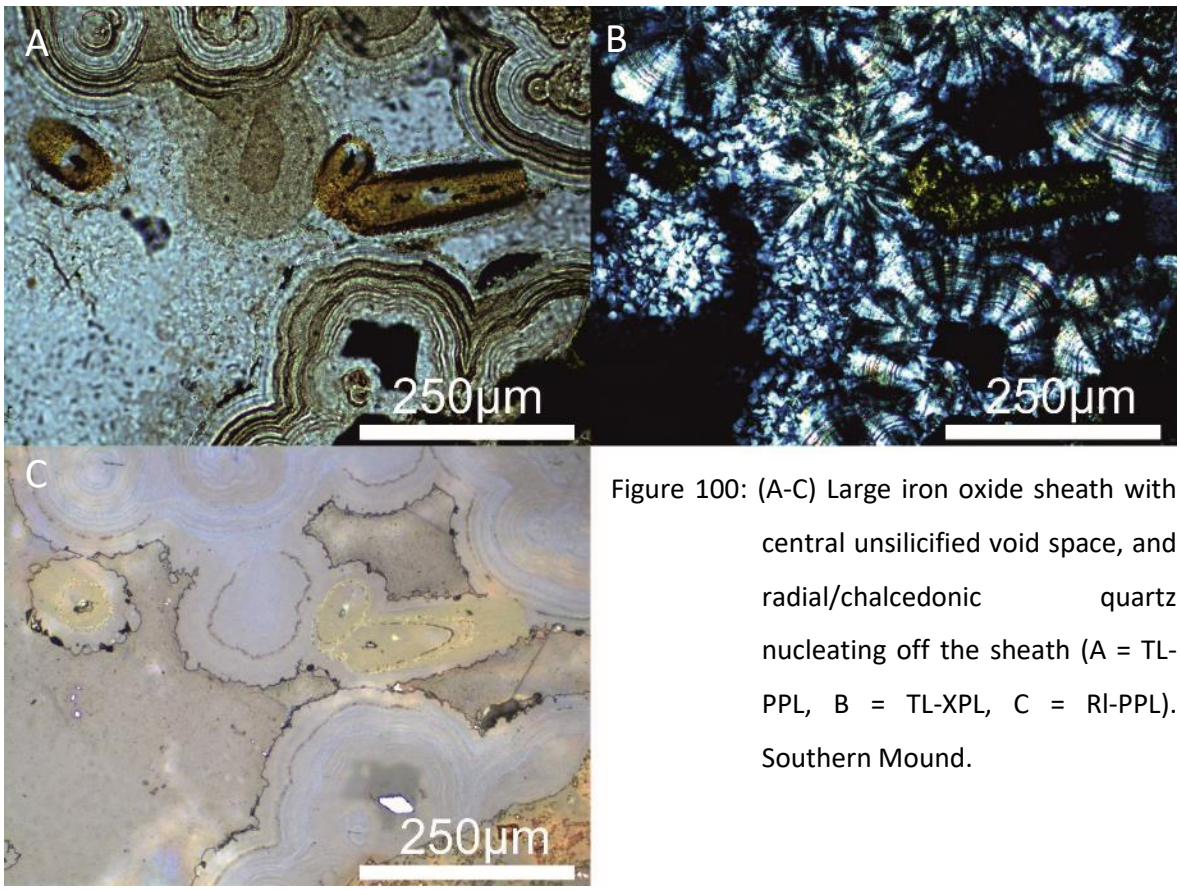

Figure 100: (A-C) Large iron oxide sheath with central unsilicified void space, and radial/chalcedonic quartz nucleating off the sheath (A = TL-PPL, B = TL-XPL, C = Rl-PPL). Southern Mound.

These two examples potentially provide the best evidence of biological involvement with the formation of the Si-Fe cap. The large iron oxide sheath observed in 050RD/P11 (Unit C – Southern Mound) exhibits fine nodules of iron oxyhydroxide material in which would be a difficult feature to replicate by abiological precipitation (García Ruiz *et al.*, 2002).

In contrast to Southern Mound, Rona Mound filamentous textures include clusters of short and randomly orientated iron oxide (and sulphide) filaments, long individual filaments, and complex intergrowths of randomly orientated filaments. Clusters of short filaments, typically of haematite, are ~ 3 to 5 microns in diameter. Where bleaching has occurred within areas of filamentous material, iron has been remobilised with residual structures preserved by silica (Figure 101).

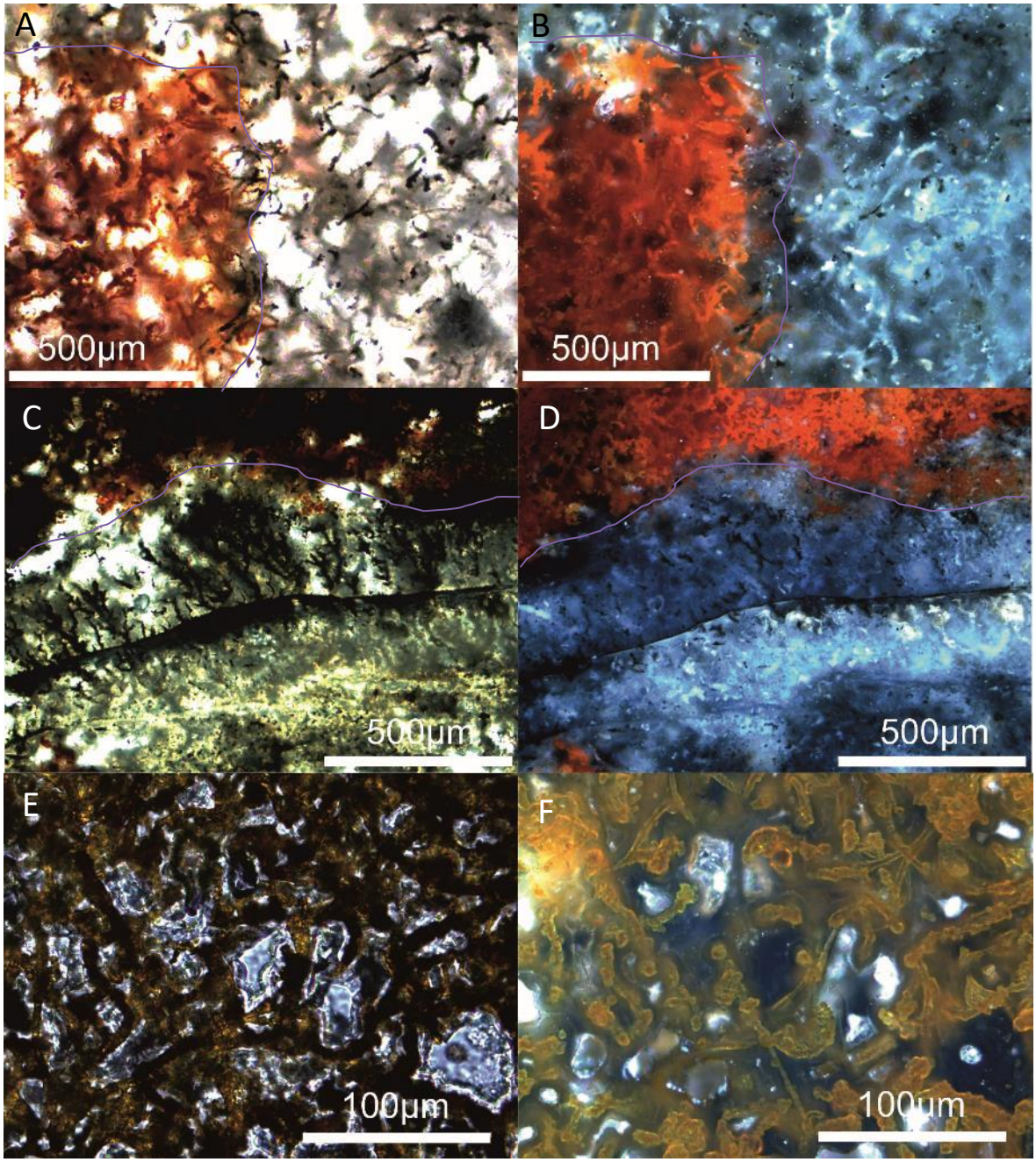

Figure 101: Filamentous textures in Rona Mound Unit C samples. Purple lines designate reduced/oxidised iron boundaries. (A,B) Transition from 'bleached' to iron oxide dominated patch with individual filaments visible across the transition (A = TL-PPL, B = RL-XPL). (C,D) Single long 'filament' with branching dendritic like growth nucleating off one surface (C = TL-PPL, D = RL-XPL). (E,F) Randomly distributed silicified overlapping iron oxide filaments (E = TL-PPL, F = RL-XPL).

5.5.4 Dendrites

Clasts of dendritic Si-Fe, similar to those observed in Unit A material in Southern Mound, are prevalent in Unit C material at Rona Mound, but no dendritic growth textures are observed throughout Unit C material at Southern Mound.

Discrete Si-Fe clasts exhibiting dendritic growth patterns, often with one preferred growth orientation, or radial growth from a central area, are distributed throughout Unit C (Figure 102). There is no obvious shared preferred orientation of dendritic growth at a thin section scale, with clasts randomly orientated throughout. Similar to Si-Fe filamentous areas, grey patches within dendritic growth structures are the result of localised reduction of iron and its remobilisation, leaving behind the residual and filamentous silica structure.

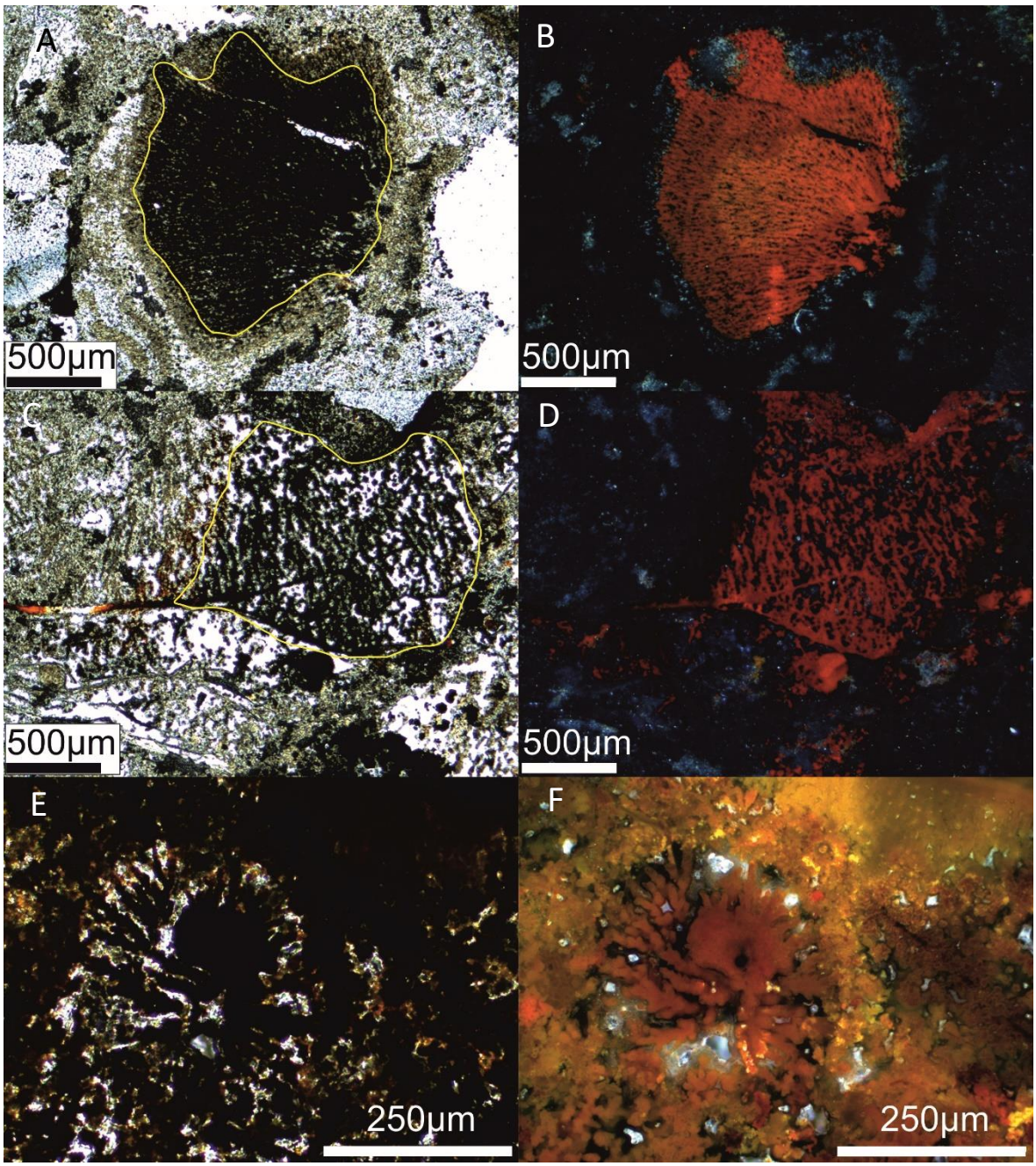

Figure 102: Three examples of dendritic clasts from Unit C material at Rona Mound. Yellow lines delineate reduced and oxidised iron areas. (A,B) Partially reduced clast of dendritic iron oxides within an opal-CT dominated area (A = TL-PPL, B = RL-XPL). (C-D) Variably reduced area of dendritic growth textures with an elongate perpendicular filament (C = TL-PPL, D = RL-XPL). (E,F) Dendritic growth in a radial pattern with no preferred growth direction (E = TL-PPL, F = RL-XPL).

5.5.5 Microfractures

Angular jigsaw brecciation, one of the defining textures of Unit B material at Southern Mound and the MIR Zone, is rare but present within Unit C material. Fractures result in angular clasts and are often infilled with quartz. One area in 050RD/P12 shows the typical jigsaw brecciation, but unusually the fractures are not infilled within quartz (Figure 103).

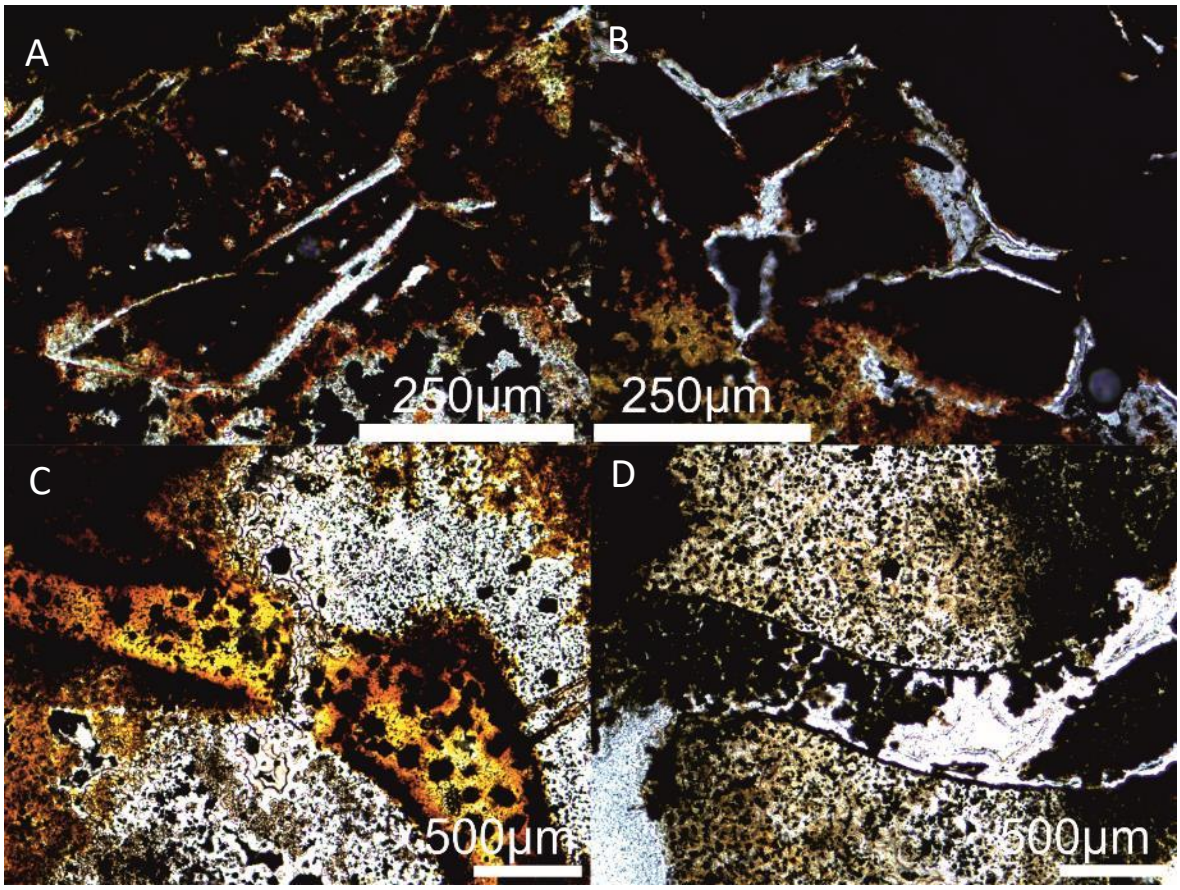

Figure 103: Desiccation cracks and fractures in Unit C material from Southern Mound. (A,B) Angular clasts with silica 'veins' similar to jigsaw brecciation in Unit B – TL-PPL. (C,D) 'Late-stage'- brecciation of early silica or Si-Fe clasts, infilled by more chalcedonic/radial quartz growth textures (TL-PPL).

Interconnected cracks visible within residual Si-Fe clasts are present at Southern Mound (050RD/P11 and 050RD/P13), and in one sample at Rona Mound (057RD/P11). At Southern Mound, these cracks are similar to those observed within clasts of Unit A material, cross cut the residual clasts, potentially indicative of desiccation of amorphous silica or opal. The cracks are infilled with quartz, and are similar to Unit B material, showing radial growth patterns of quartz after opal-CT. At Rona Mound, microfractures with 120° triple junctions resemble desiccation cracks and are present within Si-Fe. They are similar to, but not as common, as those in Unit A. Where present,

the fractured clasts are coated with a ~10 micron thick silica layer. Localised areas of iron oxide mobilisation are rarely observed at the edge of intraclast microfractures (Figure 104).

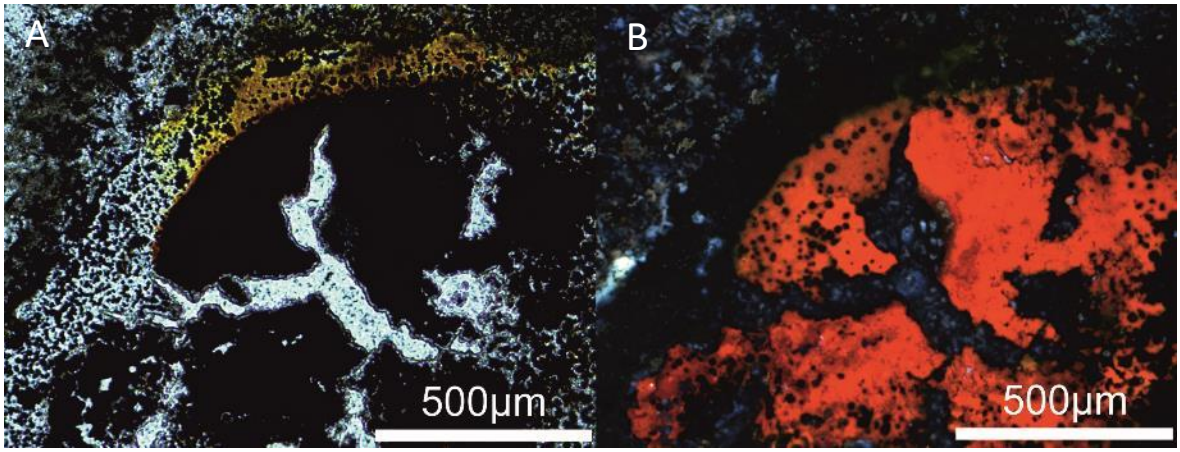

Figure 104: Preserved ~120° cracks within a Si-Fe clast in Unit C from Rona Mound (A = TL-PPL, B = RL-XPL)

5.6 Summary

Based upon the similarities and comparability in mineralogy and wide range of textures in both the hydrothermal sediments (Units M3 and M4), and all three Units of the Si-Fe cap rock (Units A-C) presented through Sections 5.2 to 5.5, it seems clear that the protolith for the Si-Fe capping materials is the hydrothermal sediments, therefore understanding how these sediments have formed, sheds light on the origins of the Si-Fe cap.

5.6.1 Origins of Unit M3 and M4

Textural and mineralogical assessment of the two hydrothermal sediment Units (M3 and M4) show distinct differences between them. Unit M3 is a goethite- and amorphous fraction-dominated sediment with preserved laminated clasts, dendritic and colloform growth textures, localised enclaves of filaments, and evidence of clasts of Si-Fe material. In contrast, Unit M4 sediment is a hematite- or amorphous fraction dominated- fine-grained sediment. It is texturally homogenous textures, shows little to no evidence of clast-like sedimentary features like Unit M3. Although quartz was identified by XRD it was not present as Si-Fe clasts.

Laminated clasts, dendritic and colloform textures observed in Unit M3 are disrupted and are not continuous throughout the Unit, implying that they have formed in a sedimentary environment, but have also been preserved before being brecciated and accumulated. This implies that Unit M3 has a contribution from sedimentary surface processes, and products of hydrothermal flow (i.e.

dendrites). Limited fractures are observed within clasts of Si-Fe material that are interpreted to be desiccation cracks, a common process associated with mineral dehydration (i.e. amorphous silica → opal-CT, or ferrihydrite → goethite → haematite (See Section 2.2). The association of microfractures with clasts of Si-Fe material, but not with silica free iron oxide material implies that this process may be a result of silica maturation, rather than iron oxide dehydration.

In general, Unit M4 sediments do not show these features, and the fine grained nature implies a colloidal formation mechanism, i.e. direct precipitation from a hydrothermal fluid, in contrast to the surface accumulatory processes interpreted for Unit M3.

5.6.2 Hydrothermal sediments as a protolith of the Si-Fe cap rocks

Based on the observed stratigraphy from Southern Mound where hydrothermal sediments and all three Si-Fe cap rock Units were recovered, five of the six occurrences of the Si-Fe cap Units share mineralogy and textural similarities with either Unit M3 or Unit M4 (Table 52).

Table 52: Interpreted protolith 'type' for the respective Si-Fe cap Units at all three mounds

	Southern Mound	**Rona Mound**	**MIR Zone**
Unit A	M3 – goethite rich	-	-
Unit B	M4 – haematite rich	N/A	M4 – haematite rich
Unit C	M4 – haematite rich	M3 – goethite rich	-

5.6.2.1 Southern Mound and the MIR Zone

Unit M3, dominated by goethite and/or amorphous fraction, contains Si-Fe clasts displaying dendritic and colloform textures. Unit A is a mixed goethite and haematite, quartz and opal-CT assemblage which displays a clast dominated breccia texture. This brecciated texture and increased silica content of Unit A is interpreted to be a product of silicification of Unit M3 sediment. Silicification has resulted in the preservation of existing sedimentary derived features and clasts that are observed in both the M3 sediment, with silica appearing to be homogenously distributed throughout the sample. SEM images, XRD and FTIR analysis determined that the silica is a mixed quartz and opal-CT and the quartz fraction is distributed throughout the 'matrix' of the sample. This mixed opal-CT and quartz assemblage, the homogenous distribution of silica, and increase in 'jasper' type textures, implies that Unit A is Unit M3 sediment that was impregnated by a silica rich gel. Subsequent maturation of the gel enabled dehydration and recrystallisation from amorphous silica through to a mixed opal-CT-quartz assemblage. During this dehydration process further desiccation can occur resulting in further fracturing, potentially increasing the brecciation.

Unit B from Southern Mound and the MIR Zone is considered to be a 'jasper', which is defined as cryptocrystalline silica stained by iron oxide, the cause of the characteristic 'blood red' colouration. The homogenous distribution of silica and iron oxide throughout the sample, can be attributed to the electrostatic attraction between negatively charged silica particles and positively charged iron oxides/oxyhydroxides within a silica gel (Grenne and Slack, 2003a, 2005). Assuming a similar silicification process as Unit M3-Unit A the lack of existing Si-Fe clasts, and the fine grained nature of Unit M4 would promote the formation of a typical 'jasper' material. This observation is further strengthened by the fact that Unit M4 sediments directly overlie Unit B material at Southern Mound, with large void spaces in the hard rock material infilled with Unit M4 sediment.

Unit C material at Southern Mound shares more similarities with Unit B material than Unit A material, again implying that it is a 'jasper'. In general few 'clasts' are observed and the iron oxide fraction is typically haematite, not goethite. However, Unit C has been altered, likely by a moderate to high temperature, sulphur rich, reduced fluid, enabling mobilisation of iron and precipitation of moderate to high temperature sulphides.

Based on the assumption that Unit A is silicified Unit M3, and Units B and C are silicified Unit M4, then the distribution of the Si-Fe cap material across a SMS deposit would be controlled by the distribution of hydrothermal sediments, and the level within the sedimentary sequence silicification reaches. The variable silicification across Southern Mound (opal-CT and quartz in Unit A, quartz only in Units B and C), and evidence of silica recrystallisation textures in Units B and C imply either stratigraphically separated silica generation or a secondary event which has altered the silica morphology. The presence of sulphides in Unit C supports the idea that a second event has occurred, bringing in high temperature sulphides.

This would explain the variable distribution of the three Si-Fe cap rock Units across Southern Mound, where different boreholes within an ~ 10 m^2 area, had different Si-Fe cap stratigraphy Figure 40).

5.6.2.2 Rona Mound

In contrast to Si-Fe cap rocks from Southern Mound and the MIR Zone, Unit B and Unit C samples from Rona mound, do not quite fit with the same interpreted silicification regime. Texturally Unit B from Rona Mound shares characteristics with the other Si-Fe material, but no other Unit is dominated by dendritic or filamentous textures. Similarly, neither hydrothermal sediment is dominated by the same filamentous and dendritic textures.

Unit C from Rona Mound shares more textural characteristics with Unit M3 sediment, and Unit A from the Si-Fe cap than Unit M4 or other Si-Fe cap Units. Clasts of Si-Fe material which exhibit

dendritic and colloform textures observed in Unit C at Rona are not observed in the theoretically equivalent Unit C samples at Southern Mound.

Silica at Rona Mound is also different to the majority of other Si-Fe cap rock samples. Only opal-CT is identified in both Units B and C, quartz is < 1 wt% of the sample, further drawing comparison with Unit A, the only other Si-Fe cap Unit which contains opal-CT. This implies that Unit C material at Rona Mound could have been formed from a Unit M3 sediment, rather than an M4 sediment.

5.6.3 Distribution of silica across the three Mounds

As summarised in Section 2.2.4, ratios of silica polymorphs can indicate a degree of maturity of silica. Amorphous silica and opal-CT represent immature (hydrous) polymorphs, whereas quartz represents the most mature, and stable silica polymorph. Silica polymorph distribution is summarised in Table 53. Unit B and C from Southern Mound, and Unit B from the MIR Zone all only contain quartz, the most mature silica polymorph. Unit A at Southern Mound has a mixed opal-CT and quartz assemblage, implying that it is more immature than other Si-Fe cap samples at Southern Mound. In contrast, only opal-CT (and potentially amorphous silica), were observed at Rona Mound, showing that the silica assemblage at Rona Mound is the most immature of all Si-Fe cap samples.

Table 53: Distribution of silica polymorphs throughout Units A-C across Southern Mound, Rona Mound, and the MIR Zone.

	Southern Mound	**Rona Mound**	**MIR Zone**
Unit A	Opal-CT and Quartz	-	-
Unit B	Quartz	Opal-CT (and amorphous?)	Quartz
Unit C	Quartz	Opal-CT (and amorphous?)	-

5.6.4 Implications for a paragenesis

The combined observations of the physical and mineralogy characteristics of the Si-Fe cap rock show that there are some general processes that have caused the formation of the Si-Fe cap, most significantly, silicification, and to a lesser degree, sulphidation (See Figure 105).

Based on the evidence presented in this Chapter, Units A-C at Southern Mound, and Unit B at the MIR Zone, can be explained as the silicification of hydrothermal sediments. Therefore, in general, iron oxide minerals are interpreted to have formed pre- or syn-silicification throughout the deposits. The Si-Fe cap at Rona Mound is interpreted to have formed in a similar way, by

silicification of existing iron oxide dominated material, however the sediment material appears to have been different to Southern Mound.

Although physical characterisation enables a good understanding of the processes that are interpreted to have formed the Si-Fe cap, a range of questions remain about the geochemical signatures of these Si-Fe cap rocks, (i.e. do they have a hydrothermal signature?) and what the physicochemical properties of the interpreted fluids were that has formed this cap. To address these questions, a range of geochemical analysis has been undertaken on the Si-Fe cap rock samples, and used in conjunction with geochemical data of the hydrothermal sediments (Unit M3 and M4) to try to constrain some parameters of the silicification process.

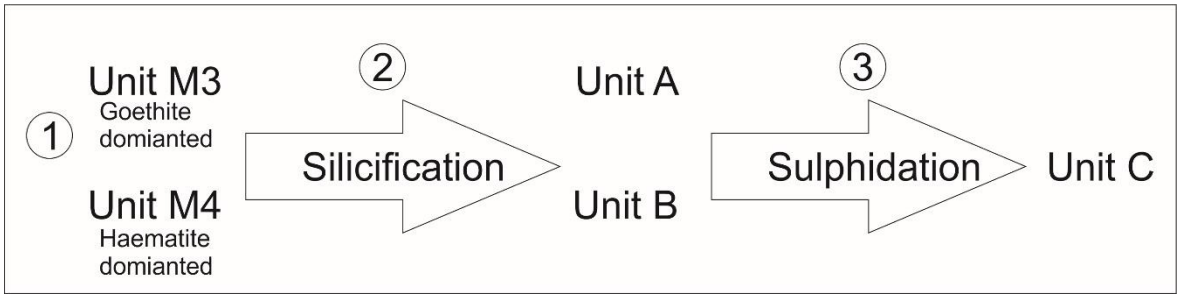

Figure 105: Generalised interpreted formation paragenesis from textural features. Step 1: Sediment accumulation, predominantly iron oxides/oxyhydroxides with minor localised silicification, forms Units M3 and M4. Step 2: Major silicification events. Evidence for at least one event to form Unit A, and at least two to form Unit B. Step 3: Sulphidation of Unit A or Unit B samples forms Unit C material.

Chapter 6 Geochemical Characterisation

6.1 Introduction

In this chapter, I explore the origins of the Si-Fe material capping the SMS ore body by geochemical characterisation of the different phases that constitute the material. Major elements are dominated by iron and silica, but the behaviour of other base metals yields insights into the processes of metal mobilisation, sulphide crystallisation, and fluid ingress. Laser ablation ICP-MS analyses of discrete mineral phases is used to compare with bulk data to help understand the elemental mobilisation during the formation of the different Si-Fe units. Hydrothermal fluids and seawater interactions are traced using rare-earth elements and their normalised relative values. Paleo-temperatures for sulphidation events are calculated from sphalerite geothermometry and, for the siliceous phases, from $\delta^{18}O$ isotopes. This chapter focuses on the presentation and analysis of the whole rock geochemistry of the Si-Fe cap, with comparison made to the interpreted hydrothermal sediment protoliths to understand the geochemical changes that have occurred during silicification.

Thirty Si-Fe whole-rock samples were processed at the University of Southampton for analysis of major and trace elements. A suite of major elements were obtained by X-Ray Fluorescence (XRF) analysis, and a suite of traces were obtained by Inductively coupled plasma mass spectrometry (ICP-MS). Total carbon (TC), total organic carbon (TOC), and total sulphur were analysed using a LECO CS225 elemental analyser at the University of Aberdeen. TC and total sulphur were obtained from 'carbonised' bulk sample powder, TOC was obtained by acid leached 'decarbonised' samples. Thirteen iron oxyhydroxide/oxide rich sediments recovered from Southern Mound were analysed by Dutrieux (2019) using a combination of ICP-OES, and ICP-MS. See Methodologies (Chapter 4) for further information.

For the Si-Fe cap samples, the accuracy and precision of the major and trace elements (including REEs) generally show 'excellent' to 'good' accuracy and precision across all three analytical techniques. The main exception is for accuracy of some trace elements measured against JR-2 (See methodologies chapter). Care and consideration have been given to the interpretation of data where accuracy or precision are poor. Table 54 and Table 55 summarises the elemental oxide, element, or value analysed by each technique that is used or discussed in this thesis.

Table 54: List of elemental oxides and elements and the analytical method used for the Si-Fe cap samples

XRF		ICP-MS		LECO	
Majors	**Trace**	**Majors**	**Trace**	**Majors**	**Other**
SiO_2, Fe_2O_{3T}, MgO, CaO, K_2O, Na_2O, P_2O_5.	Zn	Al_2O_3, TiO_2, MnO	V, Cr, Co, Ni, Cu, Sr, Mo, Cd, Ba, Pb, Th, U REEs: La, Ce, Pr, Nd, Sm, Eu, Gd, Tb, Dy, Ho, Er, Tm, Yb, Lu, Hf.	SO_3	TC, TOC

Table 55: Analytical methods used to obtain elemental data from the hydrothermal sediments (Dutrieux, 2019)

ICP-OES		ICP-MS	
Majors*	**Trace**	**Majors***	**Trace**
Al_2O_3, CaO, Fe_2O_{3T}, K_2O, MgO, MnO, Na_2O	Sr, V	TiO_2	Co, Cu, Ni, Zn, Ag, Ba, U, Pb
* = elemental oxides calculated from element composition			

6.2 Results - major elements and covariation

One of the objectives of the geochemical analyses is to identify common processes involved in the formation and evolution of the different Si-Fe units encountered at the TAGHF. Implicit in this comparison is the statistical validity of covariance between different elements and their presence in different lithological units. Two factors are considered: detection limits and the impact of concentration, accuracy and precision, and the reliability of definitions of correlations.

Al_2O_3 and TiO_2 were not detected above the detection limits of the XRF. Accuracy (between 3% - 10%) and precision (< 3%) for manganese measured by ICP-MS was considered better than XRF (between 2.5% and 37.7% accuracy, and 13.0% for precision). Therefore Al_2O_3, TiO_2, and MnO oxide concentrations were calculated from elemental ICP-MS data, and have been presented instead of the XRF. Elemental sulphur obtained from a LECO elemental analyser has been converted and

presented as SO_3. When considering total concentrations (i.e. Section 6.2), XRF data and SO_3 from LECO have been normalised to 100%. When comparing trace elements to major elements, non-normalised values have been used.

Comparison between lithological units and the behaviour of pairs of elements is limited by the low numbers of samples representative of the lithological Units: sample populations for the Units are low (typically n≤4), and even the total population is low (n=27), reducing the validity of simple correlation coefficients and least squared regressions. Instead, elemental comparisons are made using the Pearson correlation coefficient (ρ). This is used to compare elemental behaviours within the whole sample suite, or elemental concentrations between Units. The calculated ρ value is used to imply co-variance rather than a true proxy for correlation between elements. It should be noted that a correlation, or co-variance, does not automatically imply a causation. Rather, it is used here to identify potential underlying processes.

Raw whole rock geochemical data can be found in Appendix A.

6.2.1 SiO_2 and Fe_2O_{3T}, and SO_3

As anticipated from the dominant mineralogy, SiO_2 and $Fe_2O_{3(Total)}$ are the major components of the Si-Fe material found at all three mounds, and for all samples within all three Si-Fe Units, where (SiO_2+$Fe_2O_{3(Total)}$) >87.1 wt% (when XRF and LECO data is normalised to 100%).

In Southern Mound (SiO_2+$Fe_2O_{3\ (Total)}$) >98.6 wt% in Unit A, >99.4 wt% in Unit B, and >96.0 wt% in Unit C. In Rona Mound (SiO_2+$Fe_2O_{3(Total)}$) > 98.3 wt% in Unit B, and > 87.1 wt% in Unit C. In MIR Zone, (SiO_2+$Fe_2O_{3(Total)}$) in Unit B samples is all ≥ 99.1 wt%.

The lower (SiO_2+$Fe_2O_{3(Total)}$) values in Unit C material at both Southern and Rona mound can be explained by the elevated SO_3 contribution (ranging from ~ 2.4 to 12 wt%). (SiO_2+$Fe_2O_{3(Total)}$+SO_3) >99.3 wt% in all Unit C samples. SO_3 is typically <0.3 wt% throughout Unit A and B, with the exception of 057RD/P2 at 1.12 wt%, and 076RD/P8 at 0.61 wt%.

SiO_2 shows a strong negative covariance with Fe_2O_3 throughout the Si-Fe material (ρ =-0.97) (Figure 106), supporting the observation that the Si-Fe Units are predominantly a binary system. In comparison to the overlying hydrothermal sediments, the Si/Fe ratio is much higher in the Si-Fe cap (Table 56). Silica content of the Unit M3 and M4 sediments was not analysed, but are estimated based upon the difference between major element oxides (converted from ICP-MS and ICP-OES) when normalised to 100 wt%. Comparative Si-Fe atios are summarised in Table 56.

Table 56: Si:Fe ratios for hydrothermal sediments vs Si-Fe cap Units

	Hydrothermal Sediments		**Si-Fe cap**		
	Unit M3 (n=12)	**Unit M4 (n=3)**	**Unit A (n=4)**	**Unit B (n=21)**	**Unit C (n=5)**
Mean	0.78	0.42	2.19	8.46	11.60
Max	1.37	0.60	2.97	19.80	17.04
Min	0.32	0.28	1.69	2.04	4.67

SO_3 shows little to moderate positive covariance with SiO_2 and negative covariance with Fe_2O_{3T} in Unit A (ρ = 0.62 and -0.65 respectively), is substantially weaker in Unit B (ρ = 0.25 and -0.28 respectively), but very strong in Unit C where the relationships are reversed (ρ =-0.99 and 0.97 respectively). Strong positive covariance between Fe_2O_{3T} and SO_3 in Unit C samples can be explained by the occurrence of pyrite/marcasite (FeS) or iron bearing sulphides chalcopyrite (CuFeS) and/or sphalerite ((Zn,Fe)S). Pyrite has also been identified in Unit B samples (057RD/P2 from Rona Mound, and 076RD/P8 from the MIR Zone), both samples recording elevated SO_3 (in comparison to the rest of Unit B material across all mounds) (Figure 106).

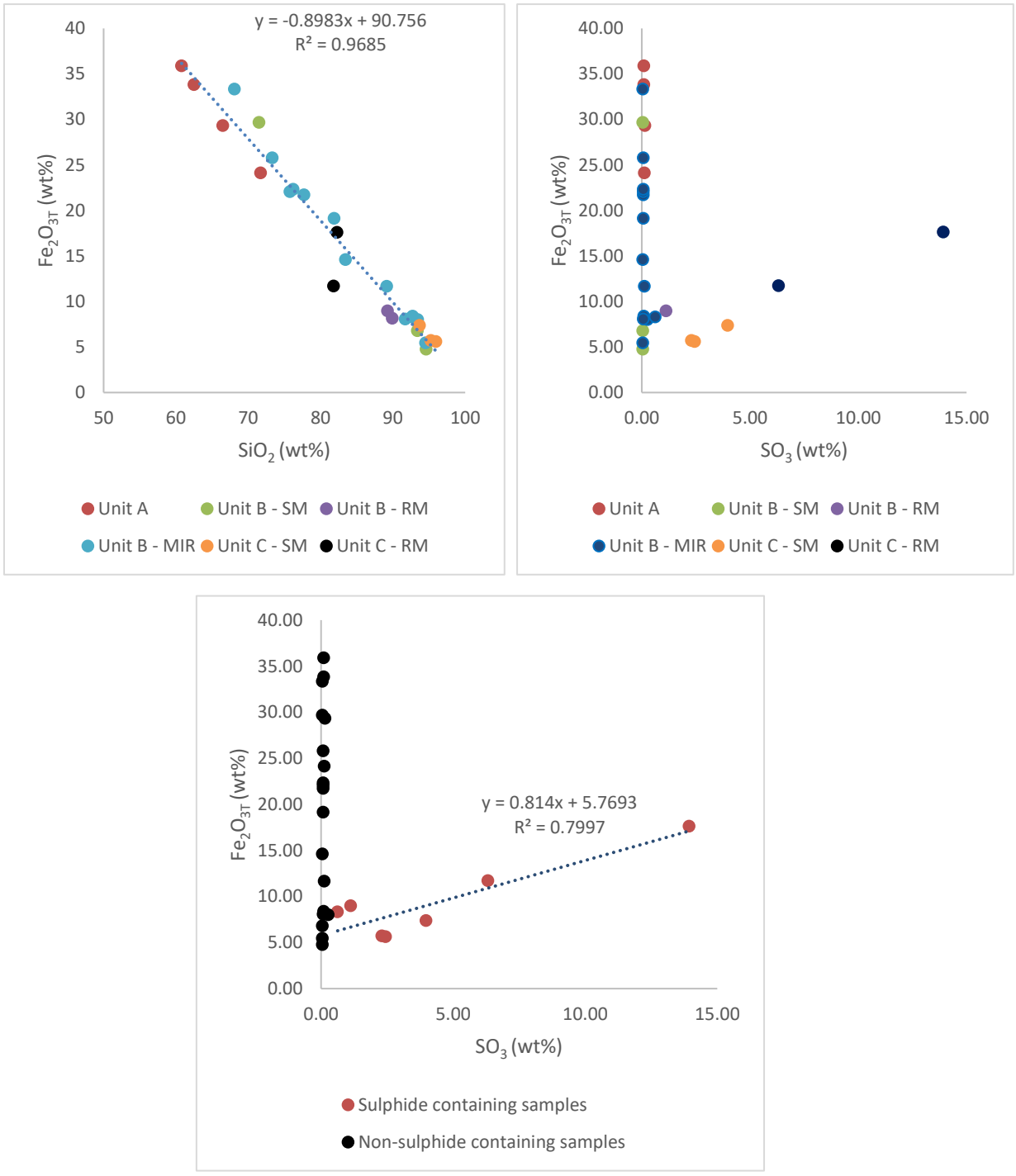

Figure 106: Bivariate plots of SiO_2 vs Fe_2O_{3T} and SO_3 vs Fe_2O_{3T} (two plots). Strong negative correlation between SiO_2 and Fe_2O_{3T}, and no correlation between SO_3 and Fe_2O_{3T} except in samples

The fact that covariance between $Fe_2O_{3(Total)}$ and SO_3 is negative in Unit A and non-existent in B material indicates that the low concentrations of sulphur in either unit (< 0.11 wt%) is unlikely to be related to sulphide minerals as a positive covariance between Fe_2O_{3T} and SO_3 would be observed (as in Unit C samples) (Figure 107).

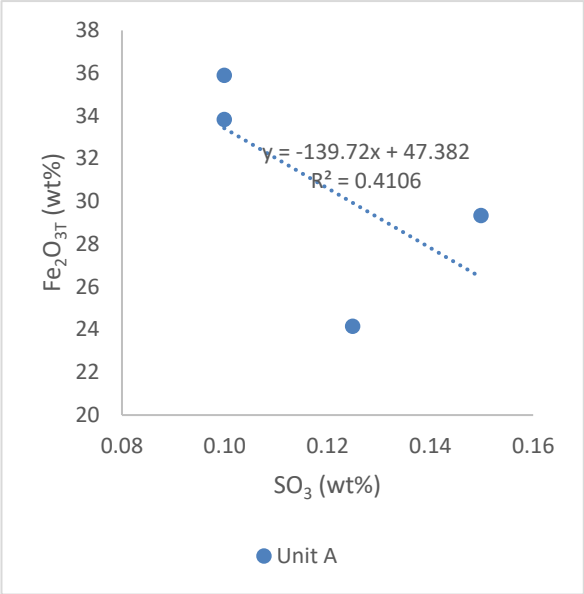

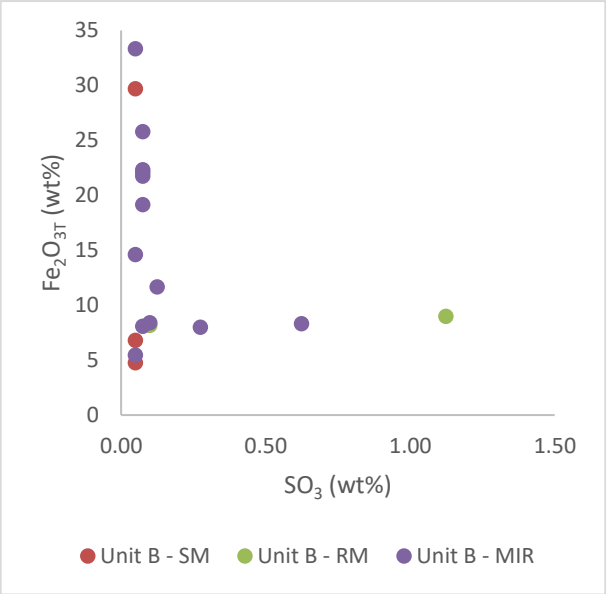

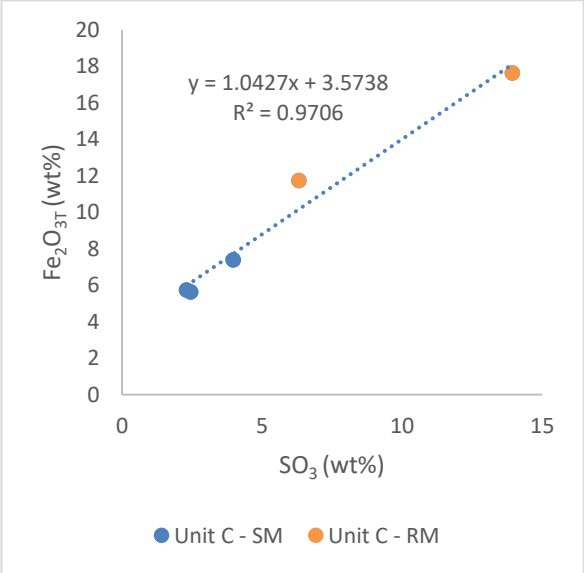

Figure 107: Bivariate plots of SO3 vs Fe2O3 for Si-Fe cap Units A, B, and C, showing the sulphide related trends

6.2.2 Other major elements, TC, and TOC

Total concentrations of the other major elements (i.e. Al_2O_3+TiO_2+MnO+MgO+CaO+K_2O+Na_2O+P_2O_5) are typically <1% by weight throughout the Si-Fe cap. Out of these, only Na_2O (0.02 – 0.83 wt%) was detected at concentrations >0.2 wt%. Concentrations of TC were not recorded greater than 0.04 wt%, with TOC not recorded greater than 0.02 wt%.

Elevated concentrations of Na_2O could be a result of residual seawater (as pore water) which was not efficiently flushed from samples during washing and drying before analysis. Low, but measurable CaO concentrations (0.02 – 0.19 wt%), low TC (< 0.04 wt%), and the lack of covariance of CaO with SO_3 (ρ = 0.25) throughout the Si-Fe cap indicates the general lack of any pelagic

carbonate sediment, gypsum ($CaSO_4.2H_2O$), or anhydrite ($CaSO_4$) commonly associated with SMS deposits (Figure 108).

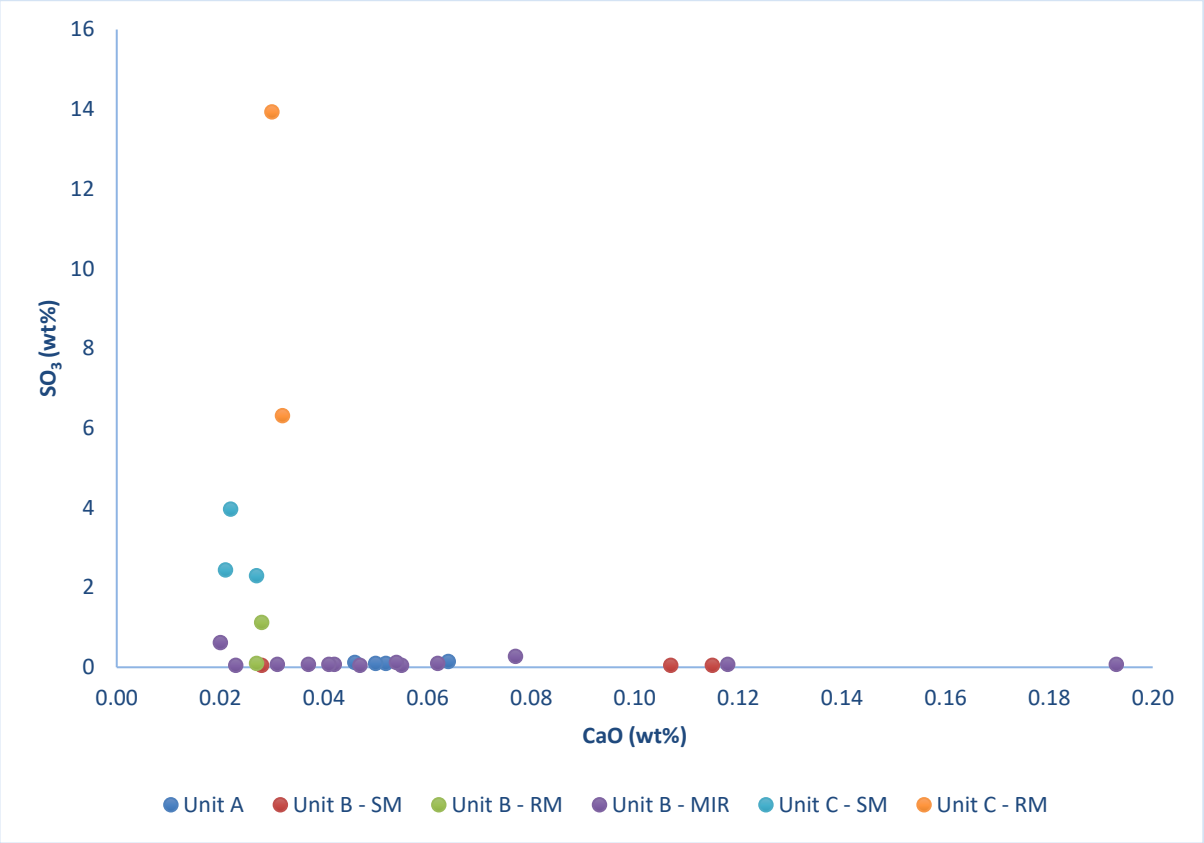

Figure 108: Bivariate CaO vs SO_3 plot for all Si-Fe cap samples

Broadly comparable concentrations of CaO and P_2O_5 (0.01 – 0.17 wt%), could be explained by trace amounts of apatite grains throughout the Si-Fe cap, which have been observed in SEM EDS maps. The CaO:P_2O_5 ratio in apatite is ~1:1.3; ten samples analysed show a similar ratio (~1.19 – 1.52) (Figure 109), implying that apatite may control the CaO and P_2O_5 contents in these samples. Apatite grains were identified by SEM EDS mapping in two thin sections of Unit B material from the MIR Zone. The samples which had the similar CaO:P_2O_5 ratios were predominantly Unit B samples from the MIR Zone (n=6) and Southern Mound (n=3), with the exception of one Unit C sample (050RD/P12) from Southern Mound. Both samples where apatite grains were identified fell on the 1:1.3 CaO:P_2O_5 trend line (Figure 109). This does not discount the presence of apatite from samples with high CaO:P_2O_5 ratios, but implies CaO and/or P_2O_5 concentrations are controlled by apatite alone.

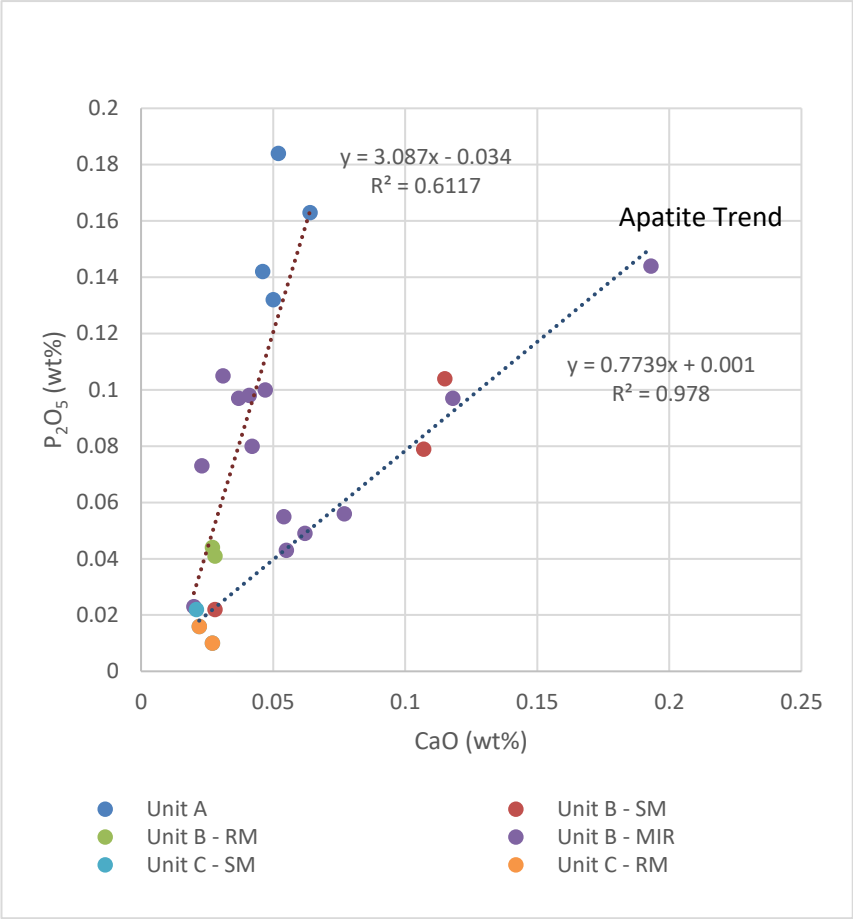

Figure 109: Bivariate plot of CaO vs P_2O_5 for all Si-Fe cap samples. Apatite trend (CaO:P_2O_5 ~ 1.3, R = 0.978) shows potential influence of apatite. It is not clear what the cause of the other trend line represents

Low concentrations of Al_2O_3 and MgO indicate that there is little contribution from aluminous clays (i.e. igneous weathering products or precipitants in the Fe-Si materials). Low concentrations of K_2O implies the lack of jarosite ($KFe^{3+}(SO_4)_2(OH)_6$, a common seafloor weathering product however natrojarosite ($NaFe^{3+}(SO_4)_2(OH)_6$) the sodic equivalent was tentatively identified by XRD (Section 5.5). Although Mn oxides are observed in the Fe-oxyhydroxide sediments overlying the Si-Fe cap rocks (Dutrieux, 2019), low concentrations of MnO (0.3 – 441 ppm) throughout the cap show that Mn oxides minerals not common throughout the Si-Fe cap.

6.3 Results - trace elements and covariation

Trace elements concentrations are generally low. Many that are at or below detection limits, or show no variance between Si-Fe units, are not considered further. Those discussed here include the base and transition metals and the rare earth elements. These elements can provide insights into sulphide mineralisation, occurrence of hydrothermal related non-sulphide minerals (i.e. barite),

and an idea of the role of hydrothermal fluids and seawater in alteration, i.e. mobilisation of redox elements.

6.3.1 Cu, Zn, Pb, Co, Cd

Pyrite/marcasite, chalcopyrite, sphalerite, and galena are common sulphide minerals observed in both SMS and VMS deposits. Pyrite/marcasite is observed in some Unit B sample (see Section 5.4.2), and mixed pyrite/marcasite, sphalerite, chalcopyrite have been observed in Unit C samples at both Southern and Rona Mounds. Therefore, it is likely that the dominant elements in said sulphides (e.g. Cu for chalcopyrite, Zn for sphalerite) would show covariance with SO_3 in the bulk geochemistry, assuming there are no other minerals that are accumulating these elements (e.g. if covariance between Pb and SO_3 is observed it could imply the presence of galena or anglesite ($PbSO_4$) despite not being observed in thin section). Other trace elements can substitute for iron (Fe^{2+}) in the sulphide crystal lattices, i.e. Co^{2+} (in any of the sulphides observed in the Si-Fe Units), or Cd^{2+} (in sphalerite) (George *et al.*, 2016; George *et al.*, 2018; Grant *et al.*, 2018), therefore they may also act as proxies for the presence of sulphide material. If there is little to no variation with SO_3, comparison with the other major geochemical components (SiO_2 and Fe_2O_{3T}) may provide an indication of which minerals, if any, are preferentially hosting these elements.

6.3.1.1 Hydrothermal Sediments Unit M3 and M4

All geochemical data for Units M3 and M4 sediment was obtained from Dutrieux, 2019. Cd was not analysed in either hydrothermal sediment Unit. Co, Cu, Zn, and Pb values have been analysed in 3 samples of Unit M4, and 12 samples of Unit M3 sediment from Southern Mound.

In Unit M3, concentrations of Co (average ~ 0.6 ppm), Cu (average ~138 ppm), Zn (average ~284 ppm), and Pb (average ~359 ppm) vary throughout the Unit but show poor covariation with each other, with Co:Cu showing the strongest (ρ = 0.57, R^2 = 0.3) (Figure 110). Furthermore, none of these elements show significant covariation with Fe_2O_{3T}, with Zn:Fe_2O_{3T} showing the most covariance (ρ = 0.55, R^2 = 0.3) (Figure 110).

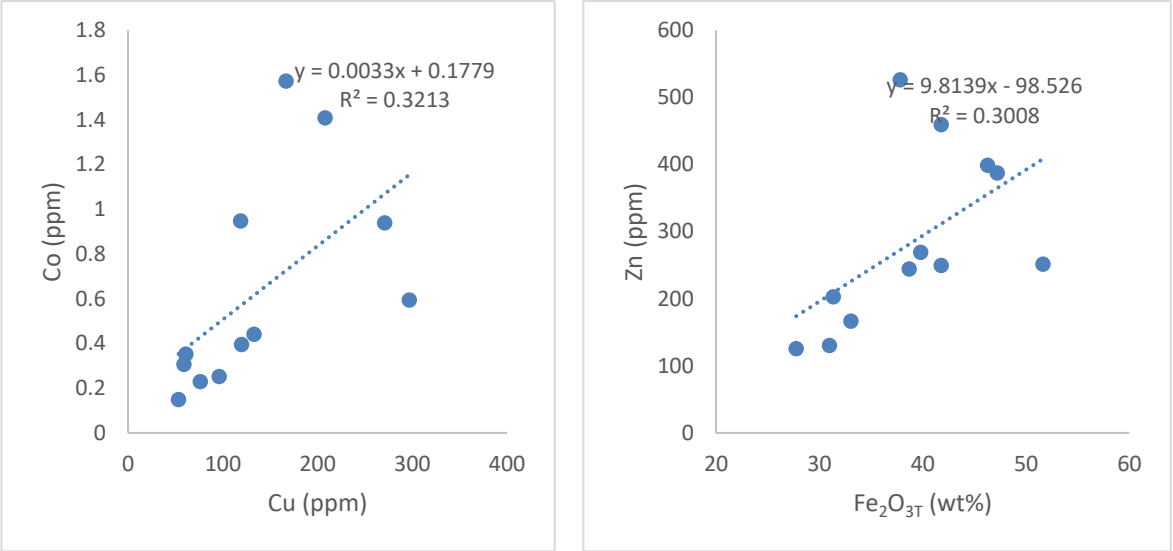

Figure 110: Bivariate plots of Co vs Cu, and Zn vs Fe_2O_{3T} for hydrothermal sediments (Unit M3). Data from Dutrieux (2019).

The general lack of covariance of Co, Cu, Zn or Pb with Fe_2O_{3T} (and also SiO_2), indicates that neither silica nor iron oxides/oxyhydroxides appear to be concentrating these elements. Unfortunately SO_3 was not analysed, therefore the covariation cannot be used to see if these elements directly related to the presence of trace sulphides.

As only 3 samples of Unit M4 were analysed, covariance values have not been used to identify trends. Concentrations of Co are on average higher (~1.5 ppm), with Cu (~77 ppm), and Zn (~135 ppm) both being lower, in comparison with Unit M3.

6.3.1.2 Unit A

Concentrations of Cu, Zn, Co, and Cd are typically consistent across Unit A at Southern Mound, with the exception of the deepest Unit A sample (050RD/P8) that has about one to two orders of magnitude lower concentrations. In contrast Pb concentrations are broadly similar across all four samples. Cu:Co, Co:Cd, Cu:Cd, all show good covariance (ρ = 0.91, 0.83, and 0.78 respectively, R^2 = 0.82, 0.64, and 0.68), but all other combinations of Cu, Zn, Co, Cd, and Pb, showed little to no trends ($-0.66 < \rho < 0.22$, $R^2 \leq 0.43$) (Figure 111).

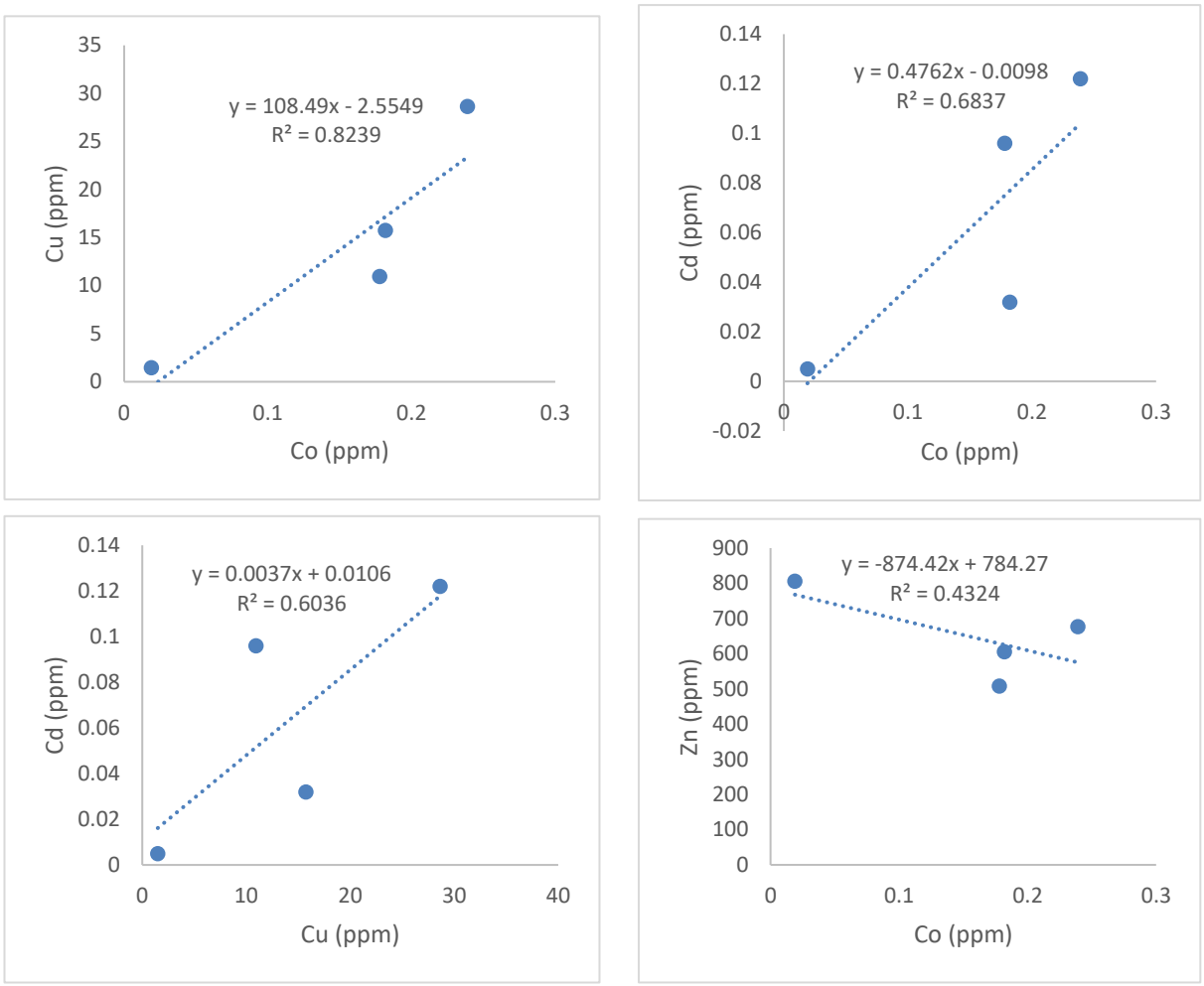

Figure 111: Bivariate plots for Unit A. Cu vs Co, Cd vs Co, Cd vs Cu, and Zn vs Co for Si-Fe Unit A

Covariance between Cu, Zn, Co, Cd, Pb and SO_3 is negative and/or poor ($-0.65 < \rho < 0.04$, $R^2 \leq 0.42$). Therefore the good covariation between Cu, Co, and Cd, and the concentrations of Cu (~1-30 ppm) and Zn (~510-805 ppm) cannot be explained by the presence of sulphides (Figure 112).

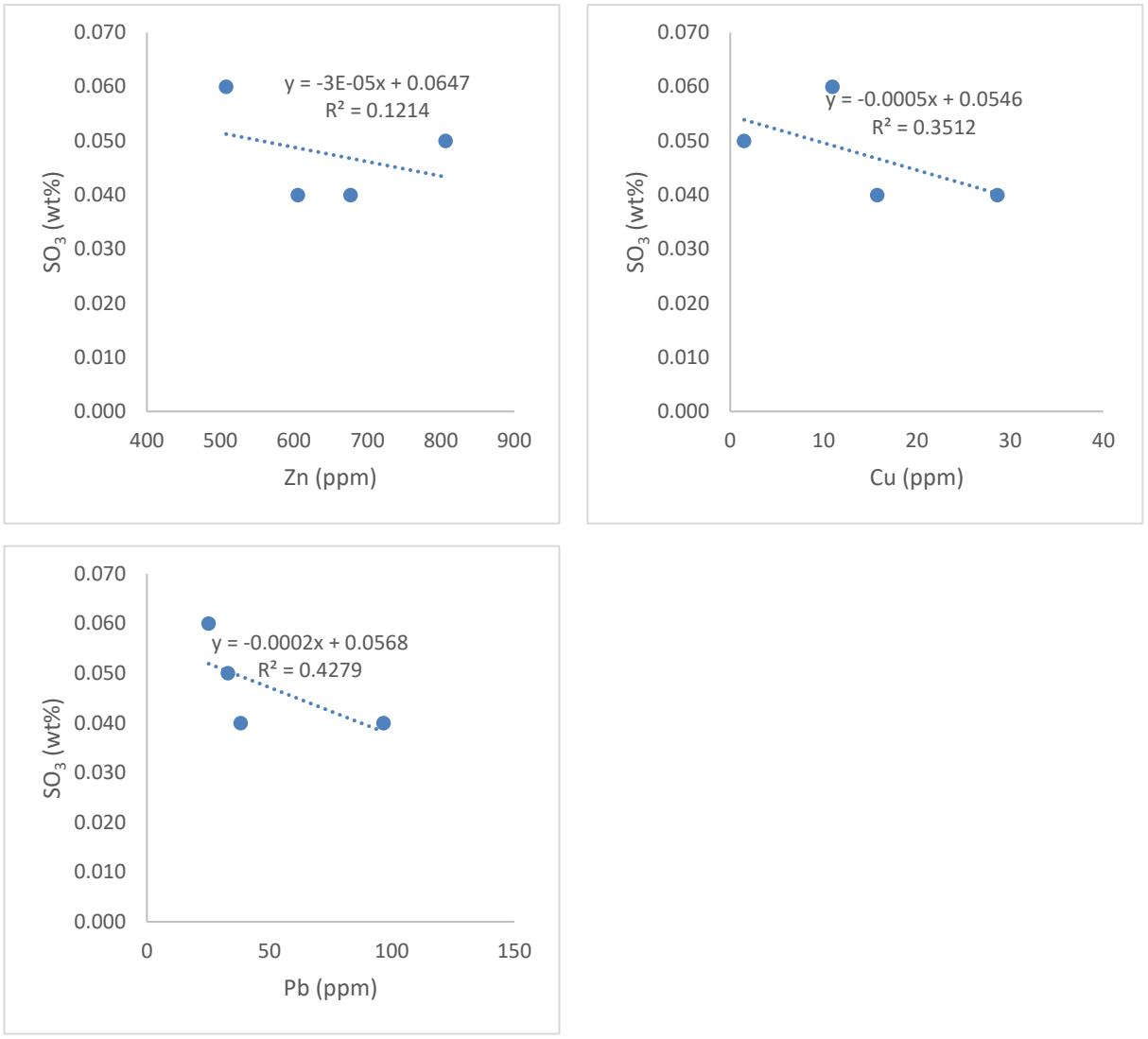

Figure 112: Bivariate plots for Unit A - Zn vs SO_3, Cu vs SO_3, and Pb vs SO_3 for Si-Fe Unit A

Cu and Co show a good positive covariance with Fe_2O_{3T} (ρ = 0.80 and 0.85, R^2 = 0.64 and 0.73 respectively), and Pb, Zn and Cd show little ($-0.49 < \rho < 0.68$, $R^2 \leq 0.47$) covariance with Fe_2O_{3T}. This suggests that Cu, Co are associated with iron oxides/oxyhydroxides within Unit A, whereas Zn, Cd, and Pb are not. Zn, Cd, and Pb show no significant trends with either SiO_2, or Fe_2O_{3T} throughout Unit A.

The lack of a positive covariance between SO_3 and the base metals, but covariation with Fe_2O_{3T}, could support the interpretation that these metals have accumulated from weathered sulphide minerals. The lack of covariance between Zn and Cd with Fe_2O_{3T}, but comparatively high Zn concentrations (~500-800 ppm) suggests a contribution from sphalerite during weathering (Figure 113). The lack of covariation between Pb and the other base metal related elements indicates that galena was not present within the interpreted pre-weathering sulphide assemblage. This is supported by the lack of galena in the underlying massive sulphide ore body at Southern Mound or

within the TAG hydrothermal field in general (Petersen *et al.*, 2000; Grant *et al.*, 2018; Lehrmann *et al.*, 2018).

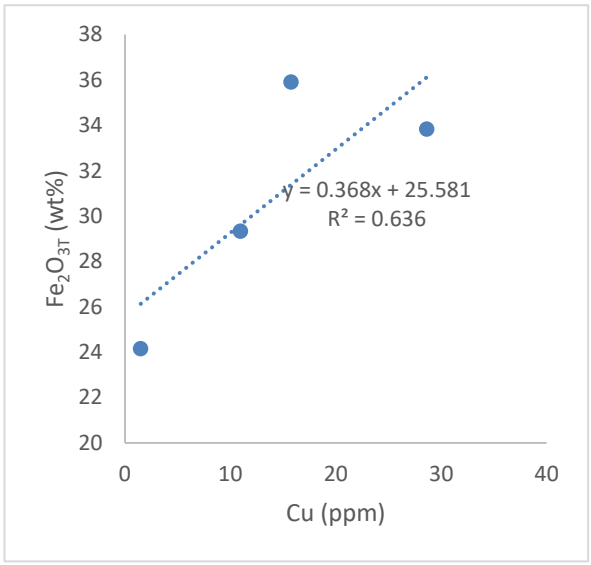

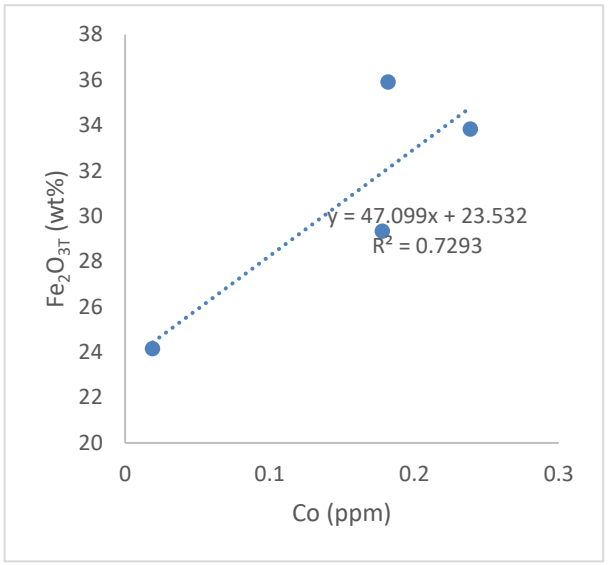

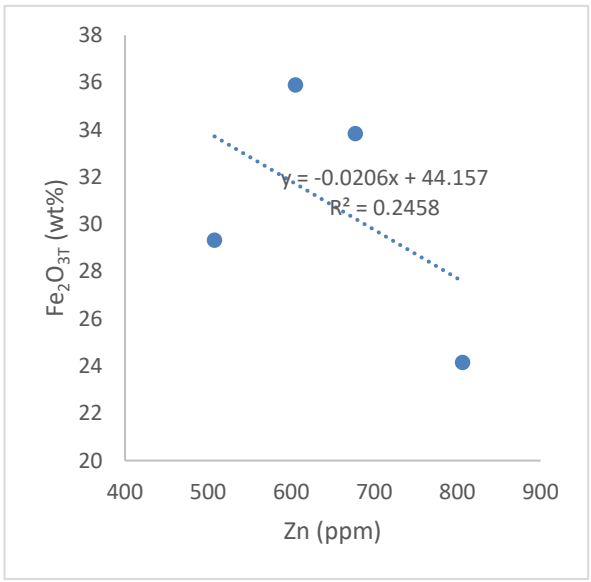

Figure 113: Bivariate plots: Cu vs Fe_2O_{3T}, Co vs Fe_2O_{3T}, and Zn vs Fe_2O_{3T} for Si-Fe Unit A

6.3.1.3 Unit B

In total 18 samples of Unit B material were analysed (3 from Southern Mound, 2 from Rona Mound, 11 from the MIR Zone). Unit B material across the three mounds had lower concentrations of Cu, Zn, Co, Cd, and Pb compared to Unit A (average total of Cu+Zn+Co+Cd+Pb = ~710 ppm in Unit A, = ~195 ppm in Unit B). Trends between Cu, Zn, Co, Cd, and Pb were typically poor with Co:Cu being the strongest trend (ρ = 0.71, R^2 = 0.50) (Figure 114).

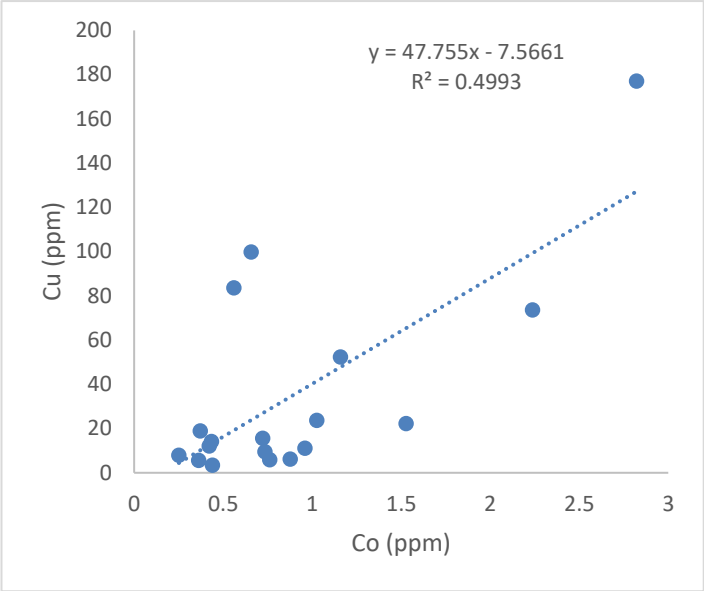

Figure 114: Bivariate plot of Co vs Cu for Si-Fe Unit B

SO_3 concentrations for Unit B materials were typically low (average = 0.05 wt%), and showed little variation with Cu, Zn, Co, Cd, or Pb ($-0.14 < \rho < 0.21$, $R^2 < 0.59$). This implies that it is unlikely that accumulation of these elements is associated primarily with sulphide minerals in Unit B, despite the observation of pyrite within several Unit B samples (Figure 115).

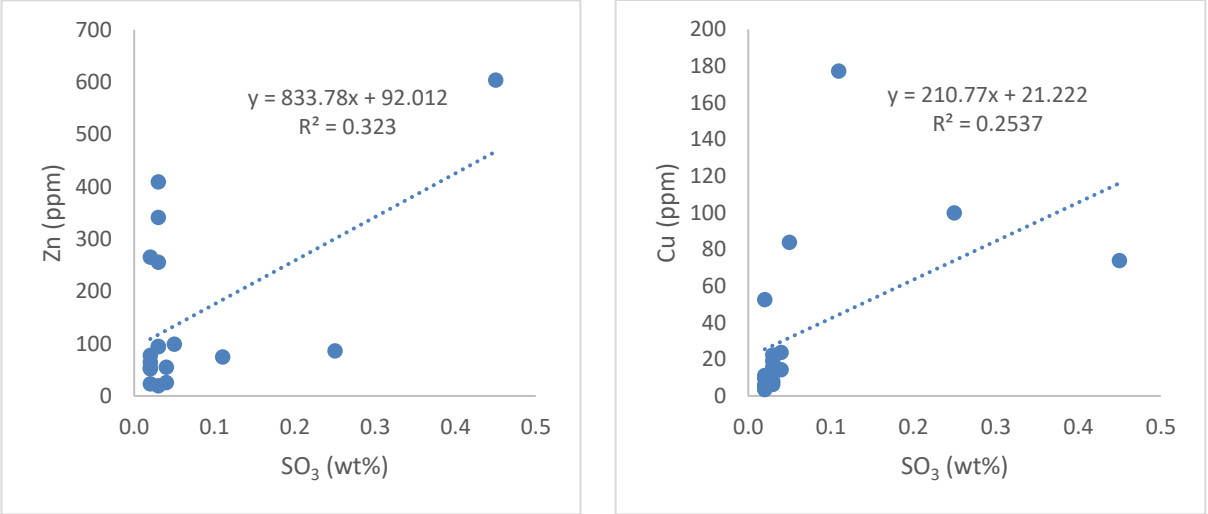

Figure 115: Bivariate plots: SO_3 vs Zn, and SO_3 vs Cu, for Si-Fe Unit B samples

Similarly there are no trends observed between Cu, Zn, Co, Cd, Pb, and Fe_2O_{3T} ($-0.49 < \rho < 0.37$, $R^2 \leq 0.23$), which implies that iron oxide/oxyhydroxide mineralogy has no control on their distribution through Unit B material. The strong inverse relationship between Fe_2O_{3T} and SiO_2 also implies poor correlation with SiO_2.

6.3.1.4 Unit C

Unit C has variable combinations of different sulphides (pyrite/marcasite, chalcopyrite, and sphalerite) in each sample (See Section 5.5.2), therefore covariation would be expected between SO_3 and Cu, Zn, Co, Cd, or Pb if sulphide minerals are acting as hosts. Zn, Co, Cd, and Pb across all samples show good covariation ($\rho > 0.72$, $R^2 > 0.52$) with each other, but not with Cu ($-0.37 < \rho < -0.14$, $R^2 < 0.14$). This could potentially be explained by the fact that only one sample contains chalcopyrite (Southern Mound Unit C sample 050RD/P13) (Figure 116).

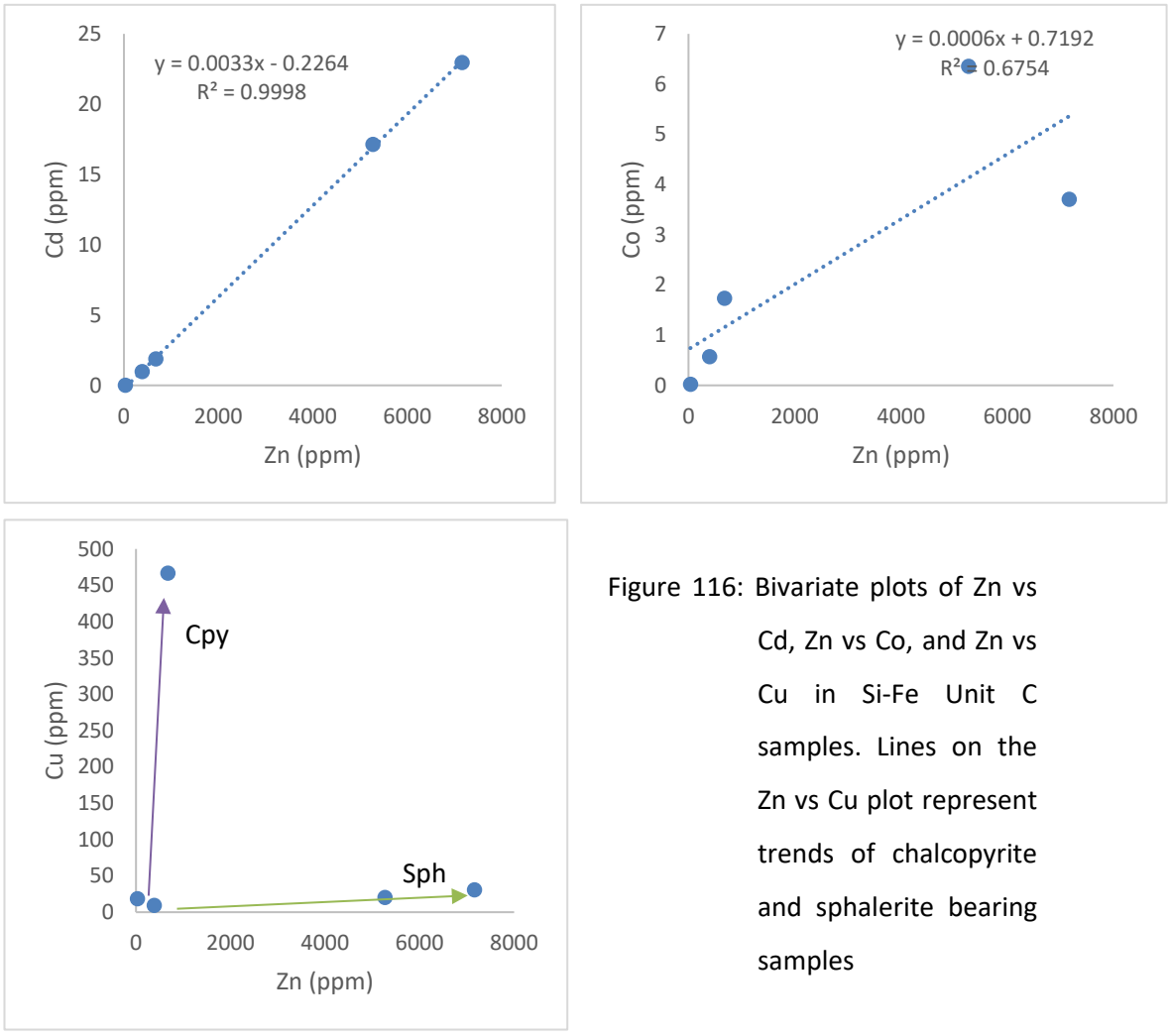

Figure 116: Bivariate plots of Zn vs Cd, Zn vs Co, and Zn vs Cu in Si-Fe Unit C samples. Lines on the Zn vs Cu plot represent trends of chalcopyrite and sphalerite bearing samples

The two highest Zn-Cd samples in Unit C are from Rona Mound (only pyrite and sphalerite observed), and the only sample of Unit C material containing chalcopyrite being the highest copper sample (050RD/P13 from Southern Mound Unit C).

Unit C samples from Rona Mound have the two highest Co concentrations throughout the Si-Fe cap (~4ppm and ~6 ppm), which is higher than any Si-Fe sample from Southern Mound (max = < 2 ppm), and all but one sample from the MIR Zone (max = ~ 3ppm, typically < 2 ppm). This may indicate a

slightly different fluid chemistry or some process accumulating Co at Rona Mound compared with Southern Mound and MIR Zone, i.e. substitution into sulphides. High Co concentrations, when associated with sulphides are typically interpreted to be a function of high temperatures, but can occur across a range of temperatures (Swanner *et al.*, 2014; Grant *et al.*, 2018).

6.3.2 Ba and Sr

Ba and Sr show a strong covariance throughout the Si-Fe cap (ρ = 0.87,R^2 = 0.76), potentially associated with the presence of barite ($BaSO_4$). Absolute concentrations vary throughout the different Units, with average concentrations being one to two orders of magnitude higher in Unit A than Units B or C. Although barite was not observed in thin section or by XRD, it was recorded in overlying hydrothermal sediments at Southern Mound where Ba concentrations ranged from similar concentrations, to an order of magnitude higher, than the Si-Fe cap Units. Both Ba and Sr show a good to strong positive covariance with SO_3 in Unit A (ρ = 0.64 and 0.61 respectively), and across all Unit C samples (ρ = 0.91 for both), again potentially supporting the occurrence of trace barite grains. No covariation was observed in Unit B material (ρ = -0.01. and -0.20 for Ba-SO_3 and Sr-SO_3), implying that Ba and Sr concentrations in Unit B is not controlled by the presence of barite (Figure 117).

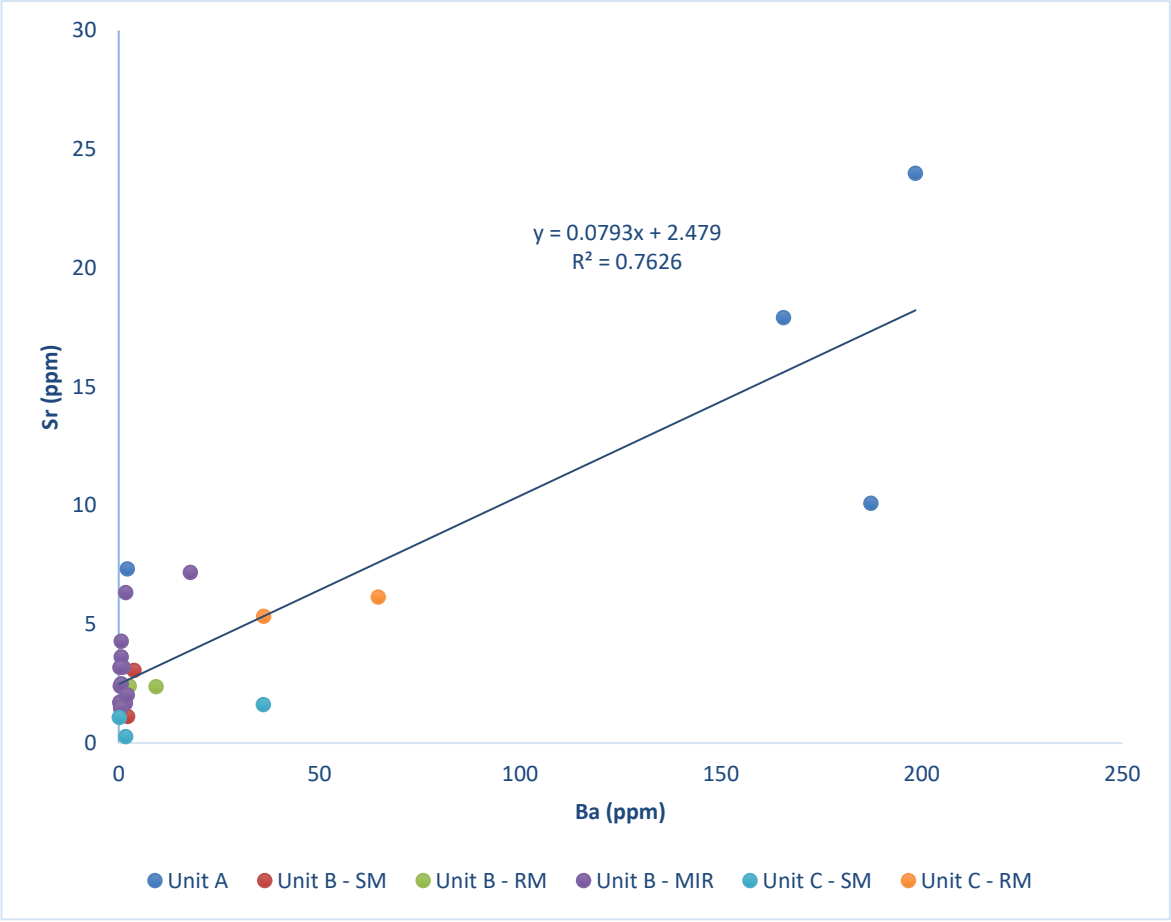

Figure 117: Bivariate plot of Ba vs Sr across all Si-Fe samples

6.3.3 V, Mo, and U

Other redox sensitive trace elements such as V, Mo, and U are enriched in hydrothermal plumes (See Section 1.1). They can also be precipitated from seawater in anoxic conditions by redox reactions, and are interpreted to adsorb onto sulphide mineral surfaces in the active TAG mound associated with seawater circulation in the mound (Grant *et al.*, 2018). High U concentrations in hydrothermal sediments have been interpreted as being related to the presence of massive sulphide grains or attributed to microbial mediation (Mills *et al.*, 1994; Ayupova *et al.*, 2018), but could also be derived from seawater. The behaviour of these elements is explored here to determine the interaction of the Si-Fe materials with seawater, as they formed, and their precursors.

The mechanism whereby V, Mo, and U are scavenged from seawater is usually attributed to adsorption onto colloidal iron oxides/oxyhydroxides under oxidising conditions (Ames *et al.*, 1993; Peacock and Sherman, 2004; Arai, 2010). Mo was not analysed in the overlying hydrothermal sediments, and V showed no covariance with Fe_2O_{3T} ($\rho = 0.20$, $R^2 = 0.04$). With the exception of one outlying sample (M4 from 022RD), U concentrations are typically < 15 ppm, and show a good

covariation with Fe_2O_{3T} (ρ = 0.79, R^2 = 0.63). This implies that U is controlled by adsorption on the surface of iron oxides/oxyhydroxides within the hydrothermally derived Units M3 and M4. The anomalous sample (~49 ppm) has U concentrations ~ 4 times higher than the other sediments, and was recovered from the sediment-hard rock interface (Figure 118).

Covariation between V, Mo, and Fe_2O_{3T} in the Si-Fe lithologies at the TAGHF is typically weak to moderate (ρ = 0.48 R^2 = 0.20, ρ = 0.58 R^2 = 0.29 respectively), implying that adsorption onto the surface of iron oxides/oxyhydroxides does not control the distribution of V, Mo throughout the Si-Fe cap. U shows a similar behaviour in the Si-Fe cap to the hydrothermal sediments, with two anomalous, high U containing samples (~38 ppm, and 43 ppm), with a weak to moderate positive covariance with Fe_2O_{3T} (ρ =0.54, R^2 = 0.32). This tentatively implies that a similar mechanism is controlling the U concentrations in the Si-Fe cap as the majority of samples fit on the same trend (Figure 118).

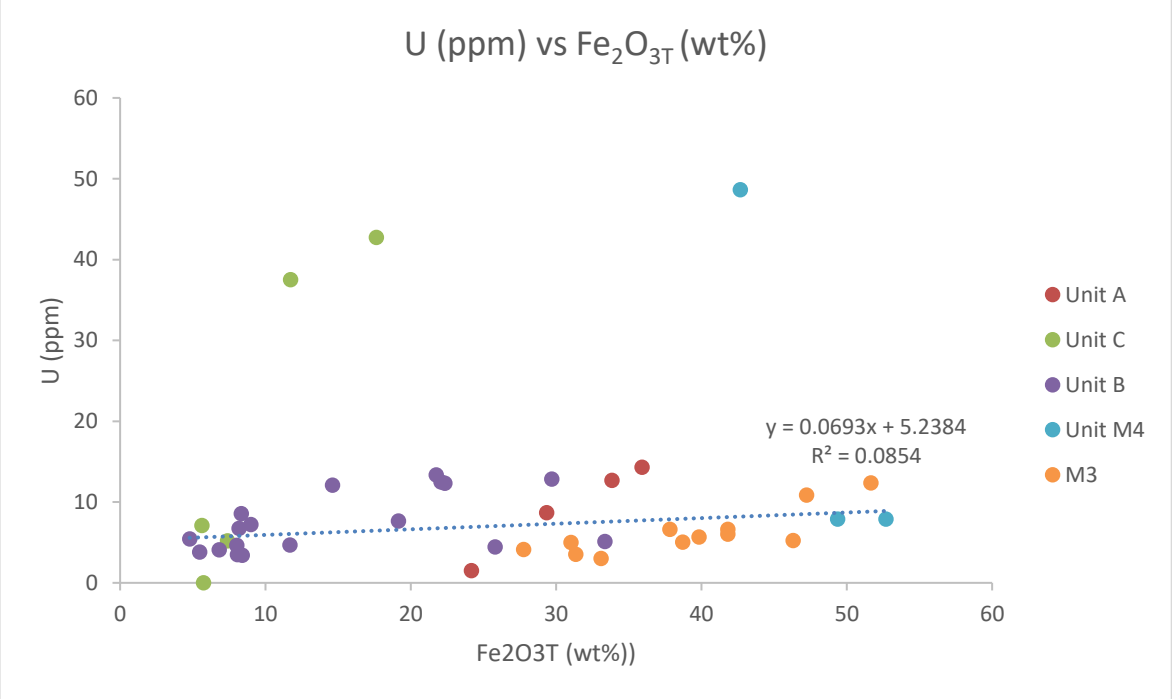

Figure 118: Bivariate plot of Fe_2O_{3T} vs U throughout the Si-Fe cap and overlying hydrothermal sediments. Two Unit C samples (from Rona Mound) and a Unit M4 sediment sample (Southern Mound) had anomalously high U concentrations.

6.4 Results - rare earth elements (REEs)

Rare earth elements (REEs) patterns, and especially Eu anomalies, reveal information about the role of hydrothermal fluids in the formation or interaction with the Si-Fe lithologies. In a hydrothermal environment sources of REEs are somewhat limited to hydrothermal fluids (black and white smoker fluids), and seawater. Positive Eu anomalies arise in hydrothermal fluids and their products largely as a result of the solubility of divalent Eu^{2+} (stable at high temperature) in reduced fluids compared with the other trivalent REEs, and preferential incorporation of REE^{3+} ions in anhydrite (Mills and Elderfield, 1995). Ce anomalies arise from interaction with oxygenated seawater and relate to the decrease in solubility that accompanies the oxidation of Ce^{3+} or Ce^{4+} (Elderfield and Schultz, 1996). These anomalies are represented as geometric values rather than linear ones. Black and white smoker fluids are typically enriched in both light REE (LREE) and heavy REE (HREE) elements (in this study a metric for LREE enrichment is the La_N/Sm_N ratio and HREE enrichment is the Sm_N/Yb_N ratio), whereas seawater is in enriched in LREEs and depleted in HREE (Klinkhammer *et al.*. 1994). Reference REE data for seawater (German *et al*., 1990 and Mitra *et al*., 1994), black smokers (Douville *et al*., 1999), and white smokers (Mitra *et al*., 1994). Observation of the presence or absence of characteristic REE patterns in the Si-Fe cap can likely be attributed to variable sources of REEs or by some mineralogical control on REE partitioning or absorption.

Throughout the Si-Fe cap, and broadly in the overlying hydrothermal sediments, total REEs (TREEs) typically correlate with Fe_2O_{3T}, with a few outliers (See Figure 119), implying that REEs are generally associated with the iron oxide/oxyhydroxide phase of the Si-Fe cap. REEs can absorb onto the surface of iron oxides/oxyhydroxides above pH 4, with a preference of HREE absorption over LREEs between pH 4 and 9, and even adsorption of REEs at pH > 9 (Liu *et al.*, 2017). Therefore, as expected the higher Fe_2O_{3T} and higher Si/Fe ratio of the sediments correlate with higher TREEs (Figure 119). This is not the case in the hydrothermal sediments, and it is not clear why this is the case.

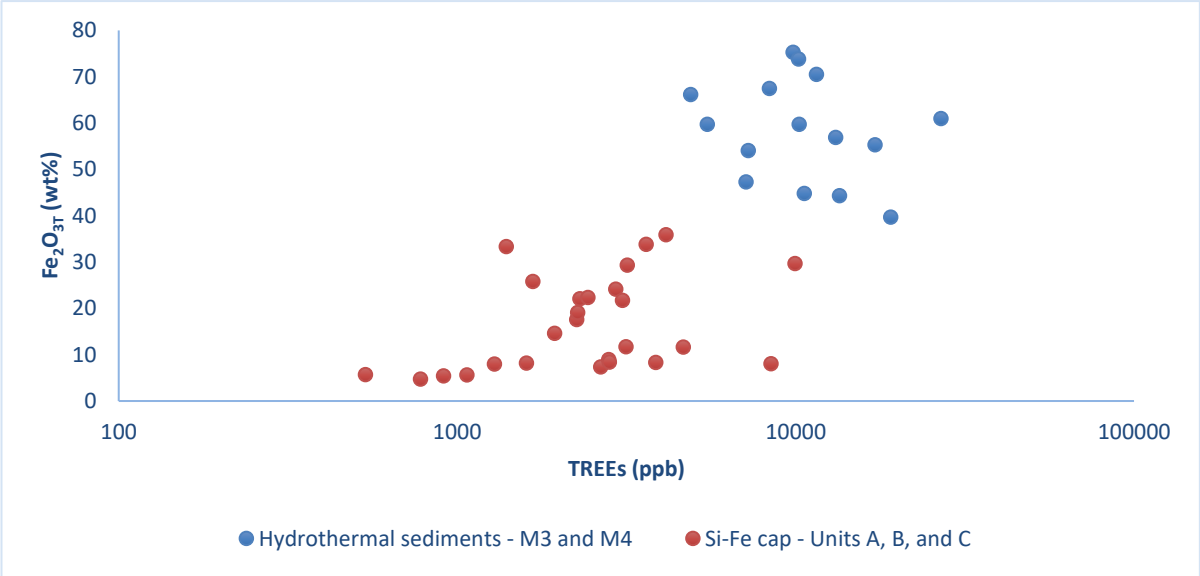

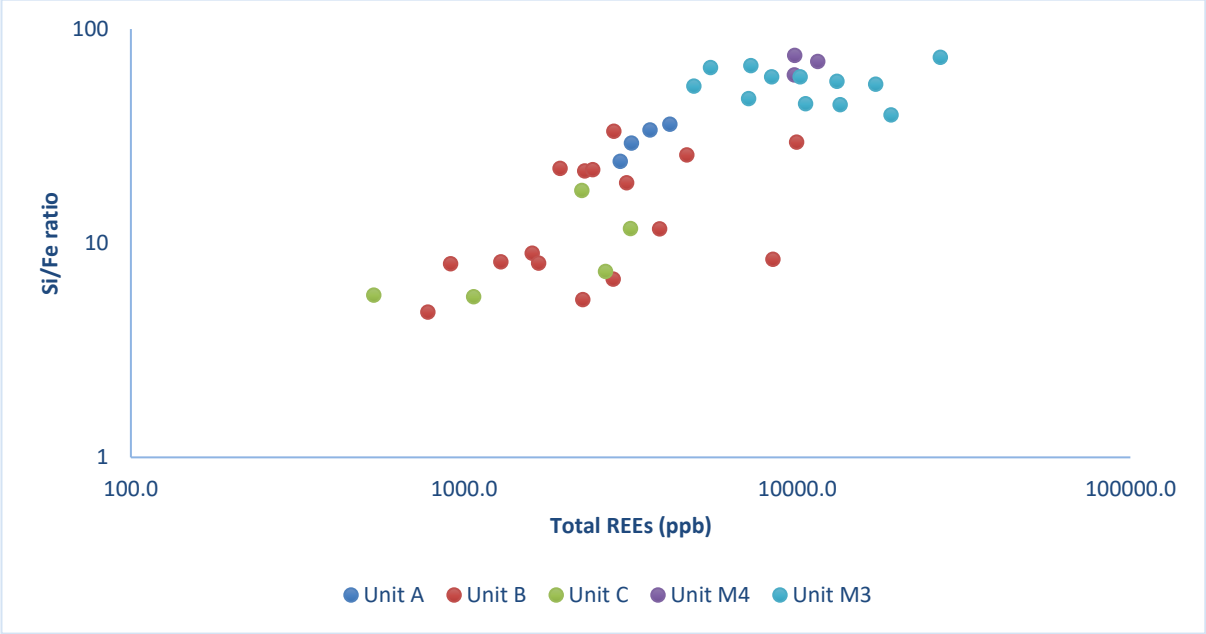

Figure 119: Bivariate plots of TREEs vs Fe_2O_{3T} and TREEs vs Si/Fe ratio for all hydrothermal sediments and Si-Fe cap rocks

6.4.1 Hydrothermal Sediment Units M3 and M4

Total REEs of the hydrothermal sediments are similar between both Unit M3 and Unit M4 samples, at around 10,000-12,000 ppb, with no real positive trend with Fe_2O_{3T} as observed in the Si-Fe cap. However, the higher Fe_2O_{3T} content of the sediments, correlates with higher TREEs (Table 57).

REE profiles for both Unit M3 and Unit M4 sediment exhibit a slightly enriched LREE profile, and an enrichment in HREEs (Figure 120, Table 57). Both Units M3 and M4 HREE fractionation (Sm_N/Yb_N = ~3) is comparable with HREE fractionation in black smoker hydrothermal fluids (Sm_N/Yb_N = 3.7), and while LREEs are enriched, they are not fractionated (La_N/Sm_N = ~ 1.7 and ~1.1 respectively) at the

same La_N/Sm_N ratio as black smoker fluids (La_N/Sm_N = 3.15), white smoker fluids (La_N/Sm_N = 6.12), or seawater (La_N/Sm_N = 4.20). This implies that despite both sediment Units showing LREE enrichment (with respect to carbonaceous chondrite), they are also exhibit a different LREE fractionation profile with respect to all three potential REE fluid sources.

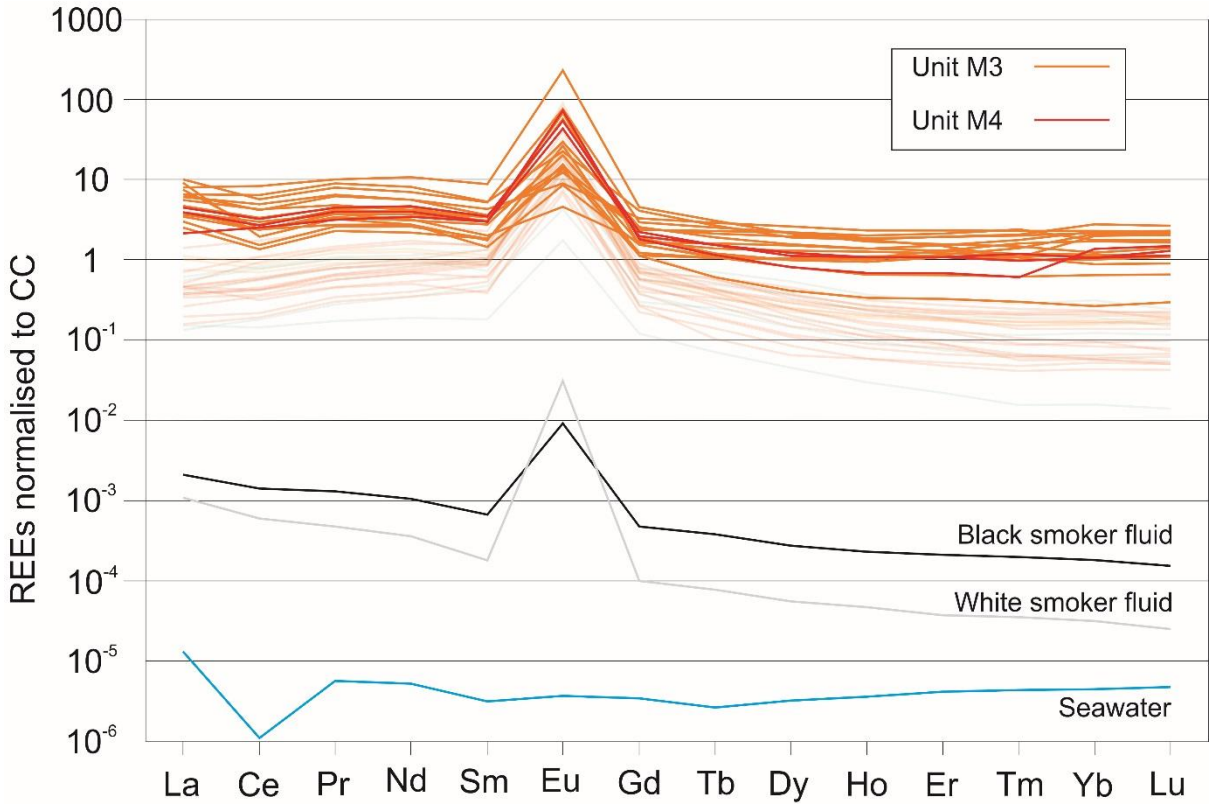

Figure 120: REE profiles for hydrothermal sediments from Units M3 and M4 (Southern Mound). Faint lines in background represent all Si-Fe cap samples (orange = Unit A, red = Unit B, grey = Unit C).

Both Unit M3 and M4 (summarised in Table 57) have strong positive Eu anomalies, with Unit M3 Eu/Eu* exhibiting a lower average anomaly (~9.29), compared to Unit M4 (~15.25). Both exhibit negative Ce/Ce* anomalies with Unit M3 anomaly being slightly lower than Unit M4. The strong Eu anomaly observed in both hydrothermal sediment Units can be attributed to interaction with black smoker fluids (Eu/Eu* = ~11) as white smoker fluid anomalies are too high (Eu/Eu* = ~150), and seawater has a slight negative Eu/Eu* anomaly (0.8). Ce/Ce* anomalies in both Units are also comparable with both black smoker (Ce/Ce* = 0.57) and white smoker (Ce/Ce* = 0.48) fluids, but are both less negative than the seawater Ce/Ce* anomaly (Ce/Ce* = 0.08).

Table 57: Summary of TREEs, HREE and LREE ratios, and Eu and Ce anomalies from hydrothermal sediment Units M3 and M4

		Total REEs (ppb)	**La_N/Sm_N**	**Sm_N/Yb_N**	**Eu/Eu***	**Ce/Ce***
Unit M3 (n = 12)	Mean	11849	1.48	3.05	9.29	0.48
	Max	26910	2.25	6.95	22.42	0.64
	Min	4893	0.91	0.89	1.66	0.38
Unit M4 (n = 3)	Mean	10391	1.10	2.78	15.25	0.51
	Max	11533	1.31	3.29	20.68	0.66
	Min	9815	0.69	2.24	11.96	0.48

The enrichment of HREEs, strong positive Eu/Eu* values, and moderately negative Ce/Ce* values all indicate that the REE profiles of both Units M3 and M4 are most comparable with black smoker REE profiles, implying a control on REEs from this fluid source. However, this cannot explain the flat and less enriched LREE values of each Unit.

6.4.2 Unit A

Total REE concentrations for Unit A (Table 58) are ~3000 ppb, on average 3 times less than hydrothermal sediment Units M3 or M4. Unit A samples exhibit relatively flat LREE profiles (La_N/Sm_N = ~ 1), and an depletion in HREEs (Sm_N/Yb_N = 6), similar to Unit M3, but with a greater HREE depletion (Figure 121, Table 58). In contrast to Unit M3, the Sm_N/Yb_N is higher, closer to that of white smoker hydrothermal fluids (Sm_N/Yb_N = 5.7), than black smoker fluids (Sm_N/Yb_N = 3.7).

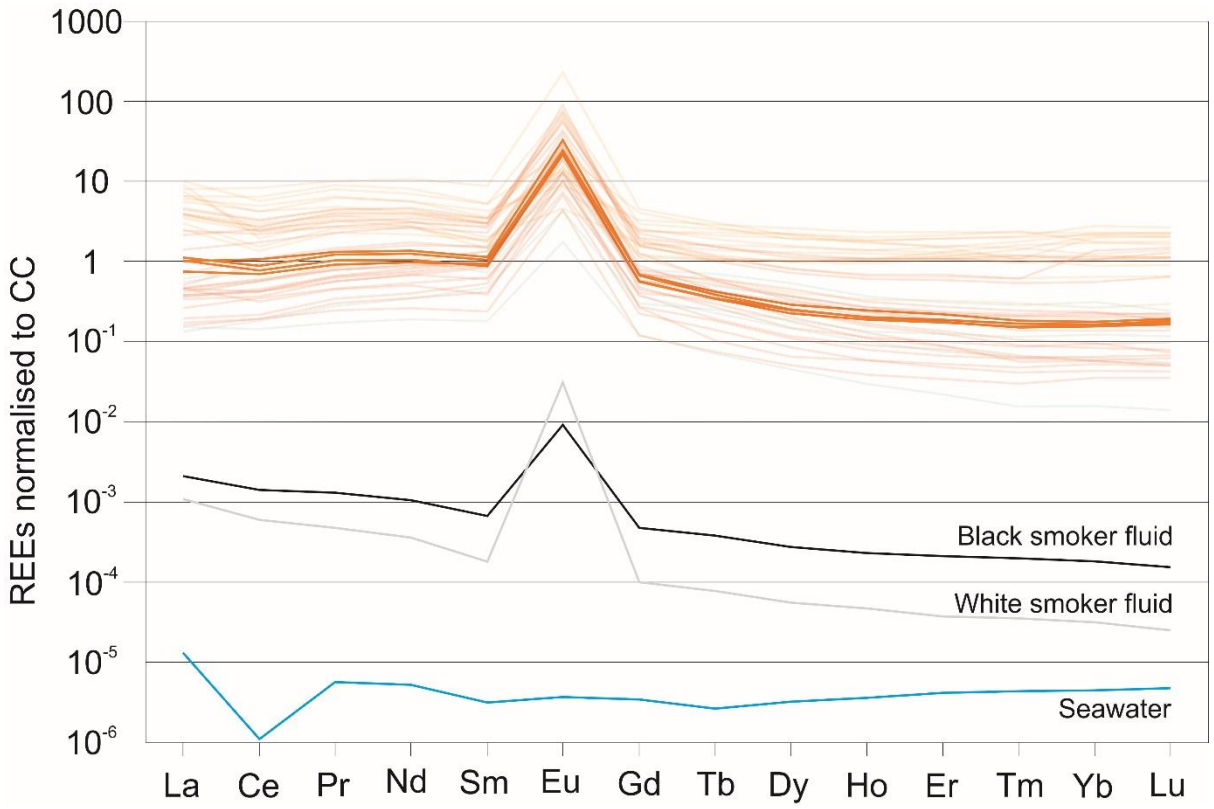

Figure 121: REE profiles for Unit A samples of the Si-Fe caprock (lines in bold). Faint lines represent Units M3 and M4 sediments, and Si-Fe cap Units B and C.

Unit A samples (summarised in Table 58) share a positive Eu/Eu* value similar to both black and white smoker fluids, with Eu/Eu* values typically somewhere between black smoker fluids (Eu/Eu* = ~11), and white smoker fluids (Eu/Eu* = ~150). The average Ce/Ce* value is the same as black smoker fluids (Ce/Ce* = 0.57), higher than both white smoker fluids (Ce/Ce* = 0.47), and seawater (Ce/Ce* = 0.08).

Therefore Unit A samples share characteristics with black and white smoker fluids with average Eu/Eu* values of ~ 21, and have depleted HREEs ratios closer to white smoker fluids than black smoker fluids (Sm_N/Yb_N = ~6). However, similar to the hydrothermal sediments their generally flat LREE profile cannot be accounted for when compared to REE profiles of all three source fluids.

Table 58: Summary of TREEs, HREE and LREE ratios, and Eu and Ce anomalies from Si-Fe cap Unit A

(n=4)	**Total REEs (ppb)**	**La_N/Sm_N**	**Sm_N/Yb_N**	**Eu/Eu***	**Ce/Ce***
Mean	3472	0.98	6.08	21.46	0.57
Max	4143	1.17	7.26	24.70	0.63
Min	2942	0.81	5.35	19.65	0.53

6.4.3 Unit B

Two Unit B samples from Southern Mound showed a significant difference in total REEs with one sample recording ~10000 ppb comparable to hydrothermal sediment Units M3 and M4, and the other 780 ppb, one of the lowest TREEs concentrations in the Si-Fe samples. REE profiles for these two Unit B samples from Southern Mound exhibit the same LREE and HREE characteristics as Unit A samples, but show more depletion in LREEs (La_N/Sm_N = 0.8), and comparable HREE depletion (Sm_N/Yb_N = ~6) (Figure 122,Table 59).

Two Unit B samples from Rona Mound recorded ~1600 and 2800 ppb TREEs, ~6 and 4 times lower in concentration than hydrothermal sediment Units M3 and M4 respectively. REE profiles share similar LREE and HREE characteristics as both Unit A samples and Unit B samples from Southern Mound but show more depletion and fractionation in LREEs (La_N/Sm_N = 0.41 and 0.43), and comparable HREE depletion and fractionation (Sm_N/Yb_N = ~4.6 and ~6.7) (Figure 122).

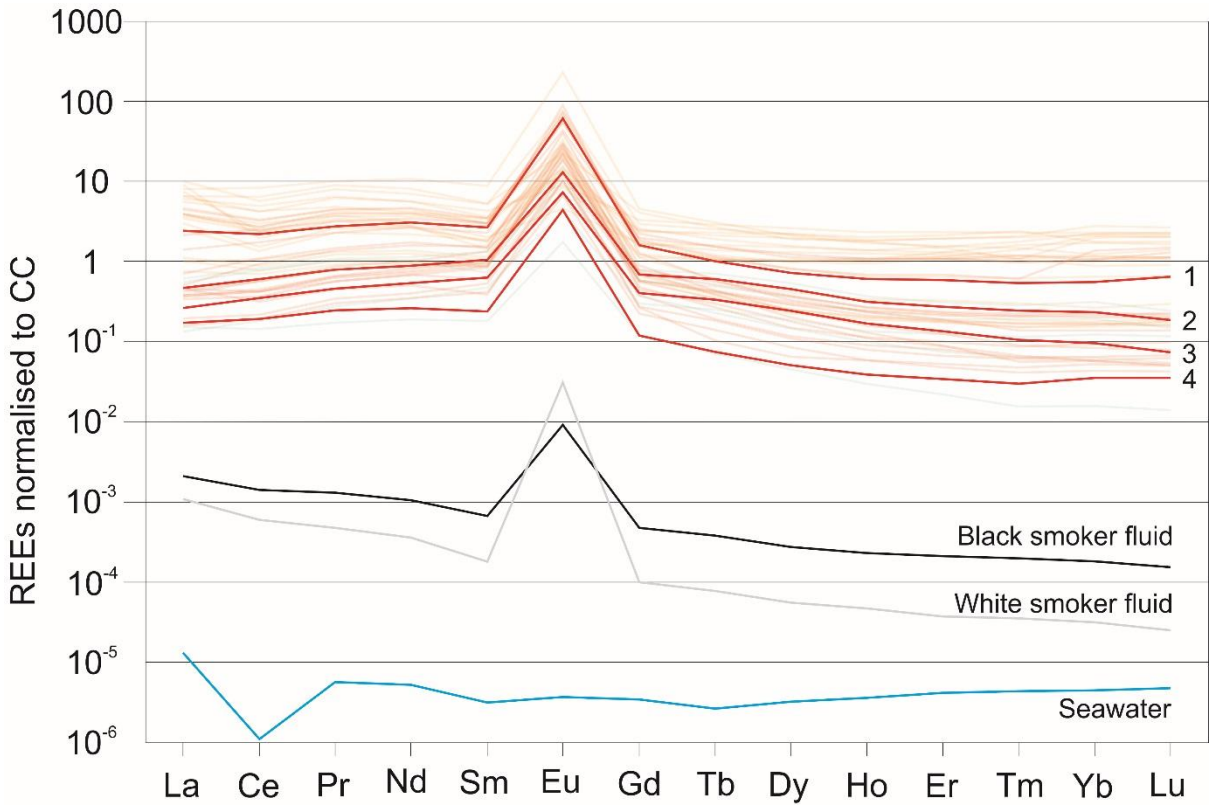

Figure 122: REE profiles for two Unit B samples from Southern Mound (profiles 1 and 4) and two Unit B samples from Rona Mound (profiles 2 and 3). Faint lines in background represent Units M3 and M4 hydrothermal sediments, Unit A and Unit C samples, and Unit B samples from the MIR Zone.

Unit B samples from Southern Mound share similar strong positive Eu/Eu* values, and negative Ce/Ce* anomalies (Table 59). Similar to Unit A, and sediment Units M3 and M4, a strong influence of hydrothermal fluids, with seemingly little interaction from seawater is interpreted from the REE patterns.

Both Unit B samples from Rona Mound exhibit strong Eu anomalies (Eu/Eu* = ~10) and weak negative Ce anomalies (Ce/Ce* = 0.65). The strong Eu/Eu* anomaly indicates strong hydrothermal influence and is broadly similar to black smoker fluids, and shows little interaction with seawater, with only a weak Ce/Ce* negative anomaly.

Table 59: TREEs, HREE and LREE ratios, and Eu and Ce anomalies from Si-Fe cap Unit B samples from Southern Mound and Rona Mound

		Total REEs (ppb)	**La_N/Sm_N**	**Sm_N/Yb_N**	**Eu/Eu***	**Ce/Ce***
Southern	022RD/CC	9966	0.88	4.90	20.68	0.60
	031RD/CC/007	779	0.71	7.05	17.48	0.64
Rona	057RD/P2	2806	0.43	4.61	10.48	0.65
	057RD/P3-8	1601	0.41	6.67	10.06	0.65

TREE concentrations for Unit B samples from the MIR zone range from ~ 900 ppb to ~8500 ppb, showing a larger range in TREEs than other Si-Fe cap rocks. REE profiles typically share similar depleted and fractionated LREEs (La_N/Sm_N average ~0.5) and depleted and fractionated HREEs (Sm_N/Yb_N = ~11) to both Unit A samples and other Unit B samples from Southern Mound and Rona Mound. One exception to this is the shallowest sample from one borehole (076RD), which shows a slight enrichment of LREEs and little to no fractionation (La_N/Sm_N = 1.19), but still shows depletion and a similar fractionation of HREEs (Sm_N/Yb_N = 7.30) (Figure 123, Table 60).

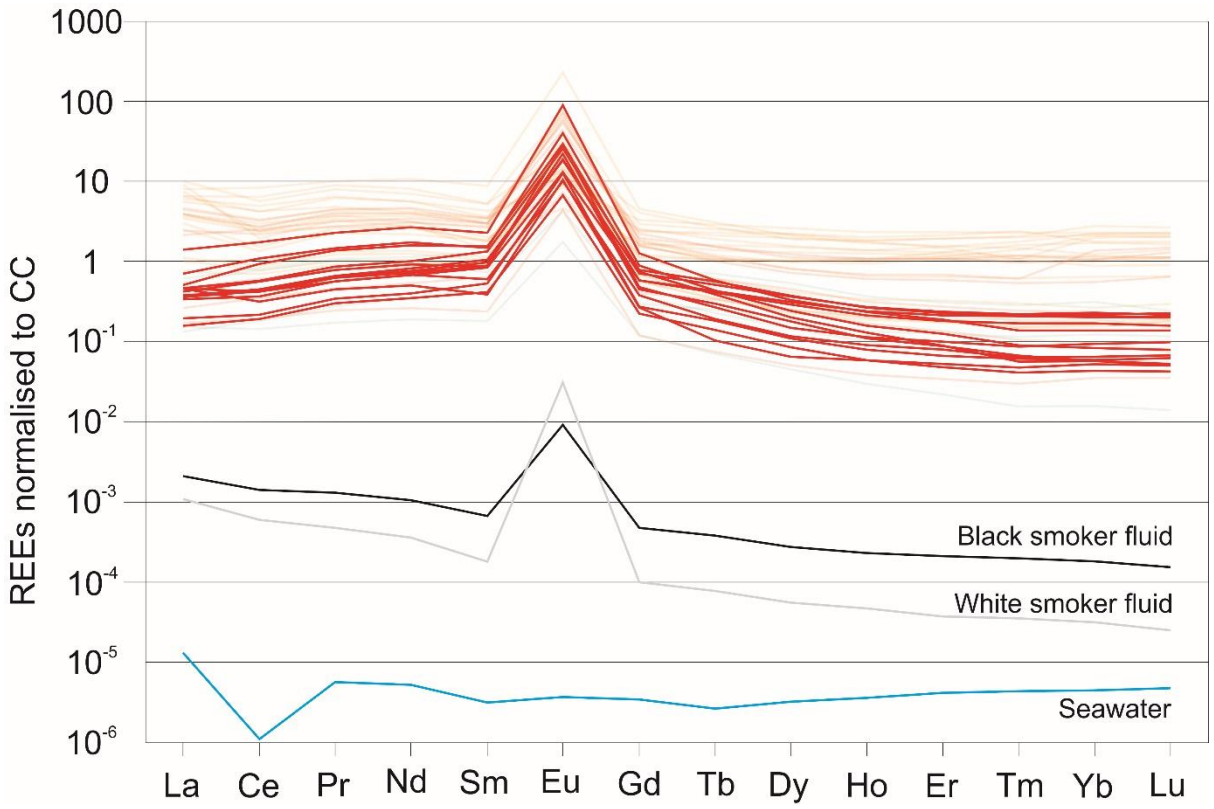

Figure 123: REE profiles of Unit B samples from the MIR Zone. Faint lines in background are hydrothermal sediment Units M3 and M4, Unit A and C, and Unit B samples from both Southern and Rona Mounds.

In general Unit B samples from the MIR Zone have strong Eu anomalies (Eu/Eu* = ~20) and weak negative Ce anomalies (Ce/Ce* = 0.6). The strong Eu/Eu* anomaly indicates strong hydrothermal influence with stronger Eu/Eu* anomalies than black smoker fluids, but weaker than white smoker Eu/Eu* anomalies.

Table 60: Summary of TREEs, HREE and LREE ratios, and Eu and Ce anomalies from Si-Fe Unit B samples from the MIR Zone

(n = 17)	**Total REEs (ppb)**	**La_N/Sm_N**	**Sm_N/Yb_N**	**Eu/Eu***	**Ce/Ce***
Mean	2853	0.50	10.95	20.02	0.59
Max	8451	1.19	27.08	34.20	0.67
Min	911	0.33	3.93	12.76	0.49

6.4.4 Unit C

Three Unit C samples from Southern Mound showed low TREE concentrations averaging ~1900 ppb, the lowest of any Si-Fe Unit. They share the same LREE and HREE characteristics as Unit A and B samples, with LREE depletion and but higher HREE depletion (Figure 124, Table 61), with comparable LREE and HREE fractionation patterns (La_N/Sm_N = 0.62, Sm_N/Yb_N = ~9).

Two Unit C samples from Rona Mound showed TREE concentrations similar to Unit A and Unit B samples (~2250 and 3150 ppb). REE profiles of the two Unit C samples from Rona Mound share similar depleted LREEs (La_N/Sm_N = ~0.5) and depletion HREEs (Sm_N/Yb_N = ~5) characteristics as the other Si-Fe cap samples (Figure 124).

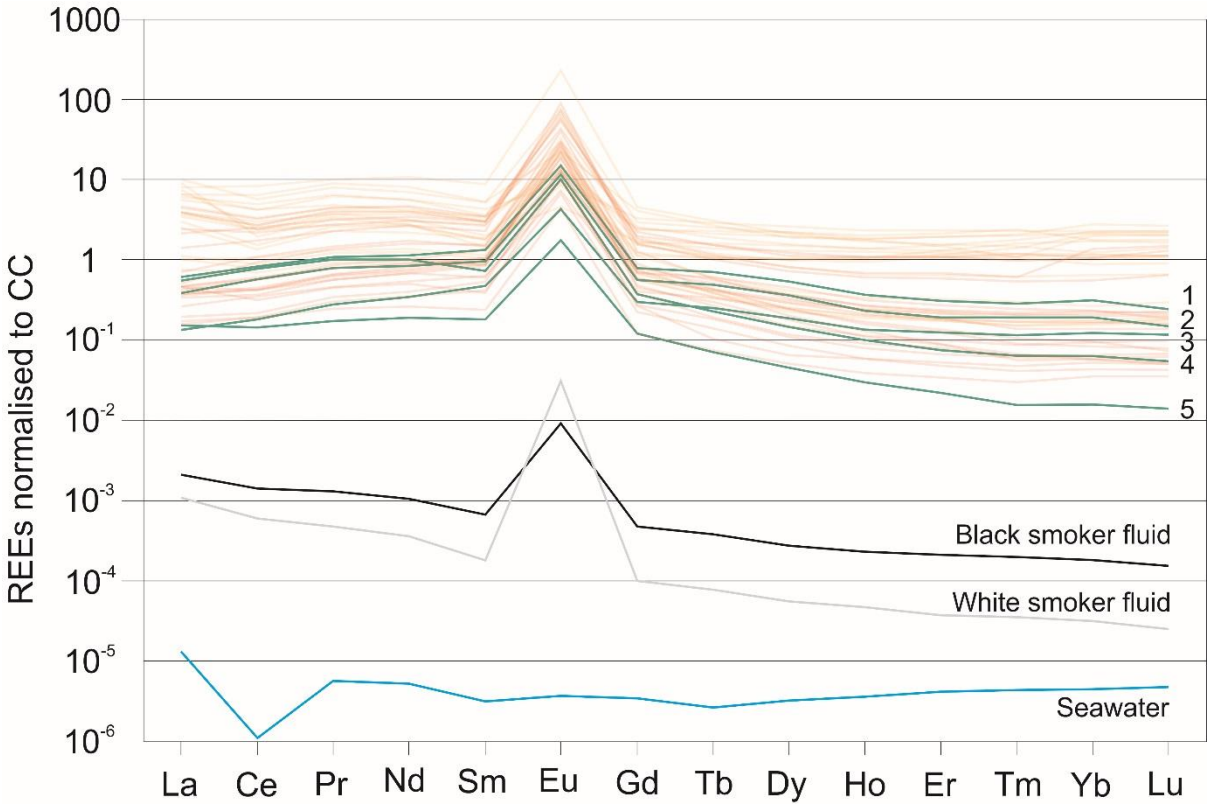

Figure 124: REE profiles from Southern Mound (profiles 3, 4, and 5), and Rona Mound (profiles 1 and 2). Faint lines in the background represent hydrothermal sediment Unit M3 and M4 samples, Unit A, and Unit B samples.

In general Unit C samples have strong positive Eu anomalies (Eu/Eu* = ~10) and weak negative Ce anomalies (Ce/Ce* = 0.65) similar to Unit B samples from Rona Mound (Table 61). The strong Eu/Eu* anomaly indicates hydrothermal influence, with Eu/Eu* anomalies comparable with black smoker fluids. The weak Ce/Ce* negative anomaly also implies a lack of seawater interaction.

Unlike samples from other Mounds, the Eu/Eu* values and Ce/Ce* values are very similar across all 4 samples from Rona Mound, implying a relatively similar influence of REE controlling factors throughout.

Table 61: Summary of TREEs, HREE and LREE ratios, and Eu and Ce anomalies from Si-Fe Unit C samples from Southern Mound (average, max, min) and Rona Mound (both samples)

		Total REEs (ppb)	**La_N/Sm_N**	**Sm_N/Yb_N**	**Eu/Eu***	**Ce/Ce***
Southern (n=3)	Mean	1420	0.62	9.10	9.77	0.65
	Max	2657	0.81	11.95	12.93	0.70
	Min	536	0.30	3.77	8.09	0.59
Rona	057RD/P10	3156	0.44	4.47	9.10	0.66
	057RD/P11	2255.5	0.39	5.13	10.45	0.66

6.4.5 Support of the interpretation of the hydrothermal sediments being the protolith for the Si-Fe cap

In general the Si-Fe cap rocks have slightly less negative Ce/Ce* values, and higher positive Eu/Eu* anomaly values than the hydrothermal sediments (Table 62). Ce/Ce* values range from ~0.55 to ~0.70 in the Si-Fe cap, with the exception of four values. All four samples are from the shallowest Si-Fe samples for their respective boreholes for Unit A samples from Southern Mound (050RD/P3, 050RD/P5 – Ce/Ce* = 0.53), and Unit B samples from the MIR Zone (073RD/P1 and 076RD/P2 - Ce/Ce* = 0.49, and 0.54 respectively).

Table 62: Average Ce/Ce* values and Eu/Eu* values for hydrothermal sediments M3 and M4, and Si-Fe cap Units A-C

	Average Ce/Ce*	**Average Eu/Eu***
Unit M3 (n = 13)	0.48	9.29
Unit M4 (n = 3)	0.51	15.25
Unit A (n = 4)	0.57	21.46
Unit B (n = 20)	0.60	18.76

Unit C (n = 5)	0.65	9.77

These four samples (highlighted by circles Figure 125) were broadly comparable with the average Ce/Ce* values of the hydrothermal protoliths Unit M3 (average Ce/Ce* = 0.51), and Unit M4 (average Ce/Ce* = 0.55), with the underlying sample at each location having less negative Ce/Ce* values (Unit A – Ce/Ce* = 0.63, and Unit B and the MIR Zone Ce/Ce* = 0.57 and 0.62).

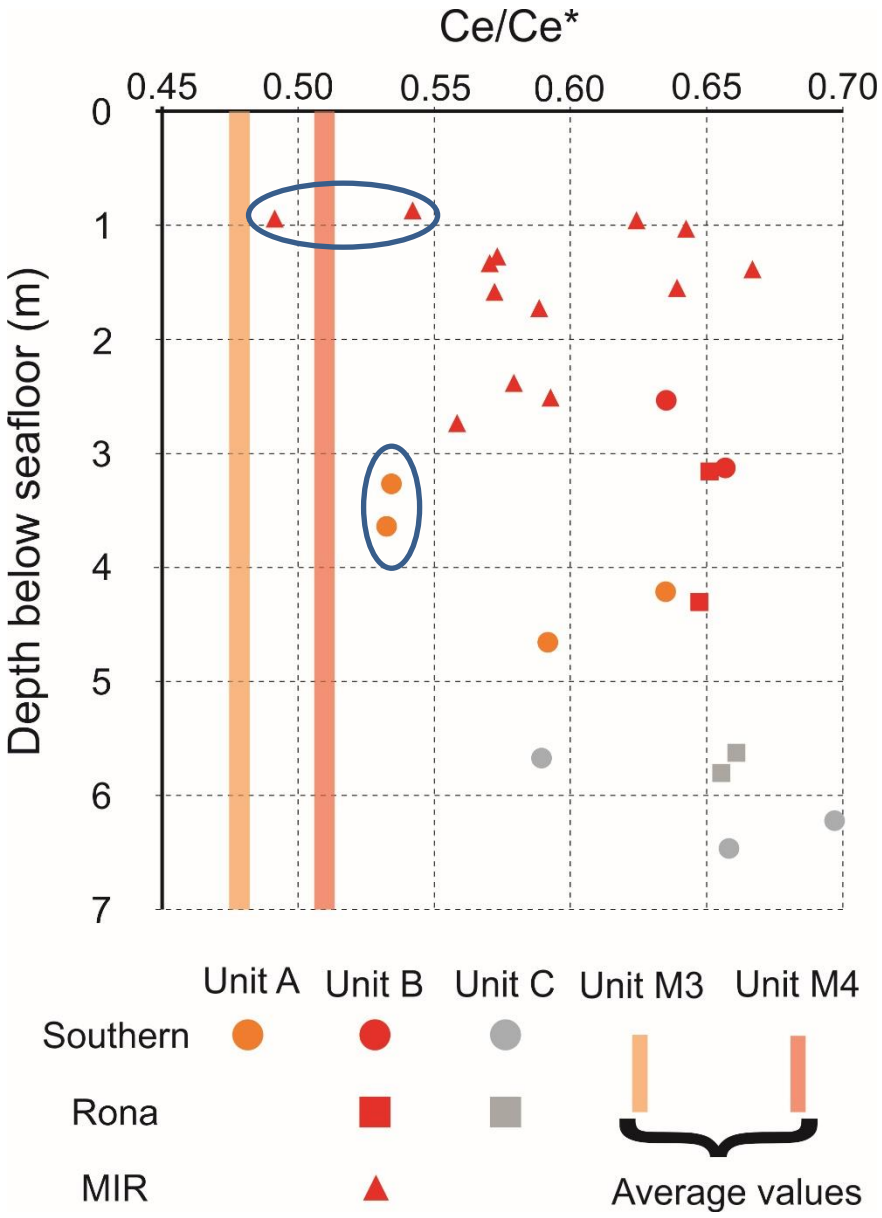

Figure 125: Ce/Ce* values of all Si-Fe samples compared with average Unit M3 and M4 hydrothermal sediment values

This variation in Ce/Ce* can be interpreted as either increased interaction with seawater after formation (i.e. fluid interaction from above the cap), or is a function of hydrothermal fluid interaction during silicification (i.e. fluid interaction from below) as a result of the hydrothermal activity, and possible silicification. As seawater ingress is typically passive, and limited to downward

diffusion into the sediment pile, there is likely no persistent seawater circulation mechanism enabling replenishment of a seawater REE source at depth. It is therefore more likely that the lessening of the Ce/Ce* negative anomaly observed in the Si-Fe cap compared to Units M3 and M4, is a function of the hydrothermal fluid influence during silicification (rather than higher seawater influence), supporting the textural and mineralogical evidence presented in Chapter 5.

6.5 Discussing the eH, pH, and temperature changes during the formation of the Si-Fe cap

The Si-Fe capping materials share striking similarities with overlying hydrothermal sediments, and thus it is interpreted that these textures, and iron oxide mineralogy, are inherited from a hydrothermal sediment protolith. This is generally supported by the interpretation that the Ce/Ce*anomaly is partially inherited, but influenced by hydrothermal fluids, from the sediments.

The main difference is the silica concentrations with the Si-Fe cap rock being ~ 30 to 60 wt% higher in silica than the hydrothermal sediments. This significant enrichment of silica results in the general decrease in all major and trace element concentrations, but it is not clear whether this is due to mobilisation by hydrothermal fluids, or just a simple dilution by the significant silica addition. The alteration of the Ce/Ce* anomaly during silicification implies that there may be some element mobilisation during silicification.

In order to investigate what, if any, elements have been mobilised during silicification, the geochemistry of both hydrothermal sediments and Si-Fe cap samples are compared. To negate the silica dilution problem, silica is 'removed' from the analyses and other elemental concentrations recalculated without silica present. All elements analysed in both sediments (Dutrieux, 2019) and the Si-Fe cap Units were converted to ppm concentration (and to elements from elemental oxides where necessary), then converted using the following formula:

$$'Silica\ free'elemental\ value\ (ppm)\ \frac{Concentration\ of\ element\ (ppm)}{Total\ concentration\ of\ all\ elements\ without\ silica\ (ppm)}$$

This was undertaken on average concentrations of hydrothermal sediment Units M3 and M4, and Si-Fe cap Units A, B, and C. To assess elemental mobility the Si-Fe cap samples were normalised to the corresponding interpreted hydrothermal sediment protolith (i.e. Unit M3 for Unit A, and Unit M4 for Units B and C).

If elemental concentrations have decreased due to dilution only (as a result of silicification of hydrothermal sediments) then 'silica free' values normalised to the sediment would be the same

(i.e. = 1). If elements have been mobilised and lost with respect to sediment material then the normalised values would be < 1, and if enriched by the altering fluids values would > 1 (Figure 126).

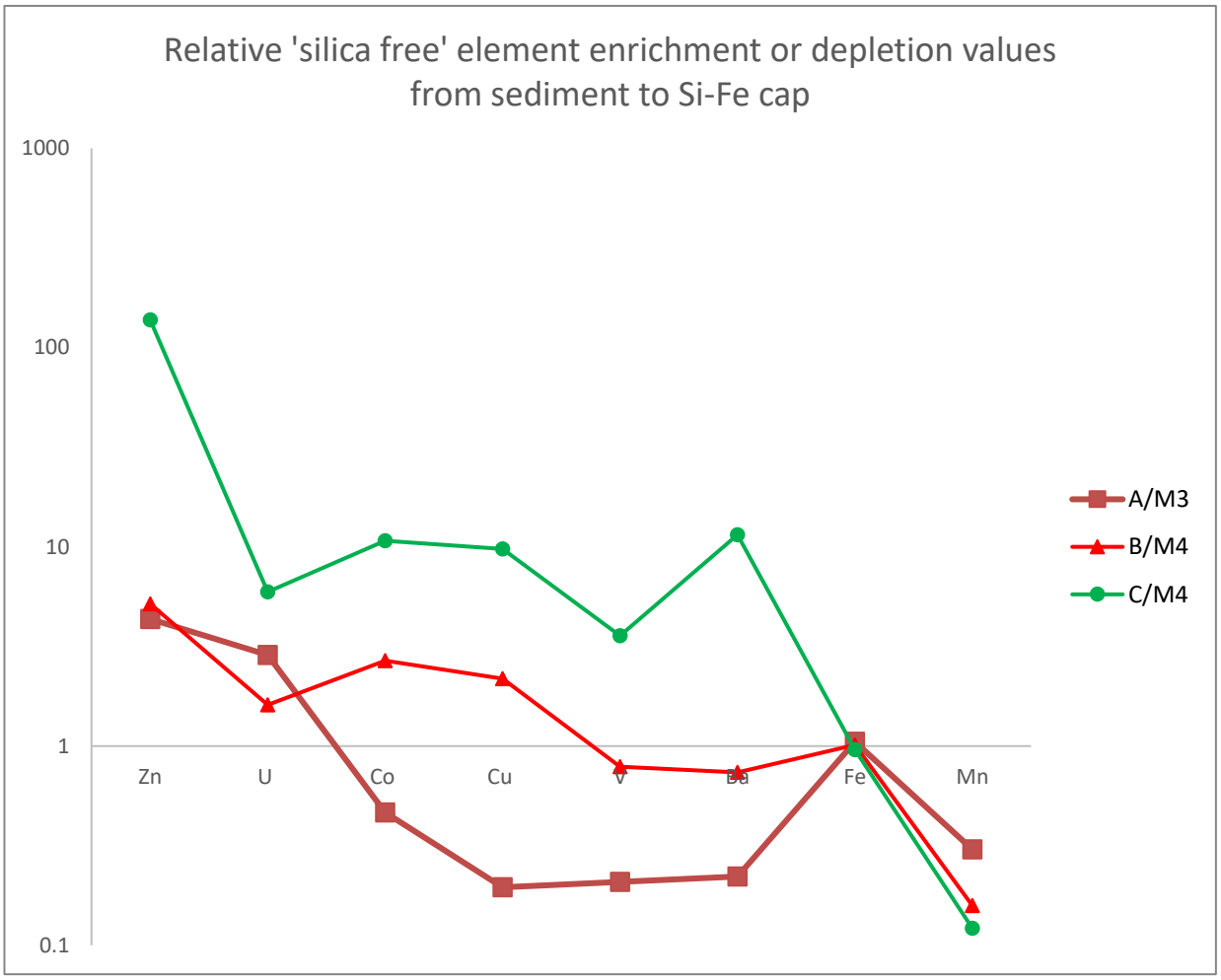

Figure 126: Relative enrichment or depletion plot for Si-Fe cap vs sediment protolith. Unit A vs Unit M3, Unit B vs Unit M4, Unit C vs Unit M4. Values < 1 are depleted with respect to the sediment protolith, values > 1 are enriched with respect to the sediment protolith. Unit A = 4 samples, Unit B = 21 samples, Unit C = 5 samples.

Out of the range of elements analysed in both hydrothermal sediments and the Si-Fe cap, several elements are known to be predominantly controlled by redox reactions and/or pH change in hydrothermal environments (i.e. Zn, Co, Cu, U, Fe, Mn, V). Elements such as Ba are commonly enriched in hydrothermal fluids and as such could indicate hydrothermal influence (i.e. barite production).

Zn and U are both enriched in all Si-Fe cap Units when compared to their respective hydrothermal sediment protoliths implying that the incoming fluids are Zn- and U-rich throughout the Si-Fe cap.

Iron remains near constant throughout the silicification process but shows a slight enrichment in Unit A (1.05), no change in Unit B (1.01), and a slight decrease in Unit C (0.96). Mn is mobilised in all Si-Fe cap samples. Co and Cu are depleted in Unit A, and enriched in Units B and C. V and Ba are depleted in Units A and B, and enriched in Unit C.

6.5.1 Evidence of redox conditions during silicification from element mobilisation

6.5.1.1 Trace elements

The consistency of iron content from hydrothermal sediments to Si-Fe cap material shows that the binary relationship between Si and Fe is predominantly a function of silica dilution, and that Fe is not significantly mobilised during silicification.

Mn is consistently depleted in all three Si-Fe Units of the cap, which is indicative of reducing conditions. Mn is very mobile under reducing conditions, and can be mobilised in sub-oxic conditions, rather than fully anoxic conditions (Burdige, 1993). This indicates that the fluids that silicified the cap are likely to be reducing, throughout the silicification process. This interpretation is supported in part by the depletion of other redox sensitive elements Co, Cu, in Unit A, and V in Units A and B. In Units B and Co and Cu are enriched with respect to the sediment protolith, implying accumulation within the cap. The presence of low quantities of sulphide grains (typically pyrite) within Unit B samples, supports the idea that reduced hydrothermal fluids have influenced the Unit. Accumulation of Cu and Co within Unit B could be attributed to lattice substitution of Cu^{2+} and Co^{2+} for Fe^{2+} in pyrite, a common process under reducing conditions and low temperatures (Stockdale *et al.*, 2010), and interpreted to be occurring in the active TAG mound (Grant *et al.*, 2018)

In Unit C, Co, Cu, and V are all enriched from the hydrothermal sediment protolith, whereas Mn is depleted. This trend along with the range of sulphides (pyrite/marcasite, chalcopyrite, and sphalerite) across Unit C samples supports the idea that Cu, Co can be substituted for iron in sulphides, and V can be potentially absorbed onto the surface of sulphides (Grant *et al.*, 2018) explaining the enrichment. Therefore the combined transportation of redox sensitive elements, and presence of sulphides supports the continued influence of reducing fluids in Unit C.

To test the theory that Co and Cu are associated with the formation of sulphides, LA-ICP-MS data has been obtained from sulphides in Units B and C (See Chapter 4 for methodologies, and appendix for full data set). This data was compared to LA-ICP-MS analysis from the literature, pyrite from surface samples from the TAG hydrothermal field (Keith *et al.*, 2016) and chalcopyrite and sphalerite from the Broken Spur hydrothermal field (Bogdanov *et al.*, 2008) in Table 63.

Table 63: Transition elements in sulphides from Units B and C of the Si-Fe cap rock, and comparable literature data from TAG surface samples and Broken Spur (basalt hosted MAR SMS deposit)

		Unit B	**Unit C**	**TAG surface samples**	**Broken Spur**
Pyrite/Marcasite	Cu (ppm)	13800$^{=}$ (n=36)	5940$^{=}$ (n=97)	483^{+} (n= 113)	730$^{+=}$ (n = 14)
	Co (ppm)	2.2$^{=}$ (n=36)	232.0$^{=}$ (n=97)	269$^{=}$ (n=61)	191$^{+=}$ (n =14)
	Zn (ppm)	96.0$^{=}$ (n=36)	3200$^{=}$ (n=97)	219$^{=}$ (n=61)	6814$^{+=}$ (n = 14)
	V (ppm)	3.3$^{=}$ (n=36)	44.1$^{=}$ (n=97)	-	1$^{=}$ (n=9)
Chalcopyrite	Cu (wt%)	-	33.1* (n=4)	-	31.9$^{+=}$ (n=28)
	Co (ppm)	-	2.5$^{=}$ (n=17)	-	181.1$^{+=}$ (n=28)
	Zn (ppm)	-	44.2 (n=17)	-	885.2$^{+=}$ (n=28)
	V (ppm)	-	1$^{=}$ (n=17)	-	< 1$^{=}$ (n=3)
Sphalerite	Cu (ppm)	-	400$^{=}$ (n=15)	-	449$^{+=}$ (n=30)
	Co (ppm)	-	0.07$^{=}$ (n=15)	-	13.5$^{+=}$ (n=30)
	Zn (wt%)	-	54.9* (n=34)	-	45.0$^{+=}$ (n=30)
	V (ppm)	-	16.7$^{=}$ (n=34)	-	< 1$^{=}$ (n=3)
* = used as internal standard for LA-ICP-MS (concentration data from SEM EDS analysis), $^{=}$ = LA-ICP-MS data only, $^{+}$ = data from EMPA analysis, $^{+=}$ = data from combined LA-ICP-MS and EMPA.					

In general Cu in pyrite is much higher than the comparative TAG surface and Broken Spur pyrite samples, which supports the idea that Cu is substituting into pyrite in both Unit B and Unit C samples. Cu in sphalerite is similar to sphalerite from Broken Spur, implying no enrichment in Cu with respect to other surface sulphides.

V in pyrite is enriched (by a factor of ~ 3) in Unit B with respect to Broken Spur samples, implying that the adsorption of V onto rare pyrite grains in Unit B may help explain the decrease in V depletion between Units A and B. Both pyrite and sphalerite in Unit C samples are significantly enriched in V when compared to Broken Spur samples (by a factor of ~ 44 and 16 respectively) and likely account for the partial enrichment of V in Unit C. Chalcopyrite in Unit C has a similar V

concentration, lower than pyrite and sphalerite in both Units implying that V does not adsorb onto the surface of chalcopyrite in this Unit.

Pyrite from Unit B, and chalcopyrite and sphalerite from Unit C all show significantly lower Co concentrations than the comparable sulphides from TAG surface samples and Broken Spur (~200 times lower). This implies that Co is not substituting into pyrite in Unit B samples, nor chalcopyrite and sphalerite in Unit B samples. Pyrite in Unit C can also be separated into three different samples, two with low Co (050RD/P11, and 057RD/P11 < 1 ppm), but the third (Co ~ 700 ppm) contains significantly more cobalt than other pyrite in the Si-Fe cap, and pyrite from the other studies of surface material (~ 3 times more than TAG pyrite). This implies that Co does substitute into pyrite in the Si-Fe cap, but may not have been observed or analysed in any other samples.

6.5.1.2 REEs

Mobilisation of redox sensitive trace elements, as discussed in the previous section, implies that the silicifying hydrothermal fluids were reducing. This implies a distinct change in redox conditions from 'oxidised' sediments to the silicified Units. REE patterns in both the hydrothermal sediment protolith and Si-Fe cap rocks further confirm this redox environment change.

The strong positive Eu/Eu* values, weak negative Ce/Ce* values, and enrichment of HREEs in hydrothermal sediments protolith can be explained by variable influence of hydrothermal fluids, and less influence from seawater, under oxidising conditions. All Si-Fe cap samples have lower total REE concentrations (average TREEs between ~2000 and 3000 ppb for Units A-C) than the hydrothermal sediments (average TREEs ~12000 ppb and ~10000 ppb for Units M3 and M4 respectively), implying that reducing fluids have mobilised REEs during silicification of the Si-Fe cap.

REEs are interpreted to be preferentially mobilised in acidic and reducing hydrothermal fluids preferentially as SO_4 complexes, then as chloride complexes, or as a 'free' REE^{3+} ions (Michard *et al.*, 1993; Haas *et al.*, 1995; Bau, 1999; Van Gosen *et al.*, 2017). Based upon the redox sensitive trace elements, the main silicifying fluids of Units A and B are interpreted to be reduced and sulphur poor and/or sulphur limited. Therefore dissolved REEs are interpreted to be either chloride complexes or free ions. The presence of sulphides in Unit C clearly indicates interaction with a reduced sulphur rich fluid, and also coincided with the lowest total REEs of the Si-Fe cap. This supports the interpretation that early silicifying fluids are sulphur poor, as total REEs would likely be low as they would have been leached by SO_4 complexes, as shown by the transition from hydrothermal sediment to Si-Fe cap rock. Experimental work implies that under acidic conditions LREE chloride complexes are more stable than HREE chloride complex (Haas *et al.*, 1995), which could provide a mechanism as to why the LREEs are depleted throughout the Si-Fe cap relative to Units M3 and M4.

When REE profiles are normalised to their respective hydrothermal sediment protolith the pattern of REE depletion is similar between all Units with LREEs and HREEs being more depleted than the MREEs (Figure 127). Only Eu shows variation in the degree of depletion, with Eu values in Units A and B being significantly less depleted than Unit C material. In general REEs are trivalent, however, at low to moderate hydrothermal temperatures (< 250˚C) Eu is mixed Eu^{2+} and Eu^{3+}, and above 250˚C is only stable as Eu^{2+} (Sverjensky, 1984). However, divalent Eu has a stable chloride complex, and is more soluble than trivalent REEs (Sverjensky, 1984), therefore at low temperatures Eu^{2+} would be preferentially mobilised over Eu^{3+} or other REE^{3+} ions. Theoretically, the Eu^{3+} ions should behave the same as the other REE^{3+} ions, so if anything Eu should be more depleted in the Si-Fe cap (with respect to the sediments). The comparison with REE plots implies the opposite is happening, with the exception of Unit C samples, where the presence of sulphides indicates that the fluids may be > 250˚C. Based on Figure 127, it seems that Eu is being mobilised to a lesser degree than all other REEs in Units A and B, but not in Unit C. It is difficult to explain this pattern of Eu, but the comparative lack of depletion in Units A and B, compared to C, explains the variation in Eu/Eu* values between the three Units.

MREE enrichment patterns have been observed when conducting leaching experiments associated with acid mine water, implying that MREEs are preferentially adsorbed onto iron oxide/oxyhydroxides over HREEs and LREEs (Worrall and Pearson, 2001), providing a potential mechanism for MREE stabilisation where both HREE and LREEs are mobilised (as shown in Units A and B in Figure 127.

Figure 127: Depletion plot of REEs when normalised to the interpreted hydrothermal sediment protoliths. Unit A = 4 samples, Unit B = 20 samples, Unit C = 5 samples.

6.5.2 Evidence of fluid pH during silicification

6.5.2.1 Trace elements

Zn and U present the most paradoxical elemental changes from sediment to Si-Fe cap. U is typically mobilised in highly oxidised fluids, whereas Zn is mobilised in reduced fluids. Zn would be expected to be mobilised or enriched by the same mechanisms as redox sensitive elements (i.e. Cu, Co, V), but it is consistently enriched in all three Units. The enrichment in Unit C can in part be explained by the presence of sphalerite. However, in Units A and B, no sphalerite is observed. The decoupling of Zn from redox sensitive elements (i.e. Cu, Co, V) could be explained by the pH of the silicifying fluids. In SMS deposits, 'zone-refining' processes, whereby Zn is mobilised and Cu is not, are attributed to a change in pH from ~ 3.35 to ~ 3 (James and Elderfield, 1996). Therefore this could imply that the silicifying fluids were typically pH of ~ 3, and the variation between Zn and the other similar redox sensitive elements could be temperature controlled, rather than pH controlled. However, this could also be a function of ligand complexation, Zn is preferentially complexed by chloride ions at high and low temperatures in high-salinity fluids over sulphide complexing (Zhong et al 2015).

U can be mobilised in reducing conditions at moderate temperatures (100-200°C), in low pH (<3 conditions) by chloride complexing (Bastrakov *et al.*, 2010). This supports the interpretation that the reducing fluids are likely pH≤ 3, enabling both U transport, and selective Zn transport over Cu.

Assuming the silicifying fluids are reduced and typically pH ≤ 3, some kind of physico-chemical change must occur within Unit A to enable accumulation and enrichment of both Zn and U. The presence of sphalerite can account for the enrichment of Zn in Unit C, however the lack of sphalerite and lack of covariance between Zn and Fe_2O_{3T} and SiO_2, implies there is not obvious mineralogical control on Zn in Units A or B.

Depending on pH and redox controls, U can be adsorbed onto the surface of iron oxyhydroxides (Waite *et al.*, 1994), sulphides (Wersin *et al.*, 1994; Grant *et al.*, 2018), or can be absorbed into silica gels (Bastrakov *et al.*, 2010). U can be adsorbed onto pyrite or iron oxyhydroxides at around pH 5 (Waite *et al.*, 1994; Wersin *et al.*, 1994), which is significantly higher than the pH <3 needed to mobilise U under reducing conditions. No significant covariance exists between U, SiO_2, Fe_2O_{3T} or SO_3. However, the two samples with the highest U concentrations have the highest SO_3 concentration and contain sulphides (Unit C samples from Rona Mound). It is therefore likely that a combination of these adsorption processes contribute to the enrichment of U in the Si-Fe cap, implying a change in pH enabling U adsorption.

6.5.2.2 REEs

The 'low' enrichment of LREEs in the hydrothermal sediments could be interpreted as a function of preferential REE adsorption onto iron oxides/oxyhydroxide. In oxidising conditions (i.e. during the formation of the iron oxide/oxyhydroxide sediments), REEs are adsorbed onto the surface of the iron oxide/oxyhydroxides (Worrall and Pearson, 2001, Davidson *et al.*, 2001). The likely source of these REEs are hydrothermal fluids (hence the strong 'inherited' Eu/Eu* anomaly), with the REEs being adsorbed onto the surface of iron oxides/oxyhydroxides when the hydrothermal fluids interact with oxygenated seawater.

Differential adsorption of LREEs over HREEs occurs at moderate to low pH (~4-6), where HREEs are preferentially adsorbed over LREEs, LREEs are typically not absorbed below pH 4 (Liu *et al.*, 2017). This would require a pH change from typical hydrothermal fluids (i.e. from ~ pH 3 (James and Elderfield, 1996) to pH > 4), to result in a degree of LREE adsorption. Differential absorption from a fluid that is enriched in LREEs and HREEs, could potentially explain how a weakly enriched LREE signature can be obtained from an enriched LREE fluid source, implying a pH control of the fluids between pH4 and 8.

6.5.3 Evidence of hydrothermal fluid influence during mass transfer?

Barite ($BaSO_4$) is a common mineral associated with hydrothermal activity, often interpreted to precipitate from a Ba-rich fluid upon interaction with seawater sulphate (Paytan *et al.*, 2002; William *et al.*, 2016). No barite was identified in the Si-Fe cap samples but barite was observed in Unit M3 implying that Ba rich fluids have been generated at Southern Mound. Ba is depleted in Units A and B, but enriched in Unit C in comparison to the hydrothermal sediments. The 'depletion' in Unit A can be explained as a function of Ba mobilisation during the transition from sediment to Si-Fe cap, or an artefact of localised Ba enrichment from the Unit M3 sediment. Theoretically, $BaSO_4$ would be dissolved by reduced Ba-undersaturated fluids, but the low reactivity may limit this reaction (Jamieson *et al.*, 2016). In Unit C enrichment in Ba could be an indicator of elevated dissolved Ba within the late-stage, sulphur rich, reduced fluids.

6.5.4 Si-Fe cap formation temperatures

The Si-Fe cap is interpreted to be a product of infusion into the unconsolidated Fe-rich material by reduced, siliceous hydrothermal fluids with variable sulphur contents. Based upon evidence from the literature and the dominance of silica minerals the cap is interpreted to be a function of low temperature hydrothermal activity, but the presence of chalcopyrite in Unit C, also implies some high temperature hydrothermal influence.

A combination of oxygen stable isotopic investigation and sphalerite geothermometry is used to identify the formation temperatures of the silica phase, the iron oxide phase, and the sulphide phase throughout the Si-Fe cap. The temperature of formation of the iron oxide phases might be inherited from any protolith, which is already shown to be the Fe-oxyhydroxide sediments above the Si-Fe units. The temperature of the siliceous fluids and the iron oxide fraction can be derived from the $\delta^{18}O$ value of the Si-Fe material. However, the relatively simple mineralogy of iron oxide (haematite/goethite) and silica (opal-CT/quartz), the microcrystalline nature of the samples, and the opaque behaviour of iron oxides requires the iron oxide and silica fractions to be separated before analysis (See Chapter 4). Oxygen isotopic investigation of the silica separate ($\delta^{18}O_{SIL}$) and the bulk sample ($\delta^{18}O_{BULK}$), enables calculation of the iron oxide oxygen isotopic fraction ($\delta^{18}O_{HAE}$), and subsequent mineral formation temperature calculations are attempted on both $\delta^{18}O_{SIL}$ and $\delta^{18}O_{HAE}$. Sphalerite geothermometry is applied to the two samples of Unit C material from Southern and Rona Mounds to constrain the formation temperatures of the sulphide phase.

Combining the two methods would help elucidate the range of fluid temperatures involved in the formation of the Si-Fe cap and provide temperature constraints for the hydrothermal fluids involved in forming the Si-Fe cap

6.5.4.1 Silica formation temperatures

Four leached samples of the Si-Fe cap rock were acquired from Unit A, three from Unit B, and three from Unit C from Southern Mound, and analysed for $\delta^{18}O$. Two Unit A samples, and a Unit C sample were repeated to check for natural variation (all summarised in Table 64).

Table 64: Summary of $\delta^{18}O_{SIL}$ values and estimated silica formation temperatures from Southern Mound. Calculations have been made assuming equilibrium with both seawater (SW), and hydrothermal fluids (HF).

					Kita (T˚C)		Sharp (T˚C)	
		n	$\delta^{18}O_{SIL}$	σ	SW	HF	SW	HF
Unit A	050RD/P3	5	26.1	1.6	66.9	76.8	70.3	80.1
	050RD/P5	1	25.9		70.0	78.0	71.4	81.3
	050RD/P7	3	27.3	1.4	60.3	69.6	63.9	73.2
	050RD/P8	1	27.4		59.8	69.1	63.4	72.5
Unit B	022RD/CC	1	18.2		121.9	137.8	125.1	141.0
	031RD/109/CC	1	19.2		113.5	128.2	116.6	131.4
	031RD/CC/007	1	19.0		115.1	130.0	118.3	133.3
Unit C	050RD/P11	1	18.9		115.9	131.0	119.1	134.2
	050RD/P12	1	14.8		155.6	176.0	159.2	180.3
	050RD/P13	3	17.7	0.3	126.4	142.8	129.6	146.1

The estimated formation temperatures for Unit A are significantly lower than both Units B and C, with one sample from Unit C (050RD/P12) showing the highest estimated formation temperatures, up to ~ 120˚C hotter than Unit A. The repeated samples yielded similar temperatures, showing that the data are repeatable and representative of the units.

On average, this implies three different formation temperatures for the three Si-Fe Units at Southern Mound: Unit A between ~60 and 80˚C, Unit B between ~110 and 140˚C, and Unit C between ~115 and 180˚C. These three formation temperature differences between Units appear to correlate with the observed mineralogy presented earlier showing that higher temperature fluids have interacted with Unit B and C (presence of quartz and sulphides), but not Unit A (no sulphides, presence of a more immature opal-CT quartz assemblage).

Two samples of Unit B and two samples of Unit C samples from Rona Mound were analysed (Table 65). In contrast to Southern Mound samples, Unit B material recorded higher temperatures (maximum estimated temperatures of ~139 and 158˚C) than Unit C material (maximum estimated temperatures of ~117 and 132 ˚C).

Table 65: Summary of $\delta^{18}O_{SIL}$ values and estimated silica formation temperatures from Rona Mound. Calculations have been made assuming equilibrium with both seawater (SW), and hydrothermal fluids (HF).

					Kita (T˚C)		Sharp (T˚C)	
		n	$\delta^{18}O_{SIL}$	σ	SW	HF	SW	HF
Unit B	057RD/P2	2	18.4	0.1	120.2	135.8	123.3	139.0
	057RD/P3-8	3	16.6	1.0	136.8	154.5	140.0	158.1
Unit C	057RD/P10	2	20.9	0.9	100.2	113.5	103.4	116.6
	057RD/P11	1	19.1		114.3	127.0	117.4	132.4

Unit B samples from Rona Mound were on average higher temperature (~120˚C to 160 ˚C), but Unit C samples were lower temperature (~100 to 130˚C), when compared to Southern Mound. It is interesting to note that at 050RD/P12 (Unit C at Southern Mound) has one of the highest silica formation temperature estimates (~155 to 180˚C), whereas a sample from Unit C at Rona Mound has one of the lowest silica formation temperatures (~100 to 115˚C).

Seventeen samples of Unit B from MIR zone were analysed, with extracts from two samples repeated three times to test for variability (Table 66).

Table 66: Summary of $\delta^{18}O_{SIL}$ values and estimated silica formation temperatures from the MIR Zone. Calculations have been made assuming equilibrium with both seawater (SW), and hydrothermal fluids (HF).

					Kita (T˚C)		Sharp (T˚C)	
		n	$\delta^{18}O_{SIL}$	σ	SW	HF	SW	HF
Unit B	073RD/P1	1	20.1		106.8	120.2	109.4	123.4
	073RD/P6	1	21.2		98.8	111.9	102.0	114.9
	073RD/P7	1	20.1		106.8	120.2	109.4	123.4
	073RD/P9	1	20.3		104.8	118.7	108.0	121.6
	073RD/10	1	20.3		104.8	118.7	108.0	121.6
	073RD/P12	1	21.0		99.5	112.6	102.6	115.8
	073RD/P14	3	20.3	0.1	104.8	118.7	108.0	121.6
	076RD/P2	3	20.4	0.2	104.0	117.6	107.1	120.8
	076RD/P3	1	20.1		106.8	120.2	109.4	123.4
	076RD/P4	1	19.9		107.9	121.9	111.0	125.1
	076RD/P6	1	20.3		104.8	118.7	108.0	121.6
	073RD/P7	1	20.4		104.0	117.6	107.1	120.8
	073RD/P8	1	19.1		114.3	129.2	117.4	132.4

All samples analysed fell within a narrow temperature window, between ~ 98 and 130˚C, which is higher than Unit A at Southern Mound, broadly comparable with Unit B from Southern Mound and Unit C at Rona Mound, but lower than Unit C and Southern Mound and Unit B at Rona Mound (summarised in Figure 128). There is no correlation between formation temperature and Si:Fe ratio,

implying that the degree of silicification of any given sample is not dependant on the fluid temperature.

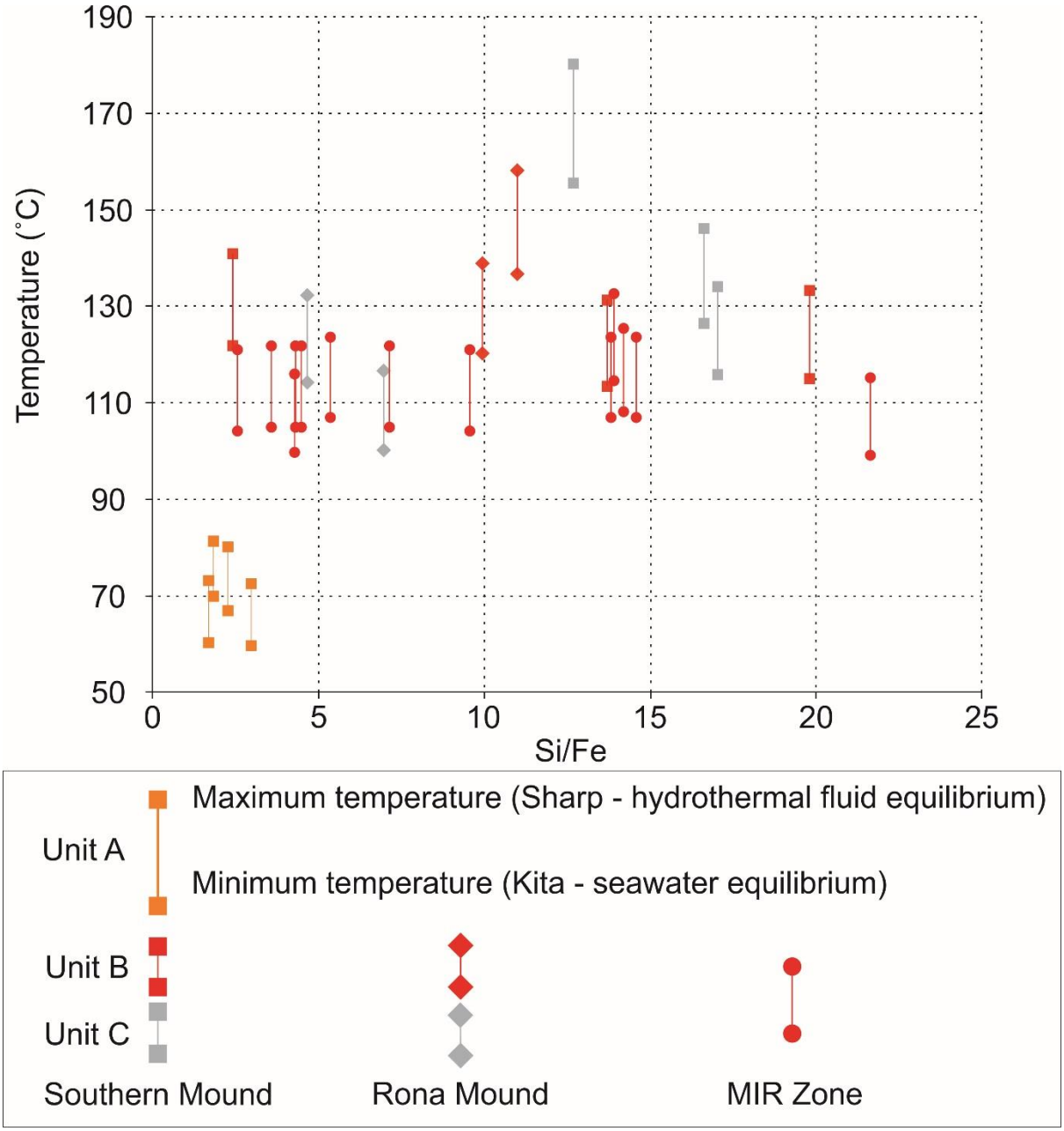

Figure 128: Maximum and minimum estimated silica formation temperatures for the Si-Fe cap units, colour denotes Unit A, B, or C, shape denotes Mound location (Southern Mound = square, Rona Mound = diamond, MIR Zone = circle).

6.5.4.2 Sulphide formation temperatures - sphalerite geothermometry

Sphalerite geothermometry is based on the principle that the Fe:Zn ratio of sphalerite is a function of formation temperature (See methodologies). Therefore estimation of the sulphide formation temperatures can be obtained by analysing the Fe:Zn ratio of sphalerite grains.

Sphalerite was typically observed in two Unit C samples, one from Southern Mound (050RD/P11) and one from Rona Mound (057RD/P11). Unit C at Southern Mound yielded 15 analyses from euhedral to subhedral sphalerite grains, which have typically grown as rims or inclusions to individual euhedral pyrite grains (Figure 129).

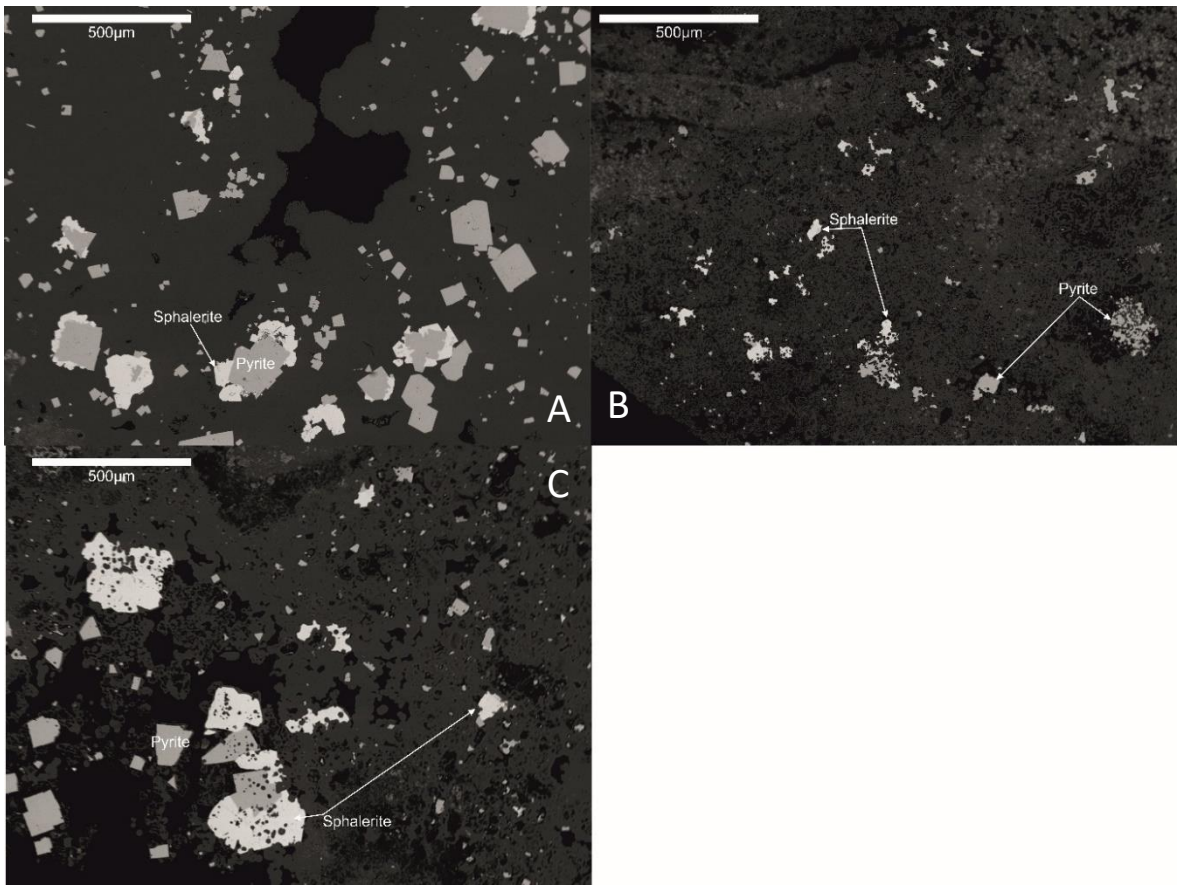

Figure 129: Backscatter SEM images of sulphides used for sphalerite geothermometry. (A) Unit C – Southern Mound late-stage sphalerite typically growing on subhedral to euhedral pyrite grains. (B) 'Area 1' – Unit C – 057RD/P11 – Rona Mound, Individual clusters of interstitial sphalerite and pyrite grains from Unit C – Rona Mound. (C) 'Area 2' – Unit C – 057RD/P11 - sphalerite as late-stage rims on pyrite and as individual grains.

The sphalerite rims have relatively consistent Fe:Zn ratios with ~ 2.6 wt% for Fe and ~ 3.5 wt% variation across all 15 analyses at Southern Mound, yielding calculated formation temperatures between ~400 to 425˚C, with an average temperature of ~ 417 ˚C (Table 67).

Two areas of sphalerite from the Unit C sample from Rona Mound (sample 057RD/P11) recorded different Fe:Zn ratios to Southern Mound Unit C. In general their Fe content was lower and their Zn content higher. The two different areas of sphalerite within the Rona Mound Unit C sample also showed slight variation in morphology. One area in the Rona Mound sample is dominated by individual interstitial sphalerite growth (Area 1), whereas the second area appears to be more

associated with pyrite, and exhibits both interstitial growth and growth as rims on pyrite (Area 2) (Figure 129).

The pyrite-free interstitial sphalerite grains (Area 1) have a higher Fe content and lower Zn content on average than the area with both pyrite and sphalerite (Area 2). Minimum Fe values and maximum Zn values are similar in both areas (Fe ~3.5-4 wt%, Zn, 61-62 wt%), but maximum Fe values and minimum Zn values vary between the two areas. Area 1 recorded maximum Fe of 15.73 wt% and minimum Zn or 53.66 wt%, and Area 2 recorded a maximum Fe value of 8.76 wt% and minimum Zn value of 59.22 wt%. These result in estimated sphalerite formation temperatures averaging ~400 ˚C in Area 1, and ~ 310 ˚C in Area 2 (summarised in Table 67).

Table 67: Fe, Zn, and calculated formation temperatures from sphalerite geothermometry, Unit C samples.

	Sample	**Southern**	**Rona**	**Rona**
		050RD/P11	**057RD/P11**	**057RD/P11**
			Area 1	**Area 2**
	n	15	9	10
Fe (wt%)	Avg	13.06	11.96	6.59
	Max	14.16	15.73	8.76
	Min	11.57	3.56	4.15
Zn (wt%)	Avg	52.74	53.66	59.22
	Max	54.55	62.22	61.19
	Min	51.04	48.09	56.55
Fe:Zn	Avg	0.25	0.22	0.11
	Max	0.26	0.25	0.14
	Min	0.23	0.07	0.07
Temperature (˚C)	Avg	417.67	398.68	312.74
	Max	426.83	421.63	337.28
	Min	401.53	284.1	283.6

6.5.4.3 Summary of silica and sulphide formation temperatures

Two clear observations are obtained from the estimated formation temperatures: 1) Silica formation temperatures are variable across all three Si-Fe Units with Unit A significantly lower than the other Si-Fe Units; and 2) Silica formation temperatures are significantly lower (≤180˚C), than even the lowest sphalerite formation temperatures (>280˚C) (See Table 68). This implies that there may be two separate temperature silicification events, and a third higher temperature sulphidation event.

Table 68: Average estimated formation temperatures from silica and sphalerite (T˚C). Values are calculated by averaging the maximum and minimum temperature values for each Unit and rounding to the nearest 10˚C.

	Southern Mound		**Rona Mound**		**MIR Zone**	
	Silica	**Sphalerite**	**Silica**	**Sphalerite**	**Silica**	**Sphalerite**
Unit A (n = 4)	~ 60-80	-	-	-	-	-
Unit B (n= 20)	~110-140	-	~120-160	-	~100-130	-
Unit C N = 5)	~115-180	~420	~100-130	~280-400	-	-

6.6 Summary

The geochemical characterisation of the Si-Fe capping Units has confirmed the mineralogical observations that this cap is a binary system, dominated by iron (i.e. Fe_2O_{3T}) and silica (SiO_2). The only other contribution from a major element is sulphur, which correlates with the samples where sulphide grains were observed throughout the Si-Fe cap.

The main conclusion of the physical characterisation of the Si-Fe cap is that the hydrothermal sediments are the protolith of the Si-Fe cap and that textures and iron oxide mineralogy is inherited from the sediments. Geochemical assessment is used to investigate the signatures that the silicifying fluids have imparted on the Si-Fe cap, including elemental mobilisation during silicification and investigation the eH, pH, and temperature conditions experienced by the Si-Fe cap.

Elemental transfer during the silicification of the cap has indicated that the silicifying fluids are reduced, resulting in the consistent depletion of Mn, and the variable depletion of other redox

controlled elements (including Co, Cu, and V). Mechanisms including adsorption onto the surface of sulphides, or lattice substitution of divalent Co and Cu for Fe in sulphides have been suggested for the enrichment of redox sensitive elements in Units B and C. LA-ICP-MS analysis of sulphide grains from within the Si-Fe cap concluded that the crystal lattice substitution of Cu^{2+} for Fe^{2+} can potentially account for the enrichment of Cu in Units B and C, despite reduced conditions, and the absorption of V onto the surface of sphalerite and pyrite can account for V enrichment in Unit C. However, significantly depleted Co values in both Unit B and Unit C sulphides with respect to other MAR SMS deposit surface samples implies that Co enrichment cannot be explained by lattice substitution. Total REE concentrations decrease from the hydrothermal sediments to the Si-Fe cap, implying mobilisation of REEs supporting the idea that the silicifying fluids were reduced.

Similar but paradoxical behaviour of Zn and U during silicification implies that the silicifying fluids were Zn- and U-rich and that the reduced fluids had to have been low to moderate temperature and pH<3 to enable preferential Zn mobilisation (over Cu), and mobilisation of U under reduced conditions. The lack of correlation of Zn and Fe_2O_{3T} or SiO_2 implies that Zn is not associated with either of the main constituents of the Si-Fe cap, and no clear accumulation mechanism for Zn is identified. Accumulation of U within the Si-Fe cap is thought to be potentially related to a pH change (to pH>3) where it can no longer be complexed by chloride, and can be absorbed onto the surface of sulphides, or be incorporated into silica gels. Assuming the black smoker fluids were pH of 3, then a black smoker:seawater fluid mixing ratio of <1:10 would be required to alter the pH from 3 to 4.

Evolution of the hydrothermal sediments can be seen through a plot of Fe_2O_{3T} (wt%) vs Eu/Eu* values (Figure 130, Figure 131). High iron contents and moderate Eu/Eu* values are characteristics of the REE sediments, where REEs are adsorbed onto the surface of iron oxides, preserving an Eu anomaly. As the sediments are silicified (Step 1) the reduced fluids mobilise REEs but some mechanism means that Eu is not as depleted as the rest, increasing the Eu/Eu* values. During the late-stage, sulphidation event (Step 2), iron oxides are reduced and no longer have REEs adsorbed to the surface, thus decreasing total REEs further, and mobilising Eu faster resulting in the decrease in Eu/Eu* to similar anomalies as the hydrothermal sediments, despite having ~ an order of magnitude less iron oxides, and iron.

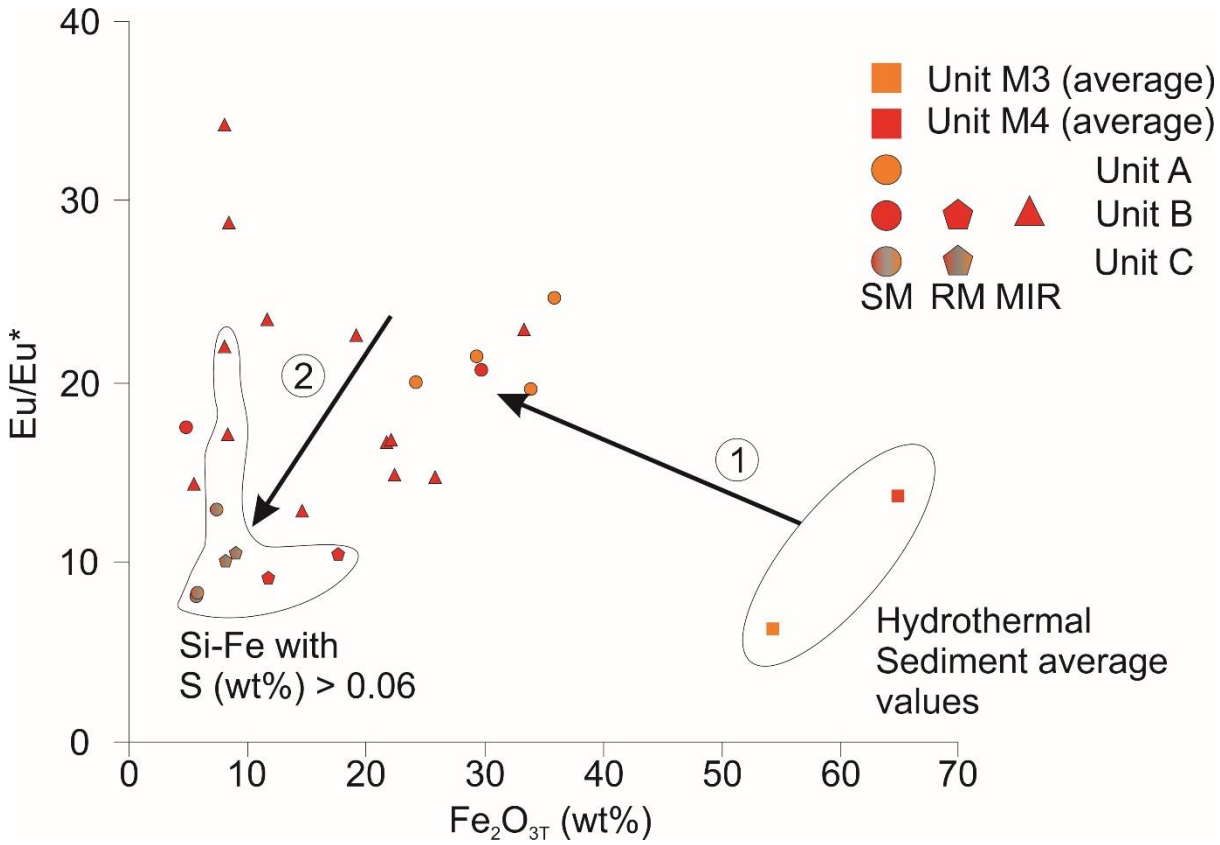

Figure 130: Fe_2O_{3T} (wt%) vs Eu/Eu*. Shows the evolution of Eu/Eu* values through silicification. Step 1 = silicification of hydrothermal sediments resulting in a decoupling of Eu versus other REEs. Step 2: Sulphidation, returning back to pre-silicification Eu/Eu* values, meaning Eu behaves in a similar way to other REEs. Thus resulting in a similar Eu/Eu* value to the sediments, but at an order of magnitude less Fe_2O_{3T} (wt%) and TREEs.

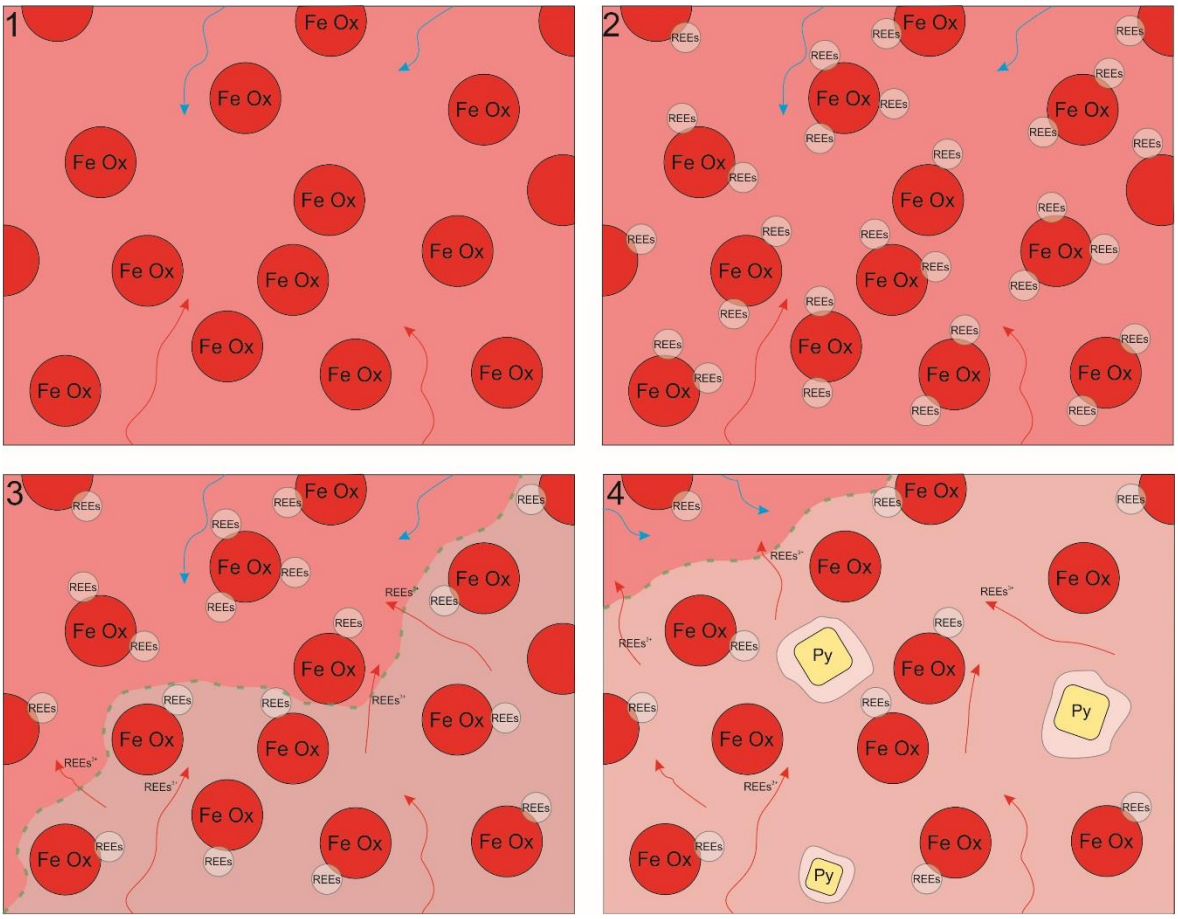

Figure 131: Schematic diagram of REE changes during silicification. 1 and 2) Early initial formation of iron oxides and adsorption of REEs onto the surface in the hydrothermal sediments. 3) Silicification results in the mobilisation of REEs by reducing fluids, but some still remain. 4) Iron oxides begin to be reduced into pyrite and so most REEs (including Eu) are released.

At Southern Mound, three different discrete formation temperatures are calculated for the silicification of Unit A, the silicification of Units B and C, and the sulphidation of Unit C (Table 68). This supports the mineralogical interpretation of multiple silicification generations, and a late-stage sulphidation event (See Chapter 5, summarised in Section 5.6). Rona Mound shows similarities with Southern Mound, and has two different silicification temperatures, and a higher temperature sulphidation event that clearly post-dates silicification (Section 5.5.2). Finally the MIR zone, has no real indication of a major late stage sulphidation event (only limited sulphidation (Figure 76, Section 5.4.2)), and oxygen isotopic constraints on a single silicification event, despite textural observations implying at least two stages of silicification, similar to Southern Mound.

The final stage, high temperature, sulphidation event evidenced in both the physical and geochemical characterisation of the Si-Fe cap, provides an insight into the potential impact that silicification could have on fluid flow through the SMS deposit. The fact that the sulphidation is only

limited to the deepest Si-Fe samples implies that it may have been physically constrained by the high silica content Si-Fe cap. This concept is tested in the following Chapter to try and constrain what effects the silicification can have on fluid flow.

Chapter 7 3D structure, porosity, and permeability

This chapter aims to investigate whether the Si-Fe capping lithologies, described here from the TAGHF, act as an impermeable boundary between the underlying massive sulphide material and overlying seawater, thereby acting to help preserve a seafloor massive sulphide ore body, especially in the early stages of burial. An approach is adopted here that acquires three-dimensional (3D) X-Ray CT scans of samples of the Si-Fe cap rock and from these volumes, calculates 3D parameters such as total porosity, connected porosity and permeability by simulating fluid flow through the material. By drawing on previous textural analyses Chapter 5, it is possible to assess changes in these parameters as silicification progressed, with a focus on the occurrence of 'late-stage' silica overgrowth related to the final stage of silicifying fluid ingress.

7.1 Introduction

7.1.1 X-Ray micro-computer tomography (micro-CT)

X-Ray micro-CT works by taking a series of two-dimensional (2D) X-Ray absorption images while rotating a sample by 360° about a vertical axis (Figure 132). Following collection of these data, a three dimensional (3D) volume can be reconstructed using the mathematical principals of tomography (Ketcham and Carlson, 2001). This volume is described by voxels (three dimensional equivalent of a pixel) where a greyscale value represents the X-Ray absorption value within the 3D volume (high values are represented as white, zero values as black). X-Ray absorption is controlled by the atomic density/thickness of the material being scanned, enabling the internal structure of the sample to be determined, provided the sample exhibits variably density.

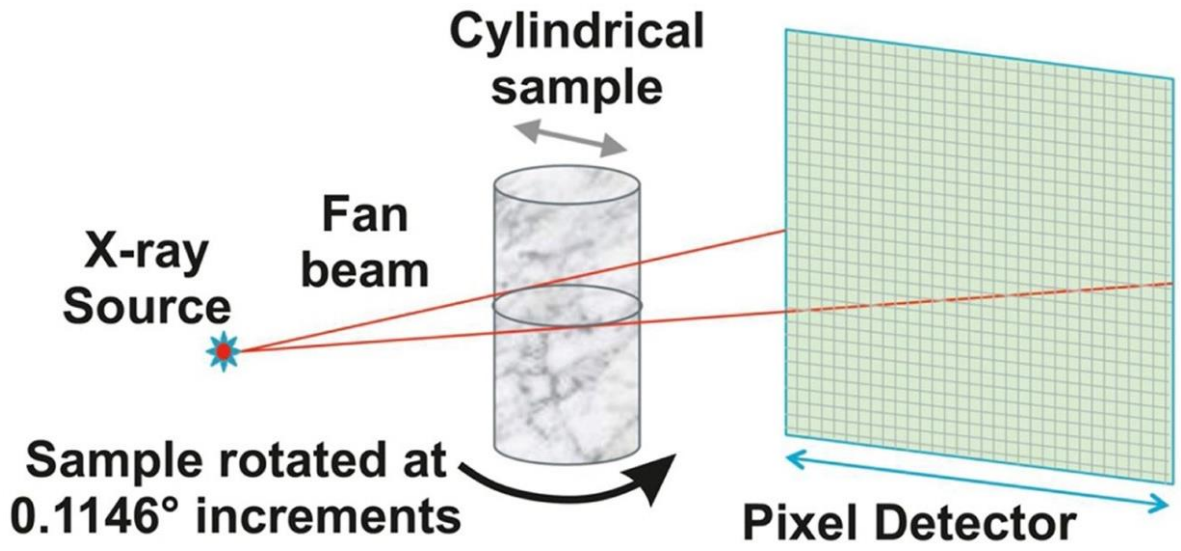

Figure 132: Diagram showing the method of micro-computer tomography (micro-CT) (Callow *et al.*, 2018)

X-Ray micro-CT scanning of the samples was undertaken to investigate the porosity and permeability of the core material and enable the modelling of simulated fluid flow through the imaged volumes (see Section 7.2.2). The scans also reveal the complex textures of the silica-iron materials in three dimensions, which is often difficult to observe in 3D from either hand specimens or thin sections alone.

Comprehensive study of the samples by microscopy, XRD, and SEM has helped identify the range of minerals within the samples of Si-Fe rocks and include: silica polymorphs (quartz, opal CT), iron oxide/oxyhydroxide (haematite, goethite), and a range of sulphides (pyrite, sphalerite, and chalcopyrite). Variation in the density and amounts of these minerals enables some distinction, at least between silica, iron oxide and sulphides within the core material (Table 69).

Table 69: Summary of the range of minerals in the Si-Fe cap Units and massive sulphide core samples with their respective densities

Mineral	**Formulae**	**Density (g/cm^3)**
Silica – Quartz	SiO_2	2.648
Silica – Opal CT	$SiO_2.nH_2O$	2.09
Iron Oxide – haematite	Fe_2O_3	5.3
Iron hydroxide – goethite	FeO.OH	3.3-4.3
Sulphide – pyrite	FeS_2	5.01

Sulphide – chalcopyrite	$CuFeS_2$	4.19
Sulphide – sphalerite	(Zn,Fe)S	4.2

The average density of silica (~2.3 g/cm^3, an average of quartz and opal-CT) is significantly lower than the average density for iron oxides (~4.7 g/cm^3, an average of haematite and goethite) and sulphides (~4.7 g/cm^3, an average of pyrite, chalcopyrite, and sphalerite); therefore, both macro crystalline sulphides and iron oxides show a density contrast with respect to silica. However, iron oxides are typically distributed within the silica as very fine (< 1µm) particles. This makes individual grains of iron oxide difficult to separate from silica due to resolution limitations, even with micro-CT scanners. This limitation still enables a differentiation between 'jasper' type material and pure silica. For example 'Jasper' material (ranging from ~60:40 to ~95:5 silica:iron) would show a proportional mixture of density contrast, i.e. a sample of 75:25 silica:iron oxide is likely to register as a material of ~3 g/cm^3, based upon the proportional densities. This assumes an even distribution of iron within the silica, which is typically observed, and that the iron oxides are present as grains that are below the resolution obtained by the CT scans.

7.1.2 Three dimensional characterisation

7.1.2.1 Unit A

Two samples of Unit A were scanned: 050RD/P3, and 050RD/P7. These two samples were considered to show the textural variability apparent in Unit A, with 050RD/P3 exhibiting more of a clast and matrix texture, where clasts are easily delineated, compared to 050RD/P7 where textures appear to be more 'massive'.

The variable density within Unit A material is interpreted to be down to the silica:iron oxide or oxyhydroxide ratios throughout the sample. No sulphides were observed in thin section, and no typical sulphide morphologies are observed as high density areas in the CT scans.

Although at the surface, 050RD/P3 appeared to be dominated by laminated clasts, CT scans show that this is only the case at the base and top of the sample. A large red clast (Figure 133) appears to be dominated by filamentous material with more visible pore space, including multiple tube-like voids running through at approximately 45˚ to the z-axis. These tube-like voids are easily identified in the CT scan by a ring of higher density (likely more iron oxide-rich) material surrounding the void space. Areas within this red haematite area almost resemble granular material.

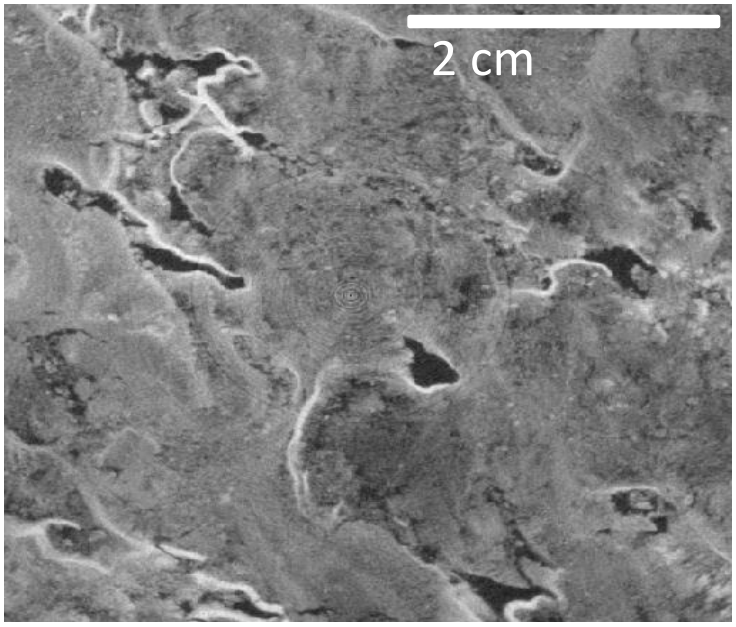

Figure 133: CT scan image of filamentous material a large red clast in Unit A - 050RD/P3 with open void/pore space 'tubes'. Highlighted in Figure 62, p.176

The rest of the sample is dominated by laminated fragments, which are tightly packed and have a much lower pore space density than the filamentous area. As observed in thin section laminated fragments are randomly orientated and show a wide range of sizes and shapes (and features such as desiccation cracks i.e. Figure 132). It is likely that some of the material precipitates in-situ, and other material is a result of mass wasting and accumulation of material, however, it is difficult to differentiate between these processes by looking at the fragments. Massive fragments are visible within the clast dominated area of the sample, but the resolution of the scans are not high enough to interpret any intraclast detail, unlike in thin section.

In comparison to 050RD/P3 the overall texture of 050RD/P8 is more similar to the filamentous red ‘area’ and it would be difficult to classify 050RD/P8 a breccia based on the three dimensional CT data. However some clast and granular material were observed throughout (< 5% of the sample).

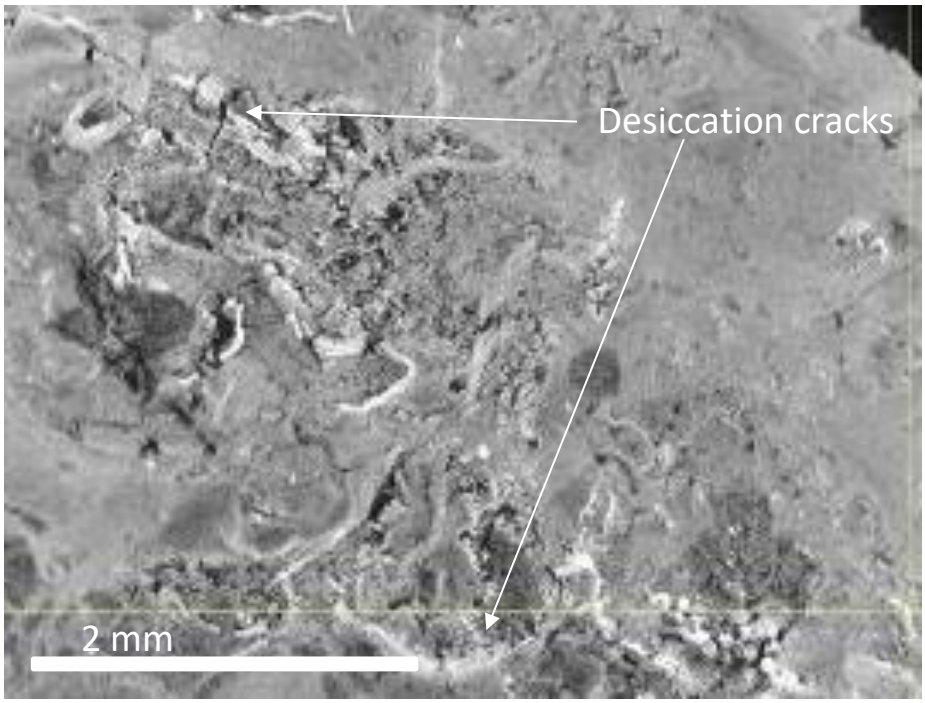

Figure 134: CT scan image of desiccation cracks preserved on the cut surface of 050RD/P3 core sample

Although the predominant texture of the non-clast material appears to be filamentous, there is significant variation of this material throughout the sample. Small enclaves or localised areas of filamentous growth can be delineated by a variable density contrast. Filamentous growth does appear to present some kind of ordering in places, with parallel and circular growth patterns observed in both thin section and in the CT scans.

7.1.2.2 Unit B

073RD/P6 shows a complex three dimensional structure with the core being dominated by massive jasper material, or by 'mesh-like veins' of jasper (Figure 135). In direct contrast to Unit A material, no visible laminated clasts or easily defined clast material can be observed in 076RD/P6. The massive areas of jasper are represented as a relatively homogenous density material. In contrast, the vein-like material forms a web or mesh like pattern, and often delineates void space and/or local areas of lower density material (likely more quartz dominated), or filamentous material.

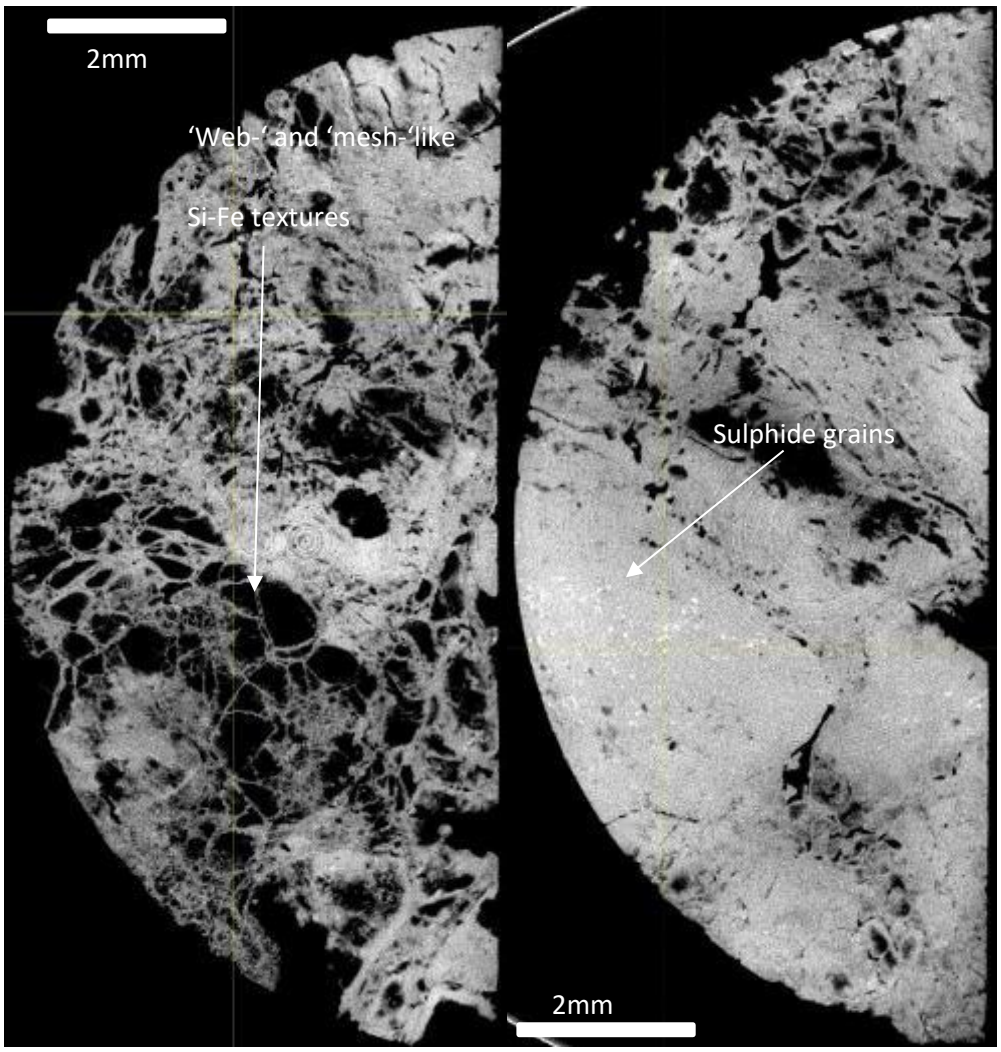

Figure 135: CT textural evidence from Unit B material (076RD/P6). (Left) 'Web-' and 'mesh-'like textures of Si-Fe material with a high degree of pore space (black). (Right) More homogenous Si-Fe material (grey) with faint sulphide grains also visible (white).

Voids delineated by vein-like textures are often subangular because of mesh or web-like vein intersections. Void space within the more homogenous jasper material appear more like intra-clast voids, or even desiccation cracks, which have been partially, potentially by recrystallisation or homogenisation of the material. Although they have little to no preferred orientation throughout the sample.

Fine-grained sulphides are interpreted to be present, observed as high density, subhedral grains. On first inspection they appear to be predominantly within massive jasper material, but they can be observed within the more vein network dominated area, but not within the 'vein' material.

073RD/P14 represents Si-Fe material which is a mixture of goethite and haematite, and in contrast to 073RD/P6 shows clear delineated, low density clasts, within a higher density matrix (Figure 136).

Clasts are both massive and laminated, and commonly have desiccation cracks. Massive clasts appear to have a speckled or granular texture on the CT scans, with high density material comparable with the matrix. Based upon the relative densities, it appears that the matrix is dominated by quartz and haematite, and the clasts are more quartz goethite rich, but it is interesting that the XRD results only show 1.2 wt% haematite.

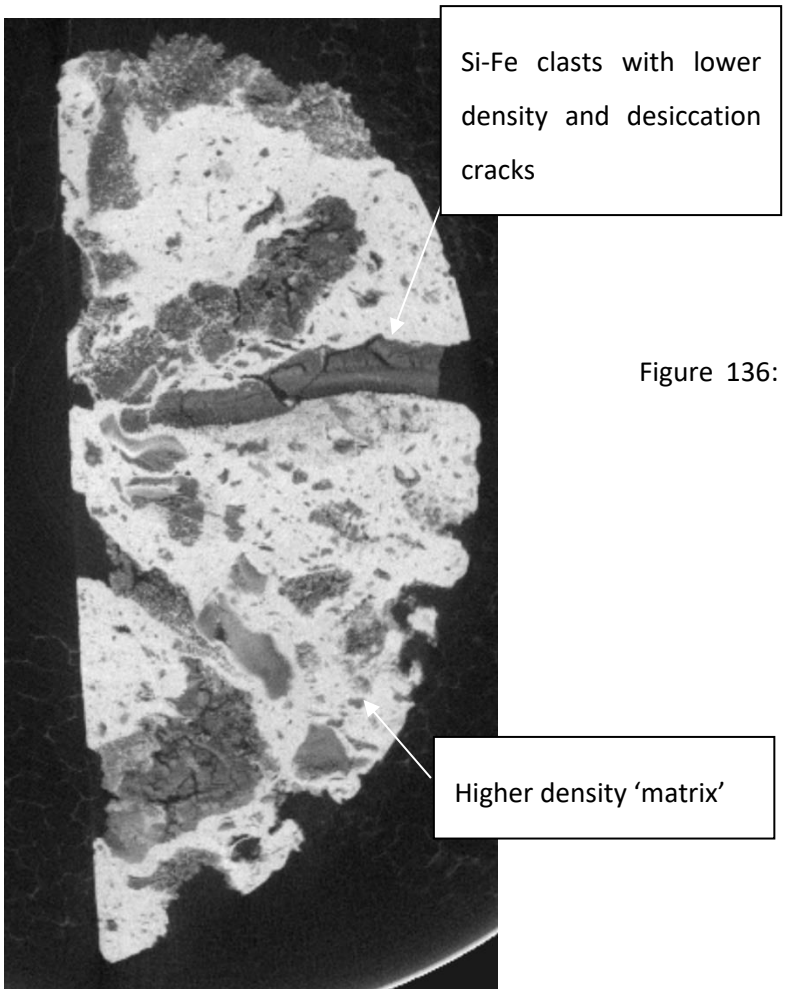

Figure 136: MIR Zone Unit B – 073RD/P14 mixed goethite and haematite rich Si-Fe sample with clear clast and matrix pattern

7.1.2.3 Unit C

050RD/P11 appears to show more textural similarities with Unit B material than Unit A. In general the core sample is a relatively homogenous density, with the exception of disseminated sulphides (Figure 137). Enclaves of sulphide rich material (i.e. grey silica) can be delineated by variable density. Porosity is present throughout, but typically in larger millimetre scale voids rather than fractures. An area of fractures is observed to be infilled with material of lower density than Si-Fe material, potentially unconsolidated sediment (based upon unsilicified sediments preserved in void space during cutting of the sample). Filamentous type structures are observed within the core sample, in particular a large ~ 5 cm diameter oval pattern of concentric filaments. This pattern is

partially obscured, likely by silica overprinting, and is only observed by the CT scanning, possibly due to the scale.

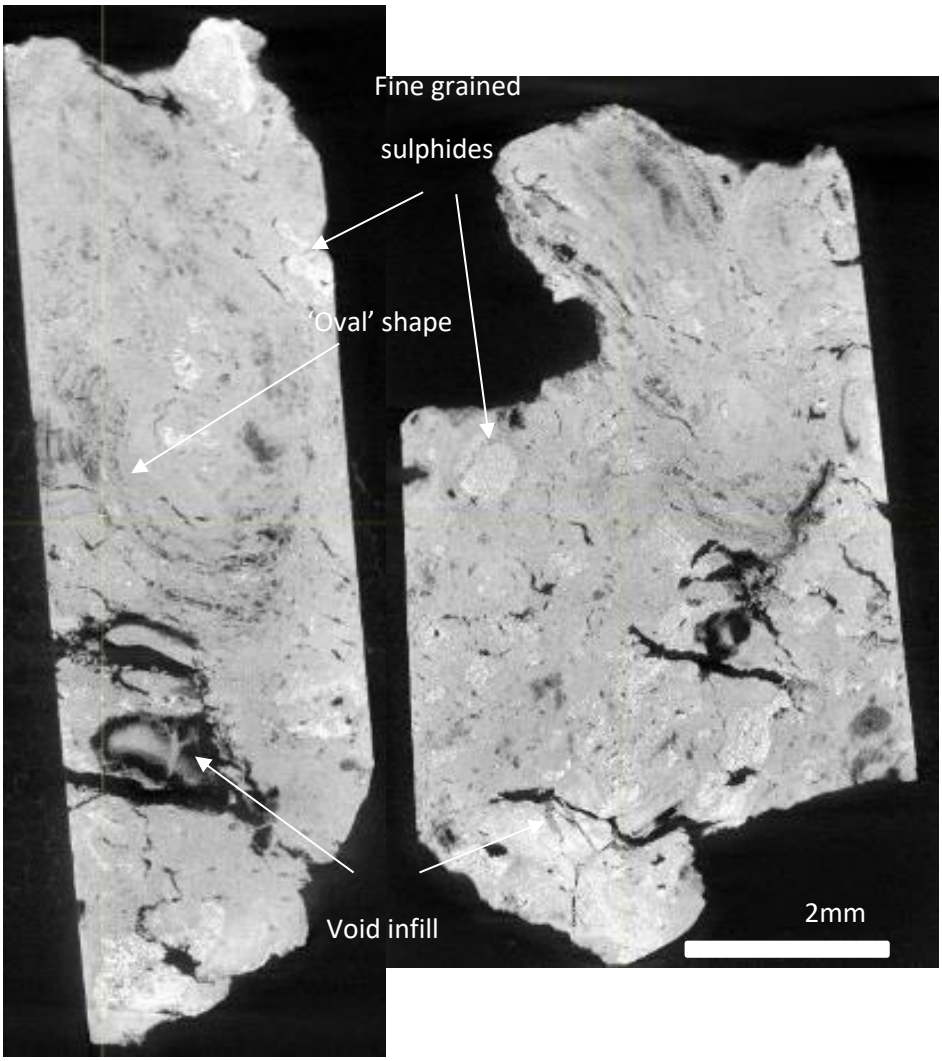

Figure 137: CT cross section images from 050RD/P11 - Southern Mound. (Left) Large void space (black) and 'oval' shaped filamentous material. (Right) Partially infilled voids, likely with sediment material. Grey = Si-Fe material, white patches = sulphides.

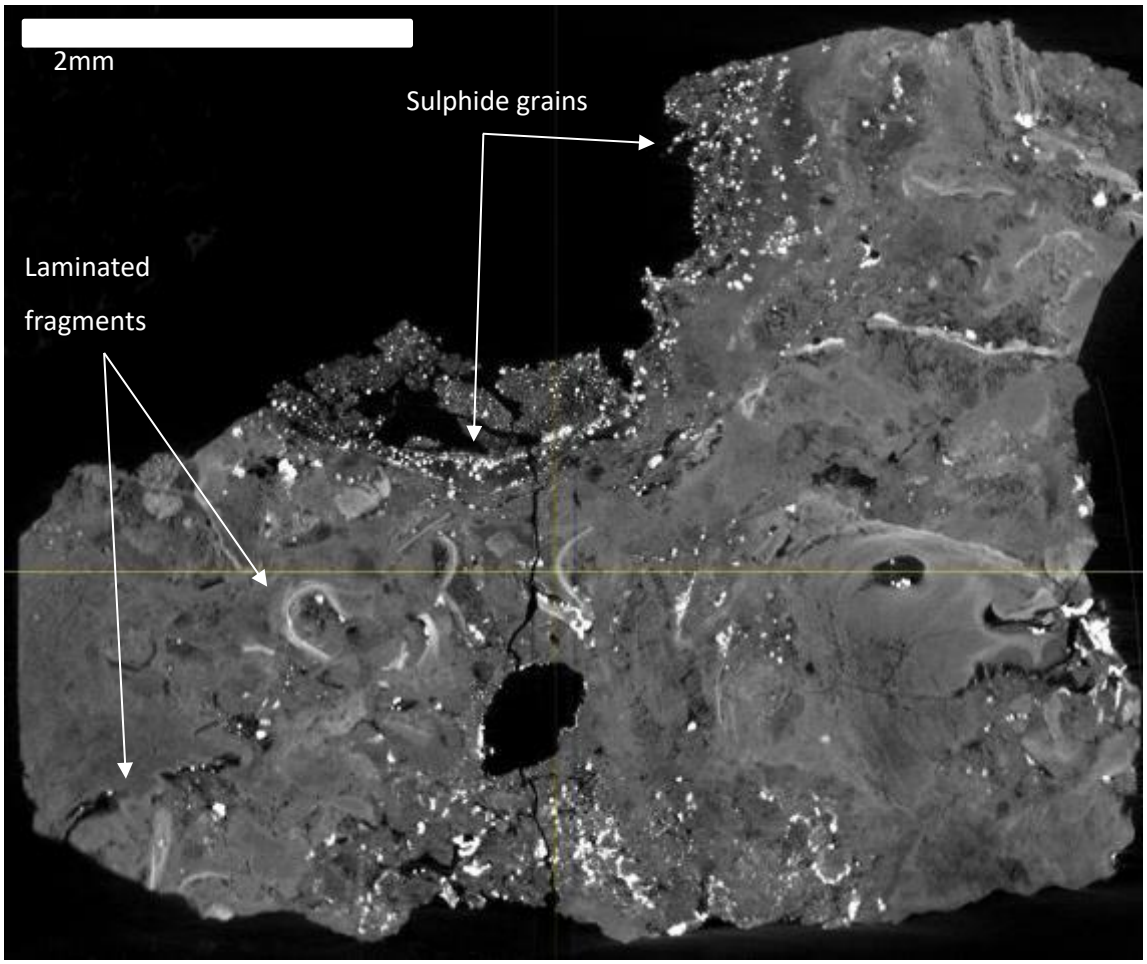

Figure 138: 057RD/P11 - Rona Mound Unit C. Clear visible clasts of laminated material and sulphide grain distribution throughout

057RD/P11 (Figure 138), in contrast to 050RD/P11 is texturally more comparable to Unit A material, with both laminated and massive clasts, and filamentous growth zones. Sulphides are relatively well distributed throughout the sample and at the macro scale do not appear to be ordered or orientated, other than being associated within iron oxide free silica.

7.1.2.4 Massive Sulphides

Two samples of massive sulphide core material were also scanned using CT techniques to compare the pore space textures of both sulphides and Si-Fe cap. Sample 065RD/P16 from Rona Mound represents a massive pyrite rich zone, which has undergone recrystallisation, and 073RD/P28 from the MIR Zone represents granular pyrite, likely a similar material to 065RD/P16, but that has not undergone recrystallisation (Figure 139).

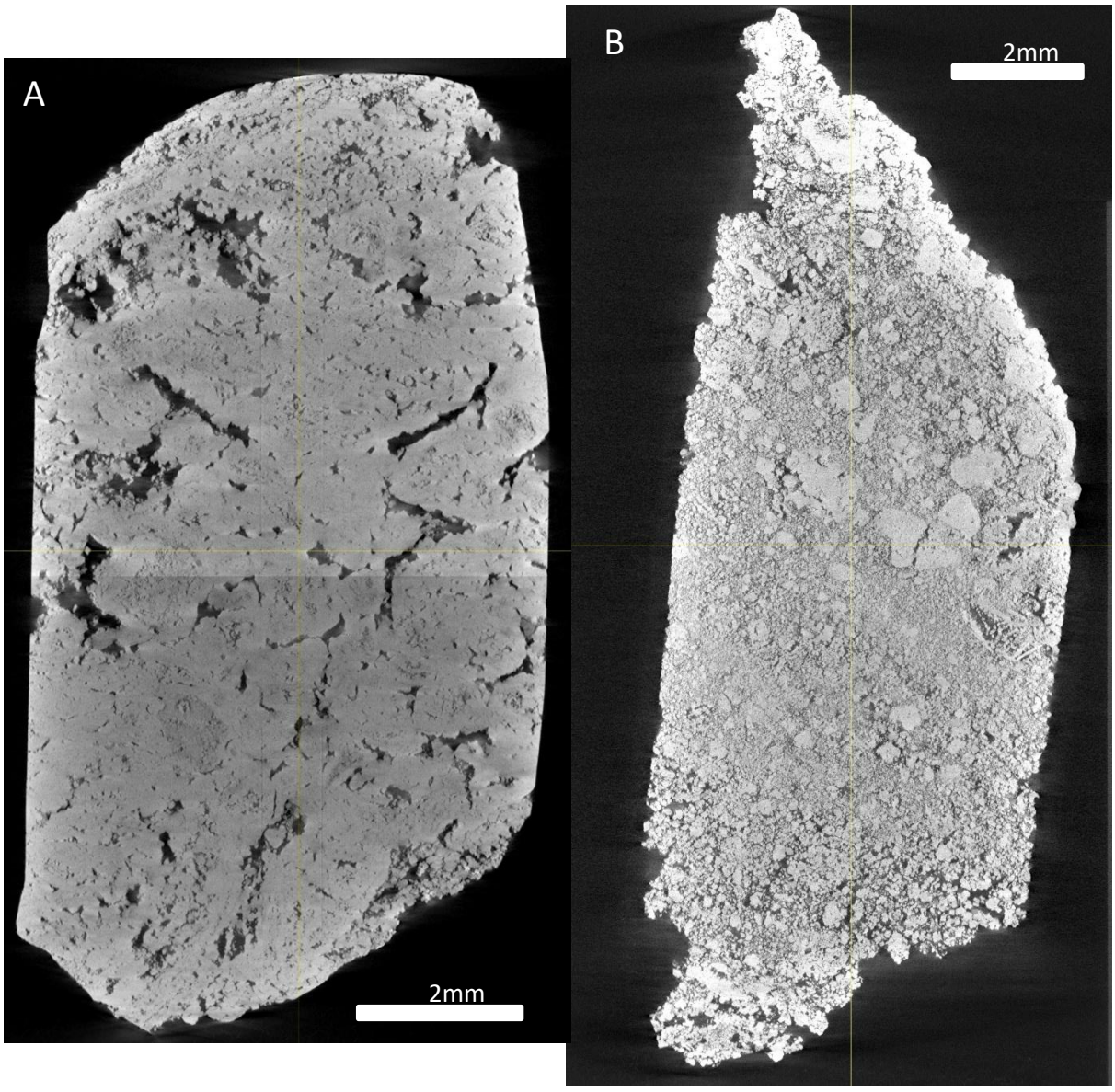

Figure 139:Massive sulphide core samples. (A) Recrystallised massive sulphide ore (065RD/P16). (B) Granular massive sulphide ore predominantly pyrite (073RD/P28).

Sample 065RD/P16 shows very little variation in density or texture, as expected from the recrystallised pyrite mineralogy. Void spaces occur regularly throughout the material with no preferred orientation. Sample 073RD/P28 also shows little variation in density, and is dominated by millimeter to centimetre sized granular pyrite. Grains are typically subhedral to anhedral and have no preferred orientation or sorting throughout the core sample. 065RD/P16 has clear separate void space (see black areas within sample), whereas the granular nature of 073RD/P28 implies a higher degree of porosity but with individual pores being visibly smaller.

7.2 CT modelling aims

The use of the non-destructive X-ray CT technique to study archive core material provides a way to determine intrinsic three-dimensional parameters by digital methods, rather than laboratory based, and potentially destructive techniques.

7.2.1 Porosity vs Connected Porosity

Total porosity and connected porosity can be easily separated from a 3D volume based upon the density difference, which corresponds to variable voxel intensity values. Therefore void space can be delineated from hard-rock material by thresholding the low density pixels (Figure 140). After total porosity has been separated, then an 'axis' connectivity module can be applied to determine whether individual pore space voxels form a connected network across the sample axes. Figure 140).

Porosity and connected porosity were initially assessed using the whole 3D volume, however this introduces a dimensional bias (as the z-axis is typically elongate compared to the other axes), and does not take into consideration the heterogeneity of the material, i.e. certain textures may be more porous and/or permeable throughout the core.

It is important to consider the heterogeneity of the textures throughout each Si-Fe sample and assess the general textures separately as the variation exhibited in these core materials may not be the representative of the Si-Fe cap lithology in general. Furthermore, the permeability is a function of connectivity between pore spaces, and these are often small channel or necks that are more difficult to resolve. Hence, the requirement to image smaller volumes of material at higher resolution, and to extrapolate the resulting interconnectivity to the larger samples.

Such connected porosity and permeability simulations have also been performed on hyperrectangle 'whole' core samples, and as cubic sub-volumes (~500x500x500 voxels) from the whole core image. A similar cubic sub-volume approach has also been undertaken to investigate 'micro-porosity' that may not be visualised in the lower resolution (~35 micron) scans of the whole core material.

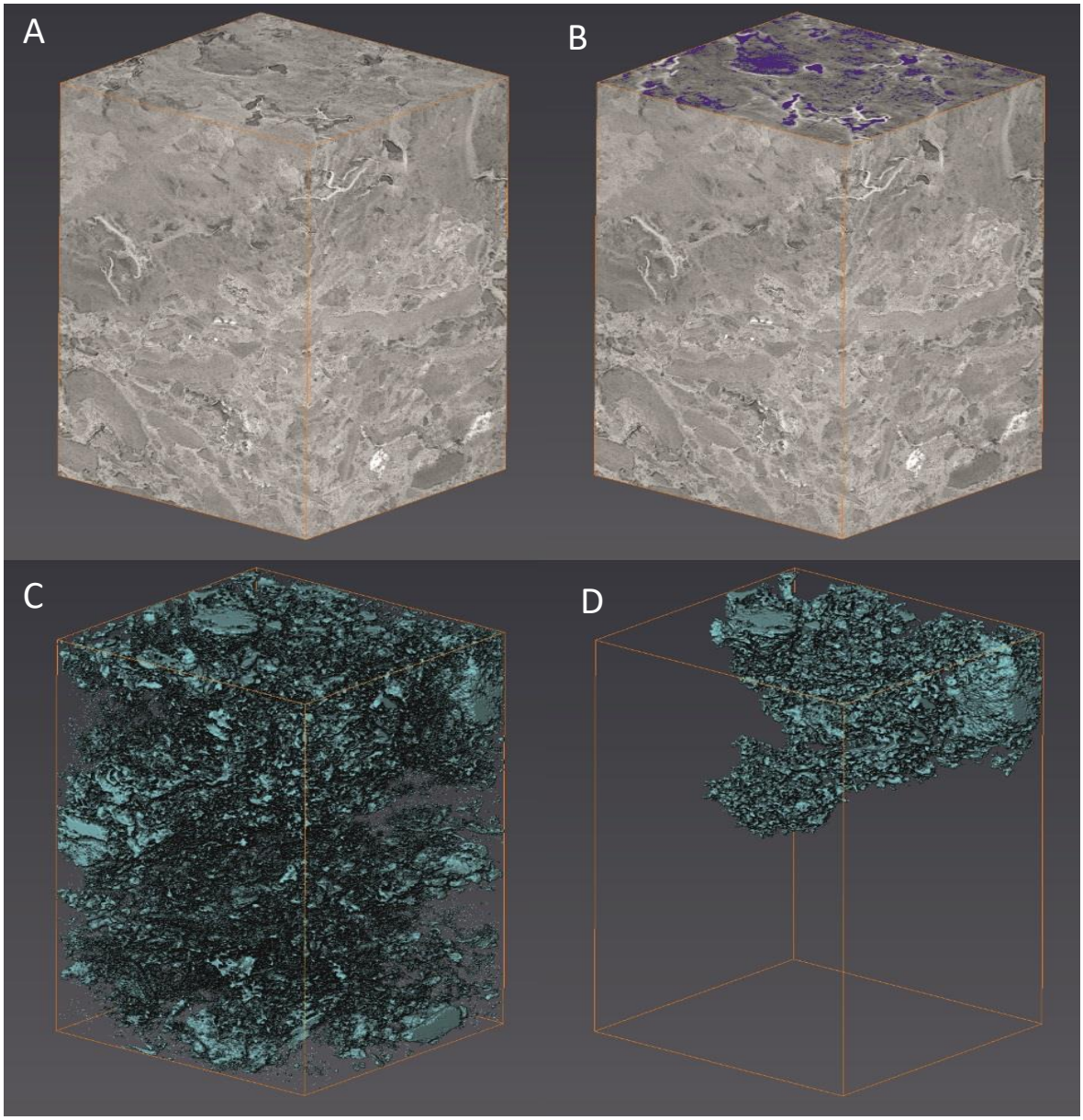

Figure 140: Four stages of connected porosity methodology. (A) 'Raw' reduced volume of a core sample. (B) Top surface displaying 'threshold' module where the pore space is highlighted on a single slice. (C) Thresholded total porosity volume, dependent on the range of selected voxel intensity. (D) Porosity that connected the 'y-axis', the only axis in this sample that has connected porosity.

7.2.2 Absolute permeability simulations

Parameters and the theory behind the simulations are provided in the Avizo Users Software guide (Avizo, 2016) and repeated here.

The permeability modelling involves simulation a permeating fluid through the volume of pore space defined in the Avizo software. The absolution permeability module then solves the Navier

Stokes equation to determine the 'global flow rate' (Q) through the sample, and then applies Darcy's Law to obtain an absolute permeability value.

The Navier-Stokes equation:

$$\left.\begin{array}{l} \vec{\nabla}.\vec{V} = 0 \\ \mu\nabla^2\vec{V} - \quad \vec{\nabla}P = \vec{0} \end{array}\right\}$$

Where $\vec{\nabla}.$ is the divergence operator, $\vec{\nabla}$ is the gradient operator, $\vec{V}$ is the velocity of the permeating fluids, μ is the dynamic viscosity of the permeating fluid, ∇^2 is the Laplacian operator, and P is the pressure of the permeating fluid. The permeating fluid is assumed to be a single phase, Newtonian fluid, with steady-state, laminar flow conditions. Boundary conditions are visually summarised in Figure 141, and are specified as:

- A no-slip condition at fluid-solid interfaces;
- a single-voxel-wide non-slip phase is added on the faces of the image that are not perpendicular to the main flow direction;
- 'experimental setup' stabilisation zones, are added on the face of the image that are perpendicular to the main flow direction to enable semi-quasi static pressure;
- Input pressure and output pressure are left at 130kPa and 100kPa, respectively (the default for the software), fluid viscosity is left at 0.001 Pa.s (default) for water.

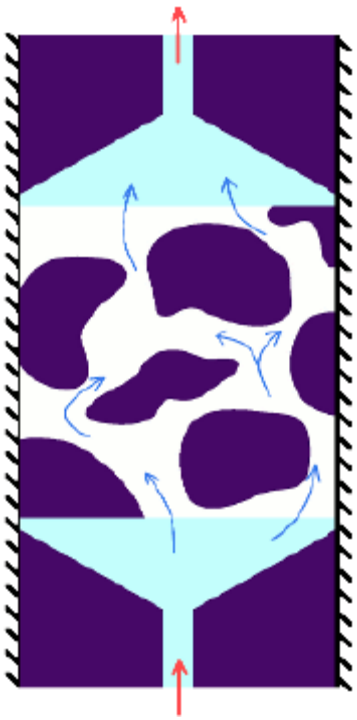

Figure 141: 2D cross section of the experimental setup for absolute permeability simulation in the Avizo software

Once Q has been calculated by the permeating fluid simulation then Darcy's Law can be rearranged to solve for the absolute permeability (k):

$$k\ (m^2) = \frac{\mu L Q}{S \Delta P}$$

Where:

- Q is the global flow rate that goes through the porous medium (m^3s^{-1}) obtained by the CT simulation;
- S is the cross section of the sample which the fluid goes through (m^2) and L is the length of the sample in the flow direction (m). Both defined by the subvolume size;
- μ is the dynamic viscosity of the flowing fluid (Pa.s) (assumed to be 0.001 Pa.s for water);
- ΔP is the pressure difference applied around the sample (Pa) (left as default =30kPa);

The output from the permeability simulation provides the permeability value (k) in both micrometers squared (μm^2), and darcy (d) (1 darcy = 0.9869233 μm^2), and spreadsheet for error values of each iteration. The permeability value calculated in these simulations is considered an intrinsic property of the sample or subsample, and is therefore not affected by the direction of fluid simulation.

7.2.3 Limitations

Porosity is based on the authors interpretation of the density differences displayed by the CT scans. This interpretation may have introduced some inherent bias based on noise within the CT scan images and therefore reproduction of these values by another person may differ. Furthermore, it is important to note that the porosity and permeability values provided from herein have been obtained using the Avizo software only. To check the validity of these values it is recommended that physical porosity and permeability experimentation of the same samples and sample volumes should be undertaken for comparison. Further mathematical testing can also be carried out, such as using the Kozney-Carmen equation to estimate permeability from porosity and pore diameters (for example in Callow *et al.*, 2018).

Without the physical or further mathematical testing caution should be given to the accuracy of the porosity and permeability values. For the purpose of this study the sample processing and modelling was constant for each sample, therefore variation between values are considered to represent true variation within the samples. Permeability simulations are typically considered at order of magnitude scales and comparative metrics are relative to each of the samples being compared (i.e. % increase or decrease).

7.3 Results - Total porosity and connected porosity – current

Results present in Table 70 show that only two out of the eight whole-core samples exhibit z-axis connectivity: one Si-Fe capping lithology, and one massive sulphide. Lateral connectivity in the x- and y-axis is more prevalent, with only the two Unit B Si-Fe capping lithology samples being completely impermeable.

This indicates that when the full three dimensional structure of each sample is resolved to ~ 35 micron resolution, the majority of the Si-Fe capping materials do not have a suitable pore network for fluid movement in the z-axis, but Unit A and C material may enable lateral fluid movement.

Investigating the porosity (Φ_{TOTAL})and connected porosity ($\Phi_{CONNECTED}$) in more detail reveals that the two samples from Unit B (both from the MIR Zone) exhibit some of the highest (076RD/P6) and lowest (073RD/P14) total porosities of any of the Si-Fe capping material, but neither exhibits connected porosity, implying that there is no relationship between porosity and permeability throughout the Si-Fe cap.

Where axis connectivity exists in more than one dimension, the pore network connects the two dimensions, therefore sharing the same volume of connected porosity. No systematic relationship exists between the volume of connected porosity compared to the volume of total porosity.

Table 70: Summary of whole core samples 'current' total porosity and connected porosity. '-' = no connected porosity

Sample	Lithology	Φ_{TOTAL} (mm^3)	$\Phi_{CONNECTED}$ (mm^3)			% of porosity connected
			x	y	z	
050RD/P3 (Southern)	Unit A	12316.2 (7.4%)		462.3 (2.8%)	-	37.8
050RD/P8 (Southern)	Unit A	2642.43 (15.8%)	1992.47 (11.9%)	1992.47 (11.9%)	-	75.3
073RD/P14 (MIR Zone)	Unit B	776.0 (2.4 %)	-	-	-	-
076RD/P6 (MIR Zone)	Unit B	4261.0 (13.5%)	-	-	-	-
050RD/P11 (Southern)	Unit C	898.4 (6.0%)	630.2 (4.2%)	-	-	70.1
057RD/P11 (Rona)	Unit C	713.6 (10.2%)	528.7 (7.5%)	-	528.7 (7.5%)	73.5
065RD/P16 (Rona)	Massive Sulphide	2139.7 (12.1%)	1509.8 (8.5%)	1509.8 (8.5%)	-	70.2
073RD/P28 (MIR Zone	Massive Sulphide	7821.8 (32.2%)	7558.0 (31.9%)	7558.0 (31.9%)	7558.0 (31.9%)	99.1

7.3.1 Changes in total porosity and connected porosity during progressive silicification

Some of the Unit B and Unit C Si-Fe lithologies exhibit different stages of growth of silica into pore space. Unit A material does not exhibit this late stage silicification (see Section 5.3) and the massive sulphide material does not contain significant concentrations of silica, hence this methodology is not appropriate.

To assess the change in porosity and connected porosity during progressive silicification, it is possible to digitally remove the outer overgrown layers of iron-oxide-free silica from inner 'jasperoidal material', provided there is a measurable difference in density. Interactive thresholding of voxel values in Units B and C is able to accommodate variation in density differences between

the ‘outer’ free-silica coatings and the ‘inner’ jasperoidal material. This reveals that three of the four samples from Units B and C have, before the second stage of silicification, three-dimensional connected porosity while one of the samples (073RD/P14) exhibits only two-dimensional connected porosity (Table 71).

Table 71: Summary of whole core samples 'pre-late-stage silicification' total porosity and connected porosity

Sample	**Lithology**	**Φ_{TOTAL} (mm^3)**	**$\Phi_{CONNECTED}$ (mm^3)**			**% of porosity connected**
			x	**y**	**z**	
073RD/P14 (MIR Zone)	Unit B	9295.2 (28.7%)	5523.5 (17.0%)	5523.5 (17.0%)	-	59.2
076RD/P6 (MIR Zone)	Unit B	12546.4 (39.7%)	12223.2 (38.6%)	12223.2 (38.6%)	12223.2 (38.6%)	97.2
050RD/P11 (Southern)	Unit C	2444.7 (16.3%)	1971.9 (13.1%)	1971.9 (13.1%)	1971.9 (13.1%)	80.4
057RD/P11 (Rona)	Unit C	1451.8 (20.7%)	1309.3 (18.7%)	1309.3 (18.7%)	1309.3 (18.7%)	90.3

Based on this new total porosity, the absolute volume change ($\Delta\Phi_{TOTAL}$) between current and pre-late stage silicification of the Si-Fe cap can be calculated (Table 72):

$$\Delta\ \Phi_{TOTAL}\ (mm^3) = \Phi_{SIL-FREE}\ (mm^3) - \Phi_{CURRENT}\ (mm^3)$$

Where $\Phi_{SIL\text{-}FREE}$ is the volume of total porosity after silica has been digitally removed, and $\Phi_{CURRENT}$ is the volume of current total porosity. The $\Delta\Phi_{TOTAL}$ is also expressed as a percentage of the $\Phi_{SIL\text{-}FREE}$ indicating the % change in porosity during this late stage silicification.

$$\%\ \Delta\ \Phi_{TOTAL}\ (\%) = \left(\frac{\Phi_{SIL\ FREE}\ (mm^3)}{\Phi_{CURRENT}\ (mm^3)} * 100\right)$$

Similarly the $\Delta\Phi_{AXIS\text{-}CON}$ (%) is also calculated using the same method:

$$\%\ \Delta\ \Phi_{AXIS-CON} = \left(\frac{\Phi_{\ SIL-FREE\ (AXIS\ CON)}\ (mm^3)}{\Phi_{CURRENT\ (AXIS\ CON)}\ (mm^3)} * 100\right)$$

Table 72: Summary of the relative change of porosity and connected porosity due to late-stage silicification

Sample	**Lithology**	**$\Delta\Phi_{TOTAL}$ (mm^3)**	**$\Delta\Phi_{TOTAL}$ (%)**	**$\Delta\Phi_{AXIS\text{-}CON}$ (%)**		
				x	**y**	**z**
073RD/P14 (MIR Zone)	Unit B	8519.2	8.3	N/A*	N/A*	-
076RD/P6 (MIR Zone)	Unit B	8285.4	34.0	N/A*	N/A*	N/A*
050RD/P11 (Southern)	Unit C	1546.3	36.8	32.0	N/A*	N/A*
057RD/P11 (Rona)	Unit C	738.2	49.2	40.4	N/A*	40.4
* = % volume change unable to quantify as initial sample had no connected porosity in this axis.						

Current total porosity ranges from between ~ 8 and 50 % of the total porosity when the late-stage silicification is removed from the 3D volume. Connected porosity is present in all three axes in both Unit C samples, and one Unit B sample, with the second Unit B sample showing connected porosity in both the x- and y- axes, but not the z-axis.

7.3.2 Current permeability

To determine whole-rock permeability, model simulations were conducted on whole core samples where axial pore-connectivity was identified. Permeability values were obtained in both μm^2 and darcy by the simulation. Both Unit A and Unit C sample 050RD/P11 recorded permeability values at 10^{-5} μm^2 (or darcy, where 1 darcy = 0.98 μm^2), with Unit C sample 057RD/P11 recording an order of magnitude higher permeability at 10^{-4} μm^2. Massive sulphide sample 065RD/P16, showed a similar permeability to the Si-Fe core materials (10^{-4} μm^2). Granular massive sulphide material (073RD/28) exhibits a permeability two orders of magnitude higher, with a value of 10^{-2} μm^2 (Table 73).

This wide range of variation in permeability is expected based upon the connected porosity variation between the samples.

Table 73: 'Current' whole core permeability values

Sample	Lithology	k (μm²)	k (d)
050RD/P3 (Southern)	Unit A	2.16×10^{-5}	2.19×10^{-5}
050RD/P8 (Southern)	Unit A	4.45×10^{-5}	4.51×10^{-5}
073RD/P14 (MIR Zone)	Unit B	-	-
076RD/P6 (MIR Zone)	Unit B	-	-
050RD/P11 (Southern)	Unit C	1.38×10^{-5}	1.40×10^{-5}
057RD/P11 (Rona)	Unit C	1.62×10^{-4}	1.64×10^{-4}
065RD/P16 (Rona)	MS	3.68×10^{-4}	3.73×10^{-4}
073RD/P28 (MIR Zone)	MS	1.74×10^{-2}	1.77×10^{-2}

7.3.3 Silica threshold permeability

Permeability values were calculated to reflect the relative increase in connected porosity by 'removing' the late-stage silica (digitally) with all samples showing late-stage silicification resulting in a decrease in permeability. Unit B samples had no calculable permeability in their current form but recorded permeability values of ~10^{-3} and 10^{-4} μm² (or darcy). Unit C samples also showed a decrease in permeability from ~10^{-4} μm² (or darcy)pre-late-stage silicification, to 10^{-4}-10^{-5} μm² (or darcy) in the current samples (Table 74).

Table 74: Pre-'late-stage' silicification permeability values

Sample	Lithology	k (μm²)	k (d)
073RD/P14 (MIR Zone)	Unit B	2.97×10^{-4}	3.01×10^{-4}
076RD/P6 (MIR Zone)	Unit B	3.05×10^{-3}	3.10×10^{-3}
050RD/P11 (Southern)	Unit C	2.55×10^{-4}	2.58×10^{-4}
057RD/P11 (Rona)	Unit C	3.12×10^{-4}	3.16×10^{-4}

7.3.4 Difference in permeability between current and silica thresholded values

As neither of the Unit B samples showed connected porosity in the whole core samples, the relative change in permeability cannot be properly quantified. Only Unit C samples displayed connected porosity in their current core form, and when the late-stage silica generation was digitally removed. Permeability values decreased to ~5 and 50% of the 'pre-silicification' permeability values (Table 75).

Relative permeability change (Δk) was calculated as follows:

$$\Delta k\ (\%) = \frac{k_{CURRENT}}{k_{SIL-FREE}} * 100$$

Table 75: Relative change in permeability due to late stage silicification

Sample	**Lithology**	**Δk (%)**
073RD/P14 (MIR Zone)	Unit B	N/A
076RD/P6 (MIR Zone)	Unit B	N/A
050RD/P11 (Southern)	Unit C	5.4
057RD/P11 (Rona)	Unit C	51.9

7.3.5 Summary of Whole core porosity/permeability across the Si-Fe cap

There is no trend between the volume of total porosity and permeability throughout the Si-Fe cap and the underlying massive sulphide samples analysed (Figure 142A). Similarly there is also little trend between volume of connected pore space and permeability (Figure 142B).

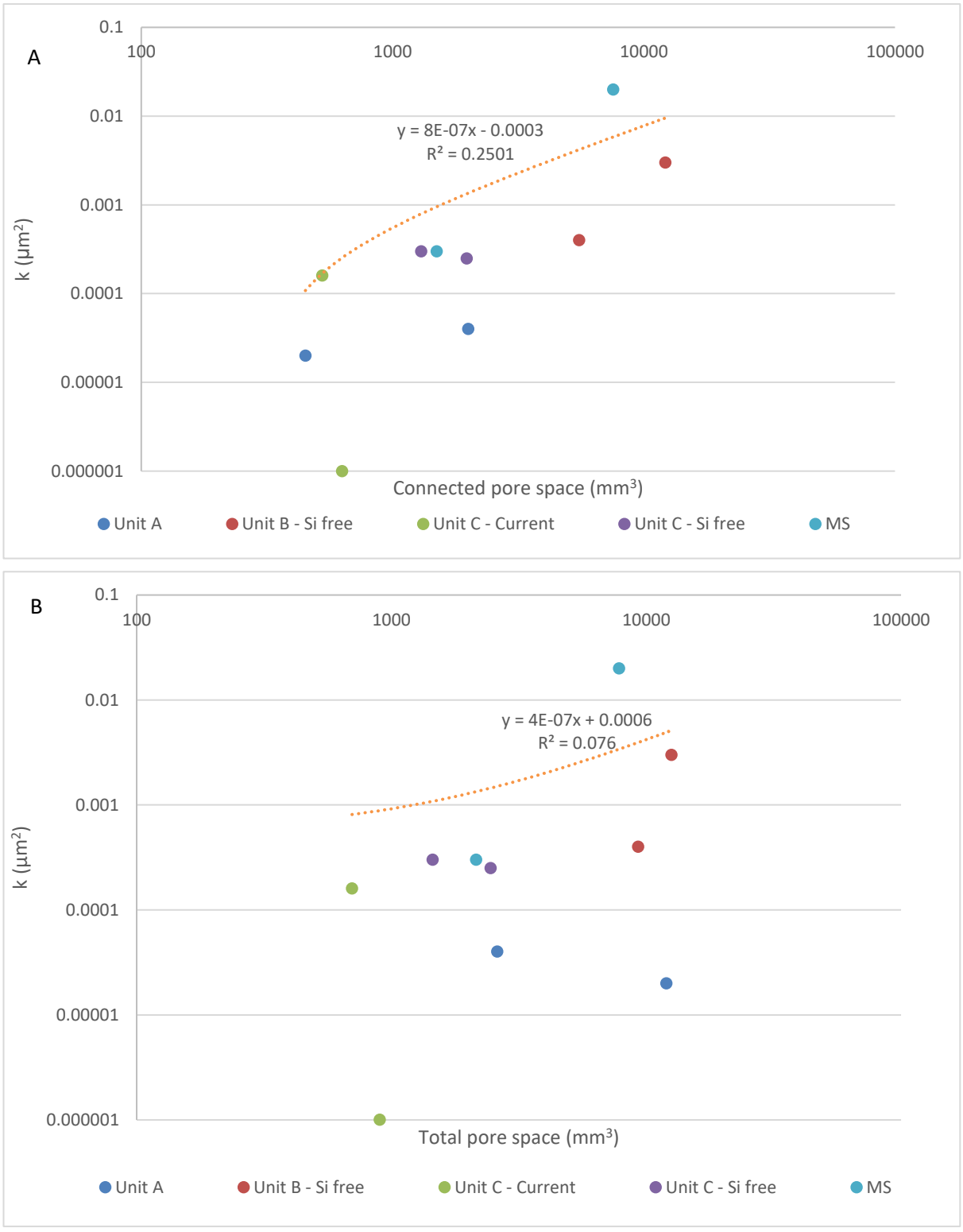

Figure 142: (A) Permeability vs connected porosity, and (B) Permeability vs total pore space plots

Comparison between Units shows that Unit B samples from the Si-Fe cap rock show the most variation (Figure 143). Late-stage silica removed 3D volumes show connected porosity in the order of ~ 10,000 mm^3, but current samples show no connected porosity, and total porosities between ~3 and 12 times lower. Similarly, permeability values are zero in current samples, but in the silica

free values were ~ 10^{-3} to 10^{-4} µm^2, broadly similar to Unit A material that has not undergone the same 'late-stage' silicification as Units B or C.

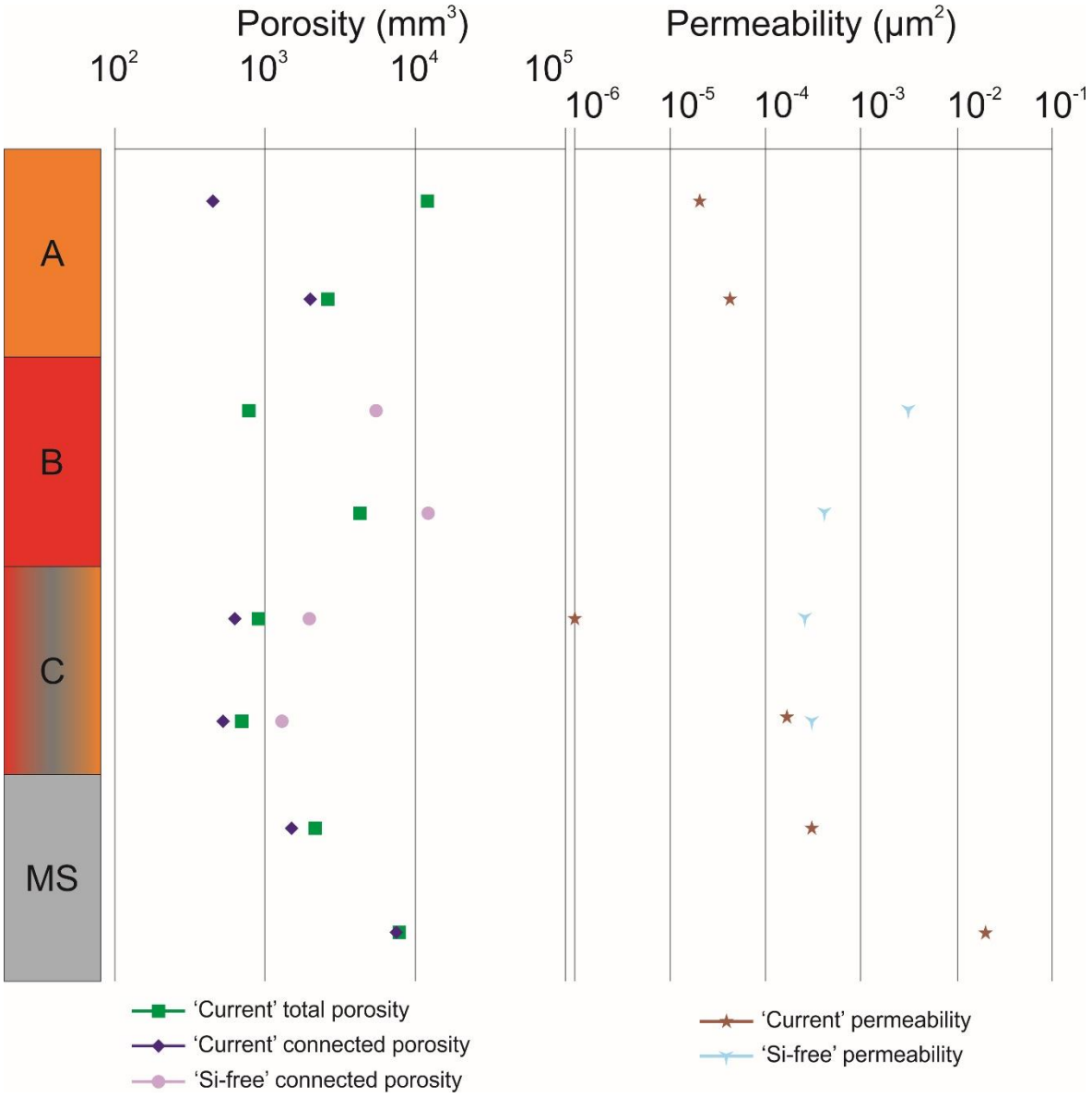

Figure 143: Summary of the current total porosity, current connected porosity, and 'Si-free' connected porosity, current permeability and 'Si-Free permeability throughout the Si-Fe cap Unit and two types of massive sulphide from the whole core samples.

7.4 Results - Porosity and Permeability of heterogeneous textures – intra-core analysis

The whole core samples of Unit B, out of all three of the Si-Fe cap Units, had no connected porosity in their current form, and had their porosity reduced between ~50% and 95% during late stage silicification. However, the whole core sample methodology does not take the heterogeneous textural variation throughout the Si-Fe cap into account.

It is possible that the variable textures may exert a control on the connected porosity and permeability. To test this, subvolumes of the heterogeneous textural variation across each of the Si-Fe samples are analysed (See Figure 144). These subvolumes are the same resolution as the whole core images, but are more representative of certain textures.

Each sub-volume is assessed for total porosity and connected porosity in all three (x-, y-, and z-) axes. Assessing the connected porosity in all three axes enables interpretation of a pore network and an understanding of which directions a fluid would be physically able to move throughout the material. If no connected porosity exists in the z-axis, but exists in either the x-, or y-axes, then fluid would be able to move horizontally, but not vertically, and vice versa. The appropriate axes for each connected porosity assessment are denoted in each table.

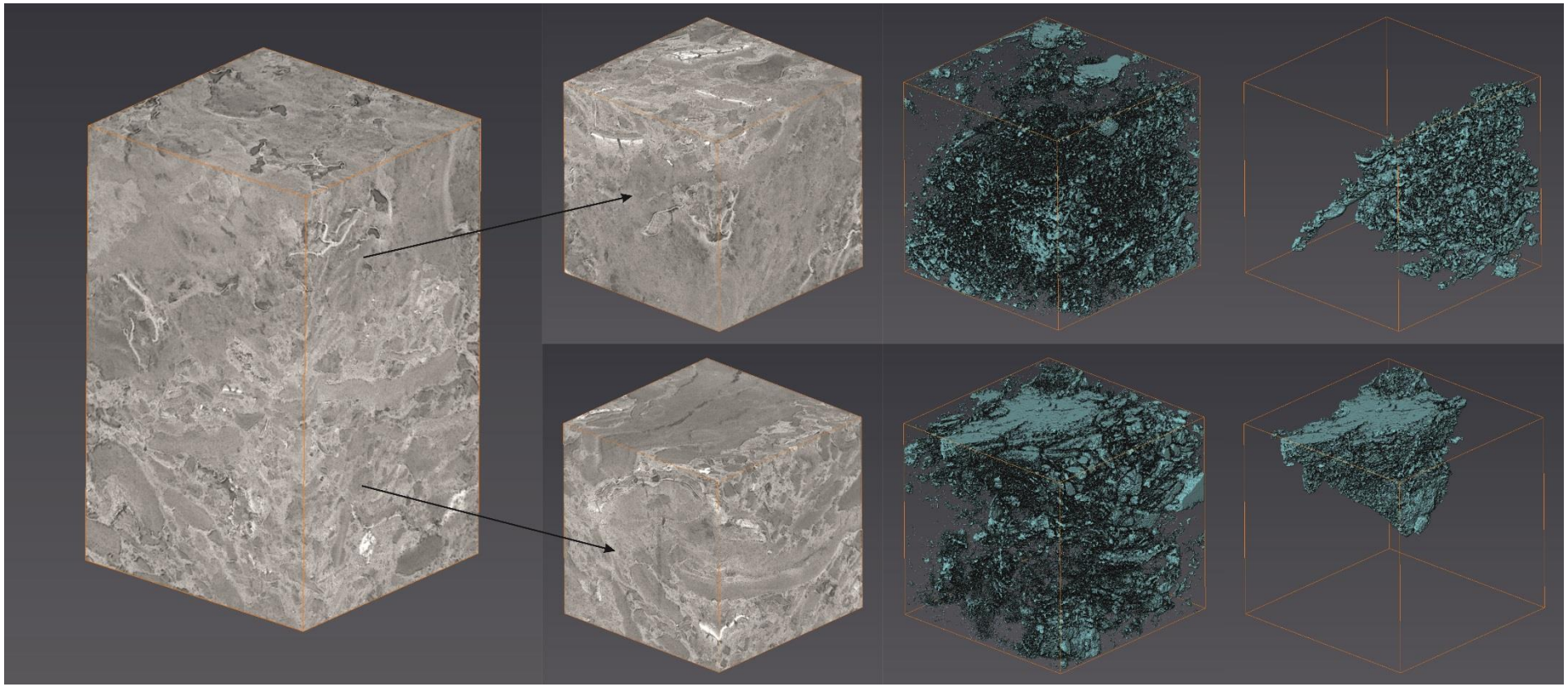

Figure 144: Example of two subvolumes extracted from the whole core, followed by thresholding for total pore space, and then connected porosity

7.4.1 Total and connected porosity - Current

7.4.1.1 Unit A

Total porosity ranges from 3.3 to 17.3 % and averages at 9.2%, with connected porosity ranging from 1.4 to 15.7 % and averaging at 6.4 % across the seven sub-volumes investigated (Table 76). On average ~60% of the porosity in sub-volumes from Unit A material are connected. Connected porosity appears to be controlled by texture, 050RD/P3 sub-volume 1 exhibited the highest porosity and the highest percentage of connected porosity. This sub-volume is representative of the more filamentous-dominated material and also contains sub-horizontal tube-like void spaces.

The connected porosity appears to not have a dominant axis with four of the seven sub-volumes analysed exhibiting connected porosity in all three axes. Two sub-volumes have connected porosity only in the horizontal planes (x or x and y), and one only in the z plane. This implies that potential fluid movement throughout Unit A is generally not limited to one direction, and does not represent significant anisotropy.

Table 76: Summary of total and connected porosity for Si-Fe Unit A samples using the subvolume method

Sample	**Sub-volume ID and descriptive feature**	**Φ_{TOTAL} (μm^3)**	**$\Phi_{CONNECTED}$ (μm^3)**			**% of porosity 'connected'**
			x	**y**	**z**	
050RD/P3	1 – filamentous area	904.3 (17.3 %)	817.4 (15.7 %)	817.4 (15.7 %)	817.4 (15.7 %)	90.4
	2 – clasts with desiccation cracks	407.5 (7.8 %)	198.0 (3.8%)	198.0 (3.8%)	198.0 (3.8%)	48.7
	3 – mixed filamentous and clast dominated	514.8 (9.9%)	-	-	333.0 (6.4%)	64.7
	4 – clasts with desiccation cracks	654.6 (12.5%)	446.0 (7.8 %)	446.0 (7.8 %)	-	68.1

050RD/P8	1 – filamentous and homogenous Si-Fe material	411.0 (7.8%)	311.4 (5.9%)	311.4 (5.9%)	311.4 (5.9%)	75.8
	2 –'granular' and homogenous Si-Fe	314.4 (6.0 %)	144.7 (2.8%)	144.7 (2.8%)	144.7 (2.8%)	46.0
	3 – desiccation cracks and filamentous	174.3 (3.3%)	-	-	72.9 (1.4%)	41.8

7.4.1.2 Unit B

Sub-volume total porosities ranged from 4.9 % to 22.9 % and average 11.1 % across the two Unit B samples studied, showing a large variation in porosity within each sample (Table 77). Despite this range of porosity, the connected porosities within each sub-volume are much smaller, ranging from 0.8 to 8.6 %, averaging 4.1%. This difference shows that even though the total porosity of the Unit B material can be quite large, there is no significant correlation between amount of total porosity and the connected porosity. On average, only 40% of the pores in Unit B are connected, ~ 20% less than in Unit A. Even though total porosities of each sub-volume are broadly comparable, the connected porosity is lower. The two sub-volumes with the largest pore volume in each Unit (Unit A - sub-volume 1 - 050RD/P3, and Unit B sub-volume 3 – 076RD/P6) recorded ~ 900 and ~1200 μm^3, however the connected porosities in each sample are ~820 and 450 μm^3 respectively.

The distribution of porosity within the sample appears to be controlled by certain textures, but connected porosity appears independent of texture. Where Unit B material is relatively homogenous (i.e. 076RD/P6 – sub-volume 1) total porosity is low, but connected porosity of ~ 3% is comparable with other sub-volumes (and so ~97% of porosity is connected in this sub-volume). In contrast, 076RD/P6 sub-volume 3 has one of the highest total porosities at 22.9%, however only 37.6% of this total porosity it connected.

Although connected porosity exists in each of the sub-volumes analysed for Unit B material, it is interesting to note that the prevailing direction of connected pores is in the horizontal, not the vertical, plane. Only 2 out of the 6 sub-volumes had connected porosity in the z axis. This implies

that although connected porosity exists there is a prevailing horizontal movement potential over vertical movement.

Table 77: Summary of total and connected porosity for Si-Fe Unit B samples using the subvolume method

Sample	**Sub-volume ID and descriptive feature**	**Φ_{TOTAL} (μm^3)**	**$\Phi_{CONNECTED}$ (μm^3)**			**% of porosity 'connected'**
			x	**y**	**z**	
073RD/P14	1 – larger area of desiccation cracks	331.4 (6.3%)	230.2 (4.4%)	230.2 (4.4%)	-	69.6
	2 – mixed clast and matrix	384.7 (7.3%)	162.3 (3.1%)	-	-	42.5
	3 – clasts and open pore space	683.9 (13.0%)	298.9 (5.7%)	125.3 (0.8%)	-	43.7 – x 18.3 - y
076RD/P6	1 – largest open void in sample	256.9 (4.9%)	158.8 (3.0%)	158.8 (3.0%)	-	61.8
	2 – more homogenous Si-Fe material	642.0 (12.3%)	156.3 (3.0%)	156.3 (3.0%)	156.3 (3.0%)	24.4
	3 - spiderweb mesh of filaments	1197.8 (22.8%)	-	-	451.6 (8.6%)	37.6

7.4.1.3 Unit C

Total porosity ranged from 7.6 to 17.6 % in Unit C samples, averaging at 12% porosity from the 5 different sub-volumes, with connected porosity ranging from 3.3 to 17.0 % and averaging at 8.6% (Table 78). Despite being the deepest Si-Fe Unit, Unit C has both the highest average total porosity value and highest average connected porosity values of the Si-Fe cap material. On average ~68% of the pores in Unit C material are connected, ~30% higher than Unit B, and ~10% higher than Unit A material.

The highest total porosity volume of Unit C (sub-volume 3 – 050RD/P11) is similar to the highest in Unit A (sub-volume 1 – 050RD/P3), and also exhibits a similar highest percentage of connected porosity at 97% compared to 90%. This high connected porosity value is associated with the largest pore space in core sample 050RD/P11 with small areas of filamentous material, in contrast to the entirely filamentous areas in 050RD/P3.

Overall, this implies that Unit C and Unit A material are broadly similar in connected porosity, both with significantly higher connected porosity volumes than Unit B material. The highest instances of connected porosity though, are directly associated with open void spaces and filamentous material. Connected porosity in Unit C is more dominated by large pore spaces, whereas Unit A is more dominated by filamentous material.

Connected porosities within four of the five sub-volumes of Unit C occur in all three axes, with the remaining sub-volume (sample 057RD/P11, sub-volume 2), exhibiting connected porosity in both the x- and z- dimensions. This shows that there is no dominant axis of connected porosity within Unit C material and fluid was free to move in all directions.

Table 78: Summary of total and connected porosity for Si-Fe Unit C samples using the subvolume method

Sample	**Sub-volume ID**	**Φ_{TOTAL} (μm^3)**	**$\Phi_{CONNECTED}$ (μm^3)**			**% of porosity 'connected'**
			x	**y**	**z**	
050RD/P11	1 – sulphide enclaves with open voids	395.7 (7.6%)	306.9 (5.9%)	306.9 (5.9%)	306.9 (5.9%)	77.6
	2 – open voids and	919.5 (17.6%)	889.9 (17.0%)	889.9 (17.0%)	889.9 (17.0%)	97.3

	filament dominated					
	3 – minor filaments and homogenous Si-Fe	477.6 (9.1%)	170.6 (3.3%)	170.6 (3.3%)	170.6 (3.3%)	35.7
057RD/P11	1 – filamentous and clasts of Si-Fe	380.1 (14.2%)	313.2 (11.7%)	313.2 (11.7%)	313.2 (11.7%)	82.4
	2 – clasts of Si-Fe, sulphides, and minor filaments	308.7 (11.5%)	142.9 (5.3%)	-	142.9 (5.3%)	46.2

7.4.1.4 Massive Sulphide

Two different massive sulphide core samples were analysed using the same CT method: a granular sample (073RD/P28), and a more massively recrystallised sample (065RD/P16).

Total porosity in the massively recrystallised material ranges from 8.9 to 16%, averaging 11. %, and connected porosity ranges from 3.1 to 15.7%, averaging 8%. Total porosity in the granular material ranges from 16.7 to 18.7% averaging 17.4%, with connected porosity ranging from 16.3 to 18.1%, averaging 16.8% (Table 79).

On average ~60% of the porosity in 065RD/P16 is connected, compared to ~95% of 073RD/P28. The granular nature of the massive sulphide accounts for the high degree of connected porosity within the material, and the percentage of connected porosity in the massive recrystallised massive sulphide material is broadly similar to the overlying Unit A and Unit C material of the Si-Fe cap rock material. This implies that the recrystallised massive sulphide material may have a similar low permeability.

Two sub-volumes from massive sulphide sample 065RD/P16 only show connected porosity in one of three axes, with the third sub-volume showing connected porosity in all three axes. Sub-volume 3 from 065RD/P16 is dominated by one of the larger void spaces in 065RD/P16, hence the higher

degree of porosity being connected. In contrast 073RD/P28 showed connected porosity in all three axes in all three sub-volumes. This shows that the recrystallisation of the sulphides likely exerts a control on the connected porosity of the material, limiting and reducing both the total and connected porosity. The recrystallisation process converts a granular material where a high amount of connected pore space is present between grains, to become a massive area of sulphide with a much lower area of connected pore space. Unlike the Si-Fe material, subvolumes of the sulphide material are relatively homogenous.

Table 79: Summary of total and connected porosity for massive sulphide samples using the subvolume method

Sample	**Sub-volume ID**	**Φ_{TOTAL} (μm^3)**	**$\Phi_{CONNECTED}$ (μm^3)**			**% of porosity 'connected'**
			x	**y**	**z**	
065RD/P16	1 – least irregular voids	557.3 (10.6%)	-	-	283.2 (5.4%)	50.8
	2 – moderate irregular voids	468.5 (8.9%)	-	160.4 (3.1%)	-	34.2
	3 – largest irregular voids	838.0 (16.0%)	823.8 (15.7%)	823.8 (15.7%)	823.8 (15.7%)	98.3
073RD/P28	1 – mixed granular	979.5 (18.7%)	946.7 (18.1%)	946.7 (18.1%)	946.7 (18.1%)	96.6
	2 – mixed granular	886.9 (16.9%)	852.4 (16.3%)	852.4 (16.3%)	852.4 (16.3%)	96.1
	3 – mixed granular	1076.7 (16.7%)	1047.6 (16.0%)	1047.6 (16.0%)	1047.6 (16.0%)	97.3

7.4.2 Late silica overgrowth: impact on total and connected porosity

7.4.2.1 Unit B

Unit B samples often exhibit jigsaw brecciation where iron oxide-free silica infills fractures and pore spaces (see Chapter 5). This lack of iron oxide often manifests as a density difference between iron free silica and 'jasper' in CT scans of Unit B samples. Therefore, variable thresholding of the samples can allow digital removal of the overgrowth silica, showing what the sample looked like without this late-stage silica addition.

To calculate the relative difference in connected porosity, the connected porosity (%) that is determined from the whole-sample volume is subtracted from the connected porosity determined from the sample volume in which the silica overgrowth has been digitally removed. The relative change is attributed to the volume change of connected porosity as a result of the late stage silicification. This is done in the z-axis direction to determine changes in the effectiveness of the cap-rock to prevent upwards or downwards migration of fluids (Table 80).

As a result of the late-stage silicification, connected porosity decreases to between ~9 and 36 % of the 'silica free' connected porosity (in sample 073RD/P14), and between ~14% and ~24%, in sample 076RD/P6 (Table 80). This significant decrease in porosity from the silica free material to the current material is the likely explanation for the lower connected porosity and pore spaces in Unit B compared to the other two Units. This implies that late-stage silicification in Unit B has a strong relationship with the control on connected porosity. It also important to note that after thresholding the last silica generation out of Unit B samples, all sub-volumes exhibited connected porosity in the z axis, something which only two sub-volumes of 076RD/P6 showed previously.

Relative change in connected porosity (% $\Delta\ \phi_{AXIS\text{-}CON}$) is calculated as follows:

$$\%\ \Delta\ \Phi_{AXIS-CON} = \left(\frac{\Phi_{\ SIL-FREE\ (AXIS\ CON)}\ (\mu m^3)}{\Phi_{CURRENT\ (AXIS\ CON)}\ (\mu m^3)} * 100\right)$$

Table 80: Summary of connected porosity and change in connected porosity due to late stage silicification in Si-Fe Unit B samples

Sample Code	**Sub-volume ID**	**$\Phi_{AXIS\ CON}$ (μm^3)**	**$\Delta\Phi_{AXIS\text{-}CON}$ (μm^3)**	**$\Delta\Phi_{AXIS\text{-}CON}$ (%)**
073RD/P14	1 – larger area of desiccation cracks	1268.34 (24.2%)	1038.18	18.2

	2 – mixed clast and matrix	445.51 (8.5%)	283.20	36.4
*	3 – clasts and open pore space	1447.22 (27.6%)	x = 1148.30 y = 1321.94	20.7 8.7
076RD/P6	1 – largest open void in sample	1127.11 (21.6%)	968.24	14.1
	2 – more homogenous Si-Fe material	1055.46 (20.2%)	899.13	14.8
	3 - spiderweb mesh of filaments	1850.30 (35.4%)	1398.68	24.4
* = Silica connected porosity is in all three axes, original porosity in x and y axes only				

7.4.2.2 Unit C

Unit C material is similar to Unit B in that it exhibits late-stage iron-sulphide-free silica overgrowths. Digital removal of the late stage silicification was undertaken to generate connected porosity values for both the original sample volume and before the late stage overgrowth.

As a result of the late-stage silicification, connected porosity decreases to between ~20 and 65% of the 'silica free' connected porosity (in both samples 050RD/P11 and 057RD/P11) (Table 81). In general, this is a much lower relative change compared with Unit B. The result is not entirely expected, based on studies of thin sections from the materials alone. There are several explanations for this: It is likely that the bleaching effect that has affected Unit C material results from a loss of iron oxide, decreasing the atomic density of the 'jasperoidal' material, and bringing it closer to that for pure silica. This makes differentiation between the bulk material and late-stage silica overgrowth harder to identify in the X-Ray CT scans. The CT scans also reveal open pore space, in spatial association with the bleached areas, indicating a causal relationship between the bleaching process and dissolution of earlier material, possibly by high temperature reduced fluids, leaving open pore spaces and bleached (iron removed) silica.

Table 81: Summary of connected porosity and change in connected porosity due to late stage silicification in Si-Fe Unit C samples

Sample Code	Sub-volume ID	$\Phi_{AXIS\ CON}$ (μm^3)	$\Delta\Phi_{AXIS\text{-}CON}$ (μm^3)	$\Delta\Phi_{AXIS\text{-}CON}$ (%)
050RD/P11	1 – sulphide enclaves with open voids	468.98 (9.0%)	162.05	65.4
	2 – open voids and filament dominated	1374.15 (26.3%)	484.22	64.8
	3 – minor filaments and homogenous Si-Fe	795.20 (15.2%)	624.57	21.5
057RD/P11	1 – filamentous and clasts of Si-Fe	480.12 (18.0%)	166.89	65.2
	2 – clasts of Si-Fe, sulphides, and minor filaments	633.19 (23.7%)	490.32	22.6

7.4.3 Absolute permeability simulations – current

7.4.3.1 Unit A

The permeability in Unit A subvolumes are broadly similar (at the same order of magnitude), with values ranging from ~2.5 x 10^{-5} μm^2 to ~5.8 x 10^{-5} μm^2, with the exception of sample 050RD/P3 sub-volume 3 (~1.2 x 10^{-1} μm^2). With the exception of sub-volume 3, permeability values across both Unit A samples average at ~ 3.0 x 10^{-5} μm^2 (Table 82).

Table 82: Absolute permeability values for Si-Fe Unit A subvolumes

Sample Code	Sub-volume ID	k (μm^2)	K (d)
050RD/P3	1 – filamentous area	5.76 x 10^{-5}	5.84 x 10^{-5}
	2 – clasts with desiccation cracks	2.89 x 10^{-5}	2.93 x 10^{-5}
	3 – mixed filamentous and clast dominated	1.23 x 10^{-1}	1.24x 10^{-1}

	4 – clasts with desiccation cracks	3.00×10^{-5}	3.04×10^{-5}
050RD/P8	1 – filamentous and homogenous Si-Fe material	3.50×10^{-5}	3.55×10^{-5}
	2 –'granular' and homogenous Si-Fe	2.77×10^{-5}	2.80×10^{-5}
	3 – desiccation cracks and filamentous	2.52×10^{-5}	2.55×10^{-5}

7.4.3.2 Unit B

The permeability of Unit B subvolumes are broadly similar (at the same order of magnitude) to each other, and Unit A material, within values ranging from ~2.2×10^{-5} to 6.5×10^{-5}. Average permeability across all six sub-volumes of Unit B material is ~ 3.5×10^{-5} μm^2 (Table 83).

Table 83: Absolute permeability values for Si-Fe Unit B subvolumes

Sample Code	**Sub-volume ID**	**k (μm^2)**	**k (d)**
073RD/P14	1 – larger area of desiccation cracks	2.20×10^{-5}	2.23×10^{-5}
	2 – mixed clast and matrix	3.15×10^{-5}	3.19×10^{-5}
	3 – clasts and open pore space	2.24×10^{-5}	2.27×10^{-5}
076RD/P6	1 – largest open void in sample	6.55×10^{-5}	6.63×10^{-5}
	2 – more homogenous Si-Fe material	2.82×10^{-5}	2.86×10^{-5}
	3 - spiderweb mesh of filaments	4.53×10^{-5}	4.59×10^{-5}

7.4.3.3 Unit C

The permeability of Unit C subvolumes are broadly similar (at the same order of magnitude) to each other, Unit A and Unit B material. Values range from ~2.3×10^{-5} to 8.8×10^{-5} and across the five sub-volumes average out at ~ 5.3×10^{-5} μm^2 (Table 84).

Table 84: Absolute permeability values for Si-Fe Unit C subvolumes

Sample Code	**Sub-volume ID**	**k (μm^2)**	**k (d)**
050RD/P11	1 – sulphide enclaves with open voids	6.51×10^{-5}	6.59×10^{-5}
	2 – open voids and filament dominated	8.72×10^{-5}	8.83×10^{-5}
	3 – minor filaments and homogenous Si-Fe	2.28×10^{-5}	2.31×10^{-5}

057RD/P11	1 – filamentous and clasts of Si-Fe	5.25×10^{-5}	5.32×10^{-5}
	2 – clasts of Si-Fe, sulphides, and minor filaments	3.6×10^{-5}	3.65×10^{-5}

7.4.3.4 Massive Sulphide

The permeability of massive sulphide subvolumes are broadly similar to the Si-Fe cap materials, but also include two sub-volumes which have higher permeability values (by an order of magnitude). Values range from ~2.5×10^{-5} to 6.0×10^{-5}, with two values at ~ 1.55×10^{-4}. Average permeability values for the massive recrystallised sulphide was ~ 7.5×10^{-5}, with average values for the granular massive sulphide material ~1.1×10^{-4} (Table 85).

Table 85: Absolute permeability values for massive sulphide subvolumes

Sample Code	**Sub-volume ID**	**k (μm^2)**	**k (d)**
065RD/P16	1 – least irregular voids	4.50×10^{-5}	4.56×10^{-5}
	2 – moderate irregular voids	2.46×10^{-5}	2.50×10^{-5}
	3 – largest irregular voids	1.54×10^{-4}	1.56×10^{-4}
073RD/P28	1 – mixed granular	1.57×10^{-4}	1.60×10^{-4}
	2 – mixed granular	5.93×10^{-5}	6.01×10^{-5}
	3 – mixed granular	7.84×10^{-6}	7.95×10^{-6}

7.4.4 Absolute permeability simulations – After silica removal

7.4.4.1 Unit B

Permeability values for the silica thresholded material are variable, but are typically an order of magnitude higher than in the non-silica thresholded material. Values range from ~ 1.3×10^{-4} to ~ 3.15×10^{-4}, with one value recorded ~ 2.5×10^{-5} and another of ~9.8×10^{-5} (Table 86). Average permeability over the six sub-volumes is ~ 1.5×10^{-4}. When compared to the current permeability values of Unit B material (~3.5×10^{-5}) the pre-late silica-overgrowth permeability is an order of magnitude higher.

Table 86: Absolute permeability values for pre-'late-stage' silicification Si-Fe Unit B subvolumes

Sample Code	Sub-volume ID	k (μm^2)	k (d)
073RD/P14	1 – larger area of desiccation cracks	2.53×10^{-5}	2.57×10^{-5}
	2 – mixed clast and matrix	1.51×10^{-4}	1.53×10^{-4}
	3 – clasts and open pore space	1.42×10^{-4}	1.44×10^{-4}
076RD/P6	1 – largest open void in sample	3.14×10^{-4}	3.18×10^{-4}
	2 – more homogenous Si-Fe material	9.73×10^{-5}	9.85×10^{-5}
	3 - spiderweb mesh of filaments	1.28×10^{-4}	1.29×10^{-4}

7.4.4.2 Unit C

Permeability values for the pre-late silica overgrown material are variable, but are typically one to two orders of magnitude higher than in the whole volume material (after overgrowth) (Table 87). Values range from ~1.9×10^{-3} to ~ 7×10^{-5} μm^2. Average permeability of pre-late silica overgrown material across the five sub-volumes is ~5×10^{-4} μm^2, and is an order of magnitude higher than current permeability values.

Table 87: Absolute permeability values for pre-'late-stage' silicification Si-Fe Unit C subvolumes

Sample Code	Sub-volume ID	k (μm^2)	k (d)
050RD/P11	1 – sulphide enclaves with open voids	1.50×10^{-4}	1.52×10^{-4}
	2 – open voids and filament dominated	1.90×10^{-3}	1.92×10^{-3}
	3 – minor filaments and homogenous Si-Fe	6.91×10^{-5}	7.00×10^{-5}
057RD/P11	1 – filamentous and clasts of Si-Fe	1.02×10^{-4}	1.03×10^{-4}
	2 – clasts of Si-Fe, sulphides, and minor filaments	2.45×10^{-4}	2.48×10^{-4}

7.4.5 Difference in Permeability between current and silica thresholded values

As expected, the decrease in connected porosity between current whole volume material and pre-late silica overgrowth material results in a significant decrease in permeability values: to between ~5% and ~85% of the permeability pre-late-stage silicification (Table 88).

Table 88: Change in porosity due to late stage silicification in Si-Fe Units B and C using the subvolume method

Sample	**Sub-volume ID**	**Δk (%)**
076RD/P6	1 – larger area of desiccation cracks	87.0
	2 – mixed clast and matrix	20.9
	3 – clasts and open pore space	15.8
073RD/P14	1 – largest open void in sample	20.9
	2 – more homogenous Si-Fe material	29.0
	3 - spiderweb mesh of filaments	35.4
050RD/P11	1 – sulphide enclaves with open voids	43.4
	2 – open voids and filament dominated	4.6
	3 – minor filaments and homogenous Si-Fe	33.3
057RD/P11	1 – filamentous and clasts of Si-Fe	51.5
	2 – clasts of Si-Fe, sulphides, and minor filaments	14.7

7.4.6 Summary of 'Subvolume' assessment of porosity and permeability

Similar to the whole core sample analysis, there is no correlation between connected porosity and permeability (Figure 145).

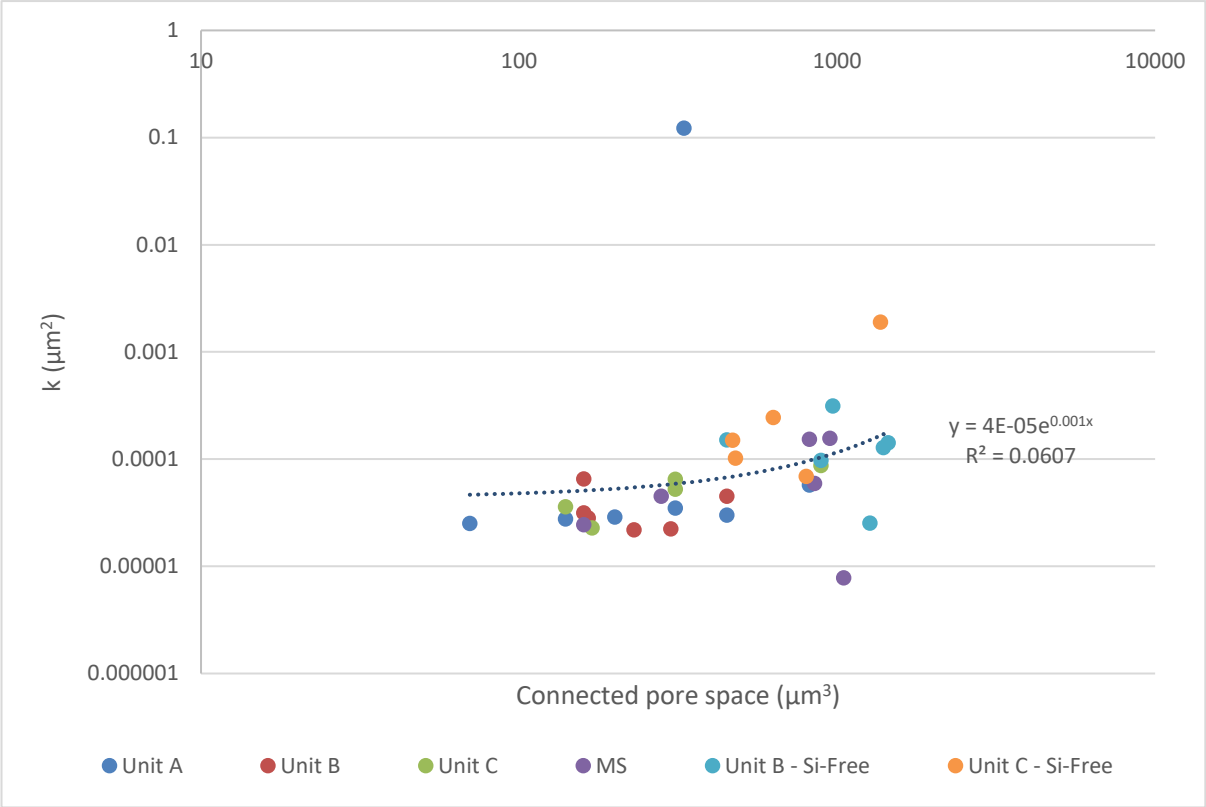

Figure 145: Plot of permeability vs connected pore space throughout the Si-Fe Unit and massive sulphide subvolumes. R^2 value of 0.06 shows the lack of trend throughout the data.

When comparing individual Units together using this methodology it appears that the general permeability is uniform throughout most of the samples between 10^{-4} and 10^{-5} µm^2. The main exception is the one subvolume from Unit A (050RD/P3) where the filamentous-dominated material shows ~ 4 orders of magnitude higher permeability than the rest of the Si-Fe cap rock samples (Figure 146). Similar to the whole core methodology, the permeability values of the silica thresholded samples are higher than the current values by ~ 1 order of magnitude.

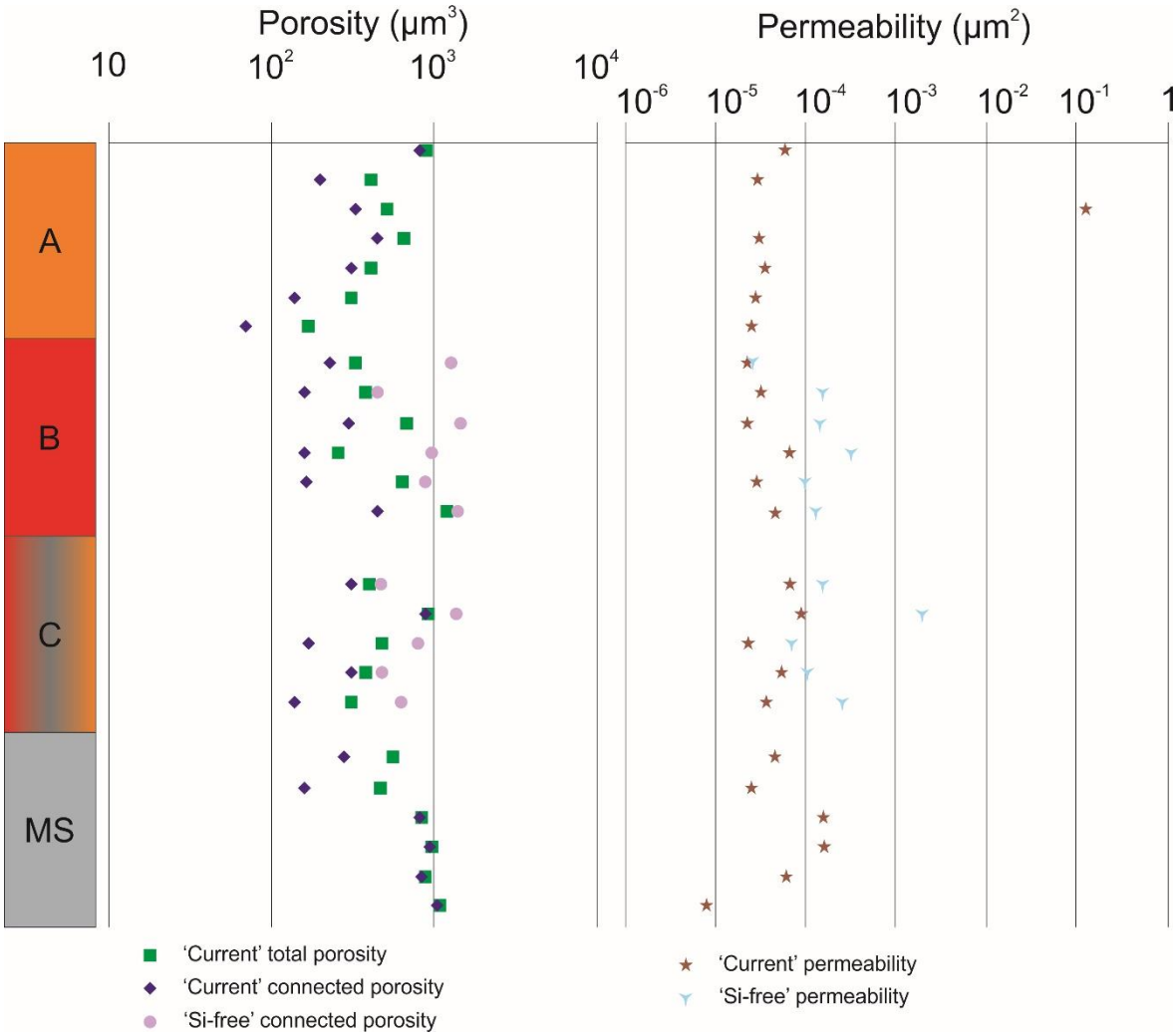

Figure 146: Summary of the current total porosity, current connected porosity, and 'Si-free' connected porosity, current permeability and 'Si-Free permeability throughout the Si-Fe cap Unit and two types of massive sulphide from the 'sub-volume' methodology.

7.5 Results - Investigating micro-porosity using higher resolution CT imaging

7.5.1 Sample scans

Three samples (Unit A - 050RD/P8, Unit C - 050RD/P11, and Unit B - 076RD/P6) were analysed at high resolution scans (~1-2 µm resolution) these appeared homogenous in the lower resolution scans (~35 µm) whole core scans. The aim was to test for 'micro-porosity' in the Si-Fe cap rock samples.

A similar reduced volume processing technique was applied to investigate porosity and permeability at this scale with sub-volumes of ~500x500x500 voxels (i.e. ~ 0.6 mm^3) investigated

(Figure 147). Reduced quality of the data was chosen as a compromise to get multiple areas in the same sample within the allotted scan time.

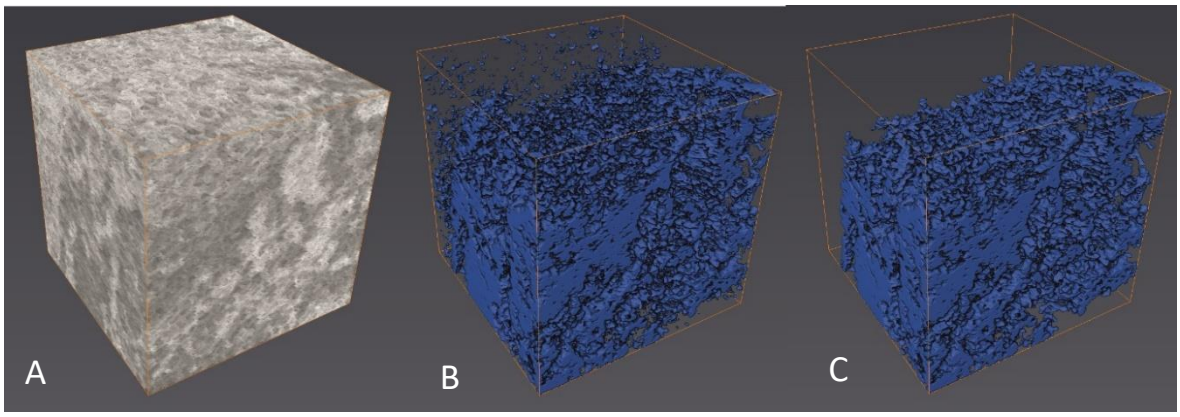

Figure 147: (A) High-resolution cubic sub-volume, with (B) total porosity, and (C) connected porosity. Subvolume is ~ 0.6 mm^3.

7.5.2 Porosity vs connected porosity

At this smaller scale, in areas which did not appear to be porous at the ~35 micron resolution, visible porosity can be detected at <2 micron resolution, indicating ~80% or greater connected porosity throughout sub-volumes (Table 89). The implication of this is that the whole core, low resolution (~35 micron) CT imaging does not take this 'micro-porosity' into account. High quantities of connected micro-porosity may lead to the interpretation that the Si-Fe samples are more permeable when this micro-porosity is taken into consideration.

In Unit B material, micro-porosity was also observed within both sub-volumes analysed, revealing high percentages of connected porosity (~ 95%) (Table 89).

Connected micro-porosity also exists within Unit C materials, but is typically lower than Units A and B, with a lower percentage of connected porosity averaging ~ 50% (Table 89).

Table 89: Summary of total porosity and connected porosity in the 'high resolution' subvolumes of Si-Fe Unit A samples

Unit, Sample ID and Location	Scan Area	Sub-volume ID	Φ_{TOTAL} (μm^3)	$\Phi_{CONNECTED}$ (μm^3)			% of porosity 'connected'
				x	y	z	
Unit A 050RD/P8 Southern Mound	1	1	20.22	19.41	19.41	19.41	96.02
		2	34.99	34.48	34.48	34.48	98.54
		3	20.45	18.53	18.53	18.53	90.63
	2	-	14.74	11.77	11.77	11.77	79.82
Unit B 076RD/P6 MIR Zone	1	-	29.72	27.80	27.80	27.80	93.66
	2	-	51.71	50.1	50.1	50.1	98.84
Unit C 050RD/P11 Southern Mound	1	-	8.11	3.79	-	3.79	46.7
	2	-	12.0	6.8	6.8	6.8	56.7

7.5.3 Absolute Permeability Simulations

Due to the similarities between total porosities and connected porosities in each of the sub-volumes analysed only two permeability simulations were undertaken in each sample.

In Unit A (sample 050RD/P8), two volumes that were assessed by permeability simulations recorded different orders of magnitude of permeability, at ~10^{-8} and ~10^{-11} μm^2, both significantly lower than the ~ 10^{-5} μm^2 permeability values for the lower resolution scans (Table 90). This implies that although micro-porosity exists within clasts and jasperoidal material of Unit A, the significantly lower permeability values would have little to no effect on the overall permeability of the sample.

In Unit B (sample 076RD/P6), two volumes investigated by permeability simulations recorded permeability values that were one and two orders of magnitude lower than the permeability values simulated in the lower resolution HMX samples (Table 90). Although these permeability values are closer to the lower resolution scan results, similar to Unit A material, this micro-porosity is not expected to have much of an impact on a sample scale.

In Unit C (sample 0505RD/P11), two areas investigated by permeability simulations recorded permeability values that were three orders of magnitude lower than the permeability values simulated in the lower resolution HMX samples (Table 90). Similar to both Units A and B samples, this significantly lower permeability values would have little to no effect on the overall permeability of the samples.

Table 90: Permeability values of Si-Fe Unit A high resolution subvolumes

Unit, Sample ID, and Location	**Scan Area**	**k (μm^2)**	**k (d)**
Unit A, 050RD/P8, Southern Mound	1	5.39×10^{-11}	5.46×10^{-11}
	2	9.17×10^{-8}	9.30×10^{-8}
Unit B, 076RD/P6, MIR Zone	1	4.40×10^{-6}	4.45×10^{-6}
	2	4.95×10^{-7}	5.02×10^{-7}
Unit C, 050RD/P11, Southern Mound	1	6.10×10^{-8}	6.18×10^{-8}
	2	6.69×10^{-8}	6.78×10^{-8}

7.5.4 Summary

This investigation has shown that the detected percentage of connected porosity in all three Si-Fe units is dependent on the resolution of the CT imaging system. Even though micro-porosity exists to a greater or lesser extent, the permeability values calculated through this material as a result of the connected micro-porosity are typically 2 or more orders of magnitude lower than permeability values calculated from the lower resolution scans. Therefore, the 'micro-porosity' identified by the high-resolution imaging does not make a significant contribution to the overall permeability of the Si-Fe capping material.

7.6 Summary

7.6.1 Porosity vs connected porosity

One of the key observations from both hand specimen and thin sections is that the Si-Fe capping material often shows porosity, however the premise is that the Si-Fe cap acts as an impermeable barrier. Therefore, the key parameter is connected porosity, rather than total porosity.

No systematic link has been identified between total porosity and connected porosity. Units A and C show some degree of axis connectivity (x and/or y), with only one Unit C sample from Rona Mound (057RD/P11) showing connectivity in the z-axis. Unit B material showed no axis connectivity at all. This implies that Unit B material from Southern Mound and MIR zone are more impermeable than the rest of the Si-Fe capping material, but the majority of the Si-Fe material analysed are impermeable in the z-axis.

In general, the Si-Fe capping materials show less connected porosity then the underlying massive sulphide material. The granular massive sulphide (sample 073RD/P28 from beneath the Si-Fe cap) exhibits axis connectivity in all three axes with the majority of the porosity connected, it exhibits the highest porosity and total porosity of any whole core sample. Sample 065RD/P16, the recrystallised massive sulphide, exhibited connected porosity in the x- and y-axes, most similar to Unit A material (sample 050RD/P8).

Investigation at the reduced sub-volume scales (~500x500x500) contrasts with the whole core samples, and reflects the heterogeneity of the core samples. Porosity varies significantly for each sub-volume in each sample and shows that textural variation exerts a significant local control on porosity and connected porosity. The majority of smaller sub-volumes in all three Si-Fe capping materials show connected porosity in at least 2 of the three axes, showing a higher degree of connectivity than the whole core samples. Z-axis connectivity is present in most of Unit A sub-volumes, and all Unit C sub-volumes, but only in one out of 6 of Unit B sub-volumes. This observation correlates well with the whole core samples showing that Unit B material has little to no pore connectivity in the z-axis.

In both whole core samples and sub-volumes, investigation and modelling clearly show that connected porosity has significantly decreased due to the late-stage silicification. In the whole core samples, Unit B samples have had either two (x- and y- 073RD/P14), or three (x-, y-, z-axes, 076RD/P8) axis sealed by the late stage silica generation with total porosity reduced to ~ 8% and 34% of the pre-late-stage silica porosity. Unit C samples show reduced total porosity volumes to ~ 37% and ~49% of pre-late-stage silica values for Southern Mound (050RD/P11) and Rona Mound (057RD/P11) respectively, with the sealing of porosity in one, and two axes, and connected porosities decreasing to ~ 30% and 40% of the pre-silicification volumes.

7.6.2 Permeability variation

Whole core Unit B samples did not display connected porosity in any axis, and therefore are considered impermeable. Where permeability could be calculated, connected porosity is typically limited to the x- or y-axes in Si-Fe samples (i.e. no axis connectivity in the z-axis), with the exception

of one Unit C sample from Rona Mound (057RD/P11). The recrystallised massive sulphide samples showed connected porosity broadly similar to Unit A samples (connected porosity in the x- and y-axes). The granular massive sulphide samples exhibit the highest connected porosity of any whole core sample, and implies permeability in all three axes.

Permeability values from whole core samples are broadly similar, at 10^{-4} to 10^{-5} μm^2, in all Si-Fe samples, despite the variation in connected porosity in Units A and C. Recrystallised massive sulphide (065RD/P16) also records a similar permeability value at a magnitude of 10^{-4} μm^2. Only the granular massive sulphide sample (073RD/P28) exhibits a significantly different permeability value at 10^{-2} μm^2, showing that the granular sulphide material is more permeable than the recrystallised sulphides and Si-Fe capping material by 2 to 3 orders of magnitude.

Upon digital removal of the late-stage silica the change in connected porosity and permeability (as a result of silicification) can be determined. Permeability values have decreased from ~10^{-3} or 10^{-4} μm^2 to being impermeable (no connected porosity in the x-, y-, or z-axes) in Unit B samples. Where connected porosity exists in the current Si-Fe samples (Unit C), the relative decrease in connected porosity due to late stage silicification is to ~20-65% of the initial 'pre-silicification' connected porosity, with permeability values decreasing to ~5 and 50% of the 'pre-silicification' permeability values.

Permeability calculations using the sub-volume method shows that the significant variation in porosity and connected porosity due to the heterogeneous material is generally not reflected in the overall permeability values. With the exception of one sub-volume in Unit A material (permeability value of ~10^{-1} μm^2), all sub-volume permeability values for Si-Fe material ranged between ~2.2 and 8.7 x 10^{-5} μm^2. The two massive sulphide samples showed a wider range of permeability values ranging from 10^{-4} to 10^{-5} μm^2 (065RD/P16) and 10^{-4} to 10^{-6} μm^2 (073RD/P28). The permeability values for the recrystallised massive sulphide sample are broadly similar to the Si-Fe capping material. However the permeability values for the granular massive sulphide sample are lower than expected based upon the whole core sample.

Digital removal of late-stage silica-overgrowth for Unit B and C samples showed that permeability values decreased to between 10^{-3} to 10^{-5} μm^2, which equated to ~5 and 90% of the 'pre-silicification' permeability values.

7.6.3 Implications from the porosity and permeability study

Ultimately, the connected porosity and permeability investigation has determined several key features of the Si-Fe cap rock that support the interpretation that it is impermeable, and provided

evidence of the impact of 'late-stage' silicification. The lack of current connected porosity in the Si-Fe core samples shows that there is no physical way for fluid to pass through the samples vertically. Lateral connected porosity (in the x- and y-axes), shows that there Si-Fe cap rocks may enable limited lateral movement.

Late-stage silicification, which had affected Units B and C, resulted in significant decrease in connected porosity in both Units. This decrease in connected porosity has resulted in no connected porosity in Unit B, and limited connected porosity in Unit C. This decrease in connected porosity has also resulted in decreased permeability values by 1 to 2 orders of magnitude, because of late-stage silicification. Thus this late-stage silicification appears to be a 'sealing' event of the Si-Fe cap. This impermeable cap would therefore inhibit vertical ingress of seawater, creating a physical barrier to the underlying massive sulphide orebody, and inhibit any vertical flow of late-stage buoyant hydrothermal fluids. This impermeable barrier has therefore likely imparted a strong control on the hydrological regime of the studied eSMS deposits, and may be a significant feature for rapid preservation of eSMS deposits.

Chapter 8 Discussion

The aim of this study was defined at the start of this thesis. It is focused on testing the hypothesis that there is some mechanism during the closing stages of hydrothermal activity, which acts to help seal a seafloor massive sulphide ore body at depth, thus restricting the ingress of oxygenated seawater and enhancing preservation of the deposit as it ages. In the preceding chapters, I have provided evidence for the extent and occurrence of a Si-Fe capping lithology (Chapter 3), explored the mechanisms of its formation, its origin, and the processes responsible for its generation (Chapter 5 - Chapter 7). Here, I bring these various strands together and make the argument that this is a common mechanism occurring at extinct SMS deposits, that has wider implications for both the metal tenor of the current ocean floor and the global metal cycle.

In bringing the strands of evidence together, I make an assessment of the textural, mineralogical, and geochemical characterisation of the hydrothermal sediments and Si-Fe cap rock Units. By drawing on this characterisation, and comparing the Si-Fe cap rocks to the occurrence and formation of similar lithologies throughout geological history, the origins of the main three constituents of the Si-Fe cap rock (iron oxide/oxyhydroxides, silica, and sulphides) can be interpreted and a paragenesis presented herein. Porosity and permeability simulations based on X-Ray CT data, coupled with textural and mineralogical assessment, provides evidence of the impermeable nature of the Si-Fe cap, and considerations of what this feature could have on the hydrological regime on eSMS deposit are considered in this Chapter.

Finally, the commonality of the processes forming the Si-Fe cap, combined with the implications the Si-Fe cap material has on preservation of eSMS deposits is considered in a wider view, with regards to seafloor oxidation rates, and the potential for base metal reservoirs on the seafloor.

8.1 Origins of the hydrothermal sediments, silicification, and sulphidation – how to from a Si-Fe cap

8.1.1 Origins of hydrothermal sediment protolith – iron oxide/oxyhydroxides

The iron oxides and oxyhydroxides in the Si-Fe cap material are interpreted to be inherited from the overlying hydrothermal sediments (summarised i Figure 105, Section 5.6.4). Therefore to understand the origin of the iron component in the cap, one must understand the accumulation processes that have formed the sediments.

As discussed in Chapter 2, iron oxides and oxyhydroxides typically form in three main ways at hydrothermal sites: during gossan formation, as exhalites, and from microbially mediated precipitation. All three of these processes can form ferrihydrite, an amorphous, metastable, hydrous iron oxyhydroxide. On a relatively short timescale, ferrihydrite can subsequently dehydrate, and transition to less hydrous, more crystalline iron oxide (i.e. haematite) or oxyhydroxide (i.e. goethite) depending on the environmental conditions. As all of these processes can form both goethite and haematite, other mineralogical, textural, or geochemical features have been investigated to shed further light on the formation mechanisms of the iron material.

8.1.1.1 Evidence of massive sulphide weathering

The chemical reactions and processes involved in sulphide weathering have been detailed in Chapter 2 with ferrihydrite and iron oxyhydroxide (likely goethite) being the primary oxidation products of pyrite, marcasite, and chalcopyrite.

The main identifying features that, in general, indicate the iron oxides are a product of sulphide weathering include: co-precipitation or formation of other secondary metal sulphides, oxides, or hydroxides, relict preserved primary sulphide textures within iron oxides, and high base metal content in the iron oxides (reflecting their origin as primary hydrothermal sulphide material).

Secondary copper minerals (i.e. covellite, chalcocite, atacamite) are common weathering products associated with both seafloor massive sulphide deposits and VMS deposits (USGS, 2012 and references therein). Atacamite was observed or recovered on massive sulphide boulders at Southern Mound, and from a weathered chimney at Rona Mound as part of this study (Section 3.2), therefore it would be likely that any gossanous material derived from the sulphides of either mound would also contain atacamite.

Few weathering product sulphides or base metal oxides were identified in any Si-Fe capping material, nor overlying hydrothermal sediments at any mounds. The sulphides in Unit C do not show any evidence of weathering, and only one sample (at Rona Mound - 057RD/P11) of the Si-Fe cap material has a tentative example of secondary weathering product, with 2.3 wt% of natrojarosite identified by XRD. Although atacamite was observed in a sediment core from the MIR Zone (Dutrieux, 2019), no secondary metal chlorides were identified in the Si-Fe cap lithologies.

This general paucity of secondary weathering products can be interpreted in three ways:

- secondary products were initially present, but continued weathering resulted in the destruction and complete mobilisation of all base metals (with the exception of iron);

- the lack of secondary minerals indicates that the iron oxides were not a product of weathering of sulphides;
- or, the limited presence of secondary products indicates a small contribution to the iron oxide/oxyhydroxide by weathering of massive sulphides. Thus, the main contribution is for another iron oxide/oxyhydroxide formation process.

One of the main processes associated with seafloor weathering, which aids seafloor gossan formation, is mass wasting. Within a typical low energy deep-sea environment, weathering of sulphide material often results in destabilisation and collapse of sulphide structures, which creates localised high-energy environments and turbidity currents. Evidence of these collapse and mass wasting events is observed in sediment sequences located distally from sulphide mounds (Murton *et al*., 2019).

Accumulation of randomly sized and orientated clasts in brecciated material in the sediment Unit M3, Unit A of Southern Mound, Unit C at Rona Mound, and Unit B in MIR zone (described throughout Chapter 5), are likely a result of a high energy mass-wasting events. The lack of clast sorting and the variation in clast size implies that the material would not have been transported far, and is likely derived from sulphide dominated surface features, thus implying a gossanous origin.

Textural observation of gossan formation from VMS deposits is often based on corroded, relict sulphide material, or chimney structures preserved within the iron oxide dominated units. Limited evidence of potential sulphide weathering material exists in the Si-Fe capping material. A clast of silicified iron oxide material in 050RD/P3 exhibits a curved shape (**Error! Reference source not found.**) which is reminiscent of a hydrothermal chimney cross section in contrast to the typical clasts described in Section 5.3. If this clast is a fragment of silicified, weathered hydrothermal chimney, it has undergone complete oxidation with no relict sulphide material remaining.

Relict, partially oxidised sulphides are rarely observed within Unit B material at both Southern Mound (022RD/CC) and MIR Zone (076RDP6-8) (Sections 5.2.3 and 5.4.2). Opaque cubic grains were initially thought to be pyrite, however in reflected light, the grain surface is clearly corroded and oxidised to haematite (Figure 75). At MIR Zone, both oxidised and non-oxidised grains exist within the same sample (Figure 76), which could be a function of differential weathering of grains from the same sulphide generation, but is more likely to represent grains from different sulphide generations with weathering of the first, but not the second.

In hydrothermal environments, iron oxyhydroxides, oxides, and manganese oxides can absorb base metals onto their surface and can therefore contain elevated base metal content. Interpretation

of surface gossanous material from the active TAG mound showed that base metal content of gossanous iron oxides is likely controlled by the original base metal content of the primary sulphide (Hannington *et al.*, 1995).

Hydrothermal sediments, which directly overlie the Si-Fe caps, contain Cu concentrations of <300 ppm, and Zn concentrations of <450 ppm. Si-Fe cap Units average ~ 14 ppm Cu and 650 ppm Zn in Unit A, ~36 ppm Cu, and ~150 ppm in Unit B, and ~110 ppm Cu, and ~2700 ppm Zn in Unit C (Section 6.3).

When compared to the gossanous material at the TAG active Mound (both gold-rich and gold poor gossans, average surface samples, and shallow surface red and grey chert), a clear difference in base metal content can be seen (Figure 148). TAG gold rich, gold poor, and surface samples all have Cu+Zn values ≥ 7000 ppm (Herzig *et al.*, 1991; Hannington *et al.*, 1995). Only one sample of the Si-Fe cap Unit C from Rona mound (057RD/P10) has comparable Cu+Zn concentrations (~7200 ppm). Two other samples from the Si-Fe cap had concentrations of ~5300 ppm (057RD/P10 – Unit C Rona Mound) and ~1150 ppm (050RD/P12 – Unit B – Southern Mound), all other samples recorded Cu+Zn concentrations between ~30 ppm and 700 ppm. Typical Cu+Zn concentrations of Si-Fe cap material are between 1 and 2 orders of magnitude lower than gossanous surface material from the TAG active mound. In contrast, the plot of red and grey chert material from the ODP drilling program falls within the spread of Si-Fe cap Unit samples from the eSMS deposits (Figure 148).

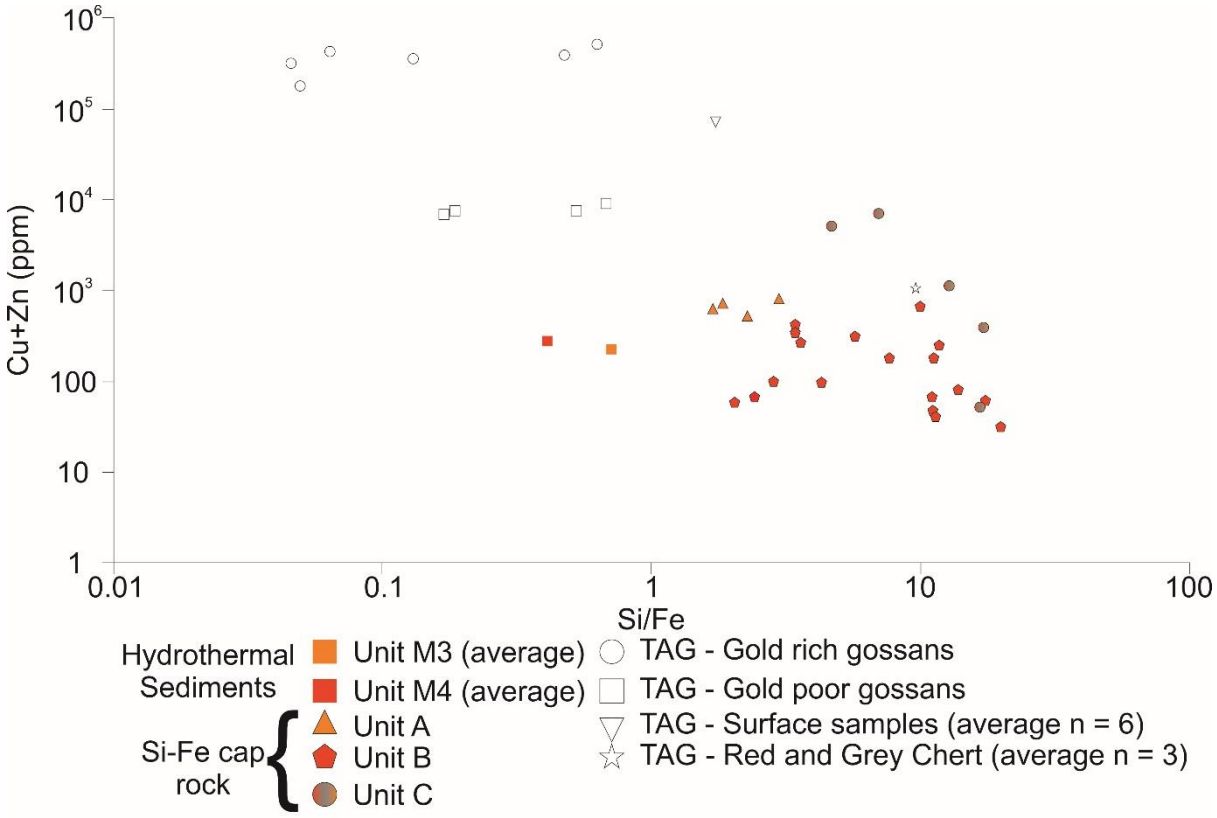

Figure 148: Plot of Si/Fe vs Cu+Zn concentrations of gossanous material from the TAG active mound, Units M3 and M3 hydrothermal sediments, and Si-Fe cap Units A-C. Additional data from Herzig *et al.* 1991, and Hannington *et al.* 1995. Unit M3 = 12 samples, Unit M4 = 3 samples, Unit A = 4 samples, Unit B = 20 samples, Unit C = 5 samples.

In general, there appears to be a negative relationship between Cu+Zn and Si/Fe ratio when comparing the TAG active mound samples (hollow symbols) to the eSMS samples (coloured symbols). This variation may be a function of silica dilution, similar to the trends observed between hydrothermal sediments and Si-Fe cap rock.

By using the technique described in Section 6.5, silica is removed from the total analyses and a silica free value can be recalculated assuming a proportional increase in all elements (Figure 149). This recalculation shows that Cu+Zn values for average Unit A and Unit B samples, and hydrothermal sediment Units M3 and M4, were still ~ 1 order of magnitude lower in concentrations than even base metal-poor TAG samples. The higher concentration of base metals in Unit C samples is solely due to the presence of late stage sulphides growth after silicification, and therefore post-date any gossan-related activity.

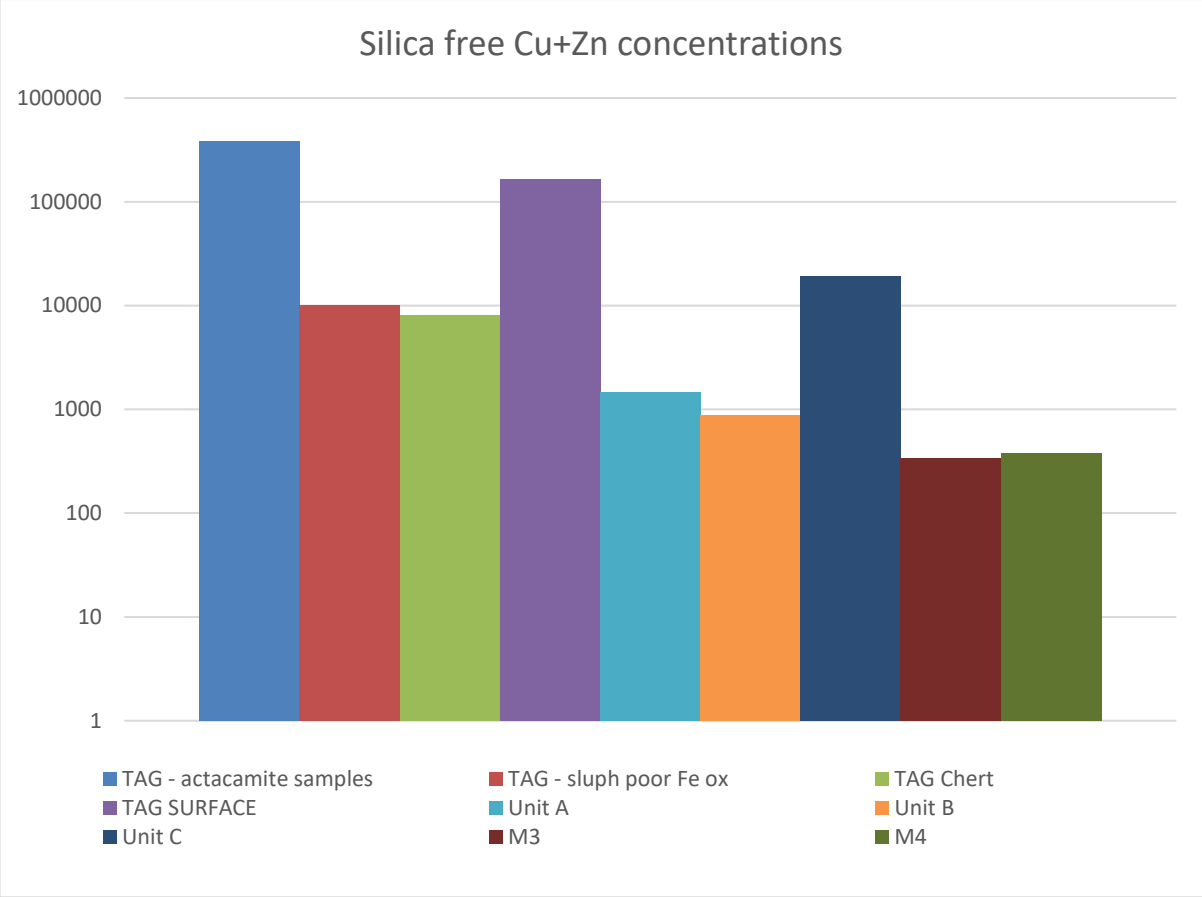

Figure 149: 'Silica removed' concentrations of Cu+Zn in a range of TAG hydrothermal field samples. Unit M3 = 12 samples, Unit M4 = 3 samples, Unit A = 4 samples, Unit B = 20 samples, Unit C = 5 samples.

This pattern shows that the Cu+Zn vs Si/Fe negative trend is not associated with simple dilution by silicification. Comparison of the hydrothermal sediments and Si-Fe cap rocks with gossanous material and even red/grey chert from the TAG active Mound have significantly lower base metal contents (~1-2 orders of magnitude).

This could be explained by:

- Gossanous processes not contributing much to the formation of the hydrothermal sediments that are interpreted to have been the protolith of the Si-Fe cap
- Or assuming gossanous process have formed the hydrothermal sediments, then either:
    - metal removal from the hydrothermal sediments has been more efficient at the eSMS deposits, than at the TAG Active Mound;
    - or the sulphide assemblage at the eSMS deposits was lower in base metal content compared to the TAG Active Mound.

Based on this investigation, it is difficult to determine which of these processes is the most likely. Textural evidence from Southern Mound (elevated Zn concentrations in Unit A samples, and potential clasts of goethite after sulphide) and the MIR Zone (observation of atacamite in a proximal sediment core to the boreholes), implies that some degree of gossan formation has contributed to the Si-Fe cap, but this is not conclusive.

The lack of secondary metal sulphides, oxides, or chlorides, the lack of preserved relict sulphide textures, and the low base metal content in comparison to gossanous material from the TAG active mound provides little evidence for the input of iron oxide from the weathering or primary massive sulphides into the hydrothermal sediment Units, which in turn became the protolith for the Si-Fe cap.

The presence of an atacamite layer within the overlying hydrothermally derived sediments at the MIR zone (Dutrieux, 2019), and the weathered pyrite grains within the Si-Fe cap implies that iron oxide/oxyhydroxides derived from the weathering of massive sulphides does contribute to the hydrothermal sediments and Si-Fe cap, but it is not likely to be a significant contribution. Therefore, another iron oxide/oxyhydroxide formation mechanism, likely direct precipitation from hydrothermal fluids, can explain the high iron oxide/oxyhydroxide contents.

8.1.1.2 Direct abiological precipitation from a hydrothermal fluid – Exhalite?

Exhalite deposits are chemical sediments formed by the accumulation of minerals precipitated from hydrothermal fluids and include sediments derived from plume fallout, replacement of existing sediments, and sub-surface precipitation of minerals . A variant called replacement exhalites are a common product in back arc VMS deposits (i.e. Kuroko, Urals etc.) as described in Section 2.3 and are typically a hydrothermal alteration product of existing overlying or associated volcanoclastic (tuffaceous) material. They occur when continued hydrothermal flow results in the alteration and replacement of volcaniclastic sediments to form iron oxides as an alteration/weathering product of hydrothermal (Mg,Fe^{2+})-smectite clay (Maslennikov *et al.*, 2012). The formation of tuffaceous material is not a common feature of mafic volcanism at mid-ocean spreading ridges and therefore it is unlikely that iron oxides are derived by halmyrolysis of volcanic-related exhalites

For the TAG hydrothermal field, there is no evidence for volcanic material (i.e. glass fragments or partially weathered igneous material) in the Si-Fe cap, nor in the overlying hydrothermal sediments. The extent of underlying volcanic material was mapped in Chapter 3, with the majority of the areas of investigation showing sediment cover over either hydrothermal material, or pillow and flow basalts. It is therefore unlikely that iron oxide material is derived from a replacement exhalite mechanism.

It is widely accepted that direct precipitation from hydrothermal fluids is one of the main iron oxide/oxyhydroxide formation mechanisms in hydrothermal settings. When a low temperature, reduced, iron rich, sulphur poor, hydrothermal fluid mixes within a seawater saturated (cool, and oxidised) sediment sequence, sub-surface precipitation can occur spontaneously. This change in redox results in the oxidation of aqueous Fe^{2+} and subsequent precipitation of amorphous ferrihydrite (Schwertmann, 1983; Schwertmann *et al.* 1999), which is a significant mechanism for iron oxide input into hydrothermal sediments, and which can be rapidly altered to more crystalline polymorphs (i.e. goethite/haematite) depending on pH and temperature. At higher temperatures, it is thermodynamically possible to directly precipitate haematite from a hydrothermal fluid by mixing (Markl *et al.*, 2006).

Because hydrothermally precipitated ferrihydrite can be converted into either haematite or goethite, the presence of goethite or haematite is not a unique indicator of sulphide weathering. Evidence for the pH conditions during Si-Fe cap diagenesis has been presented in Section 6.5, and interpreted that prevailing pH of between ~4 and 6 was necessary to create the characteristic REE patterns associated with the hydrothermal sediment Units. At these pH conditions, and low temperatures (<30˚C), goethite would be a more dominant oxidised iron product (Figure 150). At higher temperatures and more neutral to basic pH, haematite would be likely to dominate.

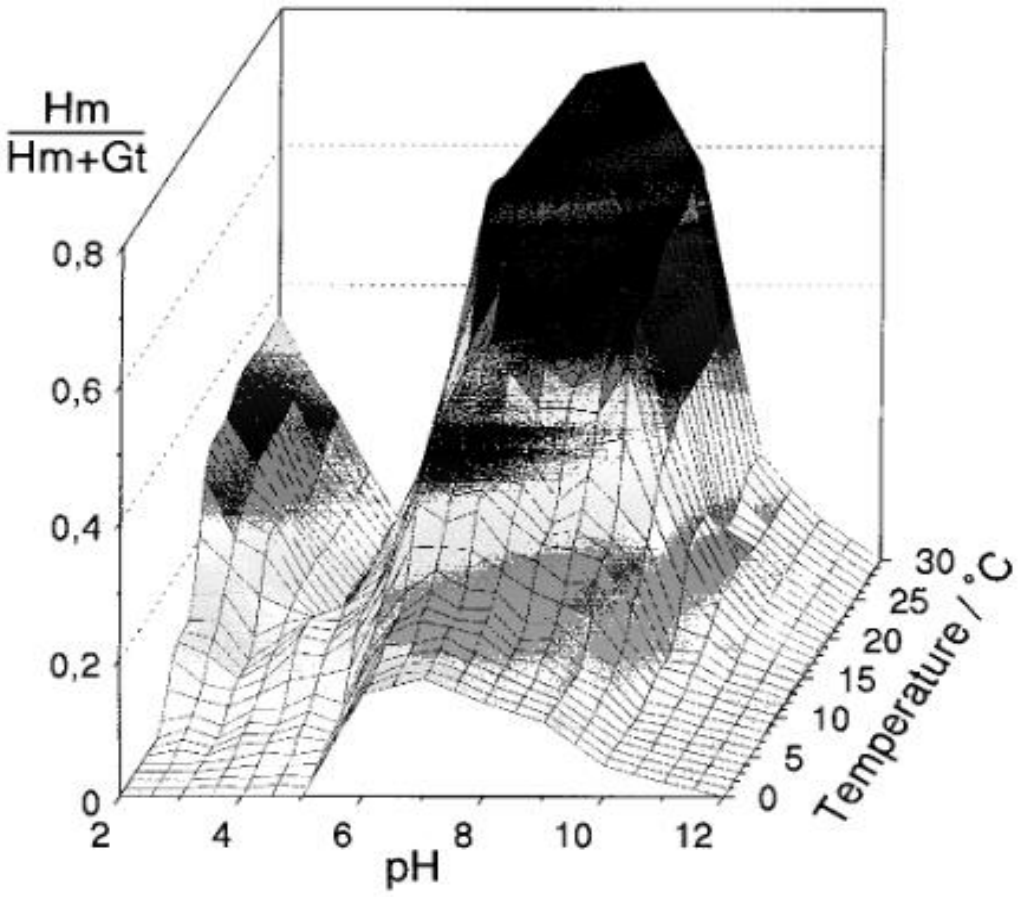

Figure 150: pH and temperature controls on the precipitation of goethite and haematite from ferrihydrite from Schwertmann *et al.* (1999). Surface represents the relative proportion of haematite and goethite precipitation, i.e. if $\frac{Hm}{Hm+Gt}$ = 0.5, then product is 50% haematite, 50% goethite.

Assuming a model in which mixing of a reduced, sulphur-poor, warm hydrothermal fluid with oxidised, cool, seawater within a hydrothermal sediment sequence causes iron oxide precipitation, and in which the goethite-haematite conversion from ferrihydrite is temperature related, then a vertical stratification of goethite over haematite might be expected. Indeed, this trend is observed throughout Southern Mound, with sediment Unit M3 and Si-Fe Unit A both being dominated by goethite, and Units M4, B, and C, being dominated by haematite. This temperature-induced trend, observed in iron oxides, is similar to the temperatures obtained by the oxygen isotope geothermometry of silica, implying cooler, temperatures at shallower depth below seafloor, and warmer temperatures at greater depth. This trend, however, is not observed at MIR zone, where oxygen isotope formation temperatures remain relatively consistent throughout, and goethite is present at depth in one borehole. This could be explained by the fact that goethite was present as part of the initial sediment and was not altered to haematite upon silicification.

Textures related to direct precipitation from hydrothermal fluids have been classified into two main types in this study: ordered; and disordered. Ordered precipitation results in some form of controlled growth textures, i.e. colloform or dendritic growth, which also provide nucleation sites promoting further precipitation. Where no organised textural growth forcing is exerted (i.e. little to no dendritic or colloformic growth), the amorphous iron oxide and iron oxyhydroxide material is typically fine grained or colloidal, representing 'disorganised' precipitation.

Hydrothermal sediment Unit M4, and to a lesser extent M3, both have high quantities of amorphous and fine-grained iron oxides/oxyhydroxides. Unit M4 is almost entirely fine-grained material, and is considered to represent a product of disorganised hydrothermal precipitation. Unit M3 appears to be a combination of disorganised precipitation, and gossanous mass wasted material.

Both colloform and dendritic iron oxide growth textures are observed in the overlying hydrothermal sediments, but are more common in the Si-Fe cap material, particularly Unit A and Unit C at Rona Mound. Colloform growth textures have historically been interpreted as fine-grained sequential mineral precipitation from a gel, but are more likely to simply represent a direct crystallisation mechanism (Roedder, 1968; Barrie *et al.*, 2009). Dendrites are considered a primary texture of direct precipitation from hydrothermal fluids. They are typically fractal in appearance, and their growth is typically thought to be a product of a diffusion limited aggregation mechanism (Chopard *et al.*, 1991; Hopkinson *et al.*, 1998). Both of these textures are a result of direct iron oxide or oxyhydroxide precipitation from supersaturated fluids (Roedder, 1968; Chopard *et al.*, 1991 and occurs throughout the sediments and is preserved in the Si-Fe capping material.

Fractal iron oxide dendrites within agates at the TAG hydrothermal field are a product of both diffusion limited aggregation and supersaturation-nucleation depletion cycles (Ortoleva *et al.*, 1987). The agates were initially a precursor silica gel, which creates the diffusion limited environment facilitating the dendritic iron oxide growth textures. Supersaturation-nucleation cycles are interpreted to be responsible for the spontaneous precipitation of iron oxides, and on precipitation, the iron oxides trigger silica crystallisation within the gel precursor. Further discussion on this mechanism can be found in Section 8.1.2. The implication behind this process is that the ordered iron oxides precipitated after the formation of a silica gel, and thus provides evidence of the relative timing of dendritic growth against silica formation.

8.1.1.2.1 Biological mediated precipitation mechanism?

The role of microbes and bacteria in the precipitation of iron oxide in hydrothermal environments is often hypothesised for ancient VMS analogues, but difficult to prove as organic material is lost

during geological preservation. In modern settings, organic material has been found, and as such microbial/bacterial presence can be directly linked to iron oxide/oxyhydroxide precipitation. The role of microbia is important because it provides a biological mechanism of iron oxidation from reduced fluids in an extreme environment, and the contribution of iron oxidation by biological process could represent a significant process of iron precipitation at seafloor vent sites (Emerson and Moyer, 2002b).

Filamentous material is common within the Si-Fe capping material from the TAGHF (Sections 5.2.4, 5.3.3, and 5.5.3). However, there is a lack of organic material in any of these samples, and hence there is a lack of direct evidence for the involvement of microbes or bacteria. This lack of a direct link is shared with Si-Fe material in ancient VMS deposits. Instead, the morphology and habit of the filamentous material offers the best method for determining the extent of biogenicity for the filamentous material throughout the Si-Fe cap.

The most likely iron oxidising bacteria in this kind of setting are *Gallionella*, *Leptothrix*, or *Sphaerotilus* (Little *et al.*, 2004), which require low temperature, near neutral pH, low oxygen fugacity (i.e. reduced conditions) and ferrous iron rich fluids to survive (Boyd and Scott, 2001). Based on the geochemical changes during formation of the Si-Fe cap rock (See Chapter 6), low temperature (minimum of ~60-80 ˚C from $\delta^{18}O$, See Section 6.5.4) reducing fluids of weakly acidic pH (pH 4-6) are interpreted to be the geochemical conditions causing silicification. These conditions appear to fit into the natural domain range of all three potential iron oxidising bacteria (Figure 151).

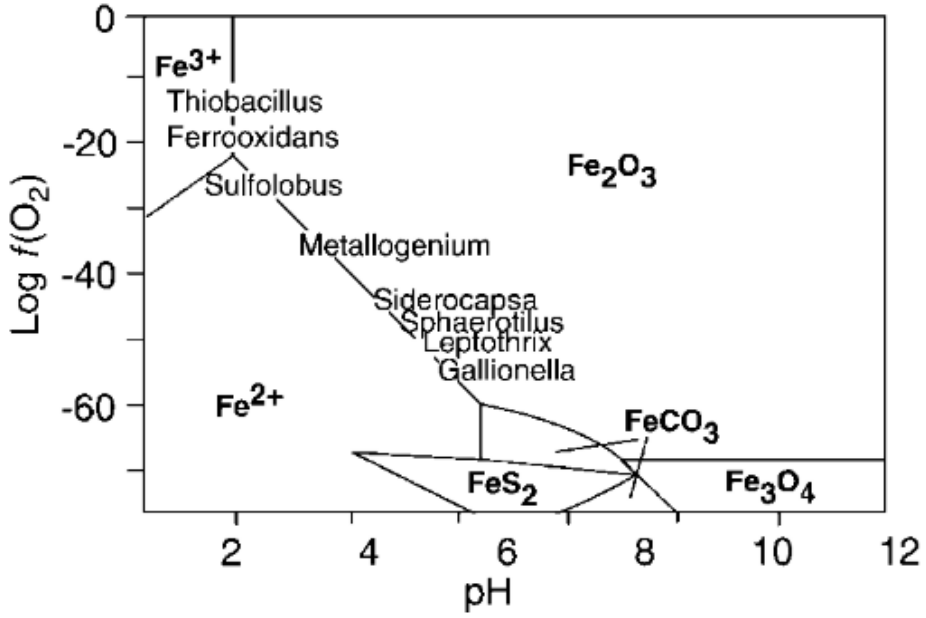

Figure 151: Oxygen fugacity vs pH diagram for a range of iron oxidising bacteria common in hydrothermal settings (from Boyd and Scott (2001))

The role of biological involvement in precipitation of ferrihydrite is a common feature at seafloor hydrothermal sites, and these processes have been well summarised in the literature ((Boyd and Scott, 2001). A condensed route taken by iron precipitated from hydrothermal fluids in the TAGHF is presented based on these interpreted processes (Figure 152).

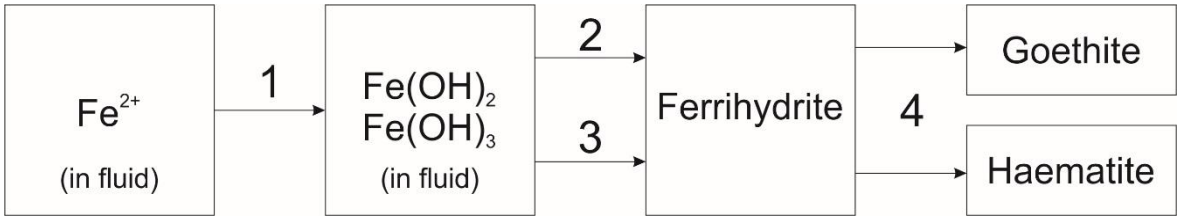

Figure 152: Interpreted processes resulting in iron oxide precipitation and formation, including biotic influence. 1) Chemical oxidation, 2) continued chemical oxidation and precipitation, 3) microbial oxidation and precipitation, 4) Phase transformation (pH and/or temperature controlled). Edited from Boyd and Scott, 2001.

8.1.2 Origins of silicification – formation of the Si-Fe cap

I have shown that the un-silicified hydrothermal sediment Units (M3 and M4) are the probable protolith of the Si-Fe cap, that have later been exposed to several silicification events . The question arises, therefore, about the origin of the silica and mechanisms for its precipitation. Two main mechanisms of seafloor silicification are known: cherts derived from biological silica; and hydrothermal silica deposits.

Examples of biogenic silica in the TAGHF hydrothermal Fe-rich sediments are restricted to sparse skeletal diatoms and radiolaria. No biogenic silica is observed in the underlying Si-Fe cap rocks despite the Fe-rich sediments being their protolith. However, the fluids impregnating the sediments with silica and converting them into the Si-Fe cap rocks will probably have destroyed any pre-existing biogenic silica during the silicification process, thus destroying any textural evidence. Even if this is the case, the amount of biogenic silica is negligible and cannot account for the increase in silica represented by the change from Fe-rich sediment to Si-Fe cap rock, and requires an external source.

Based on both historical VMS and modern-day SMS analogues (Chapter 2), and the physical, geochemical and isotope observations (Chapter 5 and Chapter 6), it is clear that the majority of silica associated with both the Si-Fe capping material, and likely the silica component of the hydrothermally derived sediments, is predominantly of hydrothermal origin.

The main mechanisms for silica precipitation in hydrothermal environments are described in Chapter 2. Considerations of phase equilibria and pH indicates that precipitation of silica appears to be a mainly a function of temperature (Carrol *et al.*, 1998). Hence, the silicification of the hydrothermal sediments is a result of cooling of silica-rich hydrothermal fluids, and not changes in pH. Although quartz can precipitate directly from silica undersaturated seawater at ocean bottom conditions (~4°C) (Mackenzie and Gees, 1971), it can also remain in solution despite being supersaturated due to its high activation energy (Krauskopf, 1956). Therefore, temperature constraints or dissolved silica concentrations of fluids influence, but may not always govern, the spontaneous precipitation of silica. As temperature decreases, so does the quartz solubility, which promotes silica precipitation from fluids with lower dissolved silica concentrations (Krauskopf, 1956). However, as temperature decreases, the kinetics of quartz precipitation slow, which further inhibits crystallisation (Krauskopf, 1956; Williams and Crerar, 1985; Williams *et al.*, 1985). These two effects cancel each other out, which often results in quartz not being precipitated, despite being supersaturated. In contrast, the kinetics of amorphous silica precipitation are faster, hence even at low temperatures amorphous silica can precipitate when the fluid is supersaturated with respect to amorphous silica, over quartz (Krauskopf, 1956; Williams and Crerar, 1985; Williams *et al.*, 1985).

Two types of silica polymorph are identified throughout the Si-Fe cap, with the textural and geochemical data implying precipitation as amorphous silica precipitation and through subsequent recrystallisation and dehydration transitions to α-quartz via hydrous metastable silica polymorphs (opal-CT, and opal-C). This supports the concept that the silica, throughout the Si-Fe cap, has been precipitated as amorphous silica that has undergone varying degrees of maturity.

Using this assumption, and the oxygen isotope formation temperatures for the two main silicification events, the minimum dissolved silica content of the silicifying fluids can be obtained from the plot of silica solubility vs temperature. Saturation limits of silica in fluids are controlled by the solubility of each silica polymorph, and the solubility is controlled by temperature (Figure 153).

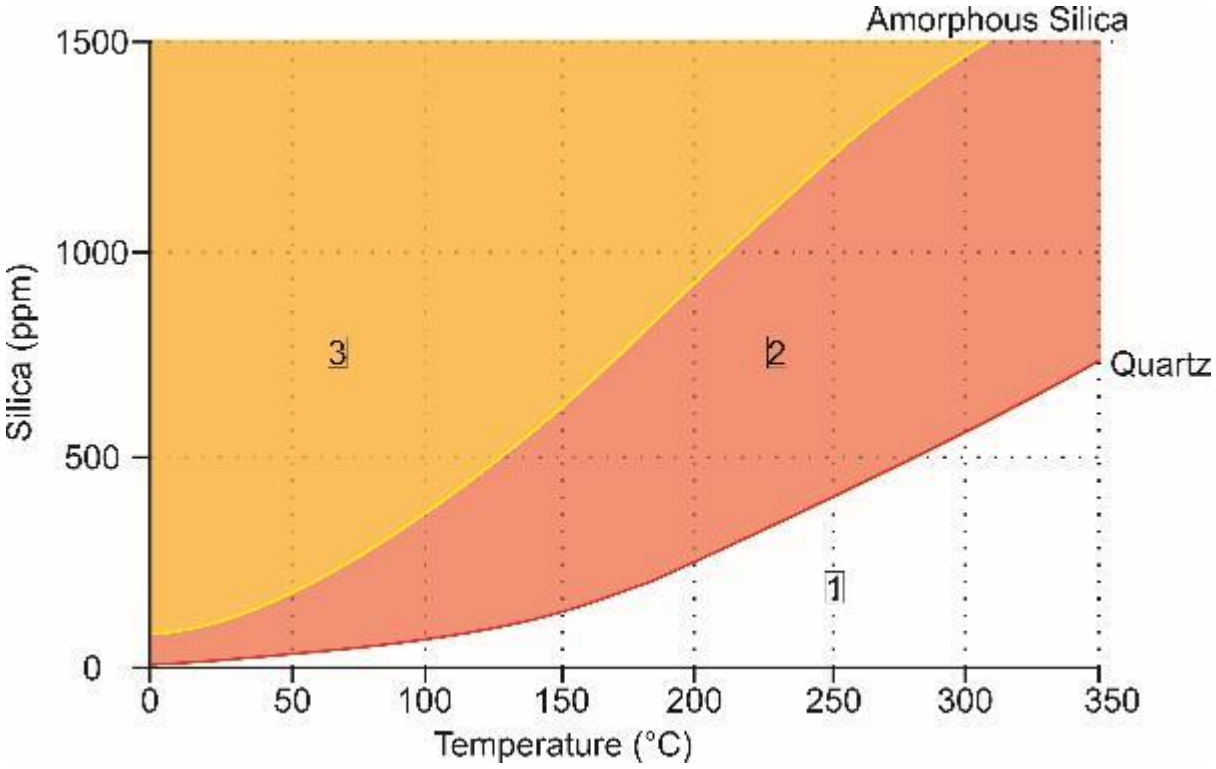

Figure 153: Silica saturation curves for quartz and amorphous silica with respect to temperature and silica (ppm). Edited from Gunnarsson & Arnorsson (2000). 1) Area where silica concentrations are not saturated with respect to either amorphous silica or quartz. 2) Area where silica concentrations are saturated with respect to quartz but not amorphous silica. 3) Area where silica concentrations are saturated with respect to both amorphous silica and quartz.

Hydrothermal fluids cool in two ways: conductive cooling of high temperature hydrothermal fluids, or fluid mixing (resulting in cooling and dilution of dissolved silica). Conductive cooling would result in little to no dilution of dissolved silica, whereas mixing hydrothermal fluids with seawater (average ~4 ppm dissolved silica), would result in silica dilution. These two mechanisms would result in different pathways on the silica solubility curve plots (Figure 154).

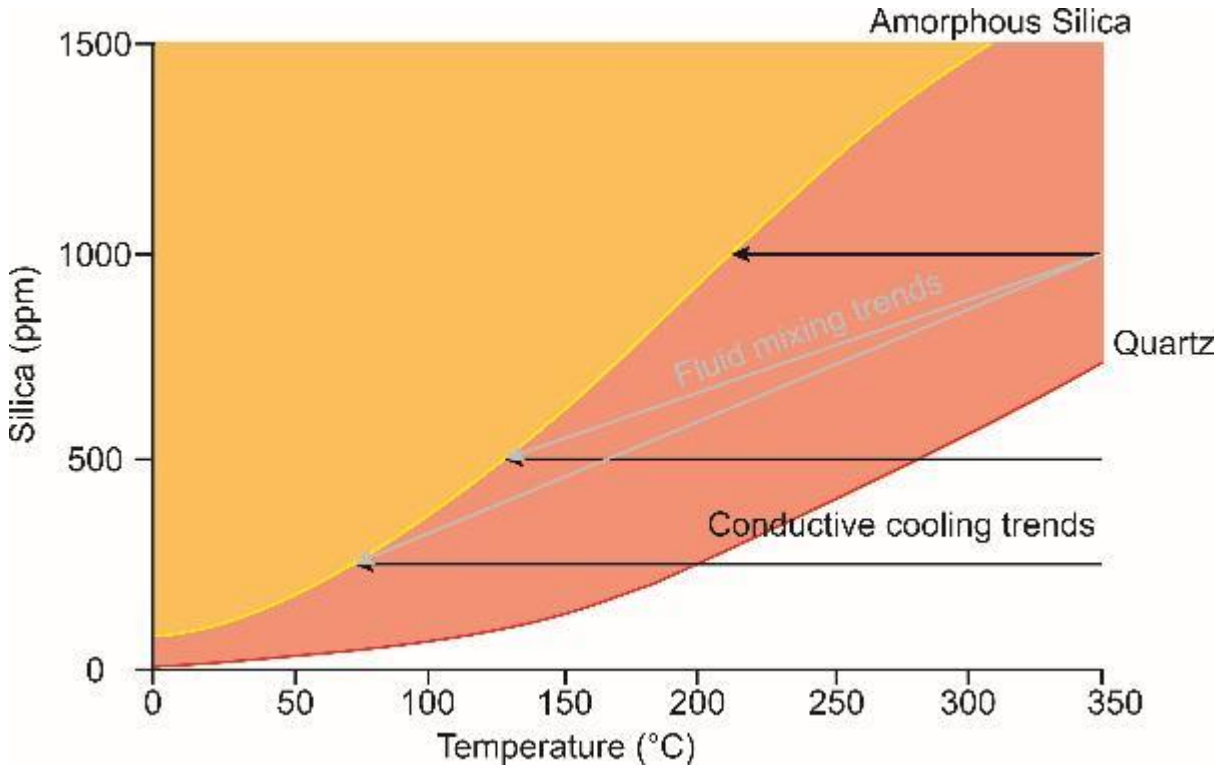

Figure 154: Conductive cooling: Three pathways for conductive cooling of three fluids containing 250, 500 and 1000 ppm silica, reaching amorphous silica saturation at temperatures of ~70, ~125, and ~210°C respectively. Fluid mixing: Two mixing trends where a single fluid of 1000 ppm 350 °C fluid mixes with variable amounts of a in cooler, lower Si content fluid, resulting in silica saturation with respect to amorphous silica at the same temperatures as conductively cooled 500 ppm and 250 ppm fluids.

Silica is being precipitated throughout the active TAG mound, estimated in the order of 10^6 or 10^7 kg/yr by considering the differing silica content of hydrothermal vent fluids (James and Elderfield 1996). Concentrations of orthosilicic acid ($Si(OH)_4$) have been recorded at ~ 22 mM/kg and ~19 mM/kg for black and white smoker fluids respectively (Tivey *et al.*, 1995; James and Elderfield,

1996). This equates to ~1300ppm and ~1100ppm of dissolved silica (SiO_2) in solution for end-member black smoker (350˚C) and white smoker (250˚C) fluids respectively (Figure 155).

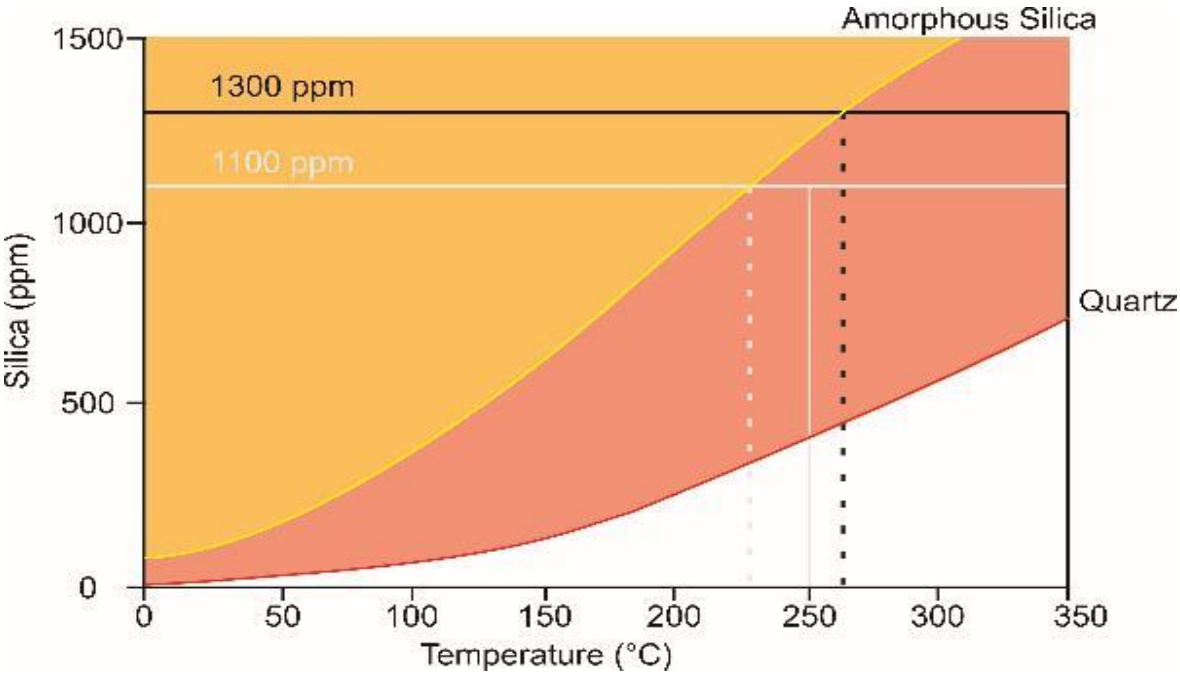

Figure 155: Conductive cooling trends of TAG black (black line) and white (grey line) smoker fluids. Dashed lines show the temperature at which the cooled fluid would become supersaturations with respect to amorphous silica, enabling precipitation.

Based on these measured concentrations of silica, both fluids are supersaturated with respect to quartz, but not supersaturated with respect to amorphous silica at their recorded temperatures. Black smoker fluids would have to be cooled to ~ 260˚C, and white smoker fluids cooled to ~230˚C to be supersaturated with respect to amorphous silica, assuming conductive cooling alone (Figure 155).

Using the maximum and minimum silica formation temperatures from oxygen stable isotopes for the Si-Fe cap materials, we can calculate the range of silica concentrations that are saturated with respect to amorphous silica (Figure 156). Assuming conductive cooling of fluids alone, the silica concentrations would have to be greater than ~210-280 ppm for Unit A (~60-80˚C), ~390-570 ppm for Unit B (~105-140˚C), and ~370-800 ppm for Unit C (100-180˚C) to be saturated with respect to amorphous silica at the estimated formation temperatures. This implies that simple conductive cooling of black or white smoker fluids is unlikely to account for the silicification of the Si-Fe capping materials, as silica formation temperatures would be expected to be >230 ˚C.

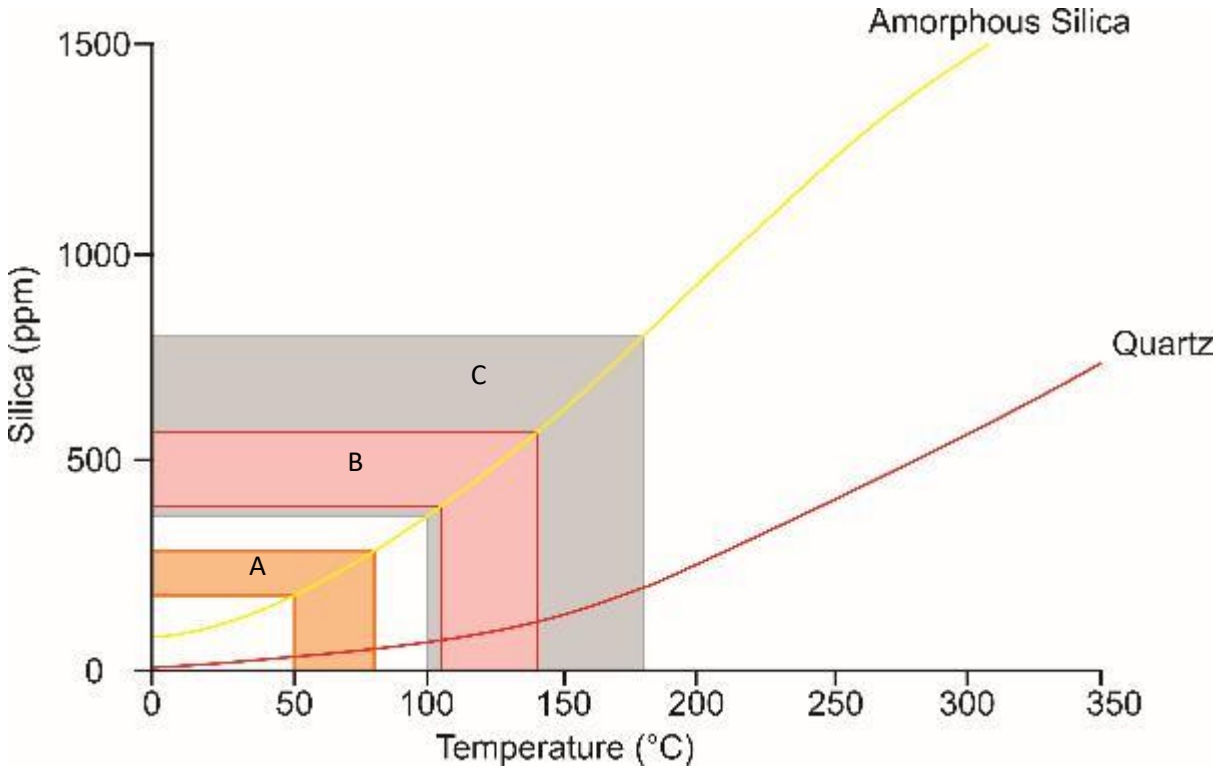

Figure 156: Range of predicted silica concentrations (max-min) of precipitating fluids for each of the three Si-Fe cap rocks, based upon their formation temperatures. Orange band = Unit A, Red band = Unit B, and Grey band = Unit C samples.

Instead, silicification is likely formed by mixing of higher temperature, silica-rich fluids, with lower temperature silica-poor fluid (i.e. seawater).

Calculations of the necessary mixing ratios of end member fluids (seawater~ 4˚C, black smoker fluids ~350˚C, and white smoker fluids ~250˚C) to form appropriate formation temperatures of the Si-Fe cap Units have been undertaken using the following formula:

$$Final\ temperature\ (^{\circ}\mathrm{C}) = \frac{(m_{F1} * c_{F1} * T_{F1} + m_{F2} * c_{F2} * T_{F2})}{(m_{F1} * c_{F1} + m_{F2} * c_{F2})}$$

The calculations assume a final total mixing volume of 100 kg of fluid, and that both fluids have the same specific heat capacity (4.2 j/g ˚K). F1 and F2 represent the two fluid endmembers being mixed, m is the necessary mass fractions (in kg) for the respective fluid (out of 100kg) necessary to create the final temperature, c is the specific heat capacity, and T is the temperature of the end member fluids in ˚C. Mixing ratios are presented in Table 91.

Table 91: Required fluid mixing ratios for black smoker fluid, white smoker fluid, and seawater to obtain the interpreted silica formation temperatures

		Temperatures (˚C)	**BS:SW ratio needed**	**WS:SW ratios needed**
Unit A	Average (n=4)	70	1:4.3	1:2.7
	Max-Min	60-80	1: 3.6 – 5.2	1: 2.2 – 3.4
Unit B	Average (n=21)	122.5	1:1.9	1: 0.9
	Max-Min	105-140	1:1.5 - 2.4	1: 0.7 – 1.2
Unit C	Average (n=5)	140	1:1.5	1: 1.2
	Max-Min	100-180	1: 1.0 - 2.6	1: 0.6 – 2.5

To test to see if it is feasible for these fluids to precipitate silica, dilution calculations have also been undertaken to determine the end silica concentrations of the mixed fluids. Seawater is assumed to have ~16 ppm dissolved silica (Fabre *et al.* 2019), and the TAG black and white smoker fluids (~1320 ppm and 1140 ppm respectively (Tivey *et al.*, 1995; Elderfield and Schultz, 1996; James and Elderfield, 1996))have been used for this calculation (Table 92).

$$Diluted\ silica\ concentration\ (ppm)\ =\ Conc_{F1} * w_{F1} + Conc_{F2} * w_{F2}$$

Where 'Conc' is concentrations in ppm (i.e. mg/kg), w is the mass fraction of mixing, and F1 and F2 represent the two end-member fluids being mixed.

Table 92: Summary of diluted silica concentrations based on the interpreted mixing ratios for black smoker, white smoker, and seawater necessary to achieve the measured silica formation temperatures

		BS:SW ratio needed	**WS:SW ratios needed**	**BS:SW diluted silica concentrations (ppm)**	**WS:SW diluted silica concentrations (ppm)**
Unit A	Average (n=4)	1:4.3	1:2.7	261	307
	Max-Min	1: 3.6 – 5.2	1: 2.2 – 3.4	224 – 298	263 – 351
Unit B	Average (n=21)	1:1.9	1: 0.9	456	538
	Max-Min	1:1.5 - 2.4	1: 0.7 – 1.2	391 – 521	461 - 615
Unit C	Average (n=5)	1:1.5	1: 1.2	521	615
	Max-Min	1: 1.0 - 2.6	1: 0.6 – 2.5	372 – 669	439 - 791

Comparison between diluted silica values and anticipated silica concentrations needed to form the respective Si-Fe cap Units general correlate well (Table 93). This shows that the diluted dissolved silica contents of variably mixed seawater and black or white smoker fluids are generally at the expected concentrations for saturation with respect to amorphous silica.

Table 93: Max-Min values of silica needed to be supersatured with respect to amorphous silica at the range of temperatures measured for silica in each of the Si-Fe cap Unit and calculated silica values from fluid mixing

		Necessary silica concentrations needed (ppm)	**BS:SW diluted silica concentrations (ppm)**	**WS:SW diluted silica concentrations (ppm)**
Unit A	Max-Min	210-280	224 – 298	263 – 351
Unit B	Max-Min	390-570	391 – 521	461 - 615
Unit C	Max-Min	370-800	372 – 669	439 - 791

When looking at the interpreted mixing lines (Figure 157), we can see that for white smoker fluids direct mixing trends for Unit A material (~70 ˚C) from the initial white smoker fluid conditions (~1100 ppm, ~250˚C) would reach supersaturation with respect to amorphous silica at higher temperatures than Unit A samples. Mixing lines from black smoker fluids, show that progressive mixing of black smoker fluid with increased seawater concentrations could account for the range of temperature observed in the Si-Fe cap.

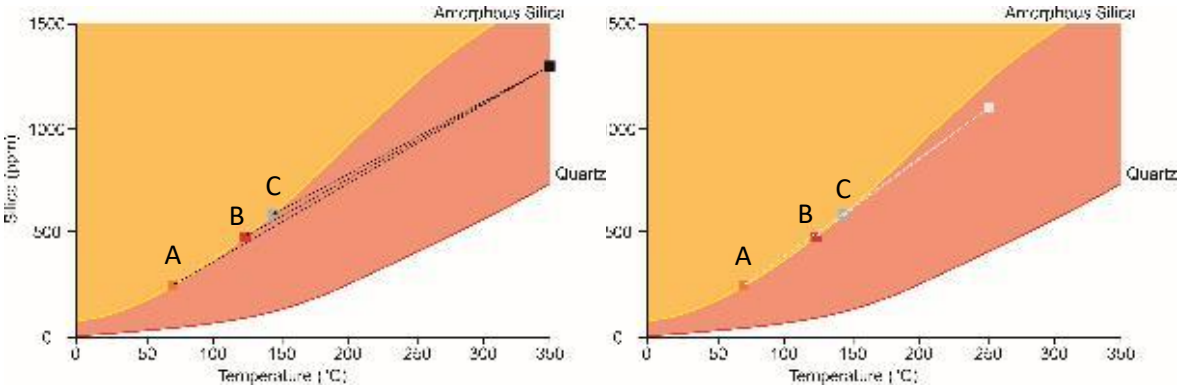

Figure 157: Fluid mixing trends from black smoker (left) and white smoker (right) fluids, assuming TAG fluid temperatures and silica concentrations

The paragenesis of the Si-Fe capping material at each of the mounds studied in this investigation imply a complex history of silicification, which appears to differ at mound scale.

8.1.2.1 Southern Mound and MIR Zone – Multiple silica generations

Southern Mound presents the most complete recorded of Si-Fe cap Units and silica genesis. Hydrothermal sediments were only recovered from Southern Mound and although rare crystalline silica was identified (by XRD), transparency in thin section and SEM EDS mapping implies that silica is present in low concentrations compared to the Si-Fe cap. In both boreholes where sediments were recovered, the only underlying Si-Fe capping material recovered was Unit B material which contained quartz (022RD, and 031RD). 050RD recorded the presence of both opal-CT and quartz silica polymorphs with oxygen isotopes registering different formation temperatures for each.

At least two generations of silica have been identified at both Southern Mound and the MIR Zone, with the assumption that the hydrothermal sediment was infiltrated by a silica rich fluid, which on cooling, precipitated an amorphous silica gel. This gel subsequently started to mature resulting in crystallisation and desiccation. It is thought that the formation of the second silica generation, interpreted to have been precipitated from a higher temperature fluid, helped increase the silica maturation rate, of the first generation while simultaneously precipitating and maturing the second generation of silica, where they overlapped spatially.

A question that remains about the distribution of silica in the Si-Fe cap (at Southern Mound), is why it varies from two similar boreholes (022RD and 031RD) to 050RD. The simplest explanation is discussed above is that any evidence of an early lower temperature silicification event overprinted was by a higher temperature event, which aided maturation of the silica polymorphs.

This presents an interesting spatial observation, implying that the early silicification event reached similar depths across southern Mound (2-3 m below the seafloor), whereas the later higher temperature generation reached variable depths (~2-3 m at 022RD and 031RD, but ~ 5-6 m at 050RD). If the two silica generations are interpreted to represent an 'isotherm' where the silica formation temperatures represent the temperature at which the hydrothermal fluids were cooled sufficiently to enable silica precipitation, then this could imply different temperature ranges across the mound between silica events.

It is possible that the type of hydrothermal sediment could indicate and play a role in silica precipitation. For example the lower temperature opal-CT silica generation is interpreted to have silicified Unit M3 sediment, is dominated by clasts of material and appears to be more porous, whereas the 'jasper' material in Units B and C does not exhibit the same degrees of porosity, and is interpreted to be silicified Unit M4 material. The higher porosity of unit M3 would have enabled more seawater to be entrained, than Unit M4, thus locally providing a larger temperature gradient during fluid mixing, and potentially decreasing the mixing fluid temperature.

Silica assemblages at TAG appear to be temperature controlled. Hopkinson *et al.* (1999) observed two temperature types of quartz, differentiated by the presence of aluminium zoning in high temperature samples (>360˚C). Aluminium is strongly hydrolysed or polymerised in typical ocean water, and as such not available for incorporation into silica at low temperatures (Frondel, 1982; Hopkinson *et al.*, 1999). None of the samples analysed as part of this investigation recorded significant aluminium concentration (10-13 ppm), implying silica formation temperatures of <360˚C. This is supported by the estimated silica formation temperatures from oxygen isotopes.

8.1.2.2 Rona Mound – 'high' temperature opal-CT

Only opal-CT, the metastable silica polymorph, is present at Rona Mound. The amorphous fraction, identified in XRD, is interpreted to be predominantly amorphous silica, based on the immaturity of the crystalline silica assemblage, and the low iron contents of the Si-Fe materials.

Silica in Unit B material is present as coating and infill of filamentous iron oxide material throughout. This texture does not suggest that the iron oxide material has formed within, or been encased by, a precursor silica gel, as observed and proposed for the TAG active mound (Hopkinson *et al.*1999).

A precursor gel would likely result in complete silicification, whereas the textures observed at Rona Mound appear to be more similar to silica precipitation on ramified iron oxides.

Unit C material presents a slightly different story, with dendritic and filamentous material appearing to show the complete silicification infill associated with a silica gel precursor. This formation mechanism is further evidenced by clear observation of the silica extent after the bleaching effect of iron oxides.

This variation could hint towards the difference in silica formation temperatures between the two Units. Unit C could be dominated by a precursor silica gel forming and beginning to crystallise, but not maturing to the extent of being a mixed opal-CT and quartz assemblage (i.e. as in Unit A). In contrast, Unit B silica could represent silica precipitation directly from a hydrothermal fluid, nucleating off existing iron oxide structures.

If the assumption is correct, that cooled TAG hydrothermal fluids are supersaturated with respect to silica (at say ~ 160 to 180˚C), then the presence of filamentous iron oxide material acting as nucleation sites could trigger spontaneous amorphous silica precipitation. Chemically similar fluids may also be responsible for the formation of the silica gel, but may not have been able to cool efficiently to form a silica gel in the shallower Unit B material, but gel formation was possible within Unit C material. This scenario would explain the higher temperatures, and the silica textural variation between Units B and C at Rona Mound, but seems counter-intuitive with 'deeper' material being cooler than shallower material.

The presence of filamentous haematite and opal-CT coatings at Rona Mound is seemingly comparable with the 'unique' haematite and opal-CT hydrothermal mounds in the East Blanco Depression (Section 2.4.1.3). These mounds are interpreted as representing iron oxide microbial mats which have been silicified by low temperature, strongly oxidised, silica- and iron- rich, and sulphur poor fluids (Hein *et al.*, 2008). This interpretation broadly fits the paragenesis of Unit B material at Rona Mound as we have predominantly filamentous and dendritic iron oxides that have provided a surface for silica precipitation. The different temperatures may be explained by two different pulses of silicification.

8.1.3 Origins of Sulphides

Partially oxidised sulphides are present in Unit B material, particularly from the MIR Zone (Section 5.4.2). These sulphides are interpreted to be relict and derived from the gossanous material derived from weathered massive sulphide and are not thought to be related to the deeper bleaching and

sulphidation of Unit C material at Southern and Rona Mounds. This implies some degree of mass wasting/weathering of existing hydrothermal material is contributing to the Si-Fe cap rocks.

Unoxidised pyrite grains, observed in Unit B material from both Rona Mound and MIR zone, exhibit an iron oxide free silica halo and are interpreted to represent bleaching of jasperoidal material by iron oxide reduction and near in-situ recrystallisation into pyrite. This texture is also observed at the TAG active mound (Petersen, 2000) and particularly within the low temperature Kremlin zone. This texture, although uncommon, implies that reduced and (probably) sulphur limited fluids were able to permeate into the Si-Fe cap material.

Clear textural evidence from both Southern and Rona mound shows that these disseminated sulphides post-date silicification in Unit C samples (Section 5.5.2). Sulphides overgrowing existing silica textures, and exhibiting interstitial growth in void spaces show that sulphidation is likely the last stage of the Si-Fe cap formation.

The hydrothermal fluids, which precipitated the sulphides in the Si-Fe cap, must have been chemically different from the fluids that precipitated iron oxide material. They are likely to have also been thermally different from the fluids that precipitated the silica.

Hydrothermal fluids that precipitated the initial iron oxides (that formed the hydrothermal sediment protolith) must have initially been reduced (becoming oxidised upon iron precipitation), low to moderate temperature, sulphur-poor and iron-rich. If the fluids were fully oxidised they would not have been able to transport iron, and if the fluids contained sulphur then iron sulphide (pyrite or marcasite) would have been precipitated rather than iron oxides. Fluids responsible for the subsequent silicification events did not exceed 180˚C. Sphalerite geothermometry (i.e. an estimation of fluid temperature of the sulphide formation) provides estimates of formation temperatures between ~250 and 400˚C, implying that the sulphide mineralising fluid was significantly hotter than previous hydrothermal fluids involved in the formation of the Si-Fe cap.

Together, this evidence indicates that the sulphides probably formed from a moderate-high temperature, chemically reduced, sulphur-rich fluid, but which was not iron-rich. The bleaching affect in Unit C shows that pre-existing iron oxide material was reduced and the iron remobilised before being incorporated into the disseminated sulphides within Unit C material. The amount of iron remobilised (during the bleaching of hard rock) is not likely to exceed ~ 10 to 15 wt%, based on the iron concentrations of Unit B or C material, therefore it is likely that remobilised iron was used to form the sulphides in addition to any that may have been dissolved in the hot late-stage fluid.

It is likely that these late stage fluids were sulphur limited, which could explain the lack of sulphides at shallower depths in the Si-Fe capping sequence. Exhaustion of the sulphur, supplied from the fluid, by reacting with the iron and precipitating sulphides at depth, would alter the physico-chemical properties of the hydrothermal fluids. There is potential that the same fluid, upon cooling and mixing with oxidised seawater, could precipitate iron oxides and/or silica, and could further contribute to the late-stage silicification of the cap. A similar mechanism is interpreted to have formed the Tetsusekiei in Kuroko type VMS deposits (Section 2.3.4). However, the most likely reason for the presence of sulphides at depth is likely to have been a physical barrier, i.e. the impermeable Si-Fe cap itself.

8.1.3.1 Source of Sulphur?

The hydrothermal fluids responsible for the precipitation of the iron oxides were sulphur poor, while the fluids responsible for silica formation had moderate temperature (<180˚C) and were also sulphur poor. Although neither of these fluids could precipitate sulphides, the occurrence of iron leaching and sulphide precipitation implies a chemical change in fluids involving the addition or increase in sulphur.

The source of sulphur in the formation of the massive sulphides could have been from magmatic, biological, or seawater sources. Without the planned sulphur isotope analysis, it is difficult to determine the exact origins of the sulphur. However, some of the textures and data observed in this study can shed some light on the potential origins of the sulphur.

The sulphidation of Unit C material post-dates silicification and by this point in the hydrothermal cycle, the Si-Fe cap is interpreted to have already formed, thus inhibiting seawater ingress. The decreased potential for seawater ingress therefore implies that the sulphur forming the disseminated sulphides at depth is unlikely to be a product of a reduction of infiltrated seawater. The contribution of reduced seawater cannot be discounted however, as the inward-dipping faults that dissect Southern and Rona Mound could provide potential fluid pathways for seawater ingress into the mound.

The origins of these faults are unknown, but are hypothesised to be a result of anhydrite dissolution at depth causing mound collapse (Murton *et al.*, 2019). As anhydrite dissolution occurs at temperatures <150˚C (Blount and Dickson, 1969) this process is interpreted to occur during the waning stage of hydrothermal circulation, similar to the formation conditions for the Si-Fe cap. It is impossible to know the temporal relationship between the faulting, or whether the two features interact with each other at depth (as the extent of the cap is only estimated), based on the current data. If the faults post-date the cap formation and late stage sulphidation, then seawater pathways

would have been limited. However if the faults pre-dated the sulphidation, and penetrated to depths beneath the Si-Fe cap, or displaced the cap (assuming the cap extends laterally for enough) it could have provided a proximal conduit for seawater ingress to contribute sulphur.

The most likely source of sulphur is magmatic, obtained during hydrothermal fluid alteration at depth. Magmatic sulphide is considered to represent a significant contribution to sulphide formation at the TAG active mound, and other seafloor massive sulphide deposits globally (Scott, 1983; Herzig, Petersen and Hannington, 1998). The occurrence of chalcopyrite, pyrite and sphalerite in the Si-Fe cap is comparable to the underlying massive sulphide ore mineralogy, particularly the relative dominance of sphalerite in the sulphide assemblage in Unit C at Rona Mound, and the underlying sulphide. Sphalerite geothermometry from the Si-Fe cap allows estimation of formation temperatures to between ~250˚C and 400˚C, which is again comparable with temperatures of precipitation from primary hydrothermal fluids, and the underlying sphalerite material (Lehrmann *et al.* 2019).

8.2 Paragenesis of the Si-Fe cap

Upon review of historical geological analogues, modern seafloor systems, and the physical and chemical observations a paragenesis for the Si-Fe capping material has been interpreted for each of the three sites investigated. All three sites have unique features that show the significant variation and diversity at mound-scale, and within a single hydrothermal field.

8.2.1 Southern Mound

The paragenesis presented in the following subsections is a generalised sequence of events based on the idealised stratigraphy, variations to this generalised paragenesis are also discussed.

8.2.1.1 Stage 1 – Accumulation of iron oxide-rich hydrothermal sediments and localised silicification

The precursor sediment to the Si-Fe capping material is iron oxide and iron oxyhydroxide-rich sediments derived from a range of processes including (schematically shown in Figure 158):

- Weathering and collapse of surface sulphide features;
- Hydrothermal plume fallout;
- Low temperature abiological precipitation;
- Biologically mediated iron oxidation.

During peak hydrothermal activity, the majority of the high-temperature hydrothermal fluids would be expelled at chimneys. However minor diffuse flow occurs all over the mound surface resulting in iron oxides and localised minor silica precipitation at and within the shallow subsurface of the mound. This process would result in partially silicified areas of laminated iron oxide-dominated sediments, of the type evidenced in both the hydrothermal sediments and preserved in Unit A material. This phenomenon is currently occurring at the TAG active mound forming a red and grey chert (Petersen, 2000). Localised areas of sediment would likely have been silicified by low temperature amorphous silica, which preserved sedimentary accumulation textures.

As the hydrothermal activity begins to wane, the system starts to cool and the low temperature diffuse venting becomes the predominant hydrothermal process. With the lack of high temperature reduced fluids sustaining the vents, cool oxygenated seawater starts to infiltrate, oxidise and destabilise the surface-exposed sulphides causing mass wasting of chimneys and the formation of accumulations of partially oxidised material. Mass wasting and gravity current transport of this material creates localised high-energy environments that caused brecciation, and entrainment of localised partially silicified material, in turbidity flows (Figure 158). Near-vent mass wasting deposits would therefore contain a mixture of partially silicified iron oxide/oxyhydroxide fragments, and weathered sulphide clasts. Continued low temperature diffuse flow would enable further disorganised iron oxide precipitation within the clasts of the mass wasted material, and could potentially also create organised dendritic growth from fluid into restricted pore spaces, increasing the thickness of hydrothermally derived sediments.

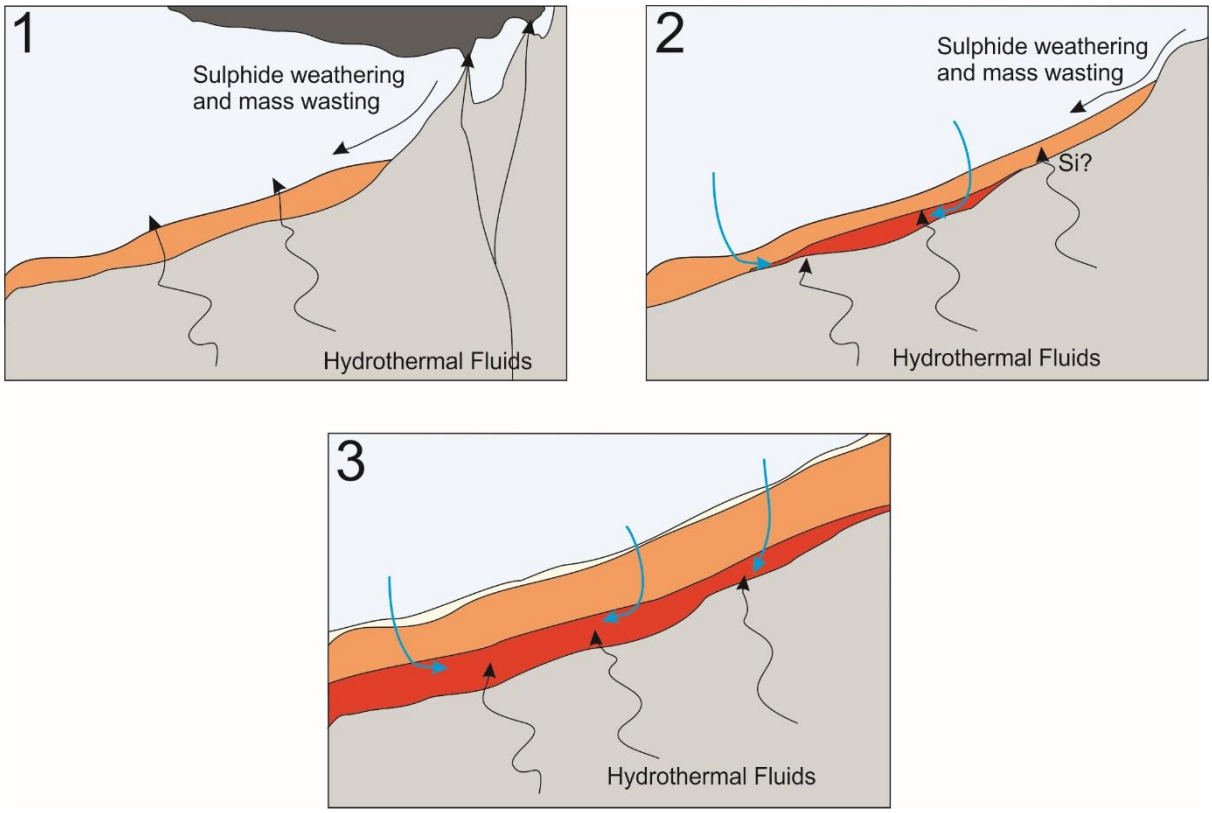

Figure 158: Generic Southern Mound hydrothermal sediment formation diagram. 1) Early sediments dominated by mass wasting of sulphide material and/or low temperature diffuse hydrothermal precipitation. 2) Continued mass wasting input, potential shift to low temperature diffuse flow resulting in subsurface iron oxide precipitation and continued surface sediment growth. Localised areas of silicification also occur during low temperature diffuse flow areas (?) enabling clasts of Si-Fe to be accumulated in the sediments as well. 3) Continuation of dominant low temperature hydrothermal precipitation, but also beginnings of carbonate sediment accumulation.

Although the presence of iron oxides/oxyhydroxides implies precipitation or formation from oxidised fluids, they retain a broadly similar REE pattern to strongly reduced hydrothermal fluids. Adsorption of REEs onto iron oxides/oxyhydroxides in an oxidised environment preferentially adsorbs HREEs over LREEs (between pH of ~4-6) (Liu *et al.*, 2017), which explains the 'low' enrichment of LREEs in the sediments compared with seawater, or in both black and white smoker hydrothermal fluids. This implies that the surface and near-subsurface conditions during hydrothermal sediment accumulation were oxidative, and with a weakly acidic pH.

8.2.1.2 Stage 2 – First major silicification event

The first mass silicification event at Southern Mound likely resulted in synchronous silicification of the thickness of the Si-Fe capping material (Figure 159). Either black smoker fluids or white smoker

fluids mixed with seawater reduced the temperature of the fluid to ~60-80˚C. At these temperatures, silica would have been precipitated as a gel-like amorphous material within hydrothermal derived sediments to form a 'proto-jasper'(Figure 159). As Unit A material was only recovered in one borehole it implies that this low temperature event reached different levels across the mound within the existing hydrothermal sediment stratigraphy than later silicification events, thus being preserved as a mixed opal-CT and quartz assemblage in 'Unit A' material at Southern Mound.

The presence of quartz is likely an indicator of the variable maturation of the Stage 2 event, indicating that some of the opal-CT has begun to recrystallised to quartz but that this transformation was not complete. FTIR data from Unit A material shows randomly distributed and intermixed quartz and opal-CT within the matrix material, further supporting the idea that the silicification is the product of a homogenous silica gel within the sediment stack.

8.2.1.3 Stage 3 – Second major silicification event

Evidence for a second major silicification event was recorded within Unit B and Unit C material. Both Units B and C material have higher silica contents, are higher density, and have lower total porosities(Figure 159). Oxygen isotope data implies that this second silicification event occurred at a higher temperature (~115 - 180˚C). Quartz is the only silica polymorph in both Unit B and C material. The latest silica growth (i.e. outer layers in pore spaces or cracks) either exhibit drusy crystal habits, implying either primary quartz growth or rapid dehydration and crystallisation, or radial growth textures that have been preserved from opal-CT growth, despite recrystallisation to quartz. This event is interpreted to be restricted spatially and has not significantly influenced the overlying material of either Unit A (if present) or hydrothermal sediment Units M3 or M4.

8.2.1.4 Stage 4 – Sulphidation

Stage 3 implies a change in temperature of the hydrothermal system, increasing from ~ 60 to 120˚C, and is an indicator of a resurgence towards higher temperature hydrothermal activity (Figure 159). This is supported by the bleaching and sulphidation of Unit C of the Si-Fe cap and, importantly, also implies a chemical change in the hydrothermal fluids. Sulphide growth in Unit C material clearly post-dates silicification and is either restricted to interstitial growth in pore space left after the last generation, or overgrows smaller silica 'globules' or silicified features.

The general chemical composition and Eh of hydrothermal fluids involved in Stages 1 to 3 are thought to be similar. The fluids must have been chemically reduced in order to transport Fe^{2+} (Stage 1), and of low to moderate temperature to precipitate iron oxide and silica (upon fluid

mixing), and to have little to no aqueous sulphur, otherwise the transported iron would precipitate as sulphide upon fluid mixing.

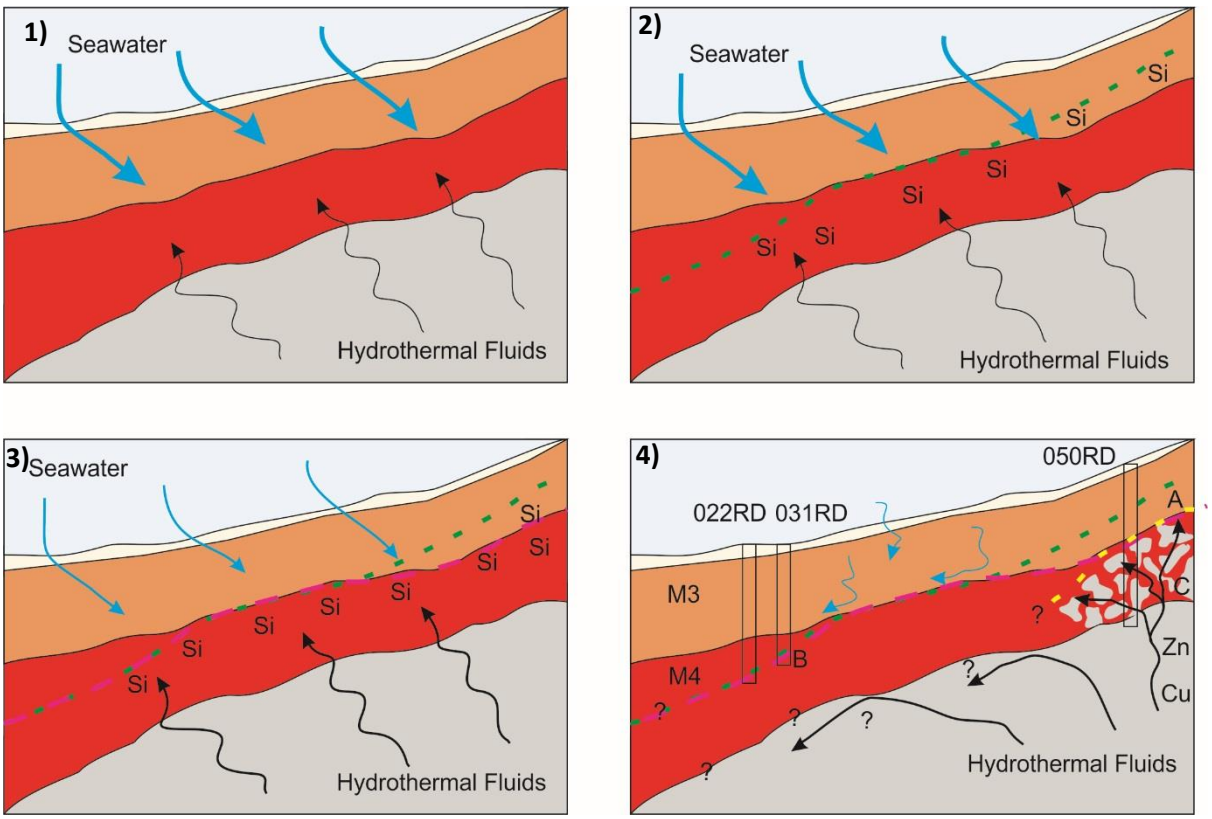

Figure 159: Four stage paragenesis of the silicification and sulphidation at Southern Mound. 1) Seawater and hydrothermal fluids mixing within a hydrothermal derived sediment sequence. 2) 'Front' of silicification, no relationship between this boundary and the boundary between Units M3 and M4 across the Mound. 3) Second stage of silicification, less seawater and a higher degree of hydrothermal fluids interacting to precipitate and mature silica faster, reached variable depths across the mound. 4) Late-stage, high temperature, reduced, sulphur and base metal rich fluids resulting in localised bleaching of the Si-Fe material and sulphide crystallisation.

The late stage growth of disseminated sulphide at depth (mainly in Units C) implies that the dissolved sulphide component of the fluids must have increased after silicification had occurred. The sphalerite geothermometry records that the temperature of the fluids had significantly increases to be closer to that of typical primary hydrothermal fluids (with temperatures ~250 – 400˚C).

8.2.2 Rona Mound

The paragenesis of Si-Fe material at Rona Mound is based on the samples recovered from 057RD as this was the only borehole to recover Si-Fe material. This means interpretation of spatial variations as observed at Southern Mound, can only be speculation.

8.2.2.1 Stage 1 – Accumulation of iron oxide rich hydrothermal sediments and localised silicification

Although no hydrothermal sediments were recovered from Rona Mound, the general sediment accumulation mechanisms as described in Section 8.1.1 are thought to have also occurred at Rona Mound. Texturally the deeper Unit C material at Rona Mound shares similarities with shallow Unit M3 sediments and Unit A material from Southern Mound. The precursor sediment for this material is interpreted to have formed from a combination of surface and sub-surface disorganised iron oxide precipitation, and accumulation of weathered gossanous material from surface sulphide material. Jasperoidal clasts in Unit C material provide the only textural evidence for localised silicification. Similar to Southern Mound, rare jasperoidal clasts exhibit desiccation cracks implying early silicification and desiccation before brecciation.

The main difference is the iron oxide protolith for Unit B material from Rona Mound, compared to both Southern Mound and the MIR Zone. Here, the iron oxide material is almost entirely composed of filamentous and dendritic growth textures with very little evidence of disorganised iron oxide precipitation. This network of dendritic and filamentous material is interpreted to be a mixture of biological and inorganic self-organised iron oxide precipitation which created a ramified network for silica to precipitate upon. Figure 160 shows a schematic final sketch of Stages 2 and 3 formation at Rona Mound.

8.2.2.2 Stage 2 – Silicification

Silicification at Rona mound is more difficult to interpret, with the main problems being the lack of diversity in silica polymorphs, the formation temperatures, and the variable textures described above.

Quartz (<0.5 wt%) is rare within Rona Mound, and opal-CT is the dominant silica polymorph. XRD analysis showed that three out of the four recovered Si-Fe samples from Rona contained high amounts of amorphous material (27 wt% to 34.5 wt%). Based on the lack of quartz, and the immaturity of the metastable silica polymorphs some, if not all, of the amorphous fraction could be amorphous silica.

Texturally, there is little evidence for more than one major silicification event. Iron oxide dendrites and filaments act as nucleation sites for silica precipitation and typically exhibit a relatively uniform thickness of silica (~10-20µm) in both Units A and C (at Rona Mound). The range of silica textures observed can be explained by the range of silica polymorphs from amorphous to opal-CT.

The formation temperatures from oxygen isotope geothermometry provide the strongest evidence for two different silicification events, as shallower Unit B materials have higher formation temperatures than deeper Unit C material. The underlying assumption is that silica is precipitated from fluid mixing of higher temperature hydrothermal fluids and low temperature seawater, the source of said hydrothermal fluids coming from below the cap, and the source of cooler fluids coming from seawater, above the deposit. Logically cooler formation temperatures (i.e. higher seawater to hydrothermal fluids ratios involved) should occur in shallow material, with hotter formation temperatures (i.e. higher hydrothermal fluid to seawater ratios involved) occurring at depth. The temperature distribution throughout a single silicification event would have formation temperatures increasing with depth, but this is not the case at Rona Mound.

The simplest explanation for this temperature variation would be two different silica generations, each at slightly different temperatures. Unlike Southern Mound, where a second, higher temperature generation has likely overgrown the early low temperature generation, the two generations at Rona Mound appear to have occurred independently of each other, and do not appear to overlap.

With the assumption that silica at Rona Mound is predominantly amorphous or opal-CT, and representative of an immature assemblage, and the occurrence of opal-CT at low temperatures at Southern Mound, it would make sense for silica precipitation to be low temperature. However, silica formation temperatures for Unit B (~120 - 160˚C) and Unit C (~100 to 130˚C) are much higher than expected. Formation temperatures at Rona Mound are comparable with the high temperature, mature quartz dominated assemblage at Southern Mound.

The most immature silica polymorph assemblages (i.e. largest amorphous and smallest opal-CT fractions) are associated with the lowest formation temperatures in Unit C material. This shows that despite a difference in absolute temperatures between the two mounds, the relationship of temperature to silica maturity exists at both mounds and implies that silicification at Rona Mound may post-date silicification at Southern Mound as the overall silica assemblage is more immature.

8.2.2.3 Stage 3 – Sulphidation

Similar to Southern Mound, Unit C materials have undergone bleaching (remobilisation of iron oxides) and the precipitation of massive sulphides (predominantly pyrite and sphalerite). This

bleaching and sulphidation is, again, evidence of a chemical change in the hydrothermal fluids with sulphide growth typically post-dating and either incorporating early silica features or growing interstitially. Again, the late stage growth of sulphide at depth implies that the dissolved sulphide component of the fluids must have increased. This is supported by the sphalerite geothermometry, which implies that the temperature of the fluids had significantly increased and was comparable to primary hydrothermal fluid temperatures (~ 250 – 400 ˚C).

Similar to Southern Mound, it is possible that cooling of these higher temperature fluids (and exhaustion of sulphur) precipitation iron oxides and/or silica could occur at shallow depths. If fluid pathways were limited but still existed through the Si-Fe cap at the time of sulphidation, and sulphur was exhausted at depth, continued upwelling of fluids, and cooling at shallower depths could have precipitated iron oxide and silica, potentially contributing to the overlying Unit B material.

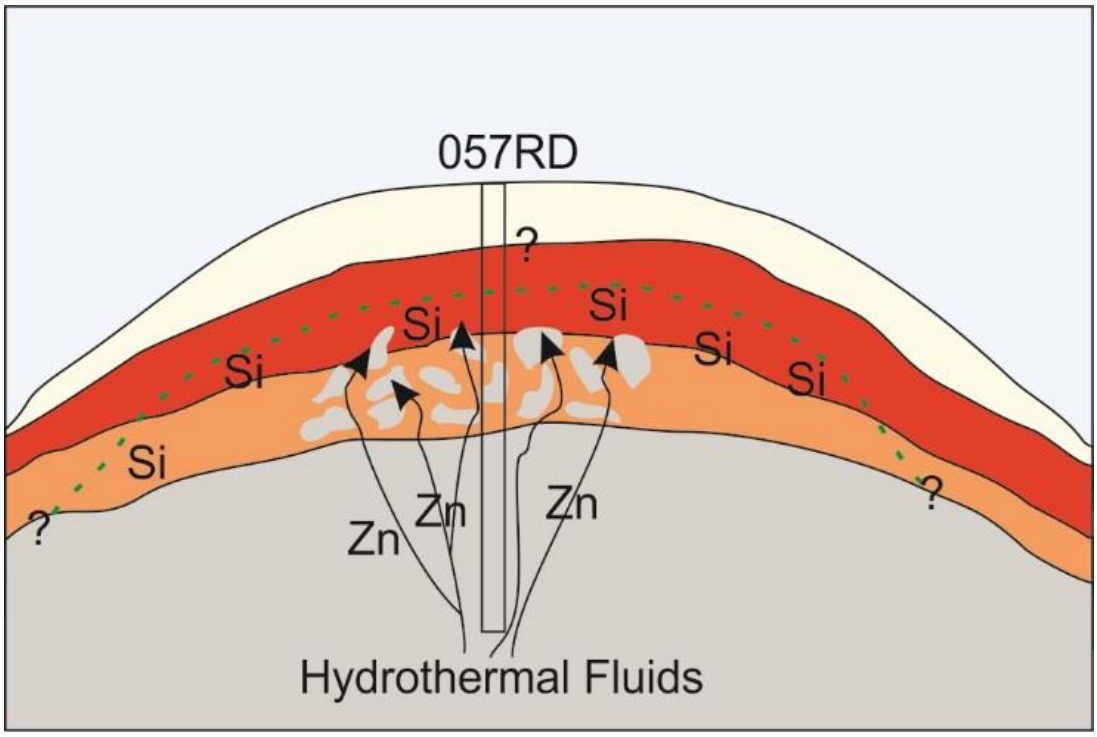

Figure 160: Summary diagram of late-stage Rona Mound paragenesis. Variable silica temperatures are likely representative of multiple silica generations but it is difficult to determine. Late stage sulphidation was caused by moderate to high temperature sulphur rich fluids, predominantly bringing Zn to precipitate sphalerite within the base of the Si-Fe cap.

8.2.3 MIR Zone

8.2.3.1 Stage 1 – Accumulation of iron oxide rich hydrothermal sediments and localised silicification

The general sediment accumulation mechanisms as described in Section 8.1.1 are interpreted to have formed the sediment precursor at the MIR zone and include:

- Weathering and collapse of surface sulphide features;
- Hydrothermal plume fallout;
- Low temperature abiological precipitation;
- Biologically mediated iron oxidation.

Only Unit B material was recovered from MIR Zone, with the majority of the core samples displaying the typical blood red haematite jasper colouration in both boreholes with the exception of deep samples at 073RD where goethite is also present. This goethite occurrence is interesting as it is the only example of Si-Fe material outside of Unit A where goethite was recovered. Assuming a similar formation mechanism as ascribed to goethite within Unit A material, then this could indicate a weathered massive sulphide contribution to the Unit B material. The is further supported by the presence of laminated clasts in the Unit B material at depth where goethite is identified, potentially a product of mass wasted, and weathered massive sulphide fragments.

Texturally the majority of the material from the MIR Zone shares similarities with Unit M4 sediments and Unit B material from Southern Mound. The precursor sediment for this Southern Mound material is interpreted to have formed from sub-surface disorganised and organised iron oxide precipitation, rather than accumulation of weathered gossanous material from surface sulphide material. However, this does not seem to be the case at MIR Zone. Although surface and subsurface organised and disorganised iron oxide precipitation likely contributes to the iron oxide generation, individual clasts show trace and relict sulphides implying that a degree of input from gossanous material has occurred. The increased presence of goethite at depth in 073RD is interpreted to be a function of the precursor sediments.

Jasperoidal clasts in Unit B material provide the only textural evidence for localised silicification. Similar to both Southern and Rona Mounds, jasperoidal clasts exhibit desiccation cracks implying early silicification and desiccation before brecciation.

Filamentous and iron oxide material occurs throughout Unit B material in the MIR Zone. It occurs as localised discrete patches and so the material is likely entrained from surface or near surface abiological precipitation or biologically mediated iron oxide material.

8.2.3.2 Stage 2 - Silicification

Formation temperatures of silica from the MIR Zone are relatively uniform and correlate between the two boreholes, at ~100-130˚C. This homogeneity implies that the silica formed at a similar temperature, and potentially came from the same event. All Unit B material at the MIR Zone contain only quartz, and is generally comparable to Unit B at Southern Mound, with respect to both temperature and mineralogy.

Textural comparison between Unit B material at Southern Mound and MIR Zone show similar jigsaw brecciation and silica veins prevalent throughout. This implies a two-stage silicification generation, where the first stage represents partial silicificiation of a mixed origin iron oxide sediment, as the silica matures and desiccates, cracks and brecciation occurs. Secondary silica precipitation occurs as veins and infilling desiccation cracks.

This two-stage interpretation could have been a result of two different temperature generations, with the last (~ 100 to 130˚C) signature preserved in the oxygen isotope values, or as two different generations at a similar temperature.

No Unit C material was recovered from MIR Zone, instead Unit B material almost directly overlies the massive sulphide material at depth. This implies that late stage sulphidation, responsible for bleaching and sulphide formations in Southern and Rona Mounds, did not occur at MIR.

8.3 Implications of the role of the Si-Fe cap in preservation of eSMS deposits

8.3.1 Current porosity of the Si-Fe cap and the change in porosity of the Si-Fe cap by silicification

Investigation of the porosity of each of the separate Si-Fe capping materials has shown that there is no link between total porosity and connected porosity. The connected porosity governs the ability of fluid to move through the sample. Investigation of connected porosity in each of three axes of each analysed sample show that out of the three sub-unit types, Unit B material from Southern Mound and the MIR Zone exhibit no connected porosity in the x-, y-, or z-axes, in their current form. Unit A material and Unit C material appear to show more connected porosity, but this is typically in the x- or y- axes only.

Based on analysis of current samples, the lack of connected porosity in the z-axis would inhibit both seawater ingress into the mound and vertical pathways of buoyant hydrothermal fluids rising up

from beneath the cap. Limited connected porosity in the x- and y-axes implies that some lateral movement of fluids is possible in both Unit A and Unit C material.

Comparison between porosity and permeability of Si-Fe samples (as they currently are) implies that the degree of porosity does not have a significant effect on permeability. All Si-Fe materials (where connected porosity exists) recorded permeability values at the same order of magnitude to each other (10^{-16} to 10^{-17} m^2). Therefore, the occurrence of connected porosity in any given axis is a more important observation than the inherent permeability value of material, with respect to fluid movement.

To test the role that silicification has played in the 'sealing' of the Si-Fe capping material connected porosity of Units B and C material were calculated once the late-stage iron oxide free silica (i.e. the last generation of silicification) was digitally removed from CT scan data (See Chapter 7). Removal of this late stage silica, showed that during silicification, connected porosity reduced to ~ 10 to 50% in volume of previous connected porosity (where connected porosity exists in the current sample). It also resulted in the sealing of connected porosity in all three axes in Unit B samples (from the MIR Zone 073RD/P14 and 076D/P6), and two (Southern Mound – 050RD/P11), and one axis (057RD/P11 – Rona Mound) in the Unit C samples.

Investigating permeability of the Si-Fe material after the late stage silica has been digitally removed shows that permeability decreased to between 5 and 50 % of pre-late-stage silicification values in Unit C, and Unit B material (which exhibited permeability of ~ 10^{-15} m^2 and 10^{-16} m^2) before silicification became completely impermeable.

8.3.2 Role of silicification in preservation?

The rapid burial of VMS deposits throughout geological history by sediments (exhalites, clastic and/or volcanoclastic) or volcanism (lava flows), is considered to one of the most important mechanisms of preservation for the underlying sulphide ore bodies (See Sections 1.5 and 2.3).

Surface evidence for the range of eSMS deposits in the TAGHF shows progressive surface weathering features from the TAG active mound, through the steep sloped Shinkai and New Mounds, to the smoother Southern and Rona Mounds (Section 3.2). Based on the range of textural features in the hydrothermal sediments at Southern Mound, surface weathering is interpreted to contribute to the formation of the Fe-rich sedimentary Units, particularly the goethite-dominated Unit M3.

Sediment cover at Southern Mound and Rona Mound (~3m) presents the first step to a physical barrier between oxygenated seawater and the eSMS ore body. Although the hydrothermal

sediment porosity was not measured, the porosity is estimated at ~ 60 to 80%, based on a series of other studies conducted of fine-grained hydrothermal sediments on the Juan de Fuca ridge (Giambalvo *et al.*, 2000) (Figure 161).

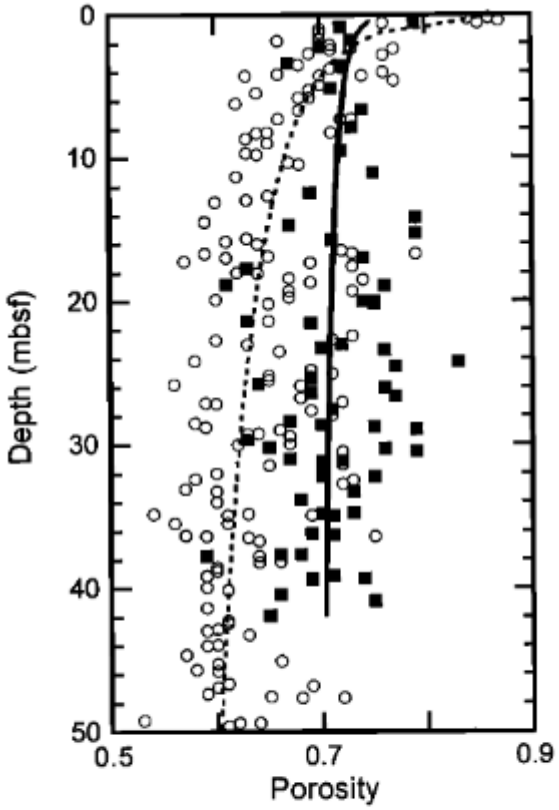

Figure 3. Porosity versus depth of fine-grained sediments at Leg 168 no-flow sites (circles and dashed line; Sites 1023-1029) and upflow sites (squares and solid line; Sites 1030 and 1031) [*Davis et al.*, 1997b]. Lines are least square best fits of the form $n=az^b$.

Figure 161: Porosity of sediments in a hydrothermal upflow zone, from the Juan de Fuca Ridge (Giambalvo *et al.*, 2000). Fine grained = predominantly composed of silt or clay grade grains size.

This matches well with the porosity estimation measured for the sediments on the top of Southern Mound at ~ 82%, by mass change during drying albeit with varying imprecision (Dutrieux, 2019). Grain size estimation of hydrothermal sediment Units M3 and M4 at Southern Mound show that Unit M3 is ~50% sand grade, 25% silt grade and 25% clay grade, whereas Unit M4 is ~90% clay grade, and 10% silt grade (Figure 162).

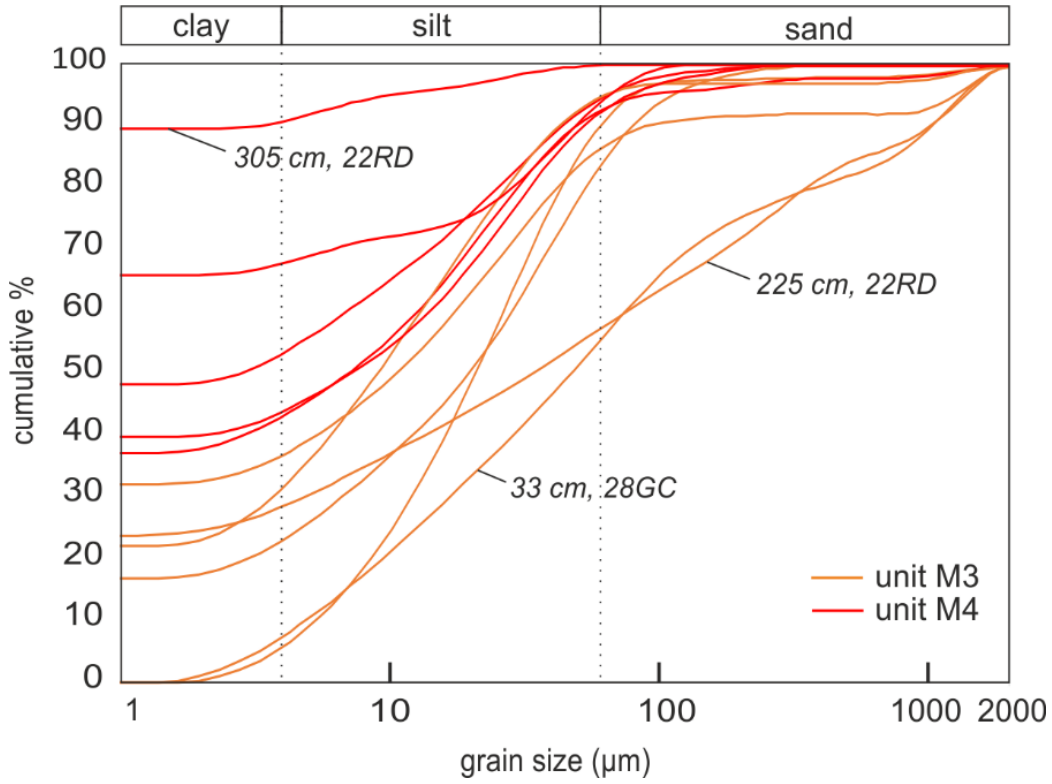

Figure 162: Figure of M3 and M4 grain size from a range of sediment cores on (see 022RD samples detailed) and around the eSMS deposits (Dutrieux, 2019)

Experimental work on the permeability of hydrothermal sediments and heat flux transfer at the Juan de Fuca Ridge show that a sediment is open to fluid convection if its permeability is >1 to 5 x 10^{-15} m^2 (Snelgrove and Forster, 1996). Sand/silt grade sediment permeability values at the seafloor are calculated to be ~ 10^{-13}, and clay grade material is ~ 3 x 10^{-15} (Snelgrove and Forster, 1996). Assuming similar values for sediments within the top 5 m of the seafloor, sand/silt grade material would not inhibit fluid convection but clay grade material may limit convection, but both still imply fluid mobility is possible. Sediments with high porosity (~80%), and permeability at values interpreted to be open for fluid convection imply that burial by <5 m of sediment would not be sufficient to create an impermeable cap for the eSMS deposits alone.

Permeability calculations undertaken on the Si-Fe cap rock samples recorded permeability values at ~10^{-16} - 10^{-17} m^2, which is at least one to two orders of magnitude lower than estimated permeability values for the overlying hydrothermal sediments. Furthermore, porosity estimates are typically ≤ 16%, compared to ~80% of the hydrothermal sediments. This presents clear evidence that the silicification of the hydrothermal sediments has resulted in a significant decrease in porosity, and permeability. When compared to the estimated fluid convection limits, the permeability of the Si-Fe cap rock would be 'closed' for fluid convection.

When the 'late-stage' silica-free generation is removed from cap rock Units B and C, permeability values were calculated at between ~10^{-15} and 10^{-16} m^2, i.e. approximately an order of magnitude higher than the calculated current permeability vales. When these permeability values are compared to the values at which sediments are considered to enable fluid convection, they sit on the boundary between 'impermeable' (i.e. no convection), and 'open', and similar to clay grade hydrothermal sediments according to Snelgrove and Forster, 1996.

Numerical modelling of ~200 m thickness of sediments with permeability values of 10^{-17} m^2 are interpreted to be impermeable with respect to fluid convection (Snelgrove and Forster, 1996). In VMS analogues, typical hanging wall rocks which are noted to overly VMS deposits throughout geological history include mafic extrusive volcanic (e.g. Troodos Cyprus type deposits) or felsic volcanic/volcaniclastic material, to clastic sediments (e.g. back arc systems). Permeability in ocean basalt material has been analysed or modelled by a range of different methods, and provided permeability values ranging from 10^{-21} to 10^{-9} m^2 (Fisher, 1998). Permeability values of centimetre scale cores would be the most comparable to the permeability values of the Si-Fe cap presented here, and have been analysed to between 10^{-21} and 10^{-17} m^2 (Fisher, 1998). Hyaloclastic material and ignimbrites from a thick volcanic sequence from the Austral Basin, Argentina, recorded permeability values of <10^{-16} to ~10^{-17} m^2) (Sruoga *et al.*, 2004). Both of these lithologies would be suitably impermeable to prevent seawater ingress and fluid convection, thus likely had some influence in preserving ancient VMS deposits.

The current permeability of the ~ 3 to 5 m Si-Fe cap is comparable to a cover of ~200 m thickness of clay dominated sediments, or the equivalent thickness of impermeable volcanic derived material that have previously been interpreted to have helped preserve ancient VMS deposits. Hence it is reasonable to conclude that the late-stage formation of hydrothermal Si-Fe deposits capping the SMS deposits contributes to the preservation of the underlying sulphide ore body, at least where the cap is present.

8.3.3 Influence of the Si-Fe cap rocks on hydrothermal fluid regime

Bleaching and precipitation of sulphides is limited to Unit C material (Figure 163), i.e. the deepest unit of the Si-Fe cap. This is evidence that the Si-Fe cap is impermeable for buoyant hydrothermal fluids. Growth textures of the majority of the sulphides from Unit C material clearly indicate that they post-date the silicification of the cap. The fluid that precipitated the massive sulphides is interpreted to be late-stage, moderate to high temperature, reduced, sulphur- and metal-rich (Cu and/or Zn), but not necessarily iron-rich, and hydrothermal in origin. This fluid is considered have a higher temperature and a higher sulphur content than the fluids that formed the early iron oxides

and sulphides. This change in physico-chemical properties is interpreted to be the result of waxing in a hydrothermal cycle, and likely aided by the Si-Fe cap limiting seawater ingress and mixing.

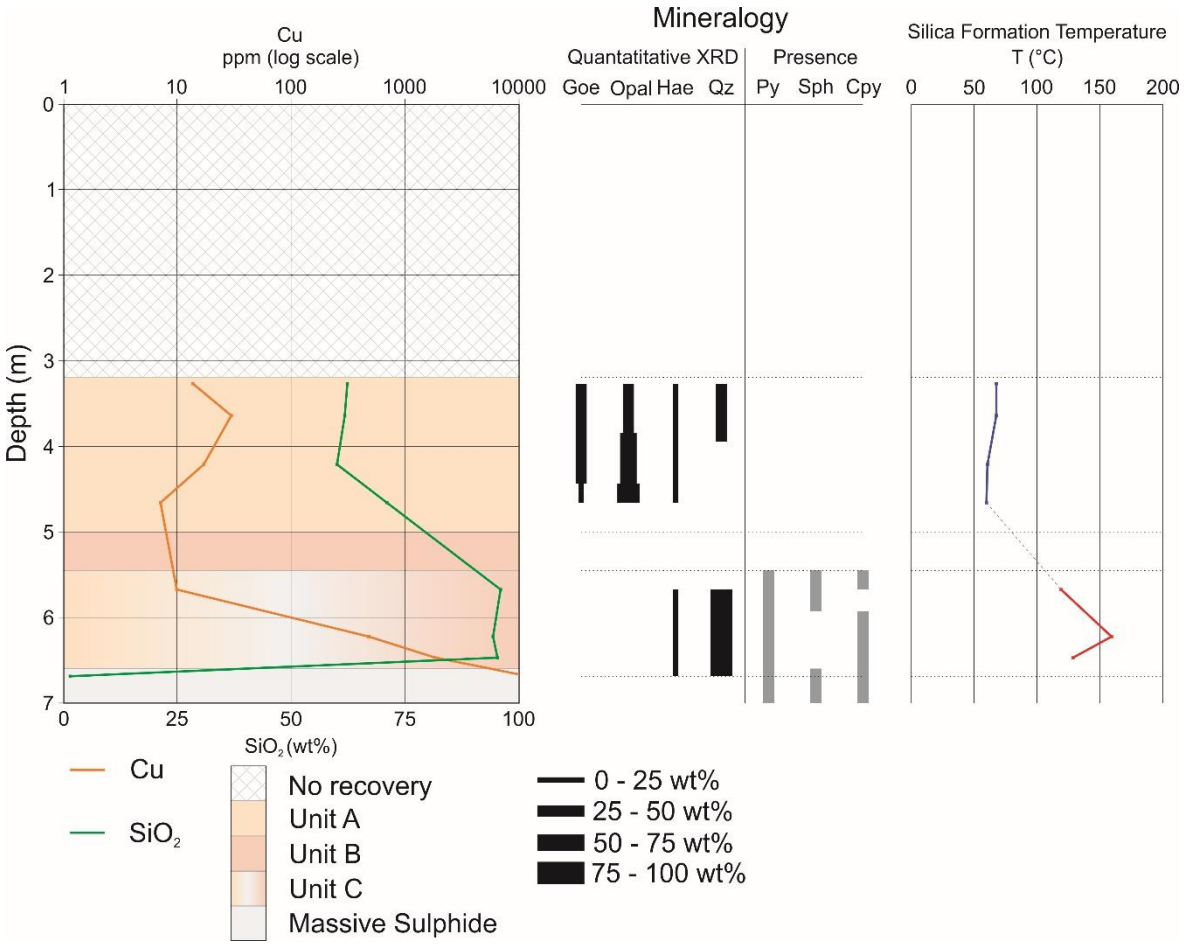

Figure 163: Summary of Cu variation with depth at Southern Mound. Note the presence of sulphides only at the base of the cap, and the corresponding elevated silica formation temperatures

The Si-Fe cap would have limited vertical fluid flow, and resulted in pooling of hydrothermal fluids at the base of the cap, eventually enabling the interstitial precipitation of the disseminated sulphides observed. This late stage fluid infiltrated the base of the Si-Fe cap, bleaching the Si-Fe material by reducing and remobilising oxidised iron, re-precipitating some if not all as iron (or iron-bearing) sulphides, and potentially precipitating late stage euhedral quartz. Iron oxide remobilisation appears to be limited by the silica armourment, where localised enclaves of silica-coated iron oxide remain unbleached. Textural evidence shows overgrowth of silica and silica-coated iron oxides by sulphide, showing that sulphidation is not 100% efficient, but can be pervasive, likely penetrating along existing fluid conduits/connected porosity within the Si-Fe cap.

The limited distribution of sulphides (Figure 163) could theoretically be explained by physico-chemical change in the hydrothermal fluids due to mineral precipitation. One explanation could be that sulphur and iron were both limited in the fluid. If a reduced, iron and sulphur-limited fluid

infiltrated the Si-Fe cap, it could remobilise iron and precipitate sulphides until the fluid sulphur was exhausted, thus limiting the further precipitation of sulphides to deep samples only. If this was the case, the fluid would continue to rise through the Si-Fe cap and, because iron is complexed by chloride in hydrothermal fluids (Douville *et al.*, 2002), further iron leaching would occur even at shallower depths.

A physical barrier is the simplest explanation of the restriction of the bleaching and sulphide precipitation in the Si-Fe cap. If the Si-Fe cap was permeable then the fluid which precipitated the sulphides at depth would continue to percolate upwards, likely resulting in continued bleaching and sulphide precipitation throughout, however this is not the case.

This interpretation leads to the question of where the fluids would go after interacting with the Si-Fe cap. If the fluid remains hot, it would still be buoyant, but would be unable to continue to flow vertically upwards due to the cap. Axis connectivity of the Si-Fe units shows more connected porosity in x- and y-axes, than the z-axis, implying that there are more pathways for lateral fluid movement than vertical (Figure 164). Assuming continued high temperature, reduced sulphur-rich fluid flow, lateral movement at the base of the Si-Fe cap would result in further bleaching and formation of Unit C material across the mound.

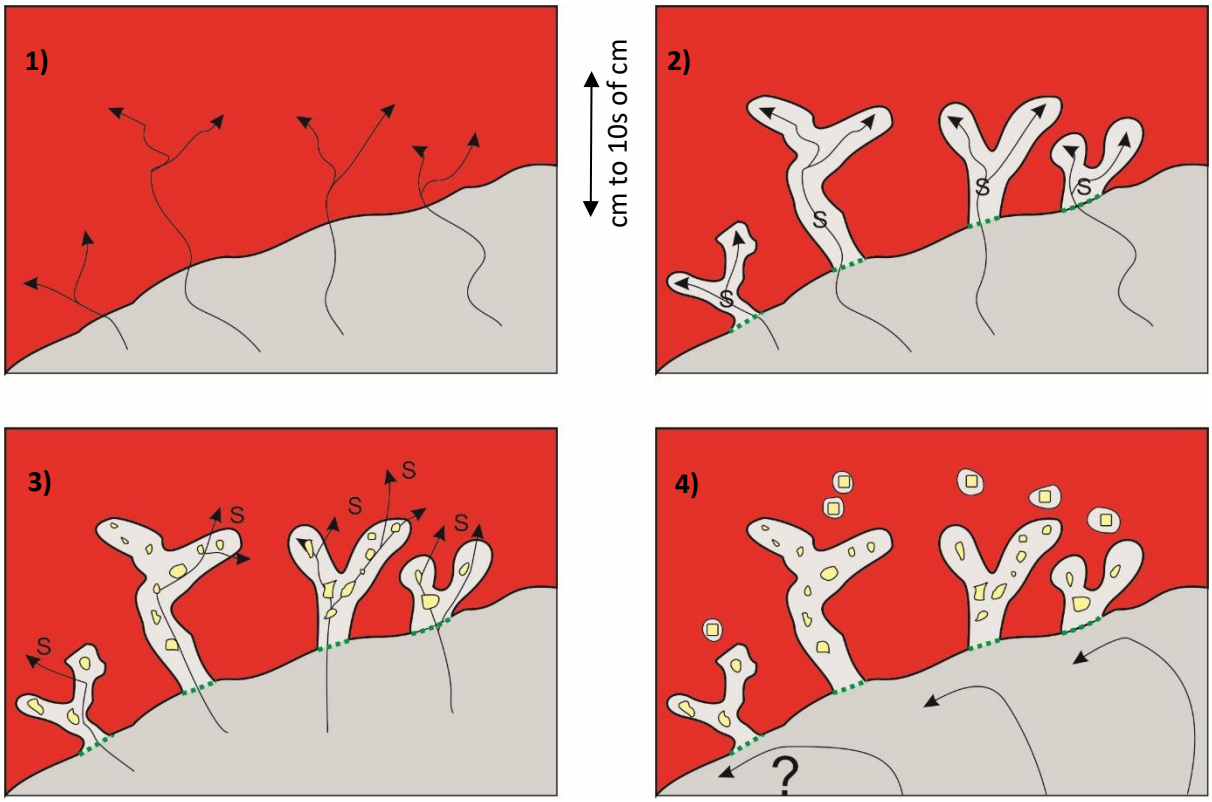

Figure 164: Interpreted mechanism of the limited permeability in the Si-Fe cap with respect to sulphide formation. 1) reduced fluids that are undersaturated with respect to iron infiltrate the base of the Si-Fe cap, 2) iron oxide is reduced and dissolved, then processed to mix with the sulphur contained with the reduced fluids, 3) sulphides precipitate out of the fluid within areas of 'iron oxide-free' silica, and fluids continue to migrate into the cap, but is limited in sulphur, and by the pre-existing silicification. As fluids cool, silica likely also precipitates sealing the pathways 4) Fluid sulphur is exhausted and pathways are sealed, resulting in no further bleaching or vertical fluid movement through the Si-Fe cap.

This process is similar to that observed in the Deep Copper Zone (DCZ) at the Bent Hill and ODP mound SMS deposits on the Juan de Fuca sedimented ridge (Section 2.4.5). In these examples, initial low porosity clastic and volcaniclastic sediments provided a suitable medium for the precipitation of silica at depth in the sediment stack, thus creating a seal, which trapped further rising hydrothermal fluids. This enabled pooling of hydrothermal fluids and eventually precipitation and replacement of existing sediments with silica and predominantly copper-rich sulphide minerals.

As the exact extent of the cap is only assumed, based on limited three-dimensional data, then it is somewhat speculative to interpret what would happen during lateral fluid movement at the base of the Si-Fe cap. However, regardless of the extent, when the Si-Fe cap rock ends, the impermeable vertical barrier would not inhibit the fluid buoyancy, likely changing from lateral flow to vertical

flow through whatever medium is present at the edge of the Si-Fe cap (if vertical flow is possible). Furthermore, it is likely that this fluid would interact with seawater and, given the silicification here is a function of fluid mixing between hydrothermal fluids and seawater, it is not unfeasible that comparable silicification processes could occur at the edge of the cap where they might grow laterally outwards from the centre, and may create new pathways to the surface, and even new chimney/sulphide deposition (Figure 165).

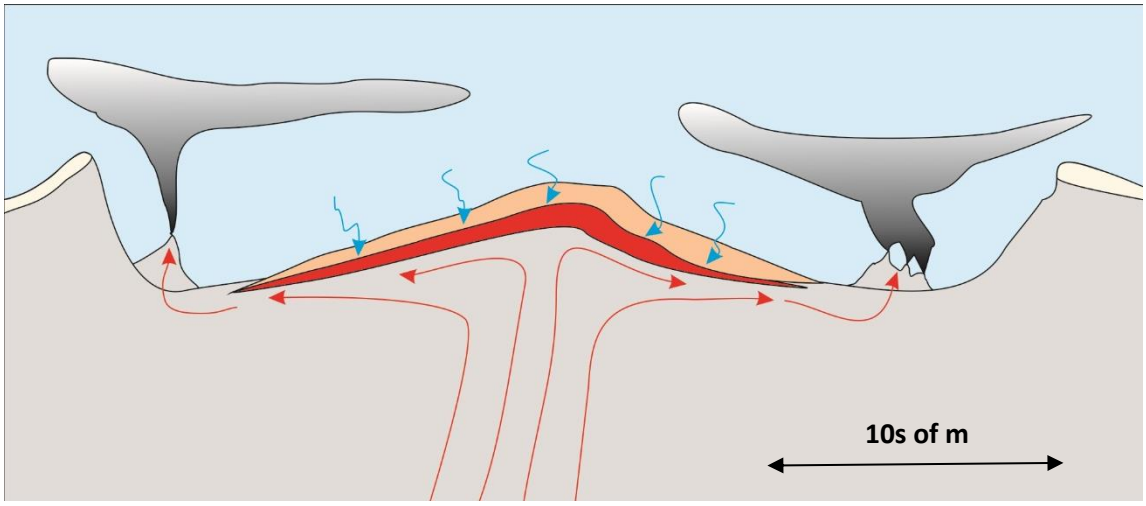

Figure 165: Sketch of potential fluid pathways after Si-Fe cap formation based off a Southern Mound structure. Could create additional vent sites at the extremes of the cap.

8.4 Wider reaching implications regarding preservation of eSMS deposits

The general aims of this project were to investigate the Si-Fe cap rock discovered at three eSMS deposits in the TAGHF, and understand the impacts this lithology could have on the potential preservation of eSMS deposits on the seafloor.

The textural and mineralogical assessment of the Si-Fe Units has identified that the Si-Fe cap is a product of silicification of hydrothermal sediments during the waning stages of a hydrothermal cycle. Although there is some variation in the manifestation of the Si-Fe cap rock across the investigated eSMS deposits, it is present at all three different deposits studied here. Combing the interpretation that silicification is a general product of waning hydrothermal activity, and that the Si-Fe cap was recovered at all three mounds drilled, it implies that this cap-rock formation is a general and common process and likely to be found at other SMS deposits during their comparable waning stages of hydrothermal activity.

This supposition is supported by the observation of red and grey chert within the shallow sub-surface of the flanks of the nearby TAG active mound, interpreted to be a function of low

temperature hydrothermal activity promoting silica precipitation. This feature does not form a cap deposit, and the TAG active mound is still venting high temperature hydrothermal fluids, with high and low temperature silica interpreted to be precipitating throughout the mound (Hopkinson *et al.*, 1999).

Assuming that the TAG active mound eventually undergoes similar processes as those at the three eSMS deposits of this study then, during waning hydrothermal activity, the combination of seafloor weathering, low temperature iron oxide precipitation, and low temperature silicification will also form a shallow Si-Fe cap over the sulphide orebody, thus increasing the chance of preservation.

8.4.1 Timing of the Si-Fe cap?

It is difficult to determine the timing of hydrothermal sediment accumulation, and silicification. Evidence from the Active TAG Mound implies that these silicified areas begin to form on the flanks of each deposit or within areas of low-temperature diffuse flow during prolonged hydrothermal activity.

The timing of Si-Fe cap formation is an important unconstrained part of the system. More specifically, how does the timing of Si-Fe cap rock formation relate to the loss of metals from eSMS deposits. If the Si-Fe cap requires a sediment protolith to form, and the sediment protolith forms from a range of surface weathering processes, then it stands to reason that some degree of weathering and loss of economically interesting metals must have occurred before the Si-Fe cap formed. If there was a particularly high degree of weathering then it is possible that high quantities of the economically interesting metals (i.e. Cu and Zn) could have been weathered and lost from the system before the Si-Fe cap could form an impermeable barrier.

Although full assessment of the underlying massive sulphide orebodies was outside the scope of this project, limited sub-surface sulphide material was recovered from beneath the Si-Fe caps at each eSMS mound. Whole rock data from these samples show that the maximum Cu+Zn concentrations were ~1 wt%, ~8.4 wt%, and ~20.4 wt% for Southern Mound, Rona Mound, and the MIR Zone, respectively. Maximum Cu+Zn concentrations at both MIR Zone and Rona Mound fit into the 'economically' interesting range of SMS deposits (Petersen *et al.*, 2016), and indicate that it is possible for interesting concentrations of metals to be present beneath the Si-Fe cap. Based on the high porosity and permeability of the weathered hydrothermal sediments, then the underlying massive sulphide ore body would be subjected to seafloor weathering even with a thin sediment cover. However, silicification would decrease the potential for further weathering. This implies that the Si-Fe cap formation may be responsible for the preservation of the high Cu+Zn concentrations observed.

8.4.2 Seafloor oxidation rates and understanding the Si-Fe cap formation in the context of seafloor exposure

Experimental studies have been carried out regarding weathering and dissolution of sulphide minerals at the seafloor. Eventually, prolonged exposure of sulphides to seawater will result in the dissolution and mobilisation of sulphide material, and with that, the loss of the economically important metals in the orebody. Oxidation rates for pyrite (and marcasite), chalcopyrite, and sphalerite have been experimentally derived at typically 10^{-10} to 10^{-12} (pyrite/marcasite), 10^{-14} (chalcopyrite) and 10^{-11} cm/s (sphalerite) (Fallon *et al.*, 2017). However, assessment of metal mobilisation during sulphide dissolution processes in seawater are difficult to derive by experimentation due to factors including: the formation of 'inert' iron oxide weathering products interfering with metal loss, and the galvanic effect of mixed sulphide assemblages (Knight *et al.*, 2018). Therefore, it would be difficult to determine how long an eSMS deposit would take to weather on the seafloor when these secondary mineralogy and burial factors are taken into consideration.

Despite this lack of ability to quantify metal loss, we can estimate the length of time that these deposits have been subjected to seawater influence, and therefore likely subject to weathering processes. Historical age dating of sulphide material and carbonate sediment dating, along with new sediment age dating (Dutrieux, 2019) provide the most complete hydrothermal history of the TAGHF to date and show that the MIR Zone hydrothermal activity has spanned from ~150kya to ~670 ya, and ALVIN Zone has spanned from ~ 80kya to 4kya (Figure 166).

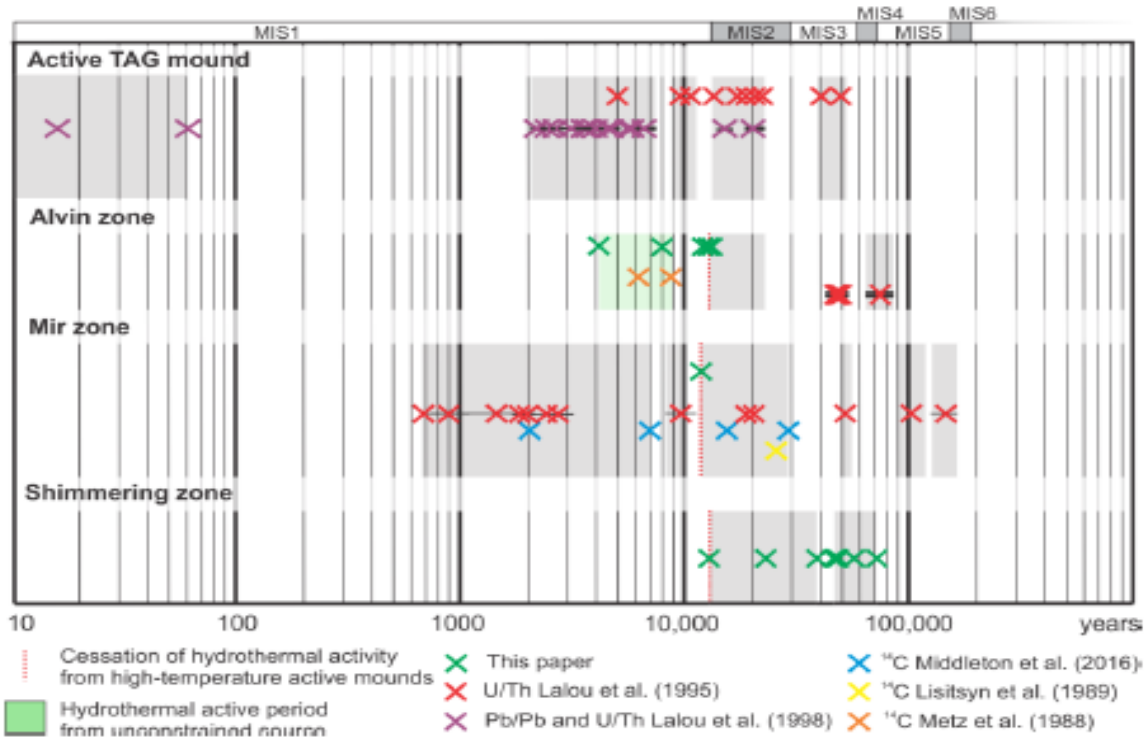

Figure 166: Summary of the age dating conducted on the TAG hydrothermal field (Dutrieux, 2019)

This age dating also highlights the fact that these deposits have likely been interacting with seawater for around 80ky-100ky. This means that during periods of hydrothermal inactivity (e.g. between ~14kya and 10kya at the ALVIN Zone), surface sulphide material would be subjected to seawater interaction and weathering, the processes interpreted to be forming the hydrothermal sediment protolith of the Si-Fe cap. Despite the lengths of time that these deposits are interpreted to have been potentially influenced by seawater, the presence of high Cu+Zn concentrations under the Si-Fe cap imply that at these timescales economically interesting base metal concentrations are likely to have been preserved by the Si-Fe cap.

Furthermore, the occurrence of high temperature sulphide minerals at the base of Southern Mound and Rona Mound (in the ALVIN Zone) could indicate that further renewed hydrothermal activity may have occurred, but did not reach the seafloor. The impermeable Si-Fe cap appears to have acted as a physical barrier to these high temperature sulphur-rich fluids and promoted sulphide precipitation in the base of the Si-Fe cap. Evidence presented in Chapter 6 implies that Zn is being mobilised in these fluids, and the wide range of sphalerite formation temperatures suggests zone refining and remobilisation of the sulphides in the Si-Fe cap by pulses of fluids with alternations in redox states and likely synchronous with the same process interpreted to be operating in the massive sulphides beneath the cap (e.g. at Rona Mound, (Lehrmann *et al.*, 2018)).

This observation could have significant implications for the resource estimates of eSMS deposits. Zone refining processes within the Active TAG Mound are interpreted to have mobilised Cu and Zn throughout the SMS deposits and essentially resulted in continually increasing Cu and Zn concentrations over multiple refining episodes. In general, Cu and Zn appear to be enriched in surface samples compared to sub-surface samples (Hannington *et al.*, 2011). However if an impermeable cap is present, the fluids would become trapped and potentially deposit sulphides at depth. This process could be similar to that observed at Bent Hill and ODP mounds (Section 2.4.5), and during resurgent hydrothermal activity could enrich the underlying orebody. This process is somewhat speculative, and further investigation and recovery of sub-seafloor sulphide material is necessary to understand whether this hypothesis is feasible.

8.4.3 Implications for potential reservoirs of base metals in the oceanic crust

Ultimately the main processes interpreted to form Si-Fe cap rocks at all three eSMS deposits derive from common hydrothermal processes: surface weathering of seafloor sulphide features, low temperature iron oxide/oxyhydroxide precipitation, and low temperature hydrothermal silicification. This is supported by the wide range of VMS deposits throughout geological history where Si-Fe materials are also interpreted to have formed in a similar way. However, as highlighted in this thesis, the occurrence at SMS or eSMS deposits is seemingly not as common.

This could be simply explained by the fact that these Si-Fe cap rocks appear to form in the sub-surface or within sedimentary sequence, therefore evidence of these processes at the seafloor are likely limited, highlighted by the comprehensive RUV surveys completed during the Blue Mining project (Section 3.3).

One poorly constrained aspect to the Si-Fe cap formation is the lateral extent over which they can and have formed. Simple estimates have been conducted (Section 3.4) and imply that they could cover as much as ~50% of Rona Mound (a small deposit), or ~25% of Southern Mound (a larger deposit). These Si-Fe caps have been proven to be impermeable, thus inhibiting weathering of sulphides, but may not cover the whole deposit.

Global metal budget of SMS deposits are based on the limited three dimensional knowledge of SMS deposits, and typically do not include stockwork zone sulphides, deposits older than 300kya, or eSMS deposits (Hannington *et al.*, 2010; Murton *et al.*, 2019). Assuming average SMS formation at 50-100ka, within 1Ma of oceanic crust across the ridge flanks on both sides of the spreading axis, then there may be 20-40 times as many eSMS deposits than hydrothermally active ones. Even if Si-Fe caps only cover and preserve 20-50% of the volumes of eSMS deposits, this would still imply 4-

20 times greater metal content preserved in the eSMS deposits than current estimates of metal reservoirs.

It is also interesting to consider the other mechanisms of deposit preservation, particularly in similar ocean ridge settings in VMS deposits. This brings us back to the Troodos ophiolite, where deposits are preserved by rapid burial by basaltic lava flows (Hall and Yang, 1994) to depths of ~ 200m. With the Troodos ophiolite presenting the closest geological analogue to SMS deposits on mid-ocean spreading ridges, it is interesting to consider the increased potential of SMS deposit preservation near volcanic centres.

Applying the VMS burial model from Troodos to modern day ocean spreading centres, it would imply that a significant amount of SMS orebodies are preserved at depth within the off-axis oceanic crust, as long as they are not buried deep enough to be destroyed by dyke intrusions. Additionally, basaltic material (10^{-17} – 10^{-21} m^2 (Fisher, 1998)) is considered to be more impermeable than Si-Fe cap materials (see Chapter 7), therefore burial by basalt flows could also provide a sensible mechanisms of eSMS preservation. This implies that large eSMS deposits could be preserved under (relatively shallow) basaltic cover within the oceanic crust where they are eventually carried by seafloor spreading to be recycled with the subduction factory and remobilised as arc-related sulphide mineralisation. This fact alone implies a recalculation is needed of the global metal cycle to better understand both the total oceanic crustal reservoir of base metals and those being recycled in subduction zone and back into the mantle.

Chapter 9 Conclusions and Further Work

9.1 Origins of the Si-Fe cap and paragenesis

In this thesis I have presented a comprehensive study of the textural, mineralogical, and geochemical assessment of Si-Fe cap rocks and determined a general paragenesis for their formation.

Firstly, a range of hydrothermally derived sediments have formed atop of a sulphide deposit by a range of processes including: sulphide weathering, low temperature hydrothermal precipitation of oxides, accumulation of material by mass-wasting. Once these sediments have formed, reduced, silica-rich, sulphur-poor, hydrothermal fluids have intruded into the sediments and started to precipitate silica by fluid mixing. At least two generations of silicification have been interpreted based upon silica formation temperatures from oxygen stable isotope geothermometry. After this silicificiation has occurred, late-stage sulphur-rich, high temperature fluids have infiltrated into the base of the Si-Fe cap, reduced iron oxides, and precipitated sulphide minerals. This late stage fluid is interpreted to be >250˚C based on sphalerite geothermometry, much higher temperatures than the silicifying fluids.

This sulphidation may represent a resurgence of higher temperature fluids in the hydrothermal system, but the formation of the Si-Fe cap has acted as a physical barrier and prevented the fluids from rising to the seafloor.

9.2 Implications for permeability of the Si-Fe cap rock

The low permeability of the Si-Fe cap rock has been assessed by X-Ray CT analysis and fluid modelling through a range of Si-Fe core samples. This supports the observations and interpretations that the Si-Fe cap rock has acted as a physical barrier to upwelling high temperature hydrothermal fluids. Furthermore, the impermeable Si-Fe cap rock would also act as a physical barrier to seawater ingress, thus protecting the underlying massive sulphide ore-body from oxidation by seawater.

The Si-Fe cap rock is interpreted to be of comparable permeability to crystalline volcanic rocks, or ~ 200 m thickness of sediments, common processes by which the geological analogues (VMS deposits) have been preserved on the seafloor.

Therefore, the combination of the interpreted formation mechanisms, and the impermeable nature of the Si-Fe cap rock, provides a potential ‘generic’ auto-preservation mechanism at eSMS deposits.

9.3 Further Work

The low sample recovery and lack of spatial variation of the Si-Fe cap across the eSMS deposits has significantly inhibited this study. Further sub-seafloor drilling and sample recovery of the same deposits would provide a better understanding of the extent of the Si-Fe cap, and help further understand the range of formation processes in this highly diverse environment. In addition, further sub-seafloor sampling of other eSMS deposits from different geological settings is recommended to investigate if this combination of generic hydrothermal related processes have combined at other sites, to form comparable auto-preservation 'caps'.

With specific regards for this study, several main aspects would be recommend for further work. The first is related the oxygen isotopic formation temperatures. This is one of the key data sets used to interpret the paragenesis of the Si-Fe cap, and has been obtained from 'bulk' silica samples. This means that the value is representative of the whole sample, and the value could be derived from variable contributions from different silicification events of differing oxygen isotope values. The underlying assumption for the interpretation of this data is that the overlapping silica generations have resulted in silica recrystallisation and re-equilibration of the oxygen isotope ratio of any existing silica with the fluid responsible for the second silica event. *In-situ* investigation of $\delta^{18}O$ variation throughout the silica generations may shed light on whether there is variation of $\delta^{18}O$ at thin section scale and thus may provide further information on the multiple silicification processes involved in forming the Si-Fe cap.

Secondly, Sulphur stable isotope analysis of the sulphides in the Si-Fe cap was planned during this project, but was not undertaken due to equipment issues. It is recommended that this is also pursued with the aim of constraining the origins of sulphur in the formation of the late-stage sulphides in the Si-Fe cap. Of particular interest is whether there is any kind of biological influence of the sulphide signature, in light of the abundance of potentially biological filaments, and the complex relationship between iron oxides and sulphides observed in the samples.

The third is related to the lack of age-datable material within the Si-Fe cap. If possible, it would be interesting to apply U-Th dating to the sulphides within the Si-Fe cap, surface samples from the eSMS mounds, and the underlying massive sulphide orebody. This could potentially link timing of processes (such as zone-refining) within the ore-body with the processes forming the Si-Fe cap. This could also provide further understanding of the evolution of the TAG hydrothermal field, and the cyclical nature of hydrothermal activity. Other novel age-dating techniques, such as thermal luminescence dating of the silica or (U/Th)-He dating of the haematite could theoretically be applied to the Si-Fe cap rock to help form a comprehensive hydrothermal history of the TAG eSMS deposits.

Finally, I believe that continued X-Ray CT study can be applied to the core material recovered. Further investigation into the use of the technique to study the porosity and permeability over more samples, and also assess the complex three dimensional textures could again provide more information of the formation processes of the Si-Fe cap. Comparison of direct permeability measurements from core samples with the calculated and modelled permeability values from the CT scanning should be undertaken to investigate the true validity of the modelled values.

Appendix A Whole rock geochemistry

Major elements with analytical techniques used.

	Unit Type	SiO_2	Al_2O_3	TiO_2	Fe_2O_{3T}	MgO	MnO
		XRF	ICP-MS	ICP-MS	XRF	XRF	ICP-MS
Southern Mound		wt%	wt%	wt%	wt%	wt%	wt%
022RD/CC	B	71.49	0.008276	0.000783	29.69	0.0304	0.026792
031RD/CC/07	B	94.59	0.003904	0.000442	4.78	0.0079	0.00356
031RD/109/CC	B	93.38	0.003242	0.002494	6.81	0.0071	0.004981
050RD/P3	A	66.46	0.002813	0.000284	29.34	0.0365	0.02798
050RD/P5	A	62.47	0.00187	0.00032	33.84	0.0489	0.044146
050RD/P7	A	60.78	0.00183	0.00033	35.91	0.0382	0.03268
050RD/P8	A	71.71	0.00042	5.29E-05	24.16	0.0419	0.004929
050RD/P11	C	95.94	0.008737	0.000464	5.63	0.0049	0.00336
050RD/P12	C	93.67	0.018744	0.000352	7.37	0.0054	0.003114
050RD/P13	C	95.26	0.000239	5.19E-05	5.73	0.0069	3.59E-05
Rona Mound							
057RD/P2	B	89.25	0.012816	0.000587	8.98	0.0044	0.002695
057RD/P3-8	B	89.92	0.005309	0.000208	8.18	0.0035	0.002746
057RD/P10	C	81.80	0.041834	0.000223	11.72	0.0039	0.002159
057RD/P11	C	82.26	0.098651	0.000266	17.62	0.0057	0.003032
MIR Zone							
073RD/P1	B	93.42	0.006024	0.000537	8.01	0.0081	0.005701
073RD/P6	B	94.53	0.001954	0.00022	5.46	0.0077	0.003925
073RD/P7	B	81.87	0.001193	0.000515	19.15	0.0067	0.005317
073RD/P9	B	77.70	0.02154	0.000872	21.75	0.0094	0.008617
073RD/P11	B	75.74	0.015834	0.0008	22.08	0.0086	0.005871
073RD/P12	B	76.20	0.007739	0.000248	22.34	0.0145	0.010532
073RD/P14	B	83.42	0.004998	0.000421	14.61	0.0112	0.008957
076RD/P2	B	68.07	0.001316	0.000271	33.35	0.0125	0.009461
076RD/P3	B	92.72	0.007303	0.000519	8.40	0.0062	0.00457
076RD/P4	B	91.69	0.006848	0.000734	8.08	0.0081	0.005581
076RD/P6	B	73.30	0.003739	0.000379	25.80	0.0147	0.01308
076RD/P7	B	89.15	0.006413	0.000316	11.68	0.0128	0.007189
076RD/P8	B	92.66	0.009852	0.000276	8.33	0.0101	0.009257

CaO	K_2O	Na_2O	P_2O_5	SO_3	TC	TOC	
XRF	XRF	XRF	ICP-MS	LECO	LECO	LECO	SUM
wt%	wt%	wt%	wt%	wt%	wt%	wt%	%
0.115	0.021	0.174	0.09627	0.05	0.04	0.01	101.76
0.028	0.009	0.13	0.023031	0.05	0.04	0.01	99.68
0.107	0.008	0.11	0.074706	0.05	0.02	0	100.57
0.064	0.045	0.809	0.122051	0.15	0.02	0.01	97.08
0.052	0.033	0.527	0.162795	0.10	0.03	0.01	97.32
0.05	0.039	0.457	0.112907	0.10	0.01	0	97.52
0.046	0.02	0.374	0.019841	0.12	0.02	0.01	96.53
0.021	0.015	0.139	0.021495	2.45	0.02	0	104.25
0.022	0.009	0.077	0.016183	3.97	0.04	0.02	105.23
0.027	0.007	0.019	0.005756	2.30	0.04	0.02	103.42
0.028	0.027	0.405	0.036895	1.12	0.02	0.01	99.90
0.027	0.016	0.262	0.040286	0.10	0.02	0.01	98.59
0.032	0.02	0.554	0.043655	6.32	0.02	0.01	100.56
0.03	0.038	0.542	0.038155	13.93	0.03	0.01	114.61
0.077	0.024	0.174	0.050713	0.27	0.03	0.02	102.10
0.055	0.01	0.227	0.037903	0.05	0.03	0.02	100.44
0.118	0.018	0.286	0.086004	0.07	0.02	0	101.63
0.042	0.027	0.441	0.091962	0.07	0.03	0.02	100.22
0.037	0.023	0.421	0.069367	0.07	0.03	0.02	98.53
0.031	0.016	0.317	0.085729	0.07	0.02	0.01	99.13
0.023	0.011	0.179	0.064371	0.05	0.04	0.02	98.45
0.047	0.035	0.378	0.08951	0.05	0.01	0	102.05
0.062	0.012	0.169	0.04629	0.10	0.03	0.02	101.58
0.193	0.012	0.144	0.131309	0.07	0.03	0.02	100.39
0.041	0.03	0.342	0.088593	0.07	0.03	0.02	99.75
0.054	0.021	0.192	0.038751	0.12	0.02	0.01	101.32
0.02	0.016	0.169	0.022898	0.62	0.03	0.01	101.92

Major elements normalised to 100 wt%.

		SiO_2	Al_2O_3	TiO_2	Fe_2O_{3T}	MgO	MnO
		XRF	ICP-MS	ICP-MS	XRF	XRF	ICP-MS
Southern Mound		wt%	wt%	wt%	wt%	wt%	wt%
022RD/CC	B	70.26	0.01	<0.01	29.18	0.03	0.03
031RD/CC/07	B	94.90	<0.01	<0.01	4.79	0.01	<0.01
031RD/109/CC	B	92.85	<0.01	<0.01	6.77	0.01	<0.01
050RD/P3	A	68.45	<0.01	<0.01	30.22	0.04	0.03
050RD/P5	A	64.19	<0.01	<0.01	34.77	0.05	0.05
050RD/P7	A	62.32	<0.01	<0.01	36.82	0.04	0.03
050RD/P8	A	74.29	<0.01	<0.01	25.03	0.04	0.01
050RD/P11	C	92.03	0.01	<0.01	5.40	<0.01	<0.01
050RD/P12	C	89.02	0.02	<0.01	7.01	0.01	<0.01
050RD/P13	C	92.11	0.00	<0.01	5.54	0.01	<0.01
Rona Mound							
057RD/P2	B	89.34	0.01	<0.01	8.99	<0.01	<0.01
057RD/P3-8	B	91.21	0.01	<0.01	8.29	<0.01	<0.01
057RD/P10	C	81.34	0.04	0.00	11.65	0.00	0.00
057RD/P11	C	71.77	0.09	0.00	15.37	0.00	0.00
MIR Zone							
073RD/P1	B	91.49	<0.01	<0.01	7.85	0.01	0.01
073RD/P6	B	94.12	<0.01	<0.01	5.44	0.01	<0.01
073RD/P7	B	80.55	<0.01	<0.01	18.84	0.01	0.01
073RD/P9	B	77.53	0.02	<0.01	21.70	0.01	0.01
073RD/P11	B	76.87	0.02	<0.01	22.41	0.01	0.01
073RD/P12	B	76.87	0.01	<0.01	22.54	0.01	0.01
073RD/P14	B	84.74	0.01	<0.01	14.84	0.01	0.01
076RD/P2	B	66.70	0.00	<0.01	32.68	0.01	0.01
076RD/P3	B	91.28	0.01	<0.01	8.27	0.01	<0.01
076RD/P4	B	91.33	0.01	<0.01	8.04	0.01	0.01
076RD/P6	B	73.48	<0.01	<0.01	25.86	0.01	0.01
076RD/P7	B	87.99	0.01	<0.01	11.52	0.01	0.01
076RD/P8	B	90.92	0.01	<0.01	8.17	0.01	0.01

CaO	K_2O	Na_2O	P_2O_5	SO_3	TC	TOC	
XRF	XRF	XRF	ICP-MS	LECO	LECO	LECO	SUM
wt%	wt%	wt%	wt%	wt%	wt%	wt%	%
0.11	0.02	0.17	0.09	0.05	0.04	0.01	100
0.03	0.01	0.13	0.02	0.05	0.04	0.01	100
0.11	0.01	0.11	0.07	0.05	0.02	0.00	100
0.07	0.05	0.83	0.13	0.15	0.02	0.01	100
0.05	0.03	0.54	0.17	0.10	0.03	0.01	100
0.05	0.04	0.47	0.12	0.10	0.01	0.00	100
0.05	0.02	0.39	0.02	0.13	0.02	0.01	100
0.02	0.01	0.13	0.02	2.35	0.02	0.00	100
0.02	0.01	0.07	0.02	3.77	0.04	0.02	100
0.03	0.01	0.02	0.01	2.22	0.04	0.02	100
0.03	0.03	0.41	0.04	1.12	0.02	0.01	100
0.03	0.02	0.27	0.04	0.10	0.02	0.01	100
0.03	0.02	0.55	0.04	6.28	0.02	0.01	100
0.03	0.03	0.47	0.03	12.16	0.03	0.01	100
0.08	0.02	0.17	0.05	0.27	0.03	0.02	100
0.05	0.01	0.23	0.04	0.05	0.03	0.02	100
0.12	0.02	0.28	0.08	0.07	0.02	0.00	100
0.04	0.03	0.44	0.09	0.07	0.03	0.02	100
0.04	0.02	0.43	0.07	0.08	0.03	0.02	100
0.03	0.02	0.32	0.09	0.08	0.02	0.01	100
0.02	0.01	0.18	0.07	0.05	0.04	0.02	100
0.05	0.03	0.37	0.09	0.05	0.01	0.00	100
0.06	0.01	0.17	0.05	0.10	0.03	0.02	100
0.19	0.01	0.14	0.13	0.07	0.03	0.02	100
0.04	0.03	0.34	0.09	0.08	0.03	0.02	100
0.05	0.02	0.19	0.04	0.12	0.02	0.01	100
0.02	0.02	0.17	0.02	0.61	0.03	0.01	100

Trace elements obtained from ICP-MS analysis, includes ppm values of major elements (Al,P,Ti, Mn)used for major element concentrations (converted to elemental oxides). All samples obtained by ICP-MS except Zn (*) obtained by XRF.

	Unit	Al	P	Ti	Mn	Co	Cu
		ppm	ppm	ppm	ppm	ppm	ppm
Southern Mound							
022RD/CC	B	43.8	420.1	4.7	207.5	0.4	3.4
031RD/CC/07	B	20.7	100.5	2.6	27.6	0.7	9.5
031RD/109/CC	B	17.2	326.0	15.0	38.6	0.8	5.9
050RD/P3	A	14.9	532.6	1.7	216.7	0.2	11.0
050RD/P5	A	9.9	710.4	1.9	341.9	0.2	28.6
050RD/P7	A	9.7	492.7	2.0	253.1	0.2	15.8
050RD/P8	A	2.2	86.6	0.3	38.2	0.0	1.5
050RD/P11	C	46.2	93.8	2.8	26.0	0.6	9.1
050RD/P12	C	99.2	70.6	2.1	24.1	1.7	466.4
050RD/P13	C	1.3	25.1	0.3	0.3	0.0	18.4
Rona Mound							
057RD/P2	B	67.8	161.0	3.5	20.9	2.2	73.7
057RD/P3-8	B	28.1	175.8	1.2	21.3	0.4	14.2
057RD/P10	C	221.4	190.5	1.3	16.7	3.7	30.6
057RD/P11	C	522.1	166.5	1.6	23.5	6.4	20.0
MIR Zone							
073RD/P1	B	31.9	221.3	3.2	44.2	2.8	177.1
073RD/P6	B	10.3	165.4	1.3	30.4	1.0	11.1
073RD/P7	B	6.3	375.3	3.1	41.2	0.9	6.2
073RD/P9	B	114.0	401.3	5.2	66.7	0.7	15.6
073RD/P11	B	83.8	302.7	4.8	45.5	0.4	12.1
073RD/P12	B	41.0	374.1	1.5	81.6	0.4	19.0
073RD/P14	B	26.5	280.9	2.5	69.4	1.2	52.4
076RD/P2	B	7.0	390.6	1.6	73.3	0.4	5.7
076RD/P3	B	38.7	202.0	3.1	35.4	1.0	23.7
076RD/P4	B	36.2	573.0	4.4	43.2	1.5	22.3
076RD/P6	B	19.8	386.6	2.3	101.3	0.3	7.9
076RD/P7	B	33.9	169.1	1.9	55.7	0.6	83.7
076RD/P8	B	52.1	99.9	1.7	71.7	0.7	99.9

Zn*	Cd	Pb	Ba	Sr	V	Mo	U	Li
ppm	ppm	ppm	ppm	ppm	ppm	ppm	ppm	ppm
65	0.02	28.62	3.85	3.06	36.12	6.12	12.84	1.07
23	0.02	6.17	2.25	1.13	6.35	1.56	5.43	0.67
78	0.66	7.82	0.60	1.44	8.63	2.22	4.10	0.94
508	0.10	25.18	198.50	23.99	13.09	4.37	8.68	0.93
677	0.12	38.21	2.19	7.33	20.42	7.03	12.70	1.02
605	0.03	96.55	165.60	17.91	9.68	6.13	14.33	2.47
806	0.01	33.06	187.40	10.10	0.90	1.18	1.52	0.10
393	0.98	20.56	0.18	1.09	2.77	2.27	7.10	1.56
678	1.87	6.91	36.05	1.62	6.24	3.53	5.22	0.28
35	0.00	0.02	1.77	0.28	0.03	0.07	0.02	0.01
603	1.51	19.11	2.64	2.41	7.81	4.88	7.24	0.15
55	0.09	7.59	9.36	2.37	2.49	3.63	6.76	0.14
7166	22.96	33.36	36.16	5.34	27.80	6.68	37.52	0.09
5274	17.13	74.85	64.70	6.16	114.90	10.48	42.77	0.12
74	0.05	13.39	0.32	1.74	9.09	7.46	4.66	1.24
52	0.01	3.35	0.31	1.69	5.15	3.31	3.83	0.68
94	0.03	6.86	1.16	3.21	5.62	4.29	7.67	1.62
255	0.06	3.08	0.66	4.29	16.96	7.75	13.37	2.43
341	0.05	1.90	0.67	3.63	13.49	6.58	12.48	2.39
409	0.08	2.59	0.34	3.18	8.61	3.86	12.32	1.40
265	0.04	0.93	0.42	2.41	9.74	3.53	12.12	1.09
54	0.02	17.11	17.86	7.18	9.57	8.05	5.12	4.27
25	0.01	2.34	1.69	1.68	6.54	2.47	3.42	1.31
19	0.01	2.01	0.69	2.50	5.90	3.25	3.50	1.32
94	0.01	10.41	1.73	6.34	8.92	6.21	4.46	2.73
99	0.02	4.02	2.18	2.03	5.94	2.40	4.68	1.14
86	0.01	9.52	0.48	1.50	9.28	2.21	8.58	1.30

Be	Ni	Cr	Rb	Y	Zr	In	Cs	Th
ppb	ppm	ppm	ppm	ppm	ppm	ppb	ppm	ppm
0.56	1.76	187.10	0.22	1.76	0.59	0.70	< 0.01	0.01
0.55	5.09	200.80	0.08	0.08	0.20	0.68	< 0.01	< 0.01
0.60	2.84	264.50	0.06	0.26	0.33	0.72	< 0.01	< 0.01
0.73	1.08	31.36	0.38	0.43	0.80	0.85	0.01	< 0.01
0.77	1.85	28.62	0.28	0.69	0.22	0.90	0.01	< 0.01
0.58	1.71	33.41	0.51	0.47	0.19	0.70	0.02	< 0.01
0.60	0.17	3.51	0.02	0.06	0.09	0.73	< 0.01	< 0.01
0.55	1.82	226.10	0.06	0.20	0.13	0.67	< 0.01	< 0.01
0.59	3.55	450.70	0.03	0.18	0.22	0.75	< 0.01	< 0.01
0.55	0.03	2.73	0.01	0.00	0.04	0.67	< 0.01	< 0.01
0.60	1.90	178.00	0.39	0.36	0.15	0.75	0.01	< 0.01
0.68	1.19	128.40	0.24	0.23	0.08	0.82	0.01	< 0.01
0.86	2.38	79.77	0.15	0.31	0.06	1.07	< 0.01	< 0.01
0.57	4.26	201.00	0.21	0.24	0.26	0.76	0.01	< 0.01
0.72	64.92	711.70	0.11	0.11	0.34	0.84	< 0.01	0.01
0.61	3.46	339.00	0.08	0.10	0.22	0.73	< 0.01	0.01
0.70	3.06	321.20	0.18	0.18	0.17	0.83	< 0.01	0.00
0.81	2.53	263.70	0.21	0.44	0.29	0.92	< 0.01	0.01
0.59	1.56	155.10	0.21	0.33	0.25	0.72	< 0.01	0.01
0.92	1.38	137.60	0.07	0.41	0.33	1.13	< 0.01	0.02
0.59	17.90	423.70	0.08	0.37	0.38	0.71	< 0.01	< 0.01
0.61	1.10	69.22	0.39	0.19	0.31	0.75	0.01	< 0.01
0.74	3.10	371.10	0.12	0.23	0.93	0.86	< 0.01	0.02
0.70	4.75	565.20	0.11	0.60	0.32	0.82	< 0.01	0.01
0.56	1.90	70.87	0.33	0.26	0.33	0.69	0.01	< 0.01
0.61	1.86	217.50	0.13	0.32	0.22	0.73	< 0.01	0.01
0.71	2.29	265.90	0.11	0.26	0.15	0.84	< 0.01	< 0.01

Analysed REEs by ICP-MS.

	Unit	La	Ce	Pr	Nd	Sm	Eu
		ppb	ppb	ppb	ppb	ppb	ppb
022RD/CC	B	647.3	2003.0	383.5	2044.0	589.6	3164.0
031RD/CC/007	B	57.5	167.6	32.8	172.3	51.0	221.8
050RD/P3	A	318.5	624.7	124.3	628.2	171.9	974.0
050RD/P5	A	344.3	712.4	149.8	749.3	203.0	1061.0
050RD/P7	A	313.8	851.9	160.6	816.4	222.0	1414.0
050RD/P8	A	230.9	565.8	112.2	587.9	180.3	939.4
050RD/P11	C	48.5	166.8	38.2	238.5	103.5	224.0
050RD/P12	C	196.0	715.4	134.4	688.3	163.9	533.3
050RD/P13	C	51.1	135.7	23.8	129.6	39.7	88.4
057RD/P2	B	157.7	538.0	108.2	585.4	229.2	639.0
057RD/P3-8	B	89.2	308.6	62.9	347.5	135.2	363.3
057RD/P10	C	188.4	661.6	131.7	686.8	269.3	630.3
057RD/P11	C	118.2	460.0	95.2	498.0	188.3	506.6
073RD/P1	B	58.7	167.4	40.5	233.1	99.3	545.1
073RD/P6	B	47.3	151.2	35.4	203.0	78.0	282.5
073RD/P7	B	114.1	327.4	73.8	420.5	168.1	945.1
073RD/P9	B	138.2	452.5	102.6	590.3	255.8	1088.0
073RD/P11	B	109.0	335.0	75.9	443.0	185.0	804.3
073RD/P12	B	111.7	348.4	77.3	471.1	196.8	786.3
073RD/P14	B	101.5	288.0	66.9	393.0	159.7	552.3
076RD/P2	B	139.4	251.0	54.3	299.0	73.6	456.4
076RD/P3	B	130.0	441.6	93.8	539.0	164.8	1213.0
076RD/P4	B	427.2	1379.0	277.1	1578.0	433.4	3805.0
076RD/P6	B	138.2	331.8	68.4	398.3	113.9	441.9
076RD/P7	B	214.8	862.6	176.1	1011.0	283.7	1727.0
076RD/P8	B	153.8	739.7	163.9	941.3	296.4	1252.0

Gd	Tb	Dy	Ho	Er	Tm	Yb	Lu
ppb	ppb	ppb	ppb	ppb	ppb	ppb	ppb
465.7	53.9	258.3	48.8	137.3	19.3	129.0	22.7
33.5	3.8	17.7	3.0	7.6	1.0	7.8	1.2
144.8	16.6	80.6	14.5	39.0	5.4	34.5	5.6
175.2	19.9	92.5	17.7	45.4	5.9	36.6	6.2
170.9	18.3	81.3	14.1	36.8	4.9	32.8	5.2
143.6	16.1	72.2	13.4	36.1	5.0	33.6	5.9
91.1	13.4	66.2	10.8	29.0	4.3	29.4	4.2
113.5	12.6	54.1	8.6	18.3	2.4	14.7	2.0
35.5	3.9	15.8	2.4	5.2	0.6	3.7	0.5
198.1	31.2	162.2	25.3	63.2	8.7	53.3	6.6
118.3	17.5	86.2	13.1	30.8	3.7	21.7	2.6
205.2	33.5	176.3	26.3	64.4	9.3	64.6	7.8
144.1	22.9	115.0	16.6	39.9	5.9	39.3	4.7
68.3	8.4	34.0	5.4	13.4	1.9	12.0	1.9
56.2	6.4	26.4	4.0	9.6	1.3	8.7	1.3
112.5	13.5	55.6	7.5	17.8	2.1	11.6	1.6
193.4	25.5	115.7	18.2	45.5	6.4	41.0	6.3
147.5	19.1	89.9	14.7	36.5	5.3	34.1	4.9
179.0	23.6	113.8	18.6	47.8	6.8	45.6	6.7
146.4	19.5	96.2	16.5	43.2	6.5	43.5	7.0
68.2	4.7	20.3	4.1	10.9	1.5	10.8	1.6
123.1	12.4	46.8	8.0	20.5	2.8	19.3	3.1
327.7	27.2	104.2	16.7	39.0	4.4	27.6	4.4
96.8	8.9	36.1	6.3	16.3	2.1	13.4	2.1
227.0	20.2	77.2	11.2	25.7	2.8	17.2	2.5
191.3	17.9	63.6	9.0	18.5	1.8	11.7	1.7

Normalised REEs (to Evensen 1978).

		La	Ce	Pr	Nd	Sm	Eu	Gd
		ppb	ppb	ppb	ppb	ppb	ppb	ppb
022RD/CC	B	2.65	2.48	3.14	3.41	3.02	72.74	1.80
031RD/CC/007	B	0.19	0.21	0.27	0.29	0.26	5.10	0.13
050RD/P3	A	1.03	0.77	1.02	1.05	0.88	22.39	0.56
050RD/P5	A	1.11	0.88	1.23	1.25	1.04	24.39	0.68
050RD/P7	A	1.01	1.05	1.32	1.36	1.14	32.51	0.66
050RD/P8	A	0.74	0.70	0.92	0.98	0.92	21.60	0.55
050RD/P11	C	0.16	0.21	0.31	0.40	0.53	5.15	0.35
050RD/P12	C	0.63	0.89	1.10	1.15	0.84	12.26	0.44
050RD/P13	C	0.16	0.17	0.19	0.22	0.20	2.03	0.14
057RD/P2	B	0.51	0.67	0.89	0.98	1.18	14.69	0.76
057RD/P3-8	B	0.29	0.38	0.52	0.58	0.69	8.35	0.46
057RD/P10	C	0.61	0.82	1.08	1.14	1.38	14.49	0.79
057RD/P11	C	0.38	0.57	0.78	0.83	0.97	11.65	0.56
073RD/P1	B	0.19	0.21	0.33	0.39	0.51	12.53	0.26
073RD/P6	B	0.15	0.19	0.29	0.34	0.40	6.49	0.22
073RD/P7	B	0.37	0.41	0.61	0.70	0.86	21.73	0.43
073RD/P9	B	0.45	0.56	0.84	0.98	1.31	25.01	0.75
073RD/P11	B	0.35	0.41	0.62	0.74	0.95	18.49	0.57
073RD/P12	B	0.36	0.43	0.63	0.79	1.01	18.08	0.69
073RD/P14	B	0.33	0.36	0.55	0.66	0.82	12.70	0.57
076RD/P2	B	0.45	0.31	0.44	0.50	0.38	10.49	0.26
076RD/P3	B	0.42	0.55	0.77	0.90	0.85	27.89	0.48
076RD/P4	B	1.38	1.71	2.27	2.63	2.22	87.47	1.27
076RD/P6	B	0.45	0.41	0.56	0.66	0.58	10.16	0.37
076RD/P7	B	0.69	1.07	1.44	1.69	1.45	39.70	0.88
076RD/P8	B	0.50	0.92	1.34	1.57	1.52	28.78	0.74

Tb	Dy	Ho	Er	Tm	Yb	Lu
ppb	ppb	ppb	ppb	ppb	ppb	ppb
1.14	0.80	0.68	0.65	0.60	0.62	0.70
0.08	0.06	0.04	0.04	0.03	0.04	0.04
0.35	0.25	0.20	0.19	0.17	0.16	0.18
0.42	0.29	0.25	0.22	0.18	0.18	0.19
0.39	0.25	0.20	0.18	0.15	0.16	0.16
0.34	0.22	0.19	0.17	0.15	0.16	0.18
0.28	0.21	0.15	0.14	0.13	0.14	0.13
0.27	0.17	0.12	0.09	0.07	0.07	0.06
0.08	0.05	0.03	0.02	0.02	0.02	0.02
0.66	0.50	0.35	0.30	0.27	0.26	0.20
0.37	0.27	0.18	0.15	0.12	0.10	0.08
0.71	0.55	0.37	0.31	0.29	0.31	0.24
0.48	0.36	0.23	0.19	0.18	0.19	0.15
0.18	0.11	0.08	0.06	0.06	0.06	0.06
0.14	0.08	0.06	0.05	0.04	0.04	0.04
0.29	0.17	0.10	0.08	0.06	0.06	0.05
0.54	0.36	0.25	0.22	0.20	0.20	0.19
0.40	0.28	0.20	0.17	0.16	0.16	0.15
0.50	0.35	0.26	0.23	0.21	0.22	0.21
0.41	0.30	0.23	0.21	0.20	0.21	0.22
0.10	0.06	0.06	0.05	0.05	0.05	0.05
0.26	0.15	0.11	0.10	0.09	0.09	0.10
0.57	0.32	0.23	0.19	0.14	0.13	0.14
0.19	0.11	0.09	0.08	0.06	0.06	0.07
0.43	0.24	0.16	0.12	0.09	0.08	0.08
0.38	0.20	0.13	0.09	0.06	0.06	0.05

Eu/Eu*	Ce/Ce*	LaN/SmN	SmN/YbN
20.68	0.60	0.88	4.90
17.48	0.64	0.71	7.05
21.45	0.53	1.17	5.35
19.65	0.53	1.07	5.94
24.70	0.63	0.89	7.26
20.03	0.59	0.81	5.76
8.09	0.59	0.30	3.77
12.93	0.70	0.75	11.95
8.29	0.66	0.81	11.59
10.48	0.65	0.43	4.61
10.06	0.65	0.41	6.67
9.10	0.66	0.44	4.47
10.45	0.66	0.39	5.13
21.86	0.54	0.37	8.89
14.27	0.57	0.38	9.64
22.51	0.57	0.43	15.60
16.57	0.59	0.34	6.69
16.71	0.58	0.37	5.82
14.78	0.59	0.36	4.62
12.76	0.56	0.40	3.93
22.81	0.49	1.19	7.30
28.76	0.62	0.50	9.15
34.20	0.64	0.62	16.84
14.65	0.57	0.76	9.13
23.37	0.67	0.48	17.64
17.03	0.64	0.33	27.08

Appendix B Unedited analysis of standards from all techniques

XRF standards for Major Elements and select trace elements

Major elements	SiO2	TiO2	Al2O3	Fe2O3	MnO	MgO	CaO	K2O
	(%)	(%)	(%)	(%)	(%)	(%)	(%)	(%)
SY-2	61.056	0.14	12	6.427	0.3163	2.585	7.861	4.397
NIM-G	75.866	0.09	12	1.948	0.0212	0.055	0.744	4.95
FER1	18.22	0.01	0	80.301	0.2301	0.241	3.061	0.013
FER2	49.946	0.18	5	39.978	0.124	2.001	2.059	1.309
FER2	49.541	0.18	5	40.216	0.1224	2.003	2.043	1.293
FER2	49.465	0.18	5	40.049	0.1236	2.02	2.06	1.31
FER2	49.803	0.18	5	39.982	0.1263	2.023	2.039	1.31
FER2	49.402	0.18	5	39.966	0.1241	2.014	2.054	1.291
FER2	49.699	0.18	5	39.853	0.1227	2.005	2.052	1.303
FER3	53.449	-0	-0	45.899	0.0824	0.915	0.766	0.016
FER4	52.887	0.06	2	42.353	0.1997	1.328	2.157	0.284
SYN 1 - 95:5	94.433	-0	-0	5.029	0.005	0	0.006	0
SYN 2 - 75:25	74.852	-0	-0	25.662	0.0037	-0.008	0.001	0
SYN 3 - 60:40	60.209	-0	-0	41.231	0.0049	-0.007	0.001	0.002

Na2O	P2O5	SO3	Sr	Zr	Ni	Cr	Pb	Zn
(%)	(%)	(%)	(ppm)	(ppm)	(ppm)	(ppm)	(ppm)	(ppm)
4.158	0.417	0	268.6	270.2	10.4	205.2	86.1	247.2
3.253	0.005	0	19.1	249.9	-15.5	203.3	46.5	64.8
0.061	2.216	0	94.5	40.8	8.1	180.9	7626	3334.9
0.432	0.244	0	68.7	60	-1.1	216.6	-1.2	48.7
0.432	0.248	0	69	53.4	6.2	222.3	-3.5	50.9
0.43	0.248	0	68.4	58.9	7.2	220.1	39.7	49.4
0.43	0.246	0	68.8	54.1	9.5	228.1	8.3	46.5
0.439	0.245	0	61.1	58.5	9.8	222.4	9.7	49.6
0.432	0.246	0	70	55.7	6.7	219.7	11.8	48.4
-0.035	0.063	0	38	25.6	-3.5	186.6	-14.9	73.8
-0.005	0.121	0	69.5	40.9	-13.5	199.1	-9.9	36
-0.04	0	0	8.7	26	-16.6	193	-11.3	40.4
-0.045	0	0	6.2	24	-19.5	192.6	-2	32.7
-0.025	0.001	0	3.9	25.7	-8.7	193.9	-12.8	202.2

Cu (ppm)	Co (ppm)	V (ppm)	Ba (ppm)	Ce (ppm)	As (ppm)	Rb (ppm)	U (ppm)
21.8	12	50.9	432.9	157	17.5	219.3	178.8
13	5.9	16.9	180.2	206.6	17.3	322.9	29.1
27.6	105.6	86.1	800.8	53.9	27.9	-12.8	22.7
18.1	53.9	45.7	197.7	54.3	17.2	79.9	14.7
17.7	52.5	46.5	171.1	77.4	17.2	91.8	17.4
17.5	53.1	44.2	202.5	43	17.2	87.6	16.3
17.4	51.9	54.6	180.6	8.7	17.2	85.6	13.3
17.7	50.6	47.3	181.1	38.9	17.2	83.2	16.1
16.8	50.1	43.7	176.9	95.6	17.2	85.8	10.2
15.8	59.2	26.9	-15.2	77.5	17.2	30.4	6.8
14.9	54.6	21.9	35.3	46	17.2	36.6	12.2
11.2	9	16.8	-18	-4.5	17.2	27.2	11
15.5	35.7	17.4	-32.8	7	17.2	17.3	16.4
25.8	56.2	13.5	4.8	22.5	17.2	30.5	16.1

ICP-MS analysis for trace elements, elements in ppm unless noted otherwise in brackets:

	Al (%)	As	Ba	Be	Cd	Ce	Co	Cr	Cs
JA2 (R1)	-	-	322	0.7892	0.13	33.49	27.46	390	5.139
JA2 (R2)	8.309	1.4	313.3	0.95101	0.126	33.89	28.15	396	5.093
JR-2 (R1)	6.529	8.43	27.9	0.99507	0.057	37.5	0.116	2.002	25.69
JR-2 (R2)	6.496	7.81	27.71	0.80046	0.063	36.81	0.12	2.071	25.15

Cu	Dy	Er	Eu	Gd	Hf	Ho	In	La	Li
29.94	2.923	1.69	0.908	3.035	2.713	0.603	0.88855	15.98	29.45
30.31	2.923	1.739	0.917	3.093	2.982	0.599	1.05216	16.37	29.85
1.55	6.668	4.544	0.099	5.698	5.105	1.454	1.05471	15.22	77.08
1.548	6.696	4.545	0.1	5.652	5.185	1.463	0.88492	14.96	77.4

Lu	Mn (%)	Mo	Nb	Nd	Ni	P (%)	Pb	Pr	Rb
0.254	0.08019	0.534	9.012	14.46	125	-	22.34	3.828	77.44
0.25	0.07869	0.727	9.389	14.61	131.1	0.06789	20.38	3.811	72.47
0.833	0.07898	2.658	17.95	19.32	0.884	0.002937	22.32	4.907	288.7
0.836	0.0788	2.556	17.57	19.23	0.871	0.003691	22.58	4.861	298.4

Re (ppb)	Sc	Sm	Sn	Sr	Ta	Tb	Th	Ti (%)	Tm
0.096487	17.91	3.084	1.524	244.7	0.914	0.488	4.918	-	0.257
0.10589	18.1	3.122	1.755	247.4	0.74	0.492	5.033	0.4237	0.257
1.05362	5.155	5.315	3.536	7.779	2.11	1.049	32.27	0.03447	0.77
0.9466	5.051	5.357	3.582	7.889	2.104	1.046	33.09	0.03372	0.764

U	V	Y	Yb	Zn	Zr
2.279	111.9	17.34	1.693	49.46	112.8
2.319	118.9	17.17	1.676	63.99	115.7
11.08	2.889	47.47	5.444	38.81	85.26
11.46	1.435	47.09	5.448	38.95	84.33

ICP-MS – REE only analyses:

	Be	Sr	Y	In	Ba	La	Ce	Pr
	ppm	ppm	ppm	ppm	ppm	ppm	ppm	ppm
JA-2 (1)	0.97106	223100	15850	0.95364	282200	14730	30720	3449
JA-2 (2)	0.6364	234900	16290	0.65197	299100	15140	31870	3674
JA-2 (3)	0.58728	224300	15510	0.60795	289800	14610	30660	3515
JR-2 (1)	1.05747	7648	48430	0.92361	28810	15060	38910	4873
JR-2 (2)	0.78393	7449	46180	0.69721	28210	14330	37150	4814
JR-2 (3)	0.70524	7280	45180	0.63606	27580	14110	36350	4733

Nd	Sm	Eu	Gd	Tb	Dy	Ho	Er	Tm
ppm	ppm	ppm	ppm	ppm	ppm	ppm	ppm	ppm
13320	2837	863.4	2776	435.9	2689	555.6	1617	238.5
14110	3007	920.1	3021	496.4	2991	606.4	1753	259.8
13900	2992	886.5	2902	482	2781	597.5	1679	243.4
19230	5316	99	5604	1034	6673	1456	4562	755.5
19130	5335	99.73	5562	1040	6703	1468	4595	760.7
18770	5225	98.02	5498	1025	6590	1442	4519	750.5

Yb	Lu	Re
ppm	ppm	ppm
1539	232.2	0.98728
1681	257.3	0.74695
1740	248.4	0.70854
5357	840.2	0.98013
5404	851.4	0.8057
5333	841.3	0.74915

LECO Carbon and Sulphur Standards:

Total Carbon (average wt%)	Average Sulphur wt%	Average Sulphur wt%	Repeats done
BCS-CRM 362	9.55%	1.48%	3
BCS-CRM 362	9.60%	1.55%	7
BCS-CRM 362	9.62%	1.49%	3
BCS-CRM 362	9.65%	1.51%	1
BCS-CRM 362	9.57%	1.50%	3
BCS-CRM 362	9.50%	1.47%	3
BCS-CRM 362	9.56%	1.48%	1
BCS-CRM 362	9.51%	1.47%	1

	Total Carbon (average wt%)	Average Sulphur wt%	Repeats done
501-502 LN 192-100-2	0.06%	0.02%	2
501-502 LN 192-100-2	0.06%	0.02%	2
501-502 LN 192-100-2	0.05%	0.02%	1
501-502 LN 192-100-2	0.07%	0.02%	2
501-502 LN 192-100-2	0.06%	0.01%	1
501-502 LN 192-100-2	0.06%	0.02%	2

	Total Carbon (average wt%)	Average Sulphur wt%	Repeats done
501-505 LN 1351	0.54%	0.02%	2
501-505 LN 1351	0.53%	0.02%	2
501-505 LN 1351	0.53%	0.02%	2
501-505 LN 1351	0.54%	0.02%	2

	Total Carbon (average wt%)	Average Sulphur wt%	Repeats done
leco 501-024 lot no. 1027	3.23%	0.05%	2
leco 501-024 lot no. 1027	3.23%	0.04%	2
leco 501-024 lot no. 1027	3.23%	0.04%	2
leco 501-024 lot no. 1027	3.23%	0.04%	2

Oxygen isotope standards:

Sample	Yield	RAW	δO^{18}_{smow}
YP2	25	3.768	29.6
YP2	14	-8.944	16.7
YP2	14.4	-8.015	17.8
YP2	11.5	-9.594	16.2
YP2	14.1	-9.292	16.2
YP2	15.5	-9.201	16.2
YP2	16.0	-8.097	17.3
YP2	14.6	-8.781	16.6
YP2	15.2	-8.953	16.5
YP2	17.8	-9.033	16.4
YP2	15.4	-7.255	18.3
YP2	15.5	-8.601	16.9
YP2	15.2	-9.119	16.4
YP2	11.2	-8.935	16.6
YP2	13.5	-9.37	16.2
YP2	11.6	-9.945	15.6
YP2	14.7	-9.109	16.5
YP2	12.4	-9.669	15.9
YP2	17.9	-9.133	16.4
YP2	13.8	-9.993	15.4
YP2	12.8	-9.528	16.4
YP2	17.5	-8.091	17.3
YP2	15.7	-8.768	16.6
YP2	14.1	-9.5	16.4
YP2	11.9	-9.282	16.6
YP2	10.6	-9.626	16.2
YP2	14.4	-9.371	16.5
YP2	19.5	-7.644	17.9
YP2	15.1	-9.093	16.4
YP2	15.4	-9.323	16.7
YP2	16.1	-9.264	16.7
YP2	19.4	-5.579	20.0
YP2	16.3	-8.422	17.2
YP2	17.9	-5.97	19.5
YP2	17.6	-9.115	16.4
YP2	17.5	-9.512	16.4
YP2	14.0	-8.944	16.7
YP2	11.5	-9.594	16.2
YP2	14.6	-8.781	16.6
YP2	15.2	-8.953	16.5
YP2	15.2	-9.119	16.4
YP2	11.2	-8.935	16.6

Sample	Yield	RAW	δO^{18}_{smow}	Sample	Yield	RAW	δO^{18}_{smow}
JJB8	15.0	4.291	30.2	UWG2	10.6	-19.79	5.6
JJB8	13.4	4.244	30.4	UWG2	13.0	-19.579	5.9
JJB8	14.8	4.773	30.5	UWG2	10.3	-19.295	6.0
JJB8	13.9	4.235	30.2	UWG2	10.4	-19.338	5.6
JJB8	14.9	4.184	30.3	UWG2	9.1	-19.178	5.7
JJB8	12.2	4.656	30.2	UWG2	11.8	-19.833	5.7
JJB8	12.5	3.966	30.2	UWG2	11.3	-19.289	5.6
JJB8	16.9	3.577	30.4	UWG2	14.6	-18.888	5.8
JJB8	15.9	3.824	30.5	UWG2	13.4	-18.41	6.5
JJB8	15.2	3.554	30.3	UWG2	15	-18.848	5.7
JJB8	15.5	5.202	30.2	UWG2	16.1	-20.029	5.6
JJB8	14.8	3.568	30.3	UWG2	15.4	-20.282	5.4
JJB8	14.5	3.603	30.3	UWG2	15.0	-19.494	5.8
JJB8	14.8	3.293	30.0	UWG2	11.4	-18.862	6.4
JJB8	14.1	3.583	30.3	UWG2	14.6	-19.521	5.7
JJB8	14.4	4.393	30.3	UWG2	11.2	-19.891	5.5
JJB8	16.7	3.938	30.2	UWG2	12.9	-19.507	5.7
JJB8	16.0	3.957	30.2	UWG2	14.2	-20.154	5.6
JJB8	16.6	3.727	29.3	UWG2	14.3	-19.794	5.8
JJB8	18.3	4.767	30.3	UWG2	11.5	-19.91	5.8
JJB8	15.0	4.291	30.2	UWG2	10.6	-19.79	5.6
JJB8	13.4	4.244	30.4	UWG2	13.0	-19.579	5.9
JJB8	14.8	4.773	30.5	UWG2	10.3	-19.295	6.0
JJB8	13.9	4.235	30.2	UWG2	10.4	-19.338	5.6
JJB8	14.9	4.184	30.3	UWG2	9.1	-19.178	5.7
JJB8	12.2	4.656	30.2	UWG2	11.8	-19.833	5.7
JJB8	12.5	3.966	30.2	UWG2	11.3	-19.289	5.6

Sample	Yield	RAW	δO^{18}_{smow}	Sample	Yield	RAW	δO^{18}_{smow}
GP147	13.7	-17.237	8.4	TOR1	16.1	-16.845	8.8
GP147	14.5	-18.164	7.5				

Appendix C LA-ICP-MS Data from Unit B and C Sulphides

		Southern Mound pyrite			Southern Mound pyrite			Rona Mound pyrite	
		050RD/P11			050RD/P13			057RD/P11	
		n = 20			n = 44			n = 33	
V	ppm	5.59	0.91		8.10	5.95		118.35	6.02
Cr	ppm	93.44	0.53		1087.58	7.50		171.77	2.43
Mn	ppm	10.97	5.53		13.72	6.10		4.62	1.30
Fe	wt%	-*	*-		-*	-*		-*	-*
Co	ppm	0.48	3.67		696.22	4.09		0.69	2.25
Ni	ppm	4.63	1.26		5.29	11.81		2.10	1.67
Cu	ppm	1606.64	8.73		15863.56	3.89		335.11	4.13
Zn	ppm	42.58	3.74		75.79	4.07		9475.39	5.71
Ga	ppm	0.18	1.86		2.54	2.53		29.48	6.49
Ge	ppm	1.19	0.85		15.82	6.90		0.77	0.70
As	ppm	68.98	3.08			-4.74		15.36	5.13
Se	ppm	0.82	6.56		484.16	3.04		1.59	6.80
Mo	ppm	5.84	3.32		69.04	6.12		19.75	3.14
Ag	ppm	10.03	1.71		2.27	4.69		84.92	4.63
Cd	ppm	-	-		-			-	-
In	ppm	-	-		-			-	-
Sn	ppm	0.13	0.66		8.69	7.93		0.34	2.85
Sb	ppm	2.59	3.06		1.97	4.04		4.93	2.91
Ba		-	-		-	-		-	-
Au	ppm	0.16	1.10		0.82	4.24		0.06	2.46
Hg	ppm	9.04	0.58		96.34	5.90		22.92	2.30
Tl	ppm	0.79	2.38		0.36	9.91		10.65	2.53
Pb	ppm	992.72	2.28		1845.52	7.23		296.67	1.72
Bi	ppm	0.01	2.28		1845.52	7.23		-	-
U	ppm	0.37	3.55		6.36	8.92		1.60	3.35

MIR Zone pyrite					Southern Mound sphalerite	
076RD/P7		076RD/P8			050RD/P11	
n = 14		n = 22			n = 7	
3.61	3.65	3.03	1.14		23.82	3.94
23.62	0.58	192.50	2.24		64.61	1.21
46.77	3.67	26.43	2.26		126.99	1.11
-*	-	*-	-		10.57	0.92
3.28	1.94	1.08	6.03		0.09	0.75
22.37	2.56	1.92	1.47		1.40	1.06
23672.09	2.95	3920.75	2.96		746.70	2.50
132.90	3.62	58.96	2.92		-*	-*
0.22	4.06		-8.75		258.09	2.13
1.99	1.89	23.69	8.10		5.41	1.24
303.05	1.94	375.71	2.09		1.64	4.63
2.78	3.88	1.09	6.43		1.40	3.42
10.47	2.52	1.42	1.67		0.94	3.49
27.32	2.80	7.61	2.30		82.11	2.20
-	-	-	-		928.67	2.74
-	-	-	-		4.62	3.11
0.12	1.32	0.20	2.15		0.14	1.15
13.08	1.47	5.96	5.95		0.47	1.46
-	-	-	-		0.69	3.69
0.52	2.71	0.40	5.40		0.24	1.62
10.73	1.95	12.25	2.38		36.97	1.04
11.63	4.10	0.05	3.22		1.15	5.15
1434.36	1.41	587.79	1.41		34.44	2.62
-	-	-	-		-	-
0.91	3.28	0.79	3.01		0.98	3.24

Rona Mound sphalerite			Southern Mound chalcopyrite	
057RD/P11			050RD/P13	
n = 8			n = 16	
9.58	2.83		0.88	1.07
68.60	0.08		121.16	0.47
48.63	0.24		1.66	0.59
6.55	0.32		28.90	0.64
0.06	0.93		2.42	3.67
0.81	0.65		1.53	2.54
50.36	1.69		-*	-*
-*	-*		44.15	4.67
235.66	1.52		1.50	0.58
0.62	0.31		1.17	0.75
-0.93	-1.36		-22.30	-1.46
0.98	1.76		27.41	1.50
0.02	2.12		2.27	3.39
49.13	0.91		0.59	2.44
1364.23	0.65		0.15	2.23
4.11	2.96		22.48	0.94
0.10	0.37		28.17	1.09
0.25	1.45		0.13	2.33
0.03	3.04		0.18	5.35
0.02	0.35		0.05	2.07
37.19	0.08		8.33	0.50
0.01	2.73		0.06	3.33
6.16	1.11		4.93	6.24
-	-		0.01	3.44
1.07	2.36		0.44	7.33

Appendix D Quantitative XRD data

SAMPLE	Unit	Goethite	Cristobalite	Tridymite	Opal-CT	Hematite
022RD/CC	B					40.8
031RD/109/CC	B					4.9
031RD/CC/007	B					4
050RD/P3	A	9.8			37.4	1.8
050RD/P5	A	24.4	14.5		14.5	0.7
050RD?P7	A	19.6	1.8	30.6	32.4	2.2
050RD?P8	A	12.5	34.1	53.4	87.5	
050RD?P11	C					0.8
050RD/P12	C					3.4
050RD/P13	C					3.7
057RD/P2	B		35.5	9.9	45.4	54.6
057RD/P3-8	B		43.1	23.2	66.3	6.2
057RD/P10	C		34.4	25.6	60	1.9
057RD/P11	C		35.2	23.3	58.5	2.3
073RD/P1	B					6.4
073RD/P6	B					3.1
073RD/P7	B					16.3
073RD/P9	B					11
073RD/P10	B					9
073RD/P12	B					2.1
073RD/P14	B					1.2
076RD/P2	B					31.5
076RD/P3	B					7.9
076RD/P4	B					6.1
076RD/P6	B					15.5
076RD/P7	B					8.6
076RD/P8	B					4.5

Quartz	Halite	Amorphous oxides	TOTAL	Error of fit	Goethite	Cristobalite	Tridymite
59.2			100				
95.1			100				
96			100				
20.8	0.7	29.5	100		0.2		
22.8	0.1	37.5	100		0.3		
0	0.5	45.3	100		0.29	0.12	0.37
			100		0.3	0.77	0.74
99.2			100				
93.9			100				
96.3			100				
			100			0.52	0.4
0.5	0	27	100			0.35	0.37
0.2		34.5	100			0.42	0.48
0.3		28.5	100			0.36	0.34
93.6			100				
96.9			100				
83.7			100				
72.7			100		0.27		
84			100		0.35		
87.4			100		0.33		
93.1			100		0.17		
68.5			100				
92.1			100				
93.9			100				
84.5			100				
91.4			100				
95.5			100				

Opal-CT	Hematite	Pyrite	Natrojarosite	Quartz	Halite	Amorphous oxides
	0.34			0.35		
	0.37			0.65		
	0.58			0.82		
0.3	0.1			0.2	0	0.9
0.9	0.1			0.2	0.1	
0.39	0.17			0	0.13	
1.07						
	0.2			0.7		
	0.23	0.25		0.53		
	0.31			0.55		
0.66	0.57					
0.51	0.15			0.11	0	
0.64	0.11	0.12		0.12		
0.50	0.12	0.13	0.22	0.13		
	0.26			0.45		
	0.54			0.73		
	0.44			0.52		
	0.23			0.3		
	0.28			0.58		
	0.15			0.34		
	0.38			0.37		
	0.57			0.81		
	0.68			0.84		
	0.39			0.52		
	0.6			0.7		
	0.54			0.67		

Appendix EOxygen stable isotopes of haematite

An attempt was made to calculate iron oxide oxygen isotope values ($\delta^{18}O_{HAEMATITE}$) and formation temperatures based upon analysis of both bulk powder ($\delta^{18}O_{BULK}$) and leached silica ($\delta^{18}O_{SIL}$). The haematite $\delta^{18}O$ is calculable from the bulk $\delta^{18}O$, and silica leach $\delta^{18}O$, based on the assumption that the only contributors to the bulk $\delta^{18}O$ are haematite and silica, and knowing the ratio of iron oxide to silica within the bulk samples based on XRF data.

Molar concentrations of oxygen contributions from SiO_2 and Fe_2O_3 were calculated using the atomic masses of oxygen, silicon, and iron as 15.999, 28.0855 and 55.845 respectively. Ratios of silica and iron oxide contributions to each sample is based upon XRF data of SiO_2 and Fe_2O_{3T}. Once the percentage contribution of both silica and iron oxide is obtained, the fraction of $\delta^{18}O$ for the iron oxide material can be back calculated from the bulk $\delta^{18}O$ and the silica leached material $\delta^{18}O$.

Table 94: Difference between $\delta^{18}O_{SIL}$ and $\delta^{18}O_{BULK}$ of all Si-Fe cap samples

	n	$\delta^{18}O_{SIL}$	n	$\delta^{18}O_{BULK}$	Difference between SIL and bulk
050RD/P3	5	26.1	4	21.6	-4.5
050RD/P5	1	25.9	-	-	
050RD/P7	3	27.3	3	19.4	-7.9
050RD/P8	1	27.4	-	-	
022RD/CC	1	18.2	2	12.4	-5.8
031RD/CC/007	1	19.0	1	17.8	-1.2
031RD/109/CC	1	19.2	1	17.1	-2.1
050RD/P11	1	18.9	2	17.0	-1.9
050RD/P12	1	14.8	3	13.0	-1.8
050RD/P13	3	17.7	1	15.5	-2.2
057RD/P2	1	18.4	2	18.7	0.3
057RD/P3-8	3	16.6	3	15.1	-1.6
057RD/P10	1	20.9	2	17.6	-3.3
057RD/P11	1	19.1	1	17.9	-1.2
073RD/P1	1	20.1	1	20.8	0.7
073RD/P6	1	21.2	1	20.1	-1.1
073RD/P7	1	20.1	1	13.6	-6.5
073RD/P9	1	20.3	1	15.4	-4.9
073RD/P10	1	20.3	1	15.4	-4.9
073RD/P12	1	21.0	1	17.6	-3.4

073RD/P14	3	20.3	1	17.2	-3.1
076RD/P2	3	20.4	1	17.9	-2.5
076RD/P3	1	20.1	1	16.5	-3.6
076RD/P4	1	19.9	1	20.1	0.2
076RD/P6	1	20.3	1	14.4	-5.9
076RD/P7	1	20.4	1	16.0	-4.4
076RD/P8	1	19.1	3	14.3	-4.8

Typically, bulk values of the samples returned lower of $\delta^{18}O$ values than the silica leaches, with only three samples recording bulk values higher than the leached material.

Initial calculations were conducted upon samples which only consist of haematite and quartz, both non-hydrous and not containing hydroxyl groups (i.e. no goethite or opal-CT) as described in the Methodology section.

Table 95: Calculated $\delta^{18}O_{HAEMATEITE}$ of Si-Fe cap samples across all three mounds that only contain haematite and quartz

Sample Code	**Mound**	**Unit**	**Calculated $\delta^{18}O_{HAEMATITE}$**
031RD/109/CC	Southern	B	-55.1
031RD/CC/007	Southern	B	-33.2
050RD/P11	Southern	C	-400.4
050RD/P12	Southern	C	-74.9
050RD/P13	Southern	C	-86.0
073RD/P1	MIR	B	38.9
073RD/P6	MIR	B	-40.8
073RD/P7	MIR	B	-45.5
076RD/P2	MIR	B	8.3
076RD/P3	MIR	B	-57.9
076RD/P4	MIR	B	25.6
076RD/P6	MIR	B	-42.6
076RD/P7	MIR	B	-66.9
076RD/P8	MIR	B	-166.2

Calculated values of $\delta^{18}O_{HAEMATITE}$ ranged from -400.4 to + 38.9. The $\delta^{18}O$ geothermometer for haematite was calibrated for formation temperatures between ~0 and 210˚C where $\delta^{18}O_{HAEMATITE}$ values ranged from -14.2 to -6.6 $\delta^{18}O_{HAEMATITE}$ (Yapp, 1990). Therefore it was thought that the wide range of calculated values of $\delta^{18}O_{HAEMATITE}$ of the iron oxide fraction were not considered representative of the true formation temperatures of the Si-Fe cap. Further calculations of goethite or opal-CT containing samples were not considered further due to this wide variation of $\delta^{18}O_{HAEMATITE}$ values.

Bibliography

Adachi, M., Yamamoto, K. and Sugisaki, R. (1986) 'Hydrothermal chert and associated siliceous rocks from the Northern Pacific: Their geological significance as indication of ocean ridge activity', *Sedimentary Geology*, 47, pp. 125–148.

Adamides, N. G. (1984) *Cyprus Volcanogenic Sulphide Deposits in Relation to their Environment of Formation*.

Adamides, N. G. (2010a) 'Mafic-dominated volcanogenic sulphide deposits in the Troodos ophiolite, Cyprus Part 1 – The deposits of the Solea graben', *Applied Earth Science*, 119(2), pp. 65–77.

Adamides, N. G. (2010b) 'Mafic-dominated volcanogenic sulphide deposits in the Troodos ophiolite, Cyprus Part 2 – A review of genetic models and guides for exploration', *Applied Earth Science*, 119(4), pp. 193–204.

Adamides, N. G. (2013) 'South Mathiatis: An unusual volcanogenic sulphide deposit in the Troodos ophiolite of Cyprus', *Applied Earth Science*, 122(4), pp. 194–206.

Alt, J. C. (1988a) 'Hydrothermal oxide and nontronite deposits on seamounts in the Eastern Pacific', *Marine Geology*, 81, pp. 227–239.

Alt, J. C. (1988b) 'The chemistry and sulfur isotope composition of massive sulfide and associated deposits on Green Seamount, eastern Pacific', *Economic Geology*, 83(5), pp. 1026–1033.

Alt, J. C., Lonsdale, P., Haymon, R. and Muehlenbachs, K. (1987) 'Hydrothermal sulfide and oxide deposits on seamounts near 21°N, East Pacific Rise', *Geological Society of America Bulletin*, 98, pp. 157–168.

Ames, D. E., Franklin, J. M. and Hannington, M. D. (1993) 'Mineralogy and geochemistry of active and inactive chimneys and massive sulfide, Middle Valley, northern Juan de Fuca Ridge; an evolving hydrothermal', *The Canadian Mineralogist*, 31(42592), pp. 997–1024.

Andrew, R. L. (1984) 'The geochemistry of selected base-metal gossans, southern Africa', *Journal of Geochemical Exploration*, 22, pp. 161–192.

Antivachis, D. N. (2015) 'The geology of the northern part of the Apliki Cyprus-type ore deposit', *Bulletin of the Geological Society of Greece*, 49, pp. 4–28.

Arai, Y. (2010) 'X-ray Absorption Spectroscopic Investigation of Molybdenum Multinuclear Sorption Mechanism at the Goethite - Water Interface', *Environmental Science & Technology*, 44, pp. 8491–

8496.

Avizo (2016) *Avizo 3D Software User's Guide. FEI*.

Ayupova, N. R. and Maslennikov, V. V. (2013) 'Biomorphic textures in the ferruginous-siliceous rocks of massive sulfide-bearing paleohydrothermal fields in the urals', *Lithology and Mineral Resources*, 48(5), pp. 438–455.

Ayupova, N. R., Maslennikov, V. V., Tessalina, S. G., Shilovsky, O. P., Sadykov, S. A., Hollis, S. P., Danyushevsky, L. V., Safina, N. P. and Statsenko, E. O. (2017) 'Tube fossils from gossanites of the Urals VHMS deposits, Russia: Authigenic mineral assemblages and trace element distributions', *Ore Geology Reviews*, 85, pp. 107–130.

Ayupova, N. R., Melekestseva, I. Y., Maslennikov, V. V., Tseluyko, A. S., Blinov, I. A. and Beltenev, V. E. (2018) 'Uranium accumulation in modern and ancient Fe-oxide sediments: Examples from the Ashadze-2 hydrothermal sulfide field (Mid-Atlantic Ridge) and Yubileynoe massive sulfide deposit (South Urals, Russia)', *Sedimentary Geology*. Elsevier B.V, 367, pp. 164–174.

Baker, E. T., German, C. R. and Elderfield, H. (1995) 'Hydrothermal Plumes Over Spreading-Centre Axes: Global Distributions and Geological Inferences', *Seafloor Hydrothermal Systems: Physical, Chemical, Biological, and Geological Interactions*, (47–71).

Baker, E. T., Massoth, G. J., Walker, S. L. and Embley, R. W. (1993) 'A method for quantitatively estimating diffuse and discrete hydrothermal discharge 1', *Earth and Planetary Science Letters*, 118, pp. 235–249.

Barrie, C. D., Boyce, A. J., Boyle, A. P., Williams, P. J., Blake, K., Wilkinson, J. J., Lowther, M., McDermott, P. and Prior, D. R. (2009) 'On the growth of colloform textures: a case study of sphalerite from the Galmoy ore body, Ireland', *Journal of the Geological Society*, 166(3), pp. 563–582.

Barriga, F. J. A. S. (1983) *Hydrothermal Metamorphism and ore genesis at Aljustrel, Portugal*.

Barriga, F. J. A. S. and Fyfe, W. S. (1988) 'Giant pyritic base-metal deposits: The example of Feitais (Aljustrel, Portugal)', *Chemical Geology*, 69(3–4), pp. 331–343.

Barriga, F. J. A. S. and Kerrich, R. (1984) 'Extreme 18O-enriched volcanics and 180-evolved marine water, Aljustrel, Iberian Pyrite Belt: transition from high to low Raylleigh number convective regimes', *Geochimica et Cosmochimica Acta*, 48(2), pp. 1021–1031.

Bastrakov, E. N., Jaireth, S. and Mernagh, T. P. (2010) *Solubility of uranium in hydrothermal fluids*

at 25 ° to 300 ° C Implications for the formation of uranium deposits Solubility of uranium in hydrothermal fluids at 25 ° to 300 ° C : Implications for the formation of uranium deposits.

Bau, M. (1999) 'Scavenging of dissolved yttrium and rare earths by precipitating iron oxyhydroxide :Experimental evidence for Ce oxidation , Y-Ho fractionation , and lanthanide tetrad effect', *Geochemica et Cosmochimica Acta*, 63(1), pp. 67–77.

Beaulieu, S. E., Baker, E. T. and German, C. R. (2015) 'Where are the undiscovered hydrothermal vents on oceanic spreading ridges?', *Deep-Sea Research Part II*. Elsevier, 121, pp. 202–212.

Becker, K., Herzen, R. Von, Kirklin, J., Evans, R., Kadko, D., Kinoshita, M., Matsubayashi, O., Mills, R., Schultz, A. and Rona, P. (1996) 'Conductive heat flow at the TAG active hydrothermal mound : Results from 1993-1995 submersible surveys', *Geophysical Research Letters*, 23(23), pp. 3463–3466.

Bekker, A., Slack, J. F., Planavsky, N., Krape??, B., Hofmann, A., Konhauser, K. O. and Rouxel, O. J. (2010) 'Iron formation: The sedimentary product of a complex interplay among mantle, tectonic, oceanic, and biospheric processes', *Economic Geology*, 105(3), pp. 467–508.

Bennett, S. A., Achterberg, E. P., Connelly, D. P., Statham, P. J., Fones, G. R. and German, C. R. (2008) 'The distribution and stabilisation of dissolved Fe in deep-sea hydrothermal plumes', *Earth and Planetary Science Letters*, 270, pp. 157–167.

Binns, R. A. and Scott, S. D. (1993) 'Actively forming polymetallic sulfide deposits associated with felsic volcanic rocks in the eastern manus back-arc basin, Papua New Guinea', *Economic Geology*, 88(8), pp. 2226–2236.

Binns, R. A., Scott, S. D., Bogdanov, Y. A., Lisitzin, A. P., Gordeev, V. V., Gurvich, E. G., Finlayson, E. J., Boyd, T., Dotter, L. E., Wheller, G. E. and Muravyev, K. G. (1993) 'Hydrothermal oxide and gold-rich sulfate deposits of Franklin seamount, western woodlark basin, Papua New Guinea', *Economic Geology*, 88(8), pp. 2122–2153.

Blount, C. W. and Dickson, F. W. (1969) 'The solubility of anhydrite (CaSO ,) in NaCI-I & O from 100 to 450 ° C and 1 to 1000 bars', *Geochimica et Cosmochimica Acta*, 33, pp. 227–245.

Bogdanov, Y. A., Lein, A. Y., Maslennikov, V. V., Li, S. and Ul'yanov, A. A. (2008) 'Mineralogical-Geochemical Features of Sulfide Ores from the Broken Spur Hydrothermal Vent Field', *Oceanology*, 48(5), pp. 679–700.

Bogdanov, Y. A., Vikent'ev, I. V., Lein, A. Y., Bogdanova, O. Y., Sagalevich, A. M. and Sivtsov, A. V. (2008) 'Low-temperature hydrothermal deposits in the rift zone of the Mid-Atlantic Ridge', *Geology*

of Ore Deposits, 50(2), pp. 119–134.

Boyd, T. D. and Scott, S. D. (2001) 'Microbial and hydrothermal aspects of ferric oxyhydroxides and ferrosic hydroxides : the example of Franklin Seamount , Western Woodlark Basin , Papua New Guinea', *Geochemical Transactions*, 7.

Boyle, J. . (1984) 'The Origin and Geochemistry of the Metalliferous Sediments of the Troodos Massif, Cyprus', (June), p. 383.

Brusnitsyn, A. I. and Zhukov, I. G. (2018) 'Geochemistry and Formation Model of Manganiferous Rocks in Jaspers of the South Urals', 53(1), pp. 14–35. doi: 10.1134/S0024490218010030.

Burdige, D. J. (1993) 'The biogeochemistry of manganese and iron reduction in marine sediments', *Earth Science Reviews*, 35, pp. 249–284.

Callow, B., Falcon-Suarez, I., Ahmed, S. and Matter, J. (2018) 'Assessing the carbon sequestration potential of basalt using X-ray micro-CT and rock mechanics', *International Journal of Greenhouse Gas Control*. Elsevier, 70(December 2017), pp. 146–156.

Calvo, G., Mudd, G., Valero, A. and Valero, A. (2016) 'Decreasing Ore Grades in Global Metallic Mining : A Theoretical Issue or a Global Reality ?', *Resources*, 5(36), pp. 1–14.

Carrol, S., Mroczek, E., Alai, M. and Ebert, M. (1998) 'Amorphous silica precipitation (60 to 120°C): Comparison of laboratory and field rates', *Geochimica et Cosmochimica Acta*, 62(8), pp. 1379–1396.

Cathles, L. M. (1983) 'An Analysis of the Hydrothermal System Responsible for Massive Sulfide Deposition in the Hokuroku Basin of Japan', *Economic Geology Monograph 5*, pp. 439–487.

Cave, R. R., German, C. R., Thomson, J. and Nesbitt, R. W. (2002) 'Fluxes to sediments underlying the Rainbow hydrothermal plume at 36 14'N on the Mid-Atlantic Ridge', *Geochimica et Cosmochimica Acta*, 66(11), pp. 1905–1923.

Chopard, B., Herrmann, H. J. and Vicsek, T. (1991) 'Structure and growth mechanism of mineral dendrites', *Letters to nature*, 353, pp. 409–412.

Constantinou, G. (1972) *The Geology and Genesis of the Sulphide Ores of Cyprus*.

Constantinou, G. and Govett, G. J. . (1973) 'Geology, Geochemistry, and Genesis of Cyprus Sulfide Deposits', *Economic Geology*, 68, pp. 843–858.

Coogan, L. A., Seyfried, W. E. and Pester, N. J. (2019) 'Environmental controls on mid-ocean ridge hydrothermal fluxes', *Chemical Geology*. Elsevier, 528(April), p. 119285.

Cope, I. L., Wilkinson, J. J., Boyce, A. J., Chapman, J. B., Herrington, R. J. and Harris, C. J. (2010) 'Genesis of the pic de fon iron oxide deposit, Simandou Range, Republic of Guinea, West Africa', *SEG Reviews*, 15, pp. 19–21.

Corliss, J. B., Dymond, J., Gor, L. I., Edmond, J. M., Herzen, R. P. Von, Bal, R. D., Green, K., Williams, D., Bainbri, A., Crane, K. and Lndel, T. H. V. A. (1979) 'Submarine Thermal Springs on the Galapagos Rift', *Science*, 203(4385), pp. 1073–1084.

Davidson, G. J., Stolz, A. J. and Eggins, S. M. (2001) 'Geochemical anatomy of silica iron exhalites: Evidence for hydrothermal oxyanion cycling in response to vent fluid redox and thermal evolution (Mt. Windsor subprovince, Australia)', *Economic Geology*, 96(5), pp. 1201–1226.

Dekov, V. M., Lalonde, S. V., Kamenov, G. D., Bayon, G., Shanks, W. C., Fortin, D., Fouquet, Y. and Moscati, R. J. (2015) 'Geochemistry and mineralogy of a silica chimney from an inactive seafloor hydrothermal field (East Pacific Rise, 18°S)', *Chemical Geology*, 415, pp. 126–140.

Dekov, V. M., Petersen, S., Garbe-Schönberg, C. D., Kamenov, G. D., Perner, M., Kuzmann, E. and Schmidt, M. (2010) 'Fe-Si-oxyhydroxide deposits at a slow-spreading centre with thickened oceanic crust: The Lilliput hydrothermal field (9°33'S, Mid-Atlantic Ridge)', *Chemical Geology*, 278(3–4), pp. 186–200.

Dilek, Y., Thy, P., Moores, E. M. and Ramsden, T. W. (1990) 'Tectonic evolution of the Troodos Ophiolite within the Tethyan Framework', *Tectonics*, 9(4), pp. 811–823.

Douville, E., Pienvenu, P., Charlou, J.L., Donval, J.P., Fouquet, Y., Appriou, P., Gamo, T. (1999) 'Yttrium and rare earth elements in fluids from various deep-sea hydrothermal systems', *Geochimica et Cosmochimica Acta*, 63(5), pp. 627-643.

Douville, E., Charlou, J. L., Oelkers, E. H., Bienvenu, P., Jove Colon, C. F., Donval, J. P., Fouquet, Y., Prieur, D. and Appriou, P. (2002) 'The rainbow vent fluids (36°14'N, MAR): The influence of ultramafic rocks and phase separation on trace metal content in Mid-Atlantic Ridge hydrothermal fluids', *Chemical Geology*, 184(1–2), pp. 37–48.

Doyle, M. G. and Allen, R. L. (2003) 'Subsea-floor replacement in volcanic-hosted massive sulfide deposits', *Ore Geology Reviews*, 23(3–4), pp. 183–222.

Dutrieux, A. M. (2019) *Rise and fall of a hydrothermal system: A tale of the metalliferous sediments (TAG hydrothermal field, MAR, 26°N)*.

Eastoe, C. J. and Gustin, M. M. (1996) 'Volcanogenic massive sulfide deposits and anoxia in the Phanerozoic oceans', *Ore Geology Reviews*, 10(3–6), pp. 179–197.

Eastoe, C. J., Güstin, M. M. and Nelson, S. E. (1987) 'Problems of recognition of olistostromes: An example from the lower Pit Formation, Eastern Klamath Mountains, California', *Geology*, (1), pp. 1–4.

Elder, J. W. (1965) 'Physical Processes in Geothermal Areas', in *Terrestrial Heat Flow*, p. 276.

Elderfield, H., Mills, R. A. and Rudnicki, M. D. (1993) 'Geochemical and thermal fluxes, high-temperature venting and diffuse flow from mid-ocean ridge hydrothermal systems: the TAG hydrothermal field, Mid-Atlantic Ridge 26˚N', in *Magmatic Processes and Plate Tectonics, Geological Society Special Publication*, pp. 295–307.

Elderfield, H. and Schultz, a. (1996) 'Mid-Ocean Ridge Hydrothermal Fluxes and the Chemical Composition of the Ocean', *Annual Review of Earth and Planetary Sciences*, 24(1), pp. 191–224.

Eldridge, C. S., Barton Jr., P. B. and Ohmoto, H. (1983) 'Mineral Textures and Their Bearing on Formation of the Kuroko Orebodies', *Economic Geology Monograph 5*, pp. 241–281.

Emerson, D. and Moyer, C. L. (2002a) 'Neutrophilic Fe-Oxidising Bacteria Are Abundant at the Lohi Seamount Hydrothermal Vents and Play a Major Role in Fe Oxide Deposition', *Applied and Environnmental Microbiology*, 68(6), pp. 3085–3093.

Emerson, D. and Moyer, C. L. (2002b) 'Neutrophilic Fe-Oxidizing Bacteria Are Abundunt at the Loihi Seamount Hydrothermal Vents and Play a Major Role in Fe Oxide Deposition', *Applied and Environmental Microbiology*, 68(6), pp. 3085–3093.

Emerson, D. and Revsbech, N. P. (1994) 'Investigation of an Iron-Oxidizing Microbial Mat Community Located near Aarhus , Denmark: Field Studies', *Applied and Environmental Microbiology*, 60(11), pp. 4022–4031.

Evensen, N. M., Hamilton, P. J. and O'Nions, R. K. (1978) 'Rare-earth abundances in chondritic meteorites', *Geochemica et Cosmochimica Acta*, 42, pp. 1199–1212.

F., T., Gonzalez Clavijo, E. and Spire, B. (1998) 'The Filon Norte orebody (Tharsis, Iberian Pyrite Belt): a proximal low-temperature shale-hosted massive sulphide in a thin-skinned tectonic belt', *Mineralium Deposita*, 33, pp. 150–169.

Fallon, E. K., Niehorster, E., Brooker, R. A. and Scott, T. B. (2018) 'Experimental leaching of massive sulphide from TAG active hydrothermal mound and implications for seafloor mining', *Marine Pollution Bulletin*. Elsevier, 126(September 2017), pp. 501–515.

Fallon, E. K., Petersen, S., Brooker, R. A. and Scott, T. B. (2017) 'Oxidative dissolution of

hydrothermal mixed-sulphide ore: An assessment of current knowledge in relation to seafloor massive sulphide mining', *Ore Geology Reviews*. Elsevier B.V., 86, pp. 309–337.

Fike, D. D., Grotzinger, J. P., Pratt, L. M. and Summons, R. E. (2006) 'Oxidation of the Ediacaran Ocean', *Letters to Nature*, 444(December), pp. 4–7.

Fisher, A. T. (1998) 'Permeability within basaltic oceanic crust', *Reviews of Geophysics*, 63(2), pp. 143–182.

Florke, O. W., Graetsch, H. and Jones, J. B. (1990) 'Hydrothermal deposition of cristobalite', *Neues Jahrbuch für Mineralogie - Abhandlungen*, pp. 81–95.

Fontaine, F. J., Wilcock, W. S. D., Foustoukos, D. E. and Butterfield, D. A. (2009) 'A Si-Cl geothermobarometer for the reaction zone of high-temperature, basaltic-hosted mid-ocean ridge hydrothermal systems', *Geochemistry, Geophysics, Geosystems*, 10(5), pp. 1–9.

Fortin, D. and Langley, S. (2005) 'Formation and occurrence of biogenic iron-rich minerals', *Earth-Science Reviews*, 72, pp. 1–19.

Fouquet, Y., Henry, K., Knott, R. and Cambon, P. (2000) 'Geochemical Section of the Tag Hydrothermal Mound', *Proceedings of the Ocean Drilling Program*, 158, pp. 363–38.

Fouquet, Y., Zierenberg, R. and Miller, D. J. (1998) 'Chapter 3: Middle Valley: Bent Hill Area (Site 1035)', *Proceedings of the Ocean Drilling Program, Initial Reports*, 169, pp. 35–152.

Franklin, J. M., Gibson, H. L., Jonasson, I. R. and Galley, A. G. (2005) 'Volcanogenic Massive Sulfide Deposits', *Economic Geology 100th Anniversary Volume*, 111, pp. 523–560.

Frew, R. D., Dennis, P. F., Heywood, K. J., Meredith, M. P. and Boswell, S. M. (2000) 'The oxygen isotope composition of water masses in the northern North Atlantic', *Deep-Sea Research I*, 47, pp. 2265–2286.

Frondel, C. (1982) 'Structural hydroxyl in chalcedony (type B quartz).', *American Mineralogist*, 67(11–12), pp. 1248–1257.

Gablina, I. F., Semkova, T. a., Stepanova, T. V. and Gor'kova, N. V. (2006) 'Diagenetic alterations of copper sulfides in modern ore-bearing sediments of the Logatchev-1 hydrothermal field (Mid-Atlantic Ridge 14°45' N)', *Lithology and Mineral Resources*, 41(1), pp. 27–44.

Galley, A., Hannington, M. D. and Jonasson, I. R. (2007) 'Volcanogenic massive sulphide deposits', *Mineral Deposits of Canada: A Synthesis of Major Deposit-Types, District Metallogeny, the Evolution of Geological Provinces, and Exploration Methods: Geological Association of Canada, Mineral*

Deposits Division, Special Publication 5, pp. 141–161.

García Ruiz, J. M., Carnerup, A., Christy, A. G., Welham, N. J. and Hyde, S. T. (2002) 'Morphology: an ambiguous indicator of biogenicity.', *Astrobiology*, 2(3), pp. 353–69.

Gass, I. G. (1968) 'Is the Troodos Massif of Cyprus a Fragment of Mesozoic Ocean Floor?', *Nature*, 220, pp. 39–42.

George, L. L., Cook, N. J. and Ciobanu, C. L. (2016) 'Partitioning of trace elements in co-crystallized sphalerite-galena-chalcopyrite hydrothermal ores', *Ore Geology Reviews*. Elsevier B.V., 77, pp. 97–116.

George, L. L., Cook, N. J., Crowe, B. B. P. and Ciobanu, C. L. (2018) 'Trace elements in hydrothermal chalcopyrite', *Mineralogical Magazine*, 82(1), pp. 59–88.

German, C.R., Elderfield, H., (1990) 'Application of the Ce anomaly as a palaeoredox indicator: the ground rules', *Palaeoceanography*, 5(5), pp. 823-833

German, C. R., Campbell, A. C. and Edmond, J. M. (1991) 'Hydrothermal scavenging at the Mid-Atlantic Ridge : Modification of trace element dissolved fluxes', *Earth and Planetary Science Letters*, 107, pp. 101–114.

German, C. R., Petersen, S. and Hannington, M. D. (2016) 'Hydrothermal exploration of mid-ocean ridges: Where might the largest sulfide deposits be forming?', *Chemical Geology*. Elsevier B.V., 420, pp. 114–126.

Giambalvo, E. R., Fisher, A. T., Martin, J. T., Darty, L. and Lowell, R. P. (2000) 'Origin of elevated sediment permeability in a hydrothermal seepage zone, eastern flank of teh Juan de Fuca Ridge, and implications for transport of fluid and heat', *Journal of Geophysical Research*, 105, pp. 913–928.

Van Gosen, B. S., Verplanck, P. L., Seal II, R. R., Long, K. R. and Gambogi, J. (2017) 'Rare-Earth Elements', in *Critical Mineral Resoruces of the United States - Economic and Environmental Geology and Prospects for Future Supply*, p. 31.

Gourcerol, B., Thurston, P. C., Kontak, D. J., Côté-Mantha, O. and Biczok, J. (2016) 'Depositional setting of Algoma-type banded iron formation', *Precambrian Research*. Elsevier B.V., 281, pp. 47–79.

Grant, H. L. J., Hannington, M. D., Petersen, S., Frische, M., Fuchs, S. H. and Helmholtz, G. (2018) 'Constraints on the behavior of trace elements in the actively-forming TAG deposit , Mid-Atlantic

Ridge , based on LA-ICP-MS analyses of pyrite', *Chemical Geology*. Elsevier, 498(June), pp. 45–71.

Grenne, T. and Slack, J. F. (2003a) 'Bedded jaspers of the Ordovician Løkken ophiolite, Norway: Seafloor deposition and diagenetic maturation of hydrothermal plume-derived silica-iron gels', *Mineralium Deposita*, 38(5), pp. 625–639.

Grenne, T. and Slack, J. F. (2003b) 'Paleozoic and Mesozoic silica-rich seawater: Evidence from hematitic chert (jasper) deposits', *Geology*, 31(4), pp. 319–322.

Grenne, T. and Slack, J. F. (2005) 'Geochemistry of jasper beds from the Ordovician Løkken ophiolite, Norway: Origin of proximal and distal siliceous exhalites', *Economic Geology*, 100(8), pp. 1511–1527.

Grenne, T. and Slack, J. F. (2018) 'Mineralogy and geochemistry of silicate , sulfide , and oxide iron formations in Norway : evidence for fluctuating redox states of early Paleozoic marine basins'. Mineralium Deposita, (7491).

Groves, D. I., Vielreicherm, R. M., Goldfarb, R. J. and Condie, K. C. (2005) 'Controls on the heterogeneous distribution of mineral deposits through time', *Mineral Deposits and Earth Evolution, Geological Society, London, Special Publications*, 248, pp. 71–101.

Gunnarsson, I. and Arnorsson, S. (2000) 'Amorphous silica solubility and the thermodynamic properties of H 4 SiO ° 4 in the range', *Geochemica et Cosmochemica Acta*, 64(13), pp. 2295–2307.

Gurvich, E. G. (2005) *Metalliferous Sediments of the World Ocean*.

Haas, J. R., Shock, E. L. and Sassani, D. C. (1995) 'Rare earth elements in hydrothermal systems : Estimates of standard partial molal thermodynamic properties of aqueous complexes of the rare earth elements at high pressures and temperatures', *Geochemica et Cosmochimica Acta*, 59(21), pp. 4329–4350.

Halbach, M., Halbach, P. and Lüders, V. (2002) 'Sulfide-impregnated and pure silica precipitates of hydrothermal origin from the Central Indian Ocean', *Chemical Geology*, 182(2–4), pp. 357–375.

Hall, J. M. and Yang, J.-S. (1994) 'A preferred environment of preservation for volcanic massive sulphide deposits in the Troodos Ophiolite (Cyprus)', *Economic Geology*, 89, pp. 851–857.

Hannington, M. D. (1993) 'The formation of atacamite during weathering of sulfides on the modern sea-floor', *Canadian Mineralogist*, 31(44492), pp. 945–956.

Hannington, M. D., Galley, A. G., Herzig, P. M. and Petersen, S. (1998) 'Comparison of the TAG Mound and stockwork complex with Cyrpus-type massive sulfide deposits', *Proceedings of the*

Ocean Drilling Programm, Scientific Results, 158, pp. 389–415.

Hannington, M. D., Jamieson, J., Monecke, T. and Petersen, S. (2010) 'Modern Sea-Floor Massive Sulfides and Base Metal Resources: Toward an Estimate of Global Sea-Floor Massive Sulfide Potential', *Society of Economic Geologists Special Publication 15*, pp. 317–338.

Hannington, M. D., Jamieson, J., Monecke, T., Petersen, S. and Beaulieu, S. (2011) 'The abundance of seafloor massive sulfide deposits', *Geology*, 39(12), pp. 1155–1158.

Hannington, M. D., Jamieson, J., Petersen, S. and Zentrum, H. (2015) 'Seafloor Massive Sulfide Deposits: Continuing Efforts Toward a Global Estimate of Seafloor Massive Sulfides', *OCEANS 2015 - Genova*. IEEE, pp. 1–3.

Hannington, M. D., de Ronde, C. E. J. and Petersen, S. (2005) 'Sea-Floor Tectonics and Submarine Hydrothermal Systems', *Economic Geology*, 100th Anni, pp. 111–141.

Hannington, M. D., Tivey, M. K., Larocque, A. C. L., Petersen, S. and Rona, P. A. (1995) 'The Occurance of Gold in Sulfide Deposits of the TAG Hydrothermal Field, Mid-Atlantic Ridge', *The Canadian Mineralogist*, 33, pp. 1285–1310.

Hein, J. R., Clauge, D. A., Koski, R. A., Embley, R. W. and Dunham, R. E. (2008) 'Metalliferous Sediment and a Silica-Hematite Deposit within the Blanco Fracture Zone, Northeast Pacific', *Marine Georesources And Geotechnology*, 26(4), pp. 317–339.

Hein, J. R., Koski, R. A., Embley, R. W., Reid, J. and Chang, S.-W. (1999) 'Diffuse-flow hydrothermal field in an oceanic fracture zone setting, Northeast Pacific: Deposit composition', *Exploration and Mining Geology*, 8(3–4), pp. 299–322.

Hekinian, R., Hoffert, M., Lamarqué, P., Cheminée, J. L., Stoffers, P. and Bideau, D. (1993) 'Hydrothermal Fe and Si Oxyhydroxide Deposits from South Pacific Intraplate Volcanoes and East Pacific Rise Axial and Off-Axial Regions', *Economic Geology*, 88, pp. 2099–2121.

Herrington, R. J., Maslennikov, V. V., Zaykov, V., Seravkin, I., Kosarev, A., Buschmann, B., Orgeval, J. J., Holland, N., Tesalina, S., Nimis, P. and Armstrong, R. (2005) 'Classification of VMS deposits: Lessons from the South Uralides', *Ore Geology Reviews*, 27(1–4), pp. 203–237.

Herzig, P. M., Hannington, M. D., Scott, S. D., Maliotis, G., Rona, P. A. and Thompson, G. (1991) 'Gold-rich sea-floor gossans in the troodos ophiolite and on the mid-Atlantic ridge', *Economic Geology*, 86(8), pp. 1747–1755.

Herzig, P. M., Petersen, S. and Hannington, M. D. (1998) 'Geochemistry and Sulfur-Isotopic

Composition of the TAG Hydrothermal Mound, Mid-Atlantic Ridge, 26°N', *Proceedings of the Ocean Drilling Program, Scientific Results*, 158, pp. 47–70.

Hollis, S. P., Cooper, M. R., Herrington, R. J., Roberts, S., Earls, G., Verbeeten, A., Piercey, S. J. and Archibald, S. M. (2015) 'Distribution, mineralogy and geochemistry of silica-iron exhalites and related rocks from the Tyrone Igneous Complex: Implications for VMS mineralization in Northern Ireland', *Journal of Geochemical Exploration*. Elsevier B.V., 159, pp. 148–168.

Hopkinson, L., Roberts, S., Herrington, R. J. and Wilkinson, J. (1998) 'Self-organization of submarine hydrothermal siliceous deposits: evidence from the TAG hydrothermal mound, 26??N Mid-Atlantic Ridge', *Geology*, 26(4), pp. 347–350.

Hopkinson, L., Roberts, S., Herrington, R. J. and Wilkinson, J. (1999) 'The nature of crystalline silica from the TAG submarine hydrothermal mound, 26°N Mid Atlantic Ridge', *Contributions to Mineralogy and Petrology*, 137(4), pp. 342–350.

Humphris, S. E., Herzig, P. M. and Miller, D. J. (1996) '158', in *ODP, Init. Repts, 158: College Station, TX (Ocean Drilling Program)*.

Humphris, S. E., Herzig, P. M., Miller, D. J., Alt, J. C., Becker, K., Brown, D., Brugmann, G., Chiba, H., Fouquet, Y., Gemmell, J. B., Guerin, G., Hannington, M. D., Holm, N. G., Honnorez, J. J., Iturrino, G. J., Knott, R., Ludwig, R., Nakamura, K., Petersen, S., Reysenbach, a L., Rona, P. A., Smith, S., Sturz, a a, Tivey, M. K. and Zhao, X. (1995) 'The internal structure of an active sea-floor massive sulfide deposit', *Nature*, pp. 713–716.

Humphris, S. E. and Kleinrock, C. (1996) 'Detailed morphology of the TAG active hydrothermal mound: Insights into its formation and growth', *Geophysical Monograph Series*, 23(23), pp. 3443–3446.

Humphris, S. E. and Tivey, M. A. M. K. (2015) 'The Trans-Atlantic Geotraverse hydrothermal field: A hydrothermal system on an active detachment fault', *Deep Sea Research Part II: Topical Studies in Oceanography*. Elsevier, pp. 1–9.

Humphris, S. E. and Tivey, M. K. (2000) 'A synthesis of geological and geochemical investigations of the TAG hydrothermal field: Insights into fluid-flow and mixing processes in a hydrothermal system', *Geological Society of America Special Papers*, 349, pp. 213–235.

Iijima, A. (1972) 'Argillaceous and Zeolitic Alteration Zones Surrounding Kuroko (Black Ore) Deposits in Odate District of Akita Prefecture', *Mine Geology*, 22(161), pp. 1–20.

Iizasa, K., Kawasaki, K., Maeda, K., Matsumoto, T., Saito, N. and Hirai, K. (1998) 'Hydrothermal

sulfide-bearing Fe-Si oxyhydroxide deposits from the Coriolis Troughs, Vanuatu backarc, southwestern Pacific', *Marine Geology*, 145(1–2), pp. 1–21. doi: 10.1016/S0025-3227(97)00112-6.

Isley, A. E. and Abbott, D. H. (1999) 'Plume-related mafic volcanism and the deposition of banded iron formation', *Journal of Geophysical Research: Solid Earth*, 104(B7), pp. 15461–15477.

James, R. H. and Elderfield, H. (1996) 'Chemistry of ore forming fluids and mineral formation rates in an active hydrothermal sulfide deposit on the Mid-Atlantic Ridge', *Geology*, 24(12), pp. 1147–1150.

Jamieson, J. W., Hannington, M. D., Tivey, M. K., Hansteen, T., Williamson, N. M. B., Stewart, M., Fietzke, J., Butterfield, D., Frische, M., Allen, L., Cousens, B. and Langer, J. (2016) 'Precipitation and growth of barite within hydrothermal vent deposits from the Endeavour Segment, Juan de Fuca Ridge', *Geochimica et Cosmochimica Acta*, 173, pp. 64–85.

Jenner, G. A. (1996) 'Trace element geochemistry of igneous rocks: geochemical nomenclature and analytical geochemistry', in *Trace element geochemisry of volcanic rocks: applications for massive sulfide exploration. Geological Assocaition of Canada, Short Course Notes*, pp. 51–77.

Jones, J. B. and Segnit, E. R. (1971) 'The nature of opal I . nomenclature and constituent phases', *Journal of the Geological Society of Australia*, 18(1), pp. 57–68.

Jones, S. (2001) *Geology and Geochemistry of the 'Caprocks' above VHMS Deposits and Myra Falls, Vancouver Island, British Columbia*.

Jones, S., Gemmell, J. B. and Davidson, G. J. (2006) 'Petrographic, geochemical, and fluid inclusion evidence for the origin of siliceous cap rocks above volcanic-hosted massive sulfide deposits at Myra Falls, Vancouver Island, British Columbia, Canada', *Economic Geology*, 101(3), pp. 555–584.

Kalogeropoulos, S. I. and Scott, S. D. (1983) 'Mineralogy and Geochemistry of Tuffaceous Exhalites (Tetsusekiei) of the Fukazawa Mine Hokuroku', *Economic Geology Monograph 5*, pp. 412–432.

Karl, D. M., Brittain, A. M. and Tilbrook, B. D. (1989) 'Hydrothermal and microbial processes at Loihi Seamount, a mid-plate hot-spot volcano', *Deep-Sea Research*, 36(11), pp. 1655–1673.

Keith, M., Haase, K. M., Klemd, R., Schwarz-Schampera, U., Franke, H., Krumm, S. and Strauss, H. (2016) 'Systematic variations of trace element and sulfur isotope compositions in pyrite with stratigraphic depth in the Skouriotissa volcanic-hosted massive sulfide deposit, Troodos ophiolite, Cyprus', *Chemical Geology*. Elsevier B.V., 423, pp. 7–18.

Keith, M., Haase, K. M., Schwarz-Schampera, U., Klemd, R., Petersen, S. and Bach, W. (2014) 'Effects

of temperature, sulfur, and oxygen fugacity on the composition of sphalerite from submarine hydrothermal vents', *Geology*, 42(8), pp. 699–702.

Keith, M., Häckel, F., Haase, K. M., Schwarz-Schampera, U. and Klemd, R. (2016) 'Trace element systematics of pyrite from submarine hydrothermal vents', *Ore Geology Reviews*, 72, pp. 728–745.

Ketcham, R. A. and Carlson, W. D. (2001) 'Acquisition, optimization and interpretation of X-ray computed tomographic imagery : applications to the geosciences', *Computers & Geosciences*, 27, pp. 381–400.

Kita, I., Taguchi, S. and Matsubaya, O. (1985) 'Oxygen isotope fractionation between amorphous silica and water at 34–93°C', *Nature*, 314(6006), pp. 83–84.

Klein, C. (2005) 'Some Precambrian banded iron-formations (BIFs) from around the world: Their age, geologic setting, mineralogy, metamorphism, geochemistry, and origin', *American Mineralogist*, 90(10), pp. 1473–1499.

Klinkhammer, G., Elderfield, H., Edmond, J.M., Mitra, A. (1994), 'Geochemical implications of rare earth element patterns in hydrothermal fluids from mid-ocean ridges', *Geochimica et Cosmochimica Acta*, 58 (23), pp. 5105-5113.

Knight, R. D., Roberts, S. and Cooper, M. J. (2018) 'Investigating monomineralic and polymineralic reactions during the oxidation of sulphide minerals in seawater: Implications for mining seafloor massive sulphide deposits', *Applied Geochemistry*. Elsevier, 90(August 2017), pp. 63–74.

Knott, R., Fouquet, Y., Honnorez, J., Petersen, S. and Bohn, M. (1998) 'Petrology of hydrothermal mineralization: A vertical section through the TAG mound', *Proceedings of the Ocean Drilling Program*, 158, pp. 5–26.

Krasnov, S. G., Cherkashev, G. a., Stepanova, T. V., Batuyev, B. N., Krotov, a. G., Malin, B. V., Maslov, M. N., Markov, V. F., Poroshina, I. M., Samovarov, M. S., Ashadze, a. M., Lazareva, L. I. and Ermolayev, I. K. (1995) 'Detailed geological studies of hydrothermal fields in the North Atlantic', *Hydrothermal Vents and Processes*, 87(87), pp. 43–64.

Krauskopf, K. B. (1956) 'Dissolution and precipitation of silica at low temperatures', *Geochemica et Cosmochemica Acta*, 10, pp. 1–26.

Kumita, K., Hashimoto, H., Yamada, T. and Sasaki, A. (1982) 'Formation and preservation of the Kuroko ore deposits, Shakanai mine: Some geologic constraints on the problem', *Mining Geology*, 32(3), pp. 225–242.

Lalou, C., Münch, U., Halbach, P. and Reyss, J. L. (1998) 'Radiochronological investigation of hydrothermal deposits from the MESO zone, Central Indian Ridge', *Marine Geology*, 149(1–4), pp. 243–254.

Lalou, C., Reyss, J. L., Brichet, E., Rona, P. A. and Thompson, G. (1995) 'Hydrothermal activity on a 10(5)-year scale at a slow spreading ridge, TAG hydrothermal field, mid-atlantic ridge 26°N', *Journal Of Geophysical Research - Solid Earth*, 100(B9), pp. 17855–17862.

Lehrmann, B., Stobbs, I. J., Lusty, P. A. J. and Murton, B. J. (2018) 'Insights into Extinct Seafloor Massive Sulfide Mounds at the TAG, Mid-Atlantic Ridge', *Minerals*, 8(302), pp. 1–17.

Leistel, J. M., Marcoux, E. and Deschamps, Y. (1997) 'Chert in the Iberian Pyrite Belt', *Mineralium Deposita*, 33(1–2), pp. 59–81.

Li, J., Peng, X., Zhou, H., Li, J. and Sun, Z. (2013) 'Molecular evidence for microorganisms participating in Fe, Mn, and S biogeochemical cycling in two low-temperature hydrothermal fields at the Southwest Indian Ridge', 118, pp. 665–679.

Lilley, M. D., Feely, R. A. and Trefry, J. H. (1995) 'Chemical and Biochemical Transformations in Hydrothermal Plumes', *Geophysical Monograph Series*, 91, pp. 369–391.

Lisitsyn, A. P., Bogdanov, Y. A., Zonenshayn, L. P., Kuz'min, M. I. and Sagalevich, A. M. (1989) 'HYDROTHERMAL PHENOMENA IN THE MID-ATLANTIC RIDGE AT LAT. 26°N (TAG HYDROTHERMAL FIELD)', *International Geology Review*. Taylor & Francis, 31(12), pp. 1183–1198.

Little, C. T. S., Glynn, S. E. J. and Mills, R. a. (2004) 'Four-Hundred-and-Ninety-Million-Year Record of Bacteriogenic Iron Oxide Precipitation at Sea-Floor Hydrothermal Vents', *Geomicrobiology Journal*, 21(September), pp. 415–429.

Liu, H., Pourret, O., Guo, H. and Bonhoure, J. (2017) 'Rare earth elements sorption to iron oxyhydroxide : Model development and application to groundwater', *Applied Geochemistry*. Elsevier, 87, pp. 158–166.

Lough, A. J. M., Homoky, W. B., Connelly, D. P., Comer-Warner, S. A., Nakamura, K., Abyaneh, M. K., Kaulich, B. and Mills, R. A. (2019) 'Soluble iron conservation and colloidal iron dynamics in a hydrothermal', *Chemical Geology*. Elsevier, 511(January), pp. 225–237.

Lydon, J. W. (1984) 'Volcanogenic Massive Sulphide Deposits Part 1: A Descriptive Model', *Geoscience Canada*, 11(4), pp. 195–202.

Lynne, B. Y. and Campbell, K. A. (2003) 'Diagenetic transformations (opal-A to quartz) of low- and

mid-temperature microbial textures in siliceous hot-spring deposits , Taupo Volcanic Zone , New Zealand 1', 1696, pp. 1679–1696.

Mackenzie, F. T. and Gees, R. (1971) 'Quartz : Synthesis at Earth-Surface Conditions', *Science*, 173(534–535), pp. 10–13.

Markl, G., Blanckenburg, F. Von and Wagner, T. (2006) 'Iron isotope fractionation during hydrothermal ore deposition and alteration', *Geochimica et Cosmochimica Acta*, 70, pp. 3011–3030.

Maslennikov, V. V., Ayupova, N. R., Herrington, R. J., Danyushevsky, L. V. and Large, R. R. (2012) 'Ferruginous and manganiferous haloes around massive sulphide deposits of the Urals', *Ore Geology Reviews*. Elsevier B.V., 47, pp. 5–41.

Massoth, G. J., Baker, E. T., Lupton, J. E., Feely, R. A., Butterfield, D. A., Von Damm, K. L., Roe, K. K. and Lebon, G. T. (1994) 'Temporal and spatial variability of hydrothermal manganese and iron at Cleft segment , Juan de Fuca Ridge', *Journal of Geophysical Research*, 99, pp. 4905–4923.

Matos, J. X., Pereira, Z., Rosa, C. J. P., Rosa, D. R. N., Oliveira, J. T. and Relvas, J. M. R. S. (2011) 'Late Strunian age: a key time frame for VMS deposit exploration in the Iberian', *SGA Biennial Meeting*, pp. 2–5.

Metz, S., Trefry, J. H. and Nelsen, T. A. (1988) 'History and geochemistry of a metalliferous sediment core from the Mid-Atlantic Ridge at 26°N', *Geochimica et Cosmochimica Acta*, 52(10), pp. 2369–2378.

Michard, A., Michard, G., Stüben, D., Stoffers, P., Cheminée, J. L. and Binard, N. (1993) 'Submarine thermal springs associated with young volcanoes: The Teahitia vents, Society Islands, Pacific Ocean', *Geochimica et Cosmochimica Acta*, 57(21–22), pp. 4977–4986.

Mills, R. a. and Elderfield, H. (1995) 'Rare earth element geochemistry of hydrothermal deposits from the active TAG Mound, 26°N Mid-Atlantic Ridge', *Geochimica et Cosmochimica Acta*, 59(17), pp. 3511–3524.

Mills, R. A., Thomson, J., Elderfield, H., Hinton, R. W. and Hyslop, E. (1994) 'Uranium enrichment in metalliferous sediments from the Mid-Atlantic Ridge', *Earth and Planetary Science Letters*, 124, pp. 35–47.

Mitra, A., Elderfield, H., Greaves, M.J. (1994) 'Rare earth elements in submarine hydrothemral fluids and plumes from the Mid-Atlantic Ridge', *Marine Chemistry*, 46 (3), pp. 217-235.

Moores, E. F., Robinson, P. T., Malpas, J. and Xenophonotos, C. (1984) 'Model for the origin of the Troodos massif, Cyprus, and other mideast ophiolites.', *Geology*, 12(8), pp. 500–503.

Murton, B. J., Lehrmann, B., Dutrieux, A. M., Martins, S., Gil, A., Iglesia, D., Stobbs, I. J., Barriga, F. J. A. S., Bialas, J., Dannowski, A., Vardy, M. E., North, L. J., Yeo, I. A. L. M., Lusty, P. A. J. and Petersen, S. (2019) 'Geological fate of seafloor massive sulphides at the TAG hydrothermal field (Mid-Atlantic Ridge)', *Ore Geology Reviews*. Elsevier, 107(October 2018), pp. 903–925.

Ohmoto, H., Mizukami, M., Drummond, S. E., Eldridge, C. S., Pisutha-Arnond, V. and Lenagh, T. C. (1983) 'Chemical Processes of Kuroko Formation', *Economic Geology Monograph 5*, pp. 570–604.

Ohmoto, H. and Skinner, B. J. (1983) *The Kuroko and Related Volcanogenic Massive Sulfide Deposits*.

Oliveira, J. T., Rosa, C. J. P., Pereira, Z., Rosa, D. R. N., Matos, J. X., Inverno, C. M. C. and Andersen, T. (2013) 'Geology of the Rosário – Neves Corvo antiform , Iberian Pyrite Belt , Portugal : new insights from physical volcanology , palynostratigraphy and isotope geochronology studies', *Mineralium Deposita*, (39), pp. 749–766.

Ortoleva, P., Merino, E., Moore, C. and Chadam, J. (1987) 'Geochemical self-organization I: Reaction-transport feedbacks and modellign approach', *American Journal of Science*, 287, pp. 979–1007.

Oudin, E. and Constantinou, G. (1984) 'Black smoker chimney fragments in Cyprus sulphide deposits', *Nature*, 310(30 August 1984), pp. 349–353.

Pantazis, T. M. and Govett, G. J. S. (1973) 'Interpretation of a detailed rock geochemical survey around mathiati mine, Cyprus', *Journal of Geochemical Exploration*, 2(1), pp. 25–36.

Parker, C. M., Von Damm, K. L., Beers, K. A., Green, D. R., Alker, B. J. and German, C. R. (2005) 'Time Series Fluid Compositions from the TAG Hydrothemral Mound, MAR: 1986-2004', in *American Geophysical Union, Fall Meeting*, p. 1.

Paytan, A., Mearon, S., Cobb, K. and Kastner, M. (2002) 'Origin of marine barite deposits : Sr and S isotope characterization', *Geology*, 30(8), pp. 747–750.

Peacock, C. L. and Sherman, D. M. (2004) 'Vanadium (V) adsorption onto goethite (α-FeOOH) at pH 1.5 to 12: A surface complexation model based on ab initio molecular geometries and EXAFS spectroscopy', *Geochemica et Cosmochimica Acta*, 68(8), pp. 1723–1733.

Petersen, S. (2000) *The Geochemical and Mineralogical Evolution of the TAG Hydrothermal Field, Mid-Atlantic Ridge, 26°N*.

Petersen, S., Hannington, M. D., Hölz, S., Krätschell, A., Klischies, M., Graber, S., Anderson, M. O., Jamieson, J. W., Grant, H. L. J. and Murton, B. J. (2019) 'Same , same , but different : recent advances in our understanding of modern seafloor hydrothermal systems', *SGA Biennial Meeting*, 1, pp. 80–82.

Petersen, S., Herzig, P. M. and Hannington, M. D. (2000) 'Third dimension of a presently forming VMS deposit: TAG hydrothermal mound, Mid-Atlantic Ridge, 26°N', *Mineralium Deposita*, 35, pp. 233–259.

Petersen, S., Krätschell, A., Augustin, N., Jamieson, J., Hein, J. R. and Hannington, M. D. (2016) 'News from the seabed – Geological characteristics and resource potential of deep-sea mineral resources', *Marine Policy*. Elsevier, 70(June), pp. 175–187.

Popoola, S. O., Han, X., Wang, Y. and Qiu, Z. (2019) 'Geochemical Investigations of Fe-Si-Mn Oxyhydroxides Deposits in Wocan Hydrothermal Field on the Slow-Spreading Carlsberg Ridge , Indian', *Minerals*, 9(1), pp. 1–17.

Popoola, S. O., Han, X., Wang, Y., Qiu, Z., Ye, Y. and Cai, Y. (2019) 'Mineralogical and Geochemical Signatures of Metalliferous Sediments in Wocan-1 and Wocan-2 Hydrothermal Sites on the Carlsberg Ridge, Indian Ocean', *Minerals*, 9(26), pp. 1–19.

Posth, N. R., Konhauser, K. O. and Kappler, A. (2011) 'Banded Iron Formations', in *Encyclopedia of Geobiology*, pp. 92–103.

Raiswell, R. (2006) 'Towards a global highly reactive iron cycle', *Journal of Geochemical Exploration*, 88, pp. 436–439.

Regelous, M., Haase, K. M., Freund, S., Keith, M., Weinzierl, C. G., Beier, C., Brandl, P. A., Endres, T. and Schmidt, H. (2014) 'Formation of the Troodos Ophiolite at a triple junction: Evidence from trace elements in volcanic glass', *Chemical Geology*. Elsevier B.V., 386, pp. 66–79.

Richards, H. G. and Boyle, J. . (1986) 'Origin, alteration and mineralization of inter-lava metalliferous sediments of the Troodos ophiolite, Cyprus', *Metallogeny of Basic and Ultrabasic Rocks. London Inst. Min. Metall*, pp. 21–31.

Roedder, E. (1968) 'The Noncolloidal Origin of " Colloform " Textures in Sphalerite Ores', *Economic Geology*, 63(1950), pp. 451–471.

Rona, P. A., Bogdanov, Y. A., Gurvich, E. G., Rimski-Korsakov, N. a, Sagalevitch, A. M., Hannington, M. D. and Thompson, G. (1993) 'Relict hydrothermal zones in the TAG Hydrothermal Field, Mid-Atlantic Ridge 26°N, 45°W', *Journal of Geophysical Research: Solid Earth*, 98(B6), pp. 9715–9730.

Rona, P. A., Hannington, M. D., Raman, C. V., Thompson, G., Tivey, M. K., Humphris, S. E., Lalou, C. and Petersen, S. (1993) 'Active and relict sea-floor hydrothermal mineralization at the TAG hydrothermal field, Mid-Atlantic Ridge', *Economic Geology*, 88(8), pp. 1989–2017.

Saez, R., Almodovar, G. R. and Pascual, E. (1996) 'Geological constraints on massive sulphide genesis in the Iberian Pyrite Belt', *Ore Geology Reviews*, 11, pp. 429–451.

Sander, S. G. and Koschinsky, A. (2011) 'Metal flux from hydrothermal vents increased by organic complexation', *Nature Geoscience*. Nature Publishing Group, 4(February), pp. 145–150.

Schultz, A., Dickson, P. and Elderfield, H. (1996) 'Temporal variations in diffuse hydrothermal flow at TAG', *Geophysical Research Letters*, 23(23), pp. 3471–3474.

Schwertmann, U. (1983) 'Effect of pH on the Formation of Goethite and Hematite from Ferrihydrite', *Clays and Clay Minerals*, 31(4), pp. 277–284.

Schwertmann, U., Friedl, J. and Stanjek, H. (1999) 'From Fe (III) Ions to Ferrihydrite and then to Hematite', *Journal of Colloid and Interface Science*, 209, pp. 215–223.

Scott, J. J., Breier, J. A., Iii, G. W. L. and Emerson, D. (2015) 'Microbial Iron Mats at the Mid-Atlantic Ridge and Evidence that Zetaproteobacteria May Be Restricted to Iron-Oxidizing Marine Systems', *PLOS ONE*, pp. 1–19.

Scott, R. ., Rona, P. A., McGregor, B. A. and Scott, M. . (1974) 'The TAG hydrothermal field', *Nature*, 248, pp. 81–82.

Scott, S. D. (1983) 'Basalt and Sedimentary Hosted Seafloor Polymetallic Sulfide Deposits and their Ancient Analogues', pp. 818–824.

Shanks III, W. C., Böhlke, J. K. and Seal II, R. R. (1995) 'Stable isotopes in mid-ocean ridge hydrothermal systems: interactions between fluids, minerals, and organisms', *Seafloor hydrothermal systems: Physical, chemical, biological, and geochemical interactions*, 91(Table 2), pp. 194–221. doi: 10.1029/GM091p0194.

Sharp, Z. D. (1990) 'A laser-based microanalytical method for the in situ determination of oxygen isotope ratios of silicates and oxides', *Geochimica et Cosmochimica Acta*, 54(5), pp. 1353–1357.

Sharp, Z. D., Gibbons, J. A., Maltsev, O., Atudorei, V., Pack, A., Sengupta, S., Shock, E. L. and Knauth, L. P. (2016) 'A calibration of the triple oxygen isotope fractionation in the SiO2-H2O system and applications to natural samples', *Geochimica et Cosmochimica Acta*. Elsevier Ltd, 186, pp. 105–119.

Singer, D. A. (2014) 'Base and precious metal resources in seafloor massive sulfide deposits', *Ore*

Geology Reviews, 59, pp. 66–72.

Slack, J. F. and Grenne, T. (2018) 'Early Ordovician anoxia and biological extinction linked to a large seafloor-hydrothermal system at Lokken, Norway', in *Goldschmidt Abstract*.

Snelgrove, A. H. and Forster, C. B. (1996) 'Impact of seafloor sediment permability and thickness on off-axis hydrothermal circulation: Juan de Fuca Ridge eastern flank', *Journal of Geophysical Research*, 101, pp. 2915–2925.

Spry, P. G., Peter, J. M. and Slack, J. F. (2000) 'Meta-Exhalites as exploration guides to ore', *Metamorphosed and metamorphic ore deposits*, p. v.11, 163-201 pp.

Sruoga, P., Rubinstein, N. and Hinterwimmer, G. (2004) 'Porosity and permeability in volcanic rocks : a case study on the Seria Tobifera, South Patagonia, Argentina', *Journal of Volcanology and Geothermal Research*, 132, pp. 31–43.

Stein, A. and Stein, S. (1994) 'Constraints on hydrothermal heat flux through the oceanic lithosphere from global heat flow', *Journal of Geophysical Research*, 99, pp. 3081–3095.

Stepanova, T. V., Krasnov, S. G. and Cherkashev, G. A. (1996) 'Mineralogy, chemical composition and structure of the MIR Mound, TAG Hydrothermal Field', *Geophysical Research Letters*, 23(23), pp. 3515–3518.

Stockdale, A., Davison, W., Zhang, H. and Hamilton-taylor, J. (2010) 'The Association of Cobalt with Iron and Manganese (Oxyhydr) oxides in Marine Sediment', *Aquatic Geochemistry*, 16, pp. 575–585.

Sun, Z., HuaiYang, Z., Yang, Q., Yin, X., Wang, H., Yao, H. and Dong, C. (2012) 'Growth model of a hydrothermal low-temperature Si-rich chimney :Example from the CDE hydrothermal field, Lau Basin', 55(10), pp. 1716–1730.

Sun, Z., Li, J., Huang, W., Dong, H., Little, C. T. S. and Li, J. (2015) 'Generation of hydrothermal Fe-Si oxyhydroxide deposit on the Southwest Indian Ridge and its implication for the origin of ancient banded iron formations', *Journal of Geophysical Research G: Biogeosciences*, 120(1), pp. 187–203.

Sun, Z., Zhou, H., Glasby, G. P., Yang, Q., Yin, X., Li, J. and Chen, Z. (2012) 'Formation of Fe – Mn – Si oxide and nontronite deposits in hydrothermal fields on the Valu Fa Ridge, Lau Basin', *Journal of Asian Earth Sciences*. Elsevier Ltd, 43(1), pp. 64–76.

Sverjensky, D. A. (1984) 'Europium redox equilibria in aqueous solution', *Earth and Planetary Science Letters*, 67, pp. 70–78.

Swanner, E. D., Planavsky, N. J., Lalonde, S. V, Robbins, L. J., Bekker, A., Rouxel, O. J., Saito, M. A., Kappler, A., Mojzsis, J. and Konhauser, K. O. (2014) 'Cobalt and marine redox evolution', *Earth and Planetary Science Letters*. Elsevier B.V., 390, pp. 253–263.

Tivey, M. A., Rona, P. A. and Kleinrock, M. C. (1996) 'Reduced crustal magnetization beneath relict hydrothermal mounds: TAG hydrothermal field, Mid-Atlantic ridge, 26 degrees N', *Geophysical Research Letters*, 23(23), pp. 3511–3514.

Tivey, M. K., Humphris, S. E., Thompson, G., Hannington, M. D. and Rona, P. A. (1995) 'Deducing patterns of fluid flow and mixing within the TAG active hydrothermal mound using mineralogical and geochemical data', *Journal of Geophysical Research*, 100(B7), p. 12527.

Tsutsumi, M. and Ohmoto, H. (1983) 'A Preliminary Oxygen Isotope Study of Tetsusekiei Ores Associated with the Kuroko Deposits in the Hokuroku District, Japan', *Economic Geology Monograph 5*, pp. 433–438.

USGS (2012) 'Volcanogenic Massive Sulfide Occurrence Model'.

Varga, R. J. and Moores, E. M. (1985) 'Spreading structure of the Troodos ophiolite, Cyprus.', *Geology*, 13(12), pp. 846–850.

Velasco, F., Herrero, J. M., Suárez, S., Yusta, I., Alvaro, A. and Tornos, F. (2013) 'Supergene features and evolution of gossans capping massive sulphide deposits in the Iberian Pyrite Belt', *Ore Geology Reviews*. Elsevier B.V., 53, pp. 181–203. doi: 10.1016/j.oregeorev.2013.01.008.

Waite, T. D., Davis, J. A., Payne, T. E., Waychunas, G. A. and Xu, N. (1994) 'Uranium(VI) adsorption to ferrihydrite: Application of a surface complexation', *Geochimica et Cosmochimica Acta*, 58(24), pp. 5465–5478.

Wersin, P., Jr, M. F. H., Persson, P. E. R., Redden, G., Leckie, J., Harris, D. W. and Stanford, G. (1994) 'Interaction between aqueous uranium (VI) and sulfide minerals : Spectroscopic evidence for sorption and reduction', *Geochimica et Cosmochimica Acta*, 58(13), pp. 2829–2843.

White, S. N., Humphris, S. E. and Kleinrock, M. C. (1998) 'New observations on the distribution of past and present hydrothermal activity in the TAG area of the mid-Atlantic ridge (26 degrees 08 ' N)', *Marine Geophysical Research*, 20(1), pp. 41–56.

William, J., Hannington, M. D., Tivey, M. K., Hansteen, T., Williamson, N. M., Stewart, M., Fietzke, J., Butterfield, D., Frische, M., Allen, L., Cousens, B. and Langer, J. (2016) 'Precipitation and growth of barite within hydrothermal vent deposits from the Endeavour Segment , Juan de Fuca Ridge', *Geochimica et Cosmochimica Acta*. Elsevier Ltd, 173, pp. 64–85.

Williams, L. A. and Crerar, D. A. (1985) 'Silica Diagenesis, II. General Mechanisms', *Journal of Sedimentary Petrology*, 55(3), pp. 312–321.

Williams, L. A., Parks, G. A. G. A. and Crerar, D. A. D. A. (1985) 'Silica Diagenesis, I. Solubility Controls', *Journal of Sedimentary Petrology*, 55(3), pp. 301–311.

Wolery, T. J. and Sleep, N. H. (1976) 'Hydrothermal Circulation and Geochemical Flux at Mid-Ocean Ridges', *The Journal of Geology*, 84(3), pp. 249–275.

Worrall, F. and Pearson, D. G. (2001) 'Water-rock interaction in an acidic mine discharge as indicated by rare earth element patterns', *Geochimica et Cosmochimica Acta*, 65(18), pp. 3027–3040.

Yang, B., Zeng, Z., Qi, H., Wang, X., Ma, Y. and Rong, K. (2015) 'Constraints on biotic and abiotic role in the formation of Fe-Si oxides from the PACMANUS hydrothermal field', *Ocean Science Journal*, 50(4), pp. 751–761.

Yapp, C. J. (1990) 'Oxygen isotopes in iron (III) oxides, 1. Mineral-water fractionation factors', *Chemical Geology*, 85, pp. 329–335.

You, C.-F. and Bickle, M. J. (1998) 'Evolution of an active sea-floor massive sulphide deposit', *Nature*, 394(6694), pp. 668–671.

Zarrouk, S. J., Woodhurst, B. C. and Morris, C. (2014) 'Geothermics Silica scaling in geothermal heat exchangers and its impact on pressure drop and performance : Wairakei binary plant , New Zealand', *Geothermics*. CNR-Istituto di Geoscienze e Georisorse, 51, pp. 445–459.

Zeng, Z. G., Wang, X. Y., Zhang, G. L., Yin, X. B., Chen, D. G. and Wang, X. M. (2008) 'Formation of Fe-oxyhydroxides from the East Pacific Rise near latitude 13°: Evidence from mineralogical and geochemical data', *Science in China, Series D: Earth Sciences*, 51(2), pp. 206–215.

Zeng, Z., Ouyang, H., Yin, X. . hua., Wang, X. and Wu, L. (2012) 'Formation of Fe–Si–Mn oxyhydroxides at the PACMANUS hydrothermal field, Eastern Manus Basin: Mineralogical and geochemical evidence', *Journal of Asian Earth Sciences*, 60, pp. 130–146.

Zepf, V., Reller, A., Rennie, C., Ashfield, M. and Simmons, J. (2014) *Material critical to the energy industry. An introduction*.

Zhong, R., Brugger, J., Chen, Y., Li, W. (2015) 'Contrasting regimes of Cu, Zn and Pb transport in ore-forming hydrothermal fluids', *Chemical Geology*, 395, pp. 154-164.

Zhu, Y. (2005) 'The preparation of nano-crystallized cristobalite under hydrothermal conditions',

Journal of Materials Science, 40, pp. 3829–3831.

Zierenberg, R. A., Fouquet, Y., Miller, D. J., Bahr, J. M., Baker, P. A., Bjerkgard, T., Brunner, C. A., Duckworth, R. C., Gable, R., Gieskes, J., Goodfellow, W. D., Groschel-Becker, H. ., Guerin, G., Ishibashi, J., Iturrine, G., James, R. H., Lackschewitz, K. S., Marquez, L. L., Nehlig, P., Peter, J. M., Rigsby, C. A., Schultheiss, P., Shanks III, W. C., Simoneit, B. R. T., Summit, M., Teagle, D. A. H., Urbat, M. and Zuffa, G. G. (1998) 'The deep structure of a sea-floor hydrothermal deposit', *Nature*, 392(April), pp. 485–488.

Zierenberg, R. A. and Miller, D. J. (2000) 'OVERVIEW OF OCEAN DRILLING PROGRAM LEG 169: SEDIMENTED RIDGES II', *Proceedings of the Ocean Drilling Program, Scientific Results*, 169(April), pp. 1–39.